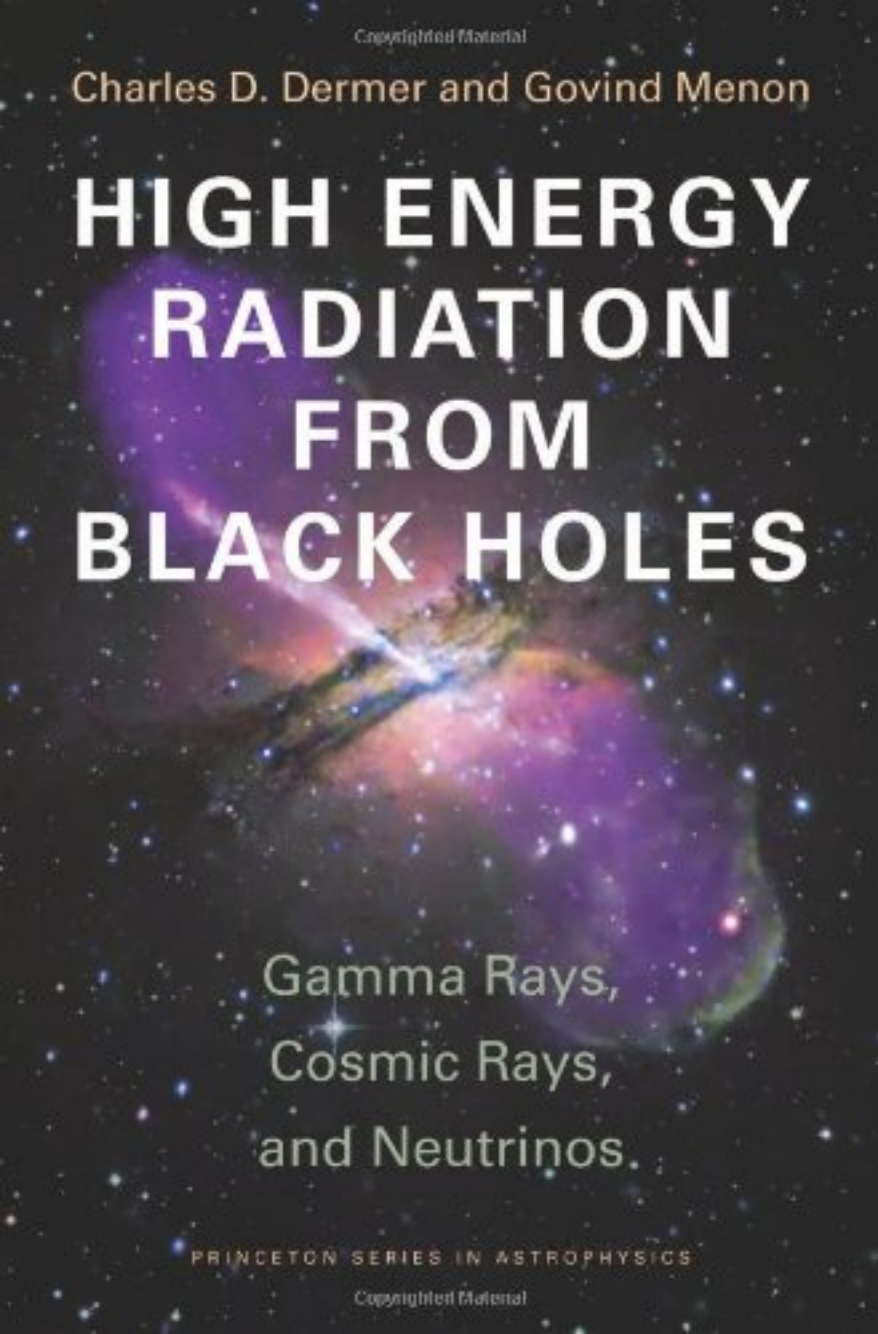


Copyrighted Material

Charles D. Dermer and Govind Menon

HIGH ENERGY RADIATION FROM BLACK HOLES



Gamma Rays,
Cosmic Rays,
and Neutrinos.

PRINCETON SERIES IN ASTROPHYSICS

Copyrighted Material

High Energy Radiation from Black Holes

Gamma Rays, Cosmic Rays, and Neutrinos

Charles D. Dermer

Govind Menon

PRINCETON UNIVERSITY PRESS
PRINCETON AND OXFORD

High Energy Radiation from Black Holes

PRINCETON SERIES IN ASTROPHYSICS

EDITED BY DAVID N. SPERGEL

Theory of Rotating Stars, *by Jean-Louis Tassoul*

Theory of Stellar Pulsation, *by John P. Cox*

Galactic Dynamics, Second Edition, *by James Binney and Scott Tremaine*

Dynamical Evolution of Globular Clusters, *by Lyman Spitzer, Jr.*

Supernovae and Nucleosynthesis: An Investigation of the History of Matter,
from the Big Bang to the Present, *by David Arnett*

Unsolved Problems in Astrophysics,
edited by John N. Bahcall and Jeremiah P. Ostriker

Galactic Astronomy, *by James Binney and Michael Merrifield*

Active Galactic Nuclei: From the Central Black Hole to the
Galactic Environment, *by Julian H. Krolik*

Plasma Physics for Astrophysics, *by Russell M. Kulsrud*

Electromagnetic Processes, *by Robert J. Gould*

Conversations on Electric and Magnetic Fields in the Cosmos,
by Eugene N. Parker

High-Energy Astrophysics, *by Fulvio Melia*

Stellar Spectral Classification,
by Richard O. Gray and Christopher J. Corbally

High Energy Radiation from Black Holes: Gamma Rays, Cosmic Rays,
and Neutrinos, *by Charles D. Dermer and Govind Menon*

High Energy Radiation from Black Holes

Gamma Rays, Cosmic Rays, and Neutrinos

Charles D. Dermer
Govind Menon

PRINCETON UNIVERSITY PRESS
PRINCETON AND OXFORD

Copyright 2009 © by Princeton University Press

Published by Princeton University Press, 41 William Street, Princeton, New Jersey 08540
In the United Kingdom: Princeton University Press, 6 Oxford Street, Woodstock,
Oxfordshire OX20 1TW

All Rights Reserved

ISBN: 978-0-691-13795-7

ISBN (pbk.): 978-0-691-14408-5

Library of Congress Control Number: 2009928093

British Library Cataloging-in-Publication Data is available

This book has been composed in Times

Printed on acid-free paper ∞

press.princeton.edu

Typeset by SR Nova Pvt Ltd, Bangalore, India

Printed in the United States of America

10 9 8 7 6 5 4 3 2 1

To Bea and Priya

This page intentionally left blank

“The black holes of nature are the most perfect macroscopic objects there are in the universe: the only elements in their construction are our concepts of space and time. And since the general theory of relativity provides only a single unique family of solutions for their descriptions, they are the simplest objects as well.”

Subrahmanyan Chandrasekhar, *The Mathematical Theory of Black Holes*

“Anyone who fights with monsters should take care that he does not in the process become a monster. And if you gaze for long into the abyss, the abyss gazes back into you.”

Friedrich Nietzsche, Aphorism 146, *Beyond Good and Evil*
(tr. M. Faber)

“angelheaded hipsters burning for the ancient heavenly connection to the starry dynamo in the machinery of night,”

Allen Ginsberg, *Howl*

This page intentionally left blank

Contents

Preface	xix
Chapter 1. Introduction	1
1.1 Black Holes in Nature	1
1.2 Energy Fluxes	8
1.3 Timing Studies and Black-Hole Mass Estimates	10
1.4 Flux Distribution	11
1.5 The Nighttime Sky	12
Chapter 2. Relativistic Kinematics	14
2.1 Lorentz Transformation Equations	14
2.2 Four-Vectors and Momentum	16
2.3 Relativistic Doppler Factor	18
2.4 Three Useful Invariants	19
2.5 Relativistic Reaction Rate	21
2.6 Secondary Production Spectra	23
Chapter 3. Introduction to Curved Spacetime	25
3.1 Special Relativity	25
3.2 Curved Space/Spacetime	29
3.3 The Schwarzschild Metric	33
Chapter 4. Physical Cosmology	36
4.1 Robertson-Walker Metric	36
4.2 Friedmann Models	39
4.2.1 Hubble Relation from the Cosmological Principle	39
4.2.2 Expansion of the Universe	40
4.2.3 Einstein–de Sitter Universe	43
4.2.4 Universe with Zero Cosmological Constant	43
4.2.5 Flat Universe	43
4.3 Luminosity and Angular-Diameter Distances	44
4.4 Event Rate of Bursting Sources	45
4.5 Flux and Intensity from Distributed Sources	47

Chapter 5. Radiation Physics of Relativistic Flows	50
5.1 Radiation Preliminaries	50
5.2 Invariant Quantities	53
5.3 Blackbody Radiation Field	53
5.4 Transformed Quantities	56
5.4.1 Transformation of Total Distribution and Energy	56
5.4.2 Transformation of Differential Distributions	56
5.5 Fluxes of Relativistic Cosmological Sources	59
5.5.1 Blob Geometry	60
5.5.2 Spherical Shell Geometry	63
5.5.3 Equivalence of Blob and Blast Wave Geometries	68
Chapter 6. Compton Scattering	70
6.1 Compton Effect	70
6.2 The Compton Cross Section	71
6.3 Transforming the Compton Cross Section	73
6.3.1 Differential Thomson Cross Section	75
6.3.2 Head-on Approximation	77
6.3.3 Differential Compton Cross Section	77
6.3.4 Moments of the Compton Cross Section	79
6.3.5 Compton Scattering in the δ -Function Approximation	80
6.4 Energy-Loss Rates in Compton Scattering	81
6.4.1 Thomson Energy-Loss Rate	81
6.4.2 Klein-Nishina Energy-Loss Rate	82
6.5 Differential Compton Cross Sections and Spectra	83
6.5.1 Comparison of Scattered Spectra for Different ERF Photon Energies	83
6.5.2 Spectral Comparisons for Isotropic Monochromatic Photons and Power-Law Electrons	84
6.6 Thomson Scattering: Isotropic Photons and Electrons	92
6.6.1 Thomson-Scattered Radiation Spectrum in the δ -Function Approximation	92
6.6.2 Spectral Comparisons for Isotropic Power-Law Photons and Electrons	93
6.7 External Photon Fields Compton-Scattered by Jet Electrons	94
6.7.1 Thomson-Scattered Spectrum for an External Point Source of Radiation from Behind	96
6.7.2 Thomson-Scattered Spectrum for External Isotropic Radiation in the δ -Function Approximation	97
6.7.3 External Isotropic Photons Compton-Scattered by Jet Electrons	99
6.7.4 Cosmic Microwave Background Radiation Compton-Scattered by Jet Electrons	103

6.8	Accretion-Disk Field Compton-Scattered by Jet Electrons	105
6.8.1	Optically Thick Shakura-Sunyaev Disk Spectrum	106
6.8.2	Integrated Emission Spectrum from Shakura-Sunyaev Disk	107
6.8.3	Transformed Accretion-Disk Radiation Field	108
6.8.4	Thomson-Scattered Shakura-Sunyaev Disk Spectrum in the Near Field	112
6.8.5	Thomson-Scattered Shakura-Sunyaev Disk Spectrum in the Far Field	113
6.8.6	Beaming Patterns	113
6.9	Broad-Line Region Scattered Radiation	114
Chapter 7. Synchrotron Radiation		117
7.1	Covariant Electrodynamics	118
7.2	Synchrotron Power and Peak Frequency	119
7.3	Elementary Synchrotron Radiation Formulae	121
7.3.1	Relations between Emitted, Received, and 90° Pitch-Angle Powers	123
7.3.2	Particle Synchrotron Radiation	126
7.3.3	Synchrotron Spectrum from a Power-Law Electron Distribution	127
7.4	δ -Function Approximation for Synchrotron Radiation	129
7.5	Equipartition Magnetic Field	131
7.5.1	Equipartition Magnetic Field: Qualitative Estimate	132
7.5.2	Equipartition Magnetic Field: Quantitative Treatment	133
7.6	Energetics and Minimum Jet Powers	135
7.7	Synchrotron Self-Compton Radiation	138
7.7.1	SSC in the Thomson Regime	138
7.7.2	SSC in the Thomson Regime for Broken Power-Law Electron Distribution	140
7.7.3	Accurate SSC for General Electron Distribution	141
7.7.4	Synchrotron/SSC Model	142
7.7.5	SSC Electron Energy-Loss Rate	143
7.8	Synchrotron Self-Absorption	143
7.8.1	Einstein Coefficients	145
7.8.2	Brightness Temperature and Self-Absorbed Flux: Qualitative Discussion	146
7.8.3	Derivation of the Synchrotron Self-Absorption Coefficient	148
7.8.4	δ -Function Approximation for Synchrotron Self-Absorption	148
7.8.5	Synchrotron Self-Absorption Coefficient for Power-Law Electrons	149

7.9	Maximum Brightness Temperature	150
7.10	Compton Limits on the Doppler Factor	153
7.11	Self-Absorbed Synchrotron Spectrum	154
7.12	Hyper-Relativistic Electrons	156
7.13	Jitter Radiation	158
Chapter 8.	Binary Particle Collision Processes	160
8.1	Coulomb Energy Losses	161
8.1.1	Stopping Power of Cold Plasma	161
8.1.2	Thermal Relaxation	163
8.1.3	Stopping Power of Thermal Plasma	164
8.1.4	Knock-On Electrons	165
8.2	Bremsstrahlung	166
8.2.1	Electron Bremsstrahlung Energy-Loss Rate	167
8.2.2	Electron Bremsstrahlung Production Spectra	167
8.3	Secondary Nuclear Production	169
8.3.1	γ Rays from π^0 Decay	171
8.3.2	Cross Section for $p + p \rightarrow \pi + X$ Production	172
8.4	Electron-Positron Annihilation Radiation	180
8.4.1	Annihilation in a Thermal Medium	181
8.4.2	Thermal Annihilation Line and Continuum Spectra	182
8.5	Nuclear γ -Ray Line Production	185
Chapter 9.	Photohadronic Processes	187
9.1	Scattering and Energy-Loss Timescales	189
9.2	Photopion Process	190
9.2.1	Photopion Cross Section	191
9.2.2	Analytic Expression for Photopion Cross Section	192
9.2.3	Numerical Calculation of Photopion Cross Section	194
9.2.4	Photopion Energy-Loss Rate	194
9.2.5	GZK Energy	196
9.2.6	Stochastic and Continuous Energy Losses	197
9.3	Photopair Process	197
9.3.1	Photopair Cross Section	198
9.3.2	Photopair Energy-Loss Timescale	198
9.3.3	Accurate Expression for Photopair Energy-Loss Rates of Ions in an Isotropic Radiation Field	201
9.3.4	Relative Importance of Photopion and Photopair Losses	203
9.4	Expansion Losses	203
9.5	Cosmogenic Neutrino Flux	204
9.6	Ultrahigh-Energy Cosmic-Ray Evolution	208
9.6.1	Normalization to Local Luminosity Density	209
9.6.2	Energy Evolution of Cosmic-Ray Protons	210
9.6.3	Rate Density Evolution and the Star Formation Rate	211

9.7	Waxman-Bahcall Bound	213
9.8	UHECR and GZK Neutrino Intensities	215
9.9	Photonuclear Reactions	219
9.9.1	Photodisintegration Reaction Rate	222
9.9.2	Effective Photodisintegration Energy-Loss Rate	224
9.9.3	Neutrinos from Photodisintegration	225
Chapter 10.	$\gamma\gamma$ Pair Production	227
10.1	$\gamma\gamma$ Pair Production Cross Section	228
10.1.1	Absorption by a Blackbody and a Modified Blackbody Photon Gas	231
10.1.2	Absorption by a Power-Law Photon Gas in a Relativistic Jet	233
10.1.3	$\gamma\gamma$ Attenuation in Anisotropic Radiation Fields	235
10.2	δ -Function Approximation for $\sigma_{\gamma\gamma}$	236
10.3	Opacity of the Universe to $\gamma\gamma$ Attenuation	237
10.3.1	$\gamma\gamma$ Optical Depth of the Universe	238
10.3.2	Measurements of the EBL	240
10.3.3	$\gamma\gamma$ Attenuation at Low Redshifts	241
10.3.4	$\gamma\gamma$ Attenuation at All Redshifts	244
10.4	The γ -Ray Horizon	244
10.5	Compactness Parameter	245
10.6	Minimum Doppler Factor from $\gamma\gamma$ Constraint	247
10.7	Correlated γ -Ray and Neutrino Fluxes	249
10.8	Electromagnetic Cascades	253
10.8.1	Cascades in Jets	254
10.8.2	Cascades in the Intergalactic Medium	256
10.9	$\gamma\gamma \rightarrow \nu$	257
Chapter 11.	Blast-Wave Physics	258
11.1	Fireballs and Relativistic Blast Waves	258
11.1.1	Blast-Wave Deceleration	260
11.1.2	Blast-Wave Equation of Motion	261
11.1.3	Dissipated Internal Energy	270
11.2	Elementary Blast-Wave Theory	270
11.2.1	Characteristic Electron Energies	271
11.2.2	Characteristic Synchrotron Frequencies	274
11.2.3	Afterglow Theory	278
11.3	Relativistic Shock Hydrodynamics	282
11.3.1	Relativistic Shock Thermodynamics	282
11.3.2	Synchrotron Radiation from a Relativistic Reverse Shock	288
11.4	Beaming Breaks and Jets	290
11.5	Synchrotron Self-Compton Radiation	292

11.6	Theory of the Prompt Phase	294
11.6.1	X-Ray Flares and γ -Ray Pulses from External Shocks	295
11.6.2	Colliding Shells and Internal Shocks	301
11.7	Thermal Photospheres	303
11.7.1	The Amati and Ghirlanda Relations	303
11.7.2	Thermodynamics of a Steady Relativistic Wind	304
11.7.3	Photospheric Radius	306
11.7.4	Pair Photosphere	308
11.8	Thermal Neutrons	310
11.9	GRB Cosmology	312
Chapter 12. Introduction to Fermi Acceleration		314
12.1	Stochastic and Shock Fermi Acceleration	316
12.2	Wave Turbulence Spectrum	317
12.3	The Hillas Condition	320
12.4	Energy Gain per Cycle from Fermi Acceleration	321
12.5	Diffusion in Physical Space	322
12.6	Maximum Particle Energy	324
Chapter 13. First-Order Fermi Acceleration		327
13.1	Nonrelativistic Shock Hydrodynamics	328
13.2	Convection-Diffusion Equation	330
13.3	Nonrelativistic Shock Acceleration	332
13.3.1	Spectral Index from Convection-Diffusion Equation	332
13.3.2	Spectral Index from Probability Arguments	334
13.3.3	Finite Shell Width	335
13.3.4	Cosmic-Ray Pressure and Shock Width	337
13.3.5	Maximum Particle Energy in Nonrelativistic Shock Acceleration	339
13.3.6	Maximum Particle Energy in Nonrelativistic Shocks	343
13.3.7	Amplification of Upstream Medium Magnetic Field	344
13.4	Relativistic Shock Acceleration	346
13.4.1	Fokker-Planck Equation for a Stationary, Parallel Shock	347
13.4.2	Spectral Index in Relativistic Shock Acceleration	348
13.4.3	Maximum Particle Energies in Relativistic Shock Acceleration	349
Chapter 14. Second-Order Fermi Acceleration		351
14.1	Power-Law Particle Spectra from Second-Order Fermi Acceleration	353
14.2	The Resonance Condition	353
14.3	Plasma Waves	355
14.4	Diffusive Particle Acceleration	359

14.5	Approximate Derivation of Diffusion Coefficients	362
14.5.1	Pitch-Angle Diffusion Coefficient	362
14.5.2	Momentum Diffusion Coefficient	363
14.6	Energy Gain and Diffusive Escape Rates	364
14.7	Momentum Diffusion Equation	367
14.7.1	Ramaty-Lee Spectrum for Hard-Sphere Scattering	368
14.7.2	Green's Function Solution	370
14.8	Maximum Particle Energy in Second-Order Fermi Acceleration	372
14.8.1	Gyroresonant Stochastic Acceleration	373
14.8.2	Stochastic Energization in Nonrelativistic Shocks	374
14.8.3	Stochastic Energization in Relativistic Flows	376
Chapter 15. The Geometry of Spacetime		379
15.1	Introduction	379
15.2	Splitting Spacetime Into Space and Time	380
15.3	The Kerr Metric	384
15.3.1	The Geodesic Equation and Its Integrability in Kerr Geometry	386
15.3.2	The Kerr Metric in Kerr-Schild Coordinates	391
15.3.3	The Ergosphere	394
15.3.4	The Event Horizon	396
15.4	The Penrose Process	397
15.5	Hawking Radiation	402
15.5.1	Scalar Fields in Curved Spacetime	402
15.5.2	The Quantum Field for a Scalar Particle in a Flat Spacetime	404
15.5.3	Particle Creation in Curved Spacetime	405
15.5.4	Particle Creation in Rindler Spacetime	408
15.5.5	Particle Creation in Schwarzschild Geometry	415
Chapter 16. Black-Hole Electrodynamics		417
16.1	3+1 Electrodynamics	417
16.2	The Energy-Momentum Tensor	424
16.3	The Blandford-Znajek Process	427
16.3.1	Explicit Expressions for the Fields and Currents	431
16.3.2	The Force-Free Constraint Equation	432
16.3.3	The Znajek Regularity Condition	433
16.3.4	Energy and Angular-Momentum Extraction from the Force-Free Magnetosphere	435
16.4	Geodesic Currents in the Magnetosphere	436
16.5	An Exact Solution	439
16.6	Fields and Energy Extraction for the Ω_- Solution	441
16.7	An Approximate Solution	442
16.8	Uniqueness of the Ω_- Solution	447

16.9	Energy Extraction for the Ω_+ Solution	448
16.10	Blandford-Znajek Process in Astrophysical Sources	450
Chapter 17. High-Energy Radiations from Black Holes		452
17.1	γ Rays	453
17.1.1	Modeling γ Rays from Black Holes	454
17.1.2	Statistics of Black-Hole Sources	456
17.1.3	Blazar Physics	457
17.1.4	GRB Classes	458
17.1.5	Unresolved and Diffuse γ -Ray Background	458
17.2	Cosmic Rays	459
17.2.1	Acceleration of Cosmic Rays at Supernova Remnant Shocks	461
17.2.2	Acceleration of UHECRs at Relativistic Blast Waves	462
17.2.3	Charged-Particle Astronomy	463
17.2.4	UHECR Propagation	466
17.2.5	UHECR Source Power Requirements	466
17.3	Neutrinos	468
17.4	Concluding Remarks	471
Appendix A: Essential Tensor Calculus		473
A.1	Introduction	473
A.2	The Tangent Vector	473
A.3	Dual Vectors	476
A.4	The Space $T^{**}(M)$	477
A.5	Tensors	478
A.6	The Metric Tensor	480
A.7	The Volume Element and the Levi-Civita Tensor	481
A.8	The Covariant Derivative	483
A.9	The Divergence Theorem	485
A.10	The Einstein Equation	486
Appendix B: Mathematical Functions		488
B.1	The Gamma Function and Error Function	488
B.2	Modified Bessel Functions of the Second Kind	488
B.3	Exponential Integral Function	489
B.4	Planck's Function	490
B.5	Bernoulli Numbers and Riemann ζ Function	490
B.6	Whittaker Functions	491
B.7	Lambert W Function	491
Appendix C: Solutions of the Continuity Equation		492
Appendix D: Basics of Monte Carlo Calculations		497

CONTENTS	xvii
Appendix E: Supplementary Information	499
Appendix F: Glossary and Acronym List	505
Bibliography	509
Index	531

This page intentionally left blank

Preface

The rapid advances in high-energy astronomy have, over the past few decades, given us a new view of the universe—a universe filled with luminous, compact, and highly variable sources best explained by the hypothesis that they are powered by black holes. Visible to great distances and early times, understanding their high-energy emissions and spectral energy distributions requires a broadband, multi-wavelength effort. Because our knowledge of black holes increasingly intersects ultrahigh-energy cosmic-ray and high-energy neutrino research, the best understanding furthermore requires a multimessenger approach.

The observational results on black holes have been accompanied by corresponding theoretical developments. Much of this research is found dispersed throughout the scientific literature. Here we attempt to organize some of the common themes in the field of nonthermal black-hole astrophysics and strong gravity by presenting a systematic study of the high-energy radiation physics and general relativity of black holes and their jets.

This book can serve as a reference to ongoing research in black-hole physics and particle and nonthermal astrophysics for graduate students, high-energy astrophysicists, astroparticle physicists, general relativists, and the interested reader who is not deterred by our attempt at a mathematical description of black holes and their high-energy radiations. First-year graduate study in physics, with emphasis on general relativity, astrophysics, and cosmology, should provide sufficient background to follow the exposition.

NOTE ON NOTATION

For clarity, we explain some conventions used here. The inequality symbols \cong , \approx , \simeq , and \sim correspond to estimates within a factor of tens of percent, 2, 5, and order of magnitude, respectively, though \sim can also represent generic uncertainty. The symbol $\mathcal{O}(x^n)$ represents the order of the next highest term in an expansion.

In quantities written as $f(x; a)$ or $f(x, y; a, b)$ and so on, the semicolon separates differential variables x, y, \dots from parameters a, b, \dots . Thus $f(x; a) = df(x; a)/dx$ and $f(x, y; a, b) = \partial^2 f(x, y; a, b)/\partial x \partial y$. Two forms of the Heaviside function are defined such that $H(x - a) = 1$ if $x \geq a$ and $H(x - a) = 0$ otherwise, and $H(x; a, b) = 1$ if $a \leq x \leq b$ and $H(x; a, b) = 0$ otherwise.

The quantity \otimes denotes tensor product, and raised and lowered repeated indices in tensors denote summation, i.e., $A_\mu B^\mu \equiv \sum_\mu A_\mu B^\mu$.

Gaussian cgs units are mainly used, so e^2/r is an energy when e is charge and r is length, and B^2 is an energy density when B stands for magnetic field. One megaparsec, Mpc, is equal to 3.086×10^{24} cm.

ACKNOWLEDGMENTS

This work is a partnership between two scientists, but could not have been possible without the support of many people.

For the first author, this book represents an opportunity to systematize research developed over more than 25 years, and obviously represents a subjective viewpoint related to my own research interests.

I would first of all like to acknowledge Professor Robert J. Gould and the late Dr. Reuven Ramaty for their teachings, and Armen Atoyán, Markus Böttcher, Edison Liang, and Reinhard Schlickeiser for fruitful collaborations. I would also like to thank Bob Berrington, Roger Blandford, Joss Bland-Hawthorn, Josh Bloom, Jim Chiang, Brenda Dings, Justin Finke, Markos Geoganopoulos, Magda González, Francis Halzen, Martin Harwit, Kevin Hurley, Demos Kazanas, Hannah Krug, Truong Le, Rich Lingenfelter, Apostolos Mastichiadis, Peter Mészáros, Kurt Mitman, Vahé Petrosian, Martin Pohl, Enrico Ramirez-Ruiz, Soeb Razzaque, Martin Rees, Yoel Rephaeli, Gerry Share, Floyd Stecker, Steve Sturmer, Lev Titarchuk, Alan Watson, Eli Waxman, Trevor Weekes, Jon Weisheit, and my family for enlightening interactions on this long strange trip. (My apologies to those whose work is overlooked or name omitted.) Special thanks to Peter Mészáros for many suggestions that improved the manuscript, Justin Finke for finding errors (those remaining belonging to me), and John McKinley for Appendix D.

Here at the Naval Research Laboratory, I have enjoyed the freedom to pursue this research in large part thanks to Jim Kurfess, the late Herb Gursky, Neil Johnson, and Jill Dahlburg. Most importantly, I thank my in-laws, Ralph and Susan Trapasso, for all those hours spent in the basement, and my children, Mikel and Sonia, for putting up with my activities. Finally, I thank Govind Menon for joining forces so that this book would become a reality.

The second author would like to thank:

Troy University, for providing me with the necessary infrastructure to do pure academic research.

John Young, my thesis advisor, for the early days.

Chuck Dermer, for piquing my interest in the astrophysical applications of General Relativity. Without him, my efforts would have been lost to the dark side of the event horizon.

M. Surendran and Kalyani Devi, my parents, for innumerable reasons why.

This research has been generously supported by the Office of Naval Research and NASA.

April 2009

High Energy Radiation from Black Holes

This page intentionally left blank

Chapter One

Introduction

1.1 BLACK HOLES IN NATURE

Because of their brilliance, black holes give us a unique view of our universe at both the smallest and largest scales. Masses of candidate black holes associated with astrophysical sources include¹ $\sim (3\text{--}10)M_{\odot}$ black holes found in our Galaxy, intermediate-mass ($\sim(10^2\text{--}10^4)M_{\odot}$) black holes observed in nearby galaxies, massive ($\sim(10^5\text{--}10^7)M_{\odot}$) black holes found in the centers of relatively nearby (redshift $z \lesssim 1$) galaxies, and supermassive ($\sim(10^8\text{--}10^9)M_{\odot}$) black holes at all redshifts (from $z \ll 1$ to $z > 7$). Moreover, newly formed black holes are thought to power the intense emissions from gamma-ray bursts² (GRBs) that occur in galaxies at all distance scales, from relatively nearby galaxies within 10^2 Mpc to structures at redshifts $z > 8$.

A supermassive black hole found at the center of an active galaxy can shine more brightly than all the stars in the galaxy. Whereas the total starlight power from a large spiral galaxy like the Milky Way may reach $\approx 10^{45}$ ergs s^{-1} , the total luminous powers of the nuclei of active galaxies, called active galactic nuclei (AGNs), commonly exceed $\sim 10^{44}$ ergs s^{-1} . The very brightest AGNs can have *apparent* isotropic bolometric powers exceeding 10^{49} ergs s^{-1} ; apparent because the radiation may be directed into a small fraction of the full sky, so that the actual luminosity is reduced by a beaming factor related to the solid angle into which the emission is radiated. Apparent isotropic GRB powers can exceed $\sim 10^{52}$ ergs s^{-1} . Jet sources from candidate black holes are often most luminous at γ -ray energies, and a variety of phenomena supports a picture of relativistic bulk plasma outflow powered by a black-hole engine.

A fundamental question is the power source of the luminous, energetic emissions from black holes. The energy sources are essentially limited to accretion and black-hole rotation. For matter accretion, dissipation of

¹One Solar mass $M_{\odot} \cong 2 \times 10^{33}$ g. The Solar luminosity $L_{\odot} \cong 4 \times 10^{33}$ ergs s^{-1} . See Appendix E.

²A glossary and acronym list is given in Appendix F.

Table 1.1 Electron and Proton Rest Mass Energies, and Units of Energy

$m_e c^2 = 8.187 \times 10^{-7} \text{ ergs} = 1.236 \times 10^{20} \text{ Hz} = 5.93 \times 10^9 \text{ K}$
$m_e c^2 = 5.11 \times 10^5 \text{ eV} = 511 \text{ keV} = 0.511 \text{ MeV} \cong 0.5 \times 10^{-3} \text{ GeV}$
$\cong 0.5 \times 10^{-6} \text{ TeV}$
$1 \text{ eV} = 2.418 \times 10^{14} \text{ Hz} = 1.602 \times 10^{-12} \text{ ergs}$
$1 \text{ MeV} \cong 1.6 \times 10^{-6} \text{ ergs} = 2.418 \times 10^{20} \text{ Hz} \simeq 10^{10} \text{ K}$
$1 \text{ TeV} \cong 2.4 \times 10^{26} \text{ Hz} \cong 1.6 \text{ ergs}$
$m_p c^2 = 1.5032 \times 10^{-3} \text{ ergs} = 2.27 \times 10^{23} \text{ Hz} \simeq 10^{13} \text{ K}$

gravitational potential energy releases $\lesssim 5\text{--}30\%$ of the rest-mass energy, depending on the spin of the black hole and how the angular momentum is deposited at the disk inner edge. The diversity of black-hole spectral states suggests that a parameter at least as important as the total black-hole mass accretion rate, \dot{M} , also plays a role. This could be the spin parameter of the black hole. Rather than describe emissions formed by quasi-spherical accretion or disk accretion onto black holes, which are likely to be quasi-thermal and are well reviewed in a number of books [1–3], here we concern ourselves with the high-energy radiation from black holes associated with relativistic jetted outflows. We consider whether the electromagnetic process can effectively extract energy from a rotating black hole to make luminous black-hole jet emissions, and other high-energy cosmic-ray and neutrino radiations. For this purpose, a formulation of general relativity is developed to understand black-hole electrodynamics and the Penrose process operating near black holes.

The theory of γ -ray emission in black-hole sources cannot be separated from the theory of synchrotron radiation, because the same electrons that Compton-scatter soft photons to γ -ray energies also radiate synchrotron photons at radio and optical frequencies. The lepton acceleration process would likewise accelerate baryons. Ultra-high-energy cosmic ray nucleons are subject to photohadronic losses, accompanied in some cases by the formation of baryonic resonances that decay into photons, leptons, neutrons, and neutrinos. To understand the underlying connections between the accelerated particles that radiate γ rays and neutrinos and those particles that become cosmic rays requires knowledge of the underlying astrophysical processes.

The goal of this monograph is to provide a systematic presentation of the theory of black-hole physics and nonthermal, high-energy radiation mechanisms. We investigate the hypothesis that the most luminous and highest-energy radiations in nature are powered by rotating black holes.

The high-energy universe of nonthermal particles and radiations begins where the hot universe leaves off: when the concept of temperature breaks down. Thermal processes involve particle distributions that are described by the Maxwell-Boltzmann form. The relativistic Maxwell-Boltzmann distribution is given by

$$\frac{dn_{\text{MB}}(p)}{dp} \equiv n_{\text{MB}}(p) = n_0 \frac{p^2 \exp(-\gamma/\Theta)}{\Theta K_2(1/\Theta)} \quad (1.1)$$

[4], where the dimensionless temperature $\Theta = k_{\text{B}}T/m_e c^2$, m_e is the rest mass of the electron (table 1.1), n_0 is the particle number density (particle number and energy densities are generally denoted by lower-case symbols), and $K_2(x)$ is a modified Bessel function of the second kind of order 2 (see Appendix B). Throughout we write the total energy E of a particle of mass m in terms of the particle Lorentz factor $\gamma = E/mc^2$, so that the particle's kinetic energy is $(\gamma - 1)mc^2$, and the particle's (dimensionless) momentum $p = \beta_{\text{par}}\gamma$, where $\beta_{\text{par}} = \sqrt{1 - \gamma^{-2}}$.³ Because relativistic particles are mainly considered, we will frequently take the $\gamma \gg 1$, $\beta_{\text{par}} \rightarrow 1$ asymptote. The particle Lorentz factor will be denoted by γ in the fluid frame, except when we consider problems involving multiple species of particles, where the Lorentz factors of the different species must be distinguished.

At relativistic temperatures, $\Theta \gg 1$, the electron-positron pair production rate increases in proportion to the square of the particle density while the pair annihilation rate declines. Pairs begin to multiply without limit above some fixed temperature ≈ 20 MeV [5,6], requiring ever-increasing energy input. Steady thermal plasmas therefore cannot exist at tens of MeV temperature and higher. Moreover, gases with temperatures $\gtrsim 10$ MeV cannot relax to a Maxwell-Boltzmann distribution, because the bremsstrahlung energy-loss rate dominates the Coulomb thermalization collision rates [7]. (Though both are proportional to the particle number densities, bremsstrahlung energy losses increase with particle energy and elastic Coulomb processes decrease with particle energy.) Thus there is no demonstrated way for the gas to thermalize. Plasma processes are often invoked to achieve rapid thermalization on a timescale related to the inverse of the plasma frequency, but special properties of the waves are required to give a quasi-thermal particle distribution. If a system of characteristic size R containing electrons with density n_e has Thomson depth $\tau_{\text{T}} = n_e \sigma_{\text{T}} R \gtrsim 1$, which is required to obtain large luminosities from small regions, then no steady, thermal plasmas with temperatures $\gg 1$ MeV can exist. Allowed system luminosities and total Thomson depths, including pairs, bifurcate into a normal and pair-dominated branch below a maximum critical temperature for fixed

³The term $\beta = \sqrt{1 - \Gamma^{-2}}$ is preserved for the β factor of bulk plasma outflow.

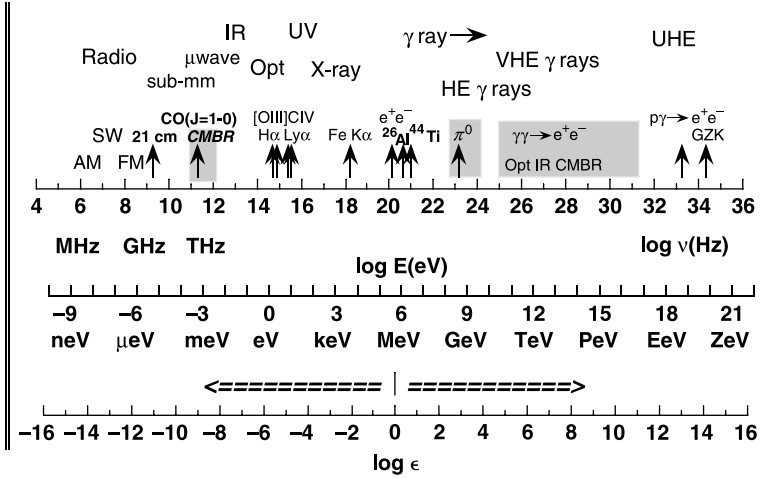


Figure 1.1 Photon and relativistic particle energy spectrum. Shown are photon or particle energies in units of Hz, eV, and electron rest mass ($\epsilon = hv/m_e c^2$), and some important astronomical lines and features. The mean energy of a cosmic microwave background (CMB) photon at the present epoch, in units of electron rest mass, is $\approx 10^{-9}$.

temperature and proton Thomson depth [8]. Photons exceeding many tens of MeV, or hundreds of MeV from pionic emissions of thermalized protons, must therefore originate from nonthermal processes. The existence of cosmic rays and GeV–TeV γ -ray sources attests to the importance of nonthermal processes throughout the universe.

The Electromagnetic Spectrum

During the past ~ 75 years,⁴ the cosmic *electromagnetic spectrum* outside the visual domain has been explored using telescopes with different limiting sensitivities and imaging capabilities over the range of frequencies ν (Hz) extending from ≈ 30 kHz to $\nu \gtrsim 10^{27}$ Hz (i.e., photon energies $E \gtrsim 10$ TeV); see figure 1.1. Absorption by interplanetary plasma limits observations from space-based radio detectors below ≈ 30 kHz, and the Earth’s ionosphere hampers observations of cosmic radio emission below ≈ 10 – 30 MHz frequencies. The sky is transparent at higher radio frequencies and in the optical waveband. Space research overcomes the limitations of the obscuring atmosphere in many wavelength ranges.

Ultraviolet and X-ray fluxes from compact sources are often attenuated by photoelectric absorption from intervening neutral or ionized matter,

⁴Karl Jansky discovered radio emission from the Galaxy in 1932.

including absorption by Milky Way gas. At TeV energies, the universe becomes opaque to pair production attenuation of very high-energy photons (γ) on cosmic infrared photons (γ'). This process, represented by the reaction $\gamma\gamma' \rightarrow e^+e^-$, prevents us from seeing extragalactic sources of multi-TeV radiation at distances $\gtrsim 1$ Gpc (redshifts $z \gtrsim 0.2$). The highest-energy cosmic photon yet detected was at ≈ 90 TeV from a Milagro source [9]. At $\gtrsim 100$ TeV energies and higher, telescopes yet lack sufficient sensitivity to detect cosmic sources or the plane of our Galaxy.

It is convenient to express the total energy E_γ of a photon in units of the electron rest-mass energy $m_e c^2$. The dimensionless energy of a photon with frequency ν is denoted by

$$\epsilon \equiv \frac{E_\gamma}{m_e c^2} = \frac{h\nu}{m_e c^2}. \quad (1.2)$$

The units of $m_e c^2$ give the energy units (table 1.1) of E_γ . The term ϵ in eq. (1.2) can also denote the dimensionless energy of highly relativistic ($\gamma \gg 1$) particles, such as cosmic rays or neutrinos. At nonrelativistic ($\gamma - 1 \ll 1$) and transrelativistic ($\gamma - 1 \approx 1$) particle energies, the total energy, kinetic energy, and momentum must be more carefully related than in the ultrarelativistic regime, where $p = \sqrt{\gamma^2 - 1} \rightarrow \gamma$ when $\gamma \gg 1$. Figure 1.1 illustrates the energy scale of astronomical photon observations in Hz, eV, and dimensionless units.

The Astroparticle Spectrum

Cosmic rays consist of nonthermal protons, ions, electrons, positrons, photons, and antiprotons. Intensities of various cosmic-ray ionic components, multiplied by $E^{2.75}$, are shown in the left panel in figure 1.2. The dashed line gives the approximation $I_p(E) = 2.2E^{-2.75}$ protons/(cm² s GeV sr) multiplied by $E^{2.75}$ (therefore a straight line in this plot) to the demodulated flux of cosmic-ray protons, valid from $E \lesssim 1$ GeV to $\approx 10^{14}$ eV. Note that α -particles and heavier nuclei make an increasing contribution to the cosmic-ray flux near the knee of the cosmic ray spectrum at ≈ 3 PeV.

At the lowest energies of the nonthermal particle spectrum, Solar energetic particles accompanying Solar flares and coronal mass ejections have been measured with energies ranging from keV/nucleon to GeV/nucleon. Cosmic rays from outside our Solar system range in energy from directly detected \sim GeV/nucleon cosmic-ray ions, at lower energies, to air shower and fluorescence events with energies exceeding $\gtrsim 10^{20}$ eV at high energies. For energies \lesssim few GeV/nucleon, the cosmic-ray flux varies with the phase of the 11-year Solar sunspot cycle. This Solar modulation of the low-energy

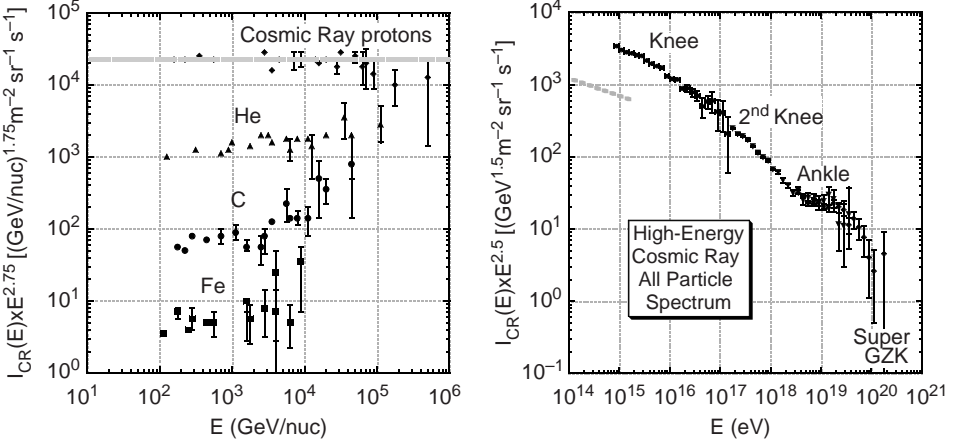


Figure 1.2 *Left panel:* Cosmic-ray number intensity multiplied by $E^{2.75}$ for cosmic-ray ions with energy $E \lesssim 10^{14}$ eV/nucleon. *Right panel:* Cosmic-ray number intensity multiplied by $E^{2.5}$ for all cosmic rays with total energy $E \gg 10^{14}$ eV. Features of the high-energy cosmic-ray all-particle spectrum are identified.

cosmic-ray flux results from adiabatic losses of the cosmic rays as they penetrate the heliosphere and diffuse through the outflowing Solar wind.

The heliosphere does not significantly perturb trajectories of cosmic rays with $E \gtrsim 10$ GeV/nucleon, and these cosmic rays sample the interstellar cosmic-ray flux. In a magnetic field with intensity B , the Larmor radius of a particle with mass m , atomic mass A , and charge Z is

$$r_L \cong \frac{mc^2 \beta_{\text{par}} \gamma}{QB} \xrightarrow{\gamma \gg 1} \frac{E}{ZeB} \cong 1.1 \frac{E (\text{PeV})}{ZB (\mu\text{G})} \text{pc} \cong \frac{A}{Z} \left(\frac{m}{m_p} \right) \frac{m_p c^2}{eB} \gamma$$

$$\cong \begin{cases} \frac{1706}{B (\text{G})} \gamma \text{ cm}, & \text{electrons,} \\ \frac{3.13 \times 10^6 A}{ZB (\text{G})} \gamma \text{ cm} \cong \frac{A/Z}{B (\mu\text{G})} \left(\frac{\gamma}{10^6} \right) \text{pc} \\ \cong \frac{E (10^{20} \text{ eV})}{ZB (10^{-10} \text{ G})} \text{Gpc}, & \text{protons or ions.} \end{cases} \quad (1.3)$$

Particles with $r_L \gg R$ will escape from or penetrate into a region of size R with mean magnetic field B , and will do this on the light crossing timescale R/c . Cosmic-ray protons with energies $E \gtrsim 10^{17}$ eV, well above the knee energy at ≈ 3 PeV, have Larmor radii comparable to the ≈ 180 pc thickness of the Galaxy's disk. At such energies, cosmic-ray protons originating in the disk of the Galaxy will escape into the halo of the Galaxy and escape

to intergalactic space. If formed beyond the Galaxy, such energetic cosmic rays can pass through the Galactic halo and into the Galaxy's disk.

The intensity of all cosmic-ray particles, irrespective of type, multiplied by $E^{2.5}$, is shown for $E \gg 10^{14}$ eV cosmic rays in the right panel of figure 1.2. Features of the high-energy spectrum are labeled. At the highest particle energies, extending from ultrahigh energies (UHE; $\gtrsim 10^{18}$ eV) to super-GZK energies ($\gtrsim 10^{20}$ eV),⁵ the different signatures of the air showers formed by a photon and a particle are not clear cut, and depend on the particle physics model used to interpret air show data [12]. The Auger collaboration report [13] that the photon fraction of the UHECR (ultrahigh-energy cosmic ray) flux at $E \cong 10^{19}$ eV is $\lesssim 2\%$. The Auger result [14] on clustering of arrival directions of $\gtrsim 6 \times 10^{19}$ eV UHECRs rules out a Galactic origin, and the large gyroradii and near isotropy of cosmic rays with $E \lesssim 4 \times 10^{19}$ eV also suggest an extragalactic origin. The energy of the transition from a Galactic disk or halo component to an extragalactic component, assuming there is a definite transition energy, could be at the second knee or at the ankle, and is an open question.

High-energy neutrinos make up another important component of the astroparticle spectrum.⁶ The high-energy nonthermal neutrino window is being opened in this decade with observations from \sim TeV to 10^{20} eV. Various estimates [16] suggest that detection of 100 TeV–100 PeV neutrinos from cosmic sources is probable with neutrino telescopes at the km scale, such as the IceCube experiment at the South Pole or a northern hemisphere neutrino telescope in the Mediterranean Sea. High-energy neutrino observations will be crucial to identify cosmic-ray accelerators and buried nonthermal sources.

The Gravitational-Wave Spectrum

The gravitational-wave spectrum offers a new window into the universe of high-energy activity. Distortions in spacetime induced by extreme events involving, for example, the coalescence of Solar mass neutron stars and black holes, induce minute strains on underground bars like those in the *Laser Interferometer Gravitational Wave Observatory* (LIGO). Relative displacements of the three-detector space-based array that forms the proposed *Laser Interferometer Space Antenna* (LISA) will be used to monitor

⁵GZK stands for Greisen, Zatsepin, and Kuzmin, an American and two Russian scientists who first pointed out that $\gtrsim 10^{20}$ eV cosmic rays would rapidly lose energy due to photohadronic interactions with the photons of the cosmic microwave background radiation (CMBR) [10,11]. See chapter 9.

⁶MeV neutrinos formed by nuclear burning in stars [15] or in dense collapsed cores of exploding stars are not treated here.

coalescence of massive black holes. LIGO is now taking data at its design sensitivity, and LISA may be developed as a NASA mission in the 2010–2020 time frame or later. Template gravitational waveform studies of merging compact objects and coalescing black holes will be a crucial tool to compare with data from these detectors. This subject, though of potentially great importance to black-hole physics, will not be treated here (see, e.g., Ref. [17]).

1.2 ENERGY FLUXES

Flux density F_ν is usually reported by radio astronomers in units of Jansky ($1 \text{ Jy} = 10^{-23} \text{ ergs cm}^{-2} \text{ s}^{-1} \text{ Hz}^{-1}$), so that the quantity νF_ν is an energy flux Φ (units of $\text{ergs cm}^{-2} \text{ s}^{-1}$, or Jy Hz , noting that $10^{10} \text{ Jy Hz} = 10^{-13} \text{ ergs cm}^{-2} \text{ s}^{-1}$). The luminosity distance d_L for a steady, isotropically emitting source is defined so that the energy flux Φ is related to the source luminosity L_* (ergs s^{-1}) according to the Euclidean expression

$$\Phi = \frac{L_*}{4\pi d_L^2} \quad (1.4)$$

(see chapter 4).

If $\phi(\epsilon)$ is the measured spectral photon flux (units of photons $\text{cm}^{-2} \text{ s}^{-1} \epsilon^{-1}$), then $\nu F_\nu = m_e c^2 \epsilon^2 \phi(\epsilon)$. Henceforth we use the notation

$$f_\epsilon = \nu F_\nu \quad (1.5)$$

for the νF_ν flux. From the definitions of Φ and f_ϵ ,

$$\Phi = \int_0^\infty d\epsilon \frac{f_\epsilon}{\epsilon}. \quad (1.6)$$

From eq. (1.4), the luminosity radiated by a source between measured photon energies ϵ_1 and ϵ_2 , or between source frame photon energies $\epsilon_1(1+z)$ and $\epsilon_2(1+z)$, is given by

$$L_*[\epsilon_1(1+z), \epsilon_2(1+z)] = 4\pi d_L^2 m_e c^2 \int_{\epsilon_1}^{\epsilon_2} d\epsilon \epsilon \phi(\epsilon) = 4\pi d_L^2 \int_{\ln \epsilon_1}^{\ln \epsilon_2} d(\ln \epsilon) f_\epsilon. \quad (1.7)$$

Equation (1.7) shows that if the νF_ν spectrum is flat with value f_ϵ^0 , corresponding to a photon flux $\phi(\epsilon) \propto \epsilon^{-2}$, then the apparent power of the source over one decade of energy is $\approx (\ln 10)L_0 \approx 2.30L_0$, where $L_0 = 4\pi d_L^2 f_\epsilon^0$.

Long-duration GRBs are thought to be powered by the core collapse of massive stars to black holes [18]. A large fraction is detected at cosmological distances, that is, at mean redshifts $\langle z \rangle \gtrsim 1$; thus their mean apparent isotropic γ -ray energy releases are

$$\mathcal{E}_* = \frac{4\pi d_L^2 \Phi \langle \Delta t \rangle}{(1+z)} \approx 10^{51} \frac{d_{28}^2}{(1+z)/2} \left(\frac{\Phi}{10^{-7} \text{ ergs cm}^{-2} \text{ s}^{-1}} \right) \left(\frac{\langle \Delta t \rangle}{20 \text{ s}} \right) \text{ ergs}, \quad (1.8)$$

where $d_L = 10^{28} d_{28}$ cm, $d_{28} \approx 2$ for a GRB at $z = 1$, and the mean duration $\langle \Delta t \rangle \approx 20$ s. The factor $1+z$ relates the observer time to the source frame time.

Blazars are thought to be supermassive black-hole sources with jets, oriented such that we are viewing nearly along the jet axis. The jet emission is strongly amplified by Lorentz-boosting of relativistic outflows, so that we can see such sources to high redshift. One such blazar is the bright flat-spectrum quasar PKS 0528 + 134 at $z = 2.06$ ($d_{28} \cong 5$). During bright γ -ray states discovered with the Energetic Gamma Ray Experiment Telescope (EGRET) on the *Compton Gamma Ray Observatory*, its apparent isotropic γ -power exceeded $\sim 10^{49}$ ergs s^{-1} [19]. The bright blazar 3C 279 at $z = 0.538$ ($d_{28} \cong 1$) also flares with apparent γ -ray luminosity $\gtrsim 10^{49}$ ergs s^{-1} [20]. Such flares, lasting for hours to days, involve apparent isotropic energy releases $\gtrsim 10^{53}$ ergs.

The relative magnitude of two sources with magnitudes m_1 and m_2 is defined as

$$m_1 - m_2 = -\frac{5}{2} \log \left(\frac{\Phi_1}{\Phi_2} \right), \quad (1.9)$$

where $\Phi_{(v)} = L_{*(v)}/4\pi d_L^2$ is the (spectral) energy flux, and $\Phi_{(v)}$ and $L_{*(v)}$ are in cgs units of ergs $\text{cm}^{-2} \text{ s}^{-1}$ (Hz^{-1}) and ergs s^{-1} (Hz^{-1}), respectively. Five magnitudes correspond to a factor 10^2 in relative energy fluxes.

Table 1.2 gives a reference optical magnitude scale [21] and the spectral energy flux $\Phi_\nu(0)$ of a zeroth magnitude star, converted to νF_ν energy fluxes $f_\epsilon(0)$ at that photon frequency. The energy flux of a zeroth magnitude star in the V band is about 10^{11} times fainter than the Solar constant ($\cong 1 \text{ kW m}^{-2}$; see Appendix E) and $\approx 10^{10}$ times brighter than a 25th magnitude galaxy (in V), which has an energy flux $\Phi \approx 10^{-15}$ ergs $\text{cm}^{-2} \text{ s}^{-1}$. The largest optical telescopes detect galaxies with $m = 30$, and therefore reach sensitivities $\Phi \lesssim 10^{-17}$ ergs $\text{cm}^{-2} \text{ s}^{-1}$. The *Hubble Space Telescope* only reaches R magnitude $m_R \cong 25$ because of its smaller mirror compared to ground-based telescopes, but its imaging is magnificent at $\sim 0.1''$.

Table 1.2 Reference Optical Magnitude Scale^a

Filter	λ_0 (μ)	ν (10^{14} Hz)	E_γ (eV)	ϵ (10^{-6})	$\Phi_\nu(0)$ ($\text{kJy} = 10^{-20}$ $\text{ergs/cm}^2 \text{ s Hz}$)	$f_\epsilon(0)$ ($\text{ergs/cm}^2 \text{ s}$)
U	0.365	8.22	3.40	6.78	1.9	1.56×10^{-5}
B	0.44	6.82	2.82	5.52	4.27	2.91×10^{-5}
V	0.56	5.40	2.24	4.38	3.54	1.91×10^{-5}
R	0.7	4.28	1.77	3.47	2.84	1.21×10^{-5}
J	1.25	2.40	0.99	1.94	1.60	3.83×10^{-6}
L	3.45	0.87	0.36	0.70	0.29	2.52×10^{-7}
M	4.8	0.62	0.257	0.50	0.163	1.02×10^{-7}

^aFlux density $\Phi_\nu(0)$ and νF_ν flux $f_\epsilon(0)$ for a zeroth magnitude star; the precise scale depends on the photometry system, filter, and bandwidth. For instance, Johnson V magnitude has central wavelength $\lambda_0 = 0.545 \mu\text{m} = 5450 \text{ \AA}$ and a bandwidth of 880 \AA .

1.3 TIMING STUDIES AND BLACK-HOLE MASS ESTIMATES

The Schwarzschild radius of a black hole of mass M is

$$R_S = \frac{2GM}{c^2} \cong 3.0 \times 10^5 \left(\frac{M}{M_\odot} \right) \text{ cm}, \quad (1.10)$$

and $R_S \approx 2 \text{ AU}$ for a $10^8 M_\odot$ black hole. To resolve the nuclear region of a cosmologically distant black hole within $\approx 10^2 R_S$ requires an imaging capability of $\approx 10^{-14}$ rad, which is beyond present technical ability. The mass of the black hole at the Galactic Center, inferred from analysis of stellar orbits, is $M_{\text{GC}} \approx 4 \times 10^6 M_\odot$ [22,23]. The Very Large Baseline Array (VLBA) has an imaging capability of $\approx 10^{-9}$ rad, sufficient to establish the source size of 42 GHz radio emission to $24(\pm 2)R_S$ [24]. The Galaxy's central black hole is the best candidate to directly image the inner regions of a black hole.

Lack of sufficient angular resolution to resolve the different radiating regions near a black hole can in principle be remedied through analysis of time histories of count or photon data. Variations in the source flux by a large factor ($\gtrsim 2$) over a time scale Δt must, from causality arguments for stationary sources, originate from an emission region of size $R \lesssim c\Delta t/(1+z)$. If the radiation were emitted from larger size scales, incoherent superposition of emissions from regions that are not in causal contact would smooth large-amplitude fluctuations. For high-quality data from bright flares, large-amplitude variations in source flux on timescale Δt would, from

this argument, imply a black-hole mass

$$\frac{M}{10^9 M_\odot} \lesssim \frac{\Delta t}{(1+z)10^4 \text{ s}}. \quad (1.11)$$

The measured size scale $R \lesssim c\Delta t/(1+z)$ reflects the physical dimensions of the energy generation region, but not necessarily the distance of the emission site from the source. For emission regions in relativistic motion with bulk Lorentz factor Γ , the actual location of the emission region can be as far as $\approx \Gamma^2 c\Delta t/(1+z)$ from the explosion center (see chapter 5). *High Energy Stereoscopic System* (HESS) detection of rapid $\sim 0.2\text{--}2$ TeV flares from PKS 2155-304 on timescales ~ 300 s, much shorter than the light crossing time across a black hole of $\approx 10^9 M_\odot$ thought to be found in this system [25], is therefore surprising [26].

There are a wide range of methods to determine the masses of Galactic and extragalactic black holes. The most reliable methods employ direct measurements of stellar or gaseous velocities in the vicinity of the black hole, or reverberation mapping of emission lines of surrounding gas in response to changes in the UV flux of the central nucleus [3]. The mass of the black hole and the mass of the bulge of the host galaxy are found to correlate in the ratio of $\approx 1 : 500$ with small, factor-of-2 scatter [27].⁷ For supermassive black holes at large redshifts where the host galaxy cannot be resolved, timing studies could offer the best hope to measure black-hole mass. Black-hole masses have been determined from analysis of X-ray data, but how precisely to determine the black-hole mass from variability data at γ -ray energies remains unclear.

1.4 FLUX DISTRIBUTION

A valuable tool for studying properties of steady or flaring sources is the statistical distribution of fluxes or fluences, called the flux (or $\log N\text{--}\log S$) distribution. The observable quantity could be peak flux within a given photon waveband, flux averaged over a long observing timescale, or fluence of a blazar flare or GRB. Expressing the sensitivity of a high-energy radiation detector in terms of a threshold flux Φ_{thr} imposes the condition that $\Phi \geq \Phi_{\text{thr}}$. For unbeamed sources with luminosity L_* and distance d ($\approx d_L$ at low redshifts), $\Phi = L_*/4\pi d^2$, and the maximum source distance for a give source flux Φ is

$$d(\Phi) = \sqrt{\frac{L_*}{4\pi\Phi}}.$$

⁷A later study [28] shows a ratio of $\approx 1 : 800$ for black holes in 72 AGNs, with more than 50% of the sample within a factor of 3 of the best-fit relation.

Hence the flux distribution for sources that are uniformly distributed with density n_0 in flat space is

$$N(>\Phi) = N(<d) = 4\pi n_0 \int_0^{d(\Phi)} dx x^2 \propto \Phi^{-3/2}, \quad (1.12)$$

as is well known.

The $\langle V/V_{\max} \rangle$ statistic [29]

$$\langle V/V_{\max} \rangle = \frac{1}{N} \sum_{i=1}^N \left(\frac{\Phi_i}{\Phi_{\text{thr}}} \right)^{-3/2} \quad (1.13)$$

expresses the deviation from 0.5 expected for a uniform Euclidean distribution of sources. Here V stands for volume, and V_{\max} is the maximum volume from which a source with flux Φ could be detected. Values of $\langle V/V_{\max} \rangle > 0.5$ represent positive evolution of sources, that is, either more sources and/or brighter sources at large distances or earlier times. Values of $\langle V/V_{\max} \rangle < 0.5$ represent negative source evolution, i.e., fewer or dimmer sources in the past. Detailed treatments of the statistical properties of black hole sources must consider cosmological effects and evolution of source properties.

Analysis of the statistics of the sources of UHECRs, needed for charged particle astronomy [14], is complicated by the unknown strength and geometry of Galactic and intergalactic magnetic fields.

1.5 THE NIGHTTIME SKY

Intergalactic space is permeated by a background glow made up of stellar and black-hole radiations, and the remnant CMBR left over from the big bang (figure 1.3). The mean intensity of light in intergalactic space is referred to here as the extragalactic background light, or EBL. In terms of energy density, the CMBR represents the dominant radiation field of the EBL in intergalactic space (see figure 1.3). The present temperature of the CMBR is 2.728 ± 0.004 K [31]. Other than the $\sim 0.1\%$ dipole anisotropy due to the Galaxy's proper motion, the CMBR shows deviations at $\lesssim 10^{-5}$ from a perfect blackbody due to acoustical imprints from the big bang.

The intensity of the diffuse background IR radiation field is difficult to measure directly because of foreground radiations, such as Galactic electron synchrotron radiation and zodiacal light scattered by dust in our Solar system. The optical component of the diffuse EBL traces, primarily, stellar radiation from spiral and elliptical galaxies. The IR component is primarily radiation from stars and black holes that has been reprocessed through large column densities of cold dust. The energy density of the dust and stellar components of the EBL is $\approx 10\%$ of the CMBR energy density at the present epoch.

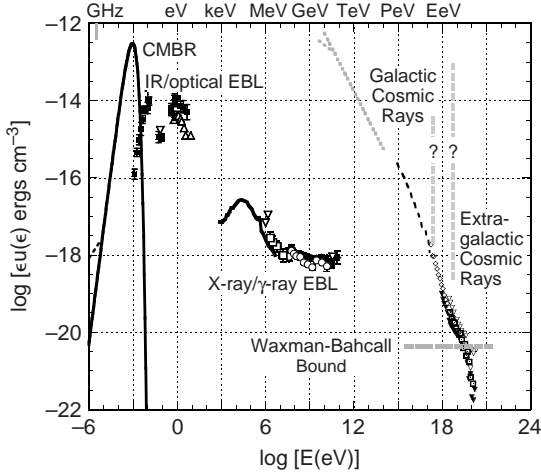


Figure 1.3 Spectral energy densities in intergalactic space of various radiations, including the CMB, the infrared (IR) and optical, X-ray, γ -ray, the extragalactic cosmic ray, and the predicted maximum energy density of cosmogenic neutrinos from photopion interactions of UHECRs with photons of the extragalactic background light (EBL) [30]. Also shown is the energy density of cosmic rays measured near Earth; the transition energy between the galactic and extragalactic components is uncertain.

The X-ray background is resolved from analysis [32] of observed populations into, primarily, Seyfert galaxies, which are star-forming (usually disk) galaxies with strong blue/UV excesses from central nuclei. Also making up the X-ray background is a significant contribution from “buried” black holes, namely accreting black holes with masses $\sim 10^5$ – $10^8 M_\odot$ that are surrounded by material with column densities exceeding $\sim 10^{24}$ H atoms cm^{-2} .

The identified extragalactic γ -ray sources in the EGRET (~ 100 MeV–10 GeV) range are blazars and GRBs. The superposition of faint blazar sources probably makes a significant contribution to the diffuse extragalactic γ -ray background [33,34] shown in figure 1.3. There are additional uncertain contributions from γ rays formed by cosmic rays accelerated in structure formation shocks, or in star-forming galaxies.

Chapter Two

Relativistic Kinematics

In this chapter, the framework of Einstein's special theory of relativity is presented. Transformations that render the spacetime interval $ds^2 = -c^2 dt^2 + dx^2 + dy^2 + dz^2$ unchanged define the category of physical theories that are Lorentz invariant. Further relativistic invariants, used to transform particle and photon distributions, are derived. The kinetic theory of reaction rates and secondary spectra occupies the final sections of this chapter.

2.1 LORENTZ TRANSFORMATION EQUATIONS

Consider two coordinate systems K and K' in uniform relative motion, defining an inertial reference system. The reference frames are aligned along the \hat{x} and \hat{x}' axes, with frame K' moving at speed $v = \beta c$ in the positive \hat{x} direction with respect to frame K (figure 2.1). Assume that a ruler and a clock are used to measure location and time in each frame. According to the postulates of special relativity, the laws of physics are the same in inertial reference systems, and the speed of light c is the same in both frames. Satisfaction of these conditions requires that the interval

$$-c^2 t^2 + x^2 + y^2 + z^2 = -c^2 t'^2 + x'^2 + y'^2 + z'^2 = 0. \quad (2.1)$$

Assuming homogeneity and isotropy of space, one can easily show that the Lorentz transformation equations are the simplest linear equations satisfying eq. (2.1) that connect location \vec{x} at time t measured in K with location \vec{x}' at time t' measured in K' . They are

$$\begin{aligned} t' &= \Gamma(t - \beta x/c), \\ y' &= y, \\ z' &= z, \\ x' &= \Gamma(x - \beta ct), \end{aligned} \quad (2.2)$$

where $\Gamma = 1/\sqrt{1 - \beta^2}$. The reverse transformations are

$$\begin{aligned} t &= \Gamma(t' + \beta x'/c), \\ y &= y', \\ z &= z', \\ x &= \Gamma(x' + \beta ct'). \end{aligned} \quad (2.3)$$

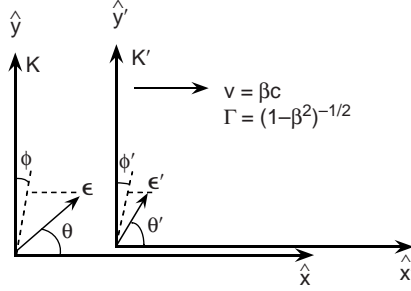


Figure 2.1 Bulk frame K' moving with speed $v = \beta c$ in the \hat{x} direction with respect to frame K . The photon or relativistic particle, with dimensionless energy ϵ , moves in a direction making an angle θ with respect to the \hat{x} axis. The azimuth ϕ is the angle between the projection of this vector on the \hat{y} - \hat{z} plane and the \hat{y} axis, and similarly for primed quantities in the K' frame.

The set of four numbers $x^\mu = (ct, \vec{x}) = (ct, x, y, z)$ defines a space-time event. Events in two inertial reference frames are related by eqs. (2.2) and (2.3).

Suppose the length of an object is measured in frame K . At the same time t , one measures the length $\Delta x = x_2 - x_1$ of an object in motion. In the K' frame, $x'_2 = \Gamma(x_2 - \beta ct)$ and $x'_1 = \Gamma(x_1 - \beta ct)$, from eq. (2.2), so that $\Delta x' = x'_2 - x'_1 = \Gamma \Delta x$. Hence $\Delta x = \Delta x' / \Gamma$, so that

$$dx = \frac{dx'}{\Gamma}. \quad (2.4)$$

The length of a moving object measured along its direction of motion is shorter than its length as measured in the proper frame of the object. This is the phenomenon of length contraction.

Now consider a clock at rest in the K' coordinate system, so x' remains constant in K' . The relationship between the time measured in the stationary frame K and that in the comoving frame K' is, from eq. (2.3), simply $\Delta t = t_2 - t_1 = \Gamma(t'_2 + \beta x'/c) - \Gamma(t'_1 + \beta x'/c) = \Gamma(t'_2 - t'_1) = \Gamma \Delta t'$, so that

$$dt = \Gamma dt'. \quad (2.5)$$

This is the phenomenon of time dilation.

In the general case, the K' frame does not travel along the \hat{x} axis. The Lorentz transformation equations for the coordinate r_{\parallel} along the direction of motion and the coordinate r_{\perp} transverse to the direction of motion can then be written as

$$t' = \Gamma(t - vr_{\parallel}/c), \quad r'_{\parallel} = \Gamma(r_{\parallel} - vt), \quad \text{and} \quad r'_{\perp} = r_{\perp}. \quad (2.6)$$

Here $\theta = \arccos \mu$ is the angle between the direction of motion of the K' system and the \hat{x} -axis of frame K , so that $r_{\parallel} = r\mu = (\vec{v} \cdot \vec{r})/v$,

$r_{\perp} = \sqrt{1 - \mu^2} |\vec{r}|$, and $vr_{\parallel} = \vec{v} \cdot \vec{r} = vr\mu$. The reverse transformation equations are

$$t = \Gamma(t' + vr'_{\parallel}/c), \quad r_{\parallel} = \Gamma(r'_{\parallel} + vt'), \quad \text{and} \quad r_{\perp} = r'_{\perp}. \quad (2.7)$$

The invariance of the interval, eq. (2.1), also implies that the spacetime interval

$$ds^2 = -c^2 dt^2 + dx^2 + dy^2 + dz^2 = -c^2 dt'^2 + dx'^2 + dy'^2 + dz'^2$$

is invariant. Consider a particle at rest in the origin of K' . Therefore

$$dt'^2 = dt^2 \left(1 - \frac{dx^2 + dy^2 + dz^2}{c^2 dt^2} \right) = dt^2 (1 - v^2/c^2).$$

Thus the proper time

$$dt' = \frac{dt}{\Gamma} = \frac{dt}{\gamma} \quad (2.8)$$

as measured in the rest frame of a particle is invariant because, in this case, the particle Lorentz factor γ equals the bulk Lorentz factor Γ . Hence $dt = \gamma dt'$, in agreement with the time dilation formula, eq. (2.5).

2.2 FOUR-VECTORS AND MOMENTUM

The four-vector spacetime coordinate $x^{\mu} = (ct, \vec{x}) = (x^0, x^1, x^2, x^3)$ transforms according to the Lorentz transformations, eqs. (2.2) and (2.3). A four-vector is defined as a set of four quantities that transform according to

$$\begin{aligned} x'^0 &= \Gamma(x^0 - \beta x^1), \\ x'^1 &= \Gamma(x^1 - \beta x^0), \\ x'^2 &= x^2, \\ x'^3 &= x^3. \end{aligned} \quad (2.9)$$

Four-vectors can be constructed from the spacetime four-vector and invariants that are unchanged by Lorentz transformations. The four-vector momentum

$$p^{\mu} = -mc \frac{dx^{\mu}}{ds} = mc\gamma(1, \vec{\beta}_{\text{par}}) = mc(\gamma, \vec{p}_{\text{par}}), \quad (2.10)$$

where $\vec{\beta}_{\text{par}} = d\vec{x}/dt$ and $\vec{p}_{\text{par}} = \vec{\beta}_{\text{par}}\gamma$, and we use the invariant $ds = -cdt' = -cdt/\gamma$, eq. (2.8), associated with the proper time of a particle moving with Lorentz factor $\gamma = 1/\sqrt{1 - \beta_{\text{par}}^2}$ in the K frame. The time component of eq. (2.10) is equal to E/c , where the total particle energy

$$E = \gamma mc^2.$$

The quantity m is the invariant particle rest mass.

Because eq. (2.10) is a four-vector, it transforms according to eq. (2.9). Thus one obtains the Lorentz transformation equations

$$\begin{aligned}\gamma' &= \Gamma(\gamma - \beta p_x) = \Gamma\gamma(1 - \beta\beta_{\text{par},x}), \\ p'_x &= \Gamma(p_x - \beta\gamma) \text{ or } \gamma'\beta'_{\text{par},x} = \gamma\Gamma(\beta_{\text{par},x} - \beta), \\ p'_y &= p_y, \\ p'_z &= p_z\end{aligned}\tag{2.11}$$

for the particle Lorentz factor and dimensionless momentum, with the reverse transformation obtained by letting $\beta \rightarrow -\beta$ and switching primed and unprimed quantities. These equations can be derived, in analogy with the Lorentz transformation equations for the spacetime event, from the invariance of $-(mc)^2 = -(E/c)^2 + (mcp_{\text{par}})^2 = -(mc)^2(\gamma^2 - \beta_{\text{par}}^2\gamma^2)$.

Because the x -component of dimensionless momentum can be written as $p_x = \gamma\beta_{\text{par},x} = \gamma\beta_{\text{par}}\mu$, where $\theta = \arccos \mu$ is the angle between the direction between the particle momentum and the \hat{x} -axis,

$$\gamma' = \Gamma\gamma(1 - \beta\beta_{\text{par}}\mu)\tag{2.12}$$

and

$$\beta'_{\text{par}}\gamma'\mu' = \Gamma\gamma(\beta_{\text{par}}\mu - \beta).\tag{2.13}$$

The ratio of eqs. (2.13) and (2.12) is

$$\beta'_{\text{par}}\mu' = \frac{\beta_{\text{par}}\mu - \beta}{1 - \beta_{\text{par}}\beta\mu}.\tag{2.14}$$

For massless photons or highly relativistic particles with $\beta_{\text{par}} \rightarrow 1$ and $\gamma \gg 1$, we let $\gamma \rightarrow \epsilon$. Thus

$$\epsilon' = \Gamma\epsilon(1 - \beta\mu),\tag{2.15}$$

$$\mu' = \frac{\mu - \beta}{1 - \beta\mu},\tag{2.16}$$

$$\phi' = \phi,\tag{2.17}$$

now writing the energy in terms of cosine angle μ and azimuth angle ϕ (figure 2.1). The reverse transformation equations for photons and relativistic particles are

$$\epsilon = \Gamma\epsilon'(1 + \beta\mu'),\tag{2.18}$$

$$\mu = \frac{\mu' + \beta}{1 + \beta\mu'},\tag{2.19}$$

$$\phi = \phi'.\tag{2.20}$$

Equations (2.15)–(2.20) can be derived for photons by considering the photon four-vector momentum $k^\mu = (\hbar/m_e c^2)(\omega, c\vec{k})$. In dimensionless form, the four-vector momentum of a photon is $p^\mu = \epsilon(1, \hat{k}/k)$.

If a photon in the bulk comoving frame is emitted at right angles to the direction of motion, then $\theta' = \pi/2$ and $\mu' = 0$. The cosine angle of the photon in frame K is $\mu = \beta$, from eq. (2.19). For highly relativistic bulk speeds, $\Gamma \gg 1$ and $\beta = \mu \approx 1 - (1/2\Gamma^2) \approx 1 - (\theta^2/2)$, so that $\theta \approx 1/\Gamma$. All photons emitted in the forward direction in K' are therefore beamed into a narrow range of angles $\theta \lesssim 1/\Gamma$ in K . This illustrates the phenomenon of relativistic beaming.

2.3 RELATIVISTIC DOPPLER FACTOR

Equation (2.15) shows that the photon energy in frame K is related to the photon energy in frame K' according to the relation

$$\frac{\epsilon}{\epsilon'} = \delta_D \equiv [\Gamma(1 - \beta\mu)]^{-1}, \quad (2.21)$$

where δ_D is the Doppler factor. In the limit of large bulk Lorentz factors and small observing angles along the line of sight,

$$\delta_D \xrightarrow{\Gamma \gg 1, \theta \ll 1} \frac{2\Gamma}{1 + \Gamma^2\theta^2}. \quad (2.22)$$

It is useful to derive the Doppler factor by considering an observer receiving photons emitted at an angle θ with respect to the direction of motion of frame K' in the stationary frame K (figure 2.2). During time Δt_* , as measured in stationary frame K , the bulk system moves a distance

$$\Delta x = \beta c \Delta t_* = \beta \Gamma c \Delta t',$$

where the last expression relates the change in distance to the comoving time element using the time dilation formula, eq. (2.5).

A light pulse emitted at stationary frame time t_* and location x is received at observer time

$$t = t_* + \frac{d}{c} - \frac{x \cos \theta}{c}, \quad (2.23)$$

where d is the distance of the observer from the origin of stationary frame K . At a later time $t_* + \Delta t_*$, a second pulse of light is emitted, which is received by the observer at time

$$t + \Delta t = t_* + \Delta t_* + \frac{d}{c} - \frac{(x + \Delta x) \cos \theta}{c}. \quad (2.24)$$

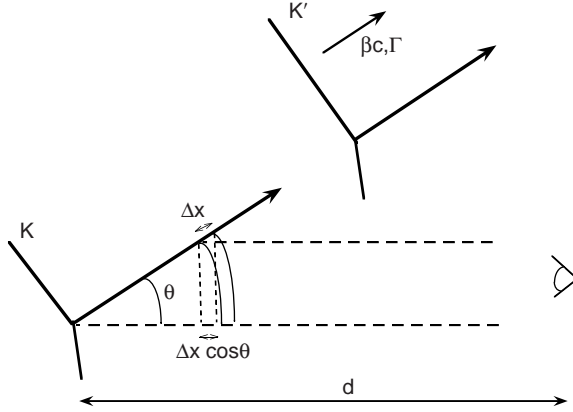


Figure 2.2 Geometry of the Doppler effect.

Subtracting eq. (2.23) from eq. (2.24) and taking the limit of differential quantities gives

$$dt = \frac{dx}{\beta c} (1 - \beta \cos \theta) = \Gamma dt' (1 - \beta \mu) = \frac{dt'}{\delta_D}. \quad (2.25)$$

Because $\epsilon = h\nu/m_e c^2$ and $\nu \propto 1/\Delta t$,

$$\frac{dt'}{dt_*} = \frac{\epsilon}{\epsilon'}, \quad (2.26)$$

and $\epsilon' = \epsilon/\delta_D$, eq. (2.15). Effects from the expansion of the universe on energy and time interval are treated in chapter 4.

2.4 THREE USEFUL INVARIANTS

The invariance of the four-volume $dt dV = dt d^3\vec{x}$ is demonstrated. Without loss of generality, align the coordinate axes along the direction of relative motion, as in figure 2.1. The quantity

$$dt dV = dt dx dy dz = J \begin{pmatrix} t & x & y & z \\ t' & x' & y' & z' \end{pmatrix} dt' dx' dy' dz', \quad (2.27)$$

where the Jacobian of the transformation, from eq. (2.3), is

$$\begin{aligned}
 J \begin{pmatrix} t & x & y & z \\ t' & x' & y' & z' \end{pmatrix} &= \begin{vmatrix} \frac{\partial t}{\partial t'} & \frac{\partial t}{\partial x'} & \frac{\partial t}{\partial y'} & \frac{\partial t}{\partial z'} \\ \frac{\partial x}{\partial t'} & \frac{\partial x}{\partial x'} & \frac{\partial x}{\partial y'} & \frac{\partial x}{\partial z'} \\ \frac{\partial y}{\partial t'} & \frac{\partial y}{\partial x'} & \frac{\partial y}{\partial y'} & \frac{\partial y}{\partial z'} \\ \frac{\partial z}{\partial t'} & \frac{\partial z}{\partial x'} & \frac{\partial z}{\partial y'} & \frac{\partial z}{\partial z'} \end{vmatrix} \\
 &= \begin{vmatrix} \Gamma & \beta/c & 0 & 0 \\ \Gamma\beta c & \Gamma & 0 & 0 \\ 0 & 0 & 1 & 0 \\ 0 & 0 & 0 & 1 \end{vmatrix} = \Gamma^2(1 - \beta^2) = 1. \quad (2.28)
 \end{aligned}$$

Thus

$$dV dt = dV' dt' = inv. \quad (2.29)$$

We now examine the transformation quantities of the momentum volume element

$$d^3 \vec{p}' = dp'_x dp'_y dp'_z = \left| \frac{\partial p'_x}{\partial p_x} \right| dp_x dp_y dp_z, \quad (2.30)$$

and show that the phase-space element $d^3 \vec{p}'/E$ is an invariant, noting that the perpendicular momentum components dp_y and dp_z are unchanged by a boost along the \hat{x} -axis. From eqs. (2.11) and (2.12),

$$\left| \frac{\partial p'_x}{\partial p_x} \right| = \Gamma - \beta\Gamma \left| \frac{\partial \gamma}{\partial p_x} \right| = \frac{\Gamma(\gamma - \beta p_x)}{\gamma} = \frac{\gamma'}{\gamma} = \frac{E'}{E}. \quad (2.31)$$

Note that $\gamma = \sqrt{1 + p^2} = \sqrt{1 + p_x^2 + p_y^2 + p_z^2}$, so that $\partial\gamma/\partial p_i = p_i/\gamma$ and $\partial\gamma/\partial p = p/\gamma$. Thus

$$\frac{d^3 \vec{p}}{E} = \frac{d^3 \vec{p}'}{E'} = inv \quad (2.32)$$

and

$$\frac{d^3 \vec{p}}{E} = \frac{p^2 dp d\Omega}{E} \rightarrow \epsilon d\epsilon d\Omega \quad (2.33)$$

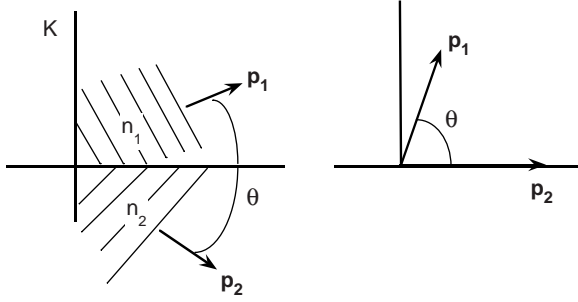


Figure 2.3 Sketch used to derive reaction rate between interacting particles or photons with stationary frame densities n_1 and n_2 .

is invariant, with the final expression applying to photons and relativistic particles.

Finally, we establish the invariance of the phase-space volume $d\mathcal{V} = d^3\vec{x}d^3\vec{p}$. Consider the invariant $d^3\vec{x}dt d^3\vec{p}/E = d\mathcal{V}dt/E$. From eq. (2.3), $dt = \Gamma dt'(1 + \beta\beta'_{\text{par},x})$. The reverse transformation of eq. (2.11) is $dE = \Gamma E'(1 + \beta\beta'_{\text{par},x})$. Thus $dt/E = dt'/E'$, which follows because dt/E is the ratio of parallel four-vectors [35].

2.5 RELATIVISTIC REACTION RATE

The relativistic reaction (or scattering) rate $\dot{n}_{\text{sc}} = dN/dV dt$ is defined as the number of collisions per unit volume per unit time between particle species “1” and “2” with masses m_1 and m_2 , respectively. Because the number of collisions dN and the product $dV dt$ are separately invariant quantities, the ratio \dot{n}_{sc} is also an invariant quantity.

Let the densities of species 1 and 2 in system K be denoted by n_1 and n_2 , respectively, as shown in figure 2.3. Due to length contraction, the densities in the proper system in which the particles are at rest are given by $n_i = \gamma_i n_i^0$, $i = 1, 2$, where $\gamma_i = (1 - \beta_i^2)^{-1/2}$ are the Lorentz factors of particles in K . Note that the density of particles is least in the proper frame. We consider for the moment particles of type i that all move with the same Lorentz factor. Transforming to the rest system of particle species 2 implies that the reaction rate in that system is

$$\dot{n}_{\text{sc}} = c\beta_r \sigma n_2^0 n_1', \quad (2.34)$$

where $c\beta_r$ is the relative speed of particles of type 1 in the rest system of particles of type 2, and $\sigma = \sigma(\gamma_r)$ is the scattering cross section. The quantity $\sigma(\gamma_r)$ is a function of the quantity $\gamma_r = (1 - \beta_r^2)^{-1/2}$, which is simply

the relative Lorentz factor of a particle of one type in the rest system of the other particle type, and as defined is obviously invariant. From our preceding considerations, $\gamma_r = p_1^\mu \cdot p_2^\mu / (m_1 m_2) = \gamma_1 \gamma_2 (1 - \vec{\beta}_1 \cdot \vec{\beta}_2)$, where p_i^μ is the four-momentum of particles of type i (eq. [2.10]). Thus

$$\beta_r = \left(\frac{(p_1^\mu \cdot p_2^\mu)^2 - m_1^2 m_2^2}{(p_1^\mu \cdot p_2^\mu)^2} \right)^{1/2}. \quad (2.35)$$

Note that $\beta_r = 1$ if either (or both) species are photons.

Let n'_1 be the density of species 1 as seen in the rest system of species 2. Therefore $n'_1 = \gamma_r n_1^0 = \gamma_r n_1 / \gamma_1$ and $n_2^0 = n_2 / \gamma_2$, implying $\dot{n}_{sc} = c \beta_r \sigma(\gamma_r) (1 - \vec{\beta}_1 \cdot \vec{\beta}_2) n_1 n_2$. This expression applies to two monoenergetic particle species each traveling in specific directions. In the general case, particles will have a distribution of directions and energies, so that it is necessary to integrate over the various directions and energies to calculate the total reaction rate. If the particle distributions are self-interacting, then the reaction rate must be multiplied by a factor of 1/2 to correct for double counting. Thus the reaction rate for two interacting distributions of particles is given by

$$\dot{n}_{sc} = \frac{c}{(1 + \delta_{12})} \int \dots \int \beta_r (1 - \vec{\beta}_1 \cdot \vec{\beta}_2) \sigma(\gamma_r) dn_1 dn_2 \quad (2.36)$$

[36, 37], where $\delta_{12} = 1$ for self-interacting particle distributions and $\delta_{12} = 0$ for interactions of different types of particles. Because of the invariance of \dot{n}_{sc} , eq. (2.36) equally gives the reaction rate in frame K , even though it was derived in the proper frame of particle species 2. Equation (2.36) is also valid for photon-particle interactions with $\beta_r \rightarrow 1$ and $\gamma_r \rightarrow \gamma_1 \epsilon (1 - \beta_1 \cos \theta_{12})$, and for photon-photon interactions with $\gamma_r \rightarrow \epsilon_1 \epsilon_2 (1 - \cos \theta_{12})$.

The differential spectral density

$$n(\vec{p}) = \frac{dn}{d^3 \vec{p}} = \frac{dn}{p^2 dp d\Omega}, \quad (2.37)$$

so that $dn = n(\vec{p}) p^2 dp d\Omega$ and $d\Omega = d\mu d\phi$. The momentum of a particle or photon of species i is denoted by \vec{p}_i . For particles, $p_i = \beta_i \gamma_i$, whereas $p_i = h\nu_i / m_e c^2 = \epsilon_i$ for photons. The general expression for the reaction rate is therefore given by

$$\begin{aligned} \dot{n}_{sc} = & \frac{c}{(1 + \delta_{12})} \oint d\Omega_1 \int_0^\infty dp_1 p_1^2 n_1(\vec{p}_1) \\ & \times \oint d\Omega_2 \int_0^\infty dp_2 p_2^2 n_2(\vec{p}_2) \beta_r (1 - \beta_1 \beta_2 \cos \psi) \sigma(\gamma_r). \end{aligned} \quad (2.38)$$

The invariant energy defining the collision strength is the relative Lorentz factor $\gamma_r = \gamma_1 \gamma_2 (1 - \beta_1 \beta_2 \cos \psi)$, and ψ is the angle between the directions

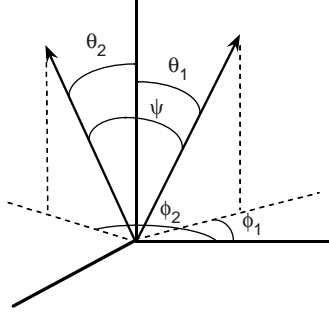


Figure 2.4 Angles in spherical geometry.

of the interacting particles or photons, given by

$$\cos \psi = \mu_1 \mu_2 + (1 - \mu_1^2)^{1/2} (1 - \mu_2^2)^{1/2} \cos(\phi_1 - \phi_2) \quad (2.39)$$

(figure 2.4), with $\mu_1 = \cos \theta_1$ and $\mu_2 = \cos \theta_2$.

Now consider the scattering rate \dot{N}_{sc} of a particle traversing a photon field. The distribution function for a single particle is $n_1(\vec{p}_1) = n_1 \delta(p - p_1) \delta(\mu_1 - 1) \delta(\phi_1) / (4\pi p_1^2)$, and eq. (2.38) implies

$$\dot{N}_{\text{sc}}(p_1) = \frac{\dot{n}_{\text{sc}}}{n_1} = c \int_0^{2\pi} d\phi \int_{-1}^1 d\mu (1 - \beta_1 \mu) \int_0^\infty d\epsilon n_{\text{ph}}(\epsilon, \Omega) \sigma(\epsilon_r), \quad (2.40)$$

where $n_{\text{ph}}(\epsilon, \Omega) = dN/dV d\epsilon d\Omega$ is the photon distribution function and $\epsilon_r = \gamma \epsilon (1 - \beta_1 \mu)$ is the invariant energy of the scattering event, which is also the photon energy in the rest frame of the particle. For photon-photon ($\gamma\gamma$) interactions of a photon with energy ϵ_1 passing through a gas of photons with energy ϵ , $\beta_1 \rightarrow 1$ and $\gamma_r \rightarrow \epsilon_r = \epsilon \epsilon_1 (1 - \mu)$. Thus the interaction rate of a photon with energy ϵ_1 passing through a background photon field $n(\epsilon, \Omega)$ is

$$\dot{N}_{\gamma\gamma}(\epsilon_1) = c \int_0^{2\pi} d\phi \int_{-1}^1 d\mu (1 - \mu) \int_0^\infty d\epsilon n_{\text{ph}}(\epsilon, \Omega) \sigma(\epsilon_r). \quad (2.41)$$

2.6 SECONDARY PRODUCTION SPECTRA

The calculation of secondary production spectra with momenta $\vec{p}_s = (p_s, \Omega_s)$ depends on knowledge of the differential cross section $d\sigma(p_1, \Omega_1, p_2, \Omega_2) / dp_s d\Omega_s$. In terms of differential densities, the results in the

previous section imply the number emissivity

$$\begin{aligned} \dot{n}_s(p_s, \Omega_s) &= \frac{dN_s}{dV dt dp_s d\Omega_s} = \frac{c}{1 + \delta_{12}} \oint d\Omega_1 \int_0^\infty dp_1 n_1(p_1, \Omega_1) \\ &\quad \times \oint d\Omega_2 \int_0^\infty dp_2 n_2(p_2, \Omega_2) \beta_r \cdot (1 - \beta_1 \beta_2 \cos \psi) \frac{d\sigma(\gamma_r)}{dp_s d\Omega_s} \end{aligned} \quad (2.42)$$

for the secondary production spectra.

The most common type of problem encountered in black-hole studies involves scattering of photons by relativistic ($p \approx \gamma \gg 1$) particles, for example, in treatments of Compton scattering and photomeson interactions. In this case, eq. (2.42) can be written as

$$\begin{aligned} \dot{n}_s(p_s, \Omega_s) &= c \oint d\Omega \int_0^\infty d\epsilon n_{\text{ph}}(\epsilon, \Omega) \oint d\Omega_{\text{par}} \\ &\quad \times \int_1^\infty d\gamma (1 - \beta_{\text{par}} \cos \psi) n_{\text{par}}(\gamma, \Omega_{\text{par}}) \frac{d\sigma(\epsilon, \Omega, \gamma, \Omega_{\text{par}})}{dp_s d\Omega_s}. \end{aligned} \quad (2.43)$$

If the particle distribution function $n_{\text{par}}(\gamma, \Omega_{\text{par}})$ is assumed to be isotropic, then $n_{\text{par}}(\gamma, \Omega_{\text{par}}) = n_{\text{par}}(\gamma)/4\pi$.

The emissivity for electron-photon scattering is given by the expression

$$\begin{aligned} j(\epsilon_s, \Omega_s) &= \frac{d\mathcal{E}}{dV dt d\epsilon_s d\Omega_s} \\ &= m_e c^2 \epsilon_s \dot{n}_s(\epsilon_s, \Omega_s) = c \epsilon_s \oint d\Omega \int_0^\infty d\epsilon \frac{u(\epsilon, \Omega)}{\epsilon} \\ &\quad \times \oint d\Omega_e \int_1^\infty d\gamma (1 - \beta_e \cos \psi) n_e(\gamma, \Omega_e) \frac{d\sigma(\epsilon, \Omega, \gamma, \Omega_e)}{d\epsilon_s d\Omega_s}, \end{aligned} \quad (2.44)$$

where the subscript “e” refers to the electron distribution. The specific spectral photon energy density $u(\epsilon, \Omega) = m_e c^2 \epsilon n_{\text{ph}}(\epsilon, \Omega)$ and scattering cosine angle

$$\cos \psi = \mu \mu_e + \sqrt{1 - \mu^2} \sqrt{1 - \mu_e^2} \cos(\phi - \phi_e), \quad (2.45)$$

from eq. (2.39).

Chapter Three

Introduction to Curved Spacetime

After a review of aspects of special relativity relevant to the discussion in this chapter, the notions of curved spacetime and geodesic motion are introduced. Schwarzschild spacetime and gravitational redshift are considered as examples. While we do rely heavily on the topics covered in Appendix A, the covariant derivative involved in geodesic motion is independently derived here from a variational principle. Good introductions to special and general relativity can also be found in [38], [39], and [40].

3.1 SPECIAL RELATIVITY

In relativity there is no unique way to separate space from time. Unlike classical physics, where we have three-dimensional vectors, in special relativity we consider four-vectors of the type

$$A^\mu = (A^0, A^1, A^2, A^3) \quad (3.1)$$

in a particular Minkowski coordinate system $\{x^0 = ct, x^1, x^2, x^3\}$. Here c is the speed of light. The vector A^μ is traditionally called a contravariant vector. The “dot” products of vectors are taken with the help of the Minkowski metric $\eta_{\mu\nu}$.

$$A \cdot B = \eta_{\mu\nu} A^\mu B^\nu \equiv \eta(A, B), \quad (3.2)$$

where

$$\eta_{\mu\nu} = \begin{bmatrix} -1 & 0 & 0 & 0 \\ 0 & 1 & 0 & 0 \\ 0 & 0 & 1 & 0 \\ 0 & 0 & 0 & 1 \end{bmatrix}. \quad (3.3)$$

Here A^μ and B^μ are the components of vectors A and B . We will also employ the following Einstein summation convention through out this book:

$$A_\mu B^\mu \equiv \sum_{\mu=0}^3 A_\mu B^\mu \quad (3.4)$$

for any two repeated indices with one index subscripted and the other superscripted. Consequently,

$$A \cdot B = -A^0 B^0 + \sum_{i=1}^3 A^i B^i. \quad (3.5)$$

In tensor notation,¹ the Minkowski metric becomes

$$\eta = -dx^0 \otimes dx^0 + dx^1 \otimes dx^1 + dx^2 \otimes dx^2 + dx^3 \otimes dx^3. \quad (3.6)$$

The canonical map between a tangent (contravariant) vector and its dual (covariant vector) is given by

$$A_0 = \eta_{0\mu} A^\mu = -A^0 \quad \text{and} \quad A_i = \eta_{i\mu} A^\mu = A^i. \quad (3.7)$$

Now consider a particle with mass m tracing out a curve

$$\alpha(\tau) = \{x^0(\tau), x^1(\tau), x^2(\tau), x^3(\tau)\}$$

in Minkowski spacetime. Its four-velocity is the tangent vector along the curve given by

$$u^\mu = \frac{dx^\mu}{d\tau}$$

such that $u^2 = \eta(u, u) = -1$. Therefore,

$$-1 = \frac{dt^2}{d\tau^2} (-c^2 + v^2). \quad (3.8)$$

Here $v^2 = \vec{v} \cdot \vec{v}$ where the three-vector

$$v^i = \frac{dx^i}{dt}$$

for $i = \{1, 2, 3\}$ is the usual three-velocity of the particle. Consequently,

$$\gamma \equiv c \frac{d\tau}{dt} = \frac{1}{\sqrt{1 - \beta^2}} \quad (3.9)$$

where $\vec{\beta} = \vec{v}/c$ is the dimensionless velocity. The four-velocity u^μ now takes the form

$$u^\mu = \gamma(1, \vec{v}/c). \quad (3.10)$$

¹The tensor product \otimes creates multilinear maps, for example,

$$dx^i \otimes dx^j(A, B) = A^i B^j,$$

for vectors A and B . For more details, see Appendix A.

The four-momentum p^μ of a particle with mass m is given by

$$p^\mu = m c^2 u^\mu = (m\gamma c^2, m\gamma\vec{v} c) = (E, \vec{p} c). \quad (3.11)$$

Here $E \equiv m\gamma c^2$ and $\vec{p} \equiv m\gamma\vec{v}$ are the energy and the three-momentum of the particle.

Massless particles such as photons, in quantum electrodynamics, have energy $\epsilon = h\nu$ and momentum $\vec{p} = \hbar\vec{k}$ such that $0 = -\epsilon^2 + c^2 p^2$. Therefore, the photon's four-momentum

$$k^\mu = (\epsilon, c\vec{p}) \quad (3.12)$$

is a constant null vector, since, while a photon may be created or annihilated, in its lifetime, the photon moves along a straight path at the speed of light with constant values of energy and momentum. Here, h is Planck's constant and $\hbar \equiv h/2\pi$. Also, ν and \vec{k} are the frequency and the wave vector of the photon. The observer who uses the Minkowski frame that we are in measures the energy of the photon to be

$$\epsilon = -\eta(k, \partial_t). \quad (3.13)$$

Here ∂_t is the four-velocity of the observer measuring the energy of the photon. Let us denote the four-velocity of an arbitrary observer by u ; then the energy ϵ of a photon with four-velocity k^μ as measured by this observer is given by

$$\epsilon = -\eta(k, u) = -\eta_{\mu\nu} k^\mu u^\nu. \quad (3.14)$$

It is easy to verify that the Minkowski metric is invariant under the following transformation:

$$\bar{x}^\mu = x^\mu + a^\mu. \quad (3.15)$$

Here, $a^\mu = \{a^0, a^1, a^2, a^3\}$ is any constant four-tuple. In addition to these space-time translations, there are other sets of transformations that leave eq. (3.6) invariant. The ordinary rotations of three-space represent one such set. Consider, for example, a rotation about the x^3 -axis given by

$$\bar{x}^\mu = R_\nu^\mu x^\nu, \quad (3.16)$$

where R_ν^μ is the matrix

$$\begin{bmatrix} 1 & 0 & 0 & 0 \\ 0 & \cos \theta & \sin \theta & 0 \\ 0 & -\sin \theta & \cos \theta & 0 \\ 0 & 0 & 0 & 1 \end{bmatrix}. \quad (3.17)$$

Throughout the book we use the convention that the upper indices refer to rows, and the lower indices refer to columns. Equation (3.16), and, in general, rotation about any arbitrary spatial axis will leave eq. (3.6) invariant.

In a similar manner, the usual Lorentz transformations leave the Minkowski metric invariant as well. In the case of a Lorentz boost along the x^3 -axis,

$$\bar{x}^\mu = \Lambda_\nu^\mu x^\nu, \quad (3.18)$$

where

$$\Lambda_\nu^\mu = \begin{bmatrix} \Gamma & 0 & 0 & -\Gamma\beta \\ 0 & 1 & 0 & 0 \\ 0 & 0 & 1 & 0 \\ -\Gamma\beta & 0 & 0 & \Gamma \end{bmatrix}. \quad (3.19)$$

Here

$$\Gamma = \frac{1}{\sqrt{1 - \beta^2}}.$$

Clearly, we want $0 \leq \beta^2 \leq 1$. The inverse of the above transformation is given by

$$[\Lambda^{-1}]_\nu^\mu = \begin{bmatrix} \Gamma & 0 & 0 & \Gamma\beta \\ 0 & 1 & 0 & 0 \\ 0 & 0 & 1 & 0 \\ \Gamma\beta & 0 & 0 & \Gamma \end{bmatrix}. \quad (3.20)$$

Coordinate transformations of tangent vectors are obtained from eq. (A.8), and under Lorentz transformations become

$$\frac{\partial \bar{x}^\mu}{\partial x^\nu} = \Lambda_\nu^\mu. \quad (3.21)$$

Similarly, the coordinate transformations of dual vectors are given by the inverse map

$$\frac{\partial x^\mu}{\partial \bar{x}^\nu} = [\Lambda^{-1}]_\nu^\mu. \quad (3.22)$$

We conclude our discussion of special relativity by writing down the covariant form of Maxwell's equations. In rationalized Heaviside-Lorentz units, Maxwell's equations are

$$\nabla \cdot D = \rho_c, \quad (3.23)$$

$$\nabla \cdot B = 0, \quad (3.24)$$

$$\partial_t B + \nabla \times E = 0, \quad (3.25)$$

$$-\partial_t D + \nabla \times H = J, \quad (3.26)$$

where ρ_c is the charge density and J is the electric three-current. Unless there are electric and magnetic susceptibilities, $E = D$ and $B = H$. The above equations can be written in a covariant form by defining the Maxwell tensor

$$F^{\mu\nu} = \begin{bmatrix} 0 & D^1 & D^2 & D^3 \\ -D^1 & 0 & H_3 & -H_2 \\ -D^2 & -H_3 & 0 & H_1 \\ -D^3 & H_2 & -H_1 & 0 \end{bmatrix} \quad (3.27)$$

and its dual,

$$*F^{\mu\nu} = \begin{bmatrix} 0 & -B^1 & -B^2 & -B^3 \\ B^1 & 0 & E_3 & -E_2 \\ B^2 & -E_3 & 0 & E_1 \\ B^3 & E_2 & -E_1 & 0 \end{bmatrix}. \quad (3.28)$$

It is easily see that the four Maxwell's equation can now be written in the form

$$\partial_\beta *F^{\alpha\beta} = 0 \quad (3.29)$$

and

$$\partial_\beta F^{\alpha\beta} = I^\alpha. \quad (3.30)$$

Here $I = (\rho_c, J^1, J^2, J^3)$. It is important to note that

$$*F^{\alpha\beta} \equiv \frac{1}{2} \epsilon^{\alpha\beta\mu\nu} F_{\mu\nu}, \quad (3.31)$$

where $\epsilon^{\alpha\beta\mu\nu}$ is the completely antisymmetric tensor such that $\epsilon^{0123} = -1$. Consequently, E , B , D , and H transform as the components of a tensor of type (0,2); we can think of these objects as three-vectors only after we fix a coordinate system.

3.2 CURVED SPACE/SPACETIME

Let us consider the simplest case of \mathfrak{N}^2 with coordinates $\{x, y\}$ and metric

$$g = dx \otimes dx + dy \otimes dy. \quad (3.32)$$

Let

$$\alpha(s) = (x(s), y(s))$$

be a curve from the point p_1 to p_2 . If we wished to compute the length of α , we would simply consider incremental lengths of the form

$$\Delta l = \sqrt{\Delta x^2 + \Delta y^2} = \Delta s \sqrt{\frac{\Delta x^2}{\Delta s^2} + \frac{\Delta y^2}{\Delta s^2}}. \quad (3.33)$$

The total, exact length of the curve can be obtained from the integral

$$l = \int ds \sqrt{\dot{x}^2 + \dot{y}^2}. \quad (3.34)$$

Here, the overdot refers to the ordinary derivative with respect to s . The above expression for the length of the curve can be written in the form

$$l = \int ds \sqrt{g_{ij} \dot{x}^i \dot{x}^j}. \quad (3.35)$$

Here, $x^1 = x$ and $x^2 = y$. While eq. (3.34) is applicable only in a Cartesian coordinate system, eq. (3.35) is a general expression valid in any coordinate system. The tangent vectors \dot{x}^i will transform according to eq. (A.8), while the metric g_{ij} will transform as a tensor of type (0,2) as given in eq. (A.25).

Now consider an arbitrary space with a given positive definite metric. The distance between any two points along a curve

$$\alpha(\tau) = (x^1(\tau), x^2(\tau), \dots, x^n(\tau)) \quad (3.36)$$

parameterized by τ is given by

$$l = \int d\tau \sqrt{g_{\mu\nu} \dot{x}^\mu \dot{x}^\nu}, \quad (3.37)$$

where μ, ν takes on values $1, 2, \dots, n$. This is nothing more than a generalization of eq. (3.35) to higher-dimensional spaces. The curve that minimizes the distance between two fixed points is referred to as a geodesic. It will be important for us to understand the nature of such curves. Clearly, such a curve would minimize the length in eq. (3.37). Minimizing eq. (3.37) is equivalent to minimizing

$$\frac{1}{2} \int g_{\mu\nu} \dot{x}^\mu \dot{x}^\nu d\tau.$$

In the usual formulation of variational mechanics, this is equivalent to choosing

$$\mathbf{L}(x, \dot{x}) = \frac{1}{2} g_{\mu\nu}(x) \dot{x}^\mu \dot{x}^\nu \quad (3.38)$$

as the Lagrangian. Geodesics are then curves generated by the Euler-Lagrange equation

$$\frac{d}{d\tau} \frac{\partial \mathbf{L}}{\partial \dot{x}^\mu} - \frac{\partial \mathbf{L}}{\partial x^\mu} = 0.$$

Consequently, along geodesics

$$\frac{d}{d\tau} g_{\mu\nu} \dot{x}^\nu - \frac{1}{2} (\partial_\mu g_{\alpha\beta}) \dot{x}^\alpha \dot{x}^\beta = 0. \quad (3.39)$$

But

$$\frac{d}{d\tau} g_{\mu\nu} \dot{x}^\nu = g_{\mu\nu} \ddot{x}^\nu + (\partial_\alpha g_{\mu\nu}) \dot{x}^\alpha \dot{x}^\nu.$$

Therefore, from eq. (3.39) and above we get

$$g_{\mu\nu} \ddot{x}^\nu + (\partial_\alpha g_{\mu\nu}) \dot{x}^\alpha \dot{x}^\nu - \frac{1}{2} (\partial_\mu g_{\alpha\beta}) \dot{x}^\alpha \dot{x}^\beta = 0.$$

This can be written in a more symmetric form as

$$g_{\mu\nu} \ddot{x}^\nu + \frac{1}{2} \{ \partial_\alpha g_{\mu\beta} + \partial_\beta g_{\mu\alpha} - \partial_\mu g_{\alpha\beta} \} \dot{x}^\alpha \dot{x}^\beta = 0.$$

Therefore,

$$\ddot{x}^\lambda + \Gamma_{\alpha\beta}^\lambda \dot{x}^\alpha \dot{x}^\beta = 0 \quad (3.40)$$

since $g^{\lambda\mu} g_{\mu\nu} = \delta_\nu^\lambda$. Here, by definition, the Christoffel symbol

$$\Gamma_{\alpha\beta}^\lambda = \frac{1}{2} g^{\lambda\mu} \{ \partial_\alpha g_{\mu\beta} + \partial_\beta g_{\mu\alpha} - \partial_\mu g_{\alpha\beta} \}. \quad (3.41)$$

Equation (3.40) is the geodesic equation. The parameter τ is referred to as an *affine parameter*.

Geodesic tangent vectors satisfy the important property that

$$\frac{d}{d\tau} [g_{\mu\nu}(x) \dot{x}^\mu \dot{x}^\nu] = 0. \quad (3.42)$$

Therefore $g_{\mu\nu}(x) \dot{x}^\mu \dot{x}^\nu = \text{const}$ along geodesics. To see this, note that

$$\begin{aligned} \frac{d}{d\tau} [g_{\mu\nu}(x) \dot{x}^\mu \dot{x}^\nu] &= \dot{x}^\mu \dot{x}^\nu \dot{x}^\alpha \partial_\alpha g_{\mu\nu} + g_{\mu\nu} \dot{x}^\nu \ddot{x}^\mu + g_{\mu\nu} \dot{x}^\mu \ddot{x}^\nu \\ &= \dot{x}^\mu \dot{x}^\nu \dot{x}^\alpha \partial_\alpha g_{\mu\nu} + g_{\mu\nu} [-\Gamma_{\alpha\beta}^\mu \dot{x}^\alpha \dot{x}^\beta \dot{x}^\nu - \Gamma_{\alpha\beta}^\nu \dot{x}^\alpha \dot{x}^\beta \dot{x}^\mu] \\ &= \dot{x}^\mu \dot{x}^\nu \dot{x}^\alpha \partial_\alpha g_{\mu\nu} - 2g_{\lambda\nu} \Gamma_{\alpha\beta}^\lambda \dot{x}^\alpha \dot{x}^\beta \dot{x}^\nu. \end{aligned}$$

Here we have changed a dummy variable in the last term above. The expression for $\Gamma_{\alpha\beta}^\lambda$ can be substituted in from above to obtain

$$\begin{aligned} \frac{d}{d\tau} [g_{\mu\nu}(x) \dot{x}^\mu \dot{x}^\nu] &= \dot{x}^\mu \dot{x}^\nu \dot{x}^\alpha \partial_\alpha g_{\mu\nu} - 2g_{\lambda\nu} \dot{x}^\alpha \dot{x}^\beta \dot{x}^\nu \frac{1}{2} g^{\lambda\mu} \\ &\quad \times \{ \partial_\alpha g_{\mu\beta} + \partial_\beta g_{\mu\alpha} - \partial_\mu g_{\alpha\beta} \} \\ &= \dot{x}^\mu \dot{x}^\nu \dot{x}^\alpha \partial_\alpha g_{\mu\nu} - \dot{x}^\alpha \dot{x}^\beta \dot{x}^\nu \{ \partial_\alpha g_{\nu\beta} + \partial_\beta g_{\nu\alpha} - \partial_\nu g_{\alpha\beta} \} = 0, \end{aligned}$$

as required.

In general relativity, the expression for the metric is not fixed, and is obtained by solving the Einstein equation. Suppose we know the metric. In a fixed background geometry, the motion of a particle can be described by a curve α in a general four-dimensional spacetime. Explicitly,

$$\alpha(\tau) = (x^0(\tau), x^1(\tau), x^2(\tau), x^3(\tau)). \quad (3.43)$$

Here, as τ varies, the curve α traces out the path taken by the particle. We use a coordinate label like x^0 , to indicate that it is a time coordinate, i.e.,

$$g_{00} < 0,$$

just as in special relativity. The tangent vector to the curve α is given by

$$u^\mu(\tau) = \dot{x}^\mu(\tau),$$

where the overdot represents the derivative with respect to τ . When gravitation is the only interaction affecting a particle, we refer to it as a *free particle*. The equation of motion of a free particle is given by the geodesic equation (eq. [3.40]). Free particles with mass must have speed less than c , and are therefore represented by timelike geodesics. In contrast, massless particles travel along null geodesics. For null geodesics

$$g_{\mu\nu}(x) \dot{x}^\mu \dot{x}^\nu = 0.$$

Therefore, in general relativity, we will treat a massless particle as an object with a worldline along null geodesics such that its momentum four-vector k^μ (as in special relativity) is the tangent vector

$$k^\mu = \dot{x}^\mu. \quad (3.44)$$

Also, *the energy ϵ of a photon with four-velocity k^μ as measured by an observer with four-velocity u^ν is*

$$\epsilon = -g(k, u) = -g_{\mu\nu} k^\mu u^\nu. \quad (3.45)$$

This is the general relativistic version of eq. (3.14). The only modification is in the explicit form of the metric. General particle motions are described by curves in spacetime. For particles with mass, we will pick the parameter τ so that the tangent $u^\mu = dx^\mu/d\tau$ of its worldline α satisfies

$$g_{\mu\nu} u^\mu u^\nu = -1.$$

We further require that u^μ is future pointing. The resulting tangent vector is the *four-velocity* of the particle. The parameter τ measures the *proper time* elapsed. The acceleration a^μ of a particle that is subject to a “nongravitational” force is given by

$$a^\mu = \ddot{x}^\mu + \Gamma_{\alpha\beta}^\mu \dot{x}^\alpha \dot{x}^\beta. \quad (3.46)$$

Clearly, a free particle has $a^\mu = 0$. The force F^μ on a particle is defined in the usual way,

$$F^\mu = ma^\mu. \quad (3.47)$$

3.3 THE SCHWARZSCHILD METRIC

In the presence of a massive, static, nonrotating object, the spacetime geometry deforms to

$$\begin{aligned}
 ds^2 = & - \left(1 - \frac{2M}{r}\right) dt \otimes dt + \frac{1}{(1 - 2M/r)} dr \otimes dr \\
 & + r^2(d\theta \otimes d\theta + \sin^2\theta d\varphi \otimes d\varphi).
 \end{aligned} \tag{3.48}$$

Here we have set c and the gravitational constant G to unity. This is the famous Schwarzschild solution [41]. For a modern derivation and analysis of this solution, see [42]. The coordinates are (t, r, θ, φ) . The parameter M represents the mass of the black hole and is solely responsible for “curving” the spacetime. As $M \rightarrow 0$, the Schwarzschild metric reduces to the Minkowski metric in a spherical coordinate system. At $r = 2M$, the Schwarzschild metric is singular since g_{rr} becomes undefined. It turns out that this singularity is unphysical as can be shown by a change in coordinate system. However, $r = 2M$ locates the position of the event horizon. The region $r < 2M$ is the interior region of the black hole that the Schwarzschild metric describes. The singularity at $r = 0$ is the true physical singularity of the spacetime and cannot be removed by a coordinate transformation. As we shall see below, the Schwarzschild metric can be obtained from the Kerr metric in the limit that the angular momentum parameter $a \rightarrow 0$. All of the singularity properties of the Schwarzschild geometry mentioned above will be explained in the context of the Kerr geometry (which is more general than the present case). For now, let us focus on the exterior geometry, i.e., $r > 2M$. In order to understand the geodesic motion of a particle in Schwarzschild geometry, we will compute the nontrivial Christoffel symbols. From eq. (3.41) we find that

$$\Gamma_{10}^0 = \frac{1}{2} g^{00} \partial_r g_{00}.$$

Therefore

$$\Gamma_{10}^0 = \frac{1}{2} f', \tag{3.49}$$

where

$$f(r) = \ln \left(1 - \frac{2M}{r}\right) \quad \text{and} \quad f' = \frac{df}{dr}.$$

In a similar manner we see that the nonzero, independent Christoffel symbols are

$$\begin{aligned}\Gamma_{00}^1 &= \frac{1}{2} f' e^{2f}, & \Gamma_{11}^1 &= -\frac{1}{2} f', & \Gamma_{22}^1 &= -r e^f, & \Gamma_{33}^1 &= -r \sin^2 \theta e^f, \\ \Gamma_{12}^2 &= \frac{1}{r} = \Gamma_{13}^3, & \Gamma_{33}^2 &= -\sin \theta \cos \theta, & \text{and} & \Gamma_{23}^3 &= \cot \theta.\end{aligned}\tag{3.50}$$

The geodesic equation of motion for the t -coordinate is given by

$$\ddot{t} + \Gamma_{01}^0 \dot{t} \dot{r} + \Gamma_{10}^0 \dot{r} \dot{t} = 0,\tag{3.51}$$

i.e.,

$$\ddot{t} + f' \dot{t} \dot{r} = 0.\tag{3.52}$$

The equations of motion for the other coordinates can be found in the same way. They are

$$\ddot{r} + \frac{1}{2} f' e^{2f} \dot{t}^2 - \frac{1}{2} f' \dot{r}^2 - r e^f \dot{\theta}^2 - r \sin^2 \theta e^f \dot{\phi}^2 = 0,\tag{3.53}$$

$$\ddot{\theta} + \frac{2}{r} \dot{\theta} \dot{r} - \cos \theta \sin \theta \dot{\phi}^2 = 0,\tag{3.54}$$

and

$$\ddot{\phi} + \frac{2}{r} \dot{\phi} \dot{r} + 2 \cot \theta \dot{\phi} \dot{\theta} = 0.\tag{3.55}$$

Just as in the classical mechanics of the two-body problem, if initially $\theta = \pi/2$ and $\dot{\theta} = 0$, then from eq. (3.54) we see that $\ddot{\theta} = 0$, and so the geodesic continues to stay in the $\theta = \pi/2$ plane. But, due to spherical symmetry, any plane can be relabeled as $\theta = \pi/2$. Therefore, for convenience, and without any loss of generality, we will consider geodesics in only the equatorial plane. Then, eq. (3.52) and eq. (3.55) can be easily integrated to give

$$\dot{t} = \frac{E}{1 - 2M/r}\tag{3.56}$$

and

$$\dot{\phi} = \frac{L}{r^2}.\tag{3.57}$$

Here E and L are integral constants of motion proportional to the energy and angular momentum of the particle moving along such geodesics as measured by an observer at infinity. This inference is made by looking at the behavior of the geodesics at large values of r , and comparing it to its counterpart in classical mechanics.

Consider a static observer near the black hole at some fixed $r = r_1$. Such an observer has four-velocity

$$u_1 = \frac{1}{\sqrt{(1 - 2M/r_1)}} \partial_t.$$

Suppose this observer were to send a photon (along a null geodesic) with four-momentum k^μ , then from eq. (3.45), the frequency of the emitted photon is

$$h\nu_1 = -g(k, u_1) = -g_{00} u_1^0 \dot{t} = \frac{E}{\sqrt{1 - 2M/r_1}}. \quad (3.58)$$

Here, ν_1 is the photon frequency at $r = r_1$. This photon, if received by another observer at $r = r_2$, has a frequency

$$h\nu_2 = \frac{E}{\sqrt{1 - 2M/r_2}} \quad (3.59)$$

since E is constant along the geodesic. Therefore,

$$\frac{\nu_1}{\nu_2} = \frac{\sqrt{1 - 2M/r_2}}{\sqrt{1 - 2M/r_1}}. \quad (3.60)$$

Thus, the frequency of the received photon decreases as it moves away from the black hole. This is an example of gravitational redshift.

Chapter Four

Physical Cosmology

In this chapter, we forsake rigor in the interests of brevity [43]. The Robertson-Walker metric for an isotropic, homogeneous universe is derived from simple arguments. A Newtonian derivation of the motion of a gravitating fluid element leads to equations for Friedmann cosmologies relating proper-frame emission time t_* to redshift z . We deduce the luminosity and angular-diameter distances for flat cosmological models, yielding equations suitable for analyzing the statistics of cosmological black-hole sources, and for deriving the intensity from unbeamed and beamed sources.

4.1 ROBERTSON-WALKER METRIC

In flat or Minkowski spacetime, a photon follows a null geodesic defined by $ds^2 = 0$, where the invariant interval is

$$\begin{aligned} ds^2 &= \eta_{\mu\nu} dx^\mu dx^\nu = -c^2 dt^2 + dx^2 + dy^2 + dz^2 = -c^2 dt^2 + d\vec{r}^2 \\ &= -c^2 dt^2 + dr^2 + r^2(d\theta^2 + \sin^2\theta d\phi^2) = -c^2 dt^2 + dr^2 + r^2 d\Omega. \end{aligned} \tag{4.1}$$

In the final two expressions of this equation, the metric is expressed in polar coordinates. Consider a homogeneous, isotropic universe. In this case, the angular dependence of the metric can be neglected, and the metric can be treated in a $3 + 1$ geometry of three spatial dimensions and one temporal dimension representing constant proper-frame time. For these time-orthogonal coordinates, the coefficients of the metric tensor are $g_{00} = -1$, and the off-diagonal elements $g_{0i} = g_{i0} = 0$ for $i = 1, 2, 3$.

Because of the assumptions of homogeneity and isotropy, we can without loss of generality consider a radial geodesic given by $ds^2 = -c^2 dt^2 + dr^2 = c^2 dt'^2$. Here t' is equal to the proper time of a particle that follows a timelike path with $ds^2 < 0$; such paths apply to events connected by time within the light cone (see figure 4.1). Material particles follow timelike world lines. Events with $ds^2 > 0$ are spacelike, that is, events that are not causally connected. Particles at rest have $dt' = dt$, and dt then represents the proper-frame time interval.

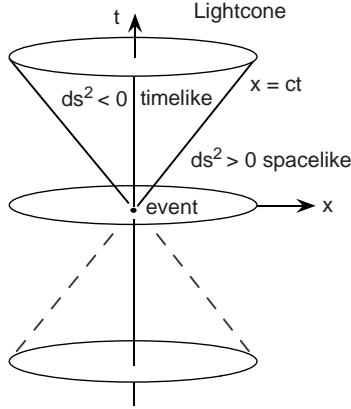


Figure 4.1 Light cone in Minkowski spacetime.

The Robertson-Walker metric for an isotropic, homogeneous world model can be derived for three-dimensional curved space by considering the analogous situation in two dimensions. Light follows a null geodesic defined by $ds^2 = -c^2 dt^2 + dx^2 + dy^2 = 0$ on a two-dimensional (2d) surface. If the surface is curved, then the equation for photon propagation is subject to the auxiliary condition $x^2 + y^2 + z^2 = \mathcal{R}^2$, where $\mathcal{R}(t)$ is the radius of curvature of the surface at time t (and cannot depend on x, y, z by the homogeneity assumption).

By analogy, photon propagation in $3 + 1$ spacetime satisfies $ds^2 = -c^2 dt^2 + dx^2 + dy^2 + dz^2 = 0$, subject to the auxiliary condition $x^2 + y^2 + z^2 + \omega^2 = r^2 + \omega^2 = \mathcal{R}^2$, where ω is a fourth spatial dimension. This condition implies $\omega = \sqrt{\mathcal{R}^2 - r^2}$, so that $d\omega = -r dr / \sqrt{\mathcal{R}^2 - r^2}$ and the squared distance interval

$$d\ell^2 = dx^2 + dy^2 + dz^2 + d\omega^2 = d\vec{r}^2 + \frac{r^2 dr^2}{\mathcal{R}^2 - r^2}. \quad (4.2)$$

From eq. (4.1),

$$d\ell^2 = \frac{dr^2}{1 - r^2/\mathcal{R}^2} + r^2 d\Omega^2,$$

so that

$$ds^2 = -c^2 dt^2 + \left(\frac{dr^2}{1 - (r/\mathcal{R})^2} + r^2 d\Omega^2 \right). \quad (4.3)$$

The Robertson-Walker metric can be rewritten in the form

$$ds^2 = -c^2 dt^2 + R^2(t) \left(\frac{d\chi^2}{1 - k\chi^2} + \chi^2 d\Omega^2 \right), \quad (4.4)$$

where the comoving radial coordinate $\chi = r/R(t)$, which has physical units, is introduced. Objects such as stars and galaxies reside on comoving coordinates. Variations in the distance between objects fixed in the Hubble flow are a consequence of changes in the dimensionless expansion scale factor $R(t)$. If we establish the convention that $R(t) = R = 1$ at the present epoch, then χ is the physical (proper) distance between objects at the present epoch t .

Particles or galaxies with fixed χ are separated by a distance that is determined only by the time variation of the scale factor $R(t)$. The curvature of space is determined by the curvature index k ; $k = +1/\mathcal{R}_0^2$ is a space of positive (spherical) curvature or a closed universe; $k = -1/\mathcal{R}_0^2$ is a space of negative (hyperbolic) curvature or an open universe; and $k = 0$ in flat space. Here \mathcal{R}_0 is the radius of curvature at the present epoch.

Photons cannot be confined to a fixed comoving coordinate. By choosing coordinates with the radial vector outward from the observer, the proper-frame time element dt_* in spacetime for a photon traveling from comoving coordinate $\chi = r$ at time t_* to $\chi = 0$ at the present epoch t is given by $c dt_* = -R(t_*) d\chi \equiv R_* d\chi$ (as the distance between the photon and the observer decreases, time increases; thus the negative sign). The proper-frame time required for transit from emission (starred) to reception (unstarred) coordinates in expanding spacetime is therefore

$$c \int_{t_*}^t \frac{d\bar{t}}{R(\bar{t})} = - \int_r^0 \frac{d\chi}{\sqrt{1 - k\chi^2}}. \quad (4.5)$$

Now imagine an event taking place Δt_* later. This event is detected at a later time $t + \Delta t$ where, for emission and reception occurring from a source on fixed comoving coordinates,

$$c \int_{t_* + \Delta t_*}^{t + \Delta t} \frac{dt'}{R(t')} = - \int_r^0 \frac{d\chi}{\sqrt{1 - k\chi^2}}. \quad (4.6)$$

Because $R(t_*)$ hardly changes between the two events separated by a small interval of time (for example, the times between two wave crests), eq. (4.6) implies

$$\frac{\Delta t}{R(t)} = \frac{\Delta t_*}{R(t_*)} \quad \text{or} \quad \Delta t = \frac{R}{R_*} \Delta t_* = (1 + z) \Delta t_*.$$

Making use of the definition

$$z = \frac{\lambda - \lambda_*}{\lambda_*} = \frac{v_*}{v} - 1$$

for the redshift (obviously, this z is different from the coordinate z), we have

$$\frac{R}{R_*} = 1 + z \quad (4.7)$$

and

$$\frac{\nu_*}{\nu} = \frac{\epsilon_*}{\epsilon} = \frac{\Delta t}{\Delta t_*} = 1 + z \quad (4.8)$$

(e.g., [44]). Combined with eqs. (2.15) and (2.25),

$$\epsilon = \frac{\delta_D \epsilon'}{1 + z} \quad (4.9)$$

and

$$dt = \frac{(1 + z) dt'}{\delta_D}. \quad (4.10)$$

4.2 FRIEDMANN MODELS

A cosmological model giving the time dependence of the scale factor $R(t)$ is needed to give an expression from which fluxes and intensities of cosmological sources can be derived. Models for homogeneous and isotropic static and expanding universes are known as Friedmann world models. Although a rigorous derivation of these equations finds solutions of Einstein's field equations, we give here simplified derivations that recover the important relations. For more detail, see Refs. [45–47].

4.2.1 Hubble Relation from the Cosmological Principle

The cosmological principle is that the universe is isotropic and homogeneous on sufficiently large scales, and that there is no preferred location. This principle is sufficient to obtain the Hubble relation that velocity is proportional to distance [48], treating the universe as a moving fluid.

Consider two observers at O and O' who measure the fluid speed of matter in the universe, as shown in figure 4.2. The two observers will measure the same speed of the fluid at P ; thus

$$\vec{v}(\vec{r}) = \vec{v}'(\vec{r}'), \quad (4.11)$$

where the unprimed and primed quantities \vec{v} and \vec{v}' refer to observations made at O and O' , respectively. The cosmological principle of isotropy means that measurements of the velocity of the flow at O in the direction \vec{r}' will give the same result as measurements at O' in the direction \vec{r}' . Thus

$$\vec{v}(\vec{r}') = \vec{v}'(\vec{r}') = \vec{v}(\vec{r} - \vec{u}), \quad (4.12)$$

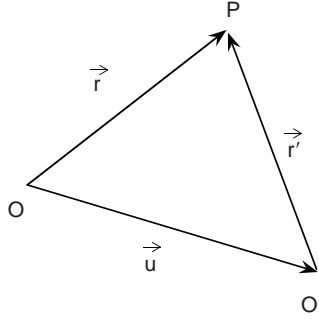


Figure 4.2 Geometry for deriving the Hubble relation from the cosmological principle.

using the relation $\vec{r}' = \vec{r} - \vec{u}$. Taking the time derivative of this vector relation gives $d\vec{r}'/dt = d\vec{r}/dt - d\vec{u}/dt$. Therefore

$$\vec{v}'(\vec{r}') = \vec{v}(\vec{r}) - \vec{v}(\vec{u}) = \vec{v}(\vec{r}') = \vec{v}(\vec{r} - \vec{u}). \quad (4.13)$$

This expression implies a linear relation between velocity and distance of the form $\vec{v}(\vec{r}) = H(t)\vec{r} = d\vec{r}/dt$. Hence

$$H(t) = \frac{1}{\vec{r}} \frac{d\vec{r}}{dt} = \frac{dR(t)/dt}{R(t)}, \quad (4.14)$$

recalling the definition of $\vec{r} = R(t)\chi\hat{r}$ in terms of the scale factor $R(t)$ and the comoving coordinate χ . The Hubble “constant” at time t_* is $H(t_*) = \dot{R}(t_*)/R(t_*) = \dot{R}_*/R_*$, and H_0 is the Hubble constant of the present epoch.

The variation of fluid density $\rho(t)$ in a homogeneous, isotropic universe satisfies the mass conservation $\dot{\rho} + \nabla \cdot (\rho\vec{v}) = 0$. With $\vec{v} = H(t)\vec{r}$, $\dot{\rho} = -3\rho H(t)$,

$$\rho(t) = \frac{\rho_0}{R^3(t)}, \quad (4.15)$$

and ρ_0 is the fluid density at the present epoch.

4.2.2 Expansion of the Universe

We provide a Newtonian derivation for the expansion of the universe. Consider the motion of a fluid element in our universe. Assuming that the fluid element is large enough that the universe is homogeneous and isotropic on this size scale, Euler’s equation for the motion of the fluid is

$$\frac{D\vec{v}}{Dt} + \frac{1}{\rho}\vec{\nabla}p - \vec{F} = 0, \quad (4.16)$$

where p and \vec{F} are the pressure and force on the fluid element, respectively. Employing Eulerian coordinates, with \vec{r} fixed in space and therefore time-independent, $D\vec{v}/Dt = \partial\vec{v}/\partial t + \vec{v} \cdot \nabla\vec{v} = \dot{H}\vec{r} + H(x\partial/\partial x + y\partial/\partial y + z\partial/\partial z)H(x\hat{x} + y\hat{y} + z\hat{z}) = (\dot{H} + H^2)\vec{r}$. Contrariwise, we could employ Lagrangian coordinates that move with the fluid, namely, comoving coordinates $\vec{r} = R\chi\hat{r}$. In this case, the total derivative becomes the time derivative, so that $D\vec{v}/Dt = d\vec{v}/dt = d(HR\chi\hat{r})/dt = \dot{H}R\chi\hat{r} + H\dot{R}\chi\hat{r} = (\dot{H} + H^2)\vec{r}$, giving the same result.

In a homogeneous universe, $\vec{\nabla}p = 0$. The expansion of the universe is counteracted by gravitational force on the expanding fluid that comprises the universe. The gravitational force per unit mass $\vec{F}_g = -GM\hat{r}/r^2$, where G is the gravitational constant. The mass contained within radius r is $M = 4\pi r^3\rho(t)/3$, and $\rho(t)$ is the mean mass density of the universe at epoch t . Hence

$$\vec{F}_g = -\frac{4\pi G}{3}\rho(t)\vec{r} = (\dot{H} + H^2)\vec{r} \quad (4.17)$$

in a pressureless universe. Taking the divergence of both sides gives $\dot{H} + H^2 = -4\pi G\rho(t)/3$. The relations $\dot{H} + H^2 = \ddot{R}/R$ and $\rho(t) = \rho_0/R^3$, where ρ_0 is the mean density at the present epoch, imply

$$R^2\ddot{R} = -\frac{4\pi}{3}G\rho_0. \quad (4.18)$$

All time dependence is found in the left-hand side of eq. (4.18).

An examination of eq. (4.18) shows that a steady-state solution can be found by adding a force term of the form

$$\vec{F} = -\frac{4\pi G}{3}\rho(t)\vec{r} + \frac{1}{3}\Lambda\vec{r}, \quad (4.19)$$

where the cosmological constant $\Lambda = 4\pi G\rho_0$ in order to get $\rho(t) = \rho_0$, independent of time. This reasoning suggests that we add a term to the density to give a repulsive force by letting $\rho \rightarrow \rho - \Lambda/4\pi G$. Hence $\ddot{R}/R = -4\pi G\rho_0/(3R^3) + \Lambda/3$, which can be integrated to give

$$\left(\frac{\dot{R}}{R}\right)^2 = \frac{8\pi G\rho(t)}{3} + \Lambda - \frac{kc^2}{R^2}. \quad (4.20)$$

The additive constant k in the integration defining the curvature of space was introduced in eq. (4.4).

The expansion scale factor $R(z) = R_0/(1+z)$; thus $R^{-1}(dR/dz) = -1/(1+z)$, and $H = \dot{R}/R = R^{-1}(dR/dz)(dz/dt) = -(dz/dt)/(1+z)$, so that

$$\frac{dt}{dz} = \frac{-1}{(1+z)H(z)}. \quad (4.21)$$

Equation (4.20) can be rewritten [46] as

$$\frac{\dot{R}}{R} = H(t) = H(z) = H_0 \sqrt{\Omega_m(1+z)^3 + \Omega_k(1+z)^2 + \Omega_\Lambda}, \quad (4.22)$$

where $H_0 = 100h \text{ km s}^{-1} \text{ Mpc}^{-1}$ is Hubble's constant, and the dimensionless density parameter associated with the mass density ρ_0 at the present epoch is given by

$$\Omega_m = \frac{8\pi G\rho_0}{3H_0^2}. \quad (4.23)$$

This term takes into account baryonic mass, cold and hot dark matter, and neutrinos. The terms

$$\Omega_\Lambda = \frac{\Lambda}{3H_0^2} \quad (4.24)$$

and

$$\Omega_k = \frac{-kc^2}{H_0^2} \quad (4.25)$$

define dimensionless density parameters for the cosmological constant and curvature densities. The dimensionless densities obey the relation $\Omega_m + \Omega_\Lambda + \Omega_k = 1$.

The condition $\Omega_m = 1$ defines a critical density

$$\rho_{cr} = \frac{3H_0^2}{8\pi G} = 1.88 \times 10^{-29} h^2 \text{ g cm}^{-3}, \quad (4.26)$$

where the Hubble constant

$$H_0 = 100h \text{ km s}^{-1} \text{ Mpc}^{-1} = 3.2404 \times 10^{-18} h \text{ s}^{-1} \cong \frac{h}{10 \text{ Gyr}}. \quad (4.27)$$

If uniformly distributed as hydrogen atoms, the critical density would be $n_{\text{H}} = 1.1 \times 10^{-5} h^2 \text{ H atoms per cm}^3$. If the normal matter content of the universe is only $\approx 5\%$ of the critical density, than the volume-averaged density of hydrogen would be proportionately smaller (compare eq. [4.23]).

From eq. (4.22), we have that

$$\frac{dt_*}{dz} = \frac{-1}{H_0(1+z)\sqrt{\Omega_m(1+z)^3 + \Omega_k(1+z)^2 + \Omega_\Lambda}}. \quad (4.28)$$

Here we have replaced t by t_* , because we will be using this equation to define the relation between proper-frame time t_* and z .

4.2.3 Einstein–de Sitter Universe

The simplest expanding-universe cosmology is the flat Einstein–de Sitter universe with no cosmological constant; thus $\Omega_\Lambda = \Omega_k = 0$ and $\Omega_m = 1$. From eq. (4.20), $\dot{R}/R \propto R^{-3/2}$ or $R^{1/2}dR \propto dt$. Hence $R(t) \propto t^{2/3}$. The Hubble constant $H(t) = \dot{R}/R = 2/3t$, so that $H_0 = 2/3t_0$. Thus $R_0/R = 1 + z = (t_0/t)^{2/3}$, and $t = t_0/(1 + z)^{3/2}$. Differentiating this expression, noting that $dt/dz = -3t_0/[2(1 + z)^{5/2}] = -1/[H_0(1 + z)^{5/2}]$, gives

$$\frac{dt_*}{dz} = \frac{-1}{H_0(1 + z)^{5/2}} \quad (4.29)$$

for the Einstein–de Sitter universe. Equation (4.29) can also be obtained directly from eq. (4.28).

4.2.4 Universe with Zero Cosmological Constant

This universe was favored before evidence for acceleration of the universe was discovered. In this cosmology, $\Omega_\Lambda = 0$ and $\Omega_m + \Omega_k = 1$, so that

$$\frac{dt_*}{dz} = \frac{-1}{H_0(1 + z)^2\sqrt{1 + \Omega_m z}}. \quad (4.30)$$

Equation (4.20) for $R(t)$ can be written in the form

$$\dot{R}^2 = H_0^2 \left[\Omega_m \left(\frac{1}{R} - 1 \right) + 1 \right]. \quad (4.31)$$

In the future $R \gg 1$, this expression becomes $\dot{R}^2 \rightarrow H_0^2(1 - \Omega_m)$. If $\Omega_m < 1$, the universe is open and continues to expand. If $\Omega_m > 1$, then expansion stops when $R = 1/(1 - \Omega_m^{-1})$, eventually causing the universe to collapse to a point. When $\Omega_m = 1$, we recover the Einstein–de Sitter universe.

4.2.5 Flat Universe

A flat universe ($\Omega_k = 0$) satisfies a number of fundamental problems, requiring that the universe went through an episode of rapid exponential inflation early in the history of the universe. For a flat universe, $\Omega_m + \Omega_\Lambda = 1$. Hence eq. (4.28) becomes

$$\frac{dt_*}{dz} = \frac{-1}{H_0(1 + z)\sqrt{\Omega_m(1 + z)^3 + \Omega_\Lambda}} \quad (4.32)$$

for a flat cosmology, with $\Omega_\Lambda = 1 - \Omega_m$. Note that $\Omega_m(1 + z)^3 + \Omega_\Lambda = (1 + \Omega_m z)(1 + z)^2 - \Omega_\Lambda(2z + z^2)$. The *Wilkinson Microwave Anisotropy Probe* (WMAP) results show that $h = 0.72 \pm 0.05$ [49] and $\Omega_\Lambda = 0.73$ [50]. The measurements are consistent with a flat universe.

4.3 LUMINOSITY AND ANGULAR-DIAMETER DISTANCES

To avoid unnecessary complications, only a flat universe is considered. The proper distance, though not directly measurable, is the distance between two objects that would be measured at the same time t . The proper distance at the present epoch is therefore just the comoving coordinate, so

$$d_{\text{prop}} = \chi = ct = c \int_0^{\chi/c} dt = c \int_0^z dz' \left| \frac{dt_*}{dz'} \right| (1 + z'). \quad (4.33)$$

The propagation distance

$$d_{\text{ppgn}} = c \int_{t_{*1}}^{t_{*2}} dt_* = c \int_0^z dz' \left| \frac{dt_*}{dz'} \right| \quad (4.34)$$

gives the distance traveled by an UHECR to reach us at the present epoch for comparison with energy-loss distances.

The energy flux for a source isotropically radiating luminosity $L = d\mathcal{E}/dt$ at proper distance d_{prop} is related to the energy flux from a source with isotropic luminosity $L_* = d\mathcal{E}_*/dt_*$ at luminosity distance d_L through the relation

$$\Phi = \frac{d\mathcal{E}}{dAdt} = \frac{d\mathcal{E}/dt}{4\pi d_{\text{prop}}^2} = \frac{d\mathcal{E}_*/dt_*}{4\pi d_L^2}. \quad (4.35)$$

The fluence $\mathcal{F}_\gamma = \int_{t_1}^{t_2} dt \Phi(t)$ measured over some time interval $t_1 - t_2$ is therefore related to the apparent isotropic energy release through the expression

$$\mathcal{E}_* = \frac{4\pi d_L^2 \mathcal{F}_\gamma}{1 + z}. \quad (4.36)$$

For an expanding universe, $d\mathcal{E}_* = \epsilon_* dN = \epsilon(1+z)dN = (1+z)d\mathcal{E}$ and $dt_* = dt/(1+z)$. Thus $d\mathcal{E}/dt = (1+z)^{-2}(d\mathcal{E}_*/dt_*)$, and

$$d_L = d_L(z) = (1+z)d_{\text{prop}} = \frac{c}{H_0} (1+z) \int_0^z dz' \frac{1}{\sqrt{\Omega_m(1+z')^3 + \Omega_\Lambda}} \quad (4.37)$$

for a flat universe. For a flat universe with zero cosmological constant, $\Omega_m = 1$ and $\Omega_\Lambda = 0$, so

$$d_L = \frac{2c}{H_0} (1+z - \sqrt{1+z}). \quad (4.38)$$

The lowest-order redshift correction to eq. (4.37), with $H_0 = 72 \text{ km s}^{-1} \text{ Mpc}^{-1}$, is

$$d_L \cong \frac{cz}{H_0} \left[1 + z \left(1 - \frac{3\Omega_m}{4} \right) + \mathcal{O}(z^2) \right], \quad (4.39)$$

so

$$d_L \cong 4160z(1 + 0.8z) \text{ Mpc}, \quad z \ll 1.$$

This approximation is within 2% of the numerical result for $z \leq 0.25$. Expressions for d_L in a Friedmann universe with positive and negative curvature are given in [51]. The expansion of the universe reduces the energy flux by two powers of the scale-factor ratio $R/R_* = (1+z)$ related to changes of time and energy between emitter and receiver. This has the effect of increasing the luminosity distance d_L by one power of $(1+z)$ over the proper distance.

We now obtain the relation between the angular diameter distance d_A and d_L . Consider a physical object at redshift z with transverse proper dimension D . The measured angle ϑ of the source is given in terms of D and the distance $R_*\chi$, referred to emission time t_* . Thus $d_A = D/\vartheta = R_*\chi$. Suppose a cosmological source radiates with isotropic luminosity $L_* = d\mathcal{E}_*/dt_*$. From the definition of d_L , the energy flux

$$\Phi = \frac{d\mathcal{E}}{dAdt} = \frac{L_*}{4\pi d_L^2} = \frac{dA}{4\pi d_L^2} \left| \frac{d\mathcal{E}_*}{d\mathcal{E}} \right| \left| \frac{dt}{dt_*} \right| \frac{d\mathcal{E}}{dAdt} = \frac{(1+z)^2 dA}{4\pi d_L^2} \Phi. \quad (4.40)$$

Therefore $dA = R^2\chi^2 d\Omega = 4\pi d_L^2/(1+z)^2$. At emission time t_* , $dA_* = R_*^2\chi^2 d\Omega_*$, and $dA = R^2\chi^2 d\Omega$, so that $dA_*/dA = 1/(1+z)^2$. This implies from the definition of the luminosity distance, letting $d\Omega = d\Omega_*$, that

$$d_L = \left(\frac{R}{R_*} \right)^2 (R_*\chi) = (1+z)^2 d_A. \quad (4.41)$$

Figure 4.3 shows d_L and d_A as a function of z for the flat Λ cold dark matter (Λ CDM) universe with parameters from *WMAP*.¹ In this model, d_A reaches a maximum and then declines with increasing z . Thus the angular diameters of objects with fixed D may become larger with increasing d_L .

4.4 EVENT RATE OF BURSTING SOURCES

The directional event rate, or event rate per sr, is

$$\frac{d\dot{N}}{d\Omega} = \frac{1}{4\pi} \int dV_* \dot{n}_*(t_*) \left| \frac{dt_*}{dt} \right| = c \int_0^\infty dz \left| \frac{dt_*}{dz} \right| \frac{(R_*\chi)^2 \dot{n}_*(z)}{(1+z)}, \quad (4.42)$$

where the burst emissivity $\dot{n}_*(z)$ gives the rate density of events at redshift z . From eq. (4.41),

$$(R_*\chi)^2 = \frac{d_L^2(z)}{(1+z)^4}, \quad (4.43)$$

¹See Ned Wright's cosmology calculator at www.astro.ucla.edu/~wright/CosmoCalc.html.

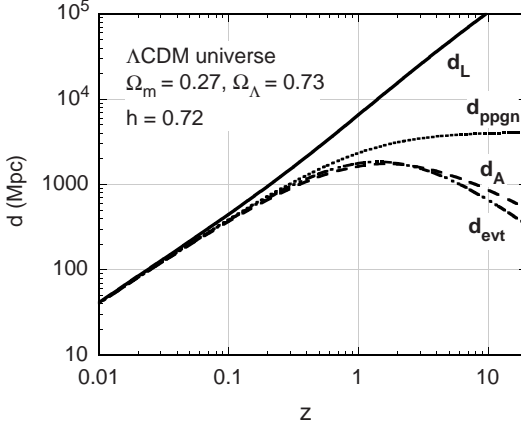


Figure 4.3 Luminosity distance d_L (eq. [4.41]), angular-diameter distance d_A (eq. [4.41]), propagation distance d_{ppgn} (eq. [4.34]), and event rate distance d_{evt} (eq. [4.46]) as a function of redshift z for standard Λ CDM cosmological parameters.

and we use eq. (4.32) for a flat Λ CDM universe. By considering the volume element in physical and comoving coordinates, one sees that constant comoving density implies that the proper density increases with redshift proportionally to $(1+z)^3$. Hence the volume density in comoving and proper coordinates is related by the expression

$$\dot{n}_*(\epsilon_*; z) = \dot{n}_{\text{co}}(\epsilon_*; z)(1+z)^3. \quad (4.44)$$

In terms of the comoving event rate $\dot{n}_{\text{co}}(z)$, the directional event rate, eq. (4.42), becomes

$$\frac{d\dot{N}}{d\Omega} = c \int_0^\infty dz \left| \frac{dt_*}{dz} \right| \frac{d_L^2(z) \dot{n}_{\text{co}}(z)}{(1+z)^2} \equiv \frac{c}{H_0} \int_0^\infty dz d_{\text{evt}}^2(z) \dot{n}_{\text{co}}(z), \quad (4.45)$$

where the event-rate distance

$$d_{\text{evt}}(z) = \frac{d_L(z)}{1+z} \sqrt{H_0 \left| \frac{dt_*}{dz} \right|} = \frac{d_L(z)}{(1+z)^{3/2} [\Omega_m(1+z)^3 + \Omega_\Lambda]^{1/4}} \quad (4.46)$$

is plotted as a function of z in figure 4.3.

If separability between the emission properties and the rate density of sources can be assumed, then $\dot{n}_{\text{co},i}(z) = \dot{n}_i \Sigma_i(z)$, where $\Sigma_i(z)$ is the structure formation history (SFH) of sources of type i . This is defined so that $\Sigma_i(z \ll 1) = 1$, and \dot{n}_i is the local ($z \ll 1$) rate density of bursting sources of type i .

The comoving density can be formally expanded as

$$\dot{n}_{\text{co}}(z) = \oint d\bar{\Omega} \int_0^\infty d\alpha N(\alpha; z) \int d\cdots \dot{n}_{\text{co}}(\bar{\Omega}, \alpha, \cdots; z) \quad (4.47)$$

[52,53]. The direction $\bar{\Omega} = (\bar{\mu} = \cos\bar{\theta}, \bar{\phi})$ specifies the orientation of the system with respect to the direction to the observer, and $N(\alpha; z)$ is a normalized distribution function for parameter α . For example, α could represent the bulk Lorentz factor Γ , the total energy radiated, the comoving-frame power, or the spectral index of the radiation. For sources oriented at random, $\dot{n}_{\text{co}}(\bar{\Omega}, \alpha, \cdots; z) = \dot{n}_{\text{co}}(\alpha, \cdots; z)/4\pi$. For two-sided jet sources, $-1 \leq \bar{\mu} \leq 1$ and $\dot{n}_{\text{co}}(\bar{\Omega}, \alpha, \cdots; z) = 2\dot{n}_{\text{co}}(\alpha, \cdots; z)/4\pi$.

If one considers persistent rather than bursting sources, an analogous derivation gives the directional number count of sources of the type i as

$$\frac{dN_i}{d\bar{\Omega}} = cn_i \int_0^\infty dz \left| \frac{dt_*}{dz} \right| \frac{d_L^2(z) \Sigma_i(z)}{(1+z)}. \quad (4.48)$$

After substituting eq. (4.47) into eq. (4.45) and placing limits on the integrals in accordance with detector specifications, model distributions of source properties can be derived.

4.5 FLUX AND INTENSITY FROM DISTRIBUTED SOURCES

Consider the problem of the intensity of radiation received from sources distributed uniformly in space and time, though with an emissivity that could, in general, depend on cosmic time t_* or redshift z . This problem applies to truly diffuse sources, or when the emissions from many sources are superposed as a result of the large field of view and limited imaging capabilities of a detector. The intensity of electron-positron annihilation or dark matter annihilation radiation is an example of this type of problem, though it could also apply to the intensity arising from the superposition of the radiation from many sources.

The photon number flux (units of $\text{cm}^{-2} \text{s}^{-1} \epsilon^{-1}$) from a cosmologically distant point source is given by $\phi(\epsilon) = dN/dAdtd\epsilon$, where ϵ represents the frequency or energy of the radiation, and $dN = \phi(\epsilon)dAdtd\epsilon$ is the differential number of photons or relativistic particles with dimensionless energies ϵ between ϵ and $\epsilon + d\epsilon$ that pass through differential area dA oriented normal to the source during the reception time interval between t and $t + dt$. The invariant differential number of photons or neutrinos radiated by a source at redshift z is given by

$$dN = \dot{n}_*(\epsilon_*, \bar{\Omega}_*; z) d\epsilon_* dt_* dV_* d\bar{\Omega}_*,$$

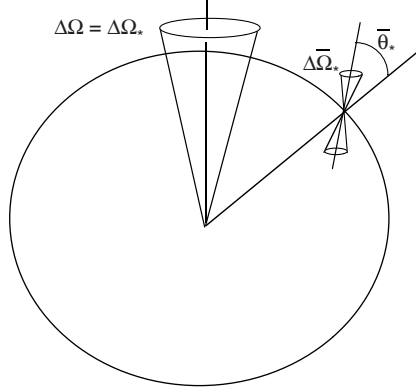


Figure 4.4 Calculation of intensity within opening angle $\Delta\Omega = \Delta\Omega_*$ for cosmological sources. If the sources are beamed, then an integration over direction $\bar{\Omega}_*$ of the source emissivity is required.

where $\dot{n}_*(\epsilon_*, \bar{\Omega}_*; z)$ ($\text{cm}^{-3} \text{s}^{-1} \epsilon_*^{-1} \text{sr}^{-1}$) is the directional photon emissivity as illustrated in figure 4.4. (The overdot always refers to the differential of proper-frame time, that is, d/dt_* .) This flux can be normalized to the mean luminosity density

$$\dot{\epsilon}(z) = \frac{d\mathcal{E}_*}{dV_* dt_*} = m_e c^2 \oint d\bar{\Omega}_* \int_0^\infty d\epsilon_* \epsilon_* \dot{n}_*(\epsilon_*, \bar{\Omega}_*; z) \quad (4.49)$$

of sources at redshift z .

For a spatial distribution of optically thin, isotropically emitting sources, the differential unattenuated radiation flux is therefore given by

$$d\phi(\epsilon) = \frac{\dot{n}_*(\epsilon_*, \bar{\Omega}_*; z) d\epsilon_* dt_* dV_* d\bar{\Omega}_*}{dAdt d\epsilon}. \quad (4.50)$$

The volume element $dV = dr(r d\theta)(r \sin\theta d\phi)$. Because $r = R(t)\chi$, we can therefore write, using the Robertson-Walker metric, eq. (4.4), specialized to a flat universe, the differential volume element at the present epoch as $dV = R^3 \chi^2 d\chi d\Omega$, where $d\Omega = \sin\theta d\theta d\phi$. The volume element at emission time t_* is $dV_* = R_*^3 \chi^2 d\chi d\Omega_*$. The area element at reception time t is $dA = R^2 \chi^2 d\Omega$ with $R = 1$. Note also that $cdt_* = R_* d\chi$. In a homogeneous isotropic expanding universe, $d\Omega = d\Omega_*$. Thus

$$d\phi(\epsilon) = \dot{n}_*(\epsilon_*; z) \left| \frac{d\epsilon_*}{d\epsilon} \right| \left| \frac{dt_*}{dt} \right| \left(\frac{R_*}{R} \right)^2 dt_* = \dot{n}_*(\epsilon_*; z) \left(\frac{R_*}{R} \right)^2 dt_*. \quad (4.51)$$

Therefore

$$\phi(\epsilon) = c \oint d\bar{\Omega}_* \int_0^\infty dz \left| \frac{dt_*}{dz} \right| \frac{\dot{n}_*(\epsilon_*, \bar{\Omega}_*; z)}{(1+z)^2}. \quad (4.52)$$

If the sources are unbeamed, $\dot{n}_*(\epsilon_*, \bar{\Omega}_*; z) = n_*(\epsilon_*; z)/4\pi$, and

$$\phi(\epsilon) = c \int_0^\infty dz \left| \frac{dt_*}{dz} \right| \frac{\dot{n}_*(\epsilon_*; z)}{(1+z)^2} \quad (4.53)$$

for isotropically emitting sources. The principal cosmological unknown in this expression is the relation between proper-frame time t_* and z , which depends on the assumed cosmology. The factor $(1+z)^{-2}$ represents the decreased flux due to the increased area that the photons pass through as the universe expands.

The intensity

$$I_\epsilon = m_e c^2 \epsilon \frac{d\phi(\epsilon)}{d\Omega} = \frac{m_e c^3}{4\pi} \int_0^\infty dz \left| \frac{dt_*}{dz} \right| \frac{\epsilon_* \dot{n}_*(\epsilon_*; z)}{(1+z)^3}, \quad (4.54)$$

and the “ νF_ν ” energy intensity

$$\epsilon I_\epsilon = \frac{m_e c^3}{4\pi} \int_0^\infty dz \left| \frac{dt_*}{dz} \right| \frac{\epsilon_*^2 \dot{n}_*(\epsilon_*; z)}{(1+z)^4}. \quad (4.55)$$

The photon emissivity $\dot{n}_*(\epsilon_*; z)$, the energy emissivity $m_e c^2 \epsilon_* \dot{n}_*(\epsilon_*; z)$, and the (spectral) luminosity density $m_e c^2 \epsilon_*^2 \dot{n}_*(\epsilon_*; z)$ are related to the luminosity density given by eq. (4.49). From eq. (4.44), $\dot{n}_*(\epsilon_*; z) = \dot{n}_{\text{co}}(\epsilon_*; z) (1+z)^3$, where $\dot{n}_{\text{co}}(\epsilon_*; z)$ is the photon emissivity per unit comoving volume. The same dependence $\propto (1+z)^3$ holds for the energy emissivity and luminosity density when referred to density expressed in physical and comoving coordinates. For sources where beaming is important, eq. (4.55) becomes

$$\epsilon I_\epsilon = \frac{m_e c^3}{4\pi} \int_0^\infty dz \left| \frac{dt_*}{dz} \right| \oint d\bar{\Omega}_* \frac{\epsilon_*^2 \dot{n}_{\text{co}}(\epsilon_*, \bar{\Omega}_*; z)}{1+z}. \quad (4.56)$$

The “ νF_ν ” intensity $\epsilon I_\epsilon = m_e c^2 \epsilon^2 \phi(\epsilon)/4\pi$ for unbeamed sources is given by

$$\epsilon I_\epsilon = \frac{m_e c^3}{4\pi} \int_0^\infty dz \left| \frac{dt_*}{dz} \right| \frac{\epsilon_*^2 \dot{n}_{\text{co}}(\epsilon_*; z)}{1+z}. \quad (4.57)$$

These equations give the intensity of truly diffuse emissions, or the intensity from the superposition of unresolved sources. The source emissivity can be assumed to follow the star formation rate history of the universe, as considered for UHECRs in chapter 9.

Chapter Five

Radiation Physics of Relativistic Flows

Elementary concepts to analyze and transform radiation fields are introduced. The properties of the Planck blackbody function are derived. The results are applied to two geometries used to treat relativistic outflows from black-hole jet sources, namely, the blob geometry consisting of a relativistic spherical ball of radiating plasma, and a relativistic spherical shell geometry. The essential equivalence of the two geometries to infer properties of relativistic flows is demonstrated.

5.1 RADIATION PRELIMINARIES

The intensity I_ϵ is defined such that $I_\epsilon d\epsilon dA dt d\Omega$ is the infinitesimal energy $d\mathcal{E}$ in photons with energy between ϵ and $\epsilon + d\epsilon$ lying within solid angle element $d\Omega$ that pass through area element dA oriented normal to the direction $\vec{\Omega}$ during differential time dt . The intensity is a local quantity; thus $I_\epsilon = I_\epsilon(\vec{x}, t)$. Other than polarization, I_ϵ provides a complete description of the radiation field. The specific spectral energy density $u(\epsilon, \Omega) = d\mathcal{E}/dV d\epsilon d\Omega$. By following a pencil beam of rays contained within differential volume $dV = c dt dA$, we see that $d\mathcal{E} = u(\epsilon, \Omega) dV d\epsilon d\Omega = u(\epsilon, \Omega) c dt dA d\epsilon d\Omega = I_\epsilon dA dt d\epsilon d\Omega$, so that

$$I_\epsilon = cu(\epsilon, \Omega). \quad (5.1)$$

Consider a pencil beam of radiation, as shown in figure 5.1, passing through area elements $dA_1 \cos \theta_1$ and $dA_2 \cos \theta_2$ separated by distance d and oriented at angles θ_1 and θ_2 , respectively, to the direction of the rays [54]. If there is no absorption or emission of photons during propagation, then energy conservation of the radiation beam passing through dA_1 and dA_2 during time dt means that $d\mathcal{E} = I_{\epsilon,1} dA_1 \cos \theta_1 dt d\Omega_1 d\epsilon_1 = I_{\epsilon,2} dA_2 \cos \theta_2 dt d\Omega_2 d\epsilon_2$. The bundle of rays passing through dA_2 lies within solid angle element $d\Omega_1 = dA_2 \cos \theta_2 / d^2$ as seen from the location of dA_1 ; likewise, the rays passing through dA_1 lie within the solid angle element $d\Omega_2 = dA_1 \cos \theta_1 / d^2$ as seen from the location of dA_2 . For constant energy rays (no cosmological redshifting, which can be treated separately), $\epsilon_1 = \epsilon_2 = \epsilon$. Thus $I_{\epsilon,1} = I_{\epsilon,2}$ or $dI_\epsilon/ds = 0$.

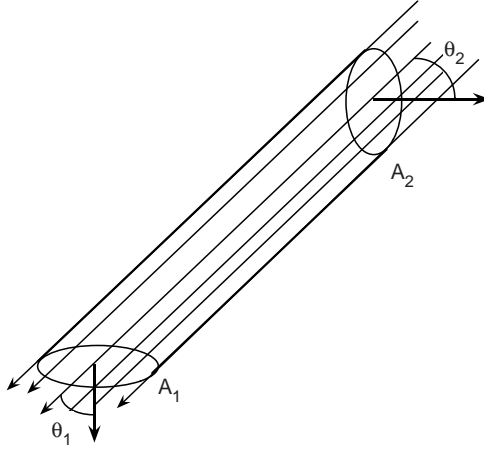


Figure 5.1 Pencil beam of rays passing through area elements A_1 and A_2 separated by distance d and oriented at angles θ_1 and θ_2 with respect to the photon direction, defined by the limit of infinitesimal area elements dA_1 and dA_2 .

Effects of absorption or emission on the evolution of the intensity over differential path length ds are described by the equation of radiative transfer, given by

$$\frac{dI_\epsilon}{ds} = -\kappa_\epsilon I_\epsilon + j(\epsilon, \Omega) \quad \text{or} \quad \frac{dI_\epsilon}{d\tau_\epsilon} = -I_\epsilon + \mathcal{S}_\epsilon. \quad (5.2)$$

Here $j(\epsilon, \Omega) = d\mathcal{E}/dV dt d\epsilon d\Omega$ is the emissivity, and the differential optical depth $\tau_\epsilon = \kappa_\epsilon ds$ is defined in terms of the spectral absorption coefficient κ_ϵ (units of inverse length). The source function

$$\mathcal{S}_\epsilon = \frac{j(\epsilon, \Omega)}{\kappa_\epsilon}. \quad (5.3)$$

The quantity $F(\epsilon) = \int_{\Omega_s} \mu I_\epsilon d\Omega$ is the spectral energy flux ($d\mathcal{E}/dAdtd\epsilon$) of radiation measured from a source subtending solid angle element Ω_s . This quantity describes the net rate of energy flow through area element dA with normal \hat{n} oriented at an angle $\mu = \hat{n} \cdot \hat{\Omega}$ with respect to rays traveling in the direction $\hat{\Omega}$. The net energy flux $F(\epsilon) = \oint d\Omega \mu I_\epsilon$ vanishes for radiation fields that can be expanded in even powers of μ . The net flux of an isotropic radiation field is zero.

Because the momentum of a photon is $h\nu/c$, the differential momentum flux on an area element with normal \hat{n} is p_ϵ (dynes $\text{cm}^{-2} \epsilon^{-1}$) = $c^{-1} \oint d\Omega \mu^2 I_\epsilon$. One factor of μ is from the projection of the area element, and the second is from the component of momentum along \hat{n} . Although I_ϵ is

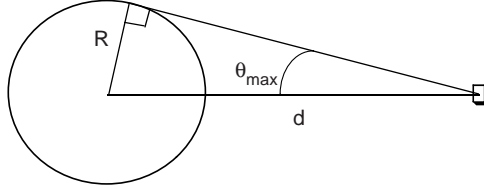


Figure 5.2 Flux received at distance d from a sphere with radius R and uniform brightness \mathcal{B} .

a positive quantity, p_ϵ can be negative if the net momentum flux is directed opposite to \hat{n} . The total radiation pressure is

$$p = c^{-1} \int_0^\infty d\epsilon \oint d\Omega \mu^2 I_\epsilon.$$

The mean intensity $\bar{I}_\epsilon = (4\pi)^{-1} \oint d\Omega I_\epsilon = cu(\epsilon)/4\pi$, and $u(\epsilon) = \oint d\Omega u(\epsilon, \Omega)$ is the spectral energy density of radiation. Thus $u(\epsilon) = 4\pi \bar{I}_\epsilon/c$. The total radiation energy density $u = \int_0^\infty d\epsilon u(\epsilon) = (4\pi/c) \int_0^\infty d\epsilon \bar{I}_\epsilon$. The radiation pressure for an isotropic radiation field with mean intensity $\bar{I}_\epsilon^{\text{iso}}$ is $p = c^{-1} \int_0^\infty d\epsilon \oint d\Omega \mu^2 \bar{I}_\epsilon^{\text{iso}} = (4\pi/3c) \int_0^\infty d\epsilon \bar{I}_\epsilon^{\text{iso}}$. From the definition of u , we have

$$p = u/3 \quad (5.4)$$

for an isotropic radiation field, valid also for the relation between the pressure and energy density of an isotropic relativistic particle distribution.

The νF_ν energy flux ($d\mathcal{E}/dAdt$, cgs units of ergs $\text{cm}^{-2} \text{s}^{-1}$) is

$$f_\epsilon = \epsilon F(\epsilon) = \epsilon \int_{\Omega_s} d\Omega \mu I_\epsilon, \quad (5.5)$$

where the integration is over the solid angle subtended by the source. The bolometric energy flux is

$$\Phi = \int_0^\infty d\epsilon F(\epsilon) = \int_0^\infty d\epsilon \int_{\Omega_s} d\Omega \mu I_\epsilon, \quad (5.6)$$

where the integration is over the solid angle Ω_s subtended by the source.

Consider the case of the energy flux from a uniform brightness sphere of radius R (figure 5.2). Here $I_\epsilon = \mathcal{B}_\epsilon$, independent of Ω , and $\mathcal{B} = \int_0^\infty d\epsilon \mathcal{B}_\epsilon$. The total energy flux at distance d from the sphere is

$$\Phi = \int_0^\infty d\epsilon \int_{\Omega_s} d\Omega \mu \mathcal{B}_\epsilon = 2\pi \mathcal{B} \int_{\sqrt{1-R^2/d^2}}^1 \mu d\mu = \pi \frac{\mathcal{B}R^2}{d^2}.$$

Thus the energy flux at the surface of a uniform brightness sphere is $\pi \mathcal{B}$.

5.2 INVARIANT QUANTITIES

The elementary invariants are the invariant four-volume $d^3\vec{x}dt = dVdt$, the invariant phase-space element $d^3\vec{p}/E$, and the invariant phase volume $d\mathcal{V} = d^3\vec{x}d^3\vec{p}$ (chapter 2). Because the number N of particles or photons is invariant,

$$\frac{dN}{d\mathcal{V}} = \frac{1}{p^2} \frac{dN}{dV dp d\Omega} \Rightarrow \frac{1}{\epsilon^2} \frac{dN}{dV d\epsilon d\Omega} = \frac{1}{m_e c^2 \epsilon^3} \frac{d\mathcal{E}}{dV d\epsilon d\Omega} \equiv \frac{1}{\epsilon^3} \frac{u(\epsilon, \Omega)}{m_e c^2}, \quad (5.7)$$

where the latter three expressions apply to photons and relativistic particles. From eq. (5.7), we see that

$$\frac{u(\epsilon, \Omega)}{\epsilon^3} = \frac{u'(\epsilon', \Omega')}{\epsilon'^3} = \text{inv.} \quad (5.8)$$

Because $u(\epsilon, \Omega) = I_\epsilon/c$, I_ϵ/ϵ^3 is also invariant.

The function

$$E \frac{dN}{d^3\vec{x}dt d^3\vec{p}} = \frac{1}{\epsilon^2} \frac{d\mathcal{E}}{dV dt d\epsilon d\Omega} \equiv \frac{1}{\epsilon^2} j(\epsilon, \Omega) \quad (5.9)$$

is invariant, noting that the last two expressions apply to photons and relativistic particles. The invariance of $\epsilon^{-3}I_\epsilon$ and $\epsilon^{-2}j(\epsilon, \Omega)$ shows, from eq. (5.2), that $\epsilon\kappa_\epsilon$ is invariant.

Let $N(\epsilon, \Omega)d\epsilon d\Omega$ represent the differential number of photons or relativistic particles with dimensionless energy between ϵ and $\epsilon + d\epsilon$ that are directed into differential solid angle interval $d\Omega$ in the direction $\vec{\Omega}$ of some physical volume. Because the total number of photons or particles is invariant, so also is the quantity

$$\frac{dN}{\epsilon d\epsilon d\Omega} = \frac{N(\epsilon, \Omega)}{\epsilon}, \quad (5.10)$$

using eq. (2.33).

5.3 BLACKBODY RADIATION FIELD

By enumerating wave modes in a blackbody cavity populated according to Boltzmann statistics, one obtains the Planck blackbody radiation formula. It is worthwhile to recall its derivation.

The average energy in wave modes populated according to Boltzmann statistics is, letting $x = e^{-h\Delta U/k_B T}$,

$$\begin{aligned} \langle U \rangle &= \frac{\sum_{n=0}^{\infty} n \Delta U e^{-n\Delta U/k_B T}}{\sum_{n=0}^{\infty} e^{-n\Delta U/k_B T}} = \Delta U \frac{\sum_{n=0}^{\infty} n x^n}{\sum_{n=0}^{\infty} x^n} = \Delta U (1-x)x \sum_{n=0}^{\infty} n x^{n-1} \\ &= \Delta U x (1-x) \frac{d}{dx} \left(\frac{1}{1-x} \right) = \frac{\Delta U}{x^{-1} - 1} = \frac{h\nu}{e^{h\nu/k_B T} - 1}, \end{aligned} \quad (5.11)$$

where the energy $\Delta U = h\nu$ in a mode of frequency ν , according to Planck's quantum hypothesis.

The wavenumber $k = 2\pi/\lambda = 2\pi\nu/c$ for a wave with wavelength λ and frequency ν . The density of modes of wavenumber k is

$$\frac{dN_k}{dV} = 2 \frac{4\pi k^2 dk}{(2\pi)^3} = \frac{8\pi \nu^2 d\nu}{c^3} \quad (5.12)$$

imposing periodic boundary conditions on the volume of a cube, and multiplying by a factor of 2 for two polarization modes. The energy density of the standing waves in a blackbody is therefore

$$\frac{\Delta \mathcal{E}}{dV} = \langle U \rangle \frac{dN_k}{dV} = \frac{8\pi h\nu^3}{c^3} \frac{d\nu}{\exp(-h\nu/k_B T) - 1}. \quad (5.13)$$

Hence the blackbody intensity ($d\mathcal{E}/dAdtd\nu d\Omega$) is

$$I_\nu^{\text{bb}}(T) = \frac{2h\nu^3}{c^2 [\exp(h\nu/k_B T) - 1]}. \quad (5.14)$$

Rewritten using dimensionless photon energy, the blackbody intensity is

$$\begin{aligned} cu_{\text{bb}}(\epsilon, \Omega; \Theta) &= I_\epsilon^{\text{bb}}(\Theta) = \frac{2m_e c^3 \epsilon^3}{\lambda_C^3 [\exp(\epsilon/\Theta) - 1]} \\ &\rightarrow \frac{2m_e c^3}{\lambda_C^3} \begin{cases} \epsilon^2 \Theta, & \epsilon \ll \Theta, & \text{Rayleigh-Jeans regime,} \\ \epsilon^3 \exp(-\epsilon/\Theta), & \epsilon \gg \Theta, & \text{Wien regime,} \end{cases} \end{aligned} \quad (5.15)$$

where $\lambda_C = h/m_e c = 2.42 \times 10^{-10}$ cm is the electron Compton wavelength, and $\Theta = k_B T/m_e c^2$ is the dimensionless temperature of the radiation field. The spectral photon density ($dN/dV d\epsilon$) of blackbody radiation is

$$n^{\text{bb}}(\epsilon; \Theta) = \frac{4\pi u^{\text{bb}}(\epsilon, \Omega)}{m_e c^2 \epsilon} = \frac{4\pi}{m_e c^3 \epsilon} I_\epsilon^{\text{bb}} = \frac{8\pi}{\lambda_C^3} \frac{\epsilon^2}{\exp(\epsilon/\Theta) - 1}. \quad (5.16)$$

For the CMBR,

$$\Theta = \Theta(z) = \frac{k_B T(z)}{m_e c^2} = \Theta_0(1+z) \cong 4.58 \times 10^{-10} (1+z) \left(\frac{T}{2.72 \text{ K}} \right), \quad (5.17)$$

and the temperature of the CMBR at the present epoch is 2.72 K. The density of photons of a blackbody radiation field is

$$\begin{aligned} n_{\text{CMB}}(\Theta) &= \int_0^\infty d\epsilon n_{\text{CMB}}(\epsilon; \Theta) \\ &= \frac{8\pi \Theta^3}{\lambda_C^3} \Gamma(3)\zeta(3) \cong 407(1+z)^3 \left(\frac{T}{2.72 \text{ K}} \right)^3 \text{ cm}^{-3}, \end{aligned} \quad (5.18)$$

where $\Gamma(n)$ is the Gamma function and $\zeta(n)$ is the Riemann zeta function (Appendix B). The mean photon energy of a blackbody radiation field is

$$\begin{aligned} \langle \epsilon_{\text{CMB}}(\Theta) \rangle &= \frac{\int_0^\infty d\epsilon \epsilon^3 / [\exp(\epsilon/\Theta) - 1]}{\int_0^\infty d\epsilon \epsilon^2 / [\exp(\epsilon/\Theta) - 1]} \\ &= \frac{\Gamma(4)\zeta(4)}{\Gamma(3)\zeta(3)} \Theta \cong 2.70\Theta \cong 1.24 \times 10^{-9} (1+z) \left(\frac{T}{2.72 \text{ K}} \right), \end{aligned} \quad (5.19)$$

so that the mean frequency of a CMBR photon at the present epoch is ≈ 150 GHz.

The energy density of a blackbody radiation field is

$$\begin{aligned} u_{\text{CMB}}(\Theta) &= \frac{4\pi}{c} \int_0^\infty d\epsilon I_\epsilon^{\text{CMB}}(\Theta) = \frac{8\pi^5 m_e c^2}{15 \lambda_C^3} \Theta^4 \\ &= 4.14 \times 10^{-13} (1+z)^4 \left(\frac{T}{2.72 \text{ K}} \right)^4 \text{ ergs cm}^{-3} \\ &\cong 0.26(1+z)^4 \left(\frac{T}{2.72 \text{ K}} \right)^4 \text{ eV cm}^{-3}. \end{aligned} \quad (5.20)$$

Note also that $u_{\text{CMB}}(\Theta) = m_e c^2 \langle \epsilon_{\text{CMB}}(\Theta) \rangle n_{\text{CMB}}(\Theta)$.

Because the blackbody radiation field is strongly peaked at photon energies $\epsilon \cong \Theta$, a monochromatic δ -function approximation oftentimes provides sufficient accuracy for calculations. A convenient approximation for the CMBR field is

$$n_{\text{CMB}}(\epsilon; z) = 407(1+z)^3 \delta[\epsilon - 1.24 \times 10^{-9}(1+z)]. \quad (5.21)$$

5.4 TRANSFORMED QUANTITIES

In this section, expressions for blackbody, isotropic, or point source photon distribution functions are derived in reference systems moving with Lorentz factor Γ with respect to the frame in which the photon distribution is characterized.

5.4.1 Transformation of Total Distribution and Energy

Consider the beaming pattern of radiation in frame K from a source that radiates isotropically in K' . Equation (5.10), describing the total photon or particle distribution in some volume, becomes

$$N(\epsilon, \Omega) = \delta_D \frac{N'(\epsilon/\delta_D)}{4\pi} = \frac{1}{\Gamma(1 - \beta\mu)} \frac{N'[\Gamma\epsilon(1 - \beta\mu)]}{4\pi}. \quad (5.22)$$

Furthermore, suppose that the spectrum of photons or particles is monochromatic in the comoving frame. In this case, $N'(\epsilon', \Omega') = N_0 \delta_D(\epsilon' - \epsilon'_0)/4\pi$, and the total photon or particle energy in the comoving frame, in units of the electron rest mass, is $\mathcal{E}' = N_0 \epsilon'_0$. The differential photon spectrum in the stationary frame is therefore

$$N(\epsilon, \Omega) = \frac{\delta_D N_0}{4\pi} \delta(\epsilon/\delta_D - \epsilon'_0)/4\pi = \frac{N_0}{4\pi \Gamma^2 (1 - \beta\mu)^2} \delta\left(\epsilon - \frac{\epsilon'_0}{\Gamma(1 - \beta\mu)}\right).$$

Examination of the μ -dependence of this expression shows that the photon distribution is highly beamed in frame K when $\Gamma \gg 1$, with the highest-energy photons or particles directed along the direction of motion of frame K' .

The total energy in frame K is

$$\mathcal{E} = \oint d\Omega \int_0^\infty d\epsilon \epsilon N(\epsilon, \Omega) = \frac{N_0 \epsilon'_0}{2} \int_{-1}^1 d\mu \delta_D^3 = \Gamma \mathcal{E}'. \quad (5.23)$$

The Lorentz boost simply adds a factor Γ to the total energy content, which is obvious by noting the symmetry of the transformation equation $\epsilon = \Gamma\epsilon'(1 + \beta\mu')$ with respect to μ' . This example illustrates how the photon distribution or total energy of a distribution of particles or photons can be calculated when dealing with more complicated angular distributions.

5.4.2 Transformation of Differential Distributions

The photon energy ϵ and angle $\theta = \cos^{-1} \mu$ in frame K are given in terms of the comoving photon energy ϵ' and direction cosine μ' through the relations

$\epsilon = \Gamma\epsilon'(1 + \beta\mu')$, $\mu = (\mu' + \beta)/(1 + \beta\mu')$, and $\phi = \phi'$. From the invariance of $u(\epsilon, \Omega)/\epsilon^3$, eq. (5.8), we have

$$u'(\epsilon', \Omega') = \frac{u(\epsilon, \Omega)}{\Gamma^3(1 + \beta\mu')^3}. \quad (5.24)$$

Assuming azimuthal symmetry of the radiation field about the axis of the boost to frame K' , which moves with bulk Lorentz factor Γ with respect to the frame K , then $u(\epsilon, \Omega) = u(\epsilon, \mu)/2\pi$. For an isotropic external photon field in the stationary frame, $u(\epsilon, \Omega) = u(\epsilon)/4\pi$ and $u'(\epsilon', \Omega') = u(\epsilon)/[4\pi\Gamma^3(1 + \beta\mu')^3]$.

External Isotropic Monochromatic Radiation Field

For an external isotropic monochromatic radiation field, $u(\epsilon, \Omega) = u_0\delta(\epsilon - \epsilon_0)/4\pi$. The comoving energy density

$$u'_0 = \int_0^\infty d\epsilon' \oint d\Omega' u'(\epsilon', \Omega') = \frac{u_0}{2\Gamma^4} \int_{-1}^1 \frac{d\mu'}{(1 + \beta\mu')^4} = u_0\Gamma^2 \left(1 + \frac{\beta^2}{3}\right) \quad (5.25)$$

[55]. The angle-dependent specific energy density $u'(\mu') = u_0/[2\Gamma^4(1 + \beta\mu')^4]$. The four powers of δ_D originate from the solid angle transformation, energy transformation, and volume transformation.

For $\Gamma \gg 1$, the specific energy density ranges in value from $\sim 8\Gamma^4 u_0$ at $\mu' = -1$ to $\sim u_0/(32\Gamma^4)$ at $\mu' = 1$. The function plummets in value when $\mu' \gtrsim -\beta$. Multiplying $u'(\mu' = -\beta) \cong \Gamma^4 u_0/2$ by the characteristic solid angle element $\delta\Omega' \sim \pi\theta'^2 \sim \pi/\Gamma^2$ gives $u'_0 \cong (\pi/2)\Gamma^2 u_0$, which approximately recovers eq. (5.25) when $\Gamma \gg 1$. The function

$$u'(\epsilon', \Omega') \cong \frac{2}{3\pi}\Gamma^2 u_0 \delta\left(\epsilon' - \frac{4}{3}\Gamma\epsilon_0\right) \delta(\mu' + 1) \quad (5.26)$$

provides a useful approximation for the aberrated comoving-frame photon distribution in the limit $\Gamma \gg 1$, noting that $u'_0/n'_0 = (1 + \beta^2/3)\Gamma\epsilon_0 m_e c^2$. For isotropic external photons, the hardest and most intense radiation is directed opposite to the direction of motion of the jet plasma in the comoving frame.

Blackbody Radiation Field

From the invariance of I_ϵ/ϵ^3 , it is easy to show that the intensity of an external blackbody radiation field like the CMBR in frame K' is

$$I'_{\epsilon'}^{\text{bb}} = \frac{2m_e c^3 \epsilon'^3}{\lambda_C^3 \{\exp[\Gamma\epsilon'(1 + \beta \cos \theta')/\Theta] - 1\}}. \quad (5.27)$$

Thus the blackbody intensity remains blackbody, though with an effective temperature $\Theta_{\text{eff}} = \Theta / [\Gamma(1 + \beta \cos \theta')]$ that depends on direction. In particular, $\Theta_{\text{eff}} / \Theta = 2\Gamma, \Gamma, 1/\Gamma,$ and $1/(2\Gamma)$ at $\cos \theta' = -1, -\beta, 0,$ and $1,$ respectively, when $\Gamma \gg 1.$

External Isotropic Power-Law Radiation Field

Consider the transformation of an isotropic, power-law radiation field described by the function

$$u(\epsilon, \mu) = k_\alpha u_0 \epsilon^{-\alpha} H(\epsilon; \epsilon_\ell, \epsilon_u); \quad (5.28)$$

α is the energy spectral index. Normalization to the total radiation energy density $u_0 = \int_0^\infty d\epsilon \int_{-1}^1 d\mu u(\epsilon, \mu)$ gives

$$k_\alpha = \begin{cases} (1 - \alpha) / [2(\epsilon_u^{1-\alpha} - \epsilon_\ell^{1-\alpha})], & \alpha \neq 1 \\ [2 \ln(\epsilon_u / \epsilon_\ell)]^{-1}, & \alpha = 1. \end{cases} \quad (5.29)$$

Equations (5.24) and (5.28) imply

$$u'(\epsilon', \mu') = \frac{k_\alpha u_0 \epsilon'^{-\alpha}}{\Gamma^3 (1 + \beta \mu')^{3+\alpha}} H[\Gamma \epsilon' (1 + \beta \mu'); \epsilon_\ell, \epsilon_u], \quad (5.30)$$

which is easily shown to be normalized to u'_{ext} given by eq. (5.25).

Point Source Monochromatic Radiation Field Behind Jet

For a jet traveling radially outward, a compact source of radiation will appear as a point source at sufficiently large distances. If the compact source radiates isotropic monochromatic emission with luminosity $L_0,$ then the specific spectral energy density

$$u(\epsilon, \Omega) = \frac{L_0}{4\pi r^2 c} \frac{\delta(\mu - 1)}{2\pi} \delta(\epsilon - \epsilon_0). \quad (5.31)$$

Equations (5.24) and (5.31) imply

$$\begin{aligned} u'(\epsilon', \Omega') &= \frac{L_0}{8\pi^2 r^2 c} \frac{\delta(\mu' - 1) \delta[\epsilon' - \epsilon_0 / \Gamma(1 + \beta)]}{\Gamma^2 (1 + \beta)^2} \\ &\xrightarrow{\Gamma \gg 1} \frac{L_0}{32\pi^2 r^2 \Gamma^2 c} \delta(\mu' - 1) \delta\left(\epsilon' - \frac{\epsilon_0}{2\Gamma}\right). \end{aligned} \quad (5.32)$$

Writing the transformed radiation field in the form $u'(\epsilon', \Omega') = u'_0 \delta(\mu' - 1) \delta(\epsilon' - \epsilon'_0) / 2\pi,$ then

$$u'_0 = \frac{L_0}{4\pi r^2 c} \frac{1}{\Gamma^2 (1 + \beta)^2}.$$

Due to radial motion away from a point source of radiation, the energy density is reduced by a factor proportional to $1/4\Gamma^2$ when $\Gamma \gg 1$ compared to the energy density measured by a source at rest. In contrast, the energy density of a surrounding external isotropic radiation field is enhanced by a factor proportional to $4\Gamma^2/3$ when $\Gamma \gg 1$ (eq. [5.25]).

Stellar Blackbody Radiation Field Intercepted by Relativistic Jet

The spectral energy density at a distance d from a star, when treated as a point source of emission from a spherical blackbody with radius R , is

$$u_*(\epsilon, \Omega; d) = \frac{\pi R^2}{d^2} \frac{I_\epsilon^{\text{bb}}}{c} \delta(\Omega - \Omega_*) = u_{*0} \frac{\epsilon^3}{\exp(\epsilon/\Theta_*) - 1} \delta(\Omega - \Omega_*), \quad (5.33)$$

using eqs. (5.1) and (5.15). Here

$$u_{*0} = \frac{15L_*}{4\pi^5 c \Theta_*^4 d^2}, \quad (5.34)$$

using the relations $L_* = 4\pi R^2 \sigma_{\text{SB}} T_*^4$ for the stellar luminosity, the stellar temperature $T_* = m_e c^2 \Theta_*/k_{\text{B}}$, and the definition of the Stefan-Boltzmann constant $\sigma_{\text{SB}} = \pi^2 k_{\text{B}}^4 / (60\hbar^3 c^2)$. The νF_ν flux of a star is therefore

$$f_\epsilon^* = \frac{15L_*}{4\pi^5 d^2} \frac{(\epsilon/\Theta_*)^4}{\exp(\epsilon/\Theta_*) - 1}. \quad (5.35)$$

5.5 FLUXES OF RELATIVISTIC COSMOLOGICAL SOURCES

Quantities in the stationary frame at rest in the Hubble flow are starred, comoving (or proper-frame) quantities are primed, and observed quantities are unscripted. The energy flux Φ , eq. (5.6), is related to the luminosity $L_{*,\text{iso}}$ (ergs s⁻¹) of an isotropically emitting source in the stationary frame according to eq. (4.35),

$$\Phi = \frac{L_{*,\text{iso}}}{4\pi d_L^2}. \quad (5.36)$$

Considering a source with a directional luminosity $L_*(\epsilon_*, \Omega_*)$, comparison with eq. (5.36) means that

$$F(\epsilon) d\epsilon = \frac{L_*(\epsilon_*, \Omega_*)}{d_L^2} d\epsilon_*. \quad (5.37)$$

As previously derived, the energies in the three frames are related by

$$\epsilon = \frac{\epsilon_*}{(1+z)} = \frac{\delta_{\text{D}} \epsilon'}{(1+z)}. \quad (5.38)$$

For a homogeneous, isotropic universe, the direction vector in the cosmological frame is equal to the direction vector in the observer frame, so that $\Omega_* = \Omega$ (this would not be true if a gravitating mass deflected the light rays during propagation). Hence

$$F(\epsilon; \Omega) = \frac{(1+z)}{d_L^2} L_*(\epsilon_*, \Omega). \quad (5.39)$$

The differential directional luminosity

$$dL_*(\epsilon_*, \Omega_*) = dV_* j_*(\epsilon_*, \Omega_*), \quad (5.40)$$

where dV_* is a differential volume element and $j(\epsilon, \Omega)/\epsilon^2$ is invariant. Hence

$$j_*(\epsilon_*, \Omega_*) = \left(\frac{\epsilon_*}{\epsilon'}\right)^2 j'(\epsilon', \Omega'). \quad (5.41)$$

Because of the invariance of the four-volume $dV dt$, $dV_* = \delta_D dV'$. Equations (5.37) and (5.40) imply

$$dF(\epsilon; \Omega) = \frac{(1+z)}{d_L^2} \delta_D^3 dV' j'(\epsilon', \Omega') \quad (5.42)$$

and

$$d[\epsilon F(\epsilon; \Omega, t)] = df_\epsilon(t) = \frac{\delta_D^4}{d_L^2} \epsilon' j'(\epsilon', \Omega'; \vec{r}', t') dV', \quad (5.43)$$

where the reception time t and emission time t' have to be properly related, and eq. (5.5) defines the νF_ν flux f_ϵ .

5.5.1 Blob Geometry

The simplest geometry to consider, as shown in figure 5.3, is a uniform blob that is spherical in the comoving frame with comoving radius r'_b and comoving volume $V'_b = 4\pi r_b'^3/3$. To avoid temporal integrations over different portions of the blob, the timescale for variation in the radiation, t'_{var} , is assumed to be longer than the light-crossing time $t'_{\text{lc}} \approx r'_b/c$. Thus

$$r'_b \lesssim ct'_{\text{var}} = c\delta_D \Delta t_{\text{var}}/(1+z), \quad (5.44)$$

making use of eq. (2.25). The measured variability timescale is Δt_{var} , and eq. (5.44) gives an upper limit to the size r'_b of the emission region given a value for the Doppler factor.

With these simplifications, and furthermore assuming that the blob moves with constant speed, we have from eq. (5.43) that

$$f_\epsilon(t) \cong \frac{\delta_D^4 V'_b}{d_L^2} \epsilon' j'(\epsilon' \Omega'; t'). \quad (5.45)$$

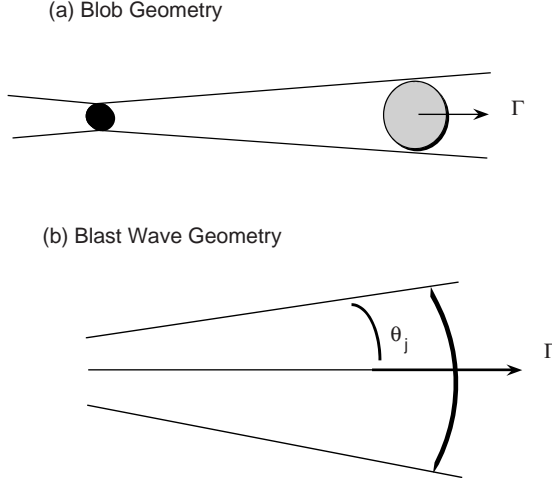


Figure 5.3 Geometries used to calculate emission properties of relativistic jets. (a) Blob geometry: $\theta_j \lesssim 1/\Gamma$. (b) Blast-wave geometry: $\theta_j \gtrsim 1/\Gamma$.

Assuming that the blob radiates isotropically in the comoving frame,

$$f_\epsilon(t) \cong \frac{\delta_D^4 V'_b}{4\pi d_L^2} \epsilon' j'(\epsilon'; t') \cong \frac{\delta_D^4 \epsilon' L'(\epsilon'; t')}{4\pi d_L^2}, \quad (5.46)$$

where the comoving spectral luminosity $L'(\epsilon'; t') \cong V'_b j'(\epsilon'; t')$.

The mean spectral energy density within the blob can be inferred from observable quantities, given the assumption of isotropic emission in the comoving blob frame. The spectral energy density $u'(\epsilon') \cong t'_{lc} j'(\epsilon')$. Because $V'_b = 4\pi r'_b{}^3/3$,

$$u'_{\epsilon'} = \epsilon' u'(\epsilon') = m_e c^2 \epsilon'^2 n'(\epsilon') \cong \frac{3d_L^2 f_\epsilon}{\delta_D^4 c r'_b{}^2} \gtrsim \frac{3d_L^2 (1+z)^2 f_\epsilon}{c^3 \delta_D^6 \Delta t_{\text{var}}^2}. \quad (5.47)$$

Consequently the relation between the total internal photon energy density u' and the total measured energy flux Φ is

$$u' \gtrsim \frac{3d_L^2 (1+z)^2 \Phi}{c^3 \delta_D^6 \Delta t_{\text{var}}^2}. \quad (5.48)$$

Beaming Factors for Blob Geometry

The dependence of the received radiation on Doppler factor for a blob that radiates an isotropic, power-law emission spectrum in the comoving blob frame is easily derived from eq. (5.46). In this case, $j'(\epsilon'; t') \propto \epsilon'^{-\alpha}$, where

α is the energy spectral index (eq. [5.28]), and $\epsilon' = (1+z)\epsilon/\delta_D$. Thus

$$f_\epsilon(t) \propto \delta_D^4 \epsilon'^{1-\alpha} \propto \delta_D^{3+\alpha} \epsilon^{1-\alpha}. \quad (5.49)$$

The beaming factor characterizing the dependence of the received flux on Doppler factor δ_D for radiation that is isotropically emitted in the comoving frame by a discrete blob is therefore $3 + \alpha$.

For a continuous jet rather than a discrete blob, $V'_b \rightarrow dV'_b = \pi r_\perp^2 dr'$, and the emission from different radiating elements along the jet radius r is integrated to obtain the received spectrum. The invariance of $dr' dt'$ implies that $dr' = (1+z)dr/\delta_D$. Substituting this expression into eq. (5.46) implies that the beaming factor for radiation that is isotropically emitted in the comoving frame by a uniform jet is $2 + \alpha$ [56].

Superluminal Motion

An unusual feature of relativistically moving ejecta is the phenomenon of apparent transverse superluminal motion, predicted by Rees [57]. An angular separation rate, $d\vartheta/dt$, is measured by charting the motions of radio-emitting features that are found mostly to move outward from a radio core. In the case of 3C 273 at redshift $z = 0.158$, Unwin et al. [58] measured two epochs of component separation with proper motion $d\vartheta/dt = 0.79 \pm 0.03 \text{ mas yr}^{-1}$ and $d\vartheta/dt = 0.99 \pm 0.24 \text{ mas yr}^{-1}$. At this redshift, $d_A = 1.7 \times 10^{27} \text{ cm}$. Because $1 \text{ mas/yr} = 1.536 \times 10^{-16} \text{ rad/s}$, the measured transverse velocity in the stationary frame (thus the factor of $1+z$) is

$$c\beta_\perp^{\text{ob}} = (1+z)d_A \left(\frac{d\vartheta}{dt} \right). \quad (5.50)$$

For 3C 273, $\beta_\perp^{\text{ob}} \cong 10[(d\vartheta/dt)/(\text{mas yr}^{-1})]$, so that the radio-emitting blobs are apparently moving faster than the speed of light.

This behavior is simply explained within a blob geometry, where the radio-emitting component follows a radial path outward from the core with constant

speed. From figure 2.2, the differential distance traveled by the blob is $dr = \beta c dt_*$, and the transverse distance is $dr_\perp = \beta c \sin \theta dt_*$. The time that it takes the blob to travel the distance dr_\perp , as measured by an observer in the local frame, is $dt = (1 - \beta \cos \theta) dt_*$. Thus

$$\beta_\perp = \frac{1}{c} \frac{dr_\perp}{dt} = \frac{\beta \sin \theta}{(1 - \beta \cos \theta)}. \quad (5.51)$$

Consider the properties of this function in the limit $\Gamma \gg 1, \theta \ll 1$. Because $(1 - \beta \cos \theta)^{-1} \rightarrow 2\Gamma^2/(1 + \Gamma^2\theta^2)$ in this limit (see eq. [5.22]),

$$\beta_\perp \rightarrow \frac{2\Gamma}{\Gamma\theta + 1/(\Gamma\theta)}. \quad (5.52)$$

From the symmetry of the final expression, it is obvious that this function reaches a maximum value when observing at $\theta = 1/\Gamma$, with maximum apparent transverse speed given by $c\beta_{\perp}^{\max} \cong c\Gamma$.

It is a simple matter to find β_{\perp}^{\max} for general Γ . From eq. (5.51),

$$\beta_{\perp}^{\max} = \beta\Gamma = \sqrt{\Gamma^2 - 1}, \quad (5.53)$$

when $\cos\theta = \beta$ or $\sin\theta = 1/\Gamma$. Apparent superluminal motion is possible when $\beta_{\perp}^{\max} > 1$, which occurs when $\beta > 1/\sqrt{2}$ or $\Gamma > \sqrt{2}$. The transverse speed $\beta_{\perp}c$ exceeds the true speed βc for all angles defined by

$$0 < \cos\theta < \frac{2\beta}{1 + \beta^2}.$$

The minimum value of Γ or β that gives a measured value of β_{\perp} is obtained from eq. (5.52). In this case, $\Gamma_{\min} = \sqrt{1 + \beta_{\perp}^2}$ and $\beta_{\min} = \beta_{\perp}/\sqrt{1 + \beta_{\perp}^2}$ [59].

5.5.2 Spherical Shell Geometry

An explosive release of energy will create a fireball that expands spherically, or as a portion of a spherical surface, as illustrated in figure 5.3. Multiple explosions can form shells moving with different speeds. Collisions between shells will convert some of the directed kinetic motion of the shells into internal energy to be radiated. This is the basis of the colliding shell model, often used to model highly variable emissions from gamma-ray bursts and blazars.

Writing eq. (5.43) as an integration over volume element $dV = d\phi d\mu dr r^2$ and using eq. (2.29), one obtains the νF_{ν} flux measured at dimensionless photon energy ϵ and time t , given by

$$f_{\epsilon}(t) = \frac{1}{d_L^2} \int_0^{2\pi} d\phi \int_{-1}^1 d\mu \int_0^{\infty} dr r^2 \delta_D^3(\mathbf{r}) \epsilon' j'(\epsilon', \mu', \phi'; \mathbf{r}, t') \quad (5.54)$$

[60], where primes refer to comoving quantities, the integration is over volume, and $\epsilon' = \epsilon(1+z)/\delta_D$. The comoving emissivity $j'(\epsilon', \Omega'; \vec{r}', t')$ may be anisotropic in the comoving frame. The angle transformations for the directional vector $\vec{\Omega} = (\mu, \phi)$ are given by $\mu' = (\mu - \beta)/(1 - \beta\mu)$ and $\phi' = \phi$, eqs. (2.16) and (2.17).

Variability and Location

Consider a relativistic spherical shell that is impulsively illuminated at some value of stationary time t_* . An observer receives emission from various portions of the spherical shell. The time delay between regions of the shell

located at an angle θ with respect to the line of sight to the observer, compared to emission from the part of the shell directed to the observer, is

$$\Delta t(\mu) = \frac{(1+z)}{c} r(1-\mu),$$

from eqs. (2.25) and (4.10).

Suppose that the shell radiates uniformly in the comoving frame, that is, the comoving emissivity is the same throughout the shell volume. Because of strong Doppler beaming, radiation emitted by portions of the shell lying outside the Doppler cone defined by the Doppler angle $\theta_D = 1/\Gamma$ is significantly reduced in intensity. Indeed, when $\Gamma \gg 1$ and $\theta \ll 1$, $\delta_D \propto \theta^{-2}$ when $\theta \gg \theta_D$ (eq. [2.22]).

We therefore neglect emission outside the Doppler cone. For an impulsive release of energy by the spherical shell, the resultant limiting variability timescale due to shell curvature is

$$\Delta t_{\text{crv}} \cong (1+z) \frac{r}{c} (1 - \cos \theta_D) \xrightarrow{\Gamma \gg 1, \theta \ll 1} (1+z) \frac{r \theta_D^2}{2c} \cong \frac{r(1+z)}{2\Gamma^2 c}. \quad (5.55)$$

If source radiation is observed to vary on a timescale Δt_{var} , then eq. (5.55) shows that the radiating site can be located at a distance

$$r \approx \eta_\Delta \frac{2\Gamma^2 c \Delta t_{\text{var}}}{1+z}, \quad \eta_\Delta \cong 1. \quad (5.56)$$

For a stationary emitting region, causality arguments imply that the region has to be smaller than $\Delta r \sim c \Delta t_{\text{var}} (1+z)$; otherwise causally disconnected regions larger than $c \Delta t_{\text{var}} (1+z)$ would superpose and wash out strong variability. Due to relativistic motions of the emission region, the location and transverse extent of the emission region can be much greater than the size scale implied by causality arguments, as seen from eqs. (5.55) and (5.56).

Curvature Relation

If a relativistic spherical shell is impulsively illuminated, the flux received by an observer will decline with time as off-axis, high-latitude emissions reach the observer. Suppose the shell, moving with speed βc , is illuminated at stationary time t_{*0} when it has reached radius $r_0 = \beta c t_{*0}$. An observer measures emission from angle θ at time t given by

$$\begin{aligned} \frac{t}{1+z} &= \left(\frac{r_0}{\beta c} \right) (1 - \beta \cos \theta) \\ &= \left(\frac{r_0}{\beta \Gamma c} \right) \delta_D^{-1} \xrightarrow{\Gamma \gg 1, \theta \ll 1} \left(\frac{r_0}{2\beta \Gamma^2 c} \right) (1 + \Gamma^2 \theta^2); \end{aligned} \quad (5.57)$$

later emission come from higher latitudes.

The differential energy flux received from angular range $d\theta$ is, from eq. (5.54), given by

$$d\mathcal{E}(\theta) \propto \delta_D^3 \epsilon' j'(\epsilon') r^2 dr d\theta, \quad (5.58)$$

for emission radiated isotropically in the comoving frame. For a flash of radiation produced at r_0 with spectral emissivity $\epsilon' j'(\epsilon') \propto \epsilon'^a$, we have from eq. (5.57) that

$$f_\epsilon(t) \propto \frac{d\mathcal{E}}{dt} \propto \epsilon^a \delta_D^{3-a} \propto \epsilon^a t^{-3+a}. \quad (5.59)$$

Hence $f_\epsilon \sim \epsilon F_\epsilon \sim \nu F_\nu \propto \epsilon^a t^{-3+a}$. Using the notation $F_\nu \propto t^{-\alpha} \nu^{-\beta}$, so $a = 1 - \beta$, gives the curvature relation [61, 62]

$$\alpha = 2 + \beta. \quad (5.60)$$

If colliding shells radiate as uniform, instantaneously illuminated portions of a spherical surface, the curvature relation also implies that the decay profile of the νF_ν spectrum should vary as $f_{\epsilon_{\text{pk}}} \propto \epsilon_{\text{pk}}^3$, where ϵ_{pk} is the peak photon energy of the νF_ν spectrum [63].

Kinematic Model for Spherical Shell

A finite-width spherical shell that is uniformly illuminated over a finite comoving interval and assumed to emit isotropically in the comoving frame produces characteristic kinematic pulses that are relevant to analyses of data from black-hole jet sources. In this idealization, the emissivity is related to the internal energy density through the relation

$$\epsilon' j'(\epsilon'; \bar{r}', t') \cong \frac{c u_{\epsilon'}(r', t')}{\Delta r'}, \quad (5.61)$$

where $\Delta r'$ is the proper shell width. For shell illumination during comoving time $t'_0 \leq t' \leq t'_0 + \Delta t'$, and approximating the spectrum by a broken power law with peak νL_ν flux at energy ϵ'_{pk} that is uniform throughout the shell,

$$u_{\epsilon'}(r', t') = u'_0 H(t'; t'_0, t'_0 + \Delta t') [x^a H(1-x) + x^b H(x-1)] \quad (5.62)$$

within the shell volume, where $a (> 0)$ and $b (< 0)$ are the νL_ν indices, and

$$x = \epsilon' / \epsilon'_{\text{pk},0} = \epsilon / \epsilon_{\text{pk},0} = (1+z) \epsilon / \delta_D \epsilon'_{\text{pk},0}. \quad (5.63)$$

Establishing constraints on the integrations over r and μ from this model gives kinematic pulse profiles as shown in figures 5.4 and 5.5. This figure shows the appearance of kinematic pulses for parameters η_r , defined in eq. (5.56),

$$\eta_\Delta = \frac{\Delta r'}{2\Gamma c \Delta t_{\text{var}} / (1+z)} \quad (5.64)$$

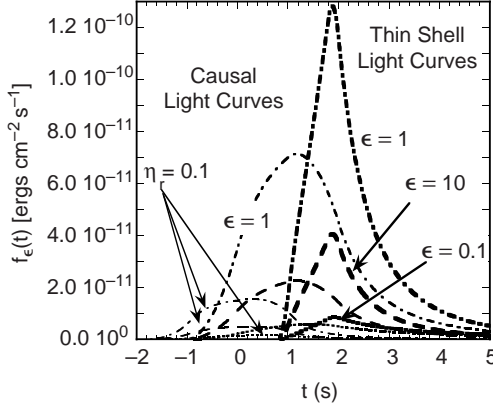


Figure 5.4 Light curves of kinematic pulses at different dimensionless observing energies ϵ as labeled. For the causal pulse, $\eta_\Delta = \eta_t = 1$ and $\eta_r = 0.1$ and 1.0 for the light and medium curves, respectively. The heavy curves are for the thin-shell case with $\eta_r = \eta_t = 1$ and $\eta_\Delta = 0.1$.

and

$$\eta_t = \frac{\Delta t'}{2\Gamma \Delta t_{\text{var}}/(1+z)} \quad (5.65)$$

characterizing the shell location, duration of emission, and shell width, respectively [63].

Three kinematic pulse profiles follow from this analysis:

1. causal pulse, with $\eta_r \cong \eta_\Delta \cong \eta_t = 1$;
2. thin-shell pulse, with $\eta_r \cong \eta_t \cong 1$, $\eta_\Delta \ll 1$;
3. curvature pulse, with $\eta_r \cong 1$, $\eta_\Delta, \eta_t \ll 1$.

A causal pulse has a characteristic rounded and weakly asymmetrical light curve, as shown in figure 5.4. The asymmetrical pulse shape is even more pronounced for a thin-shell pulse, where the asymmetry originates from the duration of the radiation and light-travel-time effects.

Pulses in the curvature limit are shown in figure 5.5, and are very asymmetrical, with a sharp leading edge. The bottom panel in figure 5.5 shows, in a log-log relation, that the flux decays as t^{-3+b} at $\epsilon > \epsilon_{\text{pk}}$. When $\epsilon < \epsilon_{\text{pk}}$, the flux decays as t^{-3+a} at early times, breaking to a t^{-3+b} behavior at late times due to curvature effects.

In the limit $\eta_\Delta \ll 1$ and $\eta_t \ll 1$, corresponding to an impulsive radiation pulse in the comoving frame, variability arises principally from curvature

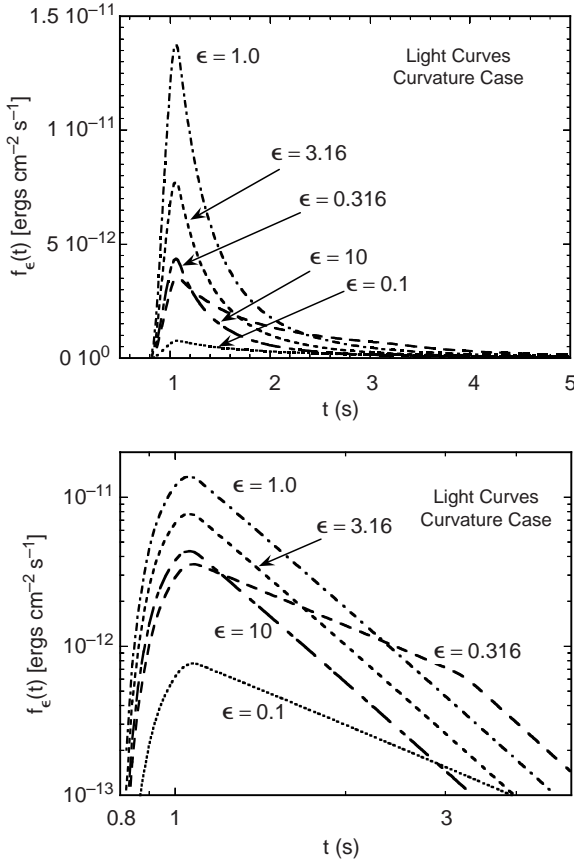


Figure 5.5 Light curves of a curvature pulse at different dimensionless observing photon energies for a model with $\eta_r = 1$ and $\eta_t = \eta_\Delta = 0.1$.

effects, and the pulse profile is analytic, given by

$$f_\epsilon(t) \cong \frac{4\eta_t c u'_0 r_0^2 \Gamma^2}{d_L^2} [x^a u^{-3+a} H(x^{-1} - u) + x^b u^{-3+b} H(x - u^{-1})] H(u - 1) \quad (5.66)$$

[63], where

$$u = \frac{2\Gamma^2 ct}{(1+z)r_0} = \frac{t}{t_{\text{var}}}.$$

At the peak of the νF_ν spectrum, $a = 0$, and

$$f_{\epsilon_{\text{pk}}} = \frac{4c u'_0 r_0^2 \Gamma^2}{d_L^2} \eta_t u^{-3}. \quad (5.67)$$

Equations (5.66) and (5.67) relate $f_\epsilon(t)$ and u'_0 in the curvature limit. The curvature limit gives the relation between the minimum internal energy density that could produce a pulse with a measured brightness and variability, for constants r_0 , Γ , and z .

Beaming Factors for Shell Geometry

The beaming factors for a shell geometry are given in terms of the Γ dependence of the received radiation. The solid angle dependence in the Doppler factor in eq. (5.54) is canceled out by the angular integration over different portions of the blast wave surface when calculating the received flux.

Consider a shell that has a constant comoving luminosity $L' = d\mathcal{E}'/dt'$. The received flux

$$\Phi = \frac{d\mathcal{E}_*/dt_*}{4\pi d_L^2} \cong \frac{\Gamma^2}{4\pi d_L^2} \frac{d\mathcal{E}'}{dt'}, \quad (5.68)$$

because $\mathcal{E}_* \cong \Gamma \mathcal{E}'$ and $dt_* \cong dt'/\Gamma$. The Γ^2 dependence of the received flux for constant internal energy density u'_0 is also found in eqs. (5.66) and (5.67).

5.5.3 Equivalence of Blob and Blast Wave Geometries

If the variability time scale Δt_{var} is equated with the full width at half maximum (FWHM) photon or count fluxes in a specified energy window, then observations can be related to model calculations. For the blast wave model in the curvature limit, $\Delta t_{\text{var}} = t_{1/2} - t_v$, where $t_{1/2} = t_v 2^{1/(3-b)}$ from eq. (5.66) when the blast wave spectrum is described by a single power law with index b (< 3). Thus

$$\Delta t_{\text{var}} = t_v [2^{1/(3-b)} - 1] = \frac{(1+z)r_0}{2\Gamma^2 c} [2^{1/(3-b)} - 1]. \quad (5.69)$$

For the blast wave model in the curvature limit, eq. (5.66) gives

$$f_\epsilon^{\text{bw,curv}} = \frac{2^4 \Gamma^6 c^3}{(1+z)^2 d_L^2} \frac{\eta_t \Delta t_{\text{var}}^2}{[2^{1/(3-b)} - 1]^2} u'_{\epsilon'}. \quad (5.70)$$

In comparison, we consistently relate the variability timescale Δt_{var} to t_f for a blob geometry, from eq. (5.47), to get

$$f_\epsilon^{\text{blob}} \rightarrow \frac{2^6 \Gamma^6 c^3 (\delta_D/2\Gamma)^6}{3(1+z)^2 d_L^2} \Delta t_{\text{var}}^2 u'_{\epsilon'}. \quad (5.71)$$

The curvature limit is realized when $\eta_t \sim 0.1$, which value effectively cancels out the denominator in brackets of eq. (5.70). By comparing eqs. (5.70) and (5.71) for $\eta_t \approx 0.1$, one sees that, to within a factor of order unity, the inferred spectral energy densities in the blob and blast wave geometries are the same. Consequently, we can even use the (simpler-to-apply) blob geometry when calculating opacity for various processes, for example, $\gamma\gamma$ and synchrotron self-absorption. The curvature limit gives the least intense internal radiation field that could produce a variable flux with given measured apparent isotropic luminosity and FWHM variability timescale Δt_{var} .

Chapter Six

Compton Scattering

The astrophysics of the Compton scattering process for relativistic particles is treated in this chapter, specialized to relativistic electrons. After deriving the elementary Compton scattering formula, the behavior of the Compton cross section in the Thomson and Klein-Nishina regimes is examined. Compton scattering regimes are determined by the value of the invariant $\bar{\epsilon} = \gamma\epsilon(1 - \beta_{\text{par}}\mu)$, which is the photon energy in the electron rest frame ($\bar{\epsilon} = \epsilon$ for electrons at rest). In the Thomson regime, $\bar{\epsilon} \ll 1$, and in the Klein-Nishina regime, $\bar{\epsilon} \gg 1$. For isotropic photon fields, analysis of the Compton energy-loss rate shows that the two regimes are characterized by the value of the parameter $\Gamma_e = 4\gamma\epsilon$.

Expressions for the differential cross section that are useful for calculations of Compton-scattered spectra are derived in the head-on approximation, and the accuracy of the different forms is examined. Applications of this process to γ -ray production from black-hole jet sources are considered. Compton scattering of surrounding target radiation fields by relativistic jet electrons is treated.

6.1 COMPTON EFFECT

Consider a photon with dimensionless energy $\epsilon = \lambda_C/\lambda$ and wavelength λ scattering an electron at rest (figure 6.1). After scattering, a photon with energy $\epsilon_s = \lambda_C/\lambda_s$ travels in a direction that makes an angle χ with respect to the direction of the incident photon. The scattered electron acquires Lorentz factor $\gamma_e = 1/\sqrt{1 - \beta_e^2}$ and is scattered in the direction θ_e with respect to the incident photon direction.

Energy conservation requires

$$1 + \epsilon = \epsilon_s + \gamma_e, \quad (6.1)$$

and conservation of momenta parallel and transverse to the initial photon direction can be expressed as

$$\epsilon = \epsilon_s \cos \chi + \beta_e \gamma_e \cos \theta_e, \quad (6.2)$$

$$\epsilon_s \sin \chi = \beta_e \gamma_e \sin \theta_e, \quad (6.3)$$

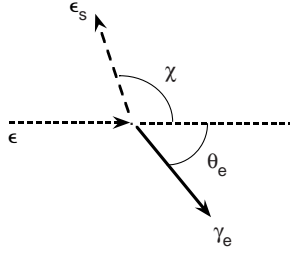


Figure 6.1 The Compton effect. In the electron rest frame (ERF), a photon with energy ϵ is scattered by a stationary electron. The scattered photon has energy ϵ_s and is scattered at angle χ with respect to the direction of the incident photon. The scattered electron has Lorentz factor γ_e .

respectively. Solving the y -momentum equation for $\cos \theta_e$ and substituting into the x -momentum equation, using $\beta_e^2 \gamma_e^2 = (\gamma_e + 1)(\gamma_e - 1) = (\epsilon - \epsilon_s)(\epsilon - \epsilon_s + 2)$ from eq. (6.1), gives

$$\cos \chi = 1 + \frac{1}{\epsilon} - \frac{1}{\epsilon_s} = 1 - \frac{1}{\lambda_C}(\lambda_s - \lambda). \quad (6.4)$$

Equation (6.4) can be rewritten as

$$\epsilon_s = \frac{\epsilon}{1 + \epsilon(1 - \cos \chi)}. \quad (6.5)$$

Due to electron recoil, the energy of the scattered photon ranges from $\epsilon/(1 + 2\epsilon)$, when scattering in the backward direction, to ϵ for forward scattering. When $\epsilon \ll 1$, then $\epsilon_s \approx \epsilon$ irrespective of the direction of scattering. The condition $\epsilon \ll 1$ defines the Thomson regime, and the condition $\epsilon \gg 1$ defines the Klein-Nishina regime.

6.2 THE COMPTON CROSS SECTION

The polarization-averaged differential Compton cross section in the ERF is given by

$$\frac{d\sigma_C}{d\epsilon_s d\Omega_s} = \frac{r_e^2}{2} \left(\frac{\epsilon_s}{\epsilon}\right)^2 \left(\frac{\epsilon_s}{\epsilon} + \frac{\epsilon}{\epsilon_s} - 1 + \cos^2 \chi\right) \delta\left(\epsilon_s - \frac{\epsilon}{1 + \epsilon(1 - \cos \chi)}\right) \quad (6.6)$$

[64], and $d\Omega_s = d\phi_s d\cos \chi$. The classical electron radius $r_e = e^2/m_e c^2$ and the Thomson cross section $\sigma_T = 8\pi r_e^2/3$. The integration of the differential cross section over scattered photon energy gives the angle-dependent

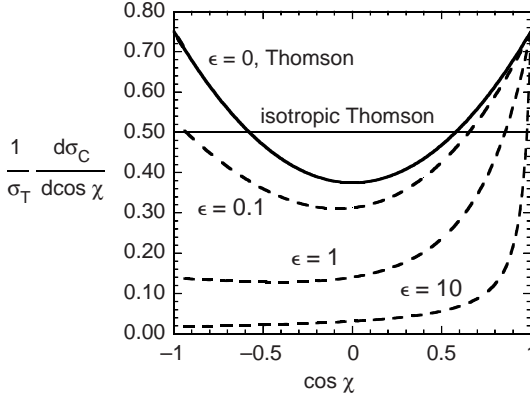


Figure 6.2 Angle-dependent Compton cross section. The differential cross section $d\sigma_C/d\cos\chi$ as a function of the cosine of the scattering angle, $\cos\chi$, is plotted for different values of incident photon energy ϵ . The limiting Thomson form of the differential cross section is shown by the heavy solid curve, and the isotropic cross section in the Thomson limit is shown by the light solid line.

Compton cross section

$$\frac{d\sigma_C}{d\Omega_s} = \frac{r_e^2}{2} [1 + \epsilon(1 - \cos\chi)^2] \left(\frac{1}{1 + \epsilon(1 - \cos\chi)} + \cos^2\chi + \epsilon(1 - \cos\chi) \right), \quad (6.7)$$

plotted in figure 6.2. In the Thomson regime $\epsilon \ll 1$, eq. (6.7) becomes

$$\frac{d\sigma_T}{d\Omega_s} = \frac{r_e^2}{2} (1 + \cos^2\chi). \quad (6.8)$$

Approximating the Thomson cross section as isotropic, then

$$\frac{d\sigma_{T,\text{iso}}}{d\Omega_s} = \frac{\sigma_T}{4\pi}. \quad (6.9)$$

Integrating eq. (6.6) over direction and scattered photon energy gives the total Compton cross section

$$\begin{aligned} \sigma_C(\epsilon) &= \int_0^\infty d\epsilon_s \oint d\Omega_s \frac{d\sigma_C}{d\epsilon_s d\Omega_s} \\ &= \frac{\pi r_e^2}{\epsilon^2} \left(4 + \frac{2\epsilon^2(1 + \epsilon)}{(1 + 2\epsilon)^2} + \frac{\epsilon^2 - 2\epsilon - 2}{\epsilon} \ln(1 + 2\epsilon) \right) \end{aligned} \quad (6.10)$$

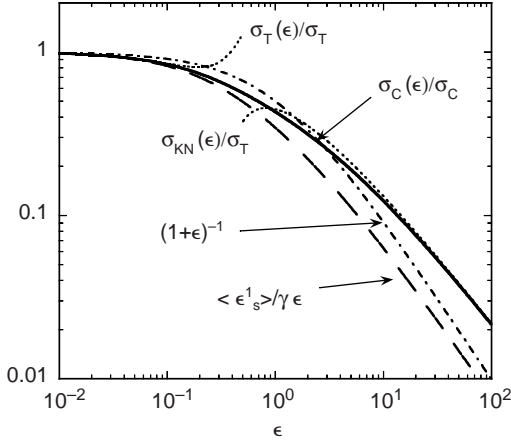


Figure 6.3 Compton cross section, approximations, and mean scattered photon energy. The total Compton cross section $\sigma_C(\epsilon)$ divided by the Thomson cross section σ_T is shown by the heavy solid curve. Dotted curves give asymptotes in the Thomson ($\epsilon \ll 1$) and Klein-Nishina ($\epsilon \gg 1$) regimes (eq. [6.11]) The light dashed curve gives the mean scattered photon energy $\langle \epsilon_s^1 \rangle$ divided by $\gamma \epsilon$ (eq. [6.40]). The dot-dashed curve shows the function $(1 + \epsilon)^{-1}$.

[65], with asymptotes

$$\sigma_C(\epsilon) \rightarrow \begin{cases} \sigma_T \left[1 - 2\epsilon + \frac{26}{5}\epsilon^2 + \mathcal{O}(\epsilon^3) \right] & \text{for } \epsilon \ll 1, \\ \frac{\pi r_e^2}{\epsilon} \left[\ln(2\epsilon) + 1/2 + \mathcal{O}(\epsilon^{-1}) \right] & \text{for } \epsilon \gg 1. \end{cases} \quad (6.11)$$

Figure 6.3 shows the dependence of σ_C on the photon energy ϵ in the ERF, and asymptotes (6.11) in the Thomson and Klein-Nishina regimes.

6.3 TRANSFORMING THE COMPTON CROSS SECTION

Having examined the properties of the Compton cross section, we now consider calculations of Compton-scattered spectra from a distribution of photons and electrons. The upper panel of figure 6.4 illustrates a system where an electron with Lorentz factor γ scatters a photon with energy ϵ to produce a scattered photon with energy ϵ_s . These quantities are defined not in the ERF, as in the previous section, but rather in a scattering frame where the

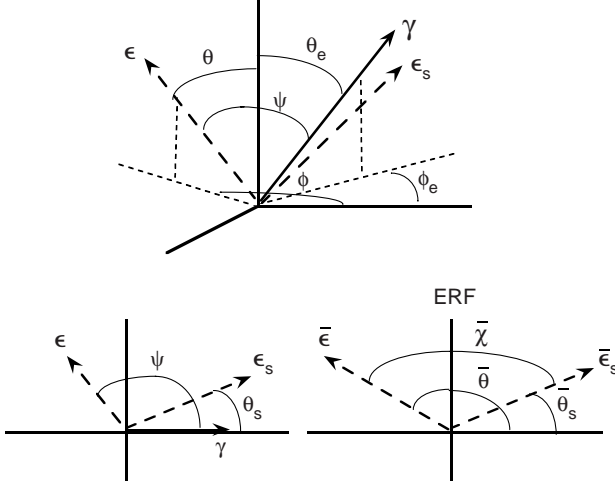


Figure 6.4 Geometry of a Compton scattering event. In the scattering frame shown in the upper panel, an electron with Lorentz factor γ scatters a photon with initial energy ϵ to final energy ϵ_s . The incident and scattered photon energies in the electron rest frame are $\bar{\epsilon}$ and $\bar{\epsilon}_s$, respectively. The differential cross section in the scattering frame is obtained by transforming the differential Compton cross section $d\sigma_C/d\bar{\epsilon}_s d\bar{\Omega}_s$ in the ERF to $d\sigma_C/d\epsilon_s d\Omega_s$ in the scattering frame. The head-on approximation has $\bar{\theta} \rightarrow \pi$ in the ERF, that is, the incident photon is directed opposite to the boost direction to the ERF.

distributions of photons and electrons are most conveniently described, for example, the comoving frame of relativistic plasma ejected by a black hole.

In the ERF, the incident photon has energy $\bar{\epsilon}$ and the scattered photon has, from eq. (6.5), energy $\bar{\epsilon}_s = \bar{\epsilon}/[1 + \bar{\epsilon}(1 - \cos \bar{\chi})]$. In the Thomson regime, $\bar{\epsilon}_s \cong \bar{\epsilon}$, and transformation back to the scattering frame gives a photon with energy $\epsilon_s = \gamma\bar{\epsilon}(1 + \beta_e \bar{\mu}_s)$. Thus photons scattered in the Thomson regime have energy $\epsilon_s = \gamma^2\epsilon(1 - \beta_e \cos \psi)(1 + \beta_e \cos \bar{\theta}_s)$, and, in the limit $\gamma \gg 1$, $\beta_e \rightarrow 1$, have energies as large as $\epsilon_s \cong 4\gamma^2\epsilon$. To ensure that the scattered photon's energy is less than the energy of the scattering electron, that is, $\epsilon_s < (\gamma - 1) \approx \gamma$, then $4\gamma\epsilon \ll 1$, the Thomson condition.

In the limit $\gamma \gg 1$, the incident photon is directed opposite to the boost direction in the ERF, so that $\cos \bar{\theta} \rightarrow -1$ and $\cos \bar{\chi} \cong -\cos \mu_s$ (lower right panel in figure 6.4). In this *head-on* approximation, discussed in more detail below, the scattered photon energy

$$\epsilon_s \approx \frac{\gamma\bar{\epsilon}(1 + \bar{\mu}_s)}{1 + \bar{\epsilon}(1 + \bar{\mu}_s)}, \quad (6.12)$$

and $\epsilon_s < \gamma$, as required.

Equation (2.44) gives the Compton-scattered emissivity

$$j_C(\epsilon_s, \Omega_s) = m_e c^3 \epsilon_s \oint d\Omega \int_0^\infty d\epsilon n_{\text{ph}}(\epsilon, \Omega) \times \oint d\Omega_e \int_1^\infty d\gamma (1 - \beta_e \cos \psi) n_e(\gamma, \Omega_e) \frac{d\sigma_C(\bar{\epsilon})}{d\epsilon_s d\Omega_s}, \quad (6.13)$$

where $\cos \psi = \mu \mu_e + \sqrt{1 - \mu^2} \sqrt{1 - \mu_e^2} \cos(\phi - \phi_e)$ is the cosine of the angle between the electron and target photon directions. The invariant quantity

$$\bar{\epsilon} = \gamma \epsilon (1 - \beta_e \cos \psi) \quad (6.14)$$

defines the collision strength; this is simply the photon energy in the ERF. The differential Compton cross section $d\sigma_C(\bar{\epsilon})/d\epsilon_s d\Omega_s$ used in eq. (6.13) is related to the differential Compton cross section $d\sigma_C/d\bar{\epsilon}_s d\bar{\Omega}_s$ defined in the ERF and discussed in the previous section by a simple Lorentz transformation. The Compton spectral luminosity of a one-zone system defined by the Compton emissivity, eq. (6.13), is

$$\epsilon_s L_C(\epsilon_s, \Omega_s) = V_b \epsilon_s j_C(\epsilon_s, \Omega_s).$$

Denoting quantities in the ERF by overbars, the invariance of $d\sigma/\epsilon d\epsilon d\Omega$ for photons implies

$$\frac{d\sigma_C}{d\epsilon_s d\Omega_s} = \frac{\epsilon_s}{\bar{\epsilon}_s} \frac{d\sigma_C}{d\bar{\epsilon}_s d\bar{\Omega}_s}. \quad (6.15)$$

From the bottom two panels of figure 6.4, we see that the scattered photon energy and angle in the ERF, expressed in terms of quantities in the scattering frame, are

$$\bar{\epsilon}_s = \gamma \epsilon_s (1 - \beta_e \mu_s) \quad \text{and} \quad \bar{\mu}_s = \frac{\mu_s - \beta_e}{1 - \beta_e \mu_s}, \quad (6.16)$$

where $\mu_s = \cos \theta_s$ and $\bar{\mu}_s = \cos \bar{\theta}_s$.

6.3.1 Differential Thomson Cross Section

The transformation of the differential Compton cross section is best illustrated using the isotropic Thomson approximation, eq. (6.9), written as

$$\frac{d\sigma_{\text{T,iso}}(\bar{\epsilon})}{d\epsilon_s d\Omega_s} = \frac{\sigma_{\text{T}}}{4\pi} \delta(\bar{\epsilon}_s - \bar{\epsilon}) = \frac{\sigma_{\text{T}}}{4\pi \gamma^2 (1 - \beta_e \mu_s)^2} \delta\left(\epsilon_s - \frac{\bar{\epsilon}}{\gamma(1 - \beta_e \mu_s)}\right). \quad (6.17)$$

Integration over ϵ_s gives the angle dependence of the scattered spectrum,

$$\frac{d\sigma_{\text{T,iso}}(\bar{\epsilon})}{d\mu_s} = \frac{\sigma_{\text{T}}}{2\gamma^2(1 - \beta_e\mu_s)^2} \xrightarrow{\gamma \gg 1, \theta_s \ll 1} \frac{2\sigma_{\text{T}}\gamma^2}{(1 + \gamma^2\theta_s^2)^2}. \quad (6.18)$$

Even for mildly relativistic electrons with $\gamma \lesssim 3$ –10, this function is highly peaked along the initial electron direction [66]. Integration of eq. (6.17) over Ω_s gives the energy dependence of the scattered spectrum,

$$\frac{d\sigma_{\text{T,iso}}(\bar{\epsilon})}{d\epsilon_s} = \frac{\sigma_{\text{T}}}{2\beta_e\gamma\bar{\epsilon}} H[\epsilon_s; \gamma\bar{\epsilon}(1 - \beta_e), \gamma\bar{\epsilon}(1 + \beta_e)]. \quad (6.19)$$

For highly relativistic electrons, $\gamma \gg 1$, eqs. (6.18) and (6.19) show that the following expression gives a good approximation to the transformed differential isotropic Thomson cross section:

$$\frac{d\sigma_{\text{T,iso}}(\bar{\epsilon})}{d\epsilon_s d\Omega_s} \cong \frac{\sigma_{\text{T}}}{2\gamma\bar{\epsilon}} H(\epsilon_s; \bar{\epsilon}/2\gamma, 2\gamma\bar{\epsilon}) \delta(\Omega_s - \Omega_e) H(1 - \bar{\epsilon}). \quad (6.20)$$

The final Heaviside function ensures that the scattering remains in the Thomson regime.

The same procedure can be followed for the angle-dependent Thomson cross section, eq. (6.8), written in the form

$$\frac{d\sigma_{\text{T}}}{d\bar{\epsilon}_s d\bar{\Omega}_s} = \frac{3\sigma_{\text{T}}}{16\pi} (1 + \cos \bar{\chi}^2) \delta(\bar{\epsilon}_s - \bar{\epsilon}), \quad (6.21)$$

where now $\cos \bar{\chi} = \bar{\mu}\bar{\mu}_s + \sqrt{1 - \bar{\mu}^2}\sqrt{1 - \bar{\mu}_s^2} \cos(\bar{\phi} - \bar{\phi}_s)$ and $\bar{\mu} = (\cos \psi - \beta_e)/(1 - \beta_e \cos \psi)$. Integration over $d\bar{\Omega}_s$ gives

$$\begin{aligned} \frac{d\sigma_{\text{T}}}{d\epsilon_s d\Omega_s} &= \frac{3\sigma_{\text{T}}}{16\beta_e\gamma\bar{\epsilon}} \left\{ 3 - \bar{\mu}^2 + \frac{(3\bar{\mu}^2 - 1)}{\beta_e^2} \left[\left(\frac{\epsilon_s}{\gamma\bar{\epsilon}} \right)^2 - \left(\frac{2\epsilon_s}{\gamma\bar{\epsilon}} \right) + 1 \right] \right\} \\ &\times H[\epsilon_s; \gamma\bar{\epsilon}(1 - \beta_e), \gamma\bar{\epsilon}(1 + \beta_e)]. \end{aligned} \quad (6.22)$$

Taking the limit $\gamma \gg 1$, $\beta_e \rightarrow 1$, $\bar{\mu} \rightarrow -1$, we find

$$\frac{d\sigma_{\text{T}}}{d\epsilon_s d\Omega_s} \cong \frac{3\sigma_{\text{T}}}{4\gamma\bar{\epsilon}} \left[1 - \frac{\epsilon_s}{\gamma\bar{\epsilon}} + \frac{1}{2} \left(\frac{\epsilon_s}{\gamma\bar{\epsilon}} \right)^2 \right] H(\epsilon_s; 0, 2\gamma\bar{\epsilon}) \delta(\Omega_s - \Omega_e) H(1 - \bar{\epsilon}). \quad (6.23)$$

for the transformed differential Thomson cross section when the scattered photons are approximated as traveling in the same direction as the scattering electron.

6.3.2 Head-on Approximation

The derivation of eq. (6.23) employed the limit $\gamma \gg 1, \beta_e \rightarrow 1$. In this limit, the incident photon travels nearly opposite to the direction of the electron when viewed in the ERF, except for those few photons lying within a solid angle element $\sim 1/\gamma^2$ sr of the direction of the relativistic electron. This is due to photon aberration, expressed by the condition that $\cos \bar{\theta} = (\cos \psi - \beta_e)/(1 - \beta_e \cos \psi) \rightarrow -1$ in the limit $\gamma \gg 1$. In this case, the scattered photon angle $\bar{\theta}_s \cong \pi - \bar{\chi}$, or $\cos \bar{\chi} \approx -\cos \bar{\theta}_s = -\bar{\mu}_s$. This is the head-on approximation [35, 67], which greatly simplifies derivations of the transformed Compton cross section. In this approximation, the Compton cross section in the ERF takes the form

$$\frac{d\sigma_C(\bar{\epsilon})}{d\bar{\epsilon}_s d\bar{\Omega}_s} \xrightarrow{\cos \bar{\chi} \rightarrow -\bar{\mu}_s} \frac{r_e^2}{2} \left(\frac{\bar{\epsilon}_s}{\bar{\epsilon}} \right)^2 \left(\frac{\bar{\epsilon}_s}{\bar{\epsilon}} + \frac{\bar{\epsilon}}{\bar{\epsilon}_s} - 1 + \bar{\mu}_s^2 \right) \times \delta \left(\bar{\epsilon}_s - \frac{\bar{\epsilon}}{1 + \bar{\epsilon}(1 + \bar{\mu}_s)} \right). \quad (6.24)$$

The transformation equations relating scattered photon energies and angles in the ERF to the scattering frame are $\bar{\epsilon}_s \cong \gamma \epsilon_s (1 - \beta_e \mu_s)$ and $\bar{\mu}_s = (\mu_s - \beta_e)/(1 - \beta_e \mu_s)$. (Here we are not allowed to let $\beta_e \rightarrow 1$ if we are to set $\mu_s \rightarrow 1$.) The reverse transformations are $\epsilon_s \cong \gamma \bar{\epsilon}_s (1 + \bar{\mu}_s)$ and $\mu_s = (\bar{\mu}_s + \beta_e)/(1 + \beta_e \bar{\mu}_s) \rightarrow 1$.

When $\gamma \gg 1$ and $\beta_e \rightarrow 1$, which is the condition for the head-on approximation, the scattered photon travels essentially in the direction of the scattering electron. In this limit, the differential Compton-scattering cross section is well approximated by the expression

$$\frac{d\sigma_C}{d\epsilon_s d\Omega_s} \cong \delta(\Omega_s - \Omega_e) \frac{d\sigma_C}{d\epsilon_s} \cong \delta(\Omega_s - \Omega_e) \oint d\bar{\Omega}_s \left(\frac{\epsilon_s}{\bar{\epsilon}_s} \right) \frac{d\sigma_C(\bar{\epsilon})}{d\bar{\epsilon}_s d\bar{\Omega}_s}. \quad (6.25)$$

The brightest emission of electrons with Lorentz factor γ is spread over solid angle $\pi\gamma^{-2}$; angular effects of the scattered photon beaming pattern need only be taken into account if variations on angular scales $\lesssim 1/\gamma$ are important.

6.3.3 Differential Compton Cross Section

Equation (6.25) can be most conveniently solved using the differential Compton cross section in the head-on approximation, eq. (6.24), by rewriting the integral in terms of $u = (1 - \beta_e \mu_s)$. Thus $\bar{\epsilon}_s = \gamma \epsilon_s u$,

$d\mu_s = -du/\beta_e$, $\bar{\mu}_s \cong (1 - \gamma^2 u)/\gamma^2 u$ for $\gamma \gg 1$, and we have

$$\frac{d\sigma_C}{d\epsilon_s} \cong \frac{\pi r_e^2}{\beta_e \gamma} \int_{1-\beta_e}^{1+\beta_e} \frac{du}{u} \left(\frac{\bar{\epsilon}_s}{\bar{\epsilon}}\right)^2 \left(\frac{\bar{\epsilon}_s}{\bar{\epsilon}} + \frac{\bar{\epsilon}}{\epsilon_s} - \frac{2}{\gamma^2 u} + \frac{1}{\gamma^4 u^2}\right) \delta\left(\bar{\epsilon}_s - \frac{\bar{\epsilon}}{1 + \bar{\epsilon}/\gamma^2 u}\right). \quad (6.26)$$

The δ -function can be rewritten as

$$\delta\left(\gamma \epsilon_s u - \frac{\bar{\epsilon}}{1 + \bar{\epsilon}/\gamma^2 u}\right) = \frac{1}{\gamma \epsilon_s y} \delta\left(u - \frac{y\bar{\epsilon}}{\gamma \epsilon_s}\right), \quad (6.27)$$

defining

$$y \equiv 1 - \frac{\epsilon_s}{\gamma} = \frac{\bar{\epsilon}_s}{\bar{\epsilon}}. \quad (6.28)$$

Solving the δ -function in eq. (6.26) using eq. (6.27) gives, in the limit $\gamma \gg 1$,

$$\frac{d\sigma_C}{d\epsilon_s} \cong \frac{\pi r_e^2}{\gamma \bar{\epsilon}} \Xi_C H\left(\epsilon_s; \frac{\bar{\epsilon}}{2\gamma}, \frac{2\gamma\bar{\epsilon}}{1 + 2\bar{\epsilon}}\right), \quad (6.29)$$

recalling that $\bar{\epsilon} = \gamma \epsilon (1 - \cos \hat{\psi})$, from eq. (6.14), with

$$\cos \hat{\psi} = \mu \mu_s + \sqrt{1 - \mu^2} \sqrt{1 - \mu_s^2} \cos \phi.$$

Here we define the Compton kernel

$$\Xi_C \equiv y + y^{-1} - \frac{2\epsilon_s}{\gamma \bar{\epsilon} y} + \left(\frac{\epsilon_s}{\gamma \bar{\epsilon} y}\right)^2. \quad (6.30)$$

Because $\epsilon_s/\gamma = 1 - y$, eq. (6.29) can also be written as

$$\frac{d\sigma_C}{d\epsilon_s} \cong \frac{\pi r_e^2}{\gamma \bar{\epsilon}^3} \left(y\bar{\epsilon}^2 + 1 + 2\bar{\epsilon} + \frac{1}{y} (\bar{\epsilon}^2 - 2\bar{\epsilon} - 2) + \frac{1}{y^2}\right) H[y; (1 + 2\bar{\epsilon})^{-1}, 1]. \quad (6.31)$$

The Compton spectral luminosity is given in the head-on approximation by the expression

$$\begin{aligned} \epsilon_s L_C(\epsilon_s, \Omega_s) &= c\pi r_e^2 \epsilon_s^2 \int_0^{2\pi} d\phi \int_{-1}^1 d\mu \int_0^{2\epsilon_s/(1-\cos \hat{\psi})} d\epsilon \frac{u(\epsilon, \Omega)}{\epsilon^2} \\ &\times \int_{\gamma_{\text{low}}}^{\infty} d\gamma N_e(\gamma, \Omega_s) \Xi_C, \end{aligned} \quad (6.32)$$

with $u(\epsilon, \Omega) = m_e c^2 \epsilon n_{\text{ph}}(\epsilon, \Omega)$. The lower limit on the electron Lorentz factor γ_{low} implied by the kinematic limits on y is

$$\gamma_{\text{low}} = \frac{\epsilon_s}{2} \left(1 + \sqrt{1 + \frac{2}{\epsilon \epsilon_s (1 - \cos \psi)}} \right). \quad (6.33)$$

6.3.4 Moments of the Compton Cross Section

The average energy of a Compton-scattered photon can be found by taking moments of the cross section. The n th moment of the cross section with respect to ϵ_s is defined as

$$\langle \epsilon_s^n \sigma \rangle \equiv \left\langle \epsilon_s^n \left(\frac{d\sigma}{d\epsilon_s d\Omega_s} \right) \right\rangle = \oint d\Omega_s \int_0^\infty d\epsilon_s \epsilon_s^n \left(\frac{d\sigma}{d\epsilon_s d\Omega_s} \right). \quad (6.34)$$

The $n = 0$ moment is the total cross section, and the $n = 1$ moment is the cross section weighted by the scattered photon energy, so that the average scattered photon energy

$$\langle \epsilon_s^1 \rangle = \frac{\langle \epsilon_s^1 \sigma \rangle}{\langle \epsilon_s^0 \sigma \rangle} \quad (6.35)$$

is the ratio of the first to the zeroth moment.

The n th moment of the differential Thomson cross section, eq. (6.23), is

$$\langle \epsilon_s^n \sigma \rangle_{\text{T}} = \frac{3\sigma_{\text{T}}}{4} (\gamma \bar{\epsilon})^n 2^{n+2} \left(\frac{1}{2(n+1)} - \frac{1}{n+2} + \frac{1}{n+3} \right). \quad (6.36)$$

Therefore the $n = 0$ moment of the differential Thomson cross section is $\langle \epsilon_s^0 \sigma \rangle_{\text{T}} = \sigma_{\text{T}}$. The $n = 1$ moment $\langle \epsilon_s^1 \sigma \rangle_{\text{T}} = \sigma_{\text{T}} \gamma \bar{\epsilon}$, so that the mean scattered energy in the Thomson limit is

$$\langle \epsilon_s^1 \rangle_{\text{T}} = \frac{\langle \epsilon_s^1 \sigma \rangle_{\text{T}}}{\langle \epsilon_s^0 \sigma \rangle_{\text{T}}} = \gamma \bar{\epsilon} = \gamma^2 \epsilon (1 - \cos \psi). \quad (6.37)$$

The n th moment of the differential Compton cross section in the head-on approximation is

$$\begin{aligned} \langle \epsilon_s^n \sigma \rangle_{\text{C}} &= \int_0^\infty d\epsilon_s \oint d\Omega_s \epsilon_s^n \left(\frac{d\sigma_{\text{C}}}{d\Omega_s d\epsilon_s} \right) = \frac{\pi r_e^2 \gamma^n}{\bar{\epsilon}^3} \int_{(1+2\bar{\epsilon})^{-1}}^1 dy (1-y)^n \\ &\quad \times [y \bar{\epsilon}^2 + (1+2\bar{\epsilon}) + y^{-1} (\bar{\epsilon}^2 - 2\bar{\epsilon} - 2) + y^{-2}]. \end{aligned} \quad (6.38)$$

The $n = 0$ moment is

$$\langle \epsilon_s^0 \sigma \rangle_{\text{C}} = \sigma_{\text{C}}(\bar{\epsilon}), \quad (6.39)$$

namely, the Compton cross section, eq. (6.10). The $n = 1$ moment of the differential Compton cross section is

$$\langle \epsilon_s^1 \sigma \rangle_C = \gamma \sigma_C(\bar{\epsilon}) - \frac{3\gamma \sigma_T}{8\bar{\epsilon}^3} \times \left[\frac{\bar{\epsilon}^2}{3} \left(\frac{(1+2\bar{\epsilon})^3 - 1}{(1+2\bar{\epsilon})^3} \right) + \frac{2\bar{\epsilon}(\bar{\epsilon}^2 - \bar{\epsilon} - 1)}{(1+2\bar{\epsilon})} + \ln(1+2\bar{\epsilon}) \right]. \quad (6.40)$$

The ratio $\langle \epsilon_s^1 \rangle_C / \langle \epsilon_s^1 \rangle_T$ of the mean scattered photon energy in Compton scattering to the Thomson-limit mean scattered photon energy goes roughly as $(1 + \bar{\epsilon})^{-1}$, as shown in figure 6.3. Simple energy conservation arguments restrict the Thomson relation $\epsilon_s \sim \gamma^2 \epsilon$ to $\gamma \epsilon \ll 1$.

The n th moment of the Compton cross section in the extreme Klein-Nishina limit $\bar{\epsilon} \gg 1$ is, from eq. (6.38), given by

$$\langle \epsilon_s^n \sigma \rangle_{\text{KN}} = \frac{\pi r_e^2 \gamma^n}{\bar{\epsilon}} \int_{1/2\bar{\epsilon}}^1 dy (1-y)^n \left(y + \frac{1}{y} \right). \quad (6.41)$$

The $n = 0$ moment is just the asymptotic Klein-Nishina cross section, eq. (6.11), given by

$$\langle \epsilon_s^0 \sigma \rangle_{\text{KN}} \rightarrow \pi r_e^2 \frac{\ln 2\bar{\epsilon} + 1/2}{\bar{\epsilon}}. \quad (6.42)$$

The $n = 1$ moment is

$$\langle \epsilon_s^1 \sigma \rangle_{\text{KN}} \rightarrow \gamma \langle \epsilon_s^0 \sigma \rangle_{\text{KN}} - \frac{4\gamma \pi r_e^2}{3\bar{\epsilon}}. \quad (6.43)$$

The mean scattered photon energy in the limit $\bar{\epsilon} \gg 1$ is therefore

$$\langle \epsilon_s^1 \rangle_{\text{KN}} = \frac{\langle \epsilon_s^1 \sigma \rangle_{\text{KN}}}{\langle \epsilon_s^0 \sigma \rangle_{\text{KN}}} \xrightarrow{\bar{\epsilon} \gg 1} \gamma \left(1 - \frac{4}{3(\ln 2\bar{\epsilon} + 1/2)} \right) \cong \gamma.$$

6.3.5 Compton Scattering in the δ -Function Approximation

A simpler form for Thomson scattering is obtained by replacing the range of scattered photon energies resulting from monoenergetic, monodirectional electrons scattering a monochromatic beam of photons by a scattered photon with fixed energy that travels in the same direction as the incident electron. The δ -function approximation to Thomson scattering is given by

$$\frac{d\sigma_{\text{T},\delta}}{d\epsilon_s d\Omega_s} \cong \sigma_T \delta(\Omega_s - \Omega_e) \delta(\epsilon_s - \gamma \bar{\epsilon}) H(1 - \bar{\epsilon}). \quad (6.44)$$

The expression

$$\begin{aligned} \frac{d\sigma_{C,\delta}}{d\epsilon_s d\Omega_s} \cong \sigma_T \left(\delta(\epsilon_s - \gamma\bar{\epsilon})H(1 - \bar{\epsilon}) \right. \\ \left. + \frac{3}{8\bar{\epsilon}} \ln(2e^{1/2}\bar{\epsilon})\delta(\epsilon_s - \gamma)H(\bar{\epsilon} - 1) \right) \delta(\Omega_s - \Omega_e) \quad (6.45) \end{aligned}$$

extends the δ -function Thomson cross section, eq. (6.44), to the KN regime [68].

6.4 ENERGY-LOSS RATES IN COMPTON SCATTERING

The general expression for the rate of change of an electron's Lorentz factor in a frame where the target photon distribution is described by $n_{\text{ph}}(\epsilon, \Omega)$ is given by

$$\begin{aligned} -\dot{\gamma} &= -\frac{d\gamma}{dt} = c \oint d\Omega \int_0^\infty d\epsilon n_{\text{ph}}(\epsilon, \Omega) (1 - \beta_e \mu) \\ &\quad \times \oint d\Omega_s \int_0^\infty d\epsilon_s (\epsilon_s - \epsilon) \frac{d\sigma(\bar{\epsilon})}{d\epsilon_s d\Omega_s} \\ &= c \oint d\Omega \int_0^\infty d\epsilon n_{\text{ph}}(\epsilon, \Omega) (1 - \beta_e \mu) (\langle \epsilon_s^1 \sigma \rangle - \epsilon \langle \epsilon_s^0 \sigma \rangle), \quad (6.46) \end{aligned}$$

taking $\mu_e = 1$ and $\phi_e = 0$. In a scattering, the electron loses energy equal to the mean scattered photon energy $\langle \epsilon_s^1 \sigma \rangle$, given by eq. (6.34), from which the initial photon energy ϵ is subtracted.

6.4.1 Thomson Energy-Loss Rate

In the Thomson limit $\bar{\epsilon} \ll 1$, $\langle \epsilon_s^1 \sigma \rangle_T \rightarrow \gamma\bar{\epsilon}\sigma_T = \gamma^2\epsilon(1 - \beta_e\mu)\sigma_T$. Substituting this expression into eq. (6.46) gives

$$-\dot{\gamma}_T = c\sigma_T \int_0^\infty d\epsilon \epsilon \int_0^{2\pi} d\phi \int_{-1}^1 d\mu [\gamma^2(1 - \beta_e\mu)^2 - 1] n_{\text{ph}}(\epsilon, \Omega). \quad (6.47)$$

For isotropic photon fields,

$$\begin{aligned}
 -\dot{\gamma}_T &= \frac{1}{2} c \sigma_T \gamma^2 \int_0^{1/\gamma} d\epsilon \in n_{\text{ph}}(\epsilon) \int_{-1}^1 d\mu [(1 - \beta_e \mu)^2 - 1] \\
 &= \frac{4}{3} c \sigma_T \beta_e^2 \gamma^2 \int_0^{1/\gamma} d\epsilon \in n_{\text{ph}}(\epsilon) \\
 &= \frac{4}{3} c \sigma_T \beta_e^2 \gamma^2 \int_0^{1/\gamma} d\epsilon u(\epsilon) \xrightarrow{\gamma \gg 1} \frac{4}{3} c \sigma_T u_T \gamma^2. \quad (6.48)
 \end{aligned}$$

The upper limit on the integration over ϵ restricts the target photons to the Thomson regime. Defining $U_T = m_e c^2 u_T = m_e c^2 \int_0^{1/\gamma} d\epsilon \in n_{\text{ph}}(\epsilon)$, the relativistic electron energy-loss rate due to Thomson scattering is therefore

$$-\left(\frac{dE}{dt}\right)_T = -m_e c^2 \dot{\gamma}_T = \frac{4}{3} c \sigma_T U_T \gamma^2, \quad (6.49)$$

as is well known.

For particles with mass m and charge Ze , the Thomson loss rate is

$$-\dot{\gamma}_T = \left(\frac{m_e}{m}\right)^3 Z^2 \frac{4}{3} c \sigma_T \left(\frac{U_T}{m_e c^2}\right) \gamma^2. \quad (6.50)$$

The replacement of the Thomson cross section with $(m_e/m)^2 Z^2 \sigma_T$, and the Compton effect, eq. (6.5) with ϵ replaced by $\epsilon(m_e/m)$, gives the scaling of the Compton process for particles other than electrons.

The scattering rate of photons in the Thomson limit is, from eq. (2.40),

$$\dot{N}_T = \frac{c \sigma_T}{4\pi} \int_0^{1/\gamma} d\epsilon \oint d\Omega (1 - \beta_e \mu) n_{\text{ph}}(\epsilon) = c \sigma_T \int_0^{1/\gamma} d\epsilon \in n_{\text{ph}}(\epsilon) = \frac{c \sigma_T u_T}{m_e c^2 \epsilon_0}, \quad (6.51)$$

where the last expression approximates the target photons as monochromatic with energy ϵ_0 . Thus the mean energy of scattered photons when an isotropic monochromatic photon distribution is scattered by relativistic electrons in the Thomson limit is

$$\langle \epsilon \rangle_T = \frac{4}{3} \epsilon_0 \gamma^2. \quad (6.52)$$

6.4.2 Klein-Nishina Energy-Loss Rate

Substitution of eqs. (6.42) and (6.43) into eq. (6.46) for an isotropic target photon field gives

$$-\dot{\gamma}_{\text{KN}} = c \pi r_e^2 \int_{1/\gamma}^{\infty} d\epsilon \frac{n_{\text{ph}}(\epsilon)}{\epsilon} \left(\ln 4\gamma\epsilon - \frac{11}{6} \right). \quad (6.53)$$

Integration of eq. (6.53), using eq. (5.16) for the blackbody spectral photon density, gives [35]

$$-\dot{\gamma}_{\text{KN,bb}} = \frac{\pi^3}{2} \frac{c\sigma_{\text{T}}}{\lambda_{\text{C}}^3} \Theta^2 \left(\ln 4\gamma\Theta - \frac{5}{6} - C_{\text{E}} - C_{\text{I}} \right), \quad (6.54)$$

where $C_{\text{E}} = 0.5772\dots$ is Euler's constant and

$$C_{\text{I}} = \frac{6}{\pi^2} \sum_{n=2}^{\infty} \frac{\ln k}{k^2} = 0.570\dots$$

Note the slow logarithmic increase of $-\dot{\gamma} \propto \ln \gamma$ versus the quadratic dependence, $-\dot{\gamma} \propto \gamma^2$, in the Thomson regime (eq. [6.50]).

The energy-loss mean free path (MFP) due to Compton losses off the CMBR in the extreme Klein-Nishina regime, $4\gamma\Theta \gg 1$ or $\gamma \gg 5 \times 10^8/(1+z)$, is

$$\lambda_{\text{KN,CMBR}} = c \left| \frac{\gamma}{\dot{\gamma}_{\text{KN,CMBR}}} \right| \cong \frac{4.2 E_{\text{EeV}}}{(1+z)^2 (\ln[3590(1+z)] E_{\text{EeV}}) - 1.98} \text{ Mpc}$$

so $\lambda_{\text{KN,CMBR}}(E_{\text{EeV}}, z \ll 1) \approx 0.67 \text{ Mpc}$. EeV photons from GZK processes made beyond a Mpc will inevitably induce a cascade γ -ray spectrum (section 10.8).

6.5 DIFFERENTIAL COMPTON CROSS SECTIONS AND SPECTRA

Equation (6.44) gives a simple form for the differential Compton scattering cross section by restricting all scattering to the Thomson regime and making a δ -function approximation for the scattered photon energy. These formulae can be compared with the differential Thomson scattering cross section, eq. (6.23), the isotropic Thomson approximation, eq. (6.20), and the differential Compton scattering cross section in the head-on approximation, eq. (6.31), accurate throughout the Thomson and Klein-Nishina regimes. We compare the accuracy of these four approximations for the problem of an isotropic, power-law distribution of electrons scattering an isotropic monochromatic photon source.

6.5.1 Comparison of Scattered Spectra for Different ERF Photon Energies

Because the scattered photon is assumed to have the same direction as the incident electron in the head-on approximation, we write

$$\frac{d\sigma}{d\epsilon_s d\Omega_s} = \frac{d\sigma}{d\epsilon_s} \delta(\Omega_s - \Omega_e). \quad (6.55)$$

The Thomson cross section, eq. (6.23) can be written as

$$\frac{d\sigma_{\text{T}}}{dx} \cong \sigma_{\text{T}} \frac{3}{2} (1 - 2x + 2x^2) H(x; 0, 1) H(1 - \bar{\epsilon}), \quad (6.56)$$

where

$$x = \frac{\epsilon_s}{2\gamma\bar{\epsilon}}$$

is the ratio of scattered photon energy ϵ_s to maximum scattered photon energy in the Thomson limit, and we have added the restriction to the Thomson regime. The isotropic Thomson approximation, eq. (6.20), is

$$\frac{d\sigma_{\text{T,iso}}}{dx} \cong \sigma_{\text{T}} H(x; 0, 1) H(1 - \bar{\epsilon}). \quad (6.57)$$

The δ -function Thomson approximation, eq. (6.44), reads

$$\frac{d\sigma_{\text{T},\delta}}{d\epsilon_s} \simeq \sigma_{\text{T}} \delta(\epsilon_s - \gamma\bar{\epsilon}) H(1 - \bar{\epsilon}). \quad (6.58)$$

The full Compton cross section in the head-on approximation, eq. (6.31), becomes

$$\frac{d\sigma_{\text{C}}}{d\hat{x}} \cong \frac{3\sigma_{\text{T}}}{4} \frac{1}{1 + 2\bar{\epsilon}} \left[\left(y + \frac{1}{y} \right) + \frac{2}{\bar{\epsilon}} \left(1 - \frac{1}{y} \right) + \frac{1}{\bar{\epsilon}^2} \left(1 - \frac{1}{y} \right)^2 \right] H(\hat{x}; 0, 1), \quad (6.59)$$

where $y = 1 - \epsilon_s/\gamma = 1 - 2\bar{\epsilon}\hat{x}/(1 + 2\bar{\epsilon})$. For the Compton cross section, the term x is generalized to

$$x \rightarrow \hat{x} = \frac{\epsilon_s}{2\gamma\bar{\epsilon}/(1 + 2\bar{\epsilon})}.$$

Figure 6.5 compares the scattered photon spectra as a function of x for different approximations to the Compton cross section. When $\bar{\epsilon} \gg 1$, the scattered spectrum begins to approach a δ -function spectrum with $\epsilon_s \approx \gamma$. The δ -function Thomson approximation, eq. (6.58), would be represented by a δ -function spectrum at $x = 1/2$ on this figure.

6.5.2 Spectral Comparisons for Isotropic Monochromatic Photons and Power-Law Electrons

We solve for the scattered photon emissivity when an isotropic photon gas described by $u(\epsilon, \Omega) = m_e c^2 \epsilon n_{\text{ph}}(\epsilon, \Omega) = u(\epsilon)/4\pi$ is scattered by an isotropic, relativistic electron distribution described by $n_e(\gamma, \Omega_e) = n_e(\gamma)/4\pi$. In this geometry, the scattered photon distribution is also isotropic, so $j(\epsilon_s, \Omega_s) = j(\epsilon_s)/4\pi$. From eqs. (6.13) and (6.55),

$$j(\epsilon_s) = \frac{c\epsilon_s}{2} \int_0^\infty d\epsilon \frac{u(\epsilon)}{\epsilon} \int_1^\infty d\gamma n_e(\gamma) \int_{-1}^1 d\mu (1 - \mu) \frac{d\sigma}{d\epsilon_s}. \quad (6.60)$$

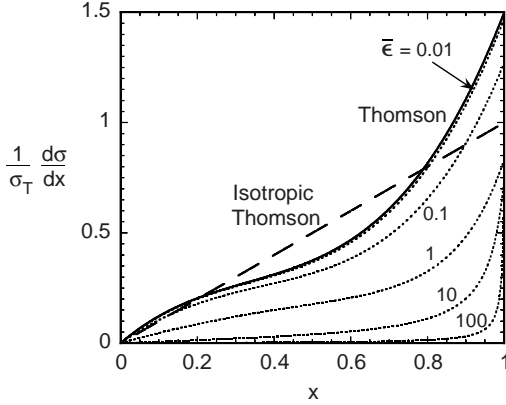


Figure 6.5 Comparison of expressions for scattered photon spectrum as a function of x , the ratio of the scattered photon energy to the maximum scattered photon energy. Solid curve gives the Thomson spectrum, eq. (6.56), the dashed curve gives the isotropic Thomson spectrum, eq. (6.57), and the dotted curves give the Compton spectra, eq. (6.59), for different values of the ERF photon energy $\bar{\epsilon}$, as labeled.

For a monochromatic photon source, $u(\epsilon, \Omega) = u_0\delta(\epsilon - \epsilon_0)/4\pi$, and eq. (6.60) becomes

$$\epsilon_s j(\epsilon_s) = \frac{cu_0\epsilon_s^2}{2\epsilon^3} \int_1^\infty d\gamma \frac{n_e(\gamma)}{\gamma^2} \int_0^{2\gamma\epsilon} d\bar{\epsilon} \bar{\epsilon} \frac{d\sigma}{d\epsilon_s}. \quad (6.61)$$

Later equations for monochromatic distributions of photons can be converted to integrations over a spectral photon distribution by letting

$$\epsilon^n u_0 \rightarrow \int d\epsilon \epsilon^n u(\epsilon).$$

For a power-law electron distribution described by the function

$$n_e(\gamma) = k_e\gamma^{-p}H(\gamma; \gamma_1, \gamma_2), \quad (6.62)$$

the total energy density in nonthermal electrons is given by

$$u_e = m_e c^2 \int_1^\infty d\gamma \gamma n_e(\gamma), \quad (6.63)$$

so that the normalization coefficient

$$k_e = \frac{(p-2)u_e}{m_e c^2 (\gamma_1^{2-p} - \gamma_2^{2-p})}. \quad (6.64)$$

Substituting the δ -function approximation, eq. (6.58), in eq. (6.61) gives

$$\epsilon_s j_{T,\delta}(\epsilon_s) = \frac{1}{2} c \sigma_T u_0 \left(\frac{\epsilon_s}{\epsilon} \right)^3 \int_{\max(\epsilon_s, \sqrt{\epsilon_s/2\epsilon})}^{\infty} d\gamma \frac{n_e(\gamma)}{\gamma^4}. \quad (6.65)$$

Restriction to the Thomson regime is provided by the condition $\gamma > \sqrt{\epsilon_s/2\epsilon}$, which follows from the conditions $\bar{\epsilon} < 2\gamma\epsilon$ and $\epsilon_s = \gamma\bar{\epsilon}$. For the power-law electron distribution given by eq. (6.62),

$$\epsilon_s j_{T,\delta}(\epsilon_s) = \frac{c \sigma_T u_0}{2(p+3)} \left(\frac{\epsilon_s}{\epsilon} \right)^3 k_e \left\{ \left[\max \left(\gamma_1, \epsilon_s, \sqrt{\frac{\epsilon_s}{2\epsilon}} \right) \right]^{-(3+p)} - \gamma_2^{-(3+p)} \right\}. \quad (6.66)$$

The solution to eq. (6.61) for the Compton-scattered emissivity in the head-on approximation is

$$\epsilon_s j_C(\epsilon_s) = \frac{3}{4} c \sigma_T u_0 \left(\frac{\epsilon_s}{\epsilon} \right)^2 \int_1^{\infty} d\gamma \frac{n_e(\gamma)}{\gamma^2} F(\epsilon_s, \gamma, 4\gamma\epsilon). \quad (6.67)$$

Here $F(\epsilon_s, \gamma, 4\gamma\epsilon)$ is a scattering kernel for different approximations to the Compton process.

For the Thomson cross section, eq. (6.56),

$$\epsilon_s j_T(\epsilon_s) = \frac{3}{4} c \sigma_T u_0 \left(\frac{\epsilon_s}{\epsilon} \right)^2 \int_{\sqrt{\epsilon_s/4\epsilon}}^{\infty} d\gamma \frac{n_e(\gamma)}{\gamma^2} F_T(\hat{\epsilon}), \quad (6.68)$$

where

$$F_T(\hat{\epsilon}) = 1 + \hat{\epsilon} - 2\hat{\epsilon}^2 + 2\hat{\epsilon} \ln \hat{\epsilon}, \quad (6.69)$$

and

$$\hat{\epsilon} = \epsilon_s/4\gamma^2\epsilon \quad (6.70)$$

is the ratio of the scattered energy to the maximum scattered energy. For the isotropic Thomson cross section, eq. (6.57),

$$F_{T,\text{iso}}(\hat{\epsilon}) = \frac{2}{3}(1 - \hat{\epsilon}). \quad (6.71)$$

No restrictions on γ have been made to ensure that scattering takes place only in the Thomson regime. Figure 6.6 compares these two expressions as a function of $\hat{\epsilon}$.

If restriction to the Thomson regime is made, then substitution of the isotropic Thomson cross section, eq. (6.57), into eq. (6.61) gives

$$\epsilon_s j_{T,\text{iso}}(\epsilon_s) = \frac{1}{2} c \sigma_T u_0 \left(\frac{\epsilon_s}{\epsilon} \right)^2 \int_{\max(\frac{\epsilon_s}{2}, \frac{1}{2}\sqrt{\epsilon_s/\epsilon})}^{\infty} d\gamma \frac{n_e(\gamma)}{\gamma^2} \left[\min \left(1, \frac{1}{2\gamma\epsilon} \right) - \hat{\epsilon} \right]. \quad (6.72)$$

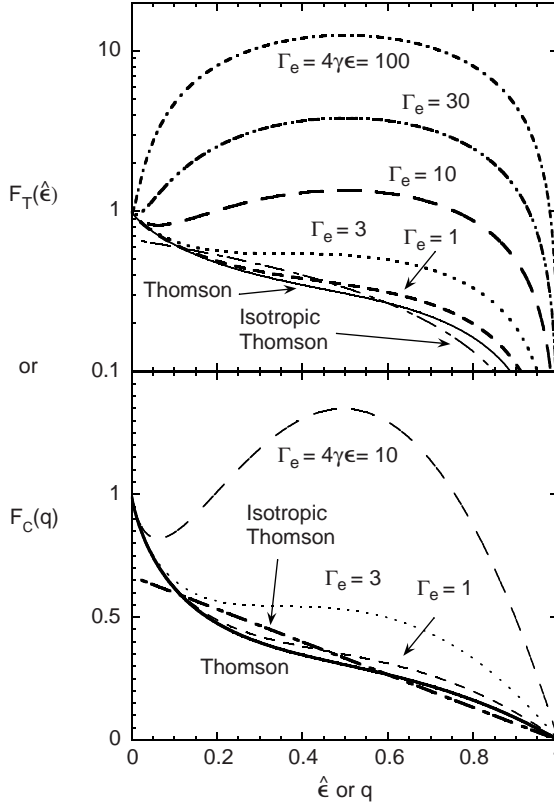


Figure 6.6 Comparison of expressions $F_T(\hat{\epsilon})$, eq. (6.69), and $F_{T,iso}(\hat{\epsilon})$, eq. (6.71), with $F_{T,C}(\hat{\epsilon})$, eq. (6.75).

Solving this for an electron distribution given by eq. (6.62) gives

$$\begin{aligned} \epsilon_s j_{T,iso}(\epsilon_s) = & \frac{k_e c \sigma_T}{4} \left(\frac{\epsilon_s}{\epsilon} \right)^2 \left(\frac{2}{p+1} (A^{-p-1} - B^{-p-1}) \right. \\ & + \frac{1}{\epsilon(p+2)} (C^{-p-2} - \gamma_2^{-p-2}) \\ & \left. - \frac{\epsilon_s}{2\epsilon(p+3)} (A^{-p-3} - B^{-p-3} + C^{-p-3} - \gamma_2^{-p-3}) \right), \end{aligned} \quad (6.73)$$

where $A = \max(\gamma_1, \frac{1}{2}\sqrt{\epsilon_s/\epsilon})$, $B = \min(\gamma_2, 1/2\epsilon)$, and $C = \max(\gamma_1, \epsilon_s/2, 1/2\epsilon)$ in this equation. When the target radiation field is synchrotron radiation from the same electrons that Thomson-scatter the radiation, the synchrotron self-Compton spectrum has a simpler form, as considered in the next chapter.

For the head-on approximation employing the full Compton cross section, eq. (6.59), the solution to eq. (6.61) for isotropic nonthermal electrons scattering photons of an isotropic external radiation field is

$$\epsilon_s j_C(\epsilon_s) = \frac{3}{4} c \sigma_T u_0 \left(\frac{\epsilon_s}{\epsilon} \right)^2 \int_1^\infty d\gamma \frac{n_e(\gamma)}{\gamma^2} F_C(q, \Gamma_e) H \left(q; \frac{1}{4\gamma^2}, 1 \right), \quad (6.74)$$

where

$$\begin{aligned} F_C(q, \Gamma_e) &= F_T(q) + \frac{1}{2} \frac{(\Gamma_e q)^2}{(1 + \Gamma_e q)} (1 - q) \\ &= 2q \ln q + (1 + 2q)(1 - q) + \frac{1}{2} \frac{(\Gamma_e q)^2}{(1 + \Gamma_e q)} (1 - q), \end{aligned} \quad (6.75)$$

$$q \equiv \frac{\epsilon_s/\gamma}{\Gamma_e(1 - \epsilon_s/\gamma)}, \quad \Gamma_e \equiv 4\gamma\epsilon, \quad (6.76)$$

and q is restricted to the range $(4\gamma^2)^{-1} \leq q \leq 1$ [35, 67]. Restriction to the Thomson regime occurs when $\Gamma_e \ll 1$ or $4\epsilon\gamma \ll 1$. The final term in eq. (6.75) dominates for scattering in the KN regime. In deriving eq. (6.75), note that $y = 1 - \epsilon_s/\gamma = 1/(1 + \Gamma_e q)$, $q\Gamma_e y = 1 - y$, and $y + y^{-1} = 2 + [(q\Gamma_e)^2/(1 + q\Gamma_e)]$. Solving for the Heaviside function in eq. (6.74) gives the results considered in section 6.6.2, below.

The general expression for the Compton emissivity when relativistic, isotropic electrons Compton-scatter an isotropic target photon distribution is

$$\epsilon_s j_C(\epsilon_s) = \frac{3}{4} c \sigma_T \epsilon_s^2 \int_{\epsilon_s}^\infty d\gamma \frac{n_e(\gamma)}{\gamma^2} \int_{\epsilon_s/4\gamma^2(1-\epsilon_s/\gamma)}^{\epsilon_s/(1-\epsilon_s/\gamma)} d\epsilon \frac{u(\epsilon)}{\epsilon^2} F_C(q, \Gamma_e). \quad (6.77)$$

Figure 6.7 compares the spectral energy emissivity $\epsilon_s j(\epsilon_s)$ derived using the differential Compton cross sections in the head-on approximation (eq. [6.74]; thick curves) with the emissivity derived using various Thomson approximations (thin curves). Here we consider an isotropic distribution of electrons with $\gamma_1 = 10^2$, $\gamma_2 = 10^7$, and $p = 2.2$, and nonthermal electron energy density $u_e = 1 \text{ ergs cm}^{-3}$. The photon distribution is assumed to be isotropic with energy density $u_e = 1 \text{ erg cm}^{-3}$, and monochromatic with dimensionless energies ϵ_0 as labeled on the curves.

Figure 6.7a shows that the δ -function approximation, eq. (6.66) (thin curves), gives a good fit in the Thomson regime of scattering, as it was designed to do, but gives very poor approximations in the low- and high-energy regimes. The νF_ν spectral slopes are easily derived from the analytic

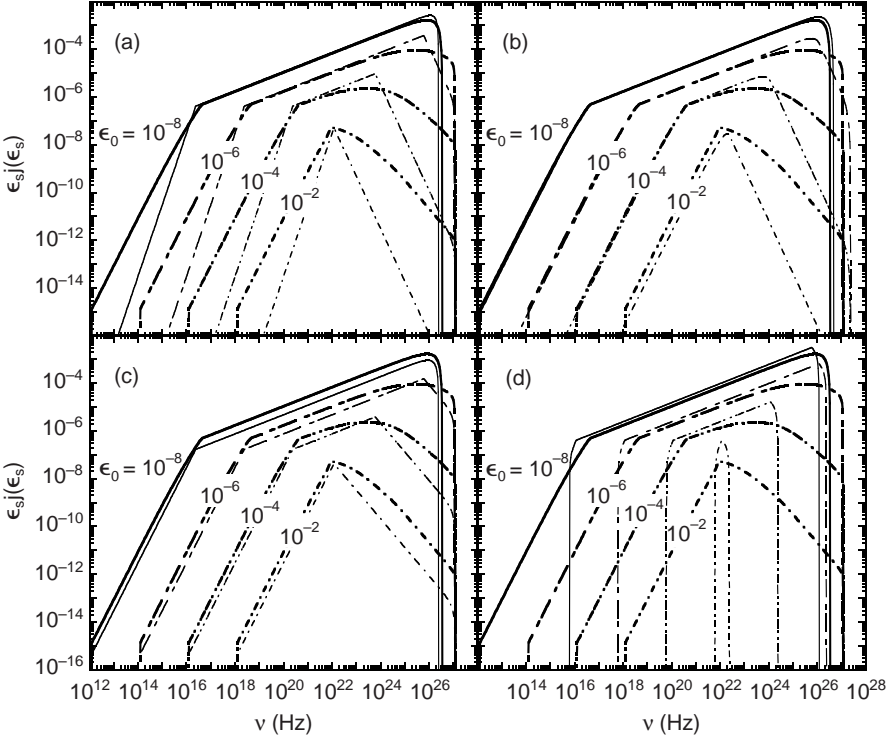


Figure 6.7 Comparison of the results obtained using the accurate Compton cross section (thick curves), given by eq. (6.74), with different approximations (thin curves) to the cross sections. All cross sections are derived in the head-on approximation. In the calculations, the electron distribution is isotropic and has a power-law spectrum with number index $p = 2.2$ and minimum and maximum Lorentz factors of 10^2 and 10^7 , respectively. The curves are labeled by the dimensionless soft photon energy ϵ_0 . Thin curves give results for the (a) δ -function Thomson approximation, eq. (6.66); (b) isotropic Thomson approximation, eq. (6.73); (c) average-angle Thomson approximation, eq. (6.80); and (d) δ -function approximation for isotropic photons and electrons, eq. (6.82).

form for the spectral energy emissivity, eq. (6.66). One finds that

$$\epsilon_s j_{T,\delta}(\epsilon_s) \propto \begin{cases} \epsilon_s^3, & \epsilon \lesssim \epsilon_s \lesssim 2\gamma_1^2 \epsilon, \\ \epsilon_s^{(3-p)/2}, & 2\gamma_1^2 \epsilon \lesssim \epsilon_s \lesssim \frac{1}{2\epsilon}, \\ \epsilon_s^{-p}, & \frac{1}{2\epsilon} \lesssim \epsilon_s. \end{cases} \quad (6.78)$$

The low-energy ($\epsilon_s \ll \epsilon$) νF_ν (or $\epsilon_s j(\epsilon_s)$) slope $\alpha_\nu \propto \epsilon_s^3$ from the analytic δ -function approximation, rather than $\alpha_\nu \propto \epsilon_s^2$ as implied by the Compton result, eq. (6.74). At the lowest energies, the scattered photons are dominated by low-energy photons in large-angle scattering events rather than by low-energy scattering from tail-on events. It is these low-energy scattering events, however, that are required in the δ -function approximation to make low-energy scattered photons.

Due to kinematic effects from the range of incident photon energies in the ERF, $\epsilon_s j(\epsilon_s) \propto \epsilon_s^3$ at energies $\epsilon \lesssim \epsilon_s \lesssim \gamma_1^2 \epsilon$. This follows by noting that

$$\frac{d\dot{N}_s}{d\epsilon_s} d\epsilon_s \propto \frac{d\dot{N}_s}{d\mu} (1 - \mu) d\mu,$$

and recalling the relation $\epsilon_s \propto \epsilon \gamma^2 (1 - \mu)$ between the electron energy, scattering direction μ , and scattered photon. The presence of the rate factor introduces an additional factor of ϵ_s , so that

$$\frac{dN_s}{d\epsilon_s} \propto \epsilon_s \quad \text{and} \quad \epsilon_s j(\epsilon_s) \propto \epsilon_s^3.$$

Comparison of low-energy results obtained using the isotropic Thomson cross section in figure 6.7b shows agreement with the accurate Compton-scattering result when $\epsilon \lesssim \epsilon_s \lesssim \gamma_1^2 \epsilon$. The inclusion of the low-energy portion of the Thomson scattered spectrum corrects the δ -function approximation. The low-energy scattered photons have the distribution

$$\frac{d\dot{N}_s}{d\epsilon_s} \propto \text{const}, \quad \text{so that} \quad \epsilon_s j(\epsilon_s) \propto \epsilon_s^2,$$

as found in the more accurate treatment. There still remain large discrepancies in the Klein-Nishina regime for the isotropic Thomson cross section.

Both the δ -function and isotropic Thomson cross sections correctly describe the spectral behavior in the Thomson regime $\gamma_1^2 \epsilon \lesssim \epsilon_s \lesssim 1/2 \epsilon$. Equation (6.78) implies that $\epsilon_s j(\epsilon_s) \propto \epsilon_s^{(3-p)/2}$, so that

$$j(\epsilon_s) \propto \epsilon_s^{-\alpha}, \quad \text{where} \quad \alpha = \frac{p-1}{2} \quad (6.79)$$

is the energy index. The νF_ν index in the Thomson regime is $\alpha_\nu = (3-p)/2$, and the number index $\alpha_\Gamma = (p+1)/2$.

The relation between photon energy index α and electron steady-state number index p can be obtained by elementary means. Target photons with energy ϵ are Thomson-scattered to ϵ_s by electrons with Lorentz factor $\gamma \cong \sqrt{\epsilon_s/\epsilon}$. Because $f_\epsilon^T \propto \gamma^3 N_e(\gamma) \propto \epsilon^{1-\alpha}$, $(3-p)/2 = 1 - \alpha$, so

$$\alpha = \frac{p-1}{2}.$$

In the Klein-Nishina regime $\epsilon_s \gtrsim 1/2\epsilon$, the δ -function approximation under estimates the actual scattered flux by having no scattering for events in the Klein-Nishina regime. The isotropic Thomson cross section in the Klein-Nishina regime is not much better. Due to residual Thomson scattering, the scattered photon spectrum in the Klein-Nishina regime varies roughly as $\epsilon_s j(\epsilon_s) \propto \epsilon_s^{-p}$ in these two approximations. The full Compton cross section gives a more rounded spectrum in the Klein-Nishina regime, with asymptotic spectral slope approaching $\epsilon_s j(\epsilon_s) \propto \epsilon_s^{1-p}$.

We consider a further ‘‘average-angle’’ approximation where the typical scattering angle is $\mu = 0$. Substituting the δ -function approximation eq. (6.58) into eq. (6.61) with the rate factor $(1 - \mu)$ set equal to unity, one obtains for the power-law electron distribution (6.62) the result

$$\epsilon_s j_{aa}(\epsilon_s) = \frac{c\sigma_T u_0}{4} \left(\frac{\epsilon_s}{\epsilon}\right)^2 \frac{k_e}{p+1} \left\{ \left[\max\left(\gamma_1, \epsilon_s, \sqrt{\frac{\epsilon_s}{2\epsilon}}\right) \right]^{-(1+p)} - \gamma_2^{-(1+p)} \right\}. \quad (6.80)$$

Figure 6.7c compares the average-angle approximation with the more accurate Compton result. The slopes are

$$\epsilon_s j_{aa}(\epsilon_s) \propto \begin{cases} \epsilon_s^2, & \epsilon \lesssim \epsilon_s \lesssim 2\gamma_1^2 \epsilon, \\ \epsilon_s^{(3-p)/2}, & 2\gamma_1^2 \epsilon \lesssim \epsilon_s \lesssim \frac{1}{2\epsilon}, \\ \epsilon_s^{1-p}, & \frac{1}{2\epsilon} \lesssim \epsilon_s. \end{cases} \quad (6.81)$$

The low-energy slope is in good agreement with the low-energy slope obtained with the full Compton cross section, though larger deviations now appear in the central part of the Thomson regime $\gamma_1^2 \epsilon_0 \lesssim \epsilon_s \lesssim 1/2\epsilon$ where most of the photon energy is radiated, compared to results obtained using the δ -function and isotropic Thomson cross sections. Although the scattered spectrum is discrepant in the Klein-Nishina regime by a factor of ≈ 10 , the average-angle approximation gives roughly the correct asymptotic slope.

The appropriate approximation depends on the accuracy needed in different problems or regimes of scattered emission. The δ -function approximation leads to the simplest analytic results, but is accurate only in the regime $\gamma_1^2 \epsilon \lesssim \epsilon_s \lesssim 1/2\epsilon$. This is, however, often the most important regime, because the νF_ν peaks of Compton-scattered photon spectra, which are the brightest parts of the spectrum, are usually found in this regime.

6.6 THOMSON SCATTERING: ISOTROPIC PHOTONS AND ELECTRONS

In this section, a δ -function approximation for the scattered spectrum from isotropic electrons and isotropic target photons is derived in the Thomson limit. Comparison is made with an accurate calculation.

6.6.1 Thomson-Scattered Radiation Spectrum in the δ -Function Approximation

We consider scattering in the Thomson regime $\bar{\epsilon} \cong \gamma^2 \epsilon \ll 1$ in the average-angle approximation, which leads to an expression involving the photon and electron distributions alone. In the ERF, $\bar{\epsilon} = \gamma \epsilon (1 - \mu) \approx \gamma \epsilon$. Because the mean scattered photon energy in Thomson scattering is $\epsilon_s = \gamma \bar{\epsilon} \cong \gamma^2 \epsilon$ for Thomson scattering, $\epsilon_s \epsilon = (\gamma \epsilon)^2 \ll 1$, and $\epsilon \ll 1/\epsilon_s$. Also, because we are considering “upscattering” and not “downscattering,” $\epsilon_s > \epsilon$ and therefore $\epsilon \ll \min(\epsilon_s, \epsilon_s^{-1})$.

For systems where the electron Lorentz factor distribution $n_e(\gamma)$ and target photon distribution $n_{\text{ph}}(\epsilon)$ are isotropic, we adopt an approximation for the Thomson-scattered spectrum consistent with the Thomson energy-loss rate, eq. (6.50), and the mean scattered photon energy $\epsilon_s \cong \gamma^2 \epsilon$ that also restricts scattering to the Thomson regime. This approximation is

$$\dot{n}_{\text{T}}(\epsilon_s) \cong \frac{2}{3} c \sigma_{\text{T}} \epsilon_s^{-1/2} \int_0^{\min(\epsilon_s, \epsilon_s^{-1})} d\epsilon \epsilon^{-1/2} n_{\text{ph}}(\epsilon) n_e \left(\sqrt{\frac{\epsilon_s}{\epsilon}} \right). \quad (6.82)$$

If the photon field is monochromatic, then $n_{\text{ph}}(\epsilon) = n_{\text{ph}}^0 \delta(\epsilon - \epsilon_0)$. For a single electron with Lorentz factor $\bar{\gamma}$, the electron distribution function takes the form $n_e(\gamma) = \delta(\gamma - \bar{\gamma})$. It is easy to verify from eq. (6.82) that

$$\int_0^\infty d\epsilon_s \epsilon_s \dot{n}_{\text{T}}(\epsilon_s) = \frac{4}{3} c \sigma_{\text{T}} n_{\text{ph}}^0 \gamma^2 \epsilon_0 = -\dot{\gamma}_{\text{T}}, \quad (6.83)$$

noting that $u_0 = m_e c^2 \epsilon_0 n_{\text{ph}}^0$ for the monochromatic radiation field. The Thomson regime of scattering holds in eq. (6.83) when $\epsilon_0 \ll 1/\gamma$.

The comoving νL_ν luminosity $\epsilon_s L(\epsilon_s) = V_b \epsilon_s j_{\text{T}}(\epsilon_s) = m_e c^2 V_b \epsilon_s^2 \dot{n}_{\text{T}}(\epsilon_s)$, where V_b is the volume of the emitting region. The Thomson-scattered photon spectrum from a monochromatic photon source in this approximation is given by

$$\epsilon_s L^{\text{T}}(\epsilon_s) \cong \frac{2}{3} c \sigma_{\text{T}} u_0 \left(\frac{\epsilon_s}{\epsilon} \right)^{3/2} N_e \left(\sqrt{\frac{\epsilon_s}{\epsilon}} \right) = \frac{2}{3} c \sigma_{\text{T}} u_0 \gamma_{\text{T}}^3 N_e(\gamma_{\text{T}}), \quad \gamma_{\text{T}} = \sqrt{\frac{\epsilon_s}{\epsilon}}, \quad (6.84)$$

noting that restriction to the Thomson regime implies $\epsilon \lesssim \min(\epsilon_s, \epsilon_s^{-1})$. The energy emissivity $m_e c^2 \epsilon_s^2 \dot{n}_T(\epsilon_s)$, with $\dot{n}_T(\epsilon_s)$ given by eq. (6.82), is compared to results obtained with the accurate Compton cross section in figure 6.7d.

6.6.2 Spectral Comparisons for Isotropic Power-Law Photons and Electrons

Expression (6.82) is used to derive an approximation for the Compton-scattered photon spectrum from isotropic power-law distributions of nonthermal electrons and photons. The electron spectrum and normalization is given by eqs. (6.62)–(6.64). For a power-law photon distribution,

$$n_{\text{ph}}(\epsilon) = n_{\text{ph}}^0 \epsilon^{-1-\alpha} H(\epsilon; \epsilon_1, \epsilon_2), \quad (6.85)$$

and normalization to the total photon energy density $u_0 = m_e c^2 \int_0^\infty d\epsilon \epsilon n_{\text{ph}}(\epsilon)$ implies

$$n_{\text{ph}}^0 = \frac{(1-\alpha)u_0}{m_e c^2 (\epsilon_2^{1-\alpha} - \epsilon_1^{1-\alpha})}. \quad (6.86)$$

Substituting these expressions into eq. (6.82) and solving gives

$$\epsilon_s j_{\text{pl}}(\epsilon_s) = \frac{4}{3} m_e c^3 \sigma_T k_e n_{\text{ph}}^0 \left(\frac{\epsilon_u^{(p-2\alpha-1)/2} - \epsilon_\ell^{(p-2\alpha-1)/2}}{p-2\alpha-1} \right), \quad (6.87)$$

where

$$\epsilon_\ell = \max\left(\frac{\epsilon_s}{\gamma_2^2}, \epsilon_1\right) \quad \text{and} \quad \epsilon_u = \min\left(\frac{\epsilon_s}{\gamma_1^2}, \epsilon_2, \epsilon_s, \epsilon_s^{-1}\right). \quad (6.88)$$

This expression provides a simple analytic form for the scattered photon spectrum when a power-law distribution of electrons with number index p Compton scatters a target photon spectrum with energy index α ; it is plotted in figure 6.8.

Figure 6.8 shows electron distributions calculated with the accurate Compton-scattered spectrum, eq. (6.74). The two-fold integration that is solved is

$$\epsilon_s j_C(\epsilon_s) = \frac{3}{4} c \sigma_T \epsilon_s^2 \int_0^\infty d\epsilon \frac{u(\epsilon)}{\epsilon^2} \int_{\gamma_{\text{min}}}^{\gamma_{\text{max}}} d\gamma \frac{n_e(\gamma)}{\gamma^2} F_C(q, \Gamma_e), \quad (6.89)$$

where $F_C(q, \Gamma_e)$ is given by eq. (6.75), and the limits

$$\gamma_{\text{min}} = \frac{\epsilon_s}{2} \left(1 + \sqrt{1 + \frac{1}{\epsilon_s}} \right) \quad (6.90)$$

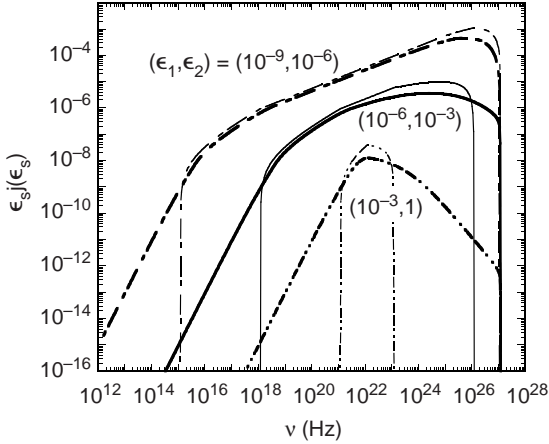


Figure 6.8 Comparison of expressions obtained using the δ -function approximation for the Thomson cross section (thin curves), and the accurate Compton (thick curves) cross sections, given by eqs. (6.87) and (6.89), respectively. The electron distribution is isotropic and has a power-law spectrum with number index $p = 2.2$ and minimum and maximum Lorentz factors of 10^2 and 10^7 , respectively. The target photon spectrum is given by a power law with energy index $\alpha = 0.5$ and soft photon energies between energies ϵ_1 and ϵ_2 , as labeled in the figure.

and

$$\gamma_{\max} = \frac{\epsilon_s}{\epsilon - \epsilon_s} H(\epsilon - \epsilon_s) + \gamma_2 H(\epsilon_s - \epsilon) \quad (6.91)$$

on γ are derived from the restriction

$$\frac{1}{4\gamma^2} \leq q = \frac{\epsilon_s/\gamma}{\Gamma_e(1 - \epsilon_s/\gamma)} \leq 1.$$

The energy densities of both the nonthermal electrons and target photons are normalized to 1 erg cm^{-3} .

6.7 EXTERNAL PHOTON FIELDS COMPTON-SCATTERED BY JET ELECTRONS

This process was proposed to explain the intense γ radiation detected from the jets of blazar active galactic nuclei [69, 70]. Theoretical treatments of scattered spectra have analyzed this problem in two ways: (i) the external radiation field is transformed to the comoving frame where the scattered spectrum is calculated and then transformed to the observer frame [68, 69];

and (ii) the electron distribution is transformed to the stationary frame, and then the external photon field is Compton-scattered [71]. The second approach can be simpler if the electron distribution is fixed. When the electrons evolve through injection, energy losses, and pitch-angle scattering, however, one must consider the electron evolution and energy losses in the comoving frame. The second approach has been limited to isotropic external radiation fields. Recent work extends this method to arbitrary anisotropic external radiation fields.

Approach (i): Transform Target and Scattered Photon Spectra

In this approach, the comoving target photon emissivity is angle dependent even if the comoving electron distribution is isotropic, because the target photon distribution is highly aberrated in the comoving frame. The emissivity for Compton scattering in the head-on approximation is, from eqs. (2.44) and (6.55), given by

$$\begin{aligned} \epsilon'_s j'(\epsilon'_s, \Omega'_s) &= c \epsilon_s'^2 \oint d\Omega' (1 - \cos \bar{\psi}) \int_0^\infty d\epsilon' \frac{u'(\epsilon', \Omega')}{\epsilon'} \\ &\times \int_1^\infty d\gamma' n'_e(\gamma', \Omega'_s) \left(\frac{d\sigma}{d\epsilon'_s} \right), \end{aligned} \quad (6.92)$$

and $\cos \bar{\psi} = \mu_s \mu + \sqrt{1 - \mu^2} \sqrt{1 - \mu'^2} \cos(\phi'_s - \phi')$. The received νF_ν spectrum, given by eq. (5.46), is

$$f_\epsilon \cong \frac{\delta_D^4 V'_b}{d_L^2} \epsilon'_s j'(\epsilon'_s, \Omega'_s), \quad (6.93)$$

with $\epsilon'_s = (1 + z)\epsilon/\delta_D$, $\mu'_s = (\mu - \beta)/(1 - \beta\mu)$, and $\phi'_s = \phi$.

Approach (ii): Transform Electron Spectrum to Stationary Frame

In this approach, due to Georganopoulos, Kirk, and Mastichiadis [71], limited in their paper to isotropic radiation fields in the stationary frame, the stationary-frame photon luminosity is calculated from the transformed stationary-frame electron distribution $N_e(\gamma, \Omega)$, using as a scattering kernel the elementary emissivity derived for a relativistic electron scattering isotropic target photons [67]. The specific spectral luminosity

$$\epsilon_s L(\epsilon_s, \Omega_s) = \int d\epsilon_* \frac{u_*(\epsilon_*, \Omega_*)}{m_e c^2} \int d\gamma N_e(\gamma, \Omega_s) \frac{d\mathcal{E}(\gamma, \epsilon_*)}{dt d\epsilon_s d\Omega_s}, \quad (6.94)$$

where the scattering kernel $d\mathcal{E}/dt d\epsilon_s d\Omega_s = V_b \epsilon_s j(\epsilon_s)/4\pi$ is accurately given in the head-on approximation by the Compton emissivity, eq. (6.77) or eq. (6.89) [72]. The νF_ν spectrum is simply given by

$$f_\epsilon = \frac{\epsilon_s L(\epsilon_s, \Omega_s)}{d_L^2} \quad (6.95)$$

with

$$\epsilon_s = (1+z)\epsilon \equiv \epsilon_z \quad \text{and} \quad \Omega_s = \Omega_*. \quad (6.96)$$

The external Compton-scattered radiation field can be obtained by adapting this approach for arbitrary external radiation fields [73]. The basic equation giving the scattered νF_ν flux from relativistic jet electrons Compton-scattering photons of an external radiation field described by $u_*(\epsilon_*, \Omega_*)$ at some location \vec{r} is, from eqs. (6.13), (6.25), and (6.29),

$$f_\epsilon^{\text{EC}} = \frac{c\pi r_e^2}{4\pi d_L^2} \epsilon_s^2 \delta_D^3 \oint d\Omega_* \int_0^{\epsilon_{*,\text{high}}} d\epsilon_* \frac{u_*(\epsilon_*, \Omega_*)}{\epsilon_*^2} \int_{\gamma_{\text{low}}}^\infty d\gamma \frac{N'_e(\gamma/\delta_D)}{\gamma^2} \Xi_C. \quad (6.97)$$

The lower limit on the electron Lorentz factor, γ_{low} , and the upper limit $\epsilon_{*,\text{high}}$ implied by the kinematic limits on y are

$$\gamma_{\text{low}} = \frac{\epsilon_s}{2} \left(1 + \sqrt{1 + \frac{2}{\epsilon_* \epsilon_s (1 - \cos \psi)}} \right) \quad (6.98)$$

and

$$\epsilon_{*,\text{high}} = \frac{2\epsilon_s}{1 - \cos \psi}. \quad (6.99)$$

Results obtained using approach (i), giving analytic results for scattering in the Thomson regime, are reviewed first.

6.7.1 Thomson-Scattered Spectrum for an External Point Source of Radiation from Behind

A point source of radiation impinging from behind the outflowing plasma jet is of interest because of the intense accretion-disk radiation fields at the base of supermassive black-hole jets. At sufficiently far distances, the accretion disk can be approximated as a point source of radiation impinging from behind, though the radial extent of the accretion disk, as described in the next section, must also be considered over a wide range of jet heights.

We derive the flux for the case of a point source behind the jet using the δ -function approximation for the Thomson cross section. The point-source approximation for the spectral energy density of a monochromatic radiation field is given in the stationary frame by eq. (5.31) and in the comoving frame of a jet streaming radially away from the point radiation field by eq. (5.32). Substituting these equations into eq. (6.92) gives

$$j'_{\text{pt}}(\epsilon'_s, \Omega'_s) = \frac{\sigma_{\text{T}} L_d (1 - \mu'_s)}{32\pi^2 r^2 \epsilon_0 \Gamma (1 + \beta)} \hat{\gamma}' n'_e(\hat{\gamma}'), \quad \hat{\gamma}' = \left(\frac{\Gamma \epsilon'_s (1 + \beta)}{\epsilon_0 (1 - \mu'_s)} \right)^{1/2}, \quad (6.100)$$

so that with eq. (6.93) we have

$$f_{\epsilon}^{\text{pt}} = \delta_{\text{D}}^6 \frac{\sigma_{\text{T}} (1 - \mu)^2}{8\pi d_L^2} \left(\frac{L_d}{4\pi r^2} \right) \tilde{\gamma}'^3 N'_e(\tilde{\gamma}') H \left(\frac{1}{\epsilon_0 (1 - \mu)} - \epsilon_z \right),$$

$$\tilde{\gamma}' \equiv \delta_{\text{D}}^{-1} \sqrt{\frac{\epsilon_z}{(1 - \mu)\epsilon_0}} \quad (6.101)$$

[69], and the Heaviside function restricts the scattering to the Thomson regime.

6.7.2 Thomson-Scattered Spectrum for External Isotropic Radiation in the δ -Function Approximation

The Compton-scattered γ -ray spectrum for an external isotropic, monochromatic radiation field is derived for scattering restricted to the Thomson regime.

Spectrum in the Limit $\Gamma \gg 1$, $\beta \rightarrow 1$

Substituting eq. (5.26) for an external isotropic monochromatic radiation field in the limit $\Gamma \gg 1$, $\beta \rightarrow 1$ into eq. (6.92) gives, using the δ -function Thomson cross section, eq. (6.58),

$$\epsilon'_s j'(\epsilon'_s, \Omega'_s) \cong \frac{c\sigma_{\text{T}} u_0}{6\pi} \Gamma^2 (1 + \mu'_s)^2 \bar{\gamma}'^3 n'_e(\bar{\gamma}', \Omega'_s) H(1 - \bar{\epsilon}),$$

$$\bar{\gamma}' = \sqrt{\frac{3\epsilon'_s}{4\Gamma\epsilon_0(1 + \mu'_s)}}. \quad (6.102)$$

Here $\bar{\epsilon} = \gamma' \epsilon' (1 + \mu'_s) = 4\gamma' \Gamma \epsilon_0 (1 + \mu'_s) / 3$. Substituting eq. (6.102) into eq. (6.93), using the Lorentz transformation equations, gives

$$f_{\epsilon}^{\text{ext}, \Gamma} \cong \delta_D^6 \frac{c \sigma_T u_0 (1 + \mu)^2}{24\pi d_L^2} \tilde{\gamma}'^3 N'_e(\tilde{\gamma}') H\left(\frac{1}{\epsilon_0(1 + \mu)} - \epsilon_z\right),$$

$$\tilde{\gamma}' \equiv \delta_D^{-1} \sqrt{\frac{3\epsilon_z}{2(1 + \mu)\epsilon_0}} \quad (6.103)$$

for electrons isotropically distributed in the comoving frame. Because the brightest fluxes are observed nearly on-axis, it is generally a good approximation to let $\mu \rightarrow 1$ in this expression.

For a power-law electron distribution, eq. (6.62),

$$N'_e(\gamma') = V'_b n'_e(\gamma') = K' \gamma'^{-p} H(\gamma'; \gamma'_1, \gamma'_2), \quad (6.104)$$

and eq. (6.103) becomes

$$f_{\epsilon}^{\text{ext}, \Gamma} \cong \frac{K'}{6\pi d_L^2} c \sigma_T u_0 \delta_D^{3+p} \left(\frac{3\epsilon_z}{4\epsilon_0}\right)^{(3-p)/2} \quad \text{for } \gamma_1'^2 \lesssim \frac{\epsilon_z}{\delta_D^2 \epsilon_0} \lesssim \gamma_2'^2. \quad (6.105)$$

Spectrum for General β , Γ

This result can be derived [74, 75] using the general transformation of the external radiation field given by eq. (5.24), so that the result is applicable even when $\Gamma - 1, \beta \ll 1$. Again use of the δ -function Thomson approximation gives

$$\epsilon'_s j'(\epsilon'_s, \Omega'_s) \cong \frac{c \sigma_T u_0}{2\Gamma(\beta + \mu'_s)} \left(\frac{\epsilon'_s}{\epsilon_0}\right)^3 \int_{\max(\gamma'_{-+}, \epsilon'_s)}^{\gamma'_{+-}} d\gamma' \gamma'^{-4} n'_e(\gamma', \Omega'_s), \quad (6.106)$$

where

$$\gamma'_{-+} = \sqrt{\frac{\Gamma \epsilon'_s (1 - \beta)}{\epsilon_0 (1 + \mu'_s)}} \quad \text{and} \quad \gamma'_{+-} = \sqrt{\frac{\Gamma \epsilon'_s (1 + \beta)}{\epsilon_0 (1 - \mu'_s)}}. \quad (6.107)$$

The νF_{ν} flux for an isotropic, power-law electron distribution is found to be

$$f_{\epsilon}^{\text{ext}, \Gamma} \cong \frac{K'(1 + \mu)^{2+\alpha}}{16\pi d_L^2 (2 + \alpha)} c \sigma_T u_0 \delta_D^{4+2\alpha} \left(\frac{\epsilon_z}{\epsilon_0}\right)^{1-\alpha} \quad \text{for } \gamma_1'^2 \lesssim \frac{\epsilon_z}{\delta_D^2 \epsilon_0 (1 + \mu)} \lesssim \gamma_2'^2, \quad (6.108)$$

which holds when $0 < \mu \leq 1$, recalling that $\alpha = (p - 1)/2$.

The expression

$$f_\epsilon^T \cong \frac{\delta_D^6}{6\pi d_L^2} c\sigma_T u_0 \gamma_T'^3 N_e'(\gamma_T') \quad \text{with} \quad \gamma_T' = \frac{1}{\delta_D} \sqrt{\frac{\epsilon_z}{2\epsilon_0}} \quad (6.109)$$

provides a simple analytic approximation for the νF_ν spectrum when nonthermal electrons Thomson-scatter photons from an external isotropic monochromatic radiation field. Restriction to the Thomson regime, from eq. (6.103), means that $\epsilon(1+z) \lesssim 1/2\epsilon_0$. For UV soft photons with $\epsilon_0 = 10^{-4}\epsilon_{-4}$, this means that Klein-Nishina effects are important already when E_γ (GeV) $\gtrsim 2/\epsilon_{-4}(1+z)$. By comparison, scattered photons remain in the Thomson regime until E_γ (TeV) $\gtrsim (\Gamma/10)^2/[(1+z)\epsilon_{-4}]$ for photons entering from behind (eq. [6.101]).

For comparison with the monochromatic expression in the δ -function approximation, eq. (6.109), we write

$$f_\epsilon = C(p) \frac{K' c\sigma_T u_0}{4\pi d_L^2} \delta_D^{3+p} \left(\frac{\epsilon_s}{\epsilon_0}\right)^{(3-p)/2}. \quad (6.110)$$

In the asymptotic, power-law portion of the Compton-scattered spectra, the coefficients C_p are given by

$$C_{T,\text{iso}}^i(p) = \frac{1}{2} \left(\frac{3}{4}\right)^{(1-p)/2}$$

for the δ -function expression, eq. (6.105),

$$C_T^i(p) = 2^{(p-1)/2}/(p+1)$$

for the Thomson expression, eq. (6.108), and

$$C_{T,\delta}^i(p) = 2^{(p-1)/2}/3$$

for the δ -function approximation, eq. (6.109), for the Thomson cross section. Values of the coefficients for the three approximations are given in table 6.1.

The range of scattered photons is determined by the range of electron energies. Because $\epsilon_s \lesssim 4\gamma'^2\epsilon_0$, $\gamma' \cong \sqrt{\epsilon_s/\epsilon_0}$, and

$$\delta_D^2 \gamma_1^2 \lesssim \frac{\epsilon_s}{\epsilon_0} \lesssim \delta_D^2 \gamma_2^2$$

(compare eq. [6.105]).

6.7.3 External Isotropic Photons Compton-Scattered by Jet Electrons

We now employ approach (ii) [71], restricting the treatment first to external isotropic radiation fields.

Table 6.1 Factors for Compton-Scattered Monochromatic Target Photons from Isotropic, Power-Law Electrons in the Thomson Regime

C_p	p				
	0	1	2	3	4
$C_{T,\text{iso}}^i(p)$	0.433	1/2	0.577	2/3	0.769
$C_T^i(p)$	0.707	1/2	0.471	1/2	0.565
$C_{T,\delta}^i(p)$	0.23	1/3	0.471	2/3	0.943
$C_{T,\text{iso}}^{ii}(p)$	2/3	1/2	0.533	2/3	0.914
$C_T^{ii}(p)$	0.733	1/2	0.525	2/3	0.936

Treating the relativistic leptons as massless particles, the invariant phase volume (5.7) for relativistic particles is given by

$$\frac{dN}{d\mathcal{V}} = \frac{dN}{dV d^3\vec{p}} = inv \Rightarrow \frac{1}{\gamma^2} \frac{dN}{d\gamma d\Omega dV} = inv,$$

implying that

$$N(\gamma, \Omega) = \frac{\gamma^2}{\gamma'^2} \frac{dV}{dV'} N'(\gamma', \Omega') = \delta_D^3 N'(\gamma', \Omega'), \quad (6.111)$$

noting that $dV/dV' = dt'/dt = \delta_D$, and $\gamma = \delta_D \gamma'$. The measurement of flux from the emitting volume at the appropriate retarded times gives the physical basis for the change in effective volume with Doppler factor.

The directional luminosity from electrons with Lorentz factor and angular distribution $N'_e(\gamma', \Omega')$ in a uniform blob is

$$\begin{aligned} \epsilon_s L(\epsilon_s, \Omega_s) &= \epsilon_s V_b j(\epsilon_s, \Omega_s) \\ &= \frac{3}{4} c \sigma_T \epsilon_s^2 \delta_D^3 \int_0^\infty d\epsilon_* \frac{u_*(\epsilon_*)}{\epsilon_*^2} \int_1^\infty d\gamma \frac{N'_e(\gamma', \Omega')}{\gamma^2} F(\hat{\epsilon}) H(1 - \hat{\epsilon}), \end{aligned} \quad (6.112)$$

where $F(\hat{\epsilon})$ is given for the various approximations to the Compton cross section. For the Thomson and isotropic Thomson cross sections, $F(\hat{\epsilon}) = F_T(\hat{\epsilon})H(1 - \gamma\epsilon)$ and $F(\hat{\epsilon}) = F_{T,\text{iso}}(\hat{\epsilon})H(1 - \gamma\epsilon)$ given by eqs. (6.69) and (6.71), respectively, with $\hat{\epsilon} = \epsilon_s/4\gamma'^2\epsilon_0$ (eq. [6.70]). The factor $H(1 - \gamma\epsilon)$ crudely restricts us to Thomson scattering.

For the full Compton cross section, $F(\hat{\epsilon})$ is replaced by $F_C(q, \Gamma_e)$, given by eq. (6.75), and $\hat{\epsilon} \rightarrow q$, given by eq. (6.76). For isotropically distributed electrons in the comoving frame, eq. (6.112) becomes

$$f_\epsilon = \frac{3}{4} \frac{c \sigma_T \epsilon_s^2}{4\pi d_L^2} \delta_D^3 \int_0^\infty d\epsilon_* \frac{u_*(\epsilon_*)}{\epsilon_*^2} \int_{\gamma_{\min}}^{\gamma_{\max}} d\gamma \frac{N'_e(\gamma')}{\gamma^2} F_C(q, \Gamma_e), \quad (6.113)$$

where $\gamma = \delta_D \gamma'$, $F_C(q, \Gamma_e)$ is given by eq. (6.75) and γ_{\min} and γ_{\max} are given by eqs. (6.90) and (6.91), respectively, with $\epsilon \rightarrow \epsilon_*$, and $(1+z)\epsilon = \epsilon_s$.

Assuming a power-law isotropic pitch-angle electron distribution given by eq. (6.104), the νF_ν spectrum (eq. [6.113]) for the isotropic external target field with monochromatic energy ϵ_0 , has dependence $f_\epsilon^C = \epsilon_s L(\epsilon_s, \Omega_s)/d_L^2 \propto \delta_D^{3+p}$. Thus the beaming factor of Compton-scattered radiation is $\propto \delta_D^{3+p} \propto \delta_D^{4+2\alpha}$ in the Klein-Nishina as well as the Thomson regime [71].

Isotropic Monochromatic Target Photons Thomson-Scattered by Power-Law Jet Electrons

The νF_ν spectrum for a blob containing relativistic electrons with an isotropic pitch-angle distribution that are entrained in a randomly oriented magnetic field is given through approach (ii) as

$$f_\epsilon^{\text{T,iso}} = \frac{3K'}{4} \frac{c\sigma_T u_0}{4\pi d_L^2} \left(\frac{\epsilon_s}{\epsilon_0}\right)^2 \delta_D^{p+3} \int_{\gamma_1'}^{\gamma_2'} d\gamma' \gamma'^{-(2+p)} F(\hat{\epsilon}). \quad (6.114)$$

For the Thomson cross sections, $\hat{\epsilon} = \epsilon_s/4\gamma_*^2\epsilon_0$, $\gamma_* = \sqrt{\epsilon_s/4\epsilon_0\hat{\epsilon}}$, and

$$d\gamma_* = -\frac{1}{2\hat{\epsilon}^{3/2}} \sqrt{\frac{\epsilon_s}{4\epsilon_0}} d\hat{\epsilon} \Rightarrow d\gamma' \gamma'^{-(2+p)} = -2^p \left(\frac{\epsilon_s}{\epsilon_0}\right)^{(3-p)/2} \hat{\epsilon}^{(p-1)/2} d\hat{\epsilon}.$$

Thus

$$f_\epsilon^{\text{T,iso}} = \frac{2^{p-2} \cdot 3K'}{4\pi d_L^2} c\sigma_T u_0 \left(\frac{\epsilon_s}{\epsilon_0}\right)^{(3-p)/2} \delta_D^{p+3} [I(\hat{\epsilon}_1) - I(\hat{\epsilon}_2)], \quad (6.115)$$

where

$$I(x) = \int^x d\hat{\epsilon} \hat{\epsilon}^{(p-1)/2} F(\hat{\epsilon}),$$

$$\hat{\epsilon}_1 = \frac{\epsilon_s}{4\gamma_1'^2\epsilon_0}, \quad \gamma_1 = \max\left(\delta_D\gamma_1', \sqrt{\frac{\epsilon_s}{4\epsilon_0}}\right), \quad \hat{\epsilon}_2 = \frac{\epsilon_s}{4\gamma_2'^2\epsilon_0}, \quad \gamma_2 = \delta_D\gamma_2'.$$

For the Thomson cross section, eq. (6.69), the integral

$$\begin{aligned} I_T(x) &= \int^x d\hat{\epsilon} \hat{\epsilon}^{(p-1)/2} (1 + \hat{\epsilon} - 2\hat{\epsilon}^2 + 2\hat{\epsilon} \ln \hat{\epsilon}) \\ &= 2 \left[\frac{x^{(p+1)/2}}{p+1} + \frac{x^{(p+3)/2}}{p+3} \left(1 + 2 \ln x - \frac{4}{p+3}\right) - \frac{2x^{(p+5)/2}}{p+5} \right]. \end{aligned} \quad (6.116)$$

For the isotropic Thomson cross section, eq. (6.71), the integral

$$I_{\text{T,iso}}(x) = \frac{2}{3} \int^x d\hat{\epsilon} \hat{\epsilon}^{(p-1)/2} (1 - \hat{\epsilon}) = \frac{4}{3} \left(\frac{x^{(p+1)/2}}{p+1} - \frac{x^{(p+3)/2}}{p+3} \right). \quad (6.117)$$

In the asymptotic power-law portion of the Thomson spectrum, $\gamma'_1 \leq \sqrt{\epsilon_s/4\epsilon_0} \ll \gamma'_2$, and in this regime $\hat{\epsilon}_1 \rightarrow 1 \gg \hat{\epsilon}_2$. Note that the Thomson regime criterion can be expressed as $\epsilon \epsilon_s \ll 1$, using the relations $\epsilon_s \cong \gamma^2 \epsilon$ and $\gamma \epsilon \ll 1$. In the notation of eq. (6.110), the coefficients C_p from approach (ii) are given by

$$C_{\text{T,iso}}^{\text{ii}}(p) = \frac{2^{p+1}}{(p+1)(p+3)},$$

and

$$C_{\text{T}}^{\text{ii}}(p) = 3 \cdot 2^{p-1} \left(\frac{3-p}{(p+1)(p+5)} + \frac{p-1}{(p+3)^2} \right).$$

Values for these quantities are given in table 6.1. Note the good agreement between the two approaches for randomly distributed, power-law jet electrons scattering external, isotropic photons in the Thomson regime.

Blackbody Photons Thomson-Scattered by Power-Law Jet Electrons

Substituting the blackbody photon distribution $u^{\text{bb}}(\epsilon; \Theta) = 8\pi m_e c^2 \epsilon^3 / \{\lambda_C^3 \times [\exp(\epsilon/\Theta) - 1]\}$, eq. (5.16), into eq. (6.113) gives, with $U_{\text{cr}} = B_{\text{cr}}^2/8\pi$ and different approximations for $F_C(q, \Gamma_e)$, the result

$$f_{\epsilon}^{\text{ECMB}} \rightarrow \frac{2^{p-3} \cdot 3K' I_{\text{T}}}{4\pi d_L^2} c\sigma_{\text{T}} \left(\frac{8\alpha_f}{\pi^2} \right) U_{\text{cr}} \epsilon_s^{(3-p)/2} \delta_{\text{D}}^{p+3} \Theta^{(5+p)/2} I_p^{\text{ECMB}}. \quad (6.118)$$

Here

$$I_p^{\text{ECMB}} = \int_0^{\infty} dx \frac{x^{(3+p)/2}}{\exp(x) - 1} = \Gamma\left(\frac{5+p}{2}\right) \zeta\left(\frac{5+p}{2}\right), \quad (6.119)$$

$$I_{\text{T}} = I_{\text{T,iso}}(p) = \frac{8}{3(p+1)(p+3)},$$

and

$$I_{\text{T}} = I_{\text{T}}(p) = 2 \left(\frac{3-p}{(p+1)(p+5)} + \frac{p-1}{(p+3)^2} \right).$$

Returning to the monochromatic form, eq. (6.115), it is simple to see that

$$f_{\epsilon}^{\text{ECMB}} \propto \begin{cases} \delta_{\text{D}}^2 (\epsilon_s/\epsilon_0)^2, & \epsilon_s \ll 4\delta_{\text{D}}^2 \gamma_1^2 \epsilon_0, \\ \delta_{\text{D}}^{3+p} (\epsilon_s/\epsilon_0)^{(3-p)/2}, & 4\delta_{\text{D}}^2 \gamma_1^2 \epsilon_0 \ll \epsilon_s \ll 4\delta_{\text{D}}^2 \gamma_2^2 \epsilon_0. \end{cases} \quad (6.120)$$

Compton-Scattered External Isotropic Radiation Field for General Nonthermal Electron Distribution

From eq. (6.89), but allowing the electron distribution to have an arbitrary comoving angular distribution, we have

$$f_\epsilon = \frac{3}{4} \frac{c\sigma_T \epsilon_s^2}{d_L^2} \delta_D^3 \int_0^\infty d\epsilon_* \frac{u_*(\epsilon_*)}{\epsilon_*^2} \int_{\gamma_{\min}}^{\gamma_{\max}} d\gamma \frac{N'(\gamma', \Omega')}{\gamma^2} F_C(q, \Gamma_e). \quad (6.121)$$

Here $\gamma' = \gamma/\delta_D$, $\mu' = (\mu - \beta)/(1 - \beta\mu)$, and $\phi' = \phi$.

6.7.4 Cosmic Microwave Background Radiation Compton-Scattered by Jet Electrons

Because of the importance of this process, and because it provides us a way to summarize the results of external Compton processes, we derive the flux when jet electrons Compton-scatter CMB photons or quasi-monochromatic photon sources. The analysis also applies to stationary synchrotron sources, e.g., the lobes of radio galaxies, by taking the limit $\delta_D \rightarrow 1$.

From eq. (6.89),

$$\epsilon_s L_C(\epsilon_s, \Omega_s) = \frac{3}{4} c\sigma_T \left(\frac{\epsilon_s}{\epsilon_*}\right)^2 u_0 \int_1^\infty d\gamma \frac{N_e(\gamma, \Omega_s)}{\gamma^2} F_C(q, \Gamma_e) H\left(q; \frac{1}{4\gamma^2}, 1\right). \quad (6.122)$$

From eqs. (6.95) and (6.113),

$$f_\epsilon^{\text{C,iso}} = \frac{3}{4} \frac{c\sigma_T \epsilon_s^2}{d_L^2} \int_0^\infty d\epsilon_* \frac{u_*(\epsilon_*)}{\epsilon_*^2} \int_{\gamma_{\min}}^\infty d\gamma \frac{N_e(\gamma, \Omega_s)}{\gamma^2} F_C(q, \Gamma_e), \quad (6.123)$$

considering only upscattering. Here, from eqs. (6.76) and (6.90),

$$q \equiv \frac{\epsilon_s/\gamma}{\Gamma_e(1 - \epsilon_s/\gamma)}, \quad \Gamma_e = 4\gamma\epsilon_*,$$

and

$$\gamma_{\min} = \frac{\epsilon_s}{2} \left(1 + \sqrt{1 + \frac{1}{\epsilon_s \epsilon_*}} \right) \xrightarrow{\epsilon_* \epsilon_s \ll 1} \sqrt{\frac{\epsilon_s}{2\epsilon_*}}.$$

For the standard jet, from eq. (6.111),

$$N_e(\gamma, \Omega_s) = \delta_D^3 \frac{N'(\gamma/\delta_D)}{4\pi}. \quad (6.124)$$

The different approximations to the Compton cross section are the full Compton cross section, eq. (6.75),

$$F_C(q, \Gamma_e) = F_T(q) + \frac{1}{2} \frac{(\Gamma_e q)^2}{1 + \Gamma_e q} (1 - q), \quad (6.125)$$

the Thomson cross section, eq. (6.69),

$$F_T(\hat{\epsilon}) = 1 + \hat{\epsilon} - 2\hat{\epsilon}^2 + 2\hat{\epsilon} \ln \hat{\epsilon}, \quad \hat{\epsilon} = \frac{\epsilon_s}{4\gamma^2\epsilon_*}, \quad (6.126)$$

and the isotropic Thomson cross section, eq. (6.71),

$$F_{T,\text{iso}}(\hat{\epsilon}) = \frac{2}{3}(1 - \hat{\epsilon}). \quad (6.127)$$

The CMBR spectrum, eq. (B.15), is

$$u_{*,\text{CMB}}(\epsilon_*) = \frac{2m_e c^2}{\lambda_C^3} \frac{\epsilon_*^3}{\exp(\epsilon_*/\Theta) - 1}. \quad (6.128)$$

Approximating the CMBR as an isotropic, monochromatic radiation field, or for such fields in general, $u_*(\epsilon_*) = u_0\delta(\epsilon_* - \epsilon_0)$. For the CMBR, $u_0 = 4 \times 10^{-13}(1+z)^4$ ergs/cm³ and $\epsilon_0 = 1.24 \times 10^{-9}(1+z)$. The condition $q < 1$ implies $\epsilon_s < \gamma/(1 + \Gamma_e^{-1})$. The differential Compton-scattered spectrum when isotropic, monoenergetic electrons Compton-upscatter isotropic, monochromatic target photons is therefore given, for the full Compton cross section, by

$$df_\epsilon^C = \frac{3}{4} \frac{c\sigma_T u_0}{d_L^2} \left(\frac{\epsilon_s}{\epsilon_*}\right)^2 \frac{N_e(\gamma, \Omega_s)d\gamma}{\gamma^2} F_C(q, \Gamma_e) H\left(\frac{\gamma}{1 + (1/4\gamma\epsilon_*)} - \epsilon_s\right), \quad (6.129)$$

for the Thomson cross section by

$$df_\epsilon^T = \frac{3}{4} \frac{c\sigma_T u_0}{d_L^2} \left(\frac{\epsilon_s}{\epsilon_*}\right)^2 \frac{N_e(\gamma, \Omega_s)d\gamma}{\gamma^2} F_T(\hat{\epsilon}) H(1 - \hat{\epsilon}), \quad (6.130)$$

and for the isotropic Thomson cross section by

$$df_\epsilon^{T,\text{iso}} = \frac{c\sigma_T u_0}{2d_L^2} \left(\frac{\epsilon_s}{\epsilon_*}\right)^2 \frac{N_e(\gamma, \Omega_s)d\gamma}{\gamma^2} (1 - \hat{\epsilon}) H(1 - \hat{\epsilon}), \quad (6.131)$$

where integration over γ is implied by the form of the expression.

Integration over the photon spectrum is accomplished, as noted earlier, by replacing u_0/ϵ_*^2 with $\int d\epsilon_* u_*(\epsilon_*)/\epsilon_*^2$, given by eq. (6.128) in the case of CMBR. Because the low-energy asymptote of the blackbody spectrum is proportional to ϵ_*^2 , like the Compton-scattered spectra, eqs. (6.129)–(6.131), the behavior $f_\epsilon \propto \epsilon^2$ sets a hardness limit on this process. A spectrum this hard is unlikely to be realized, however, because of limits on the electron spectra imposed by acceleration processes and electron cooling.

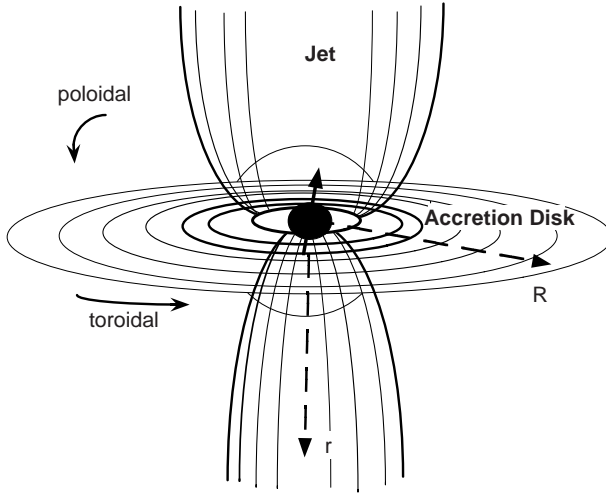


Figure 6.9 Geometry of the system of the black-hole accretion disk and jet, with magnetic field lines formed by currents in the accretion disk (top) or black-hole magnetosphere (bottom).

6.8 ACCRETION-DISK FIELD COMPTON-SCATTERED BY JET ELECTRONS

Radiation from accretion disks powering AGNs is remarkably luminous and provides a source of target photons to be scattered by nonthermal jet electrons. The target photons could originate from a cool, optically thick thermal disk or from hot, optically thin plasma formed by matter accreting onto black holes, as shown in figure 6.9.

We consider the radiation field formed by an optically thick, geometrically thin accretion disk originally considered by Shakura and Sunyaev [76]. This choice is not unique, and a quasi-spherical hot inner coronal plasma [77] could also be considered. Indeed, the choice of accretion-disk field is a matter of preference in the absence of a clear understanding of the relationship between jet and accretion state. Jets from supermassive black holes may be most active when the accretion power is low, though here the standard Shakura-Sunyaev accretion disk is treated.

A useful quantity in black-hole accretion-disk physics is the Eddington ratio

$$\ell_{\text{Edd}} = \frac{\eta_f \dot{m} c^2}{L_{\text{Edd}}}, \quad (6.132)$$

where η_f is the efficiency to transform the gravitational potential energy of accreting matter to escaping radiation. By balancing the gravitational force

$\vec{F}_g = -(GMm/r^2)\hat{r}$ with the radiation force

$$\vec{F}_{\text{rad}} = \left(\frac{dN_{\text{ph}}}{dAdt} \right) \sigma_{\text{T}} \left(\frac{h\nu}{c} \right) \hat{r} = \left(\frac{L}{4\pi r^2 h\nu} \right) \sigma_{\text{T}} \left(\frac{h\nu}{c} \right) \hat{r}$$

on protons and electrons in an optically thin plasma, one obtains the Eddington luminosity

$$L_{\text{Edd}} = \frac{4\pi GM(m_p + m_e)c}{\sigma_{\text{T}}} \cong 1.26 \times 10^{38} \frac{M}{M_{\odot}} \text{ ergs s}^{-1}. \quad (6.133)$$

The Eddington luminosity of a $10^9 M_{\odot}$ Solar mass black hole is $\approx 10^{47}$ ergs s^{-1} . Power of this magnitude requires that matter is accreting on the black hole at the rate $\dot{m} = \ell_{\text{Edd}} L_{\text{Edd}} / (\eta_f c^2) = 1.4 \times 10^{26} (\ell_{\text{Edd}} M_{\odot} / \eta_f)$ g $\text{s}^{-1} \approx 2.2 (\ell_{\text{Edd}} M_{\odot} / \eta_f)$ Solar masses per year. Because the forces of gravity and radiation are proportional to r^{-2} , super-Eddington luminosities halt the accretion of optically thin matter. Super-Eddington accretion powers may still be possible for episodic accretion, when the accreting matter is optically thick, or when the escaping radiation is collimated.

6.8.1 Optically Thick Shakura-Sunyaev Disk Spectrum

For steady flows where the energy is derived from the viscous dissipation of the gravitational potential energy of the accreting matter, the radiant surface-energy flux

$$\frac{d\mathcal{E}}{dAdt} = \frac{3GM\dot{m}}{8\pi R^3} \varphi(R) \quad (6.134)$$

[76], where R is the disk radius,

$$\varphi(R) = 1 - \beta_i (R_i/R)^{1/2} \quad (6.135)$$

for a Schwarzschild black hole, and β_i gives the fraction of angular momentum captured by the black hole at the radius R_i of the innermost stable orbit. Thus $0 \leq \beta_i \leq 1$, and $\beta_i \cong 1$ for zero stress at R_i if the accreting matter does not have time to radiate a significant fraction of its energy [78]. The innermost stable orbit of a Schwarzschild black hole, written in terms of gravitational radii $R_g = GM/c^2 = 1.48 \times 10^{14} M_{\odot} \text{ cm}$, is $R_i = 6R_g$. The unusual feature in eq. (6.134) at large radii, where a Newtonian formulation can be applied, is that the energy flux is a factor of 3/2 larger than obtained when the energy dissipated by particles in Keplerian motions at different radii is considered. This is due to energy transport from the inner regions.

If the accretion energy is dissipated as radiation, then the disk radiant luminosity is

$$L_d = 2 \times 2\pi \times \int_{R_i}^{\infty} dR \cdot R \cdot \frac{d\mathcal{E}}{dAdt} = \frac{3GM\dot{m}}{2R_i} \left(1 - \frac{2\beta_i}{3} \right), \quad (6.136)$$

where the extra factor of 2 is for a two-sided disk. When $\beta_i = 1$, the accretion efficiency for a Schwarzschild black hole is $\eta_f = 1/12$. A monochromatic approximation for the mean photon energy gives

$$T(R) = \left(\frac{3GM\dot{m}\varphi(R)}{8\pi R^3\sigma_{\text{SB}}} \right)^{1/4},$$

so that the mean photon energy radiated by an optically thick disk is

$$\bar{\epsilon}(\tilde{R}) \cong \frac{2.70k_{\text{B}}T(\tilde{R})}{m_e c^2} \cong \frac{1.51 \times 10^{-4}}{\tilde{R}^{3/4}} \left(\frac{\ell_{\text{Edd}}\varphi(\tilde{R})}{\eta_f M_9} \right)^{1/4} \equiv \frac{C}{\tilde{R}^{3/4}}. \quad (6.137)$$

Here the lengths are scaled to the gravitational radius; thus the scaled disk radius $\tilde{R} = R/R_g$, and the scaled jet height $\tilde{r} = r/R_g$ (see figure 6.10). This can also be written as

$$m_e c^2 \bar{\epsilon} \cong \frac{77}{\tilde{R}^{3/4}} \left(\frac{\ell_{\text{Edd}}}{\eta_f M_9} \right)^{1/4} \text{ eV}. \quad (6.138)$$

6.8.2 Integrated Emission Spectrum from Shakura-Sunyaev Disk

From eqs. (6.134) and (6.137), the intensity of the Shakura-Sunyaev disk at radius $R = \tilde{R}R_g$ is approximated by the expression

$$I_{\epsilon}^{\text{SS}}(\Omega; \tilde{R}) \cong \frac{3GM\dot{m}}{16\pi^2 R^3} \varphi(\tilde{R}) \delta\left(\epsilon - \frac{C}{\tilde{R}^{3/4}}\right). \quad (6.139)$$

Along the axial symmetry axis of the black-hole system, the νF_{ν} flux, from eq. (5.5), is given by

$$\begin{aligned} f_{\epsilon}^{\text{SS}} &= \epsilon_s \oint d\Omega \mu I_{\epsilon_s}^{\text{SS}}(\Omega; R) \cong \epsilon_s \frac{3GM\dot{m}}{8\pi} r^2 \\ &\times \int_{R_i}^{\infty} dR \frac{\varphi(R)}{R^2(R^2 + r^2)^2} \delta(\epsilon_s - C/\tilde{R}^{3/4}), \end{aligned} \quad (6.140)$$

noting that $\mu d\mu = -r^2 R dR / (r^2 + R^2)^2$. In the event that r reaches such large values that cosmologically redshift effects are important, then $r \rightarrow d_L$ and $\epsilon_s = (1+z)\epsilon$.

A photon emitted from a geometrically thin accretion disk at radius R that passes through the jet axis at height $r = R/\sqrt{\mu^{-2} - 1}$ makes an angle $\theta = \arccos \mu$ with respect to the jet axis, as shown in figure 6.10. Letting $\varphi \rightarrow 1$ for simplicity, eq. (6.140) can be easily solved to give

$$\begin{aligned} f_{\epsilon}^{\text{SS}} &\cong \frac{\ell_{\text{Edd}} L_{\text{Edd}}}{2\pi d_L^2 \eta_f} \left(\frac{\epsilon_s}{C} \right)^{4/3} H(\epsilon_{\text{max}} - \epsilon_s) \\ &\cong \frac{\ell_{\text{Edd}} L_{\text{Edd}}}{2\pi d_L^2 \eta_f \tilde{R}_{\text{min}}} \left(\frac{\epsilon_s}{\epsilon_{\text{max}}} \right)^{4/3} \exp(-\epsilon_s/\epsilon_{\text{max}}). \end{aligned} \quad (6.141)$$

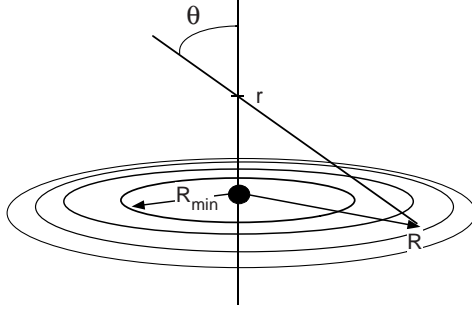


Figure 6.10 Geometry of the accretion-disk/jet system. The minimum radius R_{\min} of the accretion disk around a Schwarzschild black hole must be greater than $R_i = 6R_g$, the innermost stable orbit.

Here

$$\epsilon_{\max} \equiv \bar{\epsilon}(\tilde{R}_{\min}) \cong \frac{0.048}{\tilde{R}_{\min}^{3/4}} \left(\frac{\ell_{\text{Edd}}}{m_{\text{BH}} \eta_f / (1/12)} \right)^{1/4}, \quad (6.142)$$

where the black-hole mass m_{BH} is in Solar masses. The superposition of blackbodies in the Shakura-Sunyaev disk solution produces the characteristic spectral index $f_\epsilon \propto \epsilon^{4/3}$ with a cutoff energy $\epsilon_{\max} \propto m_{\text{BH}}^{-1/4}$. Typical maximum disk temperatures are $\approx 2 \text{ keV} \times (\ell_{\text{Edd}}/0.01)^{1/4} / m_{\text{BH}}^{1/4} \sim 10 \text{ eV} (\ell_{\text{Edd}}/0.01)^{1/4} / M_9^{1/4}$. The optically-thick disk emission is thought to make the soft high-state X-ray emission in galactic black-hole candidates and the UV “blue-bump” emission in Seyfert galaxies. If the accretion disk is oriented at an angle θ_{obs} with respect to the line of sight to the observer, the flux is reduced by the factor $\cos \theta_{\text{obs}}$.

6.8.3 Transformed Accretion-Disk Radiation Field

The target photon density from a Shakura-Sunyaev disk follows from the invariance properties of intensity. Thus,

$$u'(\epsilon', \Omega') = \left(\frac{\epsilon'}{\epsilon} \right)^3 u(\epsilon, \Omega) = \frac{u(\epsilon, \Omega)}{[\Gamma(1 + \beta\mu')]^3}, \quad (6.143)$$

implying total comoving frame energy density

$$u'_{\text{ext}} = \int_{-\beta_\Gamma}^{\mu'_{\text{max}}} d\mu' u'(\mu') = \frac{3GM\dot{m}}{8\pi cr^3\Gamma} \int_{-\beta_\Gamma}^{\mu'_{\text{max}}} d\mu' \frac{(\mu' + \beta)^3}{(1 - \mu'^2)^{3/2} (1 + \beta\mu')^4}. \quad (6.144)$$

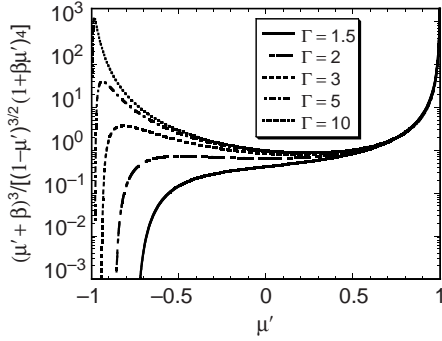


Figure 6.11 The directional or angle dependence of the photon energy density for a jet with bulk Lorentz factor Γ traveling outward along the axis of an accretion disk that radiates a Shakura-Sunyaev disk spectrum. Angle is measured with respect to axially outward. This quantity is represented by the integrand on the right-hand side of eq. (6.144).

Figure 6.11 shows the integrand of the rightmost integral in eq. (6.144). When $\Gamma \gg 1$, two dominant components of the differential energy density make up the total energy density: a component from the disk radiation field at disk radii $R \approx r$, called the *near-field* (NF) component; and a *far-field* (FF) component coming directly from behind, which dominates the disk contribution at large radii [68]. The accretion-disk radiation field, when approximated as a point source that illuminates the ejecta blob directly from behind, presents a total comoving energy density

$$u'_b = \frac{1}{\Gamma^2(1 + \beta^2)^2} \frac{3GM\dot{m}}{8\pi cr^2 R_i} \left(1 - \frac{2}{3}\beta_i\right), \quad (6.145)$$

using eq. (5.32).

The point-source approximation improves as the accretion disk becomes more like a point source following the flow in the comoving frame, that is, when

$$\mu'_{\max} = \frac{\mu_{\max} - \beta}{1 - \beta\mu_{\max}} \rightarrow 1.$$

With $\mu_{\max} \rightarrow 1 - R_{\min}^2/2r^2$,

$$\mu'_{\max} \cong \frac{1 - (R_{\min}^2/2r^2) - \beta}{1 - \beta(1 - R_{\min}^2/2r^2)} \cong 1 - 2 \left(\frac{\Gamma R_{\min}}{r}\right)^2 \rightarrow 1. \quad (6.146)$$

Consider eq. (6.144),

$$u'_{\text{ext}} = \frac{3GM\dot{m}}{8\pi c\Gamma r^3} \int_{-\beta\Gamma}^{\mu'_{\max}} d\mu' \frac{(\mu' + \beta)^3}{(1 - \mu'^2)^{3/2}(1 + \beta\mu')^4} = \frac{3GM\dot{m}}{8\pi cr^3\Gamma} (I_{\text{NF}} + I_{\text{FF}}), \quad (6.147)$$

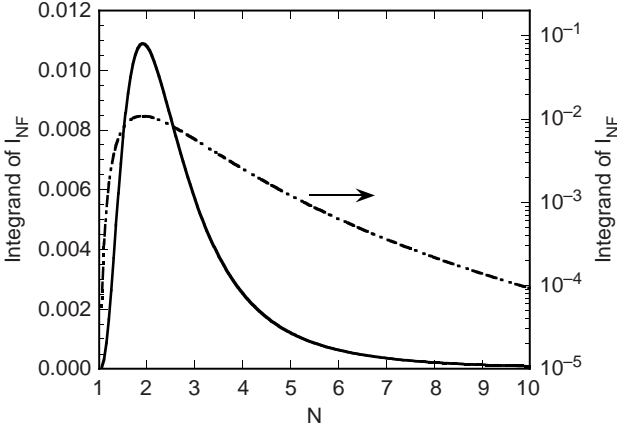


Figure 6.12 The integrand $(N^2 - 1)^3/[N^2(N^2 + 1)^4]$ of eq. (6.149).

valid in the case $\beta_i = 0$, implying an efficiency of 25% for this metric. We have divided the comoving energy density into a NF component, with $-\beta \leq \mu' < 0$, and a FF component with $0 \leq \mu' < \mu'_{\max}$.

Near-Field Integral

The expansion $\mu' = -1 + (N^2/2\Gamma^2)$ in the near-field integral gives, in the limit $\Gamma \gg 1$,

$$I_{\text{NF}} = \int_{-\beta\Gamma}^0 d\mu' \frac{(\mu' + \beta)^3}{(1 - \mu'^2)^{3/2}(1 + \beta\mu')^4} \Rightarrow 2\Gamma^3 c_d, \quad (6.148)$$

where

$$c_d \equiv \int_1^\infty dN \frac{(N^2 - 1)^3}{N^2(N^2 + 1)^4} \cong 0.023. \quad (6.149)$$

This result agrees with the estimate $c_d \cong 2 \times 3^3 / (2^2 \cdot 5^4) = 0.0216$, using the value of the integrand at $N = \Gamma\theta \cong 2$ (the integrand peaks at $\theta' \cong 1.9/\Gamma$ in the limit $\Gamma \gg 1$). Figure 6.12 presents the integrand of equation (6.149).

Far-Field Integral

The far-field integral is

$$I_{\text{FF}} = \int_0^{\mu'_{\max}} d\mu' \frac{(\mu' + \beta)^3}{(1 - \mu'^2)^{3/2}(1 + \beta\mu')^4}, \quad (6.150)$$

and $\mu'_{\max} \cong 1 - (R_{\min}^2/2r^2)$ in the limit $r \gg R_{\max}$. Hence

$$\mu'_{\max} = \frac{\mu_{\max} - \beta}{1 - \beta\mu_{\max}} = 1 - 2a^2 + \mathcal{O}(a^2/\Gamma^2), \quad (6.151)$$

in the limit $a \equiv \Gamma R_{\min}/r \ll 1$. Therefore

$$I_{\text{FF}} \xrightarrow{a \ll 1} \frac{1}{4a} = \frac{r}{4\Gamma R_{\min}}. \quad (6.152)$$

Near-Field/Far-Field Transition Radius

From eqs. (6.147), (6.148), and (6.152),

$$u'_{\text{ext}} = \frac{3GM\dot{m}}{8\pi cr^3\Gamma} \left(2\Gamma^3 c_d + \frac{r}{4\Gamma R_{\min}} \right), \quad (6.153)$$

implying for a Schwarzschild metric with $\beta_i = 0$, the NF/FF transition radius

$$\tilde{R}_{\text{NF/FF}} \cong \Gamma^4, \quad (6.154)$$

in normalized units $\tilde{r} = r/R_g$.

Near-Field/Scattered Field Transition Radius

The location r_{NX} where the NF equals the external scattered radiation field is given by the condition

$$\frac{3GM\dot{m}}{8\pi cr^3\Gamma} \times 2\Gamma^3 c_d = u'_{\text{NF}} = u'_{\text{sc}} = \Gamma^2(1 + \beta^2/3)u_* = \Gamma^2(1 + \beta^2/3) \frac{L_d \tau_{\text{sc}}}{4\pi r_{\text{sc}}^2 c}, \quad (6.155)$$

where τ_{sc} is the characteristic scattering optical depth (section 6.9). Recalling eq. (6.136), we find

$$\tilde{r}_{\text{NX}} = \frac{r_{\text{NX}}}{R_g} = c_d^{1/3} 3^{(2+\beta_i)/3} \frac{\tilde{r}_{\text{sc}}^{2/3}}{\tau_{\text{sc}}^{1/3}} \cong (0.59 - 0.85) \frac{\tilde{r}_{\text{sc}}^{2/3}}{\tau_{\text{sc}}^{1/3}}, \quad (6.156)$$

where the coefficient varies in value as β_i ranges from 0 to 1, and $r_{\text{sc}} = R_g \tilde{r}_{\text{sc}}$ is the characteristic size of the scattering region, which we identify with the broad-line region. Hence

$$\tilde{r}_{\text{NX}} \approx \frac{\tilde{r}_{\text{sc}}^{2/3}}{\tau_{\text{sc}}^{1/3}}. \quad (6.157)$$

Equation (6.157) holds when $\tilde{r}_{\text{NX}} < \tilde{r}_{\text{sc}}$ for the simplified geometry of the scattering region assumed here, requiring that $\tilde{r}_{\text{sc}} > 1/\tau_{\text{sc}}$. If $r_{\text{sc}} = 0.5$ pc around a 10^9 Solar mass black hole, then $\tilde{r}_{\text{sc}} = 10^4$. The scattered radiation will dominate the NF radiation beyond $\approx 2000(\tau_{\text{sc}}/0.01)^{-1/3} R_g$ from the black hole.

6.8.4 Thomson-Scattered Shakura-Sunyaev Disk Spectrum in the Near Field

From the analysis of the integrand of eq. (6.148) in the NF regime, we see that the NF photons originate from $\theta' \cong 1.9/\Gamma$, or from $r \approx R$ in the stationary frame. From eqs. (6.136), (6.147), and (6.148), the comoving energy density in the NF regime is

$$u'_{\text{NF}}{}^0 = \frac{L_d}{4\pi r^2 c} 4 \cdot 3^{1+\beta_i} c_d \left(\frac{R_g}{r} \right) \Gamma^2, \quad (6.158)$$

and $4 \cdot 3^{1+\beta_i} c_d = 0.28, 0.83$ when $\beta_i = 0, 1$, respectively. Taking the peak contribution from the disk at $\mu = 1/2$, we have the following approximation for the comoving energy density:

$$u'_{\text{NF}} = \frac{u'_{\text{NF}}{}^0}{2\pi} \delta(\epsilon' - \Gamma\epsilon_*/2)\delta(\mu' + 1). \quad (6.159)$$

The comoving emissivity can be derived from expression (2.44) or eq. (6.92), assuming isotropy of the comoving electron distribution function $n'_e(\gamma, \Omega_e) = n'_e(\gamma)/4\pi$. For the cross section, we take the δ -function Thomson approximation, eq. (6.58). Solving gives

$$j'(\epsilon'_s, \Omega'_s) = \frac{c\sigma_T u'_{\text{NF}}{}^0}{2\pi} \frac{(1 + \mu'_s)^2}{4\epsilon'_s} \gamma_{\text{NF}}^3 n'_e(\gamma_{\text{NF}}), \quad \gamma_{\text{NF}} = \sqrt{\frac{2\epsilon'_s}{\Gamma\epsilon_*(1 + \mu'_s)}}. \quad (6.160)$$

Making the transformation to observer frame quantities using the relation $1 + \mu'_s \rightarrow \delta(1 + \mu_s)/2\Gamma$, valid when $\Gamma \gg 1$, we obtain

$$f_\epsilon^{\text{NF}} \cong \frac{\delta_D^6 c\sigma_T u'_{\text{NF}}{}^0}{32\pi d_L^2 \Gamma^2} (1 + \mu)^2 \gamma_{\text{NF}}^3 N'_e(\gamma_{\text{NF}}), \quad \gamma_{\text{NF}} = \frac{2}{\delta_D} \sqrt{\frac{\epsilon_z}{\hat{\epsilon}_*(1 + \mu)}}, \quad (6.161)$$

where $\hat{\epsilon}_*$ is evaluated at $R \cong r$. The NF νF_ν flux can also be written as

$$f_\epsilon^{\text{NF}} \simeq \delta_D^6 \frac{\sigma_T}{12\pi d_L^2} \left(\frac{L_d R_g}{4\pi r^3} \right) \gamma_{\text{NF}}^3 N'_e(\gamma_{\text{NF}}), \quad \gamma_{\text{NF}} = \frac{1}{\delta_D} \sqrt{\frac{2\epsilon_z}{\bar{\epsilon}(\sqrt{3}r)}}, \quad (6.162)$$

where $L_d = GM\dot{m}/2R_{\text{min}}$, and $\bar{\epsilon}$ is given by eq. (6.138).

6.8.5 Thomson-Scattered Shakura-Sunyaev Disk Spectrum in the Far Field

This problem was solved earlier, eq. (6.101), with the result

$$f_{\epsilon}^{\text{FF}} \simeq \delta_{\text{D}}^6 \frac{\sigma_{\text{T}}(1-\mu)^2}{32\pi^2 r^2 d_L^2} \int_0^{[(1-\mu)\epsilon_z]^{-1}} d\epsilon_0 L(\epsilon_0) \gamma_{\text{FF}}^3 N'_e(\gamma_{\text{FF}}),$$

$$\gamma_{\text{FF}} = \frac{1}{\delta_{\text{D}}} \sqrt{\frac{\epsilon_z}{\epsilon_0(1-\mu)}}, \quad (6.163)$$

which can be applied to either the thermal accretion-disk or hot plasma modeled as a point source of radiation from behind. The FF νF_{ν} flux for the Shakura-Sunyaev disk can also be approximated by the expression

$$f_{\epsilon}^{\text{FF}} \simeq \delta_{\text{D}}^6 \frac{\sigma_{\text{T}}(1-\mu)^2}{8\pi d_L^2} \left(\frac{L_d}{4\pi r^2} \right) \gamma_{\text{FF}}^3 N'_e(\gamma_{\text{FF}}),$$

$$\gamma_{\text{FF}} = \frac{1}{\delta_{\text{D}}} \sqrt{\frac{\epsilon_z}{(1-\mu)\bar{\epsilon}(R_{\text{min}})}}. \quad (6.164)$$

6.8.6 Beaming Patterns

The beaming pattern for a relativistic blob of jet plasma scattering monochromatic photons of an external isotropic radiation field is, from eq. (6.105), given by

$$f_{\epsilon}^{\text{T}} \propto \delta_{\text{D}}^{3+p} \left(\frac{\epsilon_z}{\epsilon_0} \right)^{(3-p)/2} \propto \delta_{\text{D}}^{4+2\alpha} \left(\frac{\epsilon_z}{\epsilon_0} \right)^{1-\alpha}. \quad (6.165)$$

Thus the beaming factor for Thomson-scattered external isotropic radiation is $4 + 2\alpha$ [79], which can be compared with the beaming factor $3 + \alpha$ (eq. [5.49]) for radiation that is isotropically emitted in the comoving frame of the blob. This behavior is also followed when jet electrons scatter accretion-disk photons in the near-field limit, using a mean photon density from a point where the disk radius is about equal to the jet height (eq. [6.161]). Equation (6.165) also gives the beaming factor for scattering in the KN regime, though with a different spectral dependence, namely,

$$f_{\epsilon}^{\text{KN}} \propto \delta_{\text{D}}^{3+p} \left(\frac{\epsilon_z}{\epsilon_0} \right)^{1-p}. \quad (6.166)$$

The beaming pattern produced by an external point-source radiation field that enters the jet from behind, eq. (6.101), has the dependence

$$f_{\epsilon}^{\text{pt}} \propto (1-\mu)^2 \delta_{\text{D}}^{3-p} \left(\frac{\epsilon_z}{(1-\mu)\bar{\epsilon}} \right)^{(3-p)/2}. \quad (6.167)$$

This is the same beaming-factor dependence as for scattered accretion-disk radiation in the far-field regime, eq. (6.164), which becomes valid when the jet height is $\gg \Gamma^4 R_g$ (eq. [6.154]).

6.9 BROAD-LINE REGION SCATTERED RADIATION

The accretion-disk radiation can be scattered by material in the broad-line region (BLR) and then be intercepted by the jet [70, 80, 81]. The BLR is thought to consist of dense clouds with a specified covering factor that can be determined from AGN studies. These clouds intercept central-source radiation to produce the broad lines [82]. In addition, diffuse gas will Thomson-scatter the central-source radiation. This scattered radiation field provides important target photons for jet electrons to make γ -rays. The scattered radiation field also attenuates γ -rays produced deep within the BLR (chapter 10).

The Thomson-scattered spectral photon density can be estimated by noting that a fraction $\approx rn_e(r)\sigma_T$ of the central-source radiation with ambient photon density $n_{\text{ph}}(\epsilon_*, r) = \dot{N}_{\text{ph}}(\epsilon_*)/4\pi r^2 c$ is scattered, giving a target scattered radiation field

$$n_{\text{sc}}(\epsilon_*; r) \approx \frac{n_e(r)\sigma_T \dot{N}_{\text{ph}}(\epsilon_*)}{4\pi r c}. \quad (6.168)$$

Here $\dot{N}_{\text{ph}}(\epsilon_*) = L(\epsilon_*)/(m_e c^2 \epsilon_*)$ is the central-source photon production rate, and $L(\epsilon_*)$ is its spectral luminosity.

For the simple case of a spherically symmetric shell of scattering gas, the density is given for a power-law radial density distribution by the expression

$$n_e(R) = n_0 \left(\frac{R}{R_i} \right)^\zeta H(R; R_i, R_o) \quad (6.169)$$

extending from inner radius R_i to outer radius R_o . The shell density can be normalized to radial Thomson depth $\tau_T = \sigma_T \int_{R_i}^{R_o} dR n_e(R)$. By evaluating an expression of the form

$$n_{\text{ph}}(\epsilon_*; R) = \int dV \frac{\dot{n}(\epsilon_*; \vec{R})}{4\pi x^2 c}, \quad x^2 = R^2 + r^2 - 2rR \cos \theta,$$

one obtains [73, 83], after solving,

$$n_{\text{ph}}(\epsilon_*, \mu_*; r) = \frac{\sigma_T \dot{N}_{\text{ph}}(\epsilon_*)}{8\pi cr} \mathcal{N}(\mu_*, r), \quad (6.170)$$

where

$$\mathcal{N}(\mu_*, r) = \mathcal{N}[\mu_*, n(r)] \equiv \int_{-\mu_*}^1 d\mu n_e(\bar{y}r) \frac{\sqrt{1 + \bar{y}^2 - 2\bar{y}\mu}}{\bar{y}(1 - \mu^2)} \quad (6.171)$$

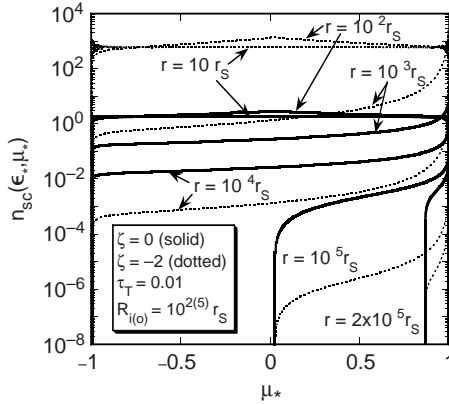


Figure 6.13 Angle-dependent density of Thomson-scattered radiation at height r along the jet axis. The radial Thomson depth of the spherically symmetric scattering medium is $\tau_T = 0.01$, and the scattering shell is assumed to extend from 10^2 to 10^5 Schwarzschild radii for a $10^9 M_\odot$ black hole. The index ζ of the density distribution is labeled in the figure, and the values of r are labeled on the curves. The luminosity of the photon source is 10^{44} ergs s^{-1} .

(units of \mathcal{N} are $1/L^3$) and

$$\bar{y} = \bar{y}(\mu, \mu_*) \equiv \frac{-\mu(1 - \mu_*^2) + \mu_*\sqrt{(1 - \mu^2)(1 - \mu_*^2)}}{\mu_*^2 - \mu^2}. \quad (6.172)$$

The Compton-scattered radiation spectrum is given, in general, by eq. (6.97). Substitution of eq. (6.170) for the target photon source gives, for a monochromatic photon source

$$\dot{N}_{\text{ph}}(\epsilon_*) = \frac{L_0 \delta(\epsilon_* - \epsilon_{*0})}{m_e c^2 \epsilon_*}, \quad (6.173)$$

the νF_ν flux

$$f_\epsilon^{\text{EC,scat}}(r) = \frac{(\pi r_e^2)^2 L_0 \delta_D^3}{12\pi^2 d_L^2 r} \left(\frac{\epsilon_s}{\epsilon_*}\right)^2 \int_{\max(-1, 1-2\epsilon_s/\epsilon_*)}^1 d\mu_* \mathcal{N}(\mu_*, r) \times \int_{\tilde{\gamma}_{\text{low}}}^\infty d\gamma \frac{N'_e(\gamma/\delta_D)}{\gamma^2} \Xi_C. \quad (6.174)$$

In this expression,

$$\tilde{\gamma}_{\text{low}} \equiv \frac{\epsilon_s}{2} \left(1 + \sqrt{1 + \frac{2}{\epsilon_* \epsilon_s (1 - \mu_*)}} \right) \quad (6.175)$$

(compare eq. [6.33]). Equation (6.175) gives [73] the Compton-scattered γ -ray νF_ν flux when the target photon field is central-source radiation Thomson-scattered by surrounding gas and dust.

Figure 6.13 shows the angle dependence of the scattered radiation field as a function of r for this idealized geometry. The scattering region is assumed to extend from 10^2 to 10^5 Schwarzschild radii for a black hole with mass equal to $10^9 M_\odot$. The radial Thomson depth of the scattering medium is $\tau_T = 0.01$, and the index of the radial distribution, eq. (6.169), is $\zeta = 0$ and -2 , as shown in the legend. As can be seen, the scattered radiation field is nearly isotropic when $r \lesssim R_i$, and starts to display increasing asymmetry peaked in the outward direction at greater heights. When $r \geq R_o$, all scattered radiation is outwardly directed. When $\zeta = -2$, most of the scattering material is near the inner edge, so that the scattered radiation field is very luminous at $r \cong R_i$.

Chapter Seven

Synchrotron Radiation

Relativistic charged particles emit synchrotron radiation when they are accelerated in the presence of a magnetic field. When both electric and magnetic fields are present, the electromagnetic force on a charged particle is given by the Lorentz force equation

$$\vec{F}_L = \frac{d}{dt}(\gamma m \vec{v}) = Q \left(\vec{E} + \frac{1}{c} \vec{v} \times \vec{B} \right). \quad (7.1)$$

Here \vec{E} is the electric field vector, Q is the charge of the particle, and $\vec{v} = \beta_{\text{par}} c$ is its velocity, so β_{par} is the particle beta factor.

In most astrophysical plasmas, the mobility of free charges causes the electric field to be shorted out. We assume this to be the case and take $\vec{E} = 0$. When a particle does not experience significant energy losses in a single gyration, γ can be treated as constant, and eq. (7.1) becomes

$$\frac{d\vec{v}}{dt} = Q \frac{\vec{v} \times \vec{B}}{\gamma m c} \equiv \omega_L \left(\vec{v} \times \frac{\vec{B}}{B} \right), \quad (7.2)$$

where the Larmor angular frequency

$$\omega_L = 2\pi \nu_L = \frac{QB}{\gamma m c} = \frac{\Omega}{\gamma} \quad (7.3)$$

is independent of pitch angle ψ (see figure 7.1). The symbol Ω represents the nonrelativistic gyrofrequency. The Larmor radius r_L , defined as the radius of gyration, is given by

$$\omega_L r_L = \beta_{\perp} c = \beta_{\text{par}} c \sin \psi, \quad (7.4)$$

so that

$$r_L = \frac{\beta_{\text{par}} \gamma m c^2 \sin \psi}{QB} \rightarrow \frac{E}{QB}, \quad (7.5)$$

where the last expression applies to an ultrarelativistic particle with $\psi = \pi/2$ and particle energy E (compare eq. [1.3]). Particles with the same Larmor radii have the same rigidity (momentum per charge); therefore the rigidity of a relativistic particle with a 90° pitch angle is $E/|Ze|$.

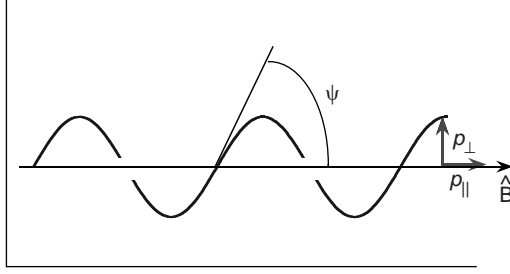


Figure 7.1 Dynamics of a particle with mass m , charge Q , pitch angle ψ , Lorentz factor γ , and dimensionless momentum $p = \beta\gamma$ in a uniform magnetic field $\vec{B} = B\hat{z}$. Note that $\tan \psi = p_{\perp}/p_{\parallel}$, so that $\sin \psi = p_{\perp}/p$.

7.1 COVARIANT ELECTRODYNAMICS

A covariant description of particle dynamics requires that the force law be cast in four-vector form. The ratio of two four-vectors is a four vector; thus we construct the 4-vector force

$$F^{\mu} = \frac{dp^{\mu}}{d\tau}, \quad (7.6)$$

where the 4-vector momentum $p^{\mu} = mu^{\mu} = m\gamma(c, \vec{v})$, and $d\tau = dt/\gamma$ is the proper time. The Lorentz force is given in manifestly covariant form by the expression

$$\frac{dp^{\mu}}{d\tau} = \frac{Q}{mc} F^{\mu\nu} p_{\nu}. \quad (7.7)$$

The field-strength tensor in Euclidean space with negligible electric permittivity and magnetic permeability (so that $D \cong E$, $B \cong H$; see eq. [3.27]) is

$$F^{\mu\nu} = \begin{pmatrix} 0 & E^1 & E^2 & E^3 \\ -E^1 & 0 & B^3 & -B^2 \\ -E^2 & -B^3 & 0 & B^1 \\ -E^3 & B^2 & -B^1 & 0 \end{pmatrix}. \quad (7.8)$$

Consider the simplest case of particle motion in the presence of zero electric field and uniform magnetic field. Thus $\vec{E} = 0$ and we set, without loss of generality, $\vec{B} = B\hat{z}$. For this system,

$$\frac{dp^{\mu}}{d\tau} = mc \begin{pmatrix} d\gamma/d\tau \\ d(\gamma\beta_x)/d\tau \\ d(\gamma\beta_y)/d\tau \\ d(\gamma\beta_z)/d\tau \end{pmatrix} = \frac{Q}{mc} F^{\mu\nu} p_{\nu} = QB \begin{pmatrix} 0 \\ \gamma\beta_y \\ -\gamma\beta_x \\ 0 \end{pmatrix}. \quad (7.9)$$

Because $dt = \gamma d\tau$, the Lorentz force equation for particle motion in a uniform magnetic field, eq. (7.2), is recovered in the form

$$\begin{aligned} \frac{d\gamma}{dt} = 0, \quad \frac{dp_x}{dt} &= \frac{QB}{\gamma mc} p_y = \omega_L p_y, \\ \frac{dp_y}{dt} &= \frac{-QB}{\gamma mc} p_x = -\omega_L p_x, \quad \text{and} \quad \frac{dp_z}{dt} = 0, \end{aligned} \quad (7.10)$$

with solution

$$\gamma(t) = \gamma_0, \quad p_x(t) = p_\perp \sin \omega_L t, \quad p_y(t) = p_\perp \cos \omega_L t, \quad \text{and} \quad p_z(t) = p_\parallel. \quad (7.11)$$

The Larmor frequency ω_L is given by eq. (7.3).

7.2 SYNCHROTRON POWER AND PEAK FREQUENCY

The acceleration of charged particles is accompanied by radiation which causes the particle to lose energy. The energy loss during a single gyration is assumed in classical synchrotron radiation theory to be a small fraction of the particle's original energy. Electrons with $\gamma \gg 10^7 / \sqrt{B(\text{G})}$ begin to lose a large fraction of their energy during a single gyration period, as can be seen by comparing the synchrotron energy-loss timescale $\sim (\sigma_T B^2 \gamma / 6\pi m_e c)^{-1}$ (see below, eq. [7.15]) with the gyration period $\nu_L^{-1} = (2\pi m_e c \gamma / QB)$. In this regime, the radiation reaction forces must be considered.

We are interested in deriving the total particle energy-loss rate per unit time per steradian, Larmor's formula, which has the form

$$\frac{dE}{dt d\Omega} = \frac{dP}{d\Omega} = -\frac{2}{3} \frac{Q^2 \vec{a}^2}{4\pi c^3}. \quad (7.12)$$

The last expression follows from dimensional analysis, noting that the quadratic dependence on Q and acceleration rate ensures net negative particle energy loss to radiation. A factor $2/3$ has been introduced to agree with more rigorous treatments [84]. A 4-vector acceleration composed of four vectors and invariant particle masses is $a^\mu = (dp^\mu/d\tau)/m$, where τ is the particle proper time. Hence the instantaneous particle energy-loss rate due to synchrotron losses for a particle with pitch angle ψ in an ordered magnetic field of strength B is

$$\begin{aligned} -\left(\frac{dE}{dt}\right)_{\text{syn}} &= \frac{2Q^2}{3m^2 c^3} \left| \frac{dp^\mu}{d\tau} \cdot \frac{dp_\mu}{d\tau} \right| = \frac{2Q^2}{3m^2 c^3} \left(\frac{QBp_\perp}{mc} \right)^2 \\ &= \frac{16\pi}{3} \left(\frac{Q^2}{mc^2} \right)^2 c \left(\frac{B^2}{8\pi} \right) \beta_{\text{par}}^2 \gamma^2 \sin^2 \psi. \end{aligned} \quad (7.13)$$

In order for an isotropic particle pitch-angle distribution to be established and maintained, pitch-angle scattering processes that cause particle isotropization should operate on a timescale shorter than the energy-loss timescale. Assuming rapid pitch-angle scattering, which allows a single particle to sample uniformly all directions in pitch-angle space, the particle loses energy at a rate found by averaging eq. (7.13) over pitch angle. The $\sin^2 \psi$ term in eq. (7.13) is replaced by the factor $\frac{1}{2} \int_{-1}^1 d \cos \psi \sin^2 \psi = 2/3$. Hence

$$-\left(\frac{dE}{dt}\right)_{\text{syn}} = \frac{4}{3} \frac{8\pi}{3} \left(\frac{Q^2}{mc^2}\right)^2 c U_B \beta_{\text{par}}^2 \gamma^2 \quad \text{with } U_B = \frac{B^2}{8\pi}, \quad (7.14)$$

from which we see that $-dE/dt|_{\text{syn}} \propto m^{-2}$, or $-\dot{\gamma}_{\text{syn}} \propto m^{-3}$.

This can also be expressed in the form

$$-\left(\frac{d\gamma}{dt}\right)_{\text{syn}} = -\dot{\gamma}_{\text{syn}} = \frac{4}{3} c \sigma_T U_B Z^4 \left(\frac{m_e}{m}\right)^3 \beta_{\text{par}}^2 \gamma^2.$$

The electron synchrotron energy-loss rate, expressed in terms of the rate of change of the electron Lorentz factor, is therefore

$$-\dot{\gamma}_{\text{syn}} = \frac{4}{3} c \sigma_T u_B \beta_{\text{par}}^2 \gamma^2 \xrightarrow{\gamma \gg 1} \frac{4}{3} c \sigma_T u_B \gamma^2, \quad (7.15)$$

where

$$u_B \equiv \frac{U_B}{m_e c^2} = \frac{B^2}{8\pi m_e c^2}. \quad (7.16)$$

The peak observed synchrotron frequency $\nu_{\text{pk}}^{\text{syn}} \approx 1/\Delta t_{\text{syn}}$ from a charged particle in relativistic circular motion can be derived qualitatively by considering the timescale Δt_{syn} during which an observer receives emission. For a particle in circular motion with Larmor timescale $t_L = 2\pi/\omega_L$, most radiation will be detected when the particle direction is within an angle $\theta_{\text{syn}} \sim \gamma^{-1}$ of the line of sight to the observer. Because the particle is traveling in the direction of the observer, the received radiation is compressed in time by a factor $\sim (1 - \beta_{\text{par}})$ along the electron's motion into a pulse of duration

$$\Delta t_{\text{syn}} \approx (2\theta_{\text{syn}}) t_L (1 - \beta_{\text{par}}) \approx \frac{2\pi m c}{Q B \gamma^2} \approx \frac{1}{\nu_{\text{pk}}^{\text{syn}}}. \quad (7.17)$$

Thus

$$\nu_{\text{pk}}^{\text{syn}} \approx \frac{Q B}{2\pi m c} \gamma^2. \quad (7.18)$$

For electrons,

$$\nu_{\text{pk}}^{\text{syn}} \cong \frac{eB}{2\pi m_e c} \gamma^2 \equiv \nu_B \gamma^2 = 2.79 \times 10^6 B(\text{G}) \gamma^2 \text{ Hz.} \quad (7.19)$$

This frequency can be written in dimensionless notation as

$$\epsilon_{\text{pk}}^{\text{syn}} = \epsilon_B \gamma^2, \quad (7.20)$$

where

$$\epsilon_B \equiv \frac{B}{B_{\text{cr}}}, \quad (7.21)$$

and the critical magnetic field

$$B_{\text{cr}} = \frac{m_e^2 c^3}{e\hbar} = 4.414 \times 10^{13} \text{ G}, \quad (7.22)$$

defined by setting the Larmor cyclotron energy $h\nu_L$ equal to the electron rest-mass energy.

The *quantum synchrotron regime*, which is primarily of interest in pulsar studies, is encountered when the energy of the radiated synchrotron photon is a large fraction of $\gamma m_e c^2$. The quantum synchrotron regime is defined by the condition that $h\nu_{\text{syn}} \gtrsim \gamma m_e c^2$, so that quantum synchrotron effects must be considered [85] when

$$\gamma B \gtrsim B_{\text{cr}}. \quad (7.23)$$

7.3 ELEMENTARY SYNCHROTRON RADIATION FORMULAE

The Larmor formula for radiated power in the direction \hat{n} is given by

$$\frac{dP}{d\Omega} = \frac{Q^2}{4\pi c} \frac{|\hat{n} \times [(\hat{n} - \vec{\beta}_{\text{par}}) \times \dot{\vec{\beta}}_{\text{par}}]|^2}{(1 - \hat{n} \cdot \vec{\beta}_{\text{par}})^5}. \quad (7.24)$$

Because the derivation of the elementary synchrotron spectral power and polarization from eq. (7.24) is performed in several other works [35,86–88] we refer the interested reader to these references for details. The particle dynamics are best treated in the frame with pitch angle $\psi = \pi/2$, followed by a boost to give the result for different pitch angles. Consider a charged particle in circular motion with 90° pitch angle in a uniform magnetic field of strength B . The particle's velocity is then given by

$$\vec{\beta}_{\text{par}} = \beta_{\text{par}}(\hat{x} \cos \omega_L t + \hat{y} \sin \omega_L t). \quad (7.25)$$

Solving eq. (7.24) leads to the spectral energy radiated per revolution at (radial) frequency $\omega = 2\pi\nu$, averaged over both polarization modes, given by

$$I^{\text{syn}}(\omega) = \frac{2e^2\omega}{\sqrt{3}\gamma^2\omega_L c} \int_{2\omega/3\omega_L\gamma^2}^{\infty} d\xi K_{5/3}(\xi). \quad (7.26)$$

The radiated power at frequency ν is $\omega_L/2\pi$ times this energy, and is therefore

$$\begin{aligned} P^{\text{syn}}(\nu) &= \left. \frac{dE}{dt d\nu} \right|_{\text{syn}} = 2\pi P^{\text{syn}}(\omega) = \omega_L I^{\text{syn}}(\omega) \\ &= \frac{\sqrt{3}e^3 B}{mc^2} \left(\frac{\nu}{\nu_c} \right) \int_{\nu/\nu_c}^{\infty} d\xi K_{5/3}(\xi), \end{aligned} \quad (7.27)$$

where, for electrons,

$$\frac{m_e c^2 \epsilon_c}{h} = \nu_c = \frac{3}{2} \left(\frac{eB}{2\pi m_e c} \right) \gamma^2 \equiv \frac{3}{2} \nu_B \gamma^2. \quad (7.28)$$

The total instantaneous power emitted by an electron spiraling with pitch angle $\psi = \pi/2$ around a uniform magnetic field with strength B is

$$P^{\text{syn}}(\epsilon) = \left. \frac{dE}{dt d\epsilon} \right|_{\text{syn}} = \frac{\sqrt{3}e^3 B}{h} \left(\frac{\epsilon}{\epsilon_c} \right) \int_{\epsilon/\epsilon_c}^{\infty} d\xi K_{5/3}(\xi) \equiv \frac{\sqrt{3}e^3 B}{h} F_{\text{syn}}(x). \quad (7.29)$$

Here $x \equiv \epsilon/\epsilon_c$ and

$$F_{\text{syn}}(x) \equiv x \int_x^{\infty} d\xi K_{5/3}(\xi) \rightarrow \begin{cases} \frac{4\pi e^3 B}{\Gamma(1/3)h} \left(\frac{\epsilon}{\epsilon_c} \right)^{1/3}, & \epsilon \ll \epsilon_c, \\ \sqrt{\frac{3\pi}{2}} \frac{e^3 B}{h} \sqrt{\frac{\epsilon}{\epsilon_c}} \exp(-\epsilon/\epsilon_c), & \epsilon \gg \epsilon_c. \end{cases} \quad (7.30)$$

The low-energy slope of the emissivity,

$$P^{\text{syn}}(\epsilon) \propto \epsilon^{1/3}, \quad \epsilon \ll \epsilon_c, \quad (7.31)$$

so that $f_{\epsilon}^{\text{syn}} \propto \epsilon^{4/3}$.

Figure 7.2 shows the elementary electron synchrotron spectral emissivity from eq. (7.30), along with the small x and large x asymptotes. The dotted curve gives the approximation [89]

$$F_{\text{ap}}(x) \cong 1.78x^{0.297} \exp(-x),$$

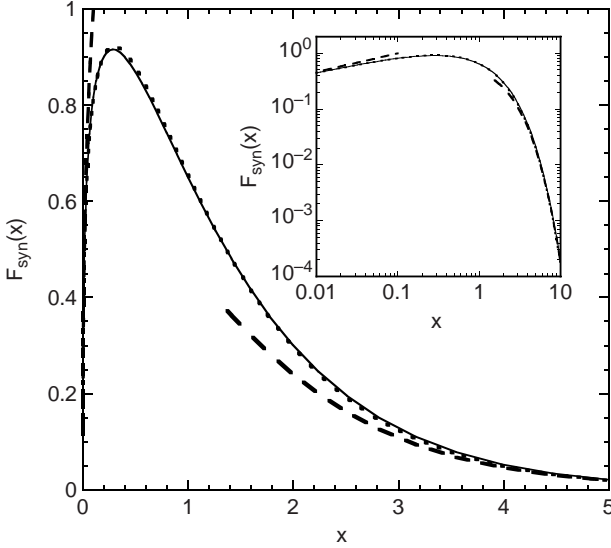


Figure 7.2 Elementary synchrotron spectral emissivity $F_{\text{syn}}(x)$, given by eq. (7.30), of a particle with 90° pitch angle in a uniform magnetic field of strength B .

which has an error of less than 5% over the range $10^{-3.5} < x < 10^{0.5}$. The mean photon energy of $F(x)$ is

$$\bar{\epsilon} = \epsilon_c \frac{\int_0^\infty du u^2 \int_u^\infty dx K_{5/3}(x)}{\int_0^\infty du u \int_u^\infty dx K_{5/3}(x)} = \frac{4\Gamma(17/6)\Gamma(7/6)}{3\Gamma(7/3)\Gamma(2/3)} \epsilon_c \cong 1.32\epsilon_c \cong 2\epsilon_B \gamma^2. \quad (7.32)$$

7.3.1 Relations between Emitted, Received, and 90° Pitch-Angle Powers

We obtain the emitted synchrotron spectral power $P_{\text{em}}^{\text{syn}}(\nu)$ from the expression, eq. (7.27), for the synchrotron spectral power in the frame in which the pitch angle $\psi = \pi/2$, which is rewritten in the 90° pitch-angle (K') frame as

$$P'^{\text{syn}}(\nu') = P'^{\text{syn}}(\nu'; \psi = \pi/2) = \frac{\sqrt{3}e^3 B}{m_e c^2} \left(\frac{\nu'}{\nu'_c} \right) \int_{\nu'/\nu'_c}^\infty d\xi K_{5/3}(\xi), \quad (7.33)$$

where

$$\nu'_c = \frac{3}{2} \left(\frac{eB}{2\pi m_e c} \right) \gamma'^2. \quad (7.34)$$

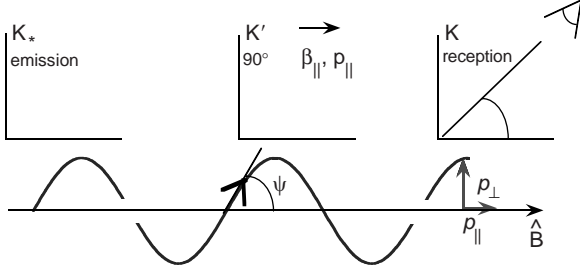


Figure 7.3 Power in stationary emission frame K_* , frame K' with electron pitch angle $\psi = \pi/2$, and reception frame K . The relationship between the electron Lorentz factor γ in K_* and the electron Lorentz factor γ' in the 90° frame is $\gamma = \gamma'/\sin\psi$ for $\gamma' \gg 1$.

Relations between the stationary or emission frame K_* , the 90° pitch-angle frame K' , and the reception frame K are illustrated in figure 7.3. The instantaneous power from electrons in the K' and K frames is invariant, provided that electrons radiate with forward-backward symmetry. Specifically, $v = \gamma_{\parallel} v' (1 + \beta_{\parallel} \cos \theta')$, so that the mean photon emission frequency averaged over θ' is $\langle \nu \rangle = \gamma_{\parallel} \nu'$, where γ_{\parallel} is the Lorentz factor relating frames K' and K_* . From figure 7.3, $\gamma = \gamma'/\sin\alpha$. Time dilation relates the stationary emission frame time $dt = \gamma_{\parallel} dt'$. Hence

$$P'^{\text{syn}} = \frac{dE}{dt'} = h\nu' \frac{dN}{dt'} = h\langle \nu \rangle \frac{dN}{dt'} = \frac{dE}{dt} = P^{\text{syn}}, \quad (7.35)$$

and $P^{\text{syn}}(\nu)d\nu = P'^{\text{syn}}(\nu')d\nu'$, so that

$$P^{\text{syn}}(\nu) = P_{\text{em}}^{\text{syn}}(\nu; \psi) = \left| \frac{d\nu'}{d\nu} \right| P'^{\text{syn}}(\nu') \cong \sin\psi P'^{\text{syn}}(\nu'), \quad (7.36)$$

noting that $\nu' = \langle \nu \rangle / \gamma_{\parallel} = \sin\psi \nu$, and

$$\gamma_{\parallel} = \frac{1}{\sqrt{1 - \beta_{\parallel}^2}} = \frac{1}{\sqrt{1 - \beta^2 \cos^2 \psi}} \cong \frac{1}{\sin\psi}, \quad \text{valid when } \gamma \gg 1, \psi \gg 1/\gamma.$$

This gives the emitted synchrotron spectral power for an electron with pitch angle ψ spiraling in an ordered magnetic field

$$P_{\text{em}}^{\text{syn}}(\nu; \psi) = \frac{\sqrt{3}e^3 B}{m_e c^2} \left(\frac{\nu}{\bar{\nu}_c} \right) \sin\psi \int_{\nu/\bar{\nu}_c}^{\infty} d\xi K_{5/3}(\xi), \quad (7.37)$$

where

$$\bar{\nu}_c = \nu_c \sin\psi = \frac{3}{2} \nu_B \gamma^2 \sin\psi, \quad \nu_B = \frac{eB}{2\pi m_e c}. \quad (7.38)$$

We now consider the relations between K' and the reception frame K . Start first with the expression for specific spectral power,

$$P(\nu, \Omega) = \frac{dE}{dt d\nu d\Omega} = h\nu^2 \left(\frac{dN}{\nu d\nu dt d\Omega} \right). \quad (7.39)$$

The term $(dN/\nu d\nu d\Omega)$ is invariant due to the invariance of $E dN/d^3\vec{p} \rightarrow \epsilon^{-1}(dN/d\epsilon d\Omega)$ for photons or relativistic particles. Also, $\nu = \delta_D \nu'$ and $dt = dt'/\delta_D$, so that $\nu dt = \nu' dt'$. For relativistic electrons,

$$\delta_D = [\gamma_{\parallel}(1 - \beta_{\parallel}\mu)]^{-1} = \gamma_{\parallel}(1 + \beta_{\parallel}\mu') \cong \gamma_{\parallel},$$

because

$$\mu' = \frac{\pi}{2} + \mathcal{O}\left(\frac{1}{\gamma'}\right).$$

Thus

$$P_{\text{rec}}^{\text{syn}}(\nu, \Omega) = \delta_D^3 P'^{\text{syn}}(\nu', \Omega').$$

Averaging this expression over angle removes two powers of δ_D , giving

$$P_{\text{rec}}^{\text{syn}}(\nu) = \delta_D P'^{\text{syn}}(\nu') = \frac{P'^{\text{syn}}(\nu')}{\sin \psi}. \quad (7.40)$$

Equations (7.36) and (7.40) imply

$$P_{\text{rec}}^{\text{syn}}(\nu) = \frac{P_{\text{em}}^{\text{syn}}(\nu)}{\sin^2 \psi}. \quad (7.41)$$

Thus we see that the received power differs from the emitted power due to the changing average distance between the electron and observer. The emitted and received powers are equal for distributions of electrons confined within a given region when the average distance between the electrons and observer does not change with time [35,86].

From these considerations,

$$L_{\nu}^{\text{syn}} = \frac{dE}{d\nu dt} = \frac{\sqrt{3}e^3 B}{m_e c^2} \oint d\Omega_{\psi} \sin \psi \int_1^{\infty} d\gamma N_e(\gamma, \Omega_{\psi}) F(x) \quad (7.42)$$

for the spectral luminosity from the random component of a synchrotron-emitting region. In this expression,

$$x = \frac{\nu}{\bar{\nu}_c} = \frac{\nu}{\frac{3}{2} \nu_B \gamma^2 \sin \psi} = \frac{2\epsilon}{3\epsilon_B \gamma^2 \sin \psi}.$$

This is the form applicable for calculations of synchrotron radiation from relativistic electrons with general pitch-angle distribution in randomly ordered magnetic field.

An analytic expression for the pitch-angle-averaged synchrotron spectral power of a single electron randomly spiraling in a magnetic field of total strength B , in units of ergs $\text{s}^{-1} \text{Hz}^{-1}$, is given by

$$\langle P^{\text{syn}}(\nu) \rangle = \left\langle \frac{dE}{dt d\nu} \right\rangle_{\text{syn}} = 4\sqrt{3}\pi r_e m_e c \nu_B x_c^2 \times \left(K_{4/3}(x_c) K_{1/3}(x_c) - \frac{3}{5} x_c [K_{4/3}^2(x_c) - K_{1/3}^2(x_c)] \right) \quad (7.43)$$

[90], where $x_c \equiv \nu/2\nu_c$. This result can be written in the form

$$\langle P^{\text{syn}}(\nu) \rangle = \frac{\sqrt{3}e^3 B}{m_e c^2} \int_1^\infty d\gamma N_e(\gamma) R(x) \quad (7.44)$$

[91], where $x = \nu/\nu_c$ (see eq. [7.28]), and

$$\begin{aligned} R(x) &= \frac{x}{2} \int_0^\pi d\theta \sin\theta \int_{x/\sin\theta}^\infty dt K_{5/3}(t) \\ &= \frac{1}{2} \pi x [W_{0, \frac{4}{3}}(x) W_{0, \frac{1}{3}}(x) - W_{\frac{1}{2}, \frac{5}{6}}(x) W_{-\frac{1}{2}, \frac{5}{6}}(x)] \end{aligned} \quad (7.45)$$

is expressed in terms of the Whittaker functions $W_{\kappa, \mu}(x)$ (see Appendix B). The asymptotes of $R(x)$ are

$$R(x) \rightarrow \begin{cases} \frac{\sqrt[3]{2}}{5} [\Gamma(1/3)]^2 x^{1/3} \cong 1.80842 x^{1/3} & \text{for } x \ll 1, \\ \frac{\pi}{2} \exp(-x) \left(1 - \frac{99}{162x} \right) & \text{for } x \gg 1 \end{cases} \quad (7.46)$$

[91]. A fit to $R(x)$ with better than 1% accuracy, useful for numerical integration, is given in [72]. The synchrotron flux from a relativistic blob is, with eq. (5.46), given by

$$\nu F_\nu^{\text{syn}} = f_\epsilon^{\text{syn}} = \frac{\delta_D^4 \nu' \langle P'^{\text{syn}}(\nu') \rangle}{4\pi d_L^2}, \quad (7.47)$$

and the primed quantities now refer to the comoving frame, so $\nu = \delta_D \nu' / (1+z)$.

7.3.2 Particle Synchrotron Radiation

We outline general synchrotron formulae for particles of mass m ($= Am_p$ for ions), charge Ze , Lorentz factor γ , and pitch angle ψ spiraling in a randomly ordered field of mean strength B . The inverse of the timescale for

synchrotron energy losses for a particle with pitch angle ψ is given from eq. (7.13) by

$$t_{\text{syn}}^{-1}(\psi) = \frac{Z^4}{(m/m_e)^3} 2c\sigma_{\text{T}}u_B\beta_{\text{par}}^2\gamma \sin^2\psi. \quad (7.48)$$

Averaging over pitch angles for an isotropic particle distribution gives

$$t_{\text{syn}}^{-1} = \frac{Z^4}{(m/m_e)^3} \frac{4}{3} c\sigma_{\text{T}}u_B\beta_{\text{par}}^2\gamma. \quad (7.49)$$

The peak synchrotron frequency

$$\bar{\nu}_c = \frac{Z}{(m/m_e)} \frac{3}{2} v_B\gamma^2 \sin\psi. \quad (7.50)$$

The frequency-dependent synchrotron power from isotropic particles in a randomly ordered field is

$$\nu L_{\nu}^{\text{syn}} = \frac{\sqrt{3}e^3 B}{mc^2} \nu \int_1^{\infty} d\gamma N(\gamma) R(x) \quad (7.51)$$

(see eqs. [7.44] and [7.45]). Here $x = 2\nu(m/m_e)/(3\nu_B\gamma^2)$ [91].

7.3.3 Synchrotron Spectrum from a Power-Law Electron Distribution

Now assume that the electron distribution takes the form

$$N_e(\gamma, \Omega_{\psi}) = K_e \frac{g(\psi)}{4\pi} \gamma^{-p} H(\gamma; \gamma_1, \gamma_2) \quad (7.52)$$

(cf. eqs. [6.62] and [6.104]), where the function $g(\psi) = 1$ for an isotropic distribution in pitch angle ψ . From eq. (7.42),

$$L_{\nu}^{\text{syn}}(p) = \frac{\sqrt{3}K_e e^3 B}{4\pi m_e c^2} \int_{\gamma_1}^{\gamma_2} d\gamma \gamma^{-p} \oint d\Omega_{\psi} g(\psi) \sin\psi F(x). \quad (7.53)$$

The integrals can be performed analytically for an isotropic pitch-angle distribution, $g(\psi) = 1$, for photon frequencies far away from the endpoints of the spectrum [35,87,91]. The result is

$$L_{\nu}^{\text{syn}}(p) = \frac{4\pi K_e e^3 B^{(p+1)/2}}{m_e c^2} \left(\frac{3e}{4\pi m_e c} \right)^{(p-1)/2} a(p) \nu^{-(p-1)/2}, \quad (7.54)$$

where

$$a(p) = \frac{2^{(p-1)/2} \sqrt{3} \Gamma[(3p-1)/12] \Gamma[(3p+19)/12] \Gamma[(p+5)/4]}{8\sqrt{\pi} (p+1) \Gamma[(p+7)/4]}. \quad (7.55)$$

Table 7.1 Factors for Synchrotron, Synchrotron Self-Absorption, and Synchrotron Self-Compton Radiation from Isotropic, Power-Law Electrons in a Randomly Ordered Magnetic Field

p	$a(p)$	ρ_δ	$b(p)$	$3^5 b(p)/2^7 \pi^2$	$c(p)$	$c_\delta(p)$	t_p
1.0	0.2833	2.55	7.456	1.43	1.191	0.74	
1.5	0.1490	1.48					
2.0	0.1032	1.137	3.498	0.67	1.396	1.396	0.49
2.5	0.08311	1.014					
3.0	0.07408	1.00	3.899	0.74	2.093	2.45	0.88
3.5	0.07117	1.063					
4.0	0.07255	1.20	6.567	1.260	3.673	4.19	1.2

The relation

$$\int_0^\infty dx x^\mu F(x) = \frac{2^{\mu+1}}{2+\mu} \Gamma\left(\frac{\mu}{2} + \frac{7}{3}\right) \Gamma\left(\frac{\mu}{2} + \frac{2}{3}\right) \quad (7.56)$$

is used to derive eq. (7.55). Values of $a(p)$ are given in table 7.1. From eq. (7.54),

$$\nu L_\nu^{\text{syn}}(p) = \frac{3^{(p+3)/2}}{2^{(p+1)/2}} a(p) \frac{4}{3} c \sigma_T U_B K_e \left(\frac{\nu}{\nu_B}\right)^{(3-p)/2}. \quad (7.57)$$

The use of eq. (7.54) is illustrated by estimating the synchrotron flux density from relativistic electrons accelerated by strong shocks ($p \cong 2$) of a supernova remnant (SNR) in the Sedov-Taylor deceleration phase. Equation (7.54) can be recast as

$$L_\nu^{\text{syn}}(p) = \frac{4\pi \mathcal{E}_e e^3 B}{\Lambda_e (m_e c^2)^2} \left(\frac{3}{2}\right)^{(p-1)/2} a(p) \left(\frac{\nu}{\nu_B}\right)^{-(p-1)/2}. \quad (7.58)$$

For $p \cong 2$, $B_{-5} = B/10\mu\text{G}$, $\nu_B = 28B_{-5} \text{ Hz}$, $\nu_{\text{GHz}} = \nu/\text{GHz}$, nonthermal electron energy $\mathcal{E}_e = 10^{48} \mathcal{E}_{48}$, and bolometric factor $\Lambda_e = 10\Lambda_1$,

$$L_\nu^{\text{syn}}(p \cong 2) \cong \frac{4 \times 10^{22} \mathcal{E}_{48} B_{-5}^{3/2}}{\Lambda_1 \sqrt{\nu_{\text{GHz}}}} \frac{\text{ergs}}{\text{s Hz}}. \quad (7.59)$$

In the Sedov-Taylor phase, the SNR shell speed v_s is given by the kinetic energy of the swept-up material from an explosion releasing $\mathcal{E}_{\text{exp}} = 10^{51} \mathcal{E}_{51}$ ergs of kinetic energy. For a fraction $\epsilon_B (\neq \epsilon_B = B/B_{\text{cr}})$ of swept-up kinetic energy converted to magnetic field energy, $B \cong \sqrt{6\mathcal{E}_{\text{exp}}\epsilon_B/R^3}$, and

$$L_\nu^{\text{syn}}(p \cong 2) \cong \frac{2 \times 10^{24} \mathcal{E}_{48} \mathcal{E}_{51}^{3/4} (\epsilon_B/0.1)^{3/2}}{(R/10 \text{ pc})^{9/4} \Lambda_1 \sqrt{\nu_{\text{GHz}}}} \frac{\text{ergs}}{\text{s Hz}}. \quad (7.60)$$

By comparing eq. (7.60) with observations of SNRs in the galaxy M33, Katz and Waxman [92] estimate that the minimum energy in relativistic hard-spectrum electrons accelerated in shell-type SNRs is $\sim 10^{47}$ ergs.

Formula (7.54) can be rewritten in the form of a $\nu L(\nu)$ or $\epsilon L(\epsilon)$ spectrum (units of ergs s^{-1}), giving

$$\epsilon L^{\text{syn}}(\epsilon) = 4\pi\alpha_f K_e h \nu_B^2 a(p) \left(\frac{3}{2}\right)^{(p-1)/2} \left(\frac{\epsilon}{\epsilon_B}\right)^{-(p-3)/2} H(\nu; \gamma_1^2 \epsilon_B, \gamma_2^2 \epsilon_B), \quad (7.61)$$

where $\alpha_f = e^2/\hbar c \cong 1/137$ is the fine structure constant. Taking into account the form of the electron spectrum, eq. (7.52), we can rewrite eq. (7.61) as

$$\epsilon L^{\text{syn}}(\epsilon) = 6c\sigma_T U_B a(p) \left(\frac{3}{2}\right)^{(p-1)/2} \gamma_s^3 N_e(\gamma_s), \quad \gamma_s = \sqrt{\frac{\epsilon}{\epsilon_B}}, \quad (7.62)$$

where $U_B = U_{\text{cr}} \epsilon_B^2 = B^2/8\pi$, and

$$U_{\text{cr}} = B_{\text{cr}}^2/8\pi = 7.75 \times 10^{25} \text{ ergs cm}^{-3}$$

is the critical magnetic field energy density. Noting that $\nu j^{\text{syn}}(\nu, \Omega) = \epsilon j^{\text{syn}}(\epsilon, \Omega)$, the synchrotron emissivity can therefore be written as

$$\nu j^{\text{syn}}(\nu, \Omega) = \frac{a(p)}{\pi} \left(\frac{3}{2}\right)^{1+\alpha} c\sigma_T U_B k_e \left(\frac{\nu}{\nu_B}\right)^{(3-p)/2} H(\nu; \gamma_1^2 \nu_B, \gamma_2^2 \nu_B), \quad (7.63)$$

with $k_e = K_e/V_b$, which is valid away from the endpoints of the spectrum in the energy range $\gamma_1^2 \epsilon_B \ll \epsilon \ll \gamma_2^2 \epsilon_B$. The power-law approximation for the nonthermal synchrotron emissivity can also be written as

$$\epsilon j^{\text{syn}}(\epsilon, \Omega) = \frac{a(p)}{\pi} \left(\frac{3}{2}\right)^{(p+1)/2} c\sigma_T U_{\text{cr}} \epsilon_B^2 \gamma_s^3 n_e(\gamma_s). \quad (7.64)$$

7.4 δ -FUNCTION APPROXIMATION FOR SYNCHROTRON RADIATION

As for Thomson scattering, a simple δ -function approximation can be employed to estimate the synchrotron radiation in problems involving isotropic electron pitch-angle distributions in a randomly oriented magnetic field with mean intensity B . In terms of the photon emissivity $\dot{n}^{\text{syn}}(\epsilon)$ (ph $\text{cm}^{-3} \text{ s}^{-1} \epsilon^{-1}$), the δ -function approximation for synchrotron emission is given by

$$\dot{n}^{\text{syn}}(\epsilon) \cong \frac{2}{3} c\sigma_T u_B \epsilon^{-1/2} \epsilon_B^{-3/2} n_e \left(\sqrt{\frac{\epsilon}{\epsilon_B}} \right), \quad (7.65)$$

recalling definition (7.16) for u_B . Note that, if $n_e = \delta(\gamma - \bar{\gamma})$ (i.e., a density of 1 electron cm^{-3}), then

$$\begin{aligned} -\dot{\gamma}_{\text{syn}} &= \int_0^\infty d\epsilon \in \dot{n}^{\text{syn}}(\epsilon) \\ &= \frac{2}{3} c\sigma_{\text{T}} u_B \int_0^\infty dx \sqrt{x} \delta(\sqrt{x} - \bar{\gamma}) = \frac{4}{3} c\sigma_{\text{T}} u_B \bar{\gamma}^2, \end{aligned} \quad (7.66)$$

so the synchrotron energy-loss rate for electrons with isotropic pitch-angle distributions is recovered. For a uniform-emitting region of volume V_b , the $\epsilon L(\epsilon)$ spectrum in the δ -function synchrotron approximation is, from eq. (7.65), given by

$$\epsilon L_\delta^{\text{syn}}(\epsilon) = m_e c^2 V_b \epsilon^2 \dot{n}^{\text{syn}}(\epsilon) \cong \frac{2}{3} c\sigma_{\text{T}} U_B \gamma_s^3 N_e(\gamma_s), \quad \gamma_s = \sqrt{\frac{\epsilon}{\epsilon_B}}. \quad (7.67)$$

The δ -function approximation for the synchrotron emissivity can be written as

$$\epsilon j_\delta^{\text{syn}}(\epsilon, \Omega) = \frac{c\sigma_{\text{T}} U_{\text{cr}} \epsilon_B^2}{6\pi} \gamma_s^3 n_e(\gamma_s). \quad (7.68)$$

The ratio of the accurate synchrotron spectrum, eq. (7.62), to the synchrotron spectrum derived in the δ -function approximation, eq. (7.67), is

$$\rho_\delta = \frac{\epsilon L^{\text{syn}}(\epsilon)}{\epsilon L_\delta^{\text{syn}}(\epsilon)} = 6a(p) \left(\frac{3}{2}\right)^{(p+1)/2}. \quad (7.69)$$

Table 7.1 also gives values of ρ_δ for various values of p . As can be seen, the δ -function approximation is accurate to better than 14% for $2.0 \leq p \leq 3.5$ in the asymptotic power-law portion of the spectrum.

For the simple *one-zone blob model*, here called the *standard one-zone (blob) model*, a randomly oriented magnetic field with intensity B is assumed to fill the volume of a spherical plasmoid-type emitter with radius r'_b and comoving volume $V'_b = 4\pi r_b'^3/3$. Nonthermal relativistic electrons are assumed to be uniformly distributed throughout the blob with an isotropic pitch-angle distribution and Lorentz-factor distribution $N'_e(\gamma')$, where $N'_e(\gamma')d\gamma'$ is the differential number of electrons with comoving Lorentz factors γ' between γ' and $\gamma' + d\gamma'$.

From eqs. (5.46) and (7.67), the νF_ν synchrotron radiation spectrum can be approximated by the expression

$$f_\epsilon^{\text{syn}} \cong \frac{\delta_{\text{D}}^4}{6\pi d_L^2} c\sigma_{\text{T}} U_B \gamma_s'^3 N'_e(\gamma_s'), \quad \gamma_s' = \sqrt{\frac{\epsilon(1+z)}{\delta_{\text{D}} \epsilon_B}}. \quad (7.70)$$

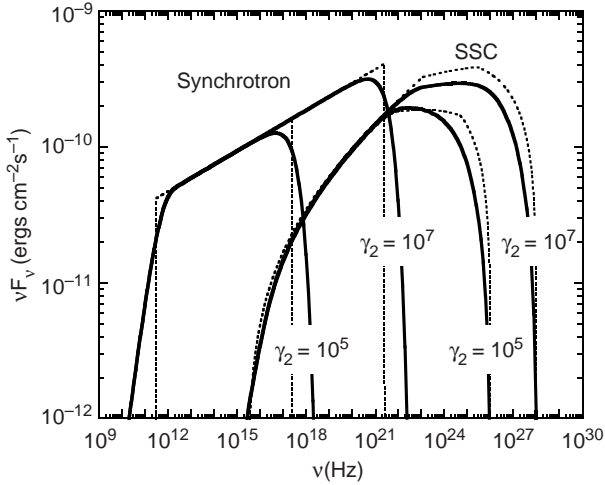


Figure 7.4 Synchrotron and synchrotron self-Compton νF_ν fluxes for an optically thin relativistically jetted blob with a nonthermal electron distribution described by a single power law with number index $p = 2.8$. Other parameters are $\Gamma = \delta_D = 10.0$ (i.e., $\mu = \beta$), $d_L = 10^{27}$ cm, $B = 1$ G, blob radius $r_b = 10^{16}$ cm, nonthermal electron energy $W'_e = 10^{48}$ ergs, $\gamma_1 = 10^2$, $\gamma_2 = 10^5$, and $\gamma_2 = 10^7$, as labeled. The solid curves show the numerical integration of eqs. (7.44) and (7.47) for synchrotron radiation, and for SSC radiation as calculated in section 7.7.3. The dotted curves show the δ -function approximation for synchrotron radiation, eq. (7.70), and SSC radiation, eqs. (7.98) and (7.99).

Figure 7.4 compares the calculation using the δ -function approximation with an accurate calculation of synchrotron radiation, for a standard one-zone blob containing a power-law electron distribution with number index $p = 2.8$. The comoving electron distribution, $N'_e(\gamma')$, can be found by inverting eq. (7.70) (section 7.7.3).

7.5 EQUIPARTITION MAGNETIC FIELD

The total energy contained in radiating plasma consists of particle and field energy. The energy in particles consists of their rest mass and kinetic energy. The particle kinetic energy can be described by the heat content of the thermal component, and by the nonthermal kinetic energy for the suprathermal and relativistic particle components. Under the assumption of a specific particle pitch-angle distribution, usually assumed to be isotropic in the comoving fluid frame, and a magnetic-field geometry, one can

calculate the kinetic energy associated with the bulk motion of the thermal and nonthermal particles. For isotropically distributed particles, the total kinetic energy is simply increased by the boost factor Γ (see eq. [5.23]).

Field energy consists of the energy in the large-scale magnetic, magnetohydrodynamic (MHD) wave energy, and photon radiation. Poynting flux refers to the field energy carried by electromagnetic radiation formed, for example, from a powerful magnetic inductor, such as is expected in electromagnetic models of black holes. Relativistic outflows have additional kinetic power from the bulk motion of the plasma, which is not considered in the qualitative derivation.

7.5.1 Equipartition Magnetic Field: Qualitative Estimate

The equipartition magnetic field and related Poynting power can be estimated by treating the black hole magnetospheric system as a magnetic dipole produced by a current flowing near the black hole, analogous to the magnetic dipole radiation produced by a pulsar [93]. The magnetized accretion disk of the black hole rotates at the rate $\Omega(R_0)$ at radius R_0 from the center of the black hole. R_0 may coincide with the radius where energy dissipation is largest, the innermost radius defined by the spin of the black hole, or the inner edge of the accretion disk. Energy is lost when the magnetic-field lines are disrupted at the light cylinder radius $R_{\text{LC}} = c/\Omega_{\text{LC}}$. For a dipole magnetic field, $B(R_{\text{LC}}) \simeq B_0(R_0/R_{\text{LC}})^3$ with $B_0 = B(R_0)$, so that the energy-loss rate in Poynting flux is

$$P_{\text{P}} \cong 4\pi R_{\text{LC}}^2 \frac{B_0^2}{8\pi} c \left(\frac{R_0}{R_{\text{LC}}} \right)^6 \cong \frac{c}{2} B_0^2 R_0^6 R_{\text{LC}}^{-4}, \quad (7.71)$$

where the light-cylinder frequency is identified with the Keplerian orbital frequency at radius R_0 ; thus $\Omega_{\text{LC}} \approx \Omega_{\text{K}}(R_0) = \sqrt{GM/R^3}$, and $\tilde{R}_{\text{LC}} = \tilde{R}_0^{3/2}$. (Recall that the tildes mean that the distances are rescaled in units of gravitational radii $R_g = GM/c^2$.)

The magnetic field is defined with respect to the observed radiant luminosity $L_{\text{rad}} = \ell_{\text{Edd}} L_{\text{Edd}}$ (eq. [6.133]) and size R_0 using the equipartition magnetic field which we define here through the Eddington relation

$$\frac{B_0^2}{8\pi} = \frac{L_{\text{rad}}}{4\pi R_0^2 c} \cong \frac{\ell_{\text{Edd}} L_{\text{Edd}}}{4\pi R_0^2 c}. \quad (7.72)$$

Normalization to supermassive black holes with masses $M = 10^9 M_9 M_\odot$ gives a magnetic-field estimate

$$B_0(\text{G}) \cong \frac{2 \times 10^4}{\tilde{R}_0} \sqrt{\frac{\ell_{\text{Edd}}}{M_9}}. \quad (7.73)$$

This suggests that the inner magnetized regions surrounding supermassive black holes should have $\mathcal{O}(\text{kG})$ magnetic fields. Equations (7.71) and (7.72) together imply

$$P_P \simeq 10^{47} \frac{M_9 \ell_{\text{Edd}}}{\tilde{R}_0^2} \text{ ergs s}^{-1}. \quad (7.74)$$

For accretion at $\ell_{\text{Edd}} \sim 1\text{--}10\%$ and energy dissipation at $\tilde{R}_0 \lesssim 10$, the Poynting power as estimated here could be compatible with supermassive black-hole jet power.

These arguments illustrate a common approach to estimating the equipartition magnetic field of a stationary emitting region. Now we treat the problem more comprehensively, considering also bulk relativistic motion.

7.5.2 Equipartition Magnetic Field: Quantitative Treatment

By using a magnetic field obtained from equipartition arguments, one can precisely derive the penalty in energy or power that must be paid when assuming a magnetic field away from equipartition. The equipartition magnetic field B_{eq} is defined by equating the magnetic field energy density $U_B = B^2/8\pi$ with the total particle energy density through the expression

$$\frac{W'_{\text{par}}}{V'_b} = \frac{(1 + \zeta_{\text{pe}})W'_e}{V'_b} = k_{\text{eq}}U_B, \quad (7.75)$$

where W'_{par} and W'_e represent the total energy in particles and nonthermal leptons (primarily electrons and positrons), respectively, in the comoving frame, and k_{eq} is the ratio of total particle energy density to U_B . The particle energy density $W'_{\text{par}} = (1 + \zeta_{\text{pe}})W'_e$, where ζ_{pe} is the ratio of total energy in hadrons compared to the lepton energy. Thus $\zeta_{\text{pe}} = 0$ for a plasma containing negligible ion content.

From eq. (7.75),

$$W'_e = \hat{k}_{\text{eq}}V'_bU_B, \quad \text{where } \hat{k}_{\text{eq}} \equiv \frac{k_{\text{eq}}}{1 + \zeta_{\text{pe}}},$$

and \hat{k}_{eq} is the ratio of nonthermal lepton energy density to U_B .

If radiation observed at energy ϵ is nonthermal synchrotron radiation from a power-law electron distribution described by

$$N'_e(\gamma') = V'_b n'_e(\gamma') = K'_e \gamma'^{-p} H(\gamma'; \gamma'_1, \gamma'_2), \quad (7.76)$$

then normalizing to the total comoving electron energy $W'_e = m_e c^2 \int_1^\infty d\gamma' \gamma' N'_e(\gamma') = K'_e m_e c^2 (\gamma_1'^{2-p} - \gamma_2'^{2-p})/(p-2)$ implies that

$$K'_e = \frac{(p-2)W'_e}{m_e c^2 (\gamma_1'^{2-p} - \gamma_2'^{2-p})} \xrightarrow{p>2, \gamma_2' \gg \gamma_1'} \frac{(p-2)W'_e \gamma_1'^{p-2}}{m_e c^2}. \quad (7.77)$$

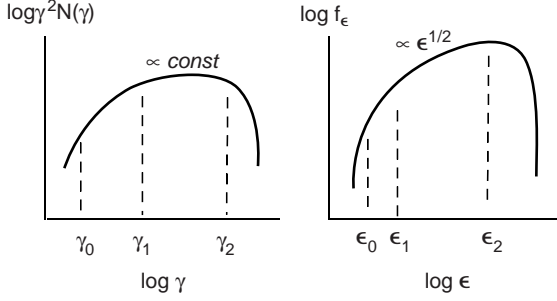


Figure 7.5 Diagram illustrating the energetics of the nonthermal lepton spectrum and the radiated synchrotron photon spectrum. Most of the particle energy is found on the $f_\epsilon \propto \epsilon^{1/2}$ branch of the spectrum. Thus $a = \alpha = 1/2$ is a critical value defining classes of sources.

We now relate the measured synchrotron νF_ν flux f_ϵ^{syn} to comoving quantities. Substituting eq. (7.77) into eq. (7.70), we obtain

$$\begin{aligned} f_\epsilon^{\text{syn}} &\cong \frac{\delta_D^4}{6\pi d_L^2} c\sigma_T U_B \frac{(p-2)W'_e}{m_e c^2 \gamma_1'^{2-p}} \left(\frac{\epsilon_z}{\delta_D \epsilon_B} \right)^{(3-p)/2} \\ &= \frac{(\delta_D \epsilon_B)^{(5+p)/2}}{6\pi d_L^2} c\sigma_T U_{\text{cr}}^2 \hat{k}_{\text{eq}} V'_b \frac{\epsilon_z^{(3-p)/2} (p-2)}{m_e c^2 \gamma_1'^{2-p}}, \end{aligned} \quad (7.78)$$

recalling that $\epsilon_z = (1+z)\epsilon$, from eq. (6.96). Solving for $\delta_D \epsilon_B = \delta_D B / B_{\text{cr}}$ gives

$$\delta_D \epsilon_B = \left(\frac{9m_e c^2 d_L^2 f_\epsilon^{\text{syn}} \gamma_1'^{2-p} \epsilon_z^{(p-3)/2}}{2c\sigma_T U_{\text{cr}}^2 (p-2) \hat{k}_{\text{eq}} r_b'^3} \right)^{2/(5+p)}. \quad (7.79)$$

The equipartition value of the quantity $y_{\text{eq}} = \delta_D \epsilon_B$ is given when $k_{\text{eq}} = 1$ and $\hat{k}_{\text{eq}} = 1/(1 + \zeta_{\text{pe}})$.

Figure 7.5 illustrates the electron spectrum and radiated synchrotron spectrum. Most of the nonthermal lepton energy is bound up in the electrons and positrons that radiate synchrotron emission in the $\alpha = 1/2$ portion of the spectrum (i.e., $F_\nu \propto \nu^{-1/2}$ and $\nu F_\nu \propto \nu^{1/2}$). The equipartition magnetic field is given when $k_{\text{eq}} = 1$, $p = 2$, or $\alpha = 1/2$, with $(p-2)\gamma_1'^{p-2} \rightarrow [\ln(\gamma_2'/\gamma_1')]^{-1} = [(1/2)\ln(\epsilon_2/\epsilon_1)]^{-1}$ in eq. (7.79), where ϵ_1 and ϵ_2 are the photon energies bounding the $\alpha = 1/2$ portion of the synchrotron spectrum. In this case,

$$\frac{B}{B_{\text{cr}}} \delta_D = \left(\frac{3\pi m_e c^2 d_L^2 f_{\epsilon_{\text{pk}}}^{\text{syn}} \ln(\epsilon_2/\epsilon_1)}{V'_b c\sigma_T U_{\text{cr}}^2 \hat{k}_{\text{eq}} \sqrt{\epsilon_2(1+z)}} \right)^{2/7}, \quad (7.80)$$

where V'_b is the comoving volume of the synchrotron source described by the spectrum $f_\epsilon = f_{\epsilon_{\text{pk}}}^{\text{syn}} (\epsilon/\epsilon_2)^{1/2}$ for $\epsilon_1 \leq \epsilon \leq \epsilon_2$.

For a flaring source that is not resolved, the size scale of the emitting region can be estimated through the relation $r_b \lesssim c\delta_D t_{\text{var}}/(1+z)$. This gives the magnetic field

$$B \text{ (G)} \cong 130 \frac{d_{28}^{4/7} f_{-10}^{2/7} [(1 + \zeta_{\text{pe}}) \ln(\nu_2/\nu_1)]^{2/7} (1+z)^{5/7}}{k_{\text{eq}}^{2/7} [t_{\text{var}}(d)]^{6/7} \delta_D^{13/7} \nu_{13}^{1/7}}, \quad (7.81)$$

which gives the equipartition comoving magnetic field B_{eq} when $k_{\text{eq}} = 1$. Note that this field depends on the value of ζ_{pe} . Here $\nu_{13} \equiv \nu/10^{13}$ Hz is the frequency where the peak flux $f_{\epsilon_{\text{pk}}}^{\text{syn}} \equiv 10^{-10} f_{-10}$ ergs cm $^{-2}$ s $^{-1}$ is measured, and we use values typical of bright blazar flares as measured with EGRET [20].

An alternative estimate of B can be derived from the ratio of the synchrotron self-Compton (SSC) γ -ray and synchrotron peak fluxes $f_{\text{SSC}}^{\text{pk}}/f_s^{\text{pk}} \cong u'_s/u'_B$ [81,94]. Thus $u'_B = Au'_s = Af_s^{\text{pk}} (2d_L^2/R^2 c\delta_D^4)$, where $A \equiv (f_s^{\text{pk}}/f_{\text{SSC}}^{\text{pk}})$. This gives

$$B = \frac{4\sqrt{\pi}(1+z)d_L}{c^{3/2}\delta_D^3 t_{\text{var}}} \sqrt{Af_s^{\text{pk}}} \cong 1.6 \frac{d_{28}(1+z)\sqrt{Af_{-10}}}{(\delta_D/10)^3 t_{\text{var}}(d)} \text{ G}. \quad (7.82)$$

This equation assumes that Klein-Nishina effects for the SSC γ -rays are unimportant, because the Compton process occurs on softer (radio-optical) photons as compared to the UV photons for external Compton scattering. In both equations (7.81) and (7.82), the strongest dependence of B is through the unknown Doppler factor. Equating these two equations gives [95] the Doppler-factor estimate

$$\delta_D \cong 8.9 \frac{d_{28}^{3/8} (1+z)^{1/4} f_{-10}^{3/16} A^{7/16} \eta^{1/4} \nu_{13}^{1/8}}{[(1 + \zeta_{\text{pe}}) \ln(\nu_2/\nu_1)]^{1/4} [t_{\text{var}}(d)]^{1/8}}. \quad (7.83)$$

7.6 ENERGETICS AND MINIMUM JET POWERS

Measurements of resolved sources of synchrotron radiation offer a method to evaluate the minimum energy associated with the mean magnetic-field and particle energy in synchrotron sources, from which minimum jet powers can be derived. As before, the magnetic-field value B is referred to the comoving frame.

Imagine a particle and plasma outflow from a stationary source. The stationary frame density n_* of the outflow at radius R is related to the total

outflow (jet) power P_j^* according to the relation

$$n_* = \frac{P_j^*}{2\Omega_j R^2 (\Gamma m_e c^2) \beta c} = \Gamma n' \quad (7.84)$$

for a two-sided jet, where Ω_j is the characteristic opening angle, in sr, of one of the jets. The jet power is of course proportional to the bulk Lorentz factor of the plasma outflow. The final relation means that the blob density is larger in the stationary frame than in the proper frame of the blob due to length contraction. Equation (7.84) implicitly assumes that electrons carry the jet power, and are cold in the comoving plasma frame. When generalized to particle distributions that consist of thermal and nonthermal components,

$$n' \rightarrow (1 + \zeta_{\text{pe}}) \frac{1}{V'_b} \int_1^\infty d\gamma' \gamma' N'_e(\gamma'),$$

where the factor ζ_{pe} takes into account the power in nonthermal hadrons.

Thus the total particle kinetic jet power in the directed rest mass and comoving nonthermal energy is

$$P_{j,\text{ke}}^* = 2\Omega_j R^2 \beta \Gamma^2 m_e c^3 \frac{(1 + \zeta_{\text{pe}})}{V'_b} \int_1^\infty d\gamma' \gamma' N'_e(\gamma'). \quad (7.85)$$

To this we add the power required to expel magnetic-field-laden plasma, given by

$$P_B^* = 2\Omega_j c R^2 \beta \Gamma^2 \left(\frac{B^2}{8\pi} \right). \quad (7.86)$$

The total jet power, referred to the stationary black-hole reference frame, is then

$$P_j^* \cong 2\pi r_b'^2 \beta c \Gamma^2 \left(\frac{B^2}{8\pi} + \frac{m_e c^2 (1 + \zeta_{\text{pe}})}{V'_b} \frac{3\pi d_L^2 f_{\epsilon_{\text{pk}}}}{c \sigma_T U_B \delta_D^4} \sqrt{\frac{\delta_D \epsilon_B}{\epsilon_{\text{pk}} (1 + z)}} \ln(\epsilon_{\text{pk}}/\epsilon_0) \right) \quad (7.87)$$

[96], taking $\pi r_b'^2 = \Omega_j R^2$; if r_b refers to the transverse width, then $r_b = r_b'$. In the final term in this expression, the synchrotron spectrum is approximated by $f_\epsilon^{\text{syn}} \cong f_{\epsilon_{\text{pk}}} (\epsilon/\epsilon_{\text{pk}})^{1/2} H(\epsilon_{\text{pk}} - \epsilon)$. The magnetic field energy density $B^2/8\pi = U_{\text{cr}} \epsilon_B^2$, and we switch from a continuous outflow model to a one-zone model.

Having switched to a blob scenario, we let $\Gamma \rightarrow \delta_D$ to derive the minimum jet power $P_{j,\text{min}}$ for a synchrotron source model [97]. The jet power

$$P_j^* = \pi r_b'^2 \beta c U_{\text{cr}} \left(\hat{k}_{\text{eq}} y_{\text{eq}}^{(5+p)/2} y^{-(1+p)/2} + y^2 \right) \quad (7.88)$$

for a synchrotron model depends only on the product

$$y \equiv \delta_D \varepsilon_B,$$

and so is degenerate. This degeneracy in δ_D and ε_B can be broken with additional observations, for example, joint X-ray/ γ -ray observations. The value of $\delta_D \varepsilon_B$ that minimizes the jet power is given by

$$y_{\min} = \left(\frac{(p+1)\hat{k}_{\text{eq}}}{4} \right)^{2/(5+p)} y_{\text{eq}}.$$

The term y_{eq} , composed entirely of observational quantities and equipartition parameters, is defined following eq. (7.79). Because most of the energy is contained in the electrons with $p = 2$, we take $p = 2$, giving

$$y_{\min} = \left(\frac{27m_e c^2 d_L^2 (1 + \zeta_{\text{pe}}) \ln(\epsilon_2/\epsilon_1) f_{\epsilon_{\text{pk}}}^{\text{syn}}}{16c\sigma_T U_{\text{cr}}^2 r_b'^3 \sqrt{\epsilon_2(1+z)}} \right)^{2/7}. \quad (7.89)$$

When the emitting region is spatially resolved, as for VLBI radio observations at GHz frequencies, this expression can be written as

$$B \text{ (G)} \cong \frac{7.0 \times 10^{-3}}{\delta_D} \frac{(1+z)^{11/7}}{d_{28}^{2/7} \vartheta_{\text{mas}}^{6/7} \epsilon_{-10}^{1/7}} [(1 + \zeta_{\text{pe}})\lambda_1 f_{-14}]^{2/7}, \quad (7.90)$$

where $\lambda_1 = \ln(\epsilon_2/\epsilon_1)/10$ is a bolometric factor, $f_i = f_\epsilon/(10^i \text{ ergs cm}^{-2} \text{ s}^{-1})$ at $\epsilon = 10^{-10} \epsilon_{-10}$, and $\epsilon_{-10} \cong 1$ corresponds to ≈ 12 GHz. The measured half-angular extent, in milliarcseconds, of the emitting region is denoted ϑ_{mas} . The minimum jet power in a pure synchrotron model, when $k_{\text{eq}} \cong 1$, is

$$\begin{aligned} P_{j,\min}^* &= P_j^*(y_{\min}) \cong 2\pi r_b'^2 \beta c U_{\text{cr}} y_{\min}^2 \\ &\cong 1.3 \times 10^{45} \beta \frac{d_{28}^{10/7} \vartheta_{\text{mas}}^{2/7}}{(1+z)^{6/7} \epsilon_{-10}^{2/7}} [(1 + \zeta_{\text{pe}})\lambda_1 f_{-14}]^{4/7} \text{ ergs s}^{-1}. \end{aligned} \quad (7.91)$$

By characterizing the size scale $r_b' = c\delta_D t_{\text{var}}/(1+z)$ in terms of the measured variability timescale $t_{\text{var}} = 1000t_3$ s, the magnetic field $B_{\text{min}L}$ giving minimum jet power is found to be

$$B_{\text{min}L} = B_{\text{cr}} \varepsilon_{B_{\text{min}L}} \cong 346 \frac{(1+z)^{5/7}}{\delta_D^{11/7}} \frac{d_{27}^{4/7} [(1 + \zeta_{\text{pe}})f_{-12}\lambda_1]^{2/7}}{t_3^{6/7} \epsilon_{-5}^{1/7}} \text{ G}. \quad (7.92)$$

The minimum jet power is

$$\begin{aligned} P_j^*(\varepsilon_{B_{\text{min}L}}) &= \frac{14}{3} \pi c \beta \Gamma^2 r_b'^2 U_{B_{\text{cr}}} \varepsilon_{B_{\text{min}L}}^2 \\ &\cong 2 \times 10^{42} \beta \frac{t_3^{2/7} d_{27}^{8/7} (1 + \zeta_{\text{pe}})^{4/7} (f_{-12}\lambda_1)^{4/7}}{(1+z)^{4/7} \delta_D^{8/7} \epsilon_{-5}^{2/7}} \text{ ergs s}^{-1}. \end{aligned} \quad (7.93)$$

The penalty paid in jet power for departures from equipartition is given by the expression

$$P_j^*(\epsilon_B) = \frac{3}{7} P_j^*(\epsilon_{B_{\min L}}) \left(u^2 + \frac{4}{3u^{3/2}} \right), \quad u \equiv \frac{\epsilon_B}{\epsilon_{B_{\min L}}}. \quad (7.94)$$

Although the jet power can be made arbitrarily small by choosing sufficiently large values of the Doppler factor, this freedom is restricted when fitting correlated observations of sources at optical/X-ray energies and at γ -ray energies and by $\gamma\gamma$ absorption (chpt. 10).

7.7 SYNCHROTRON SELF-COMPTON RADIATION

The synchrotron self-Compton (SSC) process refers to the mechanism whereby nonthermal electrons Compton-scatter the synchrotron photons that they radiate. The size scale of a synchrotron emission region can be directly measured in resolved synchrotron sources, and can be inferred from the variability timescale of the synchrotron emission. The synchrotron power and size scale imply the energy density of target synchrotron photons, which in turn implies the SSC flux.

7.7.1 SSC in the Thomson Regime

A simple expression for SSC emission from a uniform spherical emitting region is derived in the Thomson regime for a single power-law electron distribution, using δ -function approximations for the synchrotron and Thomson processes. The internal photon target is assumed to be quasi-isotropic synchrotron radiation with comoving spectral density

$$n'_{\text{syn}}(\epsilon'_i) \cong \frac{r'_b}{c} \dot{n}'_{\text{syn}}(\epsilon'_i) \cong \frac{2}{3} \sigma_T r'_b u_B \epsilon_i'^{-1/2} \epsilon_B^{-3/2} n'_e \left(\sqrt{\frac{\epsilon'_i}{\epsilon_B}} \right), \quad (7.95)$$

from eq. (7.65). Substituting this into the δ -function approximation (6.82) for Thomson scattering gives

$$\dot{n}'_{\text{SSC}}(\epsilon) \cong \frac{4}{9} \frac{c \sigma_T^2 r'_b u_B}{\epsilon'^{1/2} \epsilon_B^{3/2}} \int_0^{\min(\epsilon', 1/\epsilon')} d\epsilon'_i \epsilon_i'^{-1} n'_e \left(\sqrt{\frac{\epsilon'_i}{\epsilon'_i}} \right) n'_e \left(\sqrt{\frac{\epsilon'_i}{\epsilon_B}} \right). \quad (7.96)$$

Substituting eq. (7.76) into eq. (7.96) gives the comoving power $\epsilon' L(\epsilon') = m_e c^2 \epsilon'^2 V'_b \dot{n}'_{\text{SSC}}(\epsilon')$.

Transforming to the observer frame using relation (5.46) in the form $f_\epsilon \cong \delta_D^4 \epsilon' L'(\epsilon') / 4\pi d_L^2$ gives the SSC νF_ν flux in the δ -function approximation,

namely,

$$f_{\epsilon}^{\text{SSC}} \cong \delta_{\text{D}}^4 \frac{c\sigma_{\text{T}}^2 r_b' U_B V_b'}{12\pi d_L^2} \left(\frac{\epsilon}{\epsilon_B}\right)^{3/2} \int_0^{\min(\epsilon', 1/\epsilon')} d\epsilon_i' \epsilon_i'^{-1} n_e' \left(\sqrt{\frac{\epsilon'}{\epsilon_i'}}\right) n_e' \left(\sqrt{\frac{\epsilon_i'}{\epsilon_B}}\right). \quad (7.97)$$

The only provision made in this approximation to account for scattering in the KN regime is to terminate the scattering when $\gamma\epsilon_i' \geq 1$. For the power-law electron distribution, eq. (7.76), eq. (7.97) gives

$$f_{\epsilon}^{\text{SSC}} \cong \frac{\delta_{\text{D}}^4}{12\pi d_L^2} \frac{c\sigma_{\text{T}}^2 r_b' U_B K_e'^2}{V_b'} \hat{\gamma}_s'^{3-p} \Sigma_{\text{C}}, \quad \hat{\gamma}_s' = \sqrt{\frac{(1+z)\epsilon}{\delta_{\text{D}}\epsilon_B}} \quad (7.98)$$

[74]. Here the Compton-synchrotron logarithm

$$\Sigma_{\text{C}} = \ln \left(\frac{\min(\epsilon_B \gamma_2'^2, \epsilon'/\gamma_1'^2, \epsilon'^{-1})}{\max(\epsilon_B \gamma_1'^2, \epsilon'/\gamma_2'^2)} \right) \quad (7.99)$$

[98,99], $\epsilon' = (1+z)\epsilon/\delta_{\text{D}}$, and limits in the Compton-synchrotron logarithm restrict Compton scattering to the Thomson regime. This expression applies to nonthermal electrons scattering their own nonthermal synchrotron emission. When the electrons are described by a broken power law, one must sum a number of scattered segments (section 7.7.2). If the electrons have a low-energy cutoff in the distribution, there will be another power-law component with photon energy index $\alpha \cong -1/3$ associated with the low-energy portion of the synchrotron emissivity spectrum, and this emission will also be scattered. Figure 7.4 gives a comparison of the δ -function approximation to the SSC spectrum with an accurate calculation. Note that, even when $\gamma_2 = 10^7$, the lowest-energy photons are scattered in the Thomson regime by the highest-energy electrons. This SSC approximation breaks down with increasing γ_1 , when scattering in the KN regime is important.

By comparing eq. (7.98) with more detailed results [98], one finds that in the asymptotic quasi-power-law portion of the SSC spectrum, the coefficient 4/9 in eq. (7.96) should be replaced by $3^3 b(p)/2^5 \pi^2$. Values of $b(p)$ and the ratio $(3^3 b(p)/2^5 \pi^2)/(4/9) = 3^5 b(p)/2^7 \pi^2$ are given in table 7.1. Equation (7.98) is accurate to better than 50% when $2 \lesssim p \lesssim 3.5$ in the power-law portion of the spectrum, compared to more precise treatments.

The ratio Π of the νF_{ν} SSC and synchrotron fluxes from a power-law electron distribution can be obtained by taking the ratio of eq. (7.70) to eq. (7.98). The result is

$$\Pi \cong \frac{2}{3} (\sigma_{\text{T}} k_e r_b' \Sigma_{\text{C}}) \left(\frac{\epsilon_{\text{SSC}}}{\epsilon_{\text{syn}}} \right)^{(3-p)/2}, \quad (7.100)$$

where ϵ_{SSC} and ϵ_{syn} are the dimensionless SSC and synchrotron photon energies. The SSC-to-synchrotron flux ratio $\Pi \propto W'_e/r'_b{}^2$ increases with decreasing blob radius.

7.7.2 SSC in the Thomson Regime for Broken Power-Law Electron Distribution

For a broken power-law distribution for the nonthermal electrons, given by

$$N'_e(\gamma) = K_{\text{br}}[\gamma_1^{q-p} \gamma^{-q} H(\gamma; \gamma_0, \gamma_1) + \gamma^{-p} H(\gamma; \gamma_1, \gamma_2)], \quad (7.101)$$

normalizing to the total comoving nonthermal electron energy

$$W'_e \cong m_e c^2 \int_1^\infty d\gamma \gamma N'_e(\gamma)$$

gives

$$K_{\text{br}} = \frac{W'_e}{m_e c^2} \left(\frac{\gamma_1^{q-p} (\gamma_1^{2-q} - \gamma_0^{2-q})}{2-q} + \frac{\gamma_1^{2-p} - \gamma_2^{2-p}}{p-2} \right)^{-1}. \quad (7.102)$$

The SSC νF_ν flux from the broken power-law distribution is given by

$$f_\epsilon^{\text{SSC}} \cong \delta_D^4 \frac{c \sigma_T^2 u'_B}{16\pi^2 d_L^2 r'_b{}^2} K_{\text{br}}^2 \left(\frac{\epsilon'}{\epsilon_B} \right)^{3/2} [\gamma_1^{2(q-p)} \mathcal{I}_1 + \gamma_1^{q-p} (\mathcal{I}_2 + \mathcal{I}_3) + \mathcal{I}_4], \quad (7.103)$$

where

$$\begin{aligned} \mathcal{I}_1 &= \left(\frac{\epsilon'}{\epsilon_B} \right)^{-q/2} \ln \left[\frac{\min(\epsilon'^{-1}, \epsilon'/\gamma_0^2, \epsilon_B \gamma_1^2)}{\max(\epsilon'/\gamma_1^2, \epsilon_B \gamma_0^2)} \right], \\ \mathcal{I}_2 &= \frac{2\epsilon_B^{q/2} \epsilon'^{-p/2}}{p-q} \left\{ [\min(\epsilon'^{-1}, \epsilon'/\gamma_1^2, \epsilon_B \gamma_1^2)]^{(p-q)/2} \right. \\ &\quad \left. - [\max(\epsilon'/\gamma_2^2, \epsilon_B \gamma_0^2)]^{(p-q)/2} \right\}, \\ \mathcal{I}_3 &= \frac{2\epsilon_B^{p/2} \epsilon'^{-q/2}}{q-p} \left\{ [\min(\epsilon'^{-1}, \epsilon'/\gamma_0^2, \epsilon_B \gamma_2^2)]^{(q-p)/2} \right. \\ &\quad \left. - [\max(\epsilon'/\gamma_1^2, \epsilon_B \gamma_1^2)]^{(q-p)/2} \right\}, \end{aligned}$$

and

$$\mathcal{I}_4 = \left(\frac{\epsilon'}{\epsilon_B} \right)^{-p/2} \ln \left(\frac{\min(\epsilon'^{-1}, \epsilon'/\gamma_1^2, \epsilon_B \gamma_2^2)}{\max(\epsilon'/\gamma_2^2, \epsilon_B \gamma_1^2)} \right)$$

[94]. In deriving this expression, we assume that the mean escape time of a synchrotron photon from the uniform spherical emitting region is $3r'_b/4c$.

7.7.3 Accurate SSC for General Electron Distribution

The νF_ν synchrotron radiation spectrum can be approximated by the expression

$$f_\epsilon^{\text{syn}} \cong \frac{\delta_D^4}{6\pi d_L^2} c\sigma_T U_B \gamma_s'^3 N'_e(\gamma_s'), \quad (7.104)$$

where

$$\gamma_s' = \sqrt{\frac{\epsilon(1+z)}{\delta_D \epsilon_B}},$$

from eq. (7.70), recalling that $\epsilon_B = B/B_{\text{cr}}$, as measured in the comoving frame. Inverting this expression gives the comoving electron distribution

$$N'_e(\gamma_s') = V'_b n'_e(\gamma_s') \cong \frac{6\pi d_L^2 f_\epsilon^{\text{syn}}}{c\sigma_T U_B \delta_D^4 \gamma_s'^3}, \quad \epsilon = \frac{\delta_D \epsilon_B \gamma_s'^2}{1+z}. \quad (7.105)$$

Equation (7.105) gives a good representation of the net electron energy distributions whenever the νF_ν spectral index $a < 4/3$ (softer than $a = 4/3$), adopting the convention $f_\epsilon \propto \epsilon^a$.

In terms of the photon emissivity $\dot{n}_{\text{syn}}(\epsilon)$ ($\text{ph cm}^{-3} \text{s}^{-1} \epsilon^{-1}$), the δ -function approximation for synchrotron emission is given by

$$\dot{n}'_{\text{syn}}(\epsilon') \cong \frac{2}{3} c\sigma_T u_B \epsilon'^{-1/2} \epsilon_B^{-3/2} n'_e(\gamma_s') \cong \frac{2c\sigma_T U_{B_{\text{cr}}}}{3V'_b m_e c^2} \frac{N'_e(\gamma_s')}{\gamma_s'}, \quad \gamma_s' = \sqrt{\frac{\epsilon'}{\epsilon_B}}, \quad (7.106)$$

with $u_B = U_B/m_e c^2$. The target synchrotron radiation field is therefore given by

$$n'_{\text{syn}}(\epsilon') \cong \frac{r'_b}{c} \dot{n}'_{\text{syn}}(\epsilon') \cong \frac{3d_L^2 f_\epsilon^{\text{syn}}}{m_e c^3 r_b'^2 \delta_D^4 \epsilon_B^2 \gamma_s'^4}. \quad (7.107)$$

Jones's formula [67], eq. (6.74), with definitions given in eqs. (6.75) and (6.76), gives the Compton-scattered synchrotron self-Compton emissivity

$$\epsilon'_s J_{\text{SSC}}(\epsilon'_s) = \frac{3}{4} c\sigma_T \epsilon_s'^2 \int_0^\infty d\epsilon' \frac{u'(\epsilon')}{\epsilon'^2} \int_{\gamma'_{\text{min}}}^{\gamma'_{\text{max}}} d\gamma' \frac{N'_e(\gamma')}{\gamma'^2} F_C(q', \Gamma'_e), \quad (7.108)$$

where

$$F_C(q', \Gamma'_e) = \left(2q' \ln q' + (1+2q')(1-q') + \frac{1}{2} \frac{(\Gamma'_e q')^2}{(1+\Gamma'_e q')} (1-q') \right) \times H\left(q'; \frac{1}{4\gamma'^2}, 1\right), \quad (7.109)$$

$$q' \equiv \frac{\epsilon'_s/\gamma'}{\Gamma'_e(1 - \epsilon'_s/\gamma')}, \quad \text{and} \quad \Gamma'_e = 4\epsilon'\gamma' \quad (7.110)$$

[35,67]. From the limits on the integration over γ' implied by the limits on q , we find

$$\gamma'_{\min} = \frac{1}{2}\epsilon'_s \left(1 + \sqrt{1 + \frac{1}{\epsilon'\epsilon'_s}} \right) \quad (7.111)$$

and

$$\gamma'_{\max} = \frac{\epsilon'\epsilon'_s}{\epsilon' - \epsilon'_s} H(\epsilon' - \epsilon'_s) + \gamma'_2 H(\epsilon'_s - \epsilon'). \quad (7.112)$$

Here the maximum lepton Lorentz factor in the radiating fluid is γ'_2 .

The νF_ν SSC spectrum is therefore given by

$$f_\epsilon^{\text{SSC}} = \left(\frac{3}{2} \right)^3 \frac{d_L^2 \epsilon_s'^2}{r_b'^2 c \delta_D^4 U_B} \int_0^\infty d\epsilon' \frac{f_{\tilde{\epsilon}}^{\text{syn}}}{\epsilon'^3} \int_{\gamma'_{\min}}^{\gamma'_{\max}} d\gamma' \frac{F_C(q', \Gamma'_e) f_{\hat{\epsilon}}^{\text{syn}}}{\gamma'^5}, \quad (7.113)$$

where

$$\tilde{\epsilon} = \frac{\delta_D \epsilon'}{1+z} \quad (7.114)$$

and

$$\hat{\epsilon} = \frac{\delta_D \epsilon_B \gamma'^2}{1+z} \quad (7.115)$$

[72,73]. The only remaining uncertainties in a complete synchrotron/SSC blazar model are $\gamma\gamma$ attenuation and pair reinjection, considered in chapter 10.

7.7.4 Synchrotron/SSC Model

Any leptonic jet model will have a synchrotron and an associated SSC component. For a standard relativistic jet model, the synchrotron and SSC components, accurately accounting for Compton scattering in the self-Compton component, are [72]

$$f_\epsilon^{\text{syn}} = \frac{\delta_D^4 \epsilon' J'_{\text{syn}}(\epsilon')}{4\pi d_L^2} = \frac{\sqrt{3} \delta_D^4 \epsilon' e^3 B}{4\pi h} \int_1^\infty d\gamma' N'_e(\gamma') R(x) \quad (7.116)$$

and

$$f_{\epsilon_s}^{\text{SSC}} = \frac{9}{16} \frac{(1+z)^2 \sigma_T \epsilon_s'^2}{\pi \delta_D^2 c^2 t_{v,\min}^2} \int_0^\infty d\epsilon' \frac{f_{\tilde{\epsilon}}^{\text{syn}}}{\epsilon'^3} \int_{\gamma'_{\min}}^{\gamma'_{\max}} d\gamma' \frac{N'_e(\gamma')}{\gamma'^2} F_C(q, \Gamma). \quad (7.117)$$

7.7.5 SSC Electron Energy-Loss Rate

The energy-loss rate of electrons Compton-scattering synchrotron radiation with spectral energy density $u(\epsilon) = m_e c^2 \epsilon n_{\text{ph}}(\epsilon)$ is given by (dropping primes),

$$-m_e c^2 \dot{\gamma}_{\text{SSC}} = \frac{3}{4} \frac{c \sigma_{\text{T}}}{\gamma^2} \int_0^\infty d\epsilon \frac{u(\epsilon)}{\epsilon^2} \int_{\gamma\epsilon/(\gamma+\epsilon)}^{\Gamma_e \epsilon/(1+\Gamma_e)} d\epsilon_s \epsilon_s F_{\text{C}}(q, \Gamma_e). \quad (7.118)$$

The solution takes the form

$$-\dot{\gamma}_{\text{SSC}} = \frac{4}{3} c \sigma_{\text{T}} \int_0^\infty d\epsilon \frac{n_{\text{ph}}(\epsilon)}{\epsilon} G(\Gamma_e),$$

where

$$\begin{aligned} \frac{32}{9} G(\Gamma_e) &= \frac{2\Gamma_e}{3} \frac{1+5\Gamma_e/4}{(1+\Gamma_e)^2} - \frac{2\Gamma_e}{1+\Gamma_e} \left(\frac{1}{3} + \frac{1}{\Gamma_e} + \frac{1}{\Gamma_e^2} \right) \\ &+ \ln(1+\Gamma_e) \left(1 + \frac{12}{\Gamma_e} + \frac{12}{\Gamma_e^2} + \frac{2\ln(1+\Gamma_e)}{\Gamma_e} - \frac{4\ln\Gamma_e}{\Gamma_e} \right) \\ &- \frac{10}{\Gamma_e} + \frac{4}{\Gamma_e} \sum_{n=1}^\infty \frac{(1+\Gamma_e)^{-n}}{n^2} - \frac{2\pi^2}{3\Gamma_e} - 2 \end{aligned} \quad (7.119)$$

[67,100].¹ In the limit $\Gamma_e \ll 1$,

$$G(\Gamma_e) \rightarrow \gamma^2 \epsilon^2 \left[1 - \frac{63}{40} \Gamma_e + \frac{3^2 7^2}{2^3 5^2} \Gamma_e^2 + \mathcal{O}(\Gamma_e^3) \right]. \quad (7.120)$$

This expression applies to arbitrary radiation fields that are isotropic in the comoving frame in which the electron distribution is quasi-isotropic. In practice, the internal synchrotron field is usually the most important, and cascade radiation fields induced by ultrarelativistic electrons, generally scattered in the Klein-Nishina regime, make higher-energy emissions. External radiation fields are highly aberrated in the comoving frame of relativistic jets, and so have to be treated differently (chapter 6).

7.8 SYNCHROTRON SELF-ABSORPTION

The synchrotron flux density from a homogeneous spherical source with radius r_b is [98]

$$S_\nu = \frac{j(\nu)}{2\kappa} \left(\frac{r_b}{d_L} \right)^2 u(\tau) = \frac{j(\nu) V_b}{4\pi d_L^2} \frac{3u(\tau)}{\tau}, \quad (7.121)$$

¹This can also be written in terms of the dilogarithm function $\text{Li}_2(z) = \int_z^0 (dt/t) \ln(1-t) = \sum_{k=1}^\infty (z^k/k^2)$.

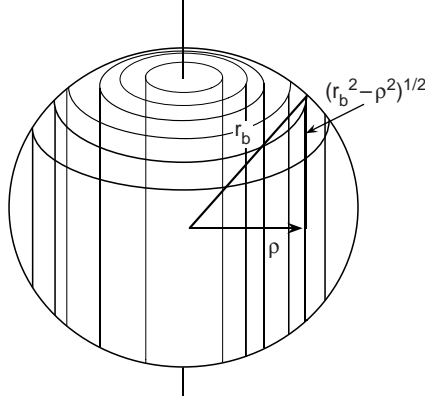


Figure 7.6 A sphere divided into shells.

where $j(\nu)$ (units of $\text{ergs s}^{-1} \text{Hz}^{-1}$) is the nonthermal synchrotron emissivity, the frequency-dependent optical depth

$$\tau \equiv 2\kappa r_b,$$

$\kappa = \kappa_\nu^{\text{SSA}}(\vec{r})$ (cm^{-1}) is the frequency-dependent synchrotron self-absorption coefficient, and

$$u(\tau) = \frac{1}{2} + \frac{\exp(-\tau)}{\tau} - \frac{1 - \exp(-\tau)}{\tau^2} = \frac{1}{2} \left(1 - \frac{2}{\tau^2} [1 - (1 + \tau) \exp(-\tau)] \right), \quad (7.122)$$

with asymptotes

$$u(\tau) \rightarrow \begin{cases} \frac{\tau}{3} - \frac{\tau^2}{8} + \mathcal{O}(\tau^3), & \tau \ll 1, \text{ optically thin,} \\ \frac{1}{2} - \tau^{-2} + \mathcal{O}(e^{-\tau}/\tau), & \tau \gg 1, \text{ optically thick.} \end{cases} \quad (7.123)$$

In the slab approximation, the term $3u(\tau)/\tau$ in eq. (7.121) is replaced with $[1 - \exp(-\tau)]/\tau$. As is easily seen from eqs. (7.121) and (7.123), $S_\nu = j(\nu)V_b/4\pi d_L^2$ in the optically thin limit.

It is worth taking a moment to derive eq. (7.122). The volume element of a sphere separated into cylindrical shells (figure 7.6) is $dV = 2\pi\rho d\rho d\ell$. The flux density when observing a spherical volume at large distances $d_L \gg r_b$ is

$$S_\nu = \frac{1}{4\pi d_L^2} \int d^3\vec{r} j(\nu; \vec{r}) \exp\left(-\int \kappa(\vec{r}') ds'\right). \quad (7.124)$$

The uniformity assumption $j(\nu; \vec{r}) = j(\nu)$ and $\kappa(\vec{r}) = \kappa$ for $r \leq r_b$ implies

$$\begin{aligned} S_\nu &= \frac{j(\nu)}{2d_L^2} \int_0^{r_b} d\rho \rho \int_0^{2\sqrt{r_b^2 - \rho^2}} d\ell \exp(-\kappa\ell) \\ &= \frac{j(\nu)}{8d_L^2\kappa^3} \int_0^{2\kappa r_b} dx x (1 - e^{-x}) = \frac{j(\nu)}{8d_L^2\kappa^3} \tau^2 u(\tau) = \frac{j(\nu)}{2\kappa} \left(\frac{r_b^2}{d_L^2} \right) u(\tau), \end{aligned} \quad (7.125)$$

which recovers eq. (7.122).

The synchrotron radiation flux from a standard model jet, with effects of synchrotron self-absorption taken into account, is given by

$$f_\epsilon^{\text{syn}} = \frac{3u(\tau)}{\tau} \frac{\delta_D^4 j'(\nu') V_b'}{4\pi d_L^2}, \quad (7.126)$$

where $\tau = \tau(\nu') = 2\kappa'_\nu r'_b$, and $\nu = \delta_D \nu' / (1 + z)$.

Because κ is a locally defined property of a magnetoactive plasma, spatially dependent values of κ can be derived for idealized geometries with different values of B and electron spectrum [98]. To derive the synchrotron self-absorption coefficient κ_ν^{SSA} , we first review Einstein's A and B coefficients.

7.8.1 Einstein Coefficients

Consider a two-level atom with electron energy states W_1 and W_2 , $W_2 > W_1$, and populations N_1 and N_2 . Populations of states in thermal equilibrium follow the Boltzmann distribution

$$\frac{N_1}{N_2} = \frac{g_1}{g_2} \exp\left(\frac{h\nu_{21}}{k_B T}\right), \quad h\nu_{21} = W_2 - W_1, \quad (7.127)$$

where g_1 and g_2 are the occupancy numbers of states 1 and 2, respectively. In steady state (no time dependence), the sum of the spontaneous and stimulated rates from state 2 to state 1 must equal the absorption rate from state 1 to state 2. Thus

$$N_2[A_{21} + I_\nu(\Omega)B_{21}] = N_1 B_{12} I_\nu(\Omega), \quad (7.128)$$

and A_{21} , B_{21} , and B_{12} are the Einstein coefficients. In thermal equilibrium, where the states are illuminated by a Planck blackbody radiation field, $I_\nu^{\text{bb}}(T)$ (eq. [5.14]), the population of states follows eq. (7.127), and one finds

$$B_{12} I_\nu^{\text{bb}}(T) = \frac{g_2}{g_1} [A_{21} + I_\nu^{\text{bb}}(T)B_{21}] \exp\left(\frac{-h\nu_{12}}{k_B T}\right). \quad (7.129)$$

In the limit of high temperatures $k_B T \gg h\nu_{12}$ and $I_\nu^{\text{bb}}(T)B_{21} \gg A_{21}$,

$$B_{12} = \frac{g_2}{g_1} B_{21}. \quad (7.130)$$

Hence

$$I_\nu^{\text{bb}}(T) = \frac{A_{21}/B_{21}}{\exp(h\nu_{12}/k_B T) - 1},$$

implying

$$\frac{A_{21}}{B_{21}} = \frac{2h\nu^3}{c^2}. \quad (7.131)$$

Spontaneous rates and transition probabilities are derived using the quantum theory of radiation. For a dipole transition with matrix element $\langle 2|\vec{r}|1\rangle$, Einstein's A coefficient

$$A_{21} \sim \alpha_f \frac{\nu_{21}^3}{c^2} |\langle 2|\vec{r}|1\rangle|^2. \quad (7.132)$$

The quantum theory of radiation is dealt with in many places [37,64,101, 102].

7.8.2 Brightness Temperature and Self-Absorbed Flux: Qualitative Discussion

Consider a source of nonthermal radiation whose spectral flux S_ν at frequency ν is measured, and whose size r_b is directly imaged or is inferred from the measured variability timescale t_{var} . As written, r_b refers to the transverse size scale, which does not change through Lorentz transformation. For a stationary spherical emitting region (i.e., no bulk relativistic motion of the radiating plasma), causality considerations imply

$$r_b \simeq \frac{t_{\text{var}}}{(1+z)c},$$

where, for definiteness, t_{var} is a measure of the time for a factor-of-2 change in flux. From this information, the source intensity I_ν is inferred.

A *thermal* plasma cannot radiate above the blackbody limit. The intensity of a plasma in thermal equilibrium is uniform, so that $dI_\nu/ds = 0$, implying from the equation of radiative transfer, eq. (5.2), that the thermal emission and absorption coefficients are related according to Kirchhoff's law,

$$\frac{j_{\text{th}}(\nu, \Omega)}{\kappa_\nu^{\text{th}}} = I_\nu^{\text{bb}} \xrightarrow{h\nu/k_B T \ll 1} \left(\frac{2\nu}{c}\right)^2 k_B T. \quad (7.133)$$

One can show that Kirchhoff's law holds for the relativistic thermal distribution function, eq. (1.1).

For *nonthermal* emissions, an effective temperature can be assigned to an observed source by relating the measured intensity I_ν to the Rayleigh-Jeans limit of the blackbody intensity for frequencies $h\nu \ll k_B T_b$, where T_b is the *brightness temperature* of the source. From eq. (5.14), the brightness temperature

$$T_b = \frac{c^2}{2\nu^2} \frac{I_\nu}{k_B}. \quad (7.134)$$

The intensity is simply related to the spectral energy flux, or flux density $S_\nu = d\mathcal{E}/dAd\nu dt$, according to

$$I_\nu \cong \frac{S_\nu}{\Delta\Omega}, \quad \Delta\Omega \cong \frac{R^2}{4d_A^2},$$

where $d_A = d_L/(1+z)^2$ is the angular diameter distance (eq. [4.41]). Thus

$$T_b = 2 \left(\frac{d_A}{r_b} \right)^2 \left(\frac{c}{\nu} \right)^2 \frac{S_\nu}{k_B}. \quad (7.135)$$

As an example, consider a ν_{GHz} GHz radio measurement of a radio source. If the source is imaged to the milliarcsecond scale, then

$$\frac{r_b}{d_A} = \vartheta \cong 4.85 \times 10^{-9} \vartheta_{\text{mas}}.$$

For this source,

$$T_b \text{ (K)} \simeq 5 \times 10^{12} \vartheta_{\text{mas}}^{-2} \nu_{\text{GHz}}^{-2} S_{\text{GHz}} \text{ (Jy)}. \quad (7.136)$$

It is interesting that $10^{12} \text{ K} \gg m_e c^2/k_B = 5.93 \times 10^9 \text{ K}$, so that the radiations originate from highly relativistic electrons with effective temperature $k_B T_b \sim \gamma m_e c^2$. Observation show sources with T_b exceeding MeV ($T_b \sim 10^{10} \text{ K}$) and even GeV ($T_b \gg 10^{12} \text{ K}$) energies, justifying the use of the Rayleigh-Jeans limit of the blackbody intensity.

Electrons with $\gamma m_e c^2 \sim k_B T_b$ are highly relativistic, and radiate their power at frequencies $\nu \approx \gamma^2 \nu_B$; see eq. (7.28). Hence

$$S_\nu \sim \left(\frac{r_b}{d_A} \right)^2 \left(\frac{\nu}{c} \right)^2 k_B T_b \sim \vartheta^2 \frac{\nu^{5/2}}{\sqrt{\nu_B}} \propto \nu^{5/2}. \quad (7.137)$$

Thus a heavily self-absorbed spectrum from synchrotron radiation radiated by a power-law nonthermal isotropic relativistic electron distribution forms a flux density $S_\nu \propto \nu^{5/2}$ for the idealized magnetized plasma considered here. This can be compared with $S_\nu \propto \nu^2$, so in principle thermal emission components can be spectrally distinguished from nonthermal synchrotron radiation.

7.8.3 Derivation of the Synchrotron Self-Absorption Coefficient

The absorption coefficient results from “true” absorption, proportional to $I_\nu(\Omega) B_{12} N(W_1)$, and stimulated emissions proportional to $I_\nu(\Omega) B_{21} N(W_2)$, $W_2 > W_1$ (eq. [7.128]). Thus it follows that

$$\kappa_\nu = \frac{h\nu}{4\pi} \sum_{W_1} \sum_{W_2} [n(W_1)B_{12} - n(W_2)B_{21}] \phi_{21}(\nu), \quad (7.138)$$

where the line profile function $\phi_{21}(\nu)$ (units of Hz^{-1}) ensures $h\nu = W_2 - W_1$, and there is no restriction to W_1 and W_2 in the summation.

From the definition

$$P(\nu, W_2) = h\nu \sum_{W_1} A_{21} \phi_{21}(\nu) = \frac{2h^2\nu^4}{c^2} \sum_{W_1} B_{21} \phi_{21}(\nu) \quad (7.139)$$

for the average power per unit frequency from levels W_2 to level W_1 (eq. [7.27]), we have

$$\begin{aligned} \kappa_\nu &= \frac{h\nu}{4\pi} \sum_{W_2} \left[\left(\frac{g_2}{g_1} n(W_2 - h\nu) - n(W_2) \right) \sum_{W_1} B_{21} \phi_{21}(\nu) \right] \\ &= \frac{c^2}{8\pi h\nu^3} \sum_{W_2} P(\nu, W_2) \left(\frac{g_2}{g_1} n(W_2 - h\nu) - n(W_2) \right). \end{aligned} \quad (7.140)$$

For the elementary quantum states (including polarization), $g_1 = g_2$, and

$$\sum_i n(W_i) \rightarrow \int d^3 \vec{p} f(\vec{p}), \quad W_2 - h\nu \rightarrow p_2^*,$$

and we use a particle distribution function formulation, where $f(\vec{p}) = dN/dV d^3 \vec{p}$. Thus

$$\kappa_\nu = \frac{c^2}{8\pi h\nu^3} \int d^3 \vec{p}_2 [f(\vec{p}_2^*) - f(\vec{p}_2)] P(\nu, W_2),$$

noting that $f(W_2 - h\nu) - f(W_2) = -h\nu \partial f / \partial p$ for processes involving continuous energy losses. Hence

$$\kappa_\nu = -\frac{1}{8\pi m_e \nu^2} \int d\gamma P(\nu, \gamma) \left[\gamma^2 \frac{\partial}{\partial \gamma} \left(\frac{n(\gamma)}{\gamma^2} \right) \right]. \quad (7.141)$$

7.8.4 δ -Function Approximation for Synchrotron Self-Absorption

We now revert to dimensionless notation. Thus $P(\nu; \gamma) d\nu = P^{\text{syn}}(\epsilon; \gamma) d\epsilon$. Use of the relation $\nu = m_e c^2 \epsilon / h$ gives

$$\kappa_\epsilon = -\frac{1}{8\pi m_e \epsilon^2} \left(\frac{\lambda_C}{c} \right)^3 \int d\gamma P^{\text{syn}}(\epsilon; \gamma) \left[\gamma^2 \frac{\partial}{\partial \gamma} \left(\frac{n(\gamma)}{\gamma^2} \right) \right]. \quad (7.142)$$

The δ -function approximation for the pitch-angle-averaged synchrotron emissivity can be written as

$$P^{\text{syn}}(\epsilon) = \frac{4}{3} c \sigma_{\text{T}} \frac{B^2}{8\pi} \gamma^2 \delta(\epsilon - 2\epsilon_B \gamma^2) = \frac{c \sigma_{\text{T}} U_{\text{cr}}}{6} \frac{\epsilon}{\gamma} \delta\left(\gamma - \sqrt{\frac{\epsilon}{2\epsilon_B}}\right). \quad (7.143)$$

Substituting eq. (7.143) in eq. (7.142) gives

$$\begin{aligned} \kappa_{\epsilon} &= \frac{\sigma_{\text{T}} U_{\text{cr}}}{48\pi m_e c^2} \frac{\lambda_{\text{C}}^3}{\epsilon} \left[\gamma \frac{\partial}{\partial \gamma} \left(\frac{n(\gamma)}{\gamma} \right) \right] \Big|_{\gamma=\sqrt{\epsilon/2\epsilon_B}} \\ &= \frac{\pi}{36} \frac{\lambda_{\text{C}} r_e}{\epsilon} \left[\gamma \frac{\partial}{\partial \gamma} \left(\frac{n(\gamma)}{\gamma} \right) \right] \Big|_{\gamma=\sqrt{\epsilon/2\epsilon_B}}, \end{aligned} \quad (7.144)$$

which in terms of frequency is

$$\kappa_{\nu} = \frac{\pi}{36} \frac{c r_e}{\nu} \left[\gamma^2 \frac{\partial}{\partial \gamma} \left(\frac{n(\gamma)}{\gamma} \right) \right] \Big|_{\gamma=\sqrt{\nu/2\nu_B}}. \quad (7.145)$$

For the power-law electron distribution given by eq. (6.62), the self-absorption coefficient is found for the δ -function approximation, eq. (7.145), to be

$$\kappa_{\nu}^{\delta} = c_{\delta}(p) \frac{c r_e k_e}{\nu} \left(\frac{\nu_B}{\nu} \right)^{(p+2)/2} \quad \text{for } \gamma_1^2 \lesssim \nu/\nu_B \lesssim \gamma_2^2, \quad (7.146)$$

where

$$c_{\delta}(p) \equiv \frac{2^{p/2}(p+2)\pi}{18}.$$

We can also write

$$\kappa_{\epsilon}^{\delta} = c_{\delta}(p) \frac{\lambda_{\text{C}} r_e k_e}{\epsilon_B} \gamma_s^{-(p+4)} \quad \text{for } \gamma_1^2 \lesssim \epsilon/\epsilon_B \lesssim \gamma_2^2. \quad (7.147)$$

7.8.5 Synchrotron Self-Absorption Coefficient for Power-Law Electrons

In detailed treatments [98], the SSA coefficient for the power-law distribution of electrons given by eq. (6.62) is

$$\kappa_{\nu} = c(p) \frac{c r_e k_e}{\nu} \left(\frac{\nu_B}{\nu} \right)^{(p+2)/2}, \quad (7.148)$$

Table 7.1 compares coefficient $c(p)$ with the coefficient $c_{\delta}(p) = \pi(p+2)2^{(p-2)/2}/9$.

From eq. (7.148) we see that, including effects of SSA, the synchrotron flux from a homogeneous spherical ball of radiating plasma with isotropic relativistic electrons and random tangled magnetic field is

$$f_v^{\text{syn}} = \frac{3}{8\pi} \frac{v_\star L_{v_\star}}{r_b \kappa_v d_L^2} u(\tau) \xrightarrow{\tau \ll 1} \frac{v_\star L_{v_\star}}{4\pi d_L^2}. \quad (7.149)$$

This expression can be generalized to give the SSA frequency in cases of relativistically moving homogeneous spheres of radiating plasma at cosmological distances. For a power-law distribution of electrons with spectral density $n_e(\gamma) = N_e(\gamma)/V'_b$ given by eqs. (7.76) and (7.77), the SSA opacity

$$\tau_{\epsilon'}^{\text{SSA}} = 2\kappa_{\epsilon'}^{\text{SSA}} r_b = \frac{3c(p)K r_e^2 \epsilon_B^{(p+2)/2}}{\alpha_f r_b^2 \epsilon'^{(p+4)/2}}, \quad (7.150)$$

where $\alpha_f = e^2/\hbar c$, $r_e = e^2/m_e c^2$, and $c(p)$ is given in table 7.1 [98]. For a spherical knot with half-angle extent ϑ , $r_b = d_L \vartheta/(1+z)^2$. The SSA frequency $\nu_{\text{SSA}} = m_e c^2 \epsilon_{\text{SSA}}/h$, when defined where $dF_\nu/d\nu = 0$, is given by

$$\epsilon_{\text{SSA}} = \left(\frac{18\pi c(p) r_e^2 f_{\epsilon_s}^s}{\alpha_f t_p c \sigma_T U_{\text{cr}}} \right)^{2/(p+4)} \left(\frac{\epsilon_B (1+z)}{\delta_D \vartheta^4 \epsilon_s^{3-p}} \right)^{1/(p+4)}, \quad (7.151)$$

where t_p is given in table 7.1 [98].

The good agreement with the detailed results for a power-law electron distribution indicates that the δ -function expression, eq. (7.144), also provides a reasonable approximation for the SSA coefficient for a homogeneous sphere of radiating magnetized plasma.

7.9 MAXIMUM BRIGHTNESS TEMPERATURE

The self-absorbed spectrum implies an upper limit on the brightness temperature T_b for a stationary source, as estimated in eq. (7.136). An improved derivation of the maximum brightness temperature of a spherical radiating plasma blob in bulk relativistic motion is now derived.

The solution to the equation for radiative transfer, eq. (5.2), which we write in the form

$$\frac{dI_\nu}{ds} = -\kappa_\nu I_\nu + j(\nu, \Omega), \quad (7.152)$$

is given, from inspection of the intensity emerging from a magnetized slab of plasma of thickness L , by

$$I_\nu = \int_0^L ds j(\nu, \Omega; \vec{r}) \exp\left(-\int_0^s d\tilde{s} \kappa_\nu(\vec{r})\right). \quad (7.153)$$

(For the case of a uniform spherical source, see eqs. [7.121] and [7.122].) Making the assumption of uniformity in this slab, then

$$I_\nu = \frac{j(\nu, \Omega)}{\kappa_\nu} (1 - e^{-\kappa_\nu L}) = j(\nu, \Omega)L \left(\frac{1 - \exp(-\tau_\nu)}{\tau_\nu} \right) \\ \rightarrow \begin{cases} j(\nu, \Omega)L, & \tau_\nu \equiv \kappa_\nu L \ll 1, \\ j(\nu, \Omega)/\kappa_\nu, & \tau_\nu \gg 1. \end{cases} \quad (7.154)$$

Consider the nonthermal emissivity and self-absorbed spectrum for an isotropic power-law electron distribution away from the endpoints of the spectrum. From eqs. (6.62) and (7.63), we can write

$$j^{\text{syn}}(\nu, \Omega) = j_0 y^{-\alpha} H(y; \gamma_1^2, \gamma_2^2), \quad (7.155)$$

where

$$y = \nu/\nu_B$$

and

$$j_0 = \frac{a(p)}{\pi} \left(\frac{3}{2} \right)^{1+\alpha} \frac{c\sigma_T U_B k_e}{\nu_B}.$$

The synchrotron self-absorption coefficient can be written, from eq. (7.148), as

$$\kappa_\nu^{\text{syn}} = \kappa_0 y^{-(p+4)/2} H(y; \gamma_1^2, \gamma_2^2) = \kappa_0 y^{-(\alpha+5/2)} H(y; \gamma_1^2, \gamma_2^2), \quad (7.156)$$

where $\kappa_0 = c(p)cr_e k_e/\nu_B$.

The nonthermal synchrotron intensity from a radiating slab, using eqs. (7.154), (7.155), and (7.156), is

$$I_\nu = \frac{j_0}{\kappa_0} y^{5/2} \left(1 - e^{-\tau_0 y^{-(\alpha+5/2)}} \right) < \frac{j_0}{\kappa_0} y^{5/2}, \quad (7.157)$$

where $\tau_0 = \kappa_0 L = c(p)cr_e k_e L/\nu_B$ and $j_0/\kappa_0 = 4(3/2)^\alpha a(p)r_e U_B/c(p)$. The transition between the optically thin and thick regimes occurs at $y \approx \tau_0^{2/(p+4)}$. Figure 7.7 shows the spectral behavior of the nonthermal synchrotron spectrum for different values of τ_0 and α .

The final inequality in eq. (7.157) must be satisfied for nonthermal synchrotron emission. This condition implies a limiting intensity for fixed values of B and ν , namely,

$$I_\nu < d(p) m_e c^2 \frac{\nu^2}{c^2} \sqrt{\frac{\nu}{\nu_B}}, \quad (7.158)$$

defining $d(p) = 2\pi(3/2)^\alpha a(p)/c(p)$. The effects of bulk relativistic motion of the intensity, using the invariance of I_ν/ν^3 , eq. (5.7), means that the limiting measured intensity is

$$I_\nu < \sqrt{\frac{\delta_D}{1+z}} d(p) m_e c^2 \frac{\nu^2}{c^2} \sqrt{\frac{\nu}{\nu_B}}, \quad (7.159)$$

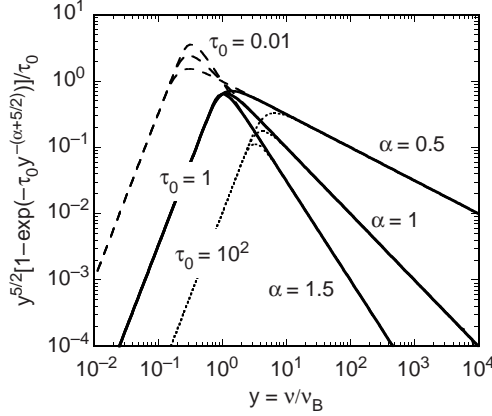


Figure 7.7 Principal frequency dependence of the analytic self-absorbed synchrotron intensity from a magnetized plasma slab with different values of τ_0 and α .

which implies an upper limit on B . Alternately, we could measure the intensity I_T at peak synchrotron frequency ν_T using high-resolution VLBA observations to assign the magnetic field within the uncertain knowledge of the Doppler factor δ_D , so that we have

$$I_T \equiv I_{\nu_T} \cong \sqrt{\frac{\delta_D}{1+z}} d(p) m_e c^2 \frac{\nu_T^2}{c^2} \sqrt{\frac{\nu_T}{\nu_B}}, \quad (7.160)$$

giving the magnetic field

$$B \cong \left(\frac{\delta_D}{1+z} \right) \left(\frac{2\pi m_e c}{e} \right) \frac{d^2(p) (m_e c^2)^2 \nu_T^5}{I_T^2 c^4} \quad (7.161)$$

of the radiating plasma, which can be written for a VLBI/VLBA radio source with intensity \mathcal{I}_T in units of $\text{Jy}/\text{mas}^2 = 4.25 \times 10^{-17} \text{ ergs}/\text{cm}^2 \text{ s sr Hz}$. The implied magnetic field intensity is

$$B \text{ (mG)} \cong 1.6 \frac{\delta_D}{1+z} \frac{d^2(p) \nu_T^5 \text{ (GHz)}}{\mathcal{I}_T^2}. \quad (7.162)$$

The Doppler factor of the radio-emitting plasma can be estimated from multi-wavelength observations of black-hole jet sources, so the system of equations is closed. These results precisely specify the model parameters and minimum powers.

Suppose a coordinated campaign on a black-hole jet source from radio to γ -ray energies clearly identified the synchrotron and synchrotron self-Compton components from detailed spectral modeling (a Compton component from scattered external radiation would have to be subtracted in many

cases). From these observables, we define the ratio of the νF_ν fluxes at the peak of the Compton and synchrotron components by

$$\Pi = \frac{(\nu F_\nu^{\text{SSC}})_{\text{max}}}{(\nu F_\nu^{\text{syn}})_{\text{max}}} \equiv \frac{f_{\epsilon^{\text{SSC}}}^{\text{SSC}}}{f_{\epsilon^{\text{syn}}}^{\text{syn}}} \cong \frac{\int d\nu' u'(\nu')}{U_B}, \quad (7.163)$$

with the final expression holding for scattering in the Thomson regime [81].

For an isotropic comoving nonthermal synchrotron radiation field, $u'(\nu') = 4\pi I'_{\nu'}/c$. Approximating the peak synchrotron intensity by a power law with index α , that is, $I'_{\nu'} = I'_0 \nu'^{-\alpha} H(\nu'; \nu'_1, \nu'_2)$, we have

$$\Pi \cong \frac{4\pi}{cU_B} \left(\frac{1+z}{\delta_D} \right)^3 \frac{I_\nu v'^\alpha (\nu_2'^{1-\alpha} - \nu_1'^{1-\alpha})}{1-\alpha}. \quad (7.164)$$

Eliminating the magnetic field between eqs. (7.161) and (7.164) fixes the Doppler factor through the intermediate expression

$$\frac{8r_e}{d^4(p)(1-\alpha)c} v'^\alpha (\nu_2'^{1-\alpha} - \nu_1'^{1-\alpha}) \left[\frac{I_\nu c^2}{m_e c^2 v^2} \frac{(1+z)}{\delta_D} \right]^5 \cong \Pi. \quad (7.165)$$

Replacing the bracketed term by the Rayleigh-Jeans expression gives an effective thermal brightness temperature

$$\begin{aligned} T_b &\cong \frac{m_e c^2}{2k_B} \frac{\delta_D}{1+z} \left(\frac{c(1-\alpha)d^4(p)\Pi}{8r_e v'^\alpha (\nu_2'^{1-\alpha} - \nu_1'^{1-\alpha})} \right)^{1/5} \\ &\cong 1.2 \times 10^{12} \left(\frac{\delta_D}{1+z} \right)^{6/5} \sqrt[5]{\frac{\Pi(1-\alpha)d^4(p)}{\bar{\nu} \text{ (GHz)}}} \text{ K} \quad \text{for } \alpha < 1. \end{aligned} \quad (7.166)$$

In practice, a maximum brightness temperature is measured when the self-absorption frequency is not well known. In the next section, the values of δ_D are worked out in the Thomson limit.

7.10 COMPTON LIMITS ON THE DOPPLER FACTOR

The ratio of the fluxes in the Compton and synchrotron portions of the spectral energy distribution (SED) give important information about black-hole jet parameters. We solve three equations to obtain δ_D from observables. Without precise knowledge of ν_T and I_T , however, this test—comparing the level of the SSC X-rays to the radio synchrotron emission—gives a minimum value of δ_D that allows the jet emission to be modeled in a nonthermal synchrotron/SSC scenario.

First it is necessary to measure the synchrotron and SSC νF_ν fluxes $f_{\epsilon^{\text{syn}}}^{\text{syn}}$ and $f_{\epsilon^{\text{SSC}}}^{\text{SSC}}$ at photon energies ϵ^{syn} and ϵ^{SSC} , respectively. From eq. (7.70), with a power-law electron distribution,

$$f_{\epsilon^{\text{syn}}}^{\text{syn}} = \frac{2\delta_D^{(p+5)/2}}{9d_L^2} cr_b^3 \sigma_T U_{B_{\text{cr}}} k_e \epsilon_z^{\text{syn} (3-p)/2} \epsilon_B^{(p+1)/2}. \quad (7.167)$$

Taking the ratio of $f_{\epsilon^{\text{SSC}}}^{\text{SSC}}$, from eq. (7.98), to eq. (7.167), gave eq. (7.100). The magnetic field is obtained from eq. (7.161), rewritten as

$$\epsilon_B \cong \left(\frac{\delta_D}{1+z} \right) \frac{d^2(p)(m_e c^2)^2 v_T^5}{I_T^2 c^4}. \quad (7.168)$$

Solving these three equations gives the Doppler factor

$$\begin{aligned} \frac{\delta_D}{1+z} &\cong \left(\frac{3f_{\epsilon^{\text{syn}}}^{\text{syn}} \Sigma_C}{c\vartheta^2 U_{B_{\text{cr}}} \Pi} \right)^{1/(4+2\alpha)} \left(\frac{I_T^2 c^4}{d^2(p) h m_e c^2 v_T^5} \right)^{(1+\alpha)/(4+2\alpha)} \\ &\times \left(\frac{\epsilon^{\text{SSC}}}{\epsilon^{\text{syn} 2}} \right)^{(1-\alpha)/(4+2\alpha)} \end{aligned} \quad (7.169)$$

in terms of measurable quantities. For a specific value of $\alpha = 0.5$ ($p = 2$), and using fiducial values for $f_{\epsilon^{\text{syn}}}^{\text{syn}} = 10^{-12} f_{-12}$ ergs $\text{cm}^{-2} \text{s}^{-1}$, $\epsilon^{\text{syn}} = 10^{-8} \epsilon_{-8}$, eq. (7.169) gives

$$\frac{\delta_D}{1+z} \cong 1.9 \left(\frac{f_{-12} \Sigma_C}{\vartheta_{\text{mas}}^2 \Pi} \right)^{1/5} \left(\frac{\mathcal{I}_T (\text{Jy}/\text{mas}^2)}{d(p)} \right)^{3/5} [v_T (\text{GHz})]^{3/2} \left(\frac{\epsilon^{\text{SSC}}}{\epsilon_{-8}^2} \right)^{0.1}. \quad (7.170)$$

A lower limit to the Doppler factor is derived if the self-absorption frequency is not measured. Note that, as the ratio Π of the SSC to synchrotron flux increases, the value of δ_D decreases, because smaller Doppler factors mean larger internal target photon densities for the SSC process [103].

Resolved or variable radio sources, if assumed stationary, have such intense internal radiation fields that the higher-order Compton scatterings should produce an intense X-ray and γ -ray emission signature while catastrophically cooling the electrons. Development of synchro-Compton theory to understand the Compton catastrophe by Burbidge, Jones, O'Dell, and Stein [104,105] helped pave the way for the acceptance of nonstationary and relativistic sources.

7.11 SELF-ABSORBED SYNCHROTRON SPECTRUM

For a uniform spherical ball of magnetized plasma ejected with relativistic speed from the central engine of a black hole, the νF_ν synchrotron spectrum

can, after examining the invariance properties of eq. (7.121), be written as

$$f_{\epsilon}^{\text{syn}} \cong \delta_D^4 \frac{\epsilon' j'(\epsilon', \Omega') V'_b}{d_L^2} \frac{3u(\tau_{\epsilon'})}{\tau_{\epsilon'}}. \quad (7.171)$$

In this equation, $\epsilon' = \epsilon_z / \delta_D = (1+z)\epsilon / \delta_D$, the invariant $\tau_{\epsilon'} = 2\kappa_{\epsilon'} r_b$, and $3u(\tau)/\tau \rightarrow 1$ in the optically thin limit $\tau \ll 1$, and $3u(\tau)/\tau \rightarrow 3/2\tau$ when $\tau \gg 1$ (eq. [7.123]).

For a power-law electron distribution with the low-energy electrons radiating synchrotron photons below the self-absorption frequency,

$$\epsilon' j'(\epsilon', \Omega') \cong \frac{6\sigma_T U_{\text{cr}} \epsilon_B^2 k_e \gamma_s^{3-p}}{6\pi}, \quad \gamma_s = \sqrt{\frac{\epsilon'}{\epsilon_B}}, \quad (7.172)$$

and κ'_{ϵ} is given by eq. (7.147). Thus

$$\frac{\epsilon' j'(\epsilon', \Omega')}{\kappa'_{\epsilon}} \cong \frac{3}{\pi^2(2+p)2^{p/2}} \frac{c\sigma_T U_{\text{cr}}}{\lambda_C r_e} \epsilon_B^3 \gamma_s^7. \quad (7.173)$$

In the optically thin limit,

$$f_{\epsilon}^{\text{syn}}(\tau \ll 1) \rightarrow \frac{2c\sigma_T U_{\text{cr}}}{9} \left(\frac{r_b}{d_L}\right)^2 (k_e r_b) \delta_D^4 \epsilon_B^2 \gamma_s^{3-p} \propto \epsilon^{1-\alpha}, \quad (7.174)$$

recalling that $\gamma_s = \sqrt{\epsilon(1+z)/\delta_D \epsilon_B}$. In the optically thick limit,

$$f_{\epsilon}^{\text{syn}}(\tau \gg 1) \rightarrow \frac{3c\sigma_T U_{\text{cr}}}{\pi(2+p)2^{p/2} \lambda_C r_e} \left(\frac{r_b}{d_L}\right)^2 \delta_D^4 \epsilon_B^3 \gamma_s^7 \propto \epsilon^{7/2}. \quad (7.175)$$

Suppose that a source radio spectrum is well-enough sampled that the measured energy flux $f_{\epsilon_T} = 10^{-14} f_{-14} \text{ ergs cm}^{-2} \text{ s}^{-1}$ and self-absorption frequency $\epsilon_T = 8.093 \times 10^{-12} \nu_T \text{ (GHz)}$ are found. Defining the self-absorption frequency as the interception of the optically thin and optically thick asymptotes, eqs. (7.174) and (7.175), then

$$k_e r_b = \frac{27}{2\pi(2+p)2^{p/2}} \frac{\epsilon_B}{\lambda_C r_e} \gamma_{sT}^{p+4}, \quad \gamma_{sT} = \sqrt{\frac{\epsilon'_T}{\epsilon_B}}. \quad (7.176)$$

From this, the half-angular size of the source ϑ , and the value of f_{ϵ_T} at $\tau = 1$, the magnetic field can be obtained through the relation

$$\epsilon_B \cong \frac{\delta_D}{1+z} \left[\left(\frac{(6e^{-1} - 3/2) m_e c^3}{2\pi^2(2+p)2^{p/2} \lambda_C^3 f_{\epsilon_T}} \right)^2 \vartheta^4 \epsilon_T^7 \right], \quad (7.177)$$

noting that $6e^{-1} - 3/2 = 0.7072 \dots$. Thus

$$B \text{ (G)} \cong 0.13 \left(\frac{\delta_D}{1+z} \right) \frac{\vartheta_{\text{mas}}^4 \nu_T^7 \text{ (GHz)}}{2^p(2+p)^2 f_{-14}^2}. \quad (7.178)$$

7.12 HYPER-RELATIVISTIC ELECTRONS

Electrons with Lorentz factor γ , traveling in a region with ordered magnetic field strength B , lose energy through synchrotron radiation at the rate

$$-\dot{\gamma}_{\text{syn}} = \frac{\sigma_{\text{T}} B^2}{4\pi m_e c} \gamma^2 \sin^2 \psi, \quad (7.179)$$

where ψ is the electron pitch angle (eq. [7.13]). The corresponding synchrotron energy-loss timescale $t_{\text{syn}} = \gamma/|d\gamma/dt|$. The gyration frequency $\omega_B = eB/\gamma m_e c$, and is independent of pitch angle. When $\omega_B t_{\text{syn}} \ll 1$, the electron loses almost all of its energy into synchrotron radiation in a time less than the gyroperiod. We use the term ‘‘hyper-relativistic’’ to refer to electrons in this radiation-reaction regime of synchrotron emission [106,107].

Electrons that cool before being deflected by an angle θ equal to the jet opening angle θ_j will emit most of their energy within θ_j . The pitch angle ψ does not change due to synchrotron losses in the limit $\gamma \gg 1$. Then $\cos \theta = \cos^2 \psi + \sin^2 \psi \cos \phi$, where $\phi = \omega_B t$ is the rotation angle. In the limit of small θ and ϕ , $\theta \cong \phi \sin \psi$. The condition $\theta \leq \theta_j$ for times $t \leq t_{\text{syn}}$ then results in the condition

$$\gamma \gtrsim \gamma_{\text{hr}}(\theta_j) = \sqrt{\frac{4\pi e}{\theta_j \sigma_{\text{T}} B \sin \psi}} \cong \frac{3 \times 10^8}{\sqrt{(\theta_j/0.1)[B(\text{G})] \sin \psi}} \quad (7.180)$$

defining hyper-relativistic electrons. Lower-energy electrons with $\gamma < \gamma_{\text{hr}}(\theta_j)$ and small-pitch-angle electrons radiate their energy over a much larger solid angle and longer time.

The characteristic synchrotron photon energy $E_\gamma = m_e c^2 \epsilon$ radiated by electrons that lose their energy within the jet opening angle θ_j is independent of ψ , and is given by

$$E_j \cong \frac{\hbar e B \sin \psi}{m_e c} \frac{\gamma_{\text{hr}}^2(\theta_j)}{(1+z)} \cong \frac{500}{(\theta_j/0.1)[(1+z)/2]} \text{ MeV}. \quad (7.181)$$

This is closely related to the maximum mean energy of synchrotron photons radiated by electrons that start to lose a large fraction of energy every Larmor cycle, which is independent of magnetic field [108,109] (see section 11.2.1).

Hyper-relativistic electrons with $\gamma > \gamma_{\text{hr}}(\theta_j)$ rapidly lose energy through synchrotron losses and deposit all of their energy along the direction of the jet. Electrons at lower energies are deflected to angles $\theta > \theta_j$, and their emission is not seen by an on-axis observer. Hence the distribution of electrons along the jet direction always has an effective low-energy cutoff at $\gamma_{\text{hr}}(\theta_j)$.

The production spectrum of the electrons can have an intrinsic cutoff γ_{co} due to the low-energy cutoff in the ultrarelativistic hadron spectrum, when photohadronic processes are responsible for the origin of the hyper-relativistic leptons. If $\rho \equiv \gamma_{\text{co}}/\gamma_{\text{hr}}(\theta_j) \geq 1$, then the observed synchrotron spectrum is a power law with -1.5 index for $E_j \lesssim E_\gamma \lesssim \rho^2 E_j$, and a photon spectrum with the same spectral index as the accelerated protons and escaping neutrons at photon energies $E_\gamma \gtrsim \rho^2 E_j$ [106]. If $\rho < 1$, then the observed photon spectrum at $E_\gamma \gtrsim E_j$ has the same spectral index as the primary hadrons.

At photon energies $E_\gamma \ll E_j$, the observed spectrum is produced by the same hyper-relativistic electrons with $\gamma \gtrsim \gamma_{\text{hr}}(\theta_j)$, but at energies ϵ well below the peak energy $3\gamma^2 \epsilon_B$, where $\epsilon_B \equiv B/B_{\text{cr}}$. The differential energy radiated per dimensionless energy interval $d\epsilon$ per differential solid angle element $d\Omega$ in the direction θ with respect to the direction of an electron moving with Lorentz factor γ is given by

$$\frac{dE}{d\epsilon d\Omega} = \frac{e^2}{3\pi^2 \lambda_C} \left(\frac{\epsilon}{\gamma \epsilon_B} \right)^2 (1 + \gamma^2 \theta^2)^2 (\Lambda_{\parallel} + \Lambda_{\perp}), \quad (7.182)$$

where $\Lambda_{\parallel} = K_{2/3}^2(\xi)$ and $\Lambda_{\perp} = (\gamma\theta)^2 K_{1/3}^2(\xi)/[1 + (\gamma\theta)^2]$ are factors for radiation polarized parallel and perpendicular to the projection of the magnetic field direction on the plane of the sky defined by the observer's direction [84]. The factor $\xi = \epsilon/\hat{\epsilon}$, where $\hat{\epsilon} = 3\epsilon_B \gamma^2/(1 + \gamma^2 \theta^2)^{3/2}$, and $K_n(x)$ is a modified Bessel function of the second kind, with asymptotes given in Appendix B.

The condition $\xi \ll 1$ corresponds to $\epsilon \ll \hat{\epsilon}$ where $K_n(\xi)$ are in their power-law asymptotes, and $\xi \gtrsim 1$ or $\epsilon \gtrsim \hat{\epsilon}$ is where $K_n(\xi)$ are in exponential decline. The characteristic energy $\hat{\epsilon}$ approaches $3\epsilon_B \gamma^2$ when $\gamma\theta \ll 1$, and $\hat{\epsilon}$ declines with θ according to the relation $\hat{\epsilon} \cong 3\epsilon_B \gamma^2/(\gamma\theta)^3$ when $\gamma\theta \gg 1$. When $\epsilon \ll \hat{\epsilon}$, then $\Lambda_{\parallel} \gg \Lambda_{\perp}$ and $dE/d\epsilon d\Omega = (dE_{\text{syn}}/d\epsilon d\Omega) \simeq 3^{1/3} (1.07e/\pi)^2 (\gamma\epsilon/\epsilon_B)^{2/3} / \lambda_C \propto \epsilon^{2/3}$. For a fixed value of ϵ , this emissivity exponentially cuts off when $\epsilon \gtrsim 3\epsilon_B/\gamma\theta^3$, or when $\theta \gtrsim \theta_{\text{max}} = (3\epsilon_B/\gamma\epsilon)^{1/3}$.

The synchrotron emission spectrum in the limit $E_\gamma \ll E_j$, integrated over solid angle, is thus

$$\frac{dE}{d\epsilon} \simeq 2\pi \int_0^{(3\epsilon_B/\gamma\epsilon)^{1/3}} d\theta \theta \left(\frac{dE_{\text{syn}}}{d\epsilon d\Omega} \right) \simeq \frac{3e^2}{\pi \lambda_C} \propto \epsilon^0. \quad (7.183)$$

This differs from the energy index $+1/3$ for synchrotron radiation radiated by electrons in the classical regime, because in this case one integrates over a complete orbit of an electron [86], so that the solid angle element $d\Omega \rightarrow d\theta \sin\theta \rightarrow d\theta \sin\psi$ in the integration in eq. (7.183). Mechanisms

for producing hyper-relativistic electrons, with synchrotron emission extending to GeV and TeV energies, were proposed by [95,110].

7.13 JITTER RADIATION

When averaging over pitch angles to derive the synchrotron formulae, we have implicitly assumed that the magnetic field is randomly oriented on size scales much smaller than the physical dimensions of the system, but that the field is unidirectional compared to the Larmor radius of the radiating particle.

An interesting limit to consider is the synchrotron “jitter” regime [111], which was motivated by spectral observations and mechanisms for magnetic field generation in the relativistic shocks of GRBs [112].

Consider a relativistic electron with $\gamma \gg 1$. Its beaming cone

$$\Delta\theta \sim \frac{1}{\gamma} \ll 1. \quad (7.184)$$

In conventional synchrotron radiation, the superposition of harmonics formed from electrons traveling at various angles gives the peak synchrotron frequency

$$\omega_c = \frac{3}{2}\gamma^2 \frac{eB \sin \psi}{m_e c}, \quad (7.185)$$

eq. (7.28). The averaging used to obtain the synchrotron emissivity function, eq. (7.27), does not apply if deflection of the electron while traveling through a magnetic domain is smaller than the beaming cone, eq. (7.184), of the electron. A magnetic domain is here roughly equated with a region on the size scale of the coherence length λ_B of the magnetic field, that is, the mean distance for the magnetic field to change in direction by $\pi/2$.

The deflection angle when passing through a magnetic domain is

$$\theta_{\text{def}} \equiv \frac{\lambda_B}{r_L}, \quad (7.186)$$

and the ratio

$$\frac{\theta_{\text{def}}}{\Delta\theta} = \frac{\lambda_B e B}{m_e c^2} \cong 5.8 \times 10^{-4} [B \text{ (G)}][\lambda_B \text{ (cm)}] \quad (7.187)$$

is independent of γ . The limit $\theta_{\text{def}} \ll \Delta\theta$ is the jitter radiation regime, and the opposite limit, $\theta_{\text{def}} \gg \Delta\theta$, is the normal synchrotron regime.

The electron passing through these magnetic domains sees an electromagnetic wave at frequency $\omega' \cong ck' \sim c/\lambda'_B \sim c\gamma/\lambda_B \approx ck_B\gamma$, which is scattered to a characteristic jitter radiation frequency

$$\omega_{\text{jit}} \sim \gamma^2 k_B c. \quad (7.188)$$

When viewed face on, the synchrotron spectra from jitter radiation

$$P^{\text{syn}}(\epsilon) \propto \epsilon^1, \quad \epsilon \ll \epsilon_{\text{jit}}, \quad (7.189)$$

so that $f_{\epsilon}^{\text{jit}} \propto \epsilon^2$, $\epsilon \ll \epsilon_{\text{jit}}$, which can be compared with standard synchrotron relation $f_{\epsilon}^{\text{syn}} \propto \epsilon^{4/3}$ for $\epsilon \ll \epsilon_c$, eq. (7.31). This is the same index as for the hyper-relativistic synchrotron emission, eq. (7.183).

From eq. (7.187), we see that the jitter regime could be relevant for magnetic domains with coherence lengths $\lambda_B \sim 10^2$ cm that could be formed with $\sim(1-10^3)$ G magnetic fields in GRBs, but is unlikely to be important for the transport of UHE electrons and positrons formed as secondaries, unless the intergalactic medium hosts \sim pc-scale magnetic-domain structure. The jitter mechanism can explain very hard, $4/3 \lesssim a \lesssim 2$ spectra of GRBs.

Chapter Eight

Binary Particle Collision Processes

This chapter considers binary particle collision processes, including

1. Coulomb interactions and ionization losses;
2. bremsstrahlung;
3. secondary nuclear production and spallation;
4. thermal electron-positron annihilation radiation; and
5. nuclear γ -ray line radiation.

The rate of thermalization and energy transfer between ionic and leptonic species is determined in the first approximation by the rate of binary collision processes. In a magnetized plasma, collective effects may be as important as binary collisions to transfer energy, and so could increase the thermalization and energy-exchange rate. Elastic binary particle collisions between electrons, positrons, and protons involve the Møller ($e+e \rightarrow e+e$), Bhabha ($e^+ + e^- \rightarrow e^+ + e^-$), and Coulomb ($e+Z \rightarrow e+Z$) cross sections [64]. Elastic scattering between two protons proceeds through Coulomb and nuclear contributions.

Bremsstrahlung has a cross section smaller by a factor $\sim \alpha_f$ than Thomson scattering. To efficiently emit bremsstrahlung, sites of rapidly varying radiation may have to be very Thomson thick, contrary to non-thermal, optically thin power-law radiations often observed from luminous, highly variable sources. Secondary radiations can be made through inelastic nuclear $p + p$ reactions, but in the relativistic jet plasma expelled from black holes, this requires large additional amounts of power to provide sufficient target density for effective energy extraction by this process. For the luminous black-hole environments in which we are most interested, binary particle processes are therefore generally less important than particle processes involving photons and fields. These processes are, however, of primary interest in cosmic-ray physics [113–115].

High-energy particles energized by black-hole engines can escape to large distances from their sources where binary particle processes become increasingly important for heating the surrounding medium through Coulomb and ionization processes, and for making pion-decay radiations from inelastic nuclear interactions. Radioactive nuclei formed by nuclear

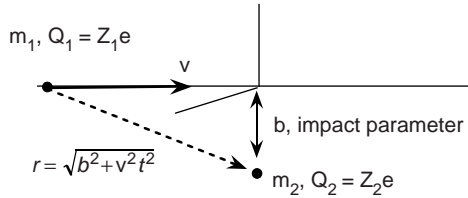


Figure 8.1 The stopping power of cold plasma. The minimum impact parameter defines the regime of validity of the Born approximation.

excitation and spallation can also reveal sites of nonthermal cosmic-ray production. For galactic black holes, positrons escaping from a compact region can annihilate with surrounding electrons to make variable $e^+ - e^-$ annihilation radiation. Only a steady Galactic annihilation glow has, however, been found with the *Oriented Scintillation Spectrometer Experiment* (OSSE) on CGRO, and the *INTERNational Gamma Ray Astrophysics Laboratory* (INTEGRAL) [116,117].

In the vicinity of Solar-mass black holes formed in stellar collapse events, secondary nuclear γ rays from radioactive species formed by the progenitor star would also be found, but may be difficult to be distinguished from radioactivities of a normal core-collapse supernova forming a neutron star.

8.1 COULOMB ENERGY LOSSES

An electron slowing down in a sea of mobile electrons and stationary protons loses energy through Coulomb processes at the rate

$$\dot{E}_{e,\text{Coul}} \sim m_e c^2 n_p c \sigma_T \ln \Lambda, \tag{8.1}$$

where n_p is the proton number density of the medium in which the electron slows down, and the Coulomb logarithm $\ln \Lambda \sim 20\text{--}40$ is the logarithm of the ratio of maximum and minimum impact parameters.

The functional dependences of particle energy losses in a plasma on mass and charge can be easily derived for Coulomb scattering in the Born approximation.

8.1.1 Stopping Power of Cold Plasma

Consider the energy lost as a fast charged particle passes through a plasma consisting of ionized protons and electrons (figure 8.1). In the Born straight-line approximation for the trajectory of the fast particle, energy is lost as the fast particle perturbs the locations of the cold particles in its path, imparting

a momentum impulse $\Delta p = \Delta p(b)$ in the transverse direction to the cold plasma particles passed at impact parameter b .

Let the fast particle “1” (with speed v_1) and cold plasma particles “2” have charges Q_1 and Q_2 and masses m_1 and m_2 , respectively. The number density of the cold plasma particles is n_2 . The energy loss in time Δt is given in the Born straight-line approximation ($\Delta p_y/p \ll 1$) by

$$\Delta E_1 = - \int db \, 2\pi b \frac{|\Delta p(b)|^2}{2m_2} n_2 v_1 \Delta t. \quad (8.2)$$

The perturbation of the speeds, and therefore the energies, of the particles in the cold plasma can be estimated from the transverse momentum impulse

$$d\vec{p} = \vec{F} dt \Rightarrow \Delta p_y = \int F_y \Delta t,$$

where the force is just the Coulomb force

$$\vec{F}_C = \frac{Q_1 Q_2}{r^2} \hat{r}. \quad (8.3)$$

Hence

$$|\Delta p_y| = 2Q_1 Q_2 \int_0^\infty \frac{b dt}{r^3} = \frac{2b Q_1 Q_2}{v_1} \frac{y}{b^2 \sqrt{b^2 + y^2}} \Big|_0^\infty = \frac{2Q_1 Q_2}{bv_1}.$$

Use of $|\Delta p_y|^2/2m_2 = 2Q_1^2 Q_2^2/b^2 v_1^2 m_2$ gives, from eq. (8.2), the result

$$-\frac{dE_1}{dt} = \frac{4\pi Z_1^2 Z_2^2 e^4 n_2}{m_2 v_1} \int_{b_{\min}}^{b_{\max}} db = \frac{4\pi Z_1^2 Z_2^2 e^4 n_2}{m_2 v_1} \ln \Lambda. \quad (8.4)$$

Because $dx = v_1 dt = \beta_1 c dt$, we can also write this as

$$-\frac{dE_1}{dx} = 4\pi \frac{Z_1^2 Z_2^2 e^4 n_2}{m_2 v_1^2} \ln \Lambda. \quad (8.5)$$

One sees from eq. (8.5) that the lightest particles are most affected by the passage of the fast particle, and contribute most to the stopping power of the plasma. For a cold electron plasma, eq. (8.5) can be written as

$$-\frac{dE_1}{dx} = \frac{3}{2} \frac{n_p \sigma_T Z^2 (m_e c^2)}{\beta_1^2} \mathcal{B}, \quad (8.6)$$

where \mathcal{B} is the stopping power and the target gas is neutral or ionized H with proton density n_p . The maximum impact parameter is defined by the energy required to excite a plasmon with energy $\hbar\omega_p$, where

$$\omega_p = \sqrt{4\pi n_p e^2 / m_e} = 5.64 \times 10^4 \sqrt{n_p \text{ (cm}^{-3}\text{)}} \text{ rad s}^{-1}$$

is the electron plasma frequency (see chapter 14).

Defining the maximum fractional energy loss $\Delta_{\text{st}} = [(\Delta E_{\text{lab}})_{\text{max}} / (m_1 v_1^2 / 2)]$, Gould [118] derives the following expressions for the stopping power of nonrelativistic electrons and positrons:

$$\mathcal{B}(\text{electron}) = \ln \left(\frac{2\sqrt{\Delta_{\text{st}}}(1 - \Delta_{\text{st}}) \times m_e v_1^2 / 2}{\hbar \omega_p} \right) + \frac{1}{2} \frac{\Delta_{\text{st}}}{(1 - \Delta_{\text{st}})} \quad (8.7)$$

and

$$\mathcal{B}(\text{positron}) = \ln \left(\frac{2\sqrt{\Delta_{\text{st}}} \times m_e v_1^2 / 2}{\hbar \omega_p} \right). \quad (8.8)$$

For distinguishable particles, $\Delta_{\text{st}} = 1$, and for indistinguishable particles, $\Delta_{\text{st}} = 1/2$. For the stopping powers of relativistic electrons and positrons,

$$\mathcal{B}_{\text{rel}}(\text{electron}) = \ln \left(\frac{\sqrt{\gamma} m_e c^2}{\hbar \omega_p} \right) \quad (8.9)$$

and

$$\mathcal{B}_{\text{rel}}(\text{positron}) = \ln \left(\frac{\sqrt{2\gamma} m_e c^2}{\hbar \omega_p} \right). \quad (8.10)$$

The stopping power for a relativistic ion in plasma is

$$\mathcal{B}_{\text{rel}}(\text{ion}) = \left[\ln \left(\frac{2\gamma m_e c^2}{\hbar \omega_p} \right) - \frac{1}{2} \beta_1^2 \right] \quad (8.11)$$

[119], and $\beta_1 = \sqrt{1 - \gamma^{-2}}$. Gould also derives stopping powers for atomic matter [120]; in this case the energy losses are referred to as ionization losses.

Equation (8.6) implies that the Coulomb energy-loss rate varies as

$$-\dot{\gamma}_{\text{Coul}} \cong \frac{c\sigma_{\Gamma} n_p}{\beta} \left(\frac{3}{2} \ln \Lambda \right), \quad (8.12)$$

displaying only a weak logarithmic increase with energy for relativistic electrons and protons. The n_p -dependent stopping power ranges from values of 20 to 40, and varies according to

$$\ln \left(\frac{m_e c^2}{\hbar \omega_p} \right) = 37.2 - \frac{1}{2} \ln[n_p (\text{cm}^{-3})]. \quad (8.13)$$

8.1.2 Thermal Relaxation

The thermalization timescale for nonrelativistic particles 1 thermalizing with a cold background test plasma 2 is defined through the relation

$$-\frac{dE_1}{dt} = \frac{m_1 v_1^2}{\tau_{1(2)}}. \quad (8.14)$$

The Born-approximation expression, eq. (8.4), for the Coulomb energy-loss rate implies the relaxation timescale

$$\tau_{1(2)} = \frac{m_1 m_2 v_1^3}{8\pi Z_1^2 Z_2^2 e^4 n_2 \ln \Lambda} \propto v_1^3; \quad (8.15)$$

thus the tail of the Maxwellian is the last to thermalize. The timescales for electrons to thermalize with ions, for ions thermalizing with themselves, and for electrons to thermalize with themselves, are, for nonrelativistic temperatures, related by the ratios

$$\tau_{e(Z)} : \tau_{Z(Z)} : \tau_{e(e)} = Z^{-2} \left(\frac{m_z}{m_e} \right) \left(\frac{n_e}{n_z} \right) : Z^{-4} \sqrt{\frac{m_z}{m_e}} \left(\frac{n_e}{n_z} \right) : 1.$$

Thus in plasmas at nonrelativistic temperatures, electrons thermalize first with themselves, and then ions with themselves, and then electrons with ions. The long timescale for electron-ion thermalization allows two-temperature electron-ion plasmas to be a plausible source model for the hot emission regions found in the vicinity of black holes [121,122].

Analytic and numerical treatments of Coulomb energy losses often employ the systematic energy-loss rate expression eq. (8.12). In (bremsstrahlung) models, where the lower-energy electrons could make a significant contribution to the emission, an accurate treatment of energy losses is required during the thermalizing process. A diffusion simulation of thermalization in relativistic plasmas is given in Ref. [7].

8.1.3 Stopping Power of Thermal Plasma

Electrons gain energy when they have thermal energies less than the thermal energy of the plasma. An expression taking this into account is

$$\dot{E}_{e,\text{Coul}}(E_e) = -\eta^e n_p \left(\frac{4\pi e^4 \mathcal{B}_{\text{th}}}{\beta_e m_e c} \right) \left(\Xi - \frac{d\Xi}{dx} \right), \quad (8.16)$$

where n_p is the proton or hydrogen density of the surrounding medium,

$$\Xi = \Xi(x) \equiv 2\pi^{-1/2} \int_0^x dy y^{1/2} \exp(-y), \quad (8.17)$$

$$\mathcal{B}_{\text{th}} = 24 - \ln \left(\frac{\sqrt{\eta^e [n_p (\text{cm}^{-3})]}}{T_e (\text{eV})} \right), \quad (8.18)$$

and

$$x = \frac{m_e v_e^2}{2k_B T_e} \quad (8.19)$$

[123]. The quantity $v_e = \beta_e c$ is the electron velocity, T_e is the plasma electron temperature, and $\eta^e = \sum Z^2 (n_Z/n_H) \cong 1.5$ is a correction factor for heavier ions, primarily He, in the interstellar medium (ISM). Nonthermal electrons diffuse in energy space with Coulomb diffusion coefficient [124]

$$D_{e,\text{Coul}}(E_e) = \eta^e n_p \left(\frac{8\pi e^4 \mathcal{B}_{\text{th}}}{\beta_e m_e c} \right) k_B T_e \Xi. \quad (8.20)$$

For ions, the energy-loss rate of a nonrelativistic test ion with mass A and charge Z in a background thermal plasma is normally dominated by Coulomb losses to electrons, and given by the asymptotic bridging formula [113]

$$-\left(\frac{dE}{dt} \right)_{\text{Coul,ion}} \cong 3 \times 10^{-7} Z^2 [n_e (\text{cm}^{-3})] \frac{\beta^2}{x_m^3 + \beta^3} \left(\frac{\ln \Lambda}{20} \right) \text{eV s}^{-1}, \quad (8.21)$$

where

$$x_m = \sqrt[3]{\frac{3\sqrt{\pi}}{4}} \beta_e \quad \text{and} \quad \beta_e \cong 0.026 \left(\frac{T_e}{2 \times 10^6 \text{K}} \right)^{1/2}. \quad (8.22)$$

The Coulomb energy-loss rate for protons with energy $E_p = m_p v^2/2$ is given by

$$\dot{E}_{p,\text{Coul}}(E_p) = -\eta^e n_p \left(\frac{4\pi e^4 \mathcal{B}_{\text{th}}}{\beta_p m_p c} \right) \left[\left(\frac{m_p}{m_e} \right) \Xi - \frac{d\Xi}{dx} \right]. \quad (8.23)$$

Due to Coulomb scattering, the protons diffuse in energy space with diffusion coefficient [123]

$$D_{p,\text{Coul}}(E_p) = \eta^e n_p \left(\frac{8\pi e^4 \mathcal{B}_{\text{th}}}{\beta_p m_p c} \right) k_B T_e \Xi. \quad (8.24)$$

8.1.4 Knock-On Electrons

Nonthermal protons knock electrons out of the thermal pool through Coulomb forces to produce a population of nonthermal knock-on electrons. The knock-on electron emissivity $\dot{n}_{\text{ko}}(\gamma_e)$, in units of $\text{cm}^{-3} \text{s}^{-1} \gamma_e^{-1}$, is given by

$$\dot{n}_{\text{ko}}(\gamma_e) = 1.75 \times 4\pi n_p(r) \int_{\gamma_1}^{\infty} d\gamma_p \Phi_k(\gamma_e, \gamma_p) J_p(\gamma_p, \Omega_p) \quad (8.25)$$

[125] where $\rho(r)$ is the density of the ISM, 1.75 accounts for the presence of heavier elements, γ_e is the Lorentz factor of the electron, γ_p is the

Lorentz factor of the proton, and $J_p(\gamma_p, \Omega_p)$ is the differential cosmic-ray proton number intensity. The differential probability for the production of an electron having a total energy per unit rest-mass energy in $d\gamma_e$ in γ_e by the collision of a cosmic ray is

$$\Phi_k(\gamma_e, \gamma_p) d\gamma_e = \frac{2\pi r_e^2}{(1 - \gamma_p^{-2})} \left(\frac{1}{(\gamma_e - 1)^2} - \frac{m_e \left(\gamma_p + \frac{m_e^2 + m_p^2}{2m_p m_e} \right)}{m_p (\gamma_e - 1) \gamma_p} + \frac{m_e^2}{2m_p^2 \gamma_p^2} \right) d\gamma_e \quad (8.26)$$

[125]. The maximum transferable energy is given by

$$\gamma_{\max} = 1 + \frac{\gamma_p^2 - 1}{\frac{m_e}{m_p} \left(\gamma_p + \frac{m_e^2 + m_p^2}{2m_e m_p} \right)}. \quad (8.27)$$

The lower bound of the integration in eq. (8.25) is determined by solving the inequality $\gamma_e \leq \gamma_{\max}$ for a given value of γ_p . The result is

$$\gamma_1 = \frac{m_p}{2m_e} (\gamma_e - 1) + \left[1 + \frac{1}{2} \left(1 + \frac{m_p^2}{m_e^2} \right) (\gamma_e - 1) + \frac{m_p^2}{4m_e^2} (\gamma_e - 1)^2 \right]^{1/2}. \quad (8.28)$$

The spectra of knock-on electrons at relativistic energies are usually soft and weak in comparison with those of directly accelerated electrons. Like suprathermal proton/inverse bremsstrahlung ($p + e \rightarrow p + e + \gamma$), where the ion is energetic and the electron is at rest [126], these processes are generally not important in black-hole environments. See [127,128] for more details. Other minor processes from the standpoint of black-hole astrophysics are direct pair production, $N + e \rightarrow N + e + e^+ + e^-$, where N can be an electron, positron, proton, or ion [129,130], double (or radiative) Compton scattering, $e + \gamma \rightarrow e + \gamma' + \gamma''$, which can provide an additional source of soft photons [37], and higher-order pair production processes, e.g., $\gamma + \gamma \rightarrow e^+ + e^- + e^+ + e^-$ [131].

8.2 BREMSSTRAHLUNG

The cross section for electron bremsstrahlung (“braking” radiation, also called free-free “ff” radiation), denoted by $e + p \rightarrow e + p + \gamma$, having an additional vertex in the Feynmann scattering diagram, has a lowest-order cross section that is one power of α_f smaller than the lowest-order Coulomb cross section [37,64].

8.2.1 Electron Bremsstrahlung Energy-Loss Rate

The relativistic bremsstrahlung energy-loss rate can be roughly approximated by the expression

$$-\dot{\gamma}_{\text{ff},e} \sim \alpha_f c \sigma_T n_p \gamma. \quad (8.29)$$

The bremsstrahlung photon number spectrum $\dot{N}_{\text{ff}}(\epsilon) \propto \epsilon^{-1}$ for $\epsilon \ll m_e c^2 \gamma$, and the mean bremsstrahlung photon energy $\langle \epsilon \rangle_{\text{ff}} \approx m_e c^2 \gamma / 3$.

For a fully ionized medium, the relativistic electron bremsstrahlung energy-loss rate [35] is given by the expression

$$-\dot{\gamma}_{\text{ff},\text{ion}} = \frac{3}{2\pi} \alpha_f c \sigma_T \gamma \left(\ln 2\gamma - \frac{1}{3} \right) \left(\sum_Z n_Z Z(Z+1) \right). \quad (8.30)$$

Effects of the shielding of the nucleus by the atomic-electron Coulomb fields must be taken into account for neutral or partially ionized gases. In this case,

$$-\dot{\gamma}_{\text{ff},\text{neutral}} = \frac{3}{8\pi} \alpha_f c \sigma_T \gamma \sum_s n_a \bar{\phi}_s(\Delta_{\text{eff}}), \quad (8.31)$$

where n_a is the number density of atomic species a ,

$$\bar{\phi}_s = \frac{4}{3} \phi_1 - \frac{1}{3} \phi_2, \quad (8.32)$$

and ϕ_1 and ϕ_2 are slowly varying transcendental functions given in Ref. [35]. The argument

$$\Delta_{\text{eff}} = (4\alpha_f \gamma Z_{\text{eff}})^{-1}, \quad (8.33)$$

and Z_{eff} is the effective nuclear charge felt by the atomic electrons. For H, $Z_{\text{eff}} = 1$, whereas $Z_{\text{eff}} \cong 1.7$ for He. The relativistic bremsstrahlung energy-loss rate can be about twice as great in ionized as in neutral plasma. See Refs. [35,132] for more details.

8.2.2 Electron Bremsstrahlung Production Spectra

The bremsstrahlung emissivity from two interacting particle distributions $n_1(p_1, \Omega_1)$ and $n_2(p_2, \Omega_2)$ is given by eq. (2.42),

$$\begin{aligned} \dot{n}_{\text{ff}}(\epsilon_s, \Omega_s) &= \frac{c}{1 + \delta_{12}} \oint d\Omega_1 \int_0^\infty dp n_1(p_1, \Omega_1) \\ &\times \oint d\Omega_2 \int_0^\infty dp_2 n_2(p_2, \Omega_2) \beta_r \cdot (1 - \beta_1 \beta_2 \cos \psi) \frac{d\sigma_{\text{ff}}(\epsilon_s; \gamma_r)}{d\epsilon_s d\Omega_s}. \end{aligned} \quad (8.34)$$

The general solution for the bremsstrahlung emissivity from two interacting isotropic particle distributions is given by a three-fold integral. Haug derived the most generally useful and accurate expressions for the electron-electron [133] and electron-positron [134] differential bremsstrahlung cross sections.

Except in plasmas at relativistic temperatures where the electron-electron and electron-positron bremsstrahlung powers can be comparable [135], electron-ion bremsstrahlung is generally the dominant bremsstrahlung emission process. For isotropic electrons interacting with protons and ions at rest, eq. (8.34) becomes

$$\dot{n}_{\text{ff},eZ} = cn_Z \int_{\sqrt{\epsilon_s(2+\epsilon_s)}}^{\infty} dp_e n_e(p_e) \frac{d\sigma_{\text{ff},eZ}(\epsilon_s; p_e)}{d\epsilon_s}; \quad (8.35)$$

the lower limit derives from the requirement that $\epsilon_s < \gamma - 1$. When the electron Lorentz factor $\gamma \lesssim m_Z/m_e$, where m_Z is the mass of an ion with charge Z , then ion recoil is small. The differential relativistic electron-ion cross section in this limit is

$$\frac{d\sigma_{\text{ff},eZ}(\epsilon_s)}{d\epsilon_s} = \frac{4Z^2\alpha_f r_e^2}{\epsilon_s} \left(1 + y^2 - \frac{2y}{3}\right) \left[\ln\left(\frac{2\gamma^2 y}{\epsilon_s}\right) - \frac{1}{2}\right], \quad (8.36)$$

where $y = 1 - \epsilon_s/\gamma$, and $y \rightarrow 1$ in the soft photon limit [35]. The electron-ion bremsstrahlung emission spectrum for cold ions and thermal electrons is given by eq. (8.35), with the thermal electron distribution

$$n_e(p; \Theta_e) = n_e \frac{p^2 \exp(-\gamma/\Theta_e)}{\Theta_e K_2(1/\Theta_e)} \xrightarrow{p \ll 1} n_e \beta_e^2 \sqrt{\frac{2}{\pi \Theta_e^3}} \exp(-\beta_e^2/2\Theta_e), \quad (8.37)$$

recalling eq. (1.1) with $\Theta_e = k_B T_e/m_e c^2$.

At nonrelativistic temperatures, the electron-ion thermal bremsstrahlung production spectrum is, using the electron-ion bremsstrahlung cross section in the nonrelativistic Born limit,

$$\dot{n}_{\text{ff},eZ}(\epsilon; \Theta_e) = 2 \left(\frac{2}{3\pi \Theta_e}\right)^{1/2} \alpha_f c \sigma_T Z^2 n_e n_Z \frac{\exp(-\epsilon/\Theta_e)}{\epsilon} G_{\text{ff}}(\epsilon/\Theta_e). \quad (8.38)$$

The Gaunt factor in the nonrelativistic Born limit is given by $G_{\text{ff}}(\epsilon/\Theta_e) = \sqrt{3} \exp(\epsilon/2\Theta_e) K_0(\epsilon/2\Theta_e)/\pi$. The nonrelativistic thermal bremsstrahlung energy emissivity is

$$\begin{aligned} \frac{d\mathcal{E}_{\text{ff},eZ}(\Theta_e)}{dV dt} &= 2 \left(\frac{2}{\pi}\right)^{3/2} \Theta_e^{1/2} Z^2 n_e n_Z \alpha_f c \sigma_T m_e c^2 G(T_e) \\ &\cong 1.57 \times 10^{-27} T_e^{1/2} Z^2 n_e n_Z G(T_e) \text{ ergs cm}^{-3} \text{ s}^{-1}, \end{aligned} \quad (8.39)$$

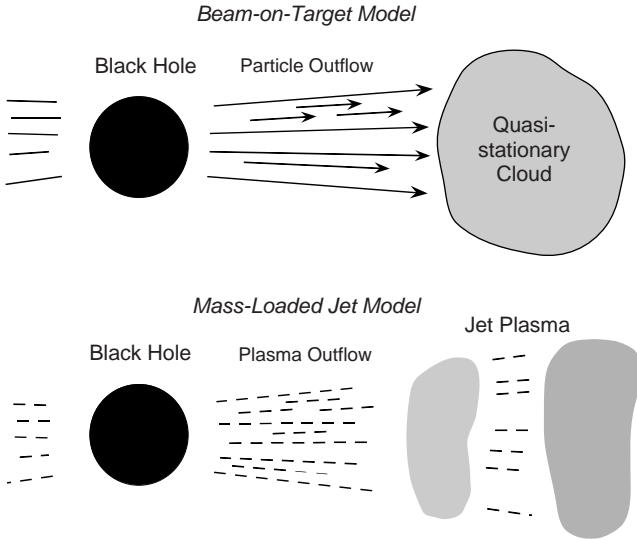


Figure 8.2 Two secondary nuclear production models from black-hole jet sources. (Upper) Beam-on-target model. (Lower) Mass-loaded jet model.

where the thermal averaged bremsstrahlung Gaunt factor $G(T_e) \cong 1.2$ in the nonrelativistic Born limit [86]. For corrections to the thermal bremsstrahlung emission spectrum and emissivity at relativistic temperatures, see Refs. [136,137].

Although bremsstrahlung emission processes are very important in cosmic-ray and Solar flare physics, nonthermal bremsstrahlung is generally not very effective in the luminous jets of black holes, because such systems would be optically thick to Thomson scattering.

8.3 SECONDARY NUCLEAR PRODUCTION

There are two classes of black-hole jet models where binary nuclear processes are important. One class is the *beam-on-target* models, so named because they resemble accelerator experiments (figure 8.2). Directed particle beams strike a target and generate high-energy radiation secondaries. This model faces the problem of requiring a large column density of target material for good energy conversion efficiency, and this model also has difficulty agreeing with time variability data of black-hole sources.

A second class is a *mass-loaded jet* model, where the density of the source is large enough that secondary nuclear production can make luminous γ -ray and neutrino emissions. This model faces energetic difficulties to have

sufficient target material in a relativistic jet in order to have good conversion efficiency of the nonthermal particles to radiation [95].

Consequently, binary nuclear processes do not seem to be especially important for making the high-energy radiation from black holes. Yet because they make secondary γ -rays and neutrinos, and because of their intrinsic interest, we review this process.

Secondary nuclear production refers to the inelastic production of pions, kaons, hyperons, baryonic resonances and baryons, and baryon-antibaryon pairs. Secondary nuclear production can also refer to spallation production, for example, when a cosmic-ray carbon ion is broken up as when it strikes the nucleus of a helium atom to produce light ions, including Li, Be, and B. The spallation cross section for proton-ion interaction and breakup can be approximated well above threshold by a simple geometrical shadowing correction factor $A^{2/3}$ to the proton-proton strong interaction cross section. A simple expression for the high-energy asymptote of the spallation cross section is [138]

$$\sigma_{\text{sp}}(E) \cong 50A^{2/3} \text{ mb.} \quad (8.40)$$

and the characteristic spallation timescale is $t_{\text{sp}} \sim 1/(n_p \sigma_{\text{sp}} c)$. Nuclear decay γ -radiation due to the production of secondary radioactive nuclides from cosmic ray/energetic particle interactions has been observed in Solar flares [139], but not yet from the plane of the Galaxy, nor from supernova remnants (SNRs).

We outline a formalism to calculate accurate spectra of secondaries produced in the simplest inelastic nuclear process,

$$p + p \rightarrow \pi^0 + X \rightarrow 2\gamma + X,$$

where X is anything else created in the collision. Equation (2.42) gives the secondary production spectrum (or number emissivity) for two interacting particle distributions. For a stationary proton target, $n_2(p_2, \Omega_2) = n_p \delta(p_2) \delta(\mu_2 - 1) / 2\pi$, giving

$$\dot{n}_s(p_s, \Omega_s) = cn_p \oint d\Omega_1 \int_0^\infty dp_1 n_1(p_1, \Omega_1) \beta_1 (1 - \beta_1 \mu_1) \frac{d\sigma(p_1, \Omega_1)}{dp_s d\Omega_s}. \quad (8.41)$$

If the particle distribution is isotropic, then $n_1(p_1, \Omega_1) = n_1(p_1) / 4\pi$. Integrating both sides over Ω_s gives

$$\dot{n}_s(p_s) = cn_p \int_0^\infty dp_1 n_1(p_1) \beta_1 \frac{d\sigma(p_1)}{dp_s}, \quad (8.42)$$

where

$$\frac{d\sigma(p_1)}{dp_s} = \oint d\Omega_s \frac{d\sigma(p_1)}{dp_s d\Omega_s}.$$

We calculate the production spectrum of secondaries $\dot{n}(T_s) = dN/dV dt dT_s$, where T_s is the kinetic energy of secondary s . The relations $dp_s \dot{n}_s(p_s, \Omega_s) = \dot{n}(T_s) dT_s / 4\pi$ and $\beta_1 c n_1(p_1) / 4\pi = J_p(T_p, \Omega_p)$ follow, where the subscripts in the last expression refer to the cosmic-ray proton. Hence

$$\dot{n}(T_s) = 4\pi n_p \int_0^\infty dT_p J_p(T_p, \Omega_p) \frac{d\sigma(T_p)}{dT_s}. \quad (8.43)$$

Now consider π^0 production from interactions of cosmic rays with gas and dust in the Galaxy. The dominant constituent of the ISM is H, and we consider only the dominant proton component of the galactic cosmic rays. A reasonable representation of the demodulated cosmic-ray proton spectrum observed in the Solar neighborhood is

$$J_p(T_p, \Omega_p) = \frac{2.2}{E_p^{2.75}} \text{ CR p cm}^{-2} \text{ s}^{-1} \text{ GeV}^{-1} \text{ sr}^{-1} \quad (8.44)$$

[140,141], namely a power-law in total energy $E_p = T_p + m_p$.

The spectral number emissivity for π^0 production from cosmic ray protons colliding with target protons or H nuclei is

$$\dot{n}_{pH \rightarrow \pi^0}(T_\pi) = 4\pi n_p \int_0^\infty dT_p J_p(T_p, \Omega_p) \frac{d\sigma_{pH \rightarrow \pi^0}(T_p)}{dT_\pi}. \quad (8.45)$$

The γ -ray emissivity from π^0 decay is

$$\dot{n}_{\pi^0 \rightarrow 2\gamma}(\epsilon) = \frac{2}{\epsilon_{\pi^0}} \int_{T_\pi^{\min}}^\infty dT_\pi \frac{\dot{n}_{pH \rightarrow \pi^0}(T_\pi)}{\sqrt{T_\pi(T_\pi + 2m_\pi)}}, \quad (8.46)$$

where $T_\pi^{\min}(\epsilon) = m_\pi [\gamma_\pi^{\min}(\epsilon) - 1]$, $\epsilon_{\pi^0} = m_{\pi^0} / m_e \cong 264$, and

$$\gamma_\pi^{\min}(\epsilon) = \frac{\epsilon}{\epsilon_{\pi^0}} + \frac{\epsilon_{\pi^0}}{4\epsilon} = \frac{1}{2} \left(\frac{2\epsilon}{\epsilon_{\pi^0}} + \frac{\epsilon_{\pi^0}}{2\epsilon} \right), \quad (8.47)$$

as we now demonstrate.

8.3.1 γ Rays from π^0 Decay

A π^0 , in its rest frame, decays into two γ -rays with energy $\epsilon' = \epsilon_{\pi^0} / 2 = \gamma_\pi \epsilon (1 - \beta_\pi \mu)$. If the π^0 decays isotropically in its own rest frame, then the γ -ray decay spectrum in the proper frame of the π^0 is

$$\frac{dN}{d\epsilon' d\Omega'} = 2 \frac{\delta(\epsilon' - \epsilon_{\pi^0} / 2)}{4\pi}. \quad (8.48)$$

For a π^0 produced with Lorentz factor γ_π , the transformation properties of $N(\epsilon, \Omega)$ imply from eq. (5.10) that

$$\frac{dN}{d\epsilon d\Omega} = \frac{\delta(\epsilon' - \epsilon_{\pi^0}/2)}{2\pi\gamma_\pi(1 - \beta_\pi\mu)}, \quad (8.49)$$

so that

$$\frac{dN}{d\epsilon} = \frac{2}{\beta_\pi\gamma_\pi\epsilon_{\pi^0}} H\left(\epsilon; \frac{1}{2}\gamma_\pi\epsilon_{\pi^0}(1 - \beta_\pi), \frac{1}{2}\gamma_\pi\epsilon_{\pi^0}(1 + \beta_\pi)\right). \quad (8.50)$$

The factor of 2 arises because two photons are produced per interaction. Substituting eq. (8.50) into eq. (8.46) gives

$$\dot{n}_{\pi^0 \rightarrow 2\gamma}(\epsilon) = \frac{2}{\epsilon_{\pi^0}} \int_{\gamma_\pi^{\min}(\epsilon)}^{\infty} d\gamma_\pi \frac{\dot{n}_{pH \rightarrow \pi^0}(\gamma_\pi)}{\beta_\pi\gamma_\pi}, \quad (8.51)$$

where $\gamma_\pi^{\min}(\epsilon)$ is given by eq. (8.47).

8.3.2 Cross Section for $p + p \rightarrow \pi + X$ Production

The cross section for π production from $p + p$ interactions can be written as

$$\frac{d\sigma_{pp \rightarrow \pi}(T_p)}{dT_\pi} = \frac{d\sigma_\pi(T_p)}{dT_\pi} = \langle \xi \sigma_\pi(T_p) \rangle \frac{dN_\pi(T_p)}{dT_\pi}. \quad (8.52)$$

The term $\langle \xi \sigma_\pi(T_p) \rangle$ is the inclusive cross section for the production of pions, irrespective of the remaining content of the secondary beam, and

$$\int_0^\infty dT_\pi \frac{dN_\pi(T_p)}{dT_\pi} = 1.$$

By contrast, exclusive cross sections are the cross sections for a specific decay channel [142]. Figure 8.3 shows the inclusive cross sections for the production of neutral and charged pions [141,143]. The pions decay according to the scheme

$$\pi^0 \rightarrow 2\gamma, \quad \pi^+ \rightarrow \mu^+ + \nu_\mu, \quad \pi^- \rightarrow \mu^- + \bar{\nu}_\mu, \quad (8.53)$$

$$\mu^+ \rightarrow e^+ + \bar{\nu}_\mu + \nu_e, \quad \mu^- \rightarrow e^- + \nu_\mu + \bar{\nu}_e \quad (8.54)$$

(see Appendix E for masses and lifetimes).

The inclusive cross section of particle i in reaction Y is the product of the inelastic cross section for reaction Y and the multiplicity ζ_i of particle i . Consequently the inclusive cross section is much larger than the inelastic

Table 8.1 Coefficients for the High-Energy Asymptotic Inclusive Cross Sections for Pion Production in p - p Collisions

X	a_π	b_π	c_π	p_{\min} (GeV/ c)
π^+	32	48.5	59.5	8
π^0	27	57.9	40.9	4
π^-	28.2	74.2	69.3	5.5

cross section well above threshold energy for the production of a given secondary. The inclusive cross sections for the production of π^+ , π^0 , and π^- in p - p collisions are fit by the function

$$\sigma_{\pi X} \text{ (mb)} = a_\pi \ln \gamma + \frac{b_\pi}{\sqrt{\gamma}} - c_\pi. \quad (8.55)$$

Coefficients for the high-energy asymptotes with proton momenta greater than p_{\min} (GeV/ c) in fits to the inclusive pion-producing reactions are given in table 8.1 and shown in figure 8.3. Fits accurate above threshold are given in Ref. [137].

The ratio of the inclusive cross section to the inelastic cross section is the π multiplicity. The high-energy, $E_p > 10$ GeV, asymptote of the $p - p$ inelastic cross section is given by

$$\sigma_{pp,\text{inel}}(E_p) \cong 30[0.95 + 0.06 \ln(E_p/\text{GeV})] \text{ mb} \quad (8.56)$$

[144], and a δ -function approximation for π production at relativistic energies can be written as

$$\frac{d\sigma_{pp,\text{inel}}(E_p)}{dE_\pi} \simeq \sigma_{pp,\text{inel}}(E_p) \delta(E_\pi - 0.17E_p). \quad (8.57)$$

A simple δ -approximation for γ -rays formed in the $p + p \rightarrow \pi^0 \rightarrow 2\gamma$ reaction is

$$\frac{d\sigma_{pp,\text{inel}}(E_p)}{dE_\gamma} \simeq 2\sigma_{pp,\pi^0}(E_p) \delta(E_\gamma - \chi E_p). \quad (8.58)$$

Here $\chi \sim 0.05$ is the ratio of the mean energy of the produced γ -ray to the energy of the incident proton. The value of χ must be adjusted at sufficiently high energies so that the total energy produced in secondaries does not exceed the inelasticity of the reaction.

Equation (8.58) is useful for making rough approximations to γ -ray production when $E_p \gg 10$ GeV. For even simple estimates, the inelastic nuclear cross section for p - p and p - A collisions is

$$\sigma_{pp}(E_p) \cong 30 \text{ mb}, \quad \sigma_{pA}(E_p) \cong 30A^{2/3} \text{ mb} \quad \text{for } E_p \gg 1 \text{ GeV}.$$

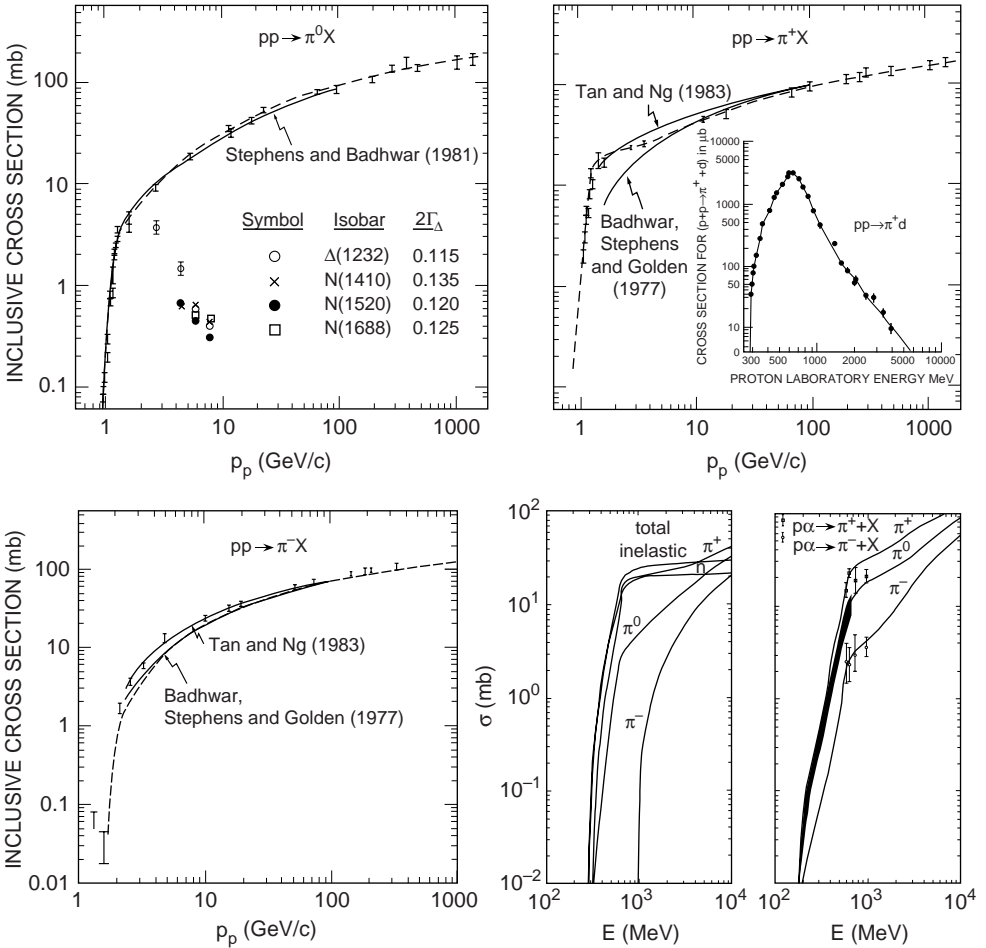


Figure 8.3 Inclusive cross sections for the production of pions in proton-proton collisions as a function of incident proton momentum. Inset in the $p + p \rightarrow \pi^+ + X$ diagram shows the cross section for the exclusive channel $p + p \rightarrow \pi^+ + d$. References to the data points, expressions for the fits (dashed lines) to the inclusive cross sections, and additional details are found in Refs. [137,143].

The inelasticity K_{pp} giving the fraction of energy lost in an inelastic $p + p \rightarrow \pi$ producing collision is ~ 0.5 , so only a few collisions are required to extract most of the cosmic ray proton's original kinetic energy.

Nonthermal protons collide with ambient protons and hydrogen nuclei to produce secondaries through a number channels. The five dominant channels are (1) $p + p \rightarrow \pi^0 + X$; (2) $p + p \rightarrow \pi^+ + X$; (3) $p + p \rightarrow \pi^- + X$;

(4) $p + p \rightarrow K^+ + X$; (5) $p + p \rightarrow K^- + X$. Here “ X ” refers to any other by-products produced in the reaction other than the particle indicated, and K^+ and K^- refer to kaons. It is also understood that channel 2 does not include the contribution resulting from the production of deuterium in the reaction $p + p \rightarrow \pi^+ + d$, which can be treated separately as a two-body process with cross section shown in figure 8.3 [145]. Secondary e^\pm and γ -ray production are dominated by the first three pion channels. Our calculation technique follows the method described in [137,141] and [146]; see also [147]. This model combines the isobaric model [148] at energies < 3 GeV and the scaling model [149] for energies > 7 GeV, with a linear combination to join the two models in the transition region between 3 and 7 GeV.

Isobaric Model

Stecker [148] developed this model for application to cosmic γ rays. For proton energies below 3 GeV, the production of pions by proton-proton collisions is mediated by the excitation of a $\Delta_{3/2}$ isobar. Assuming that the outgoing direction of the $\Delta_{3/2}$ isobar with mass m_Δ is colinear with the initial direction of the incident protons in the center-of-momentum (CM) system, and that the decay products of the isobaric resonance are isotropically produced in the frame of the baryonic resonance, the pion distribution in the laboratory system (LS) of the isobaric model is given by

$$f(T_\pi; T_p, m_\Delta) = \frac{1}{4m_\pi \gamma'_\pi \beta'_\pi \gamma_\Delta^+ \beta_\Delta^+} \left(H[\gamma_\pi; \aleph^+(-), \aleph^+(+)] + \frac{\gamma_\Delta^+ \beta_\Delta^+}{\gamma_\Delta^- \beta_\Delta^-} H[\gamma_\pi; \aleph^-(-), \aleph^-(+)] \right), \quad (8.59)$$

where the function $\aleph^\pm(\mp) = \gamma_\Delta^\pm \gamma'_\pi (1 \mp \beta_\Delta^\pm \beta'_\pi)$ and $s = 2m_p(T_p + 2m_p)$. The Lorentz factors of the forward (+) and backward (-) moving isobars are $\gamma_\Delta^\pm = \gamma_c \gamma_\Delta^* (1 \pm \beta_c \beta_\Delta^*)$, where $\gamma_c = \sqrt{s}/2m_p$ is the Lorentz factor of the CM with respect to the LS, and $\gamma_\Delta^* = (s + m_\Delta^2 + m_\pi^2)/2s^{1/2}m_\Delta$ is the Lorentz factor of the isobar in the CM. The pion Lorentz factor in the rest frame of the Δ isobar is $\gamma'_\pi = (m_\Delta^2 + m_\pi^2 - m_p^2)/2m_\Delta m_\pi$.

The pion spectrum resulting from the pp collisions is calculated by evaluating the following integral over the isobar mass spectrum:

$$\frac{dN(T_\pi, T_p)}{dT_\pi} = \int_{m_p+m_\pi}^{\sqrt{s}-m_p} dm_\Delta B_{\mathcal{W}}(m_\Delta) f(T_\pi; T_p, m_\Delta). \quad (8.60)$$

$B_{\mathcal{W}}(m_{\Delta})$ is the normalized isobar mass spectrum given by the Breit-Wigner distribution

$$B_{\mathcal{W}}(m_{\Delta}) = \frac{w_r(T_p)\Gamma_{\Delta}}{(m_{\Delta} - \langle m_{\Delta} \rangle)^2 + \Gamma_{\Delta}^2} \quad (8.61)$$

with average isobar mass $\langle m_{\Delta} \rangle$ and normalization factor

$$w_r(T_p) = \left[\arctan \left(\frac{\sqrt{s} - m_p - \langle m_{\Delta} \rangle}{\Gamma_{\Delta}} \right) - \arctan \left(\frac{m_p + m_{\pi} - \langle m_{\Delta} \rangle}{\Gamma_{\Delta}} \right) \right]^{-1}. \quad (8.62)$$

The $\Delta_{3/2}(1232)$ isobar, which has a resonance width $\Gamma_{\Delta} = 1/2 \times 115$ MeV [150], is the dominant resonance near threshold. More accurate treatments consider additional baryonic resonances.

Scaling Model

When exclusive descriptions are not feasible because of the large number of decay channels, an inclusive formalism with a scaling behavior is best suited to describe secondaries formed in nuclear production. For protons whose energies are greater than 7 GeV, we adopt a scaling model [148] to demonstrate. The Lorentz-invariant cross section given by Badhwar and Stephens [149,151] for neutral and charged pion production is written in the form

$$E_{\pi} \frac{d^3\sigma}{d^3p_{\pi}} = \mathcal{A} \mathcal{G}_{\pi}(E_p) (1 - \zeta_{\pi})^{\mathcal{Q}} \exp[-\mathcal{B}p_{\perp}/(1 + 4m_p^2/s)], \quad (8.63)$$

where we define

$$\mathcal{G}_{\pi^{\pm}}(E_p) = (1 + 4m_p^2/s)^{\mathcal{R}}, \quad (8.64)$$

$$\mathcal{G}_{\pi^0}(E_p) = (1 + 23E_p^{-2.6})(1 - 4m_p^2/s)^{\mathcal{R}}, \quad (8.65)$$

$$\mathcal{Q} = (C_1 - C_2 p_{\perp} + C_3 p_{\perp}^2) / \sqrt{1 + 4m_p^2/s}, \quad (8.66)$$

$$\zeta_{\pi} = \sqrt{x_{\parallel}^* + (4/s)(p_{\perp}^2 + m_{\pi}^2)}, \quad (8.67)$$

and

$$x_{\parallel}^* = \frac{2m_{\pi}\gamma_{\pi}\gamma_c\sqrt{s}(\beta_{\pi}\cos\theta - \beta_c)}{\sqrt{(s - m_{\pi}^2 - m_X^2)^2 - 4m_{\pi}^2m_X^2}}. \quad (8.68)$$

Here θ is the pion LS polar angle and the constants \mathcal{A} , \mathcal{B} , $C_{1,2,3}$, and \mathcal{R} are given in table 8.2 [148,149]. The quantity m_X depends on the channel under

Table 8.2 Adopted Values for Constants Defining the Invariant Cross Section for $p + p \rightarrow \pi + X$ Reactions

Constant ^a	1	2	3
\mathcal{A}	140	153	127
\mathcal{B}	5.43	5.55	5.3
C_1	6.1	5.3667	7.0334
C_2	-3.3	-3.5	-4.5
C_3	0.6	0.8334	1.667
\mathcal{R}	2	1	3

^aChannels 1, 2, and 3 refer to the production of π^0 , π^+ , and π^- , respectively.

consideration and are (1) $m_X = 2m_p$, (2) $m_X = m_p + m_n$, and (3) $m_X = 2m_p + m_\pi$ for inclusive p - p interactions leading to the production of π^0 , π^+ , and π^- , respectively. Examination of the equation for the dimensionless parallel momentum reveals the Feynman scaling limit $x_{\parallel}^* \rightarrow p_{\parallel}/p_{\parallel,\max} \rightarrow 2p_{\parallel}/\sqrt{s}$ when $s \gg m_p^2$.

To calculate the LS energy distribution of pions, we integrate the following over the pion LS polar angle:

$$Q_\pi(E_\pi, E_p) = \frac{2\pi p_\pi}{\langle \xi \sigma_\pi(E_p) \rangle} \int_{\cos \theta_{\max}}^1 d \cos \theta \left(E_\pi \frac{d^3 \sigma}{d^3 p_\pi} \right), \tag{8.69}$$

where $-1 \leq \cos \theta_{\max} \leq 1$ and is defined as

$$\cos \theta_{\max} = \frac{1}{\beta_c \gamma_c p_\pi} \left(\gamma_c E_\pi - \frac{s - m_X^2 m_\pi^2}{2\sqrt{s}} \right). \tag{8.70}$$

The pions will decay to produce muons. These muons are created fully polarized, resulting in an e^\pm decay asymmetry. The muons created by pion decay are made in the rest frame of the pion with Lorentz factor $\gamma_\mu = (m_\pi^2 + m_\mu^2)/2m_\pi m_\mu \approx 1.039$, and $\beta_\mu \approx 0.2714$. In the rest frame of the muons, the resulting electron decay spectrum is given by [152,153]

$$\frac{d^2 N}{dE_e^* d \cos \theta^*} = \frac{2\epsilon^2(3 - 2\epsilon)}{m_\mu} \left[1 + \xi \left(\frac{1 - 2\epsilon}{3 - 2\epsilon} \right) \cos \theta^* \right], \tag{8.71}$$

where E_e^* is the electron energy in the muon rest frame and helps to define the quantity $\epsilon = 2E_e^*/m_\mu$. The angle between the polarization angle of the parent muon and the resulting electron momentum is θ^* . The quantity $\xi = \pm 1$ for $\mu^\pm \rightarrow e^\pm$.

For a given electron energy E_e , the normalized electron decay energy distribution in the frame where the pions are isotropic is [137]

$$\frac{dN(E_e; \gamma_\pi)}{dE_e} = \begin{cases} \phi(\zeta_-) - \phi(\zeta_+), & \zeta_+ < \zeta_- < \omega_-, \\ \psi(\zeta_-) - \psi(\omega_-) + \phi(\omega_-) - \phi(\zeta_+), & \zeta_+ < \omega_- < \zeta_- < \omega_+, \\ \psi(\omega_+) - \psi(\omega_-) + \phi(\omega_-) - \phi(\zeta_+), & \zeta_+ < \omega_- < \omega_+ < \zeta_-, \\ \psi(\zeta_-) - \psi(\zeta_+), & \omega_- < \zeta_+ < \zeta_- < \omega_+, \\ \psi(\omega_+) - \psi(\zeta_+), & \omega_- < \zeta_+ < \omega_+ < \zeta_-, \\ 0, & \omega_+ < \zeta_-, \end{cases} \quad (8.72)$$

where we have introduced the following definitions:

$$\begin{aligned} \zeta_\pm &= \frac{E_e}{\gamma_\mu \gamma_\pi m_\mu (1 \pm \beta_\pi)} \\ \omega_\pm &= (1 \pm \beta_\mu)/2 \\ \phi(x) &= \frac{8\gamma_\mu^5 x^2}{dE_e^* d \cos \theta^*} \left[\frac{(3 - u\beta_\mu^2)(1 - \beta_\mu^2)}{2} - \frac{4x(3 + \beta_\mu^2 - 4u\beta_\mu^2)}{9} \right] \\ \psi(x) &= \frac{1}{6\beta_\mu \gamma_\mu \beta_\pi \gamma_\pi m_\mu} \left[(5 + u) \ln x - \frac{6(u + 2u\beta_\mu + 3)x^2}{(1 + \beta_\mu)^2} \right. \\ &\quad \left. + \frac{16(u + 3u\beta_\mu + 2)x^3}{3(1 + \beta_\mu)^3} \right]. \end{aligned} \quad (8.73)$$

Here $u = \xi/\beta_\mu$, and $\xi = 1$ for positrons and $\xi = -1$ for electrons. Figure 8.4 shows the energy distributions of electrons and positrons formed through pp collisions by mono-energetic protons with a variety of energies for channels 1 and 2 [154] (see also [143]). Figure 8.5 shows a calculation of the cosmic-ray induced diffuse π^0 -decay γ -ray spectrum of the Galaxy [141].

The resulting electron or positron spectrum formed by the decay of isotropically produced pions, modifying the notation from eq. (8.51), is

$$Q_e(E_e) = \int_{\bar{\gamma}_\pi(E_e)}^{\infty} d\gamma_\pi Q_\pi(\gamma_\pi) \frac{dN(E_e; \gamma_\pi)}{dE_e}, \quad (8.74)$$

where $Q_\pi(\gamma_\pi)$ is given by eq. (8.69), and $\bar{\gamma}_\pi = (E_e/E_e^{\max} + E_e^{\max}/E_e)/2$ if $E_e > E_e^{\max} = m_\mu(1 + \beta_\mu)\gamma_\mu/2 \approx 69.8$ MeV; otherwise, $\bar{\gamma}_\pi = 1$.

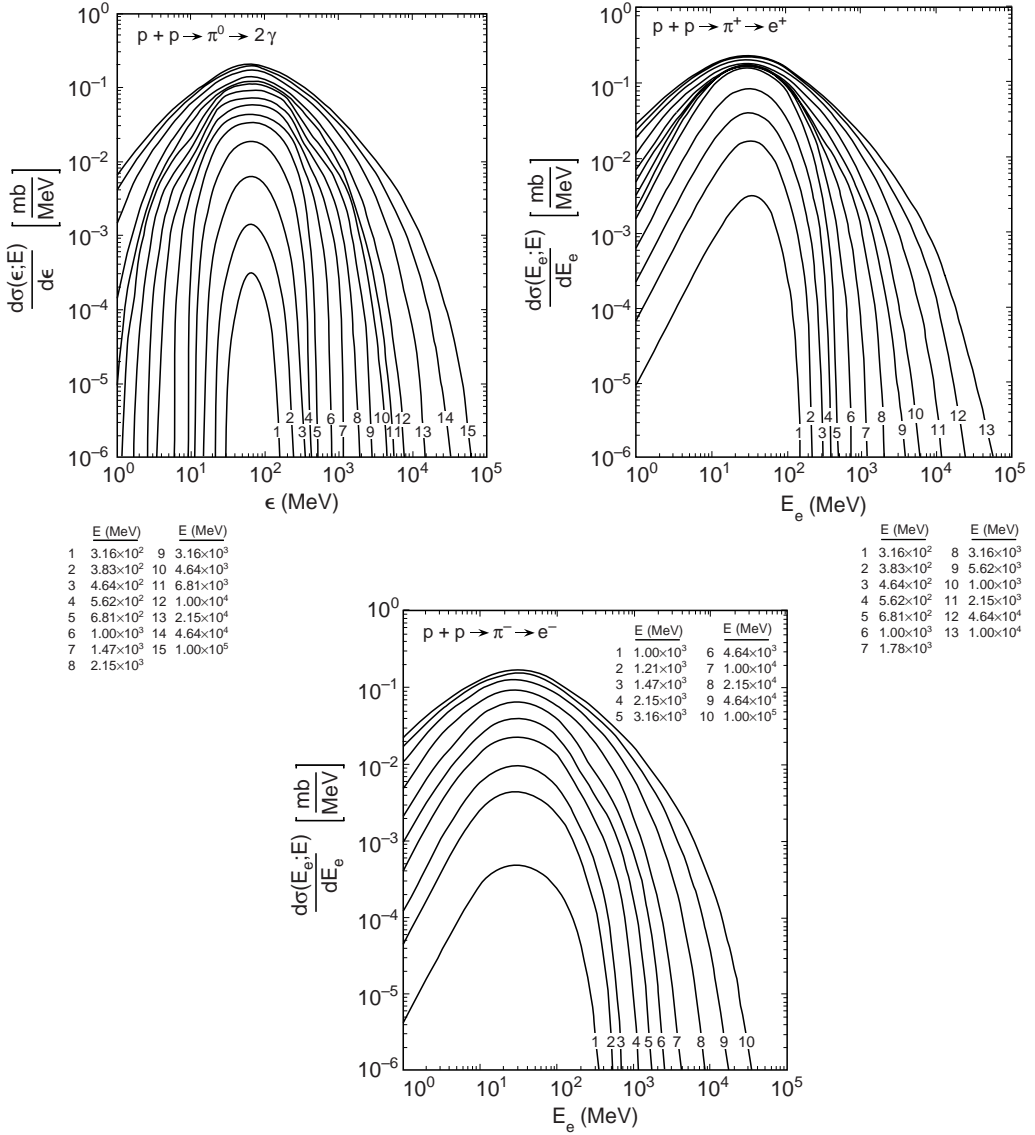


Figure 8.4 Differential cross section for the production of γ -rays, positrons, and electrons from secondary neutral and charged pions produced in p - p collisions by monoenergetic isotropic protons undergoing nuclear interactions with protons at rest [143,154]. Kinetic energies of the non-thermal protons are labeled.

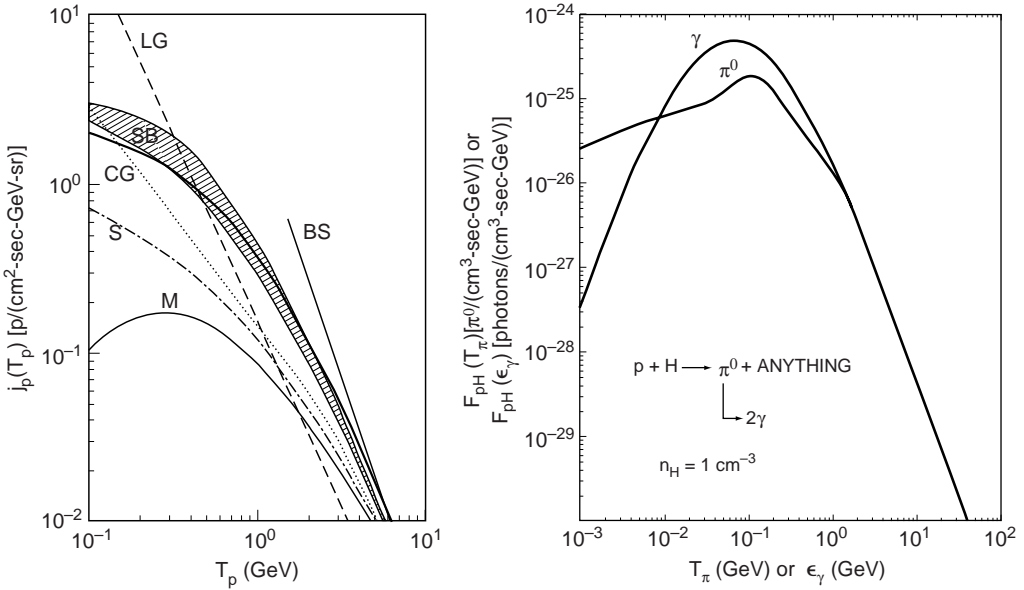


Figure 8.5 *Left:* The cosmic-ray spectrum observed during Solar minimum is labeled M, and the demodulated spectrum used in the calculation on the right is shown by the heavy solid line [140]. The demodulated spectra used in other calculations are denoted S, CG, LG, and BS (for details, see [142]). The boundaries of the region denoted by SB correspond to the curves BS and Mu of Ref. [151]. *Right:* The secondary π^0 and γ -ray emissivities from the interaction of the local demodulated cosmic-ray proton spectrum with unit density of atomic hydrogen.

More detailed treatments based on high-energy physics interaction models [155], inclusion of diffractive processes in scattering [156], and better-tested scaling representations [157] are also available to treat this process. Simple functional forms for use in astrophysical applications have also been developed and tested against nuclear interaction models [158].

8.4 ELECTRON-POSITRON ANNIHILATION RADIATION

Much interest in time-variable annihilation radiation as a marker of galactic black holes was generated in the 1980s due to low-significance detection of time-variable annihilation radiation toward the galactic center (see [159] for review). The annihilation itself would take place in a thermal environment after escape and transport. High Energy Astronomical Observatory HEAO-3 reports [160] of Cygnus X-1 with enhanced hard X-ray/soft γ -ray emission

led to the application of thermal pair cloud models to γ -ray data [8,161] in order to explain these results.

8.4.1 Annihilation in a Thermal Medium

In a sufficiently high-temperature ($T \gg 10^5$ K) phase of the ISM, or in the hot accretion plasma surrounding the black hole, target gas would be ionized plasma. In this case, positrons directly annihilate with electrons. The cross section for electron-positron annihilation in the frame of reference in which one of the particles is at rest and the other has Lorentz factor γ_r is

$$\sigma_a(\gamma_r) = \frac{\pi r_e^2}{(\gamma_r + 1)} \left[\left(\frac{\gamma_r^2 + 4\gamma_r + 1}{\gamma_r^2 - 1} \right) \ln \left(\gamma_r + \sqrt{\gamma_r^2 - 1} \right) - \frac{\gamma_r + 3}{\sqrt{\gamma_r^2 - 1}} \right] \quad (8.75)$$

[64], with asymptotes

$$\sigma_a(\gamma_r) \rightarrow \begin{cases} \pi r_e^2 / \beta_r, & \gamma_r - 1 \ll 1, \\ \pi r_e^2 \left(\frac{\ln 2\gamma_r - 1}{\gamma_r} \right), & \gamma_r \gg 1. \end{cases} \quad (8.76)$$

The thermal Doppler-broadened annihilation spectrum in a high-temperature (10^7 K $\lesssim T \lesssim 10^{10}$ K) thermal plasma was calculated numerically by Ramaty and Mészáros [162].

When positrons flow into the ISM and annihilate there, atomic effects, including positronium (Ps) formation, must be considered. Early calculations of positron annihilation in the ISM were treated by [163], and in Solar flares by [164]. Updated cross sections and processes related to the annihilation of positrons [165,166] are briefly summarized here.

Positrons injected into the ISM will annihilate directly or thermalize. Thermalization is more important than annihilation for positrons injected at MeV energies, and direct annihilation of higher-energy positrons produces a feature that is generally too broadened and weak to be easily detected. Positrons thermalize through Coulomb losses with free electrons, and through excitation and ionization energy losses with bound electrons. When a positron's energy reaches a few hundred eV, the energy-loss processes compete primarily with the formation of Ps through charge exchange in flight, as the rate of direct annihilation-in-flight is small. Thermal positrons either annihilate directly with free or bound electrons, or form Ps through radiative (re)combination and charge exchange. Charge exchange with neutral hydrogen has a 2430 Å threshold, so this process is suppressed in sufficiently low-temperature gases.

Ps is formed in the triplet (3S_1) ortho-Ps and singlet (1S_0) para-Ps ground states in a 3 : 1 ratio, with decay lifetimes of 1.4×10^{-7} s and 1.25×10^{-10} s, respectively. Cascading to the ground state can produce a Ly- α line at 6.8 eV and other lines that are very weak but, in principle, detectable [167,168]. Ps can be quenched if the density is $\gtrsim 10^{13}$ cm $^{-3}$, though this is not relevant for annihilation in the ISM. Annihilation of thermalized positrons on dust [169,170] is also an important quenching process for Ps, leading to a suppression of the 3γ continuum. These calculations are complicated by grain properties, including their sizes, charges, and compositions. The presence of dust in the warm envelopes around cold molecular cloud cores can reduce the Ps fraction, but dust is unlikely to affect the annihilation line and continuum properties in the uniform ISM.

8.4.2 Thermal Annihilation Line and Continuum Spectra

Calculating the 0.511 MeV line spectrum and relative strength of the 3γ continuum accurately requires a numerical simulation. The thermally averaged rates for the most important binary interactions involving positrons, and results of a Monte Carlo code to simulate the thermalization and Ps production of \sim MeV positrons are summarized in [171]. Charge exchange with neutral and singly ionized helium is included. Processes involving dust and H $_2$ are not considered in this simplified treatment (see [172]).

For the formation of Ps, we include radiative recombination with free electrons and charge exchange with hydrogen and neutral He. For Ps quenching, we include breakup of Ps by neutral hydrogen, ortho-Ps quenching via free electrons and via electrons bound in H, inverse charge exchange with H and He, and ionization of ortho-Ps atoms by free electrons. This last reaction, already mentioned as important in ionized gases at densities $\gtrsim 10^{13}$ cm $^{-3}$, must be considered in positron annihilation in Solar flares.

The Ps formation, quenching, and energy-loss processes along with the positron annihilation processes treated in our calculations are shown in table 8.3. The important diagnostic spectral features of annihilation radiation are the ratio $Q_{3\gamma}/Q_{2\gamma}$ and the FWHM width ΔE of the line. These two quantities depend upon the conditions of the medium where the annihilation occurs. The medium can be characterized by the temperature T , the total (neutral + ionized) hydrogen density n_H , and the ionization fractions X_{H^+} , X_{He^+} and $X_{He^{++}}$. We use the nonthermal and thermally averaged rates discussed above to solve a system of continuity equations for pair equilibrium and provide rates for positron annihilation from all of the various processes. These rates then directly give $Q_{3\gamma}/Q_{2\gamma}$. The total line spectrum is the sum of several components, some having Gaussian shapes, others not. Hence, the total line shape will not, in general, be Gaussian.

Table 8.3 Binary Interactions Involving Positrons

Energy redistribution	Positronium (Ps) formation
$e^+ \text{H} \rightarrow e^+ \text{H}^*$	$e^+ e^- \rightarrow \gamma \text{Ps}$
$e^+ \text{H} \rightarrow e^+ e^- \text{H}^+$	$e^+ \text{H} \rightarrow \text{H}^+ \text{Ps}$
$e^+ \text{He} \rightarrow e^+ \text{He}^*$	$e^+ \text{He} \rightarrow \text{He}^+ \text{Ps}$
$e^+ \text{He} \rightarrow e^+ e^- \text{He}^+$	
Positronium quenching	annihilation
$e^- \text{}^3\text{Ps} \rightarrow e^- e^- e^+$	$e^+ e^- \rightarrow 2\gamma$
$\text{H} \text{}^3\text{Ps} \rightarrow \text{H} e^- e^+$	$e^+ \text{H} \rightarrow \text{H}^+ 2\gamma$
$e^- \text{}^3\text{Ps} \rightarrow e^- \text{}^1\text{Ps}$	$e^+ \text{He} \rightarrow \text{He}^+ 2\gamma$
$\text{H} \text{}^3\text{Ps} \rightarrow \text{H} \text{}^1\text{Ps}$	$\text{}^1\text{Ps} \rightarrow 2\gamma$
$\text{H}^+ \text{Ps} \rightarrow \text{H} e^+$	$\text{}^3\text{Ps} \rightarrow 3\gamma$
$\text{He}^+ \text{Ps} \rightarrow \text{He} e^+$	

Figure 8.6 shows calculations of the annihilation line and Ps continuum for different phases of the ISM [173] with temperatures and densities given by table 8.4. The quantities $Q_{3\gamma}/Q_{2\gamma}$, giving the relative number of photons in the 3γ Ps continuum to the 0.511 MeV line, and the FWHM line width ΔE , from figures 8.6 and 8.7, are shown in the legend of figure 8.6. In the limit of a fully neutral medium, all annihilation takes place through the formation of Ps. Consequently, $Q_{3\gamma}/Q_{2\gamma} \rightarrow 9/2$, because 3/4 of the annihilations take place via ortho-Ps, giving three photons per annihilation, whereas 1/4 of the annihilations take place via para-Ps, giving two photons per annihilation. Annihilation occurs before thermalization in a fully neutral medium, so the calculated 9 keV line width for the neutral medium is broader than for partially ionized media where the positrons generally thermalize before annihilating.

As the temperature increases, the relative number of 3γ continuum to 2γ line photons decreases. This is because the Ps formation processes involving charge exchange with neutrals become less important at higher temperatures due to the fewer available neutral or partially ionized ions. The line width increases at high temperatures due to thermal broadening, and approaches the limit $\Delta E_{\text{FWHM}} = 11.0T_6^{1/2}$ keV [164,165], where T_6 is the temperature in units of 10^6 K. Ps formation can be quenched in high-temperature gas.

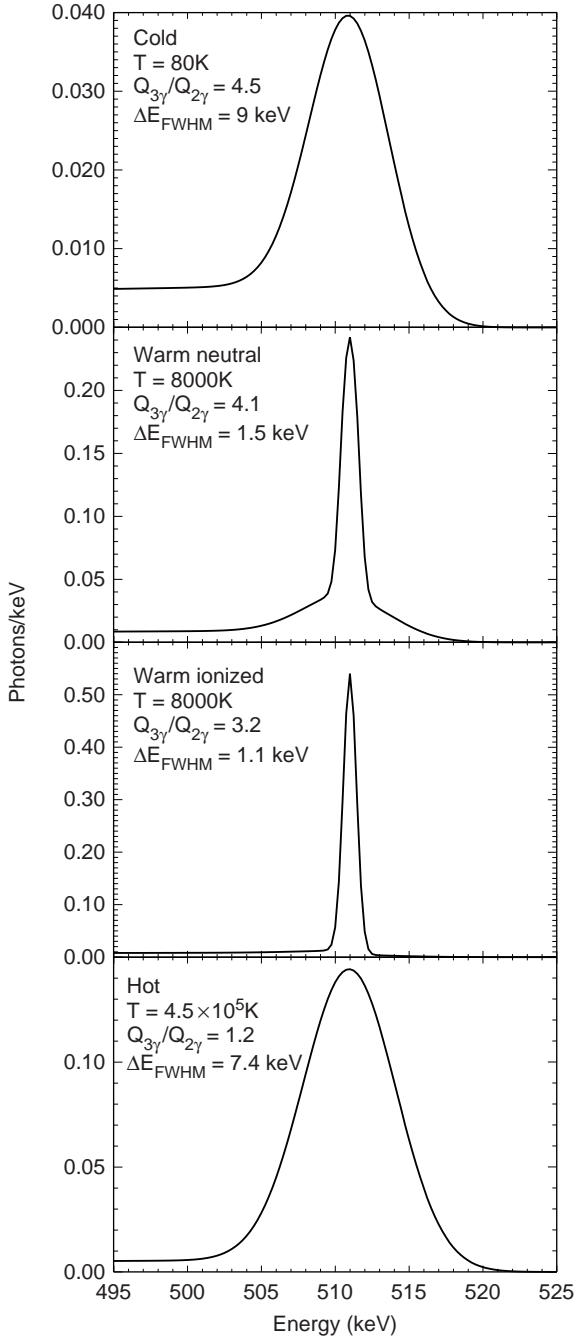


Figure 8.6 Calculations of annihilation line and Ps continuum from the injection of MeV positrons into regions with different temperatures and ionization fractions. (Figure courtesy of Ronald J. Murphy.)

Table 8.4 Temperatures and Densities, in units of cm^{-3} , of Different Phases of the ISM Used in Calculations of Annihilation Radiation

	Cold neutral	Warm neutral	Warm ionized	Hot
T (K)	80	8000	8000	4.5×10^5
n_{HI}	38	0.31	0.06	0.0
n_e	0.0	0.055	0.17	3.5×10^{-3}
n_{HI}	0.0	0.055	0.17	2.9×10^{-3}
n_{HeI}	3.8	0.036	0.023	0.0
n_{HeII}	0.0	0.0	0.0	0.0
n_{HeIII}	0.0	0.0	0.0	0.6×10^{-3}

8.5 NUCLEAR γ -RAY LINE PRODUCTION

MeV telescopes have detected nuclear line emission from Solar flares, diffuse nuclear line emissions from the Galaxy, and nuclear γ -ray line photons from SNRs and SN 1987A. Freshly synthesized nuclei formed in stellar explosions or as secondary spallation products in cosmic ray collisions may be radioactive, and decay with the emission of a γ ray on a characteristic timescale. Positron production often accompanies γ -ray production in radioactive emitters made by novae and supernovae and by low-energy (≈ 10 – 100 MeV/nucleon) cosmic rays.

With OSSE and INTEGRAL finding no signs of time-variable annihilation radiation [116,117], hopes for black-hole detection via radioactive tracers have faded. Nevertheless, nuclear γ -ray line astronomy reveals, most dramatically through maps of the 0.511 MeV annihilation line and the 1.809 MeV ^{26}Al ($\approx 10^6$ yr decay lifetime), the nuclear history of our Galaxy. Synthesis of radioactive nuclei in our Galaxy is confirmed by observations of ^{56}Co and ^{57}Co nuclear decay lines from SN 1987A, the ^{26}Al 1.809 MeV line found in clumped structure along the Galactic plane, observed in great deal with the Compton Telescope (COMPTEL) on CGRO and with INTEGRAL, and the ^{44}Ti nuclear decay line from Cas A [174,175]. (The mean lifetimes of the $^{56}\text{Ni} \rightarrow ^{56}\text{Co}$ and $^{56}\text{Co} \rightarrow ^{56}\text{Fe}$ decays in the $^{56}\text{Ni} \rightarrow ^{56}\text{Co} \rightarrow ^{56}\text{Fe}$ chain are 8.8 and 111.4 days, respectively, with a positron emitted 19% of the time in the latter reaction.)

The flux of γ -ray line emission reflects the number of SNe in the recent past, and the mass of isotopes produced in the explosion. More than a Solar mass of ^{56}Ni can be manufactured in a Type Ia SN involving white dwarf detonation or deflagration. For core-collapse Type II SNe, only $\sim 0.08M_{\odot}$

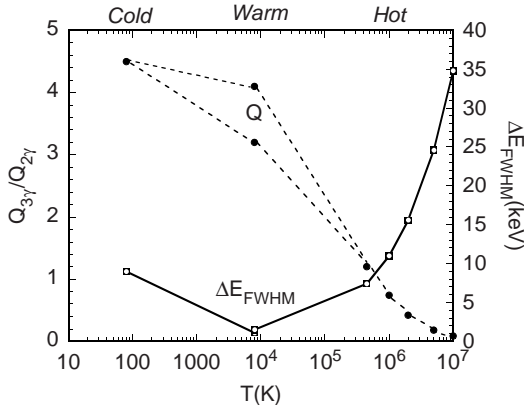


Figure 8.7 Calculations of $3\gamma/2\gamma$ ratios and FWHM line widths in different phases of the ISM.

of ^{56}Ni is synthesized per SN. The mean lifetime of the $^{44}\text{Ti} \rightarrow ^{44}\text{Sc} \rightarrow ^{44}\text{Ca}$ chain is 78 yr, and the synthesized mass of ^{44}Ti in a SN is not great, so recent supernova activity is required for detection of these nuclear lines. Calculations of masses of synthesized elements in stellar interiors are described in, e.g., Ref. [176].

Identification of sites of black-hole formation by a distinguishing nuclear line signature could be important for models of gamma-ray bursts related to a specific type of SN (specifically, SN Ib/c). Experimental advances to search for the nuclear signatures of specific types of SNe, for the radioactive decay signature of Type Ia SNe, and for the spallation nuclear γ -ray lines from low energy cosmic rays [177], will probably have to wait for an advanced nuclear γ -ray telescope. The significant bulge component of the annihilation glow suggests an origin in an old stellar population, e.g., low-mass X-ray binary neutron-star or black-hole systems.

Chapter Nine

Photohadronic Processes

In this chapter, three fundamental photohadronic processes are considered, each involving high-energy protons or ions N with atomic charge Z and atomic mass A interacting with target photons. They are the reactions

1. $N + \gamma \rightarrow N + \pi$ (denoted $\phi\pi$), photopion or photomeson production;
2. $N + \gamma \rightarrow N + e^+ + e^-$, photopair (ϕe) production; and
3. $N + \gamma \rightarrow N' + N''$, photodisintegration, for ions.

In addition, particles in intergalactic space lose energy adiabatically as the universe expands.

Charged pions formed by the photopion process decay into leptons and neutrinos, and neutral pions decay into γ rays. The secondary neutrino flavor ratio from $\phi\pi$ processes at production is

$$\nu_e : \nu_\mu : \nu_\tau = 1 : 2 : 0,$$

because the products of the decay schemes, eqs. (8.53) and (8.54), for charged pions are

$$\pi^+ \rightarrow e^+ + \nu_e + \bar{\nu}_\mu + \nu_\mu, \quad \pi^- \rightarrow e^- + \bar{\nu}_e + \nu_\mu + \bar{\nu}_\mu, \quad (9.1)$$

and are the same in photopion production as for pions formed as secondaries in nuclear production. For UHECR protons, the photopion production inelasticity $K_{\phi\pi}$, is ~ 0.2 – 0.5 , so only a few interactions are required for an UHECR proton to lose a large fraction of its initial energy. By contrast, the photopair inelasticity $K_{\phi e} \sim 2m_e/m_p$, so hundreds of scatterings are needed for an UHECR proton to lose most of its energy through this process.

The photopion process becomes less important for UHECR nucleons as an energy-loss process because of the higher threshold energy for large- A nuclei, but the photopair process, with energy-loss rates proportional to Z^2 , still remains strong. More important for ions though is photodisintegration, where nuclear resonances cause escape of protons, neutrons, and light nuclei from the nucleus.

Photopion and secondary nuclear production, examined in the previous chapter, are the two processes usually considered for high-energy ($\gtrsim \text{GeV}$) neutrino production. The flavor ratio of neutrinos formed through photopion and secondary nuclear production can be changed through different mechanisms, including neutrino oscillations. In sufficiently strong magnetic fields, a secondary muon loses its energy through synchrotron processes before decaying, thereby reducing the energy output in neutrinos and the electron neutrino content [178]. Subsequent acceleration following production can enhance neutrino energy output [179].

Neutrino detection depends on the high-energy particle physics cross sections, which are not known with certainty, and detector physics [180]. Analysis of data from optical modules placed deep in ice or water is used to discriminate the few upward-going neutrino-induced muon, electron, and τ events from the intense background of cosmic-ray-induced downward-going muons. Detection sensitivity for neutrino-induced events and opacity of the Earth to $\gg 10^{15}$ eV neutrinos [181] are central issues that must be considered in a complete high-energy astrophysical neutrino model.

Only the source and cosmic propagation problems are considered here, specialized first to the problem of UHECR protons in the CMBR. The physics of the system is illustrated by working through, in specified approximations, a central problem in cosmic-ray and high-energy neutrino astrophysics, namely, the energy spectrum of diffuse cosmogenic or GZK neutrinos formed by UHECR protons interacting with photons of the CMBR (see footnote 5, chapter 1 for the definition of GZK). Photonuclear reactions are considered in the final section of the chapter.

This analysis treats

1. scattering and energy loss timescales through photohadronic and inelastic processes;
2. the photopion ($\phi\pi$) process, including energy-loss rates of UHECR protons in the CMBR;
3. an approximate analytic treatment of the photopair (ϕe) process, including approximate and accurate UHECR ion energy-loss rates in the CMBR;
4. adiabatic losses from universal expansion;
5. formation of cosmogenic secondaries from photopion and photopair interactions between UHECR protons and CMB photons;
6. evolution of the UHECR proton spectrum and normalization to the local luminosity density and star formation rate (SFR) function of the sources of UHECRs;

7. the Waxman-Bahcall bound limiting the diffuse neutrino intensity given the measured intensity of UHECRs;
8. calculations of the diffuse neutrino background from photopion reactions between UHECRs and photons of the CMBR, for different SFRs; and
9. photodisintegration of ions.

By extending these ideas to UHECR ions, we can construct a model to confront HiRes and Auger data on the UHECR spectrum, including the GZK cutoff which was observed with the HiRes observatory in Utah [182] and the Pierre Auger Observatory (PAO) in Argentina [183]. We can also make flux predictions for high-energy neutrino astronomy, both at PeV energies from source neutrinos and at EeV energies from cosmogenic neutrinos [184].

9.1 SCATTERING AND ENERGY-LOSS TIMESCALES

Let the cross section for a photohadronic process be denoted $\sigma_{\gamma p}(\epsilon_r)$. The cross section depends only on the invariant energy of the interaction,

$$\sqrt{s_{\text{int}}} = \epsilon_r = \gamma_p \epsilon (1 - \beta_p \mu), \quad (9.2)$$

which is equal to the energy of the photon in the proton's rest frame. Here the proton has Lorentz factor $\gamma_p = E_p/m_p c^2 = (1 - \beta_p^2)^{-1/2}$, $\epsilon = h\nu/m_e c^2$, $\mu = \cos\theta$, and θ is the angle between the directions of the interacting photon and proton.

The photohadronic interaction rate (and therefore the inverse of the scattering timescale) for ultrarelativistic hadrons in a radiation field described by the spectral number density $n_{\text{ph}}(\epsilon, \Omega) = dN_{\text{ph}}/d\epsilon d\Omega dV$, which is in general anisotropic, is given by

$$\dot{N}_{\text{sc}}(\gamma_p) = c \oint d\Omega \int_0^\infty d\epsilon (1 - \beta_p \mu) n_{\text{ph}}(\epsilon, \Omega) \sigma_{\gamma p}(\epsilon_r), \quad (9.3)$$

from eq. (2.40).

In an inelastic collision leading to electron-positron pair or pion production, an ultrarelativistic proton loses, on average, a fraction $K(\epsilon_r)$ of its original energy, hence $K(\epsilon_r)$ is the inelasticity of the collision. The

inverse of the photohadronic energy-loss timescale is therefore given by

$$\begin{aligned}
 t_{\gamma p}^{-1}(\gamma_p) &= \frac{1}{\gamma_p} \left| \frac{d\gamma_p}{dt} \right|_{\gamma_p} \\
 &= c \int_0^\infty d\epsilon \int_0^{2\pi} d\phi \int_{-1}^{+1} d\mu n_{\text{ph}}(\epsilon, \Omega) (1 - \beta_p \mu) \sigma_{\gamma p}(\epsilon_r) K_{\gamma p}(\epsilon_r).
 \end{aligned} \tag{9.4}$$

The scattering timescale $t_{\text{sc}}(\gamma_p) = [\dot{N}_{\text{sc}}(\gamma_p)]^{-1}$ is generally shorter than the energy-loss timescale $t_{\gamma p}(\gamma_p)$, as it takes ~ 2 – 5 scatterings in photopion production, or hundreds of scatterings in photopair production, for the UHECR proton to lose a large fraction of its initial energy.

For an isotropic radiation field, $n_{\text{ph}}(\epsilon, \Omega) = n(\epsilon)/4\pi$, and eq. (9.4) gives

$$t_{\gamma p}^{-1}(\gamma_p) \cong \frac{c}{2\gamma_p^2} \int_0^\infty d\epsilon \frac{n_{\text{ph}}(\epsilon)}{\epsilon^2} \int_0^{2\gamma_p \epsilon} d\epsilon_r \epsilon_r \sigma_{\gamma p}(\epsilon_r) K_{\gamma p}(\epsilon_r) \tag{9.5}$$

in the limit $\gamma_p \gg 1$, $\beta_p \rightarrow 1$ [185].

The CMBR is considered here as the target background radiation field. The photon distribution of the CMBR is given, from eq. (5.16), by

$$n_{\text{CMB}}(\epsilon; z) = \frac{8\pi}{\lambda_{\text{C}}^3} \frac{\epsilon^2}{\exp[\epsilon/\Theta(z)] - 1}, \tag{9.6}$$

where $\Theta(z) \cong 4.6 \times 10^{-10}(1+z)$ is, in units of $m_e c^2$, the temperature of the CMBR at redshift z (eq. [5.17]).

9.2 PHOTOPION PROCESS

The photopion process $p\gamma \rightarrow N\pi$ has a threshold photon energy $\epsilon_{\text{thr}} = m_\pi + m_\pi^2/2m_p$ ($m_{\pi^0} = 135.0$ MeV, $m_{\pi^\pm} = 139.6$ MeV). The π^0 threshold is therefore $\cong 145$ MeV, and only the $\gamma p \rightarrow \Delta^+ \rightarrow \pi^0 p$ is kinematically allowed. At energies between the π^+ threshold, $\cong 0.150$ GeV, and ≈ 0.25 GeV, the direct pion channel $\gamma p \rightarrow \pi^+ n$ is dominant [186].

The simplest photohadronic process involves an exchange of a meson between an electromagnetic vertex for the photon interaction and a strong interaction vertex for the baryon interaction (see figure 9.1). Besides direct processes, single or multiple resonant excitations followed by decay are important at $\sqrt{s_{\text{int}}} \gtrsim 0.25$ GeV.

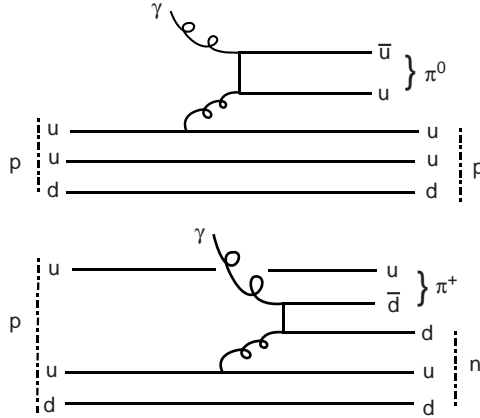


Figure 9.1 Feynman diagram for reactions $p + \gamma \rightarrow p + \pi^0$ and $p + \gamma \rightarrow n + \pi^+$. Labels u and d denote up and down quarks, respectively.

9.2.1 Photopion Cross Section

Four separate contributions to the total photopion cross section [187] are shown in figure 9.2:

1. Resonance Production

The most important resonance in photopion and secondary nuclear production is the $\Delta^+(1232)$ resonance ($m_{\Delta^+(1232)} = 1.232 \text{ GeV}$, Lorentzian width $\Gamma_{\Delta^+(1232)} = 0.115 \text{ GeV}$). For $\Delta^+(1232)$ resonance production and decay, the charge-changing reaction $p\gamma \rightarrow n\pi^+$ occurs in the ratio 1 : 2 compared to the reaction $p\gamma \rightarrow p\pi^0$ where an outgoing proton is produced. More massive resonances also contribute (the usual convention is that Δ resonances refer to isospin 3/2 particles, and N resonances to isospin 1/2 particles). The suite of baryonic resonances in $p\gamma$ reactions include the $N^+(1440)$, $N^+(1520)$, $N^+(1535)$, $N^+(1650)$, $N^+(1680)$, $\Delta^+(1700)$, $\Delta^+(1905)$, and $\Delta^+(1950)$ resonances [189]. Higher-mass resonances, such as Σ and Λ , contribute less significantly in astrophysical calculations.

2. Direct Production

This channel refers to residual, nonresonant contributions to direct two-body channels consisting of outgoing charged pions. These include the reactions $p\gamma \rightarrow n\pi^+$, $p\gamma \rightarrow \Delta^{++}\pi^-$, and $p\gamma \rightarrow \Delta^0\pi^+$. This channel contributes nearly 30% to the total photohadronic cross section for $\approx 0.25 \text{ GeV} \lesssim \sqrt{s_{\text{int}}} \lesssim 1 \text{ GeV}$. Channels with no change of the isospin I_3 vector are strongly suppressed, so that $p\gamma \rightarrow n\pi^+$ entirely dominates for this channel. This enhances the conversion of the protons to neutrons, and also

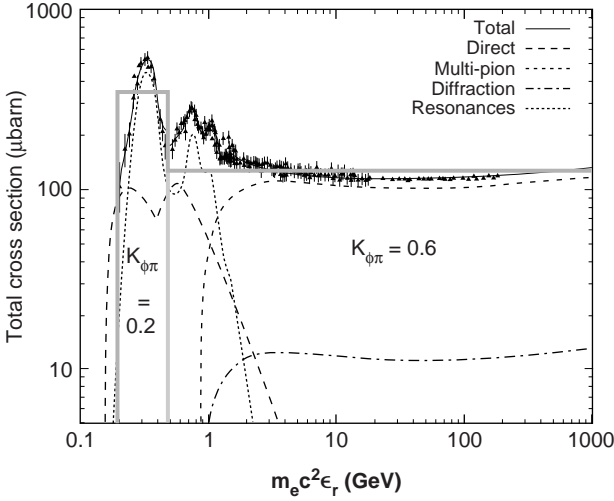


Figure 9.2 Data show the total inelastic $p\gamma$ photomeson production cross section [186,187] as a function of the photon's energy in the proton rest frame, and light curves show separate contributions of baryon resonances, the direct single-pion channel, diffractive scattering, and multipion production ($1 \mu\text{barn} = 10^{-30} \text{cm}^{-2}$; data from Ref. [188] and references therein). (Cross section figure courtesy of Anita Reimer.) Also shown by thick lines is the two-step-function approximation used in the analysis, consisting of a single-pion near-threshold channel between 200 and 500 GeV, and a multipion channel at energies $\sqrt{s_{\text{int}}} = \epsilon_r \geq 980 m_e c^2 = 500 \text{MeV}$. The inelasticities of the two channels are labeled.

increases the amount of energy in neutrinos compared to Δ^+ excitation and decay.

3. Multipion Production

Multipion production may be treated as a statistical process or expressed in terms of a scaling function, and is simulated in the SOPHIA code [187] using QCD fragmentation models.

4. Diffraction

Diffractive scattering couples photons to heavier vector mesons ρ^0 and ω .

9.2.2 Analytic Expression for Photopion Cross Section

To derive analytic expressions for total and secondary production cross sections, we follow the approach of Ref. [95] where the photopion process is approximated by the sum of two channels. In the (i) *single-pion resonance*

channel, the proton loses 20% of its energy on average through the reactions

$$p + \gamma \rightarrow \Delta^+ \rightarrow \begin{cases} p + \pi^0 \rightarrow p + 2\gamma, \\ n + \pi^+ \rightarrow n + e + 3\nu \rightarrow p + 2e + 4\nu, \end{cases}$$

with the two decay channels occurring at roughly the same rate in single-pion production.¹ In the (ii) *multipion channel*, the proton loses on average 60% of its initial energy, which is assumed to be equally divided into secondary π^0 , π^+ , and π^- particles. In the $p + \gamma \rightarrow p + \pi^0$ channel, the neutral pion decays into two γ rays, each with $\approx 10\%$ of the energy of the initial proton. Following production, the γ rays can materialize into e^+e^- pairs through the $\gamma\gamma \rightarrow e^+e^-$ absorption process, initiating an electromagnetic synchrotron/Compton/pair-production cascade.

In the $p + \gamma \rightarrow n + \pi^+$ channel, the decay of the charged pion produces three neutrinos and a positron in the reaction chain

$$\pi^+ \rightarrow \mu^+ + \nu_\mu, \quad \text{followed by the decay } \mu^+ \rightarrow e^+ + \nu_e + \bar{\nu}_\mu$$

(eqs. [8.53] and [8.54]). The neutron decays with a mean life $t_n \cong 886$ s [190] through the β -decay reaction

$$n \rightarrow p + e^- + \bar{\nu}_e. \quad (9.7)$$

The β -decay electron and neutrino have energies ≈ 1 MeV in the neutron's rest frame. In a single $p\gamma$ interaction leading to the production of a single π^+ , four neutrinos and two leptons are formed, with one of the neutrinos and one of the leptons having ≈ 50 times less energy than the others. Associated with electron β -decay is the less frequent channel known as inner bremsstrahlung, where radiation is produced from an abrupt transition in the nucleus. This energy, taken at the expense of the neutrino, produces weak secondary radiation.

We adopt a two step-function approximation [95,191] for the photopion cross section, given by

$$\sigma_{\phi\pi}(\epsilon_r) = \begin{cases} 340 \mu\text{b}, & \epsilon_{\text{thr}} = 390 \leq \epsilon_r \leq 980, \\ 120 \mu\text{b}, & \epsilon_r \leq 980, \end{cases} \quad (9.8)$$

and inelasticity

$$K_{\phi\pi}(\epsilon_r) = \begin{cases} 0.2, & 390 \leq \epsilon_r \leq 980, \\ 0.6, & \epsilon_r \leq 980; \end{cases} \quad (9.9)$$

¹Isospin statistics for this reaction give a ratio of 1:2 for the $p\gamma \rightarrow n\pi^+$ to $p\gamma \rightarrow p\pi^0$ rate; addition of the direct production channel increases the rate of the charge-changing reaction.

see figure 9.2. Hence

$$\hat{\sigma}_{\phi\pi} \equiv \sigma_{\phi\pi}(\epsilon_r) K_{\phi\pi}(\epsilon_r) \equiv \sigma_1 K_1 H(\epsilon_r - 390) \cong 70 H(\epsilon_r - 390) \mu\text{b}, \quad (9.10)$$

so $\sigma_1 K_1 \cong 70 \mu\text{b}$. Equation (9.10) provides a very versatile expression for estimating photopion energy losses for a wide range of problems.

In this approximation, the lower-energy step function approximates $\Delta(1232)$ resonance production and direct single-pion production processes, and the higher-energy step function approximates the multiphoton production process. For the Δ resonance, isospin statistics imply [192] a charge-changing ratio of 1/3 for single resonance production, but the addition of the single-pion channel, which favors the charge-changing reaction $p\gamma \rightarrow n\pi^+$, adds so that the net charge-changing probability is about equal to half of the total single-pion cross section. Thus the net resonance and single-pion channels cross sections for the $p\gamma$ process leading to a $n\pi^+$ final state is about equal to that leading to a $p\pi^0$ final state. In the multipion limit, π^+ , π^- , and π^0 are assumed to be produced in equal numbers, with the energy losses being equally distributed into the decay products consisting of leptons, neutrinos, and γ quanta.

9.2.3 Numerical Calculation of Photopion Cross Section

The cross section shown in figure 9.2 can be represented by a superposition of resonance structures, expressed as a Breit-Wigner function in the form

$$\sigma_{\Delta}(s; m_{\Delta}, \Delta, J) = \frac{\pi b_{\gamma}(2J+1)}{m_{\Delta}^2} \frac{\Delta^2 s^2}{\epsilon'^2 [(s - m_{\Delta}^2)^2 + s\Delta^2]}, \quad (9.11)$$

where ϵ' is the photon energy,

$$s = m^2 + 2m\epsilon',$$

m is the mass of the proton or ion, b_{γ} is the branching ratio, J is the angular momentum of the resonance, m_{Δ} is the resonance mass, and Δ is the resonance width. See Ref. [186] for tables of resonance masses and widths.

9.2.4 Photopion Energy-Loss Rate

Using approximation (9.10) and the CMB photon spectrum, eq. (9.6), in eq. (9.5) gives the photopion energy-loss timescale

$$t_{\phi\pi}^{-1}(\gamma_p) \cong \frac{8\pi c\sigma_1 K_1 \Theta^3}{\lambda_C^3} \int_{\omega}^{\infty} dy \frac{y^2 - \omega^2}{\exp(y) - 1}, \quad (9.12)$$

which is the inverse of the photopion energy-loss rate. The parameter

$$\omega = \frac{\epsilon_{\text{thr}}}{2\gamma_p\Theta} = \frac{4.0}{E_{20}(1+z)} \quad (9.13)$$

characterizes the different regimes of interactions of an ultrarelativistic cosmic-ray proton with energy $E_p = \gamma_p m_p c^2 = 10^{20} E_{20}$ eV with the low- and high-energy regimes of the target blackbody photons. The sub-GZK regime, where most $\phi\pi$ interactions are with the exponentially declining number of photons in the Wien regime, is defined by the condition $E_{20} \ll 4/(1+z)$ or $\omega \gg 1$. The super-GZK regime involving the highest-energy UHECR protons interacting with the target CMBR photons in the Rayleigh-Jeans portion of the spectrum is defined by $E_{20} \gg 4/(1+z)$ or $\omega \ll 1$, where $E_{20} \equiv E_p/10^{20}$ eV.

The asymptotes of the integral in eq. (9.12) in the $\omega \ll 1$ and $\omega \gg 1$ regimes (protons primarily interacting with the Rayleigh-Jeans and Wien portions of the CMBR, respectively) are

$$I = \int_{\omega}^{\infty} dy \frac{y^2 - \omega^2}{\exp(y) - 1} \rightarrow \begin{cases} \Gamma(3)\zeta(3) + \omega^2[\ln(1 - e^{-\omega}) - \frac{1}{2}], & \omega \ll 1, \\ 2(1 + \omega)e^{-\omega}, & \omega \gg 1, \end{cases} \quad (9.14)$$

where $\zeta(x)$ and $\Gamma(x)$ are Riemann's zeta function and the Gamma function, respectively, and $\Gamma(3)\zeta(3) = 2.4041 \dots$ (see Appendix B).

Substituting the $\omega \gg 1$ ($\gamma_p \ll \epsilon_{\text{thr}}/2\Theta$) asymptote into eq. (9.12), and rewriting the result in terms of the mean energy-loss length $r_{\phi\pi} = ct_{\phi\pi}$ for a proton with energy $10^{20} E_{20}$ eV, gives the result

$$r_{\phi\pi}(E_{20}) \cong \frac{13.7 \exp[4.0/E_{20}(1+z)]}{(1+z)^3 [1 + 4.0/E_{20}(1+z)]} \text{ Mpc}, \quad E_{20} \ll \frac{4}{1+z}. \quad (9.15)$$

In the opposite regime,

$$r_{\phi\pi}(E_{20}) \cong \frac{27.4 \text{ Mpc}}{(1+z)^3 \{\Gamma(3)\zeta(3) + \omega^2[\ln(1 - e^{-\omega}) - \frac{1}{2}]\}}, \quad E_{20} \gg \frac{4}{1+z}. \quad (9.16)$$

Figure 9.3 shows the low-energy asymptote for photopion losses on the CMBR at $z = 0$, compared with detailed calculations [193] of the photohadronic energy-loss pathlength. Equation (9.15) gives an excellent approximation in the regime $E_{20} \lesssim 4/(1+z)$, which is most relevant for the energy losses of UHECRs in intergalactic space and for production of GZK neutrinos [194]. The $\omega \gg 1$ asymptote is found to provide a reasonable approximation even at $\omega \ll 1$. Also shown are numerical calculations of photopair energy losses of UHECR protons with CMB photons, and photopion and photodisintegration energy-loss rates of Fe in the CMBR, as described below.

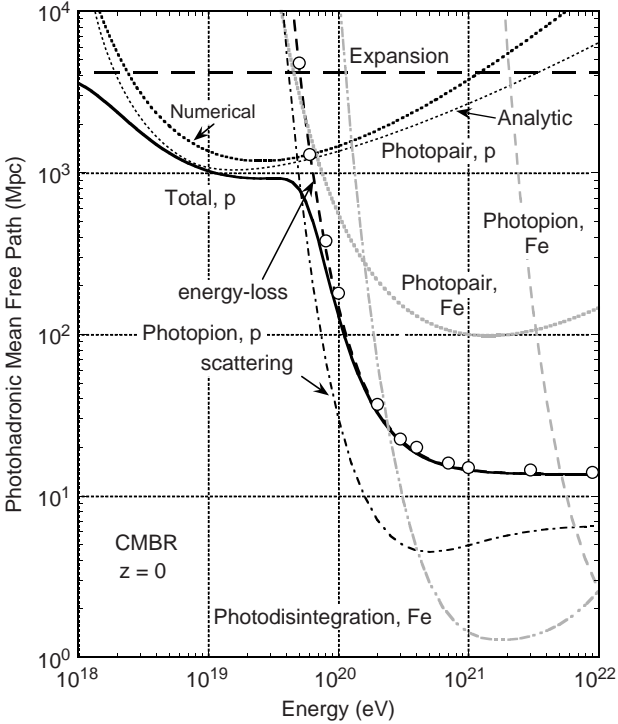


Figure 9.3 Photohadronic mean free paths for scattering, energy loss, and photodisintegration of UHECR protons and Fe in the CMBR at $z = 0$ as a function of total particle energy. The analytical approximations, eq. (9.15) and eqs. (9.30)–(9.34) for the photopion, $r_{\phi\pi}$, and photopair, $r_{\phi e}$ (with $k_{\phi e} = 1$) energy-loss pathlengths, of UHECR protons are shown by the dashed and light-dotted curves, respectively. Numerical results for $r_{\phi e}$ of UHECR protons and Fe are shown by the heavy dotted and shaded dotted curves, respectively. Open circles show numerical results [193] for the UHECR proton pathlength $r_{\phi\pi}$. Shaded dot-dashed and shaded dashed curves show the photodisintegration and photopion energy loss mean free path of UHECR Fe in the CMBR. Solid curve shows the total UHECR proton energy-loss length in the CMBR. Dot-dashed curve shows the photopion scattering MFP for UHECR protons.

9.2.5 GZK Energy

UHECR protons accelerated by distant sources lose a large fraction of their energy due to photopion interactions with photons of the CMB. For UHECR protons, we define the GZK energy by equating the Hubble radius

$$c/H_0 \cong (3 \times 10^5 / 72) \text{ Mpc} \cong 4170 \text{ Mpc} \cong 1.3 \times 10^{28} \text{ cm}$$

with the asymptotic form of the GZK photopion energy-loss mean free path in the low-redshift $z \ll 1$ limit, eq. (9.15),

$$r_{\phi\pi}(E_{20}) \cong \frac{13.7 \exp(4.0/E_{20})}{(1 + 4.0/E_{20})} \text{Mpc}. \quad (9.17)$$

The resulting transcendental equation $e^u/(1+u) = 4170/13.7 = 304$ has solution $4/E_{20} = 7.9 \dots$. The cosmic-ray *proton* GZK energy is therefore

$$E_{\text{GZK}} \cong 5 \times 10^{19} \text{eV}. \quad (9.18)$$

Even when the full extragalactic background radiation field, effects of photopair production [195], a more precise definition of the horizon (chapter 17), and photodisintegration of UHECR ions are considered, a similar value is obtained for the GZK radius. This led Greisen [10] and Zatsepin and Kuzmin [11] to argue for the end to the cosmic-ray spectrum at $E \approx 10^{20}$ eV.

9.2.6 Stochastic and Continuous Energy Losses

When the fractional energy loss per collision is large, as in photomeson production, bremsstrahlung, and Compton scattering in the Klein-Nishina regime, there are large deviations in the energy evolution of any given particle. In photomeson production, where the multipion inelasticity $K_{\phi\pi} \approx 0.6$, this introduces an additional stochastic scatter broadening of the evolving cosmic-ray proton flux beyond that given by a continuous energy-loss treatment. A Monte Carlo simulation is required for the most reliable calculations (see Appendix D). The semi-analytic model presented here gives reasonably accurate results of calculations of the UHECR spectrum and the energy distributions of outgoing secondaries.

When fractional energy loss per interaction is small, as in photopair production or Compton scattering in the Thomson limit, the energy evolution of a given particle can be accurately characterized analytically and numerically. Even for stochastic energy losses, the average energy lost can still be modeled reasonably well with an analytic approach employing average energy-loss rates [196].

9.3 PHOTOPAIR PROCESS

Now we consider the photopair reaction

$$p + \gamma \rightarrow p + e^+ + e^-,$$

which is a specific case of Bethe-Heitler pair production by a photon in the field of a charged nucleus, in this case, a singly ionized proton. In the field

of an ion, the energy-loss rate is proportional to Z^2 . This process is closely related to triplet pair production $e + \gamma \rightarrow e + e^+ + e^-$ [197]. Accurate treatments of the photopair process are given in Refs. [198] and [199], to which we return at the end of this section. Here we provide an alternative semianalytic treatment for the photopair process that yields asymptotic expressions for the rate and energy-loss behavior, following a simplified approach to triplet pair production [200].

9.3.1 Photopair Cross Section

Fits to the derived [201] cross section $\sigma_{\phi e}(\epsilon_r)$ for photopair production are given in Ref. [202]. The high-energy ($\epsilon_r \gg 1$) asymptote is

$$\sigma_{\phi e}(\epsilon_r) \cong \frac{7}{6\pi} \alpha_f \sigma_T \left(\ln 2\epsilon_r - \frac{109}{42} \right). \quad (9.19)$$

This suggests that we use the approximation

$$\sigma_{\phi e}(\epsilon_r) \approx \frac{7}{6\pi} \alpha_f \sigma_T \ln \left(\frac{\epsilon_r}{k_{\phi e}} \right), \quad (9.20)$$

where $k_{\phi e}$ is an adjustable constant. To obtain the correct high-energy asymptote, $\ln 2k_{\phi e} = 109/42$, implying $k_{\phi e} \cong 6.70$. For the cross section to vanish at threshold, $k_{\phi e} = 2$. Thus we expect $2 \lesssim k_{\phi e} \lesssim 6.7$ to give a good approximation, though we even consider a larger range of $k_{\phi e}$ to provide an adjustable parameter to improve the fit (see the inset to figure 9.4).

9.3.2 Photopair Energy-Loss Timescale

Consider a proton with Lorentz factor γ_p traveling in the $+\hat{x}$ direction that interacts with a photon with dimensionless energy ϵ directed at an angle θ with respect to the proton's momentum, as shown in figure 9.4. The invariant energy of the collision $\epsilon_r = \gamma_p \epsilon (1 - \beta_p \mu)$, eq. (9.2).

The e^+e^- pair is assumed to be formed at rest in the equal x -momentum frame of the collision [200]. The proton's dimensionless x -momentum, when transformed to the equal-momentum (K') frame found by boosting by the Lorentz factor $\gamma = (1 - \beta^2)^{-1/2}$ and speed βc along the \hat{x} -axis, is simply $p_x = \gamma \gamma_p (1 - \beta \beta_p)$. In the K' frame, the photon x -momentum is $\epsilon' \mu' = \gamma \epsilon (\mu - \beta)$, using the Lorentz transformation equations $\epsilon' = \gamma \epsilon (1 - \beta \mu)$ and $\mu' = (\mu - \beta)/(1 - \beta \mu)$. In the K' frame, therefore, $\beta_p \gamma_p - \beta \gamma_p = \beta \epsilon - \mu \epsilon$, so that

$$\gamma = \frac{\epsilon + \gamma_p}{\sqrt{(\epsilon + \gamma_p)^2 - (\beta_p \gamma_p + \epsilon \mu)^2}} \quad \text{and} \quad \beta = \frac{\beta_p \gamma_p + \epsilon \mu}{\epsilon + \gamma_p}. \quad (9.21)$$

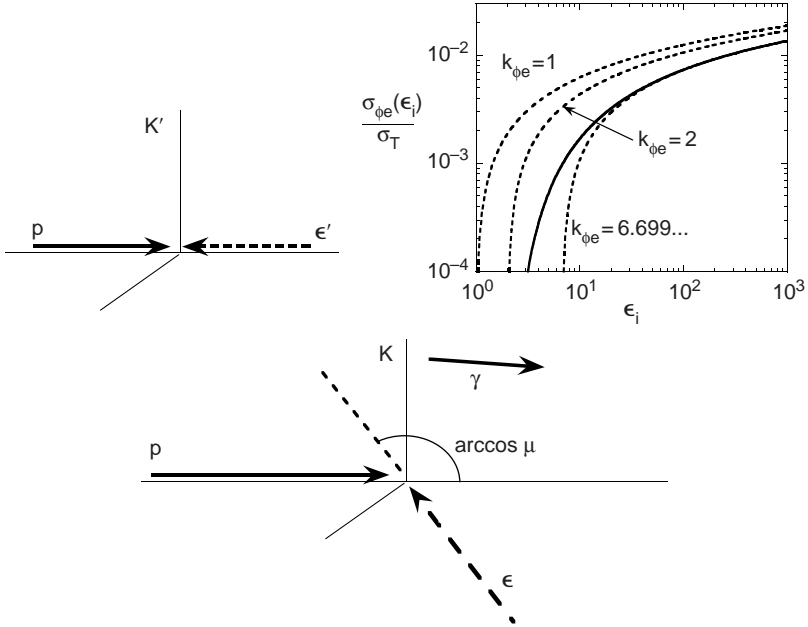


Figure 9.4 Geometry of the proton photopair process $p\gamma \rightarrow p + e^+ + e^-$. In system K , a proton with Lorentz factor γ_p interacts with a photon to produce an electron-positron pair. The proton-photon system is boosted by Lorentz factor γ to the equal- x -momentum frame K' . Inset shows the photopair cross section as a function of the invariant photon energy ϵ' (solid curve), and approximation (9.20) to the cross section for $k_{\phi e} = 1, 2$, and 6.70 , as labeled.

Equation (9.21) implies

$$\gamma = \frac{\epsilon + \gamma_p}{\sqrt{1 + 2\epsilon_r + \epsilon^2(1 - \mu^2)}} \rightarrow \frac{\gamma_p}{\sqrt{1 + 2\epsilon_r}} \tag{9.22}$$

in the regime $\epsilon \ll \epsilon_r$ considered here.

Assuming that the e^+e^- pair is formed at rest in the equal-momentum frame, the mean Lorentz factor of the produced pair is

$$\langle \gamma \rangle = \frac{\gamma_p}{\sqrt{1 + 2\epsilon_r}}. \tag{9.23}$$

The threshold condition $\epsilon_r \geq 2$ implies $\gamma_p \epsilon (1 - \beta_p \mu) \geq 2$, so that $\mu \leq \mu_{\text{th}} \equiv (\epsilon \gamma_p - 2) / \beta_p \gamma_p \epsilon$. In this approximation, the energy-loss rate of a

proton due to photopair production is

$$\begin{aligned}
 L_{\phi e}(\gamma_p) &\cong c \int_0^\infty d\epsilon \oint d\Omega n_{\text{ph}}(\epsilon, \Omega) (1 - \beta_p \mu) \sigma_{\phi e}(\epsilon_r) \cdot 2m_e c^2 \langle \gamma \rangle \\
 &\cong \frac{m_e c^3}{\gamma_p} \int_{\gamma_p^{-1}}^\infty d\epsilon \frac{n_{\text{ph}}(\epsilon)}{\epsilon^2} \int_2^{2\gamma_p \epsilon} d\epsilon_r \epsilon_r \frac{\sigma_{\phi e}(\epsilon_r)}{\sqrt{1+2\epsilon_r}}, \quad (9.24)
 \end{aligned}$$

where the last expression holds for isotropic photon targets. Note that the conditions $\epsilon_r \geq 2$ and $\mu_{\text{th}} \geq -1$ imply $\epsilon \geq \gamma_p^{-1}$.

Substituting eq. (9.19) into eq. (9.24), and considering the high-energy regime $\epsilon_r \gg 1$ so that $\sqrt{1+2\epsilon_r} \approx \sqrt{2\epsilon_r}$, we obtain the inverse of the timescale for photopair energy loss, namely the ϕe energy-loss rate, given by

$$\begin{aligned}
 t_{\phi e}^{-1}(\gamma_p) &= \left(\frac{L_{\phi e}(\gamma_p)}{m_p c^2 \gamma_p} \right) \cong \frac{7m_e \alpha_f c \sigma_T}{9\sqrt{2}\pi m_p \gamma_p^2} \int_{\gamma_p^{-1}}^\infty d\epsilon \frac{n_{\text{ph}}(\epsilon)}{\epsilon^2} \\
 &\quad \times \left\{ (2\gamma_p \epsilon)^{3/2} \left[\ln \left(\frac{2\gamma_p \epsilon}{k_{\phi e}} \right) - \frac{2}{3} \right] + \frac{2}{3} k_{\phi e}^{3/2} \right\}. \quad (9.25)
 \end{aligned}$$

Substituting eq. (9.6) for the CMBR field into eq. (9.25) gives the result

$$\begin{aligned}
 t_{\phi e}^{-1}(\gamma_p) &\cong \frac{112}{9} \frac{m_e}{m_p} \frac{\alpha_f c \sigma_T}{\lambda_C^3} \frac{\Theta^{5/2}}{\gamma_p^{1/2}} \\
 &\quad \times \left\{ I_\ell + \left[\ln \left(\frac{2\gamma_p \Theta}{k_{\phi e}} \right) - \frac{2}{3} \right] I_{3/2} + \frac{2}{3} \left(\frac{k_{\phi e}}{2\gamma_p \Theta} \right)^{3/2} I_0 \right\}. \quad (9.26)
 \end{aligned}$$

Defining

$$\mathfrak{b} \equiv \frac{1}{\gamma_p \Theta}, \quad (9.27)$$

then

$$I_\ell \equiv \int_{\mathfrak{b}}^\infty dx \frac{x^{3/2} \ln x}{\exp(x) - 1} \rightarrow \begin{cases} 0.74, & \mathfrak{b} \ll 1, \\ \mathfrak{b}^{3/2} \ln \mathfrak{b} \exp(-\mathfrak{b}), & \mathfrak{b} \gg 1, \end{cases} \quad (9.28)$$

$$I_{3/2} \equiv \int_{\mathfrak{b}}^\infty dx \frac{x^{3/2}}{\exp(x) - 1} \rightarrow \begin{cases} \Gamma(5/2)\zeta(5/2) \cong 1.783, & \mathfrak{b} \ll 1, \\ \mathfrak{b}^{3/2} \exp(-\mathfrak{b}), & \mathfrak{b} \gg 1, \end{cases} \quad (9.29)$$

and

$$I_0 \equiv \int_{\mathfrak{b}}^\infty dx [\exp(x) - 1] = -\ln[1 - \exp(-\mathfrak{b})]. \quad (9.30)$$

Expressions bridging the low- and high-energy asymptotes in eqs. (9.28) and (9.29) are

$$I_\ell \cong (0.74 + b^{3/2} \ln b) \exp(-b) \quad (9.31)$$

and

$$I_{3/2} \cong [\Gamma(5/2)\zeta(5/2) + b^{3/2}] \exp(-b), \quad (9.32)$$

respectively.

Equation (9.26) can also be expressed in terms of energy-loss length $r_{\phi e} = ct_{\phi e}$ for photopair losses, noting that $7 \cdot 2^4 m_e \alpha_f c \sigma_T / 9 m_p \lambda_C^3 = 6.90 \times 10^{10} \text{ s}^{-1}$, $\gamma_p \Theta = 0.488 E_{18}(1+z)$, and $E_{18} = E_p / 10^{18} \text{ eV}$. The result is

$$r_{\phi e}(E_{20}) = \frac{1.02 E_{18}^{1/2}}{(1+z)^{5/2} \mathcal{F}_{\phi e}(E_{18})} \text{ Gpc}, \quad (9.33)$$

where

$$\mathcal{F}_{\phi e}(E_{18}) = I_\ell + I_{3/2} \ln \left(\frac{E_{18}(1+z)}{2k_{\phi e}} \right) + 0.69 I_0 \left(\frac{k_{\phi e}}{(1+z)E_{18}} \right)^{3/2}. \quad (9.34)$$

The principal energy dependence of the photopair energy-loss length in the $b \ll 1$ or $\gamma_p \gg \Theta^{-1}$ regime is $r_{\phi e} \propto E_{18}^{1/2}$, which applies when $E_{18} \gtrsim [(1+z)/k_{\phi e}]^{2/3}$. The principal redshift dependence of $r_{\phi e}$ in the $\gamma_p \gg \Theta^{-1}$ regime is $r_{\phi e} \propto (1+z)^{-5/2}$, though $r_{\phi e} \propto (1+z)^{-3}$ at the dip or trough energy at $E_{18} \approx 20/(1+z)$.

A comparison of this analytic expression for $r_{\phi e}$ at $z = 0$ with the more detailed results [193,199] is shown in figure 9.5 with $k_{\phi e} = 1$, and with I_0 , I_ℓ , and $I_{3/2}$ given by eqs. (9.30)–(9.32). The pair production trough is at $(2-3) \times 10^{19} \text{ eV}$ when $z \rightarrow 0$. The deviation of the analytic approximation from the accurate calculation at energies above the minimum photopair length is unimportant because there photopion losses dominate.

9.3.3 Accurate Expression for Photopair Energy-Loss Rates of Ions in an Isotropic Radiation Field

The energy-loss rate due to photopair production of UHECR ions with charge Ze , mass Am_p , and Lorentz factor γ is given by

$$-\left(\frac{dE}{dt} \right)_{\phi e} = -Am_p c^2 \left. \frac{d\gamma}{dt} \right|_{\phi e} = \alpha_f r_e^2 c Z^2 m_e c^2 \int_2^\infty d\epsilon n_{\text{ph}} \left(\frac{\epsilon}{2\gamma} \right) \frac{\varphi(\epsilon)}{\epsilon^2} \quad (9.35)$$

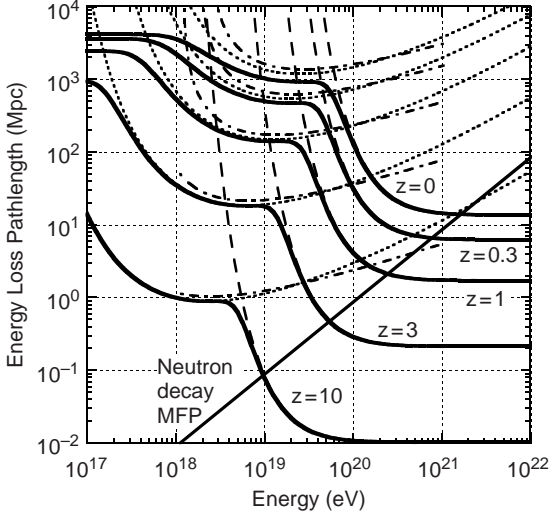


Figure 9.5 Total energy-loss mean free paths of UHECR protons interacting with photons of the CMBR, as a function of proton energy for different redshifts $z = 0, 0.3, 1, 3,$ and 10 . The total energy-loss MFP is shown by the solid curves, and is comprised of effects of adiabatic expansion, photopion (dashed curves), and photopair (dotted curves) energy losses. The analytic expression for the mean photopion energy-loss MFP, $r_{\phi\pi}$, eq. (9.15), and numerical values of $r_{\phi e}$, section 9.3.3, are used to derive the total energy-loss MFP. Analytic expressions for photopair losses, given by eq. (9.26) and eqs. (9.30)–(9.34), are shown by the dot-dashed curves as a function of proton energy at different redshifts. Expansion losses are obtained from eq. (9.42). The energy-loss trough formed by the three loss processes is at $\approx 10^{19}/(1+z)$ eV. The solid line gives the decay MFP of relativistic neutrons as a function of energy.

[198] when traveling through an isotropic radiation field denoted by $n_{\text{ph}}(\epsilon)$. To accuracy better than 1.5×10^{-3} , the fitting functions

$$\varphi(\epsilon) \cong \frac{\pi}{12} \frac{(\epsilon - 2)^4}{1 + \sum_{i=1}^4 c_i (\epsilon - 2)^i} \quad \text{for } 2 \leq \epsilon < 25, \quad (9.36)$$

where $c_1 = 0.8048$, $c_2 = 0.1459$, $c_3 = 1.137 \times 10^{-3}$, $c_4 = -3.879 \times 10^{-6}$, and

$$\varphi(\epsilon) \cong \frac{\epsilon \sum_{i=0}^3 d_i (\ln \epsilon)^i}{1 - \sum_{i=1}^3 f_i \epsilon^{-i}} \quad \text{for } \epsilon \geq 25, \quad (9.37)$$

where $d_0 \cong -86.07$, $d_1 \cong 50.96$, $d_2 \cong -14.45$, $d_3 = 8/3$, $f_1 = 2.910$, $f_2 = 78.35$, and $f_3 = 1837$, are convenient to use [199].

The characteristic energy-loss pathlength for ions losing energy through photopair losses with photons of a surrounding isotropic radiation field is

$$r_{\phi e} = ct_{\phi e} = c \left| \frac{1}{E} \left(\frac{dE}{dt} \right)_{\phi e} \right|^{-1}. \quad (9.38)$$

9.3.4 Relative Importance of Photopion and Photopair Losses

From eq. (9.23), the photopair inelasticity is

$$K_{\phi e} \cong \frac{2m_e}{m_p \sqrt{1 + 2\epsilon_r}} \simeq \frac{m_e}{m_p} \quad (9.39)$$

for reactions near threshold. The product of the inelasticity and the cross section for photopair production is $K_{\phi e} \sigma_{\phi e} \cong (m_e/m_p) \alpha_f \sigma_T \cong 2.6 \mu\text{b}$, which can be compared with $\hat{\sigma} = 70 \mu\text{b}$ for photopion losses. Hence the relative photopion and photopair energy-loss rates for protons interacting with the peak of the νF_ν spectrum of the target photon distribution is

$$\frac{K_{\phi\pi} \sigma_{\phi\pi}}{K_{\phi e} \sigma_{\phi e}} \approx 100.$$

Considering the different threshold behaviors, this explains the relative energy-loss rates at $E_p \cong 4 \times 10^{20}/(1+z)$ eV for photopion production and at $E_p \cong 2 \times 10^{19}/(1+z)$ eV for photopair production, as can be seen from figure 9.5.

9.4 EXPANSION LOSSES

Radiation undergoes adiabatic energy losses from the expansion of the universe, as do particles coupled with the background radiation in intercluster space. However, particles found in regions decoupled from the Hubble flow, like clusters of galaxies, will experience losses that depend on the behavior of this flow. Thus universal expansion losses need not apply to a particle during certain episodes of its life history, as UHECRs may become trapped in the cluster environment for a long time before escaping to intercluster space.

From the first law of thermodynamics for an adiabatic system, namely, a closed expanding system with no addition of heat energy Q ,

$$dQ = 0 = dU + p dV, \quad (9.40)$$

where $U = uV$ is the total internal energy, u is the energy density, p in this section is pressure (not momentum), and V is the volume. Hence $(u + p)dV = -V du$. For a relativistic gas consisting of either particles or

photons, $p = u/3$ (eq. [5.4]), so that $u \propto V^{-4/3}$ or $U \propto V^{-1/3} \propto R^{-1}$, where R is the size (or scale factor) of the universe. Thus the energy of particles in a relativistic gas changes according to the relation $dU \rightarrow d\gamma \propto -R^{-2}dR$, and

$$-\frac{\dot{\gamma}}{\gamma} = \frac{1}{R} \frac{dR}{dt} = \frac{1}{3} \frac{d \ln V}{dt}. \quad (9.41)$$

In eq. (9.41), the result $dV/V = dx/x + dy/y + dz/z = 3dR/R$ is used, implying that the characteristic cosmic expansion timescale is $\approx 1/(3H_0) \approx 4.5 \times 10^9$ yr. If one solves a continuity equation for the evolution of particle spectra defined in terms of proper differential density $n_*(\gamma_*)$, then a term $-3H_0 n_*(\gamma_*)$, representing the change in the volume element due to volume expansion must be included; this term is omitted if the density is defined in terms of comoving coordinates [132].

From eqs. (4.32) and (9.41), the energy-loss rate of a particle of mass m due to the expansion of the universe is given by $mc^2\dot{\gamma}_{\text{exp}}$, where

$$-\dot{\gamma}_{\text{exp}}(z) = (1+z)^{-1} \left| \frac{dz}{dt} \right| \gamma = H_0 \sqrt{\Omega_m(1+z)^3 + \Omega_\Lambda} \gamma. \quad (9.42)$$

Figure 9.5 shows the analytic expression for the loss lengths $r_{\phi\pi}$ and $r_{\phi e}$ at various redshifts, with the total including adiabatic energy losses, for $H_0 = 72 \text{ km s}^{-1} \text{ Mpc}^{-1}$, $\Omega_\Lambda = 0.73$, and $\Omega_m = 0.27$.

9.5 COSMOGENIC NEUTRINO FLUX

Following section 4.5, we define the photon or neutrino emissivity by the expression $\dot{n}_*^i(\epsilon_*, \Omega_*; z)$, where the quantity $\dot{n}_*^i(\epsilon_*, \Omega_*; z)d\epsilon_* dt_* d\Omega_* dV_*$ is the differential number of secondaries of type i with energies between ϵ_* and $\epsilon_* + d\epsilon_*$ that are emitted from differential volume dV_* during differential time dt_* and directed into differential solid angle $d\Omega_*$ in the direction of Ω_* . The starred quantities refer to proper frame emission. The function $\dot{n}_*^i(\epsilon_*, \Omega_*; z)$ is described in the proper frame at rest in the Hubble flow at redshift z (measured using meter sticks and clocks) and is related to the comoving emissivity (yardsticks expand with the universe) through the relation $\dot{n}_{co}^i(\epsilon_*, \Omega_*; z) = (1+z)^{-3} \dot{n}_*^i(\epsilon_*, \Omega_*; z)$, where $\epsilon_* = (1+z)\epsilon$, and ϵ is the measured photon or particle energy.

The energy intensity of secondaries of type i , for example, neutrinos, leptons, or photons, from a distribution of sources described by this emissivity function is given by

$$\epsilon I_\epsilon^i = \frac{c}{4\pi} \int_0^\infty dz \left| \frac{dt_*}{dz} \right| \oint d\Omega_* \frac{\epsilon_*^2 \dot{n}_{co}^i(\epsilon_*, \Omega_*; z)}{(1+z)}, \quad (9.43)$$

from eq. (4.56). In this expression, the independent energy variable ϵ_* can just as well have photon or particle energies in physical units, e.g., ergs or GeV.

Let the differential density of UHECR protons at redshift z be given by the function

$$n_p(\gamma_p, \Omega_p; z) = \frac{dN_p(\gamma_p, \Omega_p; z)}{d\gamma_p dV d\Omega_p}. \quad (9.44)$$

From eq. (2.42), the emissivity of secondary i , where i refers to neutrinos (ν), electrons and positrons (e), γ rays (γ), neutrons (n), and protons (p), is

$$\begin{aligned} \dot{n}_*^i(\epsilon_*, \Omega_*; z) = c \oint d\Omega \int_0^\infty d\epsilon_\gamma n_{ph}(\epsilon_\gamma, \Omega; z) \\ \times \oint d\Omega_p \int_1^\infty d\gamma_p n_p(\gamma_p, \Omega_p; z) (1 - \beta_p \cos \psi) \frac{d\sigma_i(\epsilon')}{d\epsilon_* d\Omega_*}, \end{aligned} \quad (9.45)$$

where $\cos \psi = \mu\mu_p + \sqrt{1 - \mu^2} \sqrt{1 - \mu_p^2} \cos(\phi - \phi_p)$, $\epsilon' = \gamma_p \epsilon_\gamma (1 - \beta_p \cos \psi)$ is the invariant collision energy, and $[d\sigma_i(\epsilon')/d\epsilon_* d\Omega_*] d\epsilon_* d\Omega_*$ is the differential cross section for producing secondaries with energies between ϵ_* and $\epsilon_* + d\epsilon_*$ into the solid angle element $d\Omega_*$ in the direction Ω_* . Here we let the secondary energy be given in physical units and the target photon energy ϵ_γ be described in dimensionless units.

Following the description of photohadronic interactions, we approximate the secondary production cross section for the single-pion (s) and multipion (m) channels by the expression

$$\frac{d\sigma_i^{s,m}(\epsilon')}{d\epsilon_* d\Omega_*} \cong \zeta_i^{s,m} \sigma_{\phi\pi}^{s,m} H(\epsilon'_l; \epsilon'_l, \epsilon'_u) \delta(\Omega_* - \Omega_p) \delta(\epsilon_* - \chi_i^{s,m} m_p c^2 \gamma_p), \quad (9.46)$$

where $\zeta_i^{s,m}$ is the multiplicity of secondary i , and $\chi_i^{s,m}$ is the mean fractional energy of the produced secondary compared to the incident primary proton. For secondaries formed in single-pion production, $\sigma_{\phi\pi}^s = 340 \mu\text{b}$, $\epsilon'_l = 390$, and $\epsilon'_u = 980$, whereas for neutrinos produced in multipion production, $\sigma_{\phi\pi}^m = 120 \mu\text{b}$, $\epsilon'_l = 980$, and $\epsilon'_u \rightarrow \infty$. In both cases, $\chi_\nu = 1/20$. Table 9.1 gives the mean multiplicities and fractional energies of secondaries formed in the single- and multipion channels, consistent with the assumed inelasticity and number of decay products. These channels also include neutron β -decay electrons and neutrinos. This assumes that neutrons will decay before undergoing a further photohadronic interaction. For the propagation of UHECRs in galaxy cluster fields or interstellar space, this is a good approximation for $\gtrsim 10^{20}$ eV neutrons when $z \lesssim 3$ (figure 9.5), but begins to break down for $\gtrsim 3 \times 10^{20}$ eV neutrons even when $z \gtrsim 1$.

Table 9.1 Multiplicities ζ and Mean Fractional Energies χ of Secondaries Formed in Photomeson Production

Species	Single π		Multi- π	
Neutrinos	$\zeta_v^s = 3/2$	$\chi_v^s = 0.05$	$\zeta_v^m = 6$	$\chi_v^m = 0.05$
Leptons	$\zeta_e^s = 1/2$	$\chi_e^s = 0.05$	$\zeta_e^m = 2$	$\chi_e^m = 0.05$
γ -rays	$\zeta_\gamma^s = 1$	$\chi_\gamma^s = 0.1$	$\zeta_\gamma^m = 2$	$\chi_\gamma^m = 0.1$
Neutrons	$\zeta_n^s = 1/2$	$\chi_n^s = 0.8$	$\zeta_n^m = 0.5$	$\chi_n^m = 0.4$
Protons	$\zeta_p^s = 1/2$	$\chi_p^s = 0.8$	$\zeta_p^m = 0.5$	$\chi_p^m = 0.4$
β -electrons	$\zeta_{\beta,e}^s = 1/2$	$\chi_{\beta,e}^s = 10^{-3}$	$\zeta_{\beta,e}^m = 1/2$	$\chi_{\beta,e}^m = 10^{-3}$
β -neutrinos	$\zeta_{\beta,\nu}^s = 1/2$	$\chi_{\beta,\nu}^s = 10^{-3}$	$\zeta_{\beta,\nu}^m = 1$	$\chi_{\beta,\nu}^m = 10^{-3}$

Substitution of eq. (9.46) into eq. (9.45) gives

$$\begin{aligned} \dot{n}_*^i(\epsilon_*, \Omega_*; z) &= \frac{c\sigma_{\phi\pi}^i \zeta_i}{8\pi} \int_0^\infty d\epsilon_\gamma n_{\text{ph}}(\epsilon_\gamma) \int_{-1}^1 d\mu (1 - \beta_p \mu) \\ &\times \int_1^\infty d\gamma_p n_p(\gamma_p; z) H(\epsilon'_l; \epsilon'_u) \delta(\epsilon_* - \chi_i m_p c^2 \gamma_p), \end{aligned} \quad (9.47)$$

assuming isotropy of the photon and UHECR proton spectra. Equation (9.47) can be simplified to the form

$$\begin{aligned} \dot{n}_*^i(\epsilon_*, \Omega_*; z) &= \frac{\zeta_i c \sigma_{\phi\pi}^i n_p(\bar{\gamma}_p; z)}{16\pi \chi_i m_p c^2 \bar{\gamma}_p^2} \int_{\epsilon'_l/2\bar{\gamma}_p}^\infty d\epsilon_\gamma \frac{n_{\text{ph}}(\epsilon_\gamma; z)}{\epsilon_\gamma^2} \\ &\times \left[\left[\min(2\bar{\gamma}_p \epsilon_\gamma, \epsilon'_u) \right]^2 - \epsilon'^2_l \right], \end{aligned} \quad (9.48)$$

where

$$\bar{\gamma}_p \equiv \epsilon_* / \chi_i m_p c^2.$$

For the CMBR spectrum, eq. (9.6), eq. (9.48) becomes

$$\begin{aligned} \dot{n}_*^i(\epsilon_*, \Omega_*; z) &= \frac{2\zeta_i c \sigma_{\phi\pi}^i n_p(\bar{\gamma}_p; z) \Theta^3(z)}{\lambda_C^3 \chi_i m_p c^2} \\ &\times \left[I_0(y_\ell, y_u) + y_\ell^2 \ln(1 - e^{-y_\ell}) - y_u^2 \ln(1 - e^{-y_u}) \right], \end{aligned} \quad (9.49)$$

where

$$y_{\ell,u} \equiv \frac{\epsilon'_{\ell,u}}{2\bar{\gamma}_p \Theta(z)} = \frac{\chi_i \epsilon'_{\ell,u} m_p c^2}{2\epsilon(1+z)\Theta(z)} \quad (9.50)$$

and

$$I_0(y_\ell, y_u) \equiv \int_{y_\ell}^{y_u} dy \frac{y^2}{e^y - 1}. \quad (9.51)$$

Substitution of eq. (9.49) for the evolving neutrino emissivity into eq. (9.43) gives the diffuse background intensity

$$\begin{aligned} \epsilon I_\epsilon^{i, \phi\pi} &= \frac{2\xi_i c^2 \sigma_{\phi\pi}^i}{\lambda_C^3 \chi_i} \left(\frac{\epsilon}{m_p c^2} \right) \epsilon \int_0^\infty dz \left| \frac{dt_*}{dz} \right| \frac{n_p(\bar{\gamma}_p; z) \Theta^3(z)}{(1+z)^2} \\ &\times [I_0(y_\ell, y_u) + y_\ell^2 \ln(1 - e^{-y_\ell}) - y_u^2 \ln(1 - e^{-y_u})] \end{aligned} \quad (9.52)$$

of neutrinos produced from channel i (single- and multiple channels, and β -decay neutrinos) formed in photopion interactions of UHECRs with the CMBR. The units of ϵI_ϵ^i are given by the units of ϵ .

Approximate behaviors of $I_0(y_\ell, y_u)$ can be obtained by examining asymptotes of the associated function

$$\int_x^\infty dy \frac{y^2}{e^y - 1} \rightarrow \begin{cases} (x^2 + 2x + 2) \exp(-x), & x \gg 1, \\ 2\zeta(3) - x^2/2, & x \ll 1, \end{cases} \quad (9.53)$$

noting also for the evaluation of eq. (9.52) that $\ln(1 - e^{-y}) \rightarrow \ln y$ when $y \ll 1$ and $\ln(1 - e^{-y}) \rightarrow -e^{-y}$ when $y \gg 1$.

After deriving the form of the temporally evolving UHECR proton spectrum, which we do in the next section, the neutrino and lepton emissivity can be obtained numerically by evaluating eq. (9.52), using multiplicities and fractional energy production values given in table 9.1. Four channels of neutrino production are treated in this way: two photopion channels associated with single-resonance- π and multiple- π production, and two more from the β -decay neutrinos created by decaying neutrons formed in photopion processes.

These expressions can also be used to derive the unobserved injection emissivity of electromagnetic secondaries (leptons and γ rays) from photopion production using the appropriate entries from table 9.1. This is unobserved because leptons and γ -rays injected at such high energies cascade through synchrotron and Compton processes through interactions with ambient photons, so that the injection spectrum of photons is not preserved, as generally is the case for neutrinos. In this case, a full cascade calculation must be done, as considered in the next chapter.

An important quantity to consider for energy deposition in electromagnetic secondaries from photopion processes is the bolometric intensity of

secondary channel i , given by

$$\mathcal{I}^i = \int_0^\infty d\epsilon I_\epsilon^i = \int_0^\infty dz \frac{d\mathcal{I}^i}{dz}. \quad (9.54)$$

The bolometric injection rate of secondaries of type i formed in photopion processes of UHECR protons with CMBR photons, differential in redshift, is given by

$$\begin{aligned} \frac{d\mathcal{I}^{i,\phi\pi}}{dz} &= \frac{2\xi_i c^2 \sigma_{\phi\pi}^i}{\lambda_C^3} \left| \frac{dt_*}{dz} \right| \Theta^3(z) \chi_i(1+z) m_p c^2 \int_1^\infty d\bar{\gamma}_p \bar{\gamma}_p n_{p,\text{co}}(\bar{\gamma}_p; z) \\ &\quad \times [I_0(y_\ell, y_u) + y_\ell^2 \ln(1 - e^{-y_\ell}) - y_u^2 \ln(1 - e^{-y_u})], \end{aligned} \quad (9.55)$$

using eq. (9.50). An approximate calculation of the diffuse cosmogenic γ -ray intensity can be made by employing eq. (9.55) and assuming that all electromagnetic secondaries emerge with photon energies where the universe becomes transparent to γ rays.

The bolometric injection rate of e^+e^- pairs formed in photopair processes of isotropically distributed target photons with comoving photon number density $n_{\text{ph}}(\epsilon)$ and comoving UHECR ion spectrum $n_{Z,\text{co}}(\gamma; p)$ of ion Z , differential in redshift, is given by

$$\frac{d\mathcal{I}^{\phi e}}{dz} = \frac{\alpha_f m_e c^4 r_e^2 Z^2}{4\pi(1+z)} \left| \frac{dt_*}{dz} \right| \int_0^\infty d\gamma n_{Z,\text{co}}(\gamma; p) \int_2^\infty d\epsilon n_{\text{ph}}\left(\frac{\epsilon}{2\gamma}\right) \frac{\varphi(\epsilon)}{\epsilon^2}, \quad (9.56)$$

using eqs. (9.36) and (9.37) for $\varphi(\epsilon)$. The subsequent reprocessing by Compton-synchrotron cascades with the CMBR is weakly dependent on the pair injection energy for \gg PeV injection (see next chapter). The strongly increasing energy losses at high redshifts means that all UHECR protons originate from a maximum depth of a few hundred Mpc, and even from closer distances if the diffusion mean free path is a small fraction of the energy-loss mean free path.

The secondary neutrino and lepton emissivity depends on photopion, photopair, and cosmological expansion energy-loss rates. We have yet only derived the $\phi\pi$ losses for protons, and have not considered ion breakup through photo-erosion. The main unknown for calculating secondary neutrinos and γ rays is the evolving UHECR proton spectrum $n_{p,\text{co}}(\gamma_p; z)$.

9.6 ULTRAHIGH-ENERGY COSMIC-RAY EVOLUTION

The comoving differential UHECR proton density $n_{p,\text{co}}(\gamma_p; z)$ at redshift z is related to the proper frame differential UHECR proton density $n_{p*}(\gamma_p; z)$

through the relation $n_{p,\text{co}}(\gamma_p; z) = (1+z)^{-3} n_{p^*}(\gamma_p; z)$ (eq. [(4.44)]). These differential densities are the superposition of cosmic rays emitted at redshifts $z' \geq z$, and

$$n_{p,\text{co}}(\gamma_p; z) = \int_z^\infty dz' \left| \frac{dt_*}{dz} \right| \dot{n}_{p,\text{co}}(\gamma_{p^*}; z) \left| \frac{d\gamma_{p^*}}{d\gamma_p} \right|. \quad (9.57)$$

If the comoving UHECR emissivity $\dot{n}_{p,\text{co}}(\gamma_p^*; z)$ is assumed to be described by a power-law injection spectrum with discrete low-energy and exponential high-energy cutoffs, then

$$\dot{n}_{p,\text{co}}(\gamma_p^*; z) = \frac{dN_p}{d\gamma_p^* dt^* dV_{\text{co}}} = K(s) \gamma_p^{*-s} \exp(-\gamma_p^*/\gamma_{\text{max}}) \Sigma(z) H(\gamma_p^* - \gamma_{\text{min}}). \quad (9.58)$$

Implicit in this expression is that sources accelerate UHECRs with similar spectra throughout time (this assumption is easily relaxed, but introduces parameters unconstrained by available data), though the comoving UHECR source rate density described by the *star-formation rate* function $\Sigma(z)$ could vary (see below). Moreover, eq. (9.57) gives the emissivity averaged over a volume containing many sources, and does not describe inhomogeneous matter and star formation activity within ≈ 100 Mpc, which is important for super-GZK cosmic ray production.

9.6.1 Normalization to Local Luminosity Density

The UHECR emissivity is normalized to the local ($z \rightarrow 0$) luminosity density through the relation

$$m_p c^2 \int_{\gamma_{\text{min}}}^\infty d\gamma_p^* \gamma_p^* \dot{n}_{\text{co}}(\gamma_p^*; 0) = \dot{\mathcal{E}}_p \equiv 10^{44} \dot{\mathcal{E}}_{44} \text{ ergs Mpc}^{-3} \text{ yr}^{-1}. \quad (9.59)$$

The normalization coefficient $K(s)$ is then given by

$$K(s) = \frac{\dot{\mathcal{E}}_p}{m_p c^2} \begin{cases} (s-2) \gamma_{\text{min}}^{s-2}, & s > 2, 1 \ll \gamma_{\text{min}} \ll \gamma_{\text{max}}, \\ \gamma_{\text{max}}^{s-2} / \Gamma(2-s), & s < 2, 1 \ll \gamma_{\text{min}} \ll \gamma_{\text{max}}, \\ E_1(\gamma_{\text{min}}/\gamma_{\text{max}}), & s = 2, \end{cases} \quad (9.60)$$

for the injection spectrum, eq. (9.58). The properties of the exponential integral $E_1(x)$ are briefly described in Appendix B.

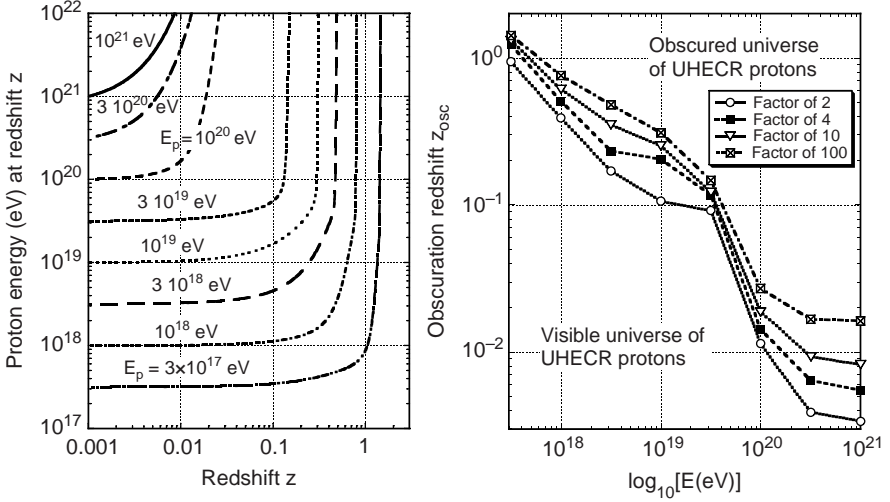


Figure 9.6 (a) Evolution of a cosmic-ray proton's energy with redshift z due to cosmic expansion and to photopair and photopion losses on the CMBR. (b) Boundary redshift $z_{\text{osc}}(E_p)$ separating the universe from which protons with energy 2, 4, 10, and 100 times their measured energy E_p could originate. The analytic forms of the $r_{\phi\pi}$ and $r_{\phi e}$ are used in this calculation.

9.6.2 Energy Evolution of Cosmic-Ray Protons

The differential change $d\gamma_p^*$ in the Lorentz factor of UHECR protons at epoch z during the proper time interval $dt_* = dz|dt_*/dz|$ is given by

$$\gamma_p^*(z + \Delta z) = \gamma_p^*(z) \left[1 + \Delta z \left(\frac{1}{1+z} + c \left| \frac{dt_*}{dz} \right| [r_{\phi\pi}^{-1}(\gamma_p^*) + r_{\phi e}^{-1}(\gamma_p^*)] \right) \right], \quad (9.61)$$

where $r_{\phi\pi}$ and $r_{\phi e}$ are given analytically by eqs. (9.15) and (9.33), respectively. The Jacobian $|d\gamma_p^*/d\gamma_p|$ is solved numerically by calculating the energy evolution of two cosmic ray protons with nearly the same Lorentz factors.

Figure 9.6a shows the evolution of cosmic-ray proton energy with redshift, calculated from eq. (9.61). If an UHECR proton with a given energy is detected, then the source of higher-energy cosmic rays, which have since evolved to the measured energy at the present epoch, must be found within an obscuration redshift z_{osc} ; otherwise the UHECR protons would have lost too much energy to be presently observed. The redshift z_{osc} separating the visible universe from the obscured, or veiled universe is not sharp, due

also to the stochastic nature of photopion energy losses (section 9.2.3). For UHECR protons, z_{osc} is a function only of the presently measured proton energy.

Figure 9.6b shows the obscuration redshift z_{osc} from which UHECR protons with measured energy E_p were produced by a source at $z = z_{\text{osc}}$ with energy a factor $\mu_{\mathcal{F}} = 2, 4,$ and $10 \times E_p$. As is clear from figure 9.6b, detection of UHECR protons with $E \approx 6 \times 10^{19}$ eV means that sources capable of producing UHECRs with $E \approx 6 \times 10^{20}$ eV must be found within a few hundred Mpc, and even closer if the UHECRs propagate diffusely. Sources accelerating UHECR protons with energies up to $\approx 10^{21}$ eV must be found within ≈ 100 Mpc, and the source of the 3×10^{20} eV cosmic ray event, if a proton, must likely be within ≈ 40 Mpc. A model-independent definition of the horizon radius is obtained by choosing $\mu_{\mathcal{F}} = e$. See Ref. [203] for a model-dependent calculation of the cosmic ray horizon.

9.6.3 Rate Density Evolution and the Star Formation Rate

Astronomical observations restrict the evolving comoving density or rate-density evolution of UHECR sources connected to the hypothesized astronomical source class of UHECRs, for example, GRBs, blazars and radio galaxies, or clusters of galaxies. One possibility is that the rate density of UHECRs follows the star formation rate (SFR) history derived from the blue and UV luminosity density of distant galaxies [204], which is reasonable if GRBs are the sources of UHECRs. The SFR activity can be approximated by an analytic fitting profile given by [205]

$$\Sigma(z) = \frac{1 + a_1}{(1 + z)^{-a_2} + a_1(1 + z)^{a_3}}. \quad (9.62)$$

Two model SFRs that bracket the uncertainty in the extinction corrections for the SFR are the lower SFR (LSFR) and upper SFR (USFR) rate factors shown in figure 9.7. The lower optical/UV curve shown here is in accord with a lower limit to the SFR evolution, while a much stronger evolution of the SFR is found [216] after correcting for dust extinction. Also shown in figure 9.7 is the rate function $\Sigma(z) = (1 + z)^4$ used by Berezhinsky and his colleagues [217] to model hypothetical sources of UHECRs. The corresponding ‘‘SFR’’ activity for producing UHECRs from AGNs could be much steeper than in the star formation activity associated with spiral and star-forming galaxies.

A variety of models for the SFR factor—which are not strictly ‘‘star formation rates,’’ but rather fueling or growth rates of explosive events—are shown in figure 9.7. These SFR factors $\Sigma_i(z)$, $i = 1, \dots, 7$, are assumed

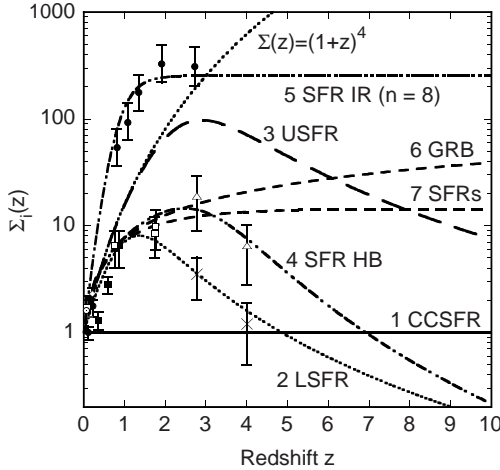


Figure 9.7 Model star formation rates (SFRs) and data as a function of redshift. The line labeled “CCSFR” is the constant comoving rate, the LSFR and USFR curves bound the inferred SFR densities (normalized with respect to a SFR of $0.09 M_{\odot} \text{ Mpc}^{-3} \text{ yr}^{-1}$), the curve “SFR HB” is the SFR from Hopkins and Beacom’s study [206], curve “SFR IR” is eq. (9.64) with $n = 8$ that is used to fit IR luminosity density data from IR luminous galaxies [207], and curves labeled “GRB SFHs” are SFR histories used to fit GRB data [53]. Other data give relative SFR densities from measurements of galactic optical/UV emission (see [208]). The data are denoted by a filled circle [209], an open square [210], an open diamond [211], filled squares [212], open squares [213], and crosses [214]. High-redshift data with corrections for dust extinction are given by the open triangles [215]. An estimate of the maximum extinction [216] is shown by the USFR. The curve labeled $\Sigma(z) = (1+z)^4$ is considered in Ref. [217].

to be proportional to the redshift-dependent comoving rate density $\dot{n}_{i,\text{co}}(z) = \Sigma_i(z)\dot{n}_{i,\text{co}}$, where the local comoving rate density $\dot{n}_{i,\text{co}}$ of species i normalizes the event rate. Different classes of sources can, of course, contribute to the UHECRs observed in the Solar neighborhood.

The SFR factors used to calculate the UHECR spectrum are

1. Constant comoving rate density, $\Sigma_1(z) = 1$, considered for mathematical convenience.
2. LSFR $\Sigma_2(z)$, described by eq. (9.62) with by $a_1 = 0.005$; $a_2 = 3.3$, and $a_3 = 3.0$.
3. USFR $\Sigma_3(z)$ described by eq. (9.62) with by $a_1 = 0.0001$, $a_2 = 4.0$, and $a_3 = 3.0$.

4. Comoving SFR \propto the blue/UV luminosity density, which is assumed to track the SFR of the universe [206],

$$\Sigma_4(z) = \frac{1 + 6.78z}{1 + (z/3.3)^{5.2}}. \quad (9.63)$$

5. SFR IR; Comoving rate \propto sub-mm/far-IR luminosity density associated with luminous IR galaxies [207], fit using the analytic form

$$\Sigma_{IR,n}(z) = \frac{1 + 2^{-n}}{(1 + z)^{-n} + 2^{-n}}. \quad (9.64)$$

A good fit to the IR luminosity density data is obtained with $n = 8$, as shown in figure 9.7. If IR-luminous galaxies are caused by galactic merger events, as indicated by morphological and spectral evidence [218], this would connect blazars and the formation of supermassive black holes to galaxy collisions. Although related to supermassive black hole growth, the IR luminosity density does not, however, directly measure the activity of supermassive black holes, because the IR radiation is a convolution of the photon luminosity which is then reprocessed through thick columns of material. Hence we have generalized the form with a single adjustable parameter, n , that represents a range of blazar formation histories. Only the $\Sigma_{IR,8}$ form is shown in figure 9.7, so $\Sigma_5(z) = \Sigma_{IR,8}$.

6. SFRs 6 and 7: Upper and lower range of SFRs that give a good fit to Swift and pre-Swift GRB redshift distributions and pre-Swift opening angle distribution [53]. The analytic forms of these functions are $\Sigma_6 = (1 + 0.12z/0.011)/(1 + \sqrt{z/3})$, and $\Sigma_7 = (1 + 0.12z/0.015)/(1 + \sqrt{z/1.3})$.

9.7 WAXMAN-BAHCALL BOUND

Waxman and Bahcall propose [30,219] that measurements of the UHECR flux set an upper bound to UHE ν production from sources at redshifts $z \lesssim 1$. They argue that astrophysical systems such as clusters of galaxies or magnetized relativistic outflows cannot contain the highest-energy cosmic rays, so that the measured UHECR intensity implies an associated maximum flux of ‘‘GZK-neutrinos’’ formed by photomeson interactions of UHECRs with the CMBR.

To derive an estimate of this bound, consider that from eq. (5.2) for optically-thin radiative transfer, the neutrino intensity

$$I_\nu \cong j_\nu \Delta s \cong j_\nu R_H$$

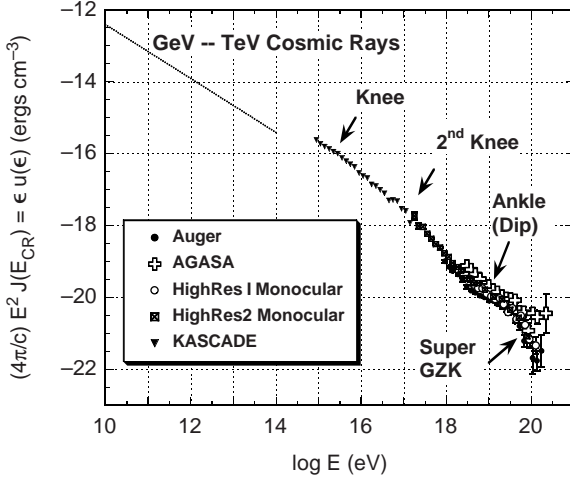


Figure 9.8 Cosmic-ray energy density observed near Earth. The two solid curves show extrapolations to model fits of the observed cosmic-ray proton [140] and all-particle [220] spectrum at \lesssim and $\gtrsim 10^{14}$ eV, respectively; thus the discontinuity. The UHECR data points are from observations taken with the Akeno Giant Air Shower Array (AGASA) [221].

where $R_H \cong c/H_0 \cong 4000$ Mpc is the Hubble radius. Cosmological factors rapidly reduce the contribution at $z \gg 1$.

In single-resonance production, about $3/2 \times 0.05 \cong 7.5\%$ of the energy of the proton is transformed to neutrinos, rising to a value of $\approx 30\%$ for multipion production. In single-resonance production, the relative fraction of energy lost in neutrinos compared to all secondary energy is $\approx 3/8$, whereas this fraction is $\approx 1/2$ for multipion production (table 9.1). We use an intermediate value $\approx 20\%$ for the fractional energy in a photopion interaction.

If the timescale for photopion energy losses of a proton with Lorentz factor γ_p is denoted by $t_{\phi\pi}(\gamma_p)$, then the muon neutrino energy emissivity is

$$\epsilon_\nu j_{\nu_\mu}(\epsilon_\nu, \Omega) \cong \frac{0.2}{2} \frac{u_{CR}(\gamma_p)}{4\pi t_{\phi\pi}(\gamma_p)}$$

where $u_{CR}(\gamma_p)$ is the cosmic-ray energy density, $\epsilon_\nu \cong m_p c^2 \gamma_p / 20$, and the factor $1/2$ is for oscillations into ν_e and ν_τ (neutrino telescopes are most sensitive to ν_μ).

Figure 9.8 is a sketch of the cosmic-ray energy density, showing that $u_{CR}(10^{20} \text{ eV}) \approx 10^{-21} \text{ ergs cm}^{-3}$. The photopion energy-loss timescale at 10^{20} eV is $\approx 140 \text{ Mpc}/c = 1.44 \times 10^{16} \text{ s}$ ($\cong 0.5 \text{ Gyr}$; see figure 9.3). Thus

$$\epsilon_\nu I_{\nu_\mu}(5 \times 10^{18} \text{ eV}, \Omega) \cong 5 \times 10^{-9} \frac{\text{GeV}}{\text{cm}^2 \text{ s sr}}.$$

Waxman and Bahcall [30] estimate an upper bound of the neutrino intensity equal to

$$\epsilon_\nu I_{\nu_\mu + \bar{\nu}_\mu}^{\text{WB}} \cong 1.5 \times 10^{-8} \xi_z \frac{\text{GeV}}{\text{cm}^2 \text{ s sr}}, \quad (9.65)$$

where ξ_z , a factor of order unity, is a correction factor for high-redshift sources. This Waxman-Bahcall value is ≈ 3 larger than the value derived here. The difference is found in the larger AGASA energy density, by a factor ≈ 2 , they assume for the $\gtrsim 10^{20}$ eV cosmic rays energy density, and counting ν_μ and $\bar{\nu}_\mu$ without oscillations. The associated energy density $\epsilon u_{\text{WB}}(\epsilon) = 4\pi\epsilon I_\epsilon^{\text{WB}}/c \approx 10^{-20} \xi_z \text{ erg cm}^{-3}$ (figure 1.3).

Though our estimate here gives a somewhat smaller neutrino flux, the estimate assumes no evolution, yet any astrophysical model of UHECRs must involve one or more source classes whose activity changes with time. The SFR factors are generally strongly positively evolving (more in the past), so that intensities comparable to the original Waxman-Bahcall estimate are calculated.

Even though the bound applies to GZK neutrinos with energies $\approx 10^{18}$ – 10^{19} eV, Waxman and Bahcall also claim that it applies to lower-energy neutrino fluxes because cosmic-ray sources inject cosmic rays with number spectral indices ≈ -2 . This seems a questionable extension of the bound; cosmic ray sources can accelerate softer particle spectra, and these cosmic rays need not escape the galaxies or clusters where they are formed. Yet the Waxman-Bahcall bound may still hold at the lower TeV–PeV energies for sources where the UHECRs do not suffer large photohadronic losses with the EBL, provided that the UHECR protons and ions escape with negligible photohadronic energy losses. Importantly, the Waxman-Bahcall bound does not apply to high-redshift sources, or buried sources from which UHECRs cannot escape, though from which an escaping flux of UHE neutrinos can be detected [222].

The HiRes collaboration [223] measures a factor ≈ 4 less energy density in $\gtrsim 10^{20}$ eV particles than AGASA, and the Auger collaboration [183] measures $\approx 40\%$ less than the HiRes result (figure 9.9). The HiRes-2 Monocular (denoted by solid dots in later figures) and the HiRes-1 Monocular data (denoted by open circles) [223] are used to compare model with data. The error bars are given by the statistical errors, so the measurement uncertainty is greater than shown due to additional systematic errors.

9.8 UHECR AND GZK NEUTRINO INTENSITIES

All of the necessary apparatus needed to calculate the UHECR proton and neutrino flux has been developed, to be compared with sensitivities of

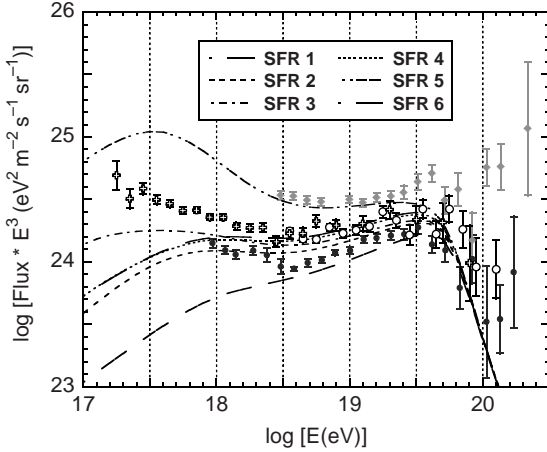


Figure 9.9 Calculations of UHECR proton intensity spectra, multiplied by E^3 , measured at Earth, compared with measurements of the UHECR spectrum by AGASA (filled diamonds), HiRes (open symbols), and Auger (filled circles). The different SFR factors used in the calculation are shown in figure 9.7.

present day UHE neutrino telescopes, and also with the Waxman-Bahcall estimate.

Figure 9.9 shows calculations of the UHECR proton intensity spectra measured at the present epoch due to UHECR protons injected in the shape of an exponentially truncated power-law spectrum with injection index $s = 2.2$, low-energy cutoff $E_{\min} = m_p c^2 \gamma_{\min} = 10^{14}$ eV, and high-energy exponential cutoff $E_{\max} = 10^{20}$ eV. The local energy emissivity in UHECRs is $\dot{\mathcal{E}}_{44} = 60$ (eq. [9.59]).

As is apparent from figure 9.9, the constant comoving SFR 1 could explain a few of the highest energy UHECRs, but fails to explain much else. The lower star formation rate, SFR 2, begins to reproduce much of the high-energy data. When star formation evolves positively by a factor of 5–10 between the present epoch and $z \approx 1-2$, the model can well fit the UHECR spectrum from the ankle energy $\approx 4 \times 10^{18}$ eV and above. For SFRs 3, 4, and 6, a two-component galactic/extragalactic model, with a lower-energy galactic component, can give high-quality fits to the data. Figure 9.9 also shows the UHECR proton intensity spectrum for SFR 6, which is similar to SFR 7. These SFRs were found [53] to give the best fit to the Swift and pre-Swift redshift distributions of GRBs and the pre-Swift opening angle distribution. A SFR that follows the IR luminosity density, SFR 5, seems to be ruled out.

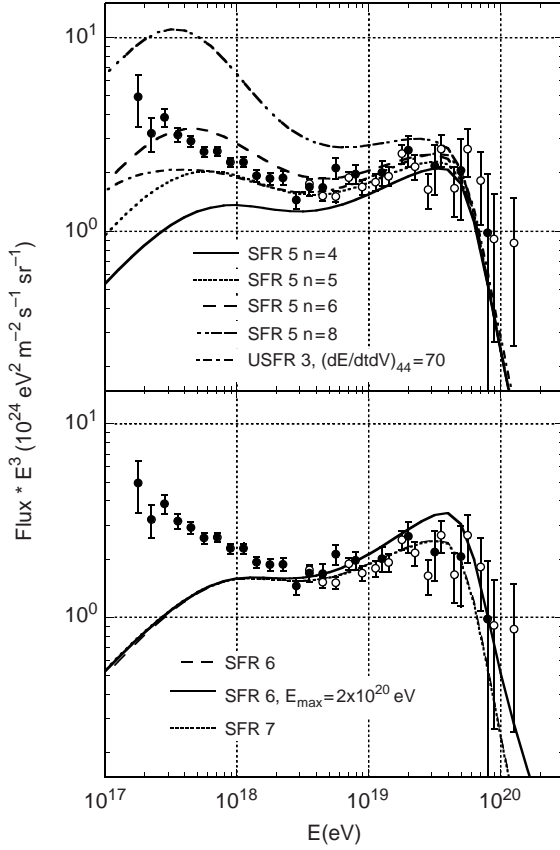


Figure 9.10 Calculations of UHECR proton intensity spectra multiplied by E^3 received at Earth. The rate density of UHECR sources is proportional to the different SFR factors. *Upper panel:* UHECR proton intensity spectrum for SFR 5, eq. (9.64), with different values of parameter n , as labeled. Also calculated here is the USFR model of Ref. [208] with $\dot{\mathcal{E}}_{44} = 70$ (otherwise $\dot{\mathcal{E}}_{44} = 60$). *Lower panel:* UHECR proton intensity spectrum for SFR 6, $\dot{\mathcal{E}}_{44} = 60$, and $E_{\max} = 1 \times 10^{20}$, 2×10^{20} eV, and SFR 7 with $\dot{\mathcal{E}}_{44} = 60$ and $E_{\max} = 1 \times 10^{20}$ eV.

The best-fit model of Ref. [208] uses USFR 3 and $\dot{\mathcal{E}}_{44} = 70$: the model fit using these parameters is found in the upper panel of figure 9.10. Also shown there are UHECR intensity spectra using the modified IR SFR function, eq. (9.64), with $n = 4, 5, 6, 8$ (SFR 5) (using $\dot{\mathcal{E}}_{44} = 60$). The lower panel of Figure 9.10 shows SFR 6 with $E_{\max} = 10^{20}$ and 10^{21} eV, and SFR 7 with $E_{\max} = 10^{20}$ eV. These SFRs are found by [53] to give the best fit to the Swift and pre-Swift redshift distributions of GRBs, and the pre-Swift opening angle distribution. Inspection of these results indicates that

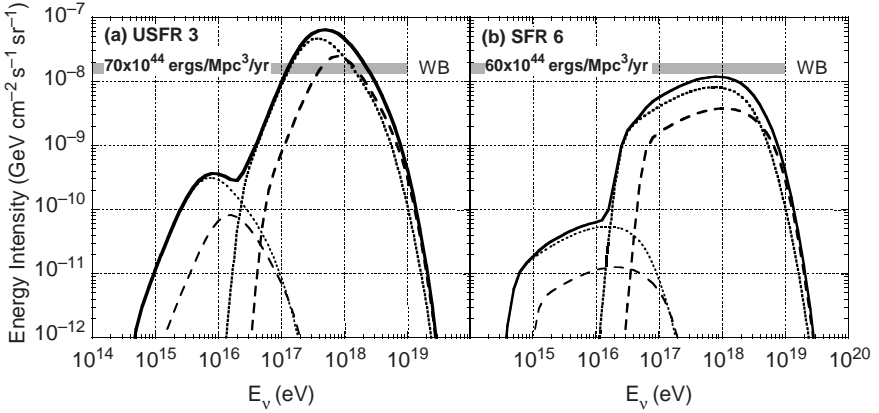


Figure 9.11 GZK neutrino fluxes from two different models of UHECR proton production shown in figure 9.10. *Left panel:* USFR 3 of Ref. [208]. *Right panel:* SFR 6 of Ref. [53].

the sources of UHECRs do not accelerate, on average, many particles to energies $\gtrsim 2 \times 10^{20}$ eV.

A number of features are apparent from these spectra. First is the dramatic “GZK” cutoff at energies $\gtrsim 6 \times 10^{19}$ eV resulting from UHECR interactions with the CMBR. The second is the pile-up of protons at $\approx 4 \times 10^{19}$ eV as a result of energy losses on the CMBR, and the third is the photopair dip at $\approx (2-5) \times 10^{18}$ eV. The energy of the pair production valley is rather robust for vigorous UHECR source activity at $z \cong 1-2$ compared with the present epoch, which may be more easily fulfilled with blazar AGNs than with GRB sources. Berezhinskii [217,224] argues that the ankle feature is a consequence of pair-production losses by UHECRs on target photons of the CMBR, using models with injection indices $s \cong 2.7$.

Figure 9.11 shows predictions of the GZK neutrino intensity spectrum for the USFR 3 model [208] associated with the UHECR spectrum shown in the upper panel of figure 9.10, and for SFR 6 shown in the lower panel of figure 9.10. For the model of Ref. [208], the total neutrino intensity exceeds the Waxman-Bahcall bound due to its increased SFR activity at $z \approx 1-2$. SFRs 6 (and 7) produce a low-energy diffuse neutrino ledge due to photopion processes occurring at large redshifts.

Predictions for the total diffuse neutrino spectrum for various models are shown in figure 9.12 in comparison with the ANITA sensitivity for a 45 day flight [227]. Long-duration balloon-borne high-energy neutrino telescopes seem close to discovering the guaranteed flux of GZK neutrinos that seriously restrict models for UHECR origin. The cosmogenic neutrino flux is difficult to detect with IceCube (see [226] for IceCube sensitivities to point sources).

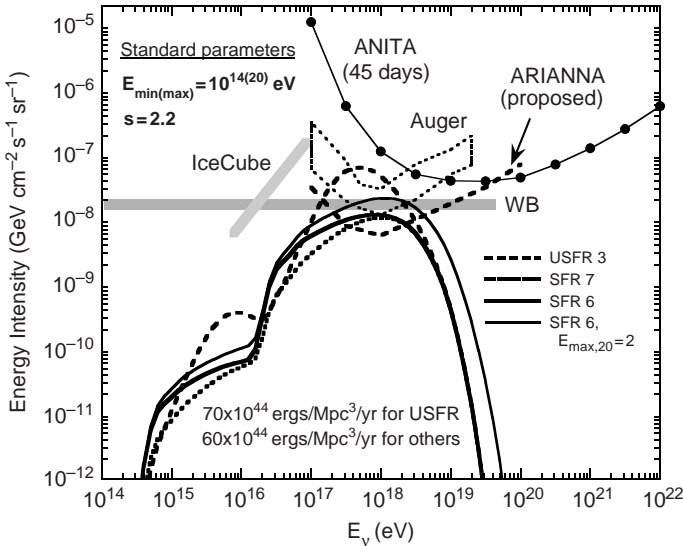


Figure 9.12 Comparison of model calculations of GZK neutrino intensities for neutrinos of all flavors with sensitivity curves of ANITA, IceCube, and proposed ARIANNA detectors [225]. IceCube sensitivity is for 3 years assuming a -2 spectrum [226]. The original Waxman-Bahcall estimate is at the level of $1.5 \times 10^{-8} \text{ GeV cm}^{-2} \text{ s}^{-1} \text{ sr}^{-1}$ (eq. [9.65]).

The spectral injection and propagation signatures in the UHECR spectrum and the diffuse high energy neutrino intensity are important clues to the sources of UHECRs. Besides making a diffuse flux of GZK neutrinos, the secondary leptons and γ rays formed through photopair and photopion processes make an electromagnetic cascade that emerges at photon energies where the universe is transparent to $\gamma\gamma$ pair production on the diffuse ambient EBL, as we discuss in more detail in the next chapter. Semikoz and Sigl [228] have shown that to fit the AGASA data with a top-down exotic particle physics model in the Z-burst scenario [229] makes a diffuse intensity of cascade γ -rays that would overproduce the diffuse γ -ray background measured with the EGRET telescope. See Ref. [230] for a discussion of UHE neutrino astronomy, including particle physics issues and top-down models.

9.9 PHOTONUCLEAR REACTIONS

For UHECR ions, total energy E is dominated by the kinetic energy of the A nucleons found in a nucleus of atomic mass A and charge Z . Thus the γ factor of a nucleus is A times less than for an UHECR proton with the same

energy. The mean photon energy is consequently smaller by a factor A in the rest frame of an UHECR ion than of an UHECR proton with the same energy. For a heavy nucleus with $E \sim 10^{20}$ eV, the photopion production rate with photons of the CMBR is therefore at a much reduced level compared to an UHECR proton with the same value of E , because the number of CMBR photons above the photopion threshold is smaller.² The proportional to Z^2 increase in the photopair energy-loss rate for ions counteracts threshold effects from photopair losses for heavy ions to make photopair losses with the CMBR an important energy-loss mechanism for ions. The photopion and photopair losses are graphed for Fe in figure 9.3.

Besides pair- and pion-production energy losses, the composition of UHECR ions during propagation can be changed by photoerosion through resonant and nonresonant processes leading to the breakup of the nucleus. The best-known resonant photonuclear process is the giant dipole resonance, where one or two nucleons are ejected from a nucleus, thereby changing the atomic mass and charge. Nuclear dipole vibrations excited by the γ -ray—though generally with wavelength far larger than the characteristic nuclear size—drive the protons through the neutron fluid, leaving the nucleus in an excited state, where it decays by the evaporation of one or two protons or neutrons [231]. The characteristic energy of the electric dipole transition is

$$h\nu_{\text{GDR}} \cong \frac{40}{A^{1/3}} \text{ MeV}$$

[232], and the characteristic excitation width $\Delta \approx 3 - 10$ MeV [233].

For electromagnetic dipole transitions, the Thomas-Reiche-Kuhn sum rule over oscillator strengths gives the energy-integrated cross section

$$\begin{aligned} \Sigma_d &= \int_0^\infty dE_\gamma \sigma_{\text{GDR}}(E_\gamma) \\ &= \frac{2\pi^2 e^2 \hbar}{m_p c} \frac{(A-Z)Z}{A} \cong 29.9Z \left(\frac{1-Z/A}{1/2} \right) \text{ MeV mb.} \end{aligned} \quad (9.66)$$

In the approach of Puget, Stecker, and Bredekamp [234,235], the giant dipole resonance cross section for nuclide (Z, A) is represented by a Gaussian (rather than a Lorentzian) with single $[(\gamma, n)$ or $(\gamma, p)]$ or double $[(\gamma, 2n)$ (γ, np) , $(\gamma, 2p)]$ nucleon loss, in addition to a flat part above 30 MeV to match the data. With these approximations, the nuclear

²The photopion threshold $E_\gamma^{\text{thr}} = m_\pi + m_\pi^2/2Am_p \cong 140 \text{ MeV} + 10.5/A \text{ MeV}$ is not much different between protons and heavy ions.

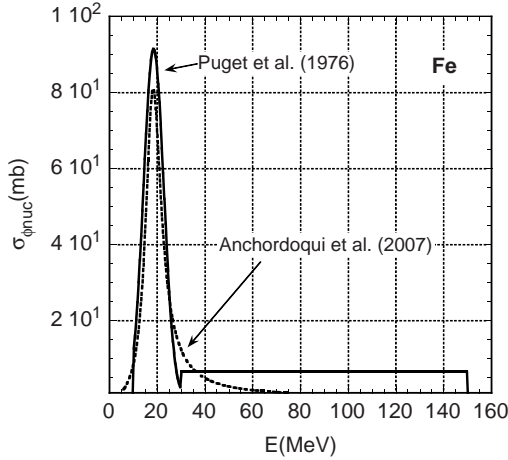


Figure 9.13 Comparison of photodisintegration cross section for Fe from [234] and [236].

photodisintegration cross section takes the form

$$\begin{aligned} \sigma_{\phi_{\text{nuc}}}(E_{\gamma}) = & \frac{\sum_d \xi_i}{W_i} \exp\left(\frac{-2(E_{\gamma} - E_{\gamma}^i)^2}{\Delta_i^2}\right) H(E_{\gamma}; E_0, E_1) \\ & + \sum_d \zeta_d \frac{H(E_{\gamma}; E_1, E_2)}{(E_2 - E_1)} \end{aligned} \quad (9.67)$$

(see figure 9.13), where $i = 1, 2$ refers to single- or double-nucleon emission during excitation, $E_0, E_1,$ and E_2 are assigned the values of 2, 30, and 150 MeV, respectively, and tables of values of $E_{\gamma}^i, \Delta_i, \xi_i, \zeta_d,$ are given in Ref. [234].³ The normalization factor

$$W_i = \Delta_i \sqrt{\frac{\pi}{8}} \left[\operatorname{erf}\left(\frac{E_1 - E_{\gamma}^i}{\Delta_i/\sqrt{2}}\right) + \operatorname{erf}\left(\frac{E_{\gamma}^i - E_0}{\Delta_i/\sqrt{2}}\right) \right].$$

The first term in eq. (9.67) describes the giant dipole resonance, and the second term describes nonresonant processes in which the transition matrix connects directly to the ground state. Note that the reaction $\gamma + d \rightarrow p + n,$ the inverse of the deuterium-forming reaction $p + n \rightarrow d + \gamma$ (2.2 MeV), is not a dipole resonance excitation [232]. Equation (9.66) can be used to calculate the survival probability of UHECR ions in the CMBR or, indeed, in an arbitrary background radiation field. A more accurate treatment would also consider the pygmy dipole resonance excited by surface

³Updated experimental giant dipole resonance parameters can be found at <http://www-nds.iaea.org/RIPL-2/gamma.html>.

Table 9.2 Anders-Grevesse [238] Abundances, by Number, Relative to H

Element	Z	A ^a	Solar photosphere abundance	Meteoritic abundance
H	1	1	1.0	1.0
He	2	4	0.98×10^{-2}	0.080
C	6	12	3.63×10^{-4}	4.44×10^{-4}
N	7	14	1.2×10^{-4}	1.15×10^{-4}
O	8	16	8.51×10^{-4}	8.75×10^{-4}
Ne	10	20	1.23×10^{-4}	1.38×10^{-4}
Mg	12	24	3.80×10^{-5}	3.95×10^{-4}
Al	13	27	2.95×10^{-6}	3.12×10^{-6}
Si	14	28	3.55×10^{-5}	3.68×10^{-5}
S	16	32	1.62×10^{-5}	1.89×10^{-5}
Ca	20	40	2.29×10^{-6}	2.24×10^{-6}
Fe	26	56	4.68×10^{-5}	3.31×10^{-5}

^aMost common isotope.

nuclear oscillations (e.g., [237]). Though its cross section is smaller than that of the giant dipole resonance, it is peaked at a lower-energy radiation, so that the threshold energy is lower.

An accurate treatment of UHECR ion propagation requires a reaction network to follow creation and destruction of UHECR nuclei and energy loss during transport. There is a general monotonic decrease of the composition of heavier ions in the Solar photospheric abundances (see table 9.2). This also holds true for the meteoritic abundances and, taking into account spallation processes during transport, the composition patterns of the GeV–TeV cosmic rays. If the abundances of accelerated UHECR ions follow the Solar photospheric abundance, the addition of new nuclides during transport from photodestruction of heavier nuclides can be neglected in a simple examination of the problem.

9.9.1 Photodisintegration Reaction Rate

We now make a simple guess for the photonuclear destruction or disintegration rate of UHECR ions by photons of the CMBR. The photonuclear cross section can be written in the δ -function form

$$\sigma_{\phi\text{nuc}}(E) \cong \frac{\sum_d}{m_e} \delta(\epsilon - \bar{\epsilon}_r), \quad (9.68)$$

where the total particle energy $E = Am_p c^2 \gamma$. The peak of the photonuclear cross section is typically near 20 MeV, so

$$\bar{\epsilon}_r \cong \frac{20}{m_e c^2} \text{ MeV} \cong 40 \left(\frac{h\nu_{\text{GDR}}}{20 \text{ MeV}} \right) \equiv 40\bar{\epsilon}_{40}.$$

By subdividing the cross section, eq. (9.68), into a superposition of δ -functions with coefficients that sum to $\Sigma_d/m_e c^2$, successively better approximations to the photonuclear cross section can be made.

Another δ -function approximation for the photodisintegration cross section of nucleus A is given by

$$\sigma_A(\epsilon_r) \cong \frac{\pi}{2} \sigma_{0,A} \Delta_{\text{GDR}} \delta(\epsilon_r - \epsilon_{r,A}) \quad (9.69)$$

[138,236,239], where

$$\sigma_{0,A} = 1.45A \text{ mb}, \quad \Delta_{\text{GDR}} \cong 15.6, \quad \epsilon_{r,A} \cong 83.5A^{-0.21},$$

and $\epsilon_r = \gamma\epsilon(1 - \mu)$ is the invariant dimensionless photon energy in the ion's rest frame.

From eq. (9.3), the photonuclear reaction rate of a nuclide with Lorentz factor γ passing through an isotropic radiation field denoted by $n_{\text{ph}}(\epsilon)$ is

$$\dot{N}_{\phi\text{nuc}}(\gamma, z) = \frac{c}{2\gamma^2} \int_0^\infty d\epsilon \frac{n_{\text{ph}}(\epsilon)}{\epsilon^2} \int_0^{2\gamma\epsilon} d\epsilon_r \epsilon_r \sigma_{\phi\text{nuc}}(\epsilon_r), \quad (9.70)$$

where $\gamma = E/Am_p c^2$ and $\beta \rightarrow 1$. Substitution of eq. (9.68) for the cross section and eq. (9.6) for the CMBR radiation field gives

$$\dot{N}_{\phi\text{nuc}}(\gamma, z, A, Z) = \frac{-4\pi c \tilde{\Sigma}_d \Theta(z) \bar{\epsilon}_r}{\lambda_C^3 \gamma^2} \ln \left[1 - \exp \left(\frac{-\bar{\epsilon}_r}{2\gamma \Theta(z)} \right) \right]. \quad (9.71)$$

Here $\tilde{\Sigma}_d = (\Sigma_d/0.511 \text{ MeV}) \times 10^{-27} \text{ cm}^2$ (eq. [9.66]). Photonuclear reactions of ion (A, Z) with energy $E = 10^{20} E_{20} \text{ eV}$ with $E_{20} \ll 0.4A\bar{\epsilon}_{40}/(1+z)$ take place with Wien photons of the CMBR. In this asymptote, eq. (9.71) gives the photonuclear interaction pathlength

$$\begin{aligned} r_{\phi\text{nuc}}(E_{20}, z, A, Z) &= \frac{c}{\dot{N}_{\phi\text{nuc}}(\gamma, z, A, Z)} \\ &\rightarrow \frac{4.0E_{20}^2}{\bar{\epsilon}_{40} Z A^2 (1+z)} \exp \left(\frac{0.41A\bar{\epsilon}_{40}}{E_{20}(1+z)} \right) \text{ Mpc}, \end{aligned} \quad (9.72)$$

using eq. (9.66) for the energy-integrated cross section and treating ions heavier than He. This proves to be a poor approximation, as shown in figure 9.14.

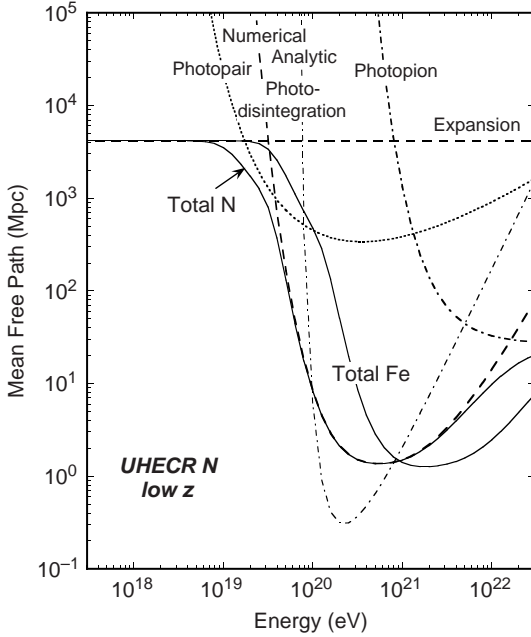


Figure 9.14 Photonuclear destruction pathlengths $r_{\phi_{\text{nuc}}}$, for low-redshift UHECR nitrogen nuclei interacting with CMBR photons. Separate effective mean free paths for photopion, photopair, photodisintegration, and universal expansion losses are shown for N, including total effective mean free path for N and Fe. Analytic photodisintegration mean free path for N is also shown.

9.9.2 Effective Photodisintegration Energy-Loss Rate

When a single proton or neutron is ejected, then a fraction A^{-1} of the original energy E is lost to the original nucleon, and with the ejection of two nucleons, a fraction $2/A$ of energy is lost. For multinucleon injection, an average fractional energy loss k_A/A is used [234], where $k_A = 1.2, 3.6,$ and 4.349 for $A = 4, 10 \leq A \leq 22,$ and $23 \leq A \leq 56,$ respectively. The photodisintegration energy-loss MFPs have only a generalized meaning in terms of the mean distance for an UHECR nucleon to be broken up into mostly lower energy protons and neutrons and a nucleon with A about half of the original nucleonic mass. Photodisintegration of Fe, for example, leads to significant fraction of $A \lesssim 15$ nucleon secondaries [234].

In the δ -function approximation for the GDR, eq. (9.69), the inverse of the effective energy-loss timescale of an UHECR ion due to photodisintegration

processes with photons of the CMBR, namely, the photodestruction rate, is

$$t_E^{-1}(E, A) = \frac{2\pi^2 c \Delta_{\text{GDR}} k_A \epsilon_{r,A} \Theta}{\gamma^2 A \lambda_C^3} \ln \left(\frac{1}{1 - \exp(-w_{r,A})} \right) \\ \cong 3.2 \times 10^{-15} \frac{k_A A^{1.79} (1+z)}{E_{20}^2} \ln \left(\frac{1}{1 - \exp(-w_{r,A})} \right) \text{ s}^{-1}, \quad (9.73)$$

where

$$w_{r,A} \equiv \frac{\epsilon_{r,A}}{2\gamma\Theta} = \frac{0.83 A^{0.79}}{E_{20}(1+z)}.$$

The effective path length for photodisintegration in the δ -function approximation for the GDR is therefore

$$\lambda_E = \lambda_E(E, A) = ct_E(E, A) \rightarrow \frac{3.0 E_{20}^2 \exp \{0.83 A^{0.79} / [(1+z) E_{20}]\}}{k_A A^{1.79} (1+z)} \text{ Mpc} \quad (9.74)$$

in the limit $w_{r,A} \gg 1$, that is, $E_{20} \ll 5(A/10)^{0.79}$. The analytic MFP is not very accurate, as shown for UHECR nitrogen in figure 9.14. The calculated MFPs provide inputs for Monte Carlo calculations (see Refs. [203,240]). Figure 9.14 also shows the effective photodisintegration energy-loss pathlengths of UHECR Fe in the CMBR at low redshift, using a low-energy threshold of 10 MeV [236]. This pathlength is an overestimate because of the neglect of the diffuse infrared radiation field, considered in the next chapter.

9.9.3 Neutrinos from Photodisintegration

The “guaranteed” cosmogenic GZK neutrino flux is actually quite sensitive to the ionic composition of UHECRs [241]. As we have seen, the diffuse neutrinos from UHECRs originate from photopion production and neutron β -decay. Many neutrons formed as secondaries in photodisintegration of ions will β -decay and, because of the large number of produced secondaries, make a flux of $\sim 10^{16}$ eV neutrinos. But the fractional energy to neutrinos in β -decay, with electron neutrinos taking $\approx 0.04\%$ of the neutron’s energy, makes it hard for ions to make a more detectable diffuse neutrino flux than protons, where a neutrino takes $\approx 5\%$ of the cosmic ray proton’s energy.

This factor reduces the efficiency for neutrino production compared to a pure proton composition. Consider that the threshold condition for photopion production by protons is $\gamma_p \langle \epsilon \rangle \gtrsim m_\pi / m_e$, $\langle \epsilon \rangle \approx 2.70\Theta \approx 1.2 \times 10^{-9}$, giving a threshold energy

$$E_p = m_p c^2 \gamma_p \gtrsim 2 \times 10^{20} \text{ eV}. \quad (9.75)$$

For an ion with energy E_N , by comparison, the threshold for interaction with the GDR is $\gamma_N \langle \epsilon \rangle \gtrsim \epsilon_{r,A}$, so

$$E_N = Am_p c^2 \gamma_N \cong 4 \times 10^{20} (A/10)^{0.79} \text{ eV}, \quad (9.76)$$

and the typical energy of a β -decay neutrino formed from photodisintegration is $\langle E_\nu \rangle \sim 2 \times 10^{16} (A/10)^{-0.21} \text{ eV}$.

If the upper energy of the UHECR ion injection spectrum extends to 10^{22} or 10^{23} eV, then a significant flux of high-energy neutrinos can be made through both photopion and photodisintegration processes. Besides fitting the UHECR proton and ion data [184], a model for the cosmogenic neutrinos must in addition underproduce the diffuse galactic γ -ray background intensity.

Chapter Ten

$\gamma\gamma$ Pair Production

In this chapter, the astrophysical importance of the $\gamma\gamma \rightarrow e^+e^-$ process that destroys γ rays and creates electron-positron pairs is considered. This reaction is the inverse of the pair annihilation process considered in section 8.4.

Topics include:

1. the $\gamma\gamma \rightarrow e^+e^-$ cross section $\sigma_{\gamma\gamma}(s)$ and the $\gamma\gamma$ pair-attenuation optical depth per unit pathlength, $d\tau_{\gamma\gamma}(\epsilon_1)/dx$, for a γ ray with energy ϵ_1 ;
2. δ -function approximation to the $\gamma\gamma \rightarrow e^+e^-$ cross section and an estimate of the $\gamma\gamma$ opacity $\tau_{\gamma\gamma}(\epsilon_1)$;
3. calculations of the $\gamma\gamma \rightarrow e^+e^-$ opacity of the universe for ~ 100 GeV – multi-TeV γ rays emitted from a source at redshift z that interact with photons of the EBL (extragalactic background light);
4. calculations of the $\gamma\gamma$ opacity in compact sources;
5. minimum Doppler factor in standard relativistic jet model from observations of a variable source of γ rays;
6. γ -ray suppression during periods of most luminous neutrino emission; and
7. electromagnetic cascades induced by leptonic or hadronic primaries interacting with ambient photons.

The $\gamma\gamma$ pair production optical depth $\tau_{\gamma\gamma}(\epsilon_1)$ is an integral quantity defined along a specific path. In the absence of other γ -ray sources in the path, the source flux is reduced by the factor $\exp(-\tau_{\gamma\gamma})$. By this mechanism, $\gtrsim 10$ GeV–TeV γ rays are attenuated by interacting with photons of the ambient diffuse EBL at IR and optical wavelengths. Measurements of pair production features from sources at different redshifts offer the prospect of measuring the diffuse and evolving IR and optical EBL. The amount of absorption for sources at different redshifts reveals the integral bolometric energy generated by stars and black holes, which make up the primary astrophysical sources of power. Much of this stellar and/or black-hole accretion and rotation power may be reprocessed into infrared wavelengths if the powerhouses are surrounded by thick columns of gas or dust. Attenuation of \gtrsim TeV radiation should be apparent by $z \cong 0.15$, which makes it a surprise

that HESS detects multi-TeV radiation from moderate redshift TeV blazars, including 1ES 1101-232 at $z = 0.186$ [242].

If the source medium is also the attenuating medium, then the emergent flux depends on the values of the energy-dependent emissivity $j(\epsilon, \Omega)$ and absorption coefficient κ_ϵ . For a radiating slab of width L , the emergent intensity, from eq. (7.154), is given by $I_\epsilon = j(\epsilon, \Omega)L [1 - \exp(-\tau_{\gamma\gamma})]/\tau_{\gamma\gamma}$ and for a uniform spherical source, by eqs. (7.121) and (7.122).

When a source is compact to γ rays with dimensionless energy ϵ_1 , $\tau_{\gamma\gamma}(\epsilon_1) > 1$, and γ rays with energy $\approx m_e c^2 \epsilon_1$ are absorbed by the source photons. The absorbed γ -ray materializes into an e^+e^- pair. Subsequent Compton and synchrotron emissions by these energetic secondary leptons can produce new γ rays that are again subject to γ -ray annihilation. In some cases, many generations of γ rays are formed in the electromagnetic cascade. Either high-energy leptons or hadrons can, depending on source conditions, induce these cascades. PeV neutrino detection from relativistic jet sources would confirm the acceleration of hadrons in these sources, likely solving the problem of UHECR origin.

As already mentioned in the previous chapter, cosmogenic γ rays formed as the decay products of secondaries produced in photopair and photopion processes between UHECRs and target photons of the EBL make a guaranteed source of diffuse extragalactic background γ rays. We conclude this chapter with a consideration of cascades induced by UHECRs at the sources and throughout intergalactic space.

10.1 $\gamma\gamma$ PAIR-PRODUCTION CROSS SECTION

From the methods of quantum electrodynamics [37,64], one obtains the $\gamma\gamma$ pair-production cross section

$$\sigma_{\gamma\gamma}(s) = \frac{1}{2}\pi r_e^2 (1 - \beta_{\text{cm}}^2) \left[(3 - \beta_{\text{cm}}^4) \ln \left(\frac{1 + \beta_{\text{cm}}}{1 - \beta_{\text{cm}}} \right) - 2\beta_{\text{cm}}(2 - \beta_{\text{cm}}^2) \right], \quad (10.1)$$

where $\beta_{\text{cm}} = (1 - \gamma_{\text{cm}}^{-2})^{1/2} = \sqrt{1 - s^{-1}}$, and $\sqrt{s} = \gamma_{\text{cm}}$ is the center-of-momentum frame Lorentz factor of the produced electron and positron. The strength of a collision is characterized by the invariant energy $\sqrt{s_{\text{tot}}}$, defined in terms of four-vectors p_1^μ and p_2^μ by

$$s_{\text{tot}} = (p_1^\mu + p_2^\mu)^2 = (\epsilon_1 + \epsilon)^2 - (\epsilon_1 + \epsilon\mu)^2 - \epsilon^2(1 - \mu^2) = 2\epsilon\epsilon_1(1 - \mu). \quad (10.2)$$

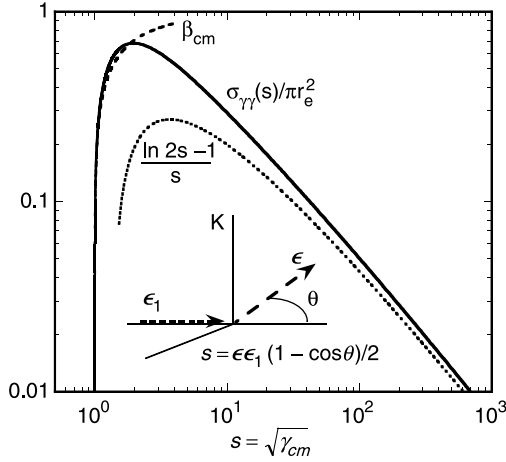


Figure 10.1 Cross section for $\gamma\gamma$ pair production, $\sigma_{\gamma\gamma}(s)$, as a function of invariant s , along with asymptotes at $s - 1 \ll 1$ and $s \gg 1$.

At threshold, two leptons are formed at rest with total energy $2m_e c^2$, so that $s_{\text{tot}} = 4$ at threshold. Above threshold, $s_{\text{tot}} = 4\gamma_{\text{cm}}^2$. Hence

$$s = \gamma_{\text{cm}}^2 = \frac{1}{2}[\epsilon\epsilon_1(1 - \mu)] = \frac{s_{\text{tot}}}{4}. \tag{10.3}$$

The asymptotes of the cross section are

$$\sigma_{\gamma\gamma}(s) = \pi r_e^2 \begin{cases} \beta_{\text{cm}}, & \beta_{\text{cm}} \ll 1, \\ \frac{\ln 2s - 1}{s}, & s \gg 1. \end{cases} \tag{10.4}$$

Equations (10.1) and (10.4), plotted in figure 10.1, give the $\gamma\gamma$ pair-production cross section as a function of s . The interaction angle $\theta = \arccos \mu$ is the angle between the directions of ϵ_1 and ϵ . For a γ -ray photon with energy ϵ_1 passing through a background of photons with energy ϵ and angle θ , the cross section is invariant with respect to fixed values of the interaction energy $s = \epsilon\epsilon_1(1 - \mu)/2$. Note the strong peaking of the cross section when $s \approx 2$, which consequently favors collisions near threshold. The assumption $s \approx 2$ gives a good approximation to this process except when the target photon spectrum is so hard that $s \gg 1$ interactions become important.

For γ rays passing through isotropic photon fields, $s \rightarrow \epsilon\epsilon_1$ for head-on collisions. For approximations, $s \rightarrow \epsilon\epsilon_1/2$ (assuming typical collision angle $\theta \cong \pi/2$) gives reliable estimates for a typical interaction with isotropic target photons. The threshold for pair production in $\gamma\gamma$ processes is $\beta_{\text{cm}} > 0$,

$\gamma_{\text{cm}} > 1$, implying $s > 1$. Relations of interest for pair production are

$$\gamma_{\text{cm}} = \sqrt{\frac{\gamma_r + 1}{2}} \quad \text{and} \quad \gamma_r = 2\gamma_{\text{cm}}^2 - 1,$$

where γ_r is the Lorentz factor of one produced lepton in the rest frame of the second antilepton.

The absorption probability per unit pathlength is

$$\frac{d\tau_{\gamma\gamma}(\epsilon_1)}{dx} = \frac{\dot{N}_{\text{sc}}}{c} = \oint d\Omega (1 - \mu) \int_0^\infty d\epsilon n_{\text{ph}}(\epsilon, \Omega) \sigma_{\gamma\gamma}(s), \quad (10.5)$$

from eq. (2.40), where \dot{N}_{sc} is the γ -ray absorption rate, and the dependence on ϵ_1 is contained in the definition of s , eq. (10.3). For an *isotropic* photon field,

$$\frac{d\tau_{\gamma\gamma}}{dx} = \frac{1}{2} \int_{-1}^1 d\mu (1 - \mu) \int_0^\infty d\epsilon n_{\text{ph}}(\epsilon) \sigma_{\gamma\gamma}(s). \quad (10.6)$$

This can be written [243–245] in the form

$$\frac{d\tau_{\gamma\gamma}}{dx} = \frac{\pi r_e^2}{\epsilon_1^2} \int_{1/\epsilon_1}^\infty d\epsilon \epsilon^{-2} n_{\text{ph}}(\epsilon) \bar{\varphi}(s_0), \quad (10.7)$$

where $s_0 \equiv \epsilon\epsilon_1$, and

$$\bar{\varphi}(s_0) = 2 \int_1^{s_0} ds \frac{s\sigma_{\gamma\gamma}(s)}{\pi r_e^2}. \quad (10.8)$$

From the formulae of Gould and Schröder [244], corrected in [245],

$$\begin{aligned} \bar{\varphi}(s_0) = & \frac{1 + \beta_0^2}{1 - \beta_0^2} \ln w_0 - \beta_0^2 \ln w_0 - \ln^2 w_0 - \frac{4\beta_0}{1 - \beta_0^2} \\ & + 2\beta_0 + 4 \ln w_0 \ln(1 + w_0) - 4L(w_0), \end{aligned} \quad (10.9)$$

where $\beta_0^2 = 1 - 1/s_0$, $w_0 = (1 + \beta_0)/(1 - \beta_0)$, and

$$L(w_0) = \int_1^{w_0} dw w^{-1} \ln(1 + w) = \frac{1}{2} \ln^2 w_0 + \frac{\pi^2}{12} - \sum_{n=1}^{\infty} (-)^{n-1} n^{-2} w_0^{-n}. \quad (10.10)$$

Equation (10.9) can also be written as

$$\begin{aligned} \bar{\varphi}(s_0) = & \left(2s_0 - 2 + \frac{1}{s_0} \right) \ln w_0 + 2(1 - 2s_0) \sqrt{1 - s_0^{-1}} \\ & + \ln w_0 [4 \ln(1 + w_0) - 3 \ln w_0] - \frac{1}{3} \pi^2 + 4 \sum_{n=1}^{\infty} (-)^{n-1} n^{-2} w_0^{-n}. \end{aligned} \quad (10.11)$$

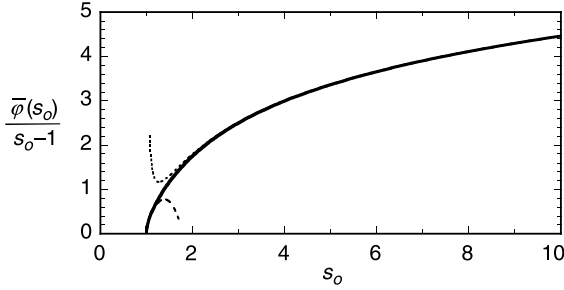


Figure 10.2 Graph of the function $\bar{\varphi}(s_0)/(s_0 - 1)$ used to calculate $\tau_{\gamma\gamma}$ in an isotropic photon field, including asymptotes at small and large values of s_0 , from eq. (10.12).

The asymptotes of $\bar{\varphi}(s_0)$ are

$$\bar{\varphi}(s_0) \rightarrow \begin{cases} 2s_0(\ln 4s_0 - 2) + \ln 4s_0(\ln 4s_0 - 2) - \frac{\pi^2 - 9}{3} \\ \quad + s_0^{-1}(\ln 4s_0 + 9/8) + \dots, & s_0 \gg 1, \\ \frac{4}{3}(s_0 - 1)^{3/2} + \frac{6}{5}(s_0 - 1)^{5/2} \\ \quad - (253/70)(s_0 - 1)^{7/2} + \dots, & s_0 - 1 \ll 1 \end{cases} \quad (10.12)$$

(see figure 10.2).

10.1.1 Absorption by a Blackbody and a Modified Blackbody Photon Gas

The number spectrum of a blackbody photon gas, from eq. (5.16), is given by

$$n_{\text{bb}}(\epsilon; \Theta) = \frac{8\pi}{\lambda_C^3} \frac{\epsilon^2}{\exp(\epsilon/\Theta) - 1}. \quad (10.13)$$

We generalize this formula to treat modified blackbody spectral energy densities of the form

$$\epsilon u(\epsilon) = u_0 \frac{w^k}{\exp(w) - 1} = m_e c^2 \epsilon^2 n_{\text{ph}}(\epsilon), \quad (10.14)$$

where $w = \epsilon/\Theta$. For a blackbody, $k = 4$ and $u_0 = 8\pi m_e c^2 \Theta^4 / \lambda_C^3$.

Substitution of the blackbody spectrum, eq. (10.13), into eq. (10.7) gives

$$\frac{d\tau_{\gamma\gamma}^{\text{bb}}}{dx} = \frac{2\alpha_f^2}{\lambda_C} \epsilon_1^{-2} \int_{1/\epsilon_1}^{\infty} d\epsilon \frac{\bar{\varphi}(s_0)}{\exp(\epsilon/\Theta) - 1} \equiv \frac{2\alpha_f^2}{\lambda_C} \Theta^3 \mathcal{F}(v) \quad (10.15)$$

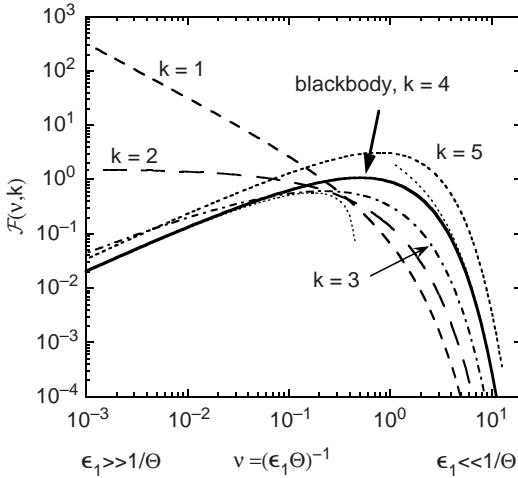


Figure 10.3 Graph of the function $\mathcal{F}(v)$ ($\equiv \mathcal{F}(v, 4)$), eq. (10.17), used to calculate $\tau_{\gamma\gamma}$ in a blackbody photon field, including asymptotes (dotted curves) from eq. (10.18). Also shown are the functions $\mathcal{F}(v, k)$, eq. (10.22), for $k = 1, 2, 3, 4$ (blackbody), and 5.

for the differential $\gamma\gamma$ opacity through a blackbody radiation field, where

$$v \equiv \frac{1}{\epsilon_1 \Theta} \tag{10.16}$$

and

$$\mathcal{F}(v) = v^2 \int_v^\infty dw \frac{\bar{\varphi}(w/v)}{\exp(w) - 1}. \tag{10.17}$$

The asymptotes of $\mathcal{F}(v)$ are

$$\mathcal{F}(v) \rightarrow \begin{cases} \sqrt{\pi v} \exp(-v) \left(1 + \frac{9}{4v}\right), & v \gg 1 \text{ or } \epsilon_1 \ll 1/\Theta, \\ \frac{\pi^2 v}{3} \ln(0.47/v), & v \ll 1 \text{ or } \epsilon_1 \gg 1/\Theta \end{cases} \tag{10.18}$$

[131,244,245]. Figure 10.3 is a graph of the function $\mathcal{F}(v)$, along with its asymptotes.

The asymptotes of the $\gamma\gamma$ optical depth through the local $z \ll 1$ CMBR for a photon of energy E (PeV) from a source at distance d are given, from eqs. (10.15) and (10.18), by the expressions

$$\tau_{\gamma\gamma}(E \text{ (PeV)}, d) \cong \left(\frac{d}{10 \text{ kpc}}\right) \begin{cases} (2.5/\sqrt{E \text{ (PeV)}}) \exp(-1.16/E_{\text{PeV}}), & E_{\text{PeV}} \ll 1, \\ (5.0/E_{\text{PeV}}) \ln(0.40 E \text{ (PeV)}), & E_{\text{PeV}} \gg 1. \end{cases} \tag{10.19}$$

The source distance for unity optical depth in the redshift- z CMBR is, therefore,

$$\lambda_{\gamma\gamma}^{\text{CMB}} (\text{kpc}) \cong \begin{cases} \frac{4\sqrt{E} (\text{PeV})}{(1+z)^{5/2}} \exp\{-1.16/[E (\text{PeV})](1+z)\}, & (1+z)E (\text{PeV}) \ll 1, \\ \frac{2.1 E (\text{PeV})}{(1+z)^2 \ln\{0.42[E (\text{PeV})](1+z)\}}, & (1+z)E (\text{PeV}) \gg 1. \end{cases} \quad (10.20)$$

PeV sources in our Galaxy should show significant attenuation from the CMBR, as well as from stellar radiation fields [246].

For the modified blackbody, eq. (10.14), eq. (10.7) gives

$$\frac{d\tau_{\gamma\gamma}^{\text{mbb}}}{dx} = \frac{\pi r_e^2}{\Theta m_e c^2} u_0 \mathcal{F}(v, k), \quad (10.21)$$

where eq. (10.17) is generalized to

$$\mathcal{F}(v, k) = v^2 \int_v^\infty dw \frac{w^{k-4} \bar{\varphi}(w/v)}{\exp(w) - 1}. \quad (10.22)$$

Figure 10.3 is a graph of the function $\mathcal{F}(v, k)$, for $k = 1, 2, 3, 4$ (blackbody), and 5. Thus $\mathcal{F}(v) = \mathcal{F}(v, 4)$. The $v \gg 1$ asymptote of $\mathcal{F}(v, k)$ is

$$\mathcal{F}(v, k) \xrightarrow[v \gg 1]{} \sqrt{\pi} v^{k-7/2} \exp(-v). \quad (10.23)$$

10.1.2 Absorption by a Power-Law Photon Gas in a Relativistic Jet

The $\gamma\gamma$ optical depth of γ rays interacting with lower-energy target photons with a broken power-law target photon spectrum in a relativistic flow is treated here. The target photon spectrum is defined in the fluid frame of a relativistic jet, and is assumed to have low- and high-energy cutoffs. We restore the primes to quantities in the proper frame of the relativistic bulk flow, and then transform to the observer frame through the relations $\epsilon'_1 = (1+z)\epsilon_1/\delta_D$ for the γ -ray energy and $\epsilon' = (1+z)\epsilon/\delta_D$ for the target photon energy.

Consider a uniform spherical radiating blob of volume $V'_b = 4\pi r_b^3/3$. The measured vF_v flux is related to the comoving emissivity according to

the relation

$$\nu F_\nu = f_\epsilon \cong \frac{\delta_D^4 V'_b}{d_L^2} \epsilon' j'(\epsilon', \Omega') \rightarrow \frac{\delta_D^4 V'_b}{4\pi d_L^2} \epsilon' j'(\epsilon'), \quad (10.24)$$

where $j'(\epsilon', \Omega')$ is the comoving emissivity (see section 5.5), Ω is the direction vector, and the final expression in eq. (10.24) assumes isotropic emission in the comoving frame. Equation (10.24) is an approximation because we have implicitly assumed that the light travel time across the blob is smaller than the duration of the flare in order to avoid integrations over different portions of the emitting plasma, consistent with causality arguments for a discrete intense flare or pulse. The expression $dt = (1+z)dt'/\delta_D$ relating observer and comoving differential times implies $r'_b \lesssim ct'_{\text{var}} = c\delta_D t_{\text{var}}/(1+z)$.

The comoving spectral energy density $u'_{\epsilon'} = m_e c^2 \epsilon'^2 n'(\epsilon')$ is related to the isotropic emissivity $j'(\epsilon')$ through the relation $\epsilon' j'(\epsilon') \cong u'_{\epsilon'}/\langle t'_{\text{esc}} \rangle \cong cu'_{\epsilon'}/r'_b$, where $\langle t'_{\text{esc}} \rangle$ is the mean photon escape time and $n'(\epsilon')$ is the spectral photon number density (eq. [5.47]). Thus

$$u'_{\epsilon'} \cong \frac{3d_L^2}{cr'_b{}^2\delta_D^4} f_\epsilon = \frac{3d_L^2}{cr'_b{}^2\delta_D^4} f_{\epsilon_{\text{pk}}} S(x), \quad (10.25)$$

where $x = \epsilon/\epsilon_{\text{pk}} = \epsilon'/\epsilon'_{\text{pk}}$ and the spectral function $S(x)$ defines the shape of the νF_ν spectrum.

If the target SED is approximated by a broken power law with peak energy flux $f_{\epsilon_{\text{pk}}}$ at $\epsilon = \epsilon_{\text{pk}}$ with νF_ν indices a (>0) and b (<0) at low and high frequencies, respectively, then

$$S(x) = x^a H(x; x_a, 1) + x^b H(x; 1, x_b). \quad (10.26)$$

Equations (10.7) and (10.25) give

$$\begin{aligned} \tau_{\gamma\gamma}(\epsilon_1) &= \frac{3\pi r_e^2 d_L^2 f_{\epsilon_{\text{pk}}}}{cr'_b{}^2\delta_D^4 m_e c^2} \frac{1}{\epsilon_1'^2 \epsilon_{\text{pk}}'^3} \int_{1/\epsilon_1' \epsilon_{\text{pk}}'}^{\infty} dx x^{-4} S(x) \bar{\varphi}(x\epsilon_1' \epsilon_{\text{pk}}') \\ &= \frac{3\pi r_e^2 d_L^2 f_{\epsilon_{\text{pk}}}}{m_e c^4 t_{\text{var}} \epsilon_1'^2 \epsilon_{\text{pk}}'^3 (1+z)^4} \int_{\omega^{-1}}^{\infty} dx x^{-4} S(x) \bar{\varphi}(x\omega) \\ &= \frac{3\pi r_e^2 d_L^2 f_{\epsilon_{\text{pk}}}}{m_e c^4 t_{\text{var}} \epsilon_1'^2 \epsilon_{\text{pk}}'^3 (1+z)^4} \left[H\left(1 - \frac{1}{\omega}\right) \int_{\max(x_a, 1/\omega)}^1 dx \frac{\bar{\varphi}(x\omega)}{x^{4-a}} \right. \\ &\quad \left. + \int_{\max(1, 1/\omega)}^{x_b} dx \frac{\bar{\varphi}(x\omega)}{x^{4-b}} \right], \quad (10.27) \end{aligned}$$

where $\omega = (1+z)^2 \epsilon_1 \epsilon_{\text{pk}} / \delta_D^2$, and the final expression uses the broken power-law spectrum, eq. (10.26). The asymptotic behavior of low-energy γ -rays

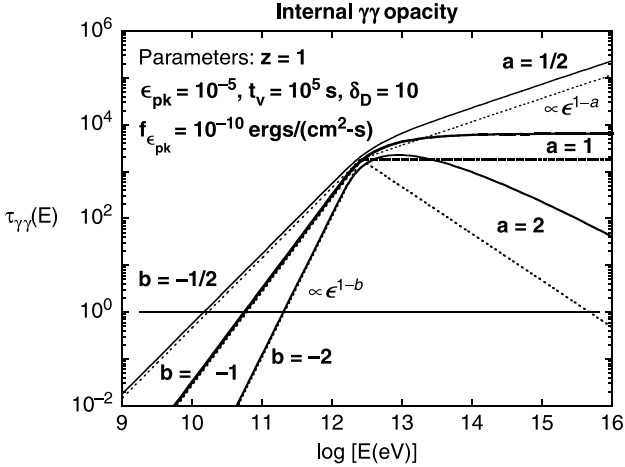


Figure 10.4 $\gamma\gamma$ opacity $\tau_{\gamma\gamma}(\epsilon_1)$ as a function of photon energy for parameters shown, with Doppler factor $\delta_D = 10$ and $z = 1$. The target photon SED is approximated as a broken power law, eq. (10.26), with νF_ν flux peaking at $\epsilon_{pk} = 10^{-5}$. Heavy and light curves for $\tau_{\gamma\gamma}(\epsilon_1)$ are accurate numerical integration, eq. (10.27), and δ -function approximation, eq. (10.34), respectively.

($\epsilon_1 \ll \epsilon_{pk}$) interacting with the high-energy portion of the target isotropic photon spectrum is given by

$$\tau_{\gamma\gamma}(\epsilon_1) \rightarrow \frac{3\pi r_e^2 d_L^2 f_{\epsilon_{pk}}}{cr_b' \delta_D^4 m_e c^2} \epsilon_{pk}^{1-b} \epsilon_1^{1-b} \int_1^{x_b \epsilon_{pk}' \epsilon_1'} ds s^{b-4} \bar{\varphi}(s) \propto \epsilon_1^{1-b}, \quad (10.28)$$

where the behavior expressed in the last relation holds when $x_b = \epsilon_b/\epsilon_{pk} \gg 1/\epsilon_{pk}' \epsilon_1'$, or when $\delta_D^2/(1+z)^2 \epsilon_{pk} \gg \epsilon_1 \gg \delta_D^2/(1+z)^2 \epsilon_b$. Likewise, the asymptotic behavior of high-energy γ rays when $\delta_D^2/(1+z)^2 \epsilon_a \gg \epsilon_1 \gg \delta_D^2/(1+z)^2 \epsilon_{pk}$ is $\tau_{\gamma\gamma}(\epsilon_1) \propto \epsilon_1^{1-a}$,

Figure 10.4 shows a numerical calculation of the opacity of photons traveling through a target power-law photon field for a model blazar, using eq. (10.27). The photon SED is given by eq. (10.26), with different values of a and b as shown in the figure. The parameters of the calculation are shown in the figure legend, and $\delta_D = 10$.

10.1.3 $\gamma\gamma$ Attenuation in Anisotropic Radiation Fields

By integrating eq. (10.5) over the pathlength of the γ ray, one can derive the total $\gamma\gamma$ optical depth for a photon with measured energy ϵ_1 [247]. For a Shakura-Sunyaev disk field with intensity $I_\epsilon^{SS}(\Omega; \vec{R})$ given by eq. (6.139),

the absorption optical depth $\tau_{\gamma\gamma}$ can be calculated by substituting the photon intensity $n_{\text{ph}}^{\text{SS}}(\epsilon_*, \Omega_*) = I_{\epsilon_*}^{\text{SS}}(\Omega_*; \tilde{R})/\epsilon_* m_e c^3$ into eq. (10.5) and integrating x from r to ∞ . The optical depth to $\gamma\gamma$ pair production attenuation for a γ ray traveling outward along the jet axis starting at height \tilde{R} is [73]

$$\tau_{\gamma\gamma}^{\text{SS}}(\epsilon_1, \tilde{r}) \cong 6 \times 10^6 \frac{\ell_{\text{Edd}}^{3/4} M_9^{1/4}}{\eta_f^{3/4}} \int_{\tilde{R}}^{\infty} \frac{d\tilde{x}}{\tilde{x}^2} \int_6^{\infty} \frac{d\tilde{R}}{\tilde{R}^{5/4}} \times \frac{[\phi(\tilde{R})]^{1/4} H(\tilde{s} - 1)}{(1 + \tilde{R}^2/\tilde{x}^2)^{3/2}} \left(\frac{\sigma_{\gamma\gamma}(\tilde{s})}{\pi r_e^2} \right) (1 - \mu_*), \quad (10.29)$$

where $\tilde{s} \equiv (\epsilon(\tilde{R}))_{\epsilon_1} (1+z)(1 - \mu_*)/2$ and $\mu_* = 1/\sqrt{1 + \tilde{R}^2/\tilde{x}^2}$. For the Shakura-Sunyaev disk extending to the innermost stable orbit of a Schwarzschild black hole, one sees from eq. (10.29) that $\tau_{\gamma\gamma}^{\text{SS}}(\epsilon_1, \tilde{R})/M_9 \propto \xi \equiv (\ell_{\text{Edd}}/M_9 \eta_f)^{1/4}$.

For the case of a photon traversing a radiation field scattered by BLR gas, we consider a radially symmetric scattering shell, as in section 6.9. Substitution of eq. (6.170) into eq. (10.5) for a monochromatic photon source, eq. (6.173), gives

$$\tau_{\gamma\gamma}(\epsilon_1, r) = \frac{\sigma_{\text{T}} L_0}{8\pi m_e c^3 \epsilon_*} \int_r^{\infty} \frac{dx}{x} \times \int_{-1}^{1-2/[\epsilon_1 \epsilon_* (1+z)]} d\mu_* (1 - \mu_*) \mathcal{N}(\mu_*, x) \sigma_{\gamma\gamma}(s) \quad (10.30)$$

for the opacity of a photon with measured energy ϵ_1 emitted outward along the jet axis at height r . The $\gamma\gamma$ opacity vanishes when $\epsilon_1 \leq 1/[\epsilon_*(1+z)]$ due to the $\gamma\gamma$ pair-production threshold. Blandford and Levinson [80, 248] introduced the concept of a pair horizon to describe a source radiation environment that strongly attenuates GeV and TeV photons from the jet. See also Refs. [83, 249].

10.2 δ -FUNCTION APPROXIMATION FOR $\sigma_{\gamma\gamma}$

In cases where the external radiation can be approximated as isotropic, a mean interaction takes place with $\theta \approx \pi/2$ or $\mu = 0$. In this case, we can write

$$\frac{d\tau_{\gamma\gamma}}{dx} \cong \int_{2/\epsilon_1}^{\infty} d\epsilon \sigma_{\gamma\gamma}(\epsilon_1 \epsilon) n_{\text{ph}}(\epsilon; x). \quad (10.31)$$

Given this assumption, the simplest invariant cross section that can be formed from the (quasi-)invariant $\epsilon\epsilon_1$ is

$$\sigma_{\gamma\gamma}(\epsilon\epsilon_1) \cong \frac{2}{3}\sigma_T \delta(\epsilon\epsilon_1 - 2) \cong \frac{2}{3}\frac{\sigma_T}{\epsilon_1} \delta\left(\epsilon - \frac{2}{\epsilon_1}\right) \cong \frac{1}{3}\sigma_T \epsilon \delta\left(\epsilon - \frac{2}{\epsilon_1}\right) \tag{10.32}$$

[250], where the coefficient improves comparison with numerical results.

The photoabsorption optical depth for a γ -ray photon with energy ϵ_1 in a radiation field with spectral photon density $n_{\text{ph}}(\epsilon', \mu'; r')$ ($\approx n_{\text{ph}}(\epsilon')/2$ for a uniform isotropic radiation field in the comoving frame) is [244]

$$\begin{aligned} \tau_{\gamma\gamma}(\epsilon'_1) &= \int_{r'_1}^{r'_2} dr' \int_{-1}^1 d\mu'(1 - \mu') \\ &\quad \times \int_{2/\epsilon'_1(1-\mu')}^{\infty} d\epsilon' \sigma_{\gamma\gamma}[\epsilon'\epsilon'_1(1 - \mu')]n_{\text{ph}}(\epsilon', \mu'; r') \\ &\cong r'_b \int_0^{\infty} d\epsilon' \sigma_{\gamma\gamma}(\epsilon', \epsilon'_1) n'_{\text{ph}}(\epsilon'). \end{aligned} \tag{10.33}$$

Using the approximation (10.32) for the cross section and making the substitutions in eq. (10.33) gives [251]

$$\tau_{\gamma\gamma}(\epsilon_1) = \tau_{\gamma\gamma}^{\text{pk}} \left[\left(\frac{\epsilon_1}{\epsilon_1^{\text{pk}}}\right)^{1-b} H(\epsilon_1^{\text{pk}} - \epsilon_1) + \left(\frac{\epsilon_1}{\epsilon_1^{\text{pk}}}\right)^{1-a} H(\epsilon_1 - \epsilon_1^{\text{pk}}) \right], \tag{10.34}$$

where

$$\tau_{\gamma\gamma}^{\text{pk}} = \frac{\sigma_T d_L^2 f_{\epsilon_{\text{pk}}}}{2m_e c^4 t_{\text{var}} \delta_D^4 \epsilon_{\text{pk}}} \tag{10.35}$$

and

$$\epsilon_1^{\text{pk}} = \frac{2\delta_D^2}{(1+z)^2 \epsilon_{\text{pk}}}. \tag{10.36}$$

Comparison of numerical calculations with the approximate form of $\tau_{\gamma\gamma}$, eq. (10.35), is shown in fig. 10.4. Note that a factor 1/2 was added in eq. (10.35) to improve agreement with the numerical calculations of $\tau_{\gamma\gamma}$ in the low-energy asymptote.

10.3 OPACITY OF THE UNIVERSE TO $\gamma\gamma$ ATTENUATION

The EBL consists of separate emission components that evolve differently through cosmic time, the most energetically important of which is the

Table 10.1 Relations Between γ -Ray Energy and Target Photon Frequency for $\gamma\gamma$ Attenuation

λ (μm)	1	2	4	8	12	25	60	100	1000
ν (10^{12} Hz)	300	150	75	37.5	25	12	5	3	0.3
E (eV)	1.24	0.62	0.32	0.16	0.10	0.50	0.21	0.012	0.0012
E_1 (TeV)	0.42	0.84	1.68	3.4	5	10	25	42	420

CMBR (section 1.5). The EBL is additionally formed by the superposition of stellar, galactic, black hole, dark matter, etc., emissions since the onset of structure formation. The EBL at IR wavelengths is difficult to measure directly because of foreground contamination by zodiacal light and galactic cosmic-ray electron synchrotron emission. The cosmological importance of measuring the diffuse cosmic IR and optical background lies in the fact that its intensity is determined primarily by stellar processes, and gives a bolometric calorimetry of normal matter processes.

Because of the peaking of $\sigma_{\gamma\gamma}(\epsilon_r)$ at $\epsilon_r \cong 2$, photons with energy ϵ_1 are preferentially attenuated by photons with energy ϵ according to the relation $\epsilon_1\epsilon \cong 2$ or, in dimensional units,

$$E_1 \text{ (TeV)} \cong 0.4\lambda \text{ (\mu m)} \quad (10.37)$$

where $\lambda = h/m_e c\epsilon$ is the wavelength of the target photon. Table 10.1 shows values of GeV and TeV photon energies E_1 which are most strongly attenuated by infrared photons with wavelength λ between 1 and 1000 μm . One micron or ≈ 1 eV photons effectively attenuate ~ 0.5 TeV γ rays. Photons detected with the Fermi Gamma Ray Space Telescope at ~ 10 GeV will be preferentially attenuated at large redshift, so eq. (10.37) does not hold below $\approx 1 \mu$.

10.3.1 $\gamma\gamma$ Optical Depth of the Universe

The optical depth per unit distance traveled through the universe by a γ -ray photon with energy ϵ_1 (measured at the present epoch) is, starting from eq. (10.7),

$$\frac{d\tau_{\gamma\gamma}(\epsilon_1, z)}{dx} = \frac{\pi r_e^2}{\epsilon_1^2(1+z)^2} \int_{1/\epsilon_1(1+z)}^{\infty} d\epsilon \frac{n_{\text{ph}}(\epsilon; z)}{\epsilon^2} \bar{\varphi}[\epsilon\epsilon_1(1+z)]. \quad (10.38)$$

Because $dx = cd t_*$, the total $\gamma\gamma$ optical depth becomes

$$\begin{aligned} \tau_{\gamma\gamma}(\epsilon_1, z) &= \frac{c\pi r_e^2}{\epsilon_1^2} \int_0^z dz' \left| \frac{dt^*}{dz'} \right| \frac{1}{(1+z')^2} \\ &\times \int_{1/\epsilon_1(1+z')}^\infty d\epsilon \frac{n_{\text{ph}}(\epsilon; z')}{\epsilon^2} \bar{\varphi}[\epsilon \epsilon_1(1+z')]. \end{aligned} \quad (10.39)$$

For a modified blackbody radiation field described by eq. (10.14), and the flat Λ CDM cosmological relation $|dt^*/dz|$, eq. (4.32), we find

$$\tau_{\gamma\gamma}(\epsilon_1, z) = \frac{c\pi r_e^2}{m_e c^2 H_0} \int_0^z dz' \frac{u_0(z') \mathcal{F}(v, k)}{\Theta(z')(1+z') \sqrt{\Omega_m(1+z')^3 + \Omega_\Lambda}} \quad (10.40)$$

with $v^{-1} = \epsilon_1(1+z')\Theta(z')$ and $\mathcal{F}(v, k)$ from eq. (10.22).

The $\gamma\gamma$ optical depth to cosmic blackbody radiation (CBR, not CMBR, because the CBR ceases to be primarily microwave radiation at high redshift) is

$$\tau_{\gamma\gamma}^{\text{CBR}}(\epsilon_1, z) = \frac{2\alpha_f^2 c}{H_0 \lambda_C} \Theta_0^3 \int_0^z dz' \frac{(1+z')^3 \mathcal{F}[v(z')]}{\sqrt{\Omega_m(1+z')^3 + \Omega_\Lambda}} \quad (10.41)$$

from eq. (10.15), where $v(z') = 1/[\epsilon_1 \Theta_0(1+z')]$ (see eqs. [10.16] and [5.17]). The opacity of X-rays and γ -rays in evolving blackbody radiation fields, including Compton scattering with gas and higher-order processes such as $\gamma\gamma \rightarrow \gamma\gamma$ scattering, was treated in detail by Zdziarski and Svensson [131,252].

Equations (4.32) and (4.57) give the expression

$$\epsilon I_\epsilon = \frac{c}{4\pi H_0} \int_0^{z_{\text{max}}} dz \frac{\epsilon_* j_{\text{co}}(\epsilon_*; z)}{(1+z)^2 \sqrt{\Omega_m(1+z)^3 + \Omega_\Lambda}} \quad (10.42)$$

for the present intensity of radiation in a flat universe from sources described by isotropic emissivity functions; thus $j_{\text{co}}(\epsilon_*; z) = 4\pi m_e c^2 \epsilon_* \dot{N}_{\text{co}}(\epsilon_*, \Omega_*; z)$. The maximum redshift of the emission is $z = z_{\text{max}}$. For radiation fields produced by cosmic sources, the photon spectral density at redshift z , given by $n_{\text{ph}}(\epsilon; z) = 4\pi \epsilon I_\epsilon / (m_e c^3 \epsilon^2)$, is

$$n_{\text{ph}}(\epsilon; z) = \frac{1}{H_0} \int_z^{z_{\text{max}}} dz' \frac{\dot{n}_{\text{co}}(\epsilon_*; z')}{\sqrt{\Omega_m(1+z')^3 + \Omega_\Lambda}}, \quad (10.43)$$

from eq. (4.57). In this expression, $\dot{N}_{\text{co}}(\epsilon_*; z')$ is the photon emissivity at z' , and

$$\epsilon_* = \frac{(1+z')}{(1+z)} \epsilon.$$

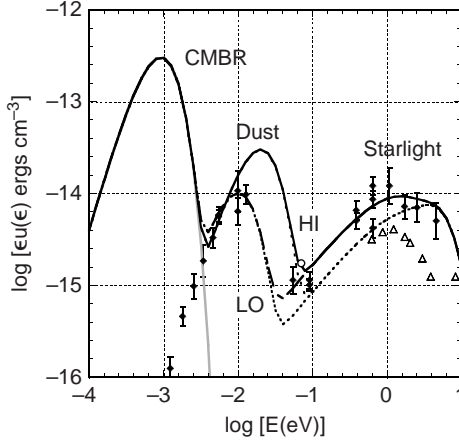


Figure 10.5 Measurements of the EBL at optical and infrared frequencies [253], and empirical fits to the EBL using modified blackbody functions, plotted in terms of spectral energy density $\epsilon u(\epsilon)$. Data triangles pointed upwards are lower limits. The spectral energy density of the CMBR at $z = 0$ is also shown.

10.3.2 Measurements of the EBL

Figure 10.5 shows measurements of the intensity of the unresolved IR and optical EBL at the present epoch from the review by Hauser and Dwek [253], including an upper limit at ≈ 0.1 eV inferred from γ -ray observations [254]. Motivated by the appearance of two distinct peaks in the SED of luminous infrared galaxies and normal star-forming galaxies like the Milky Way, we fit these two peaks with the modified blackbody functions, eq. (10.14). The lower-energy emission feature peaking near ≈ 0.01 eV, probably due to radiation reprocessed by dust, is referred to as the dust component. The higher-energy emission feature peaking near 2 eV is referred to as the stellar component.

The relationship giving u_0 and Θ in terms of the peak spectral energy density $u_{\text{pk}} = \epsilon_{\text{pk}} u(\epsilon_{\text{pk}})$ at peak dimensionless photon energy ϵ_{pk} is, from eq. (10.14), given by

$$u_0 \equiv u_{\text{pk}} \omega_k = u_{\text{pk}} \frac{\exp(a_k) - 1}{a_k^k}, \quad (10.44)$$

where a_k is a solution to the equation

$$(k - a_k) \exp(a_k) = k, \quad (10.45)$$

Table 10.2 Functions Defined in Eqs. (10.44) and (10.45)

k	a_k	$\omega_k = \frac{\exp(a_k) - 1}{a_k^k}$	$\Gamma(k)\zeta(k)$
2.0	1.659	1.545	1.6449
2.5	2.23	1.18	1.7826
3.0	2.82	0.703	2.404
3.5	3.38	0.40	3.745
3.8	3.707	0.273	5.145
4.0	3.92	0.209	6.494

$\Theta = \epsilon_{pk}/a_k$, and

$$u_{\text{tot}} = u_0 \int_0^\infty dx \frac{x^{k-1}}{\exp(x) - 1} = u_0 \Gamma(k)\zeta(k).$$

Solutions to eq. (10.45) and values of ω_k and $\Gamma(k)\zeta(k)$ are given in table 10.2. Fits to the EBL data shown in figure 10.5 are described below.

10.3.3 $\gamma\gamma$ Attenuation at Low Redshifts

The EBL does not evolve much at $z \ll 1$. The $\gamma\gamma$ opacity can therefore be estimated using the photon spectrum given in the $\epsilon u(\epsilon)$ form, as shown in figure 10.5. The $\gamma\gamma$ optical depth, eq. (10.21), for a photon traveling a distance $d = 10^{27} d_{27}$ (corresponding to $z \cong 0.08$ or a distance of ≈ 350 Mpc for the standard Λ CDM described in section 4.2.5) can be written as

$$\tau_{\gamma\gamma} \cong \frac{\pi r_e^2 d}{m_e c^2} \sum_{i=1}^N \frac{u_{0,i}}{\Theta_i} \mathcal{F}(v_i, k_i) \cong 1.6 d_{27} \sum_{i=1}^N \frac{u_{-14,i}}{T_i \text{ (eV)}} \mathcal{F}(v_i, k_i), \tag{10.46}$$

where $u_{-14,i} = u_{0,i}/(10^{-14} \text{ ergs cm}^{-3})$, and i represents the CMBR, dust, and stellar contributions (see table 10.3). The limitation here is that $z \ll 1$, $d_{27} \lesssim$ a few.

It is simple to perform the numerical calculation starting with eq. (10.40) for the superposition of N blackbody or modified blackbody distributions

$$\tau_{\gamma\gamma}(\epsilon_1, z) = \frac{c\pi r_e^2}{m_e c^2 H_0} \sum_{i=1}^N \int_0^z dz' \frac{u_{0,i}(z') \mathcal{F}(v_i, k_i)}{\Theta_i(z')(1+z')\sqrt{\Omega_m(1+z')^3 + \Omega_\Lambda}}, \tag{10.47}$$

with, as before, $v^{-1} = \epsilon_1(1+z')\Theta(z')$ and $\mathcal{F}(v, k)$ given in eq. (10.22). This approach can be straightforwardly generalized for line emission using

Table 10.3 Parameters of Empirical Fits to the Local Long-Wavelength EBL

Component	k_i	$\Theta_i(z)$	T_i (K)	$u_{0,i}(z \ll 1)$ (10^{-14} ergs cm^{-3})
CMBR	4	$4.58 \times 10^{-10}(1+z)$	$2.72(1+z)$	6.38
Dust (high)	3.8	1.06×10^{-8}	62	0.819
Dust (low)	3.8	5.3×10^{-9}	31	0.273
Star 1 (high)	2.0	1.2×10^{-6}	7,100	1.1
Star 1 (low)	2.0	1.2×10^{-6}	7,100	0.55
Star 2	3.0	2.8×10^{-6}	16,600	0.5

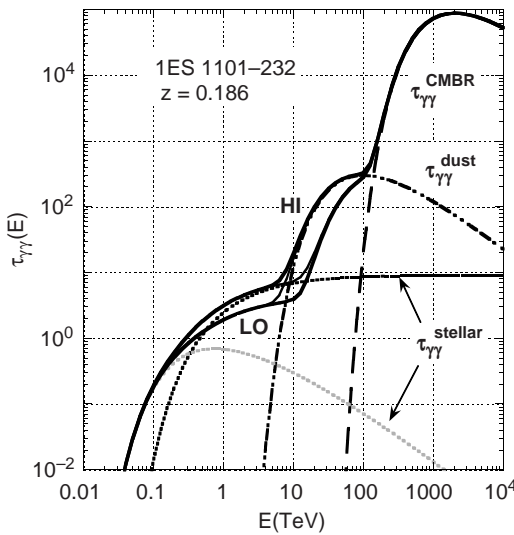


Figure 10.6 Optical depth to $\gamma\gamma$ absorption with photons of the optical and IR radiation fields, described as modified blackbody spectral for a stellar component and dust component, respectively.

Breit-Wigner functions for the IR line radiation, for example, the IR lines of the polycyclic aromatic hydrocarbons found in the ISM.¹

The optical depth $\tau_{\gamma\gamma}$ to the stellar and dust components of the EBL, using the fits shown in figure 10.5, is shown in figure 10.6. For photon energies

¹The Breit-Wigner function for line emission,

$$S(E) = \frac{(G/2)^2}{(E - E_0)^2 + (G/2)^2}$$

(with FWHM energy G), was introduced in eq. (8.61) to describe the cross section for resonant nuclear scattering. Note that $S(E_0 + G/2) = 1/2 = S(E_0)/2$.

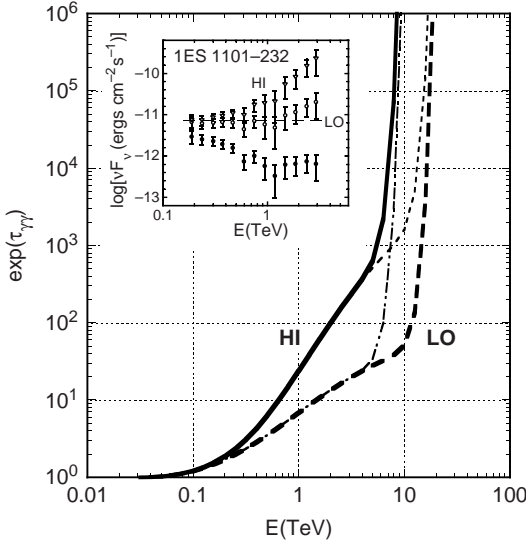


Figure 10.7 Attenuation factor for the low and high forms of the EBL, for 1ES 1101-232 at $z = 0.186$. Inset shows the effects of the low and high EBLs on the intrinsic spectrum of 1ES 1101-232 [242,258].

$\lesssim 10$ TeV, the opacity is dominated by the stellar component. For the source 1ES 1101-232 at $z = 0.186$, with $d_{27} \cong 2.4$, the high-EBL attenuation factor at 1 TeV is $\approx \exp(-3) \cong 0.05$, so that the intrinsic luminosity at 1 TeV is ≈ 20 times greater than the observed luminosity. The spectral index of the intrinsic photon number spectrum of 1ES 1101-232, using the optical depth calculated in figure 10.5, is softer than -1.5 , in agreement with expectations from the intrinsic spectra of nearby TeV blazars like Mrk 421 and Mrk 501 [242].

Figure 10.6 shows the optical depth to $\gamma\gamma$ pair production attenuation for γ rays with measured energies E detected from the TeV X-ray selected BL Lac object 1ES 1101-232 at $z = 0.186$ [242]. Separate components for the CMBR, dust, and stellar radiation fields are shown for the low EBL in the figure. In making this calculation, only the CMBR field evolves with redshift, and the dust and stellar radiation field energy densities remain constant. This assumption becomes increasingly less reliable at higher redshifts.

The attenuation factor, from which the intrinsic spectrum of 1ES 1101-232 is obtained, is plotted in figure 10.7. As can be seen from the index, the use of the low EBL means that the intrinsic photon spectral index of 1ES 1101-232 from ≈ 0.2 –3 TeV is ≈ -2.0 . If we adopt as a general rule, consistent with our knowledge of the GeV spectra of flat-spectrum radio quasars (FSRQs) [255] and GeV–TeV spectra of BL Lacs like Mrk 421 and

Mrk 501, that the intrinsic spectrum is softer than -2 , then the low EBL is favored (cf. [256,257]). A low EBL between 1 and 10μ solves the problem of the unusually hard γ -ray spectrum of 1ES 1101-232 [242,258], avoids the necessity to construct acceleration scenarios not operating in Mrk 421 and Mrk 501, and explains the lack of evidence of hard synchrotron components associated with a hard electron energy distributions in X-ray selected BL Lac objects (XBLs) observed at TeV energies.

10.3.4 $\gamma\gamma$ Attenuation at All Redshifts

Two methods have been employed to determine the evolving EBL over a range of redshifts: (i) empirically adding up the optical/infrared emissions from sources at various redshifts; and (ii) developing a model of the universe from large-scale structure formation theory to give the integrated infrared emission. In approach (i), developed in the work of Stecker and collaborators [259–261], the Infrared Astronomical Satellite (IRAS) data at 12, 25, 60, and 100μ , and data from the *Infrared Space Observatory* and other telescopes, for example, the Kuiper Airborne Observatory, are used to derive luminosity-dependent galaxy SEDs from the optical through the IR. Integrations over cosmic time given the evolving luminosity density permit $\tau_{\gamma\gamma}$ to be derived.

In approach (ii) of Primack and collaborators [262], models of galaxy formation, taking into account physical processes such as star formation, supernova feedback and metal production in merging of dark matter halos, are used to derive the EBL at different redshifts. The Primack model predicts an EBL with a steep spectrum between 2 and $10 \mu\text{m}$.

10.4 THE γ -RAY HORIZON

The low and high EBL SEDs represent the likely range of the local $z \ll 1$ intergalactic medium (IGM) IR and optical radiation fields. We can use this field to calculate the γ -ray photon horizon, defined by the relation $\tau_{\gamma\gamma}(E_{\text{osc}}, z_{\text{osc}}) = 1$ [244,263] (known as the Fazio-Stecker relation). Figure 10.8 shows the γ -ray photon energy E_{osc} as a function of obscuration redshift z_{osc} from Refs. [261] and [262].

The left panel in figure 10.8 illustrates that PeV γ rays can be detected from sources within our Galaxy, though they might be subject to modest attenuation from the CMBR. The IR and stellar radiation fields can also contribute significant $\gamma\gamma$ opacity at $\sim 100 \text{TeV}$. Anisotropy effects of Galactic radiation fields on opacity have recently been calculated in [246]. Attenuated spectra of TeV–PeV γ -ray sources could in principle give a distance measure of specific sources in the Milky Way and nearby galaxies.

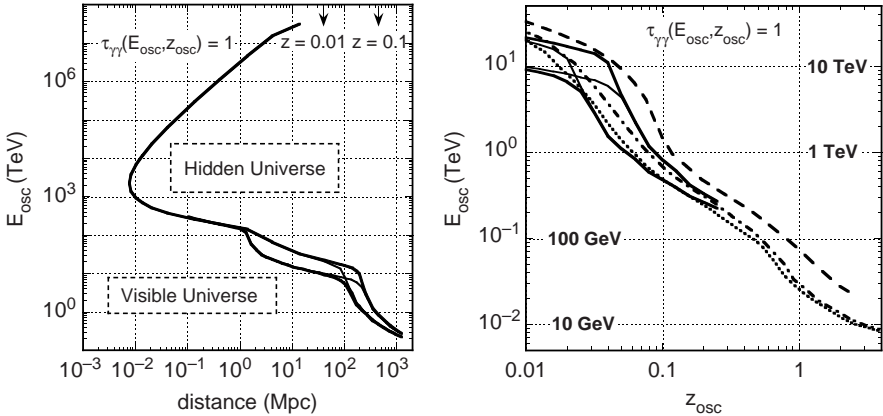


Figure 10.8 The γ -ray horizon due to attenuation by EBL light. (Left) Low-redshift ($z \leq 0.25$) γ -ray horizon giving the relationship between obscuration photon energy E_{osc} and obscuration redshift z_{osc} or distance d_{osc} where $\tau_{\gamma\gamma}(E_{\text{osc}}, z_{\text{osc}}) = 1$ for the low and high EBLs shown in figure 10.5. (Right) The dashed curve is the γ -ray horizon from the work of Primack et al. [262], and the dotted and dot-dashed curves are the horizons for different evolutionary scenarios for IR luminous galaxies from the work of Stecker et al. [261]. (The dotted curve shows a fast-evolution model.) The solid curves show the γ -ray horizon calculated here from empirical fits to the EBL.

The right panel compares detailed calculations of the γ -ray horizon with the empirical approach, valid at low redshifts when the IR and optical radiation fields have not changed appreciably over time, calculated here. The dotted and dot-dashed curves in the right panel are the γ -ray horizon from Stecker et al. [261], and the dashed curve is the γ -ray horizon from Primack et al. [262]. This diagram is primarily illustrative, and should be used cautiously to compare with data. For example, at the redshift of 1ES 1101-232, namely, $z = 0.186$, this diagram says that the exponential cutoff energy is at $\approx 300\text{--}400$ GeV, and that the low and high EBLs are not significantly different. In fact, no exponential cutoff is seen in the 1ES 1101-232 TeV spectrum, because the actual attenuation is very sensitive to the full spectrum of the EBL.

10.5 COMPACTNESS PARAMETER

Consider a spherical emission region with radius R that is at rest in the stationary frame. Suppose also that this region emits a luminosity L_γ at

≈ 500 keV ($\epsilon \approx 1$). The number density of $\approx 1/2$ MeV photons in the source is therefore

$$n_\gamma \approx \frac{L_\gamma}{\epsilon m_e c^3 \cdot 4\pi R^2 c} \approx \frac{L_\gamma}{4\pi R^2 m_e c^3}. \quad (10.48)$$

The numerical coefficient in eq. (10.48) depends on geometry. Note that the photon distribution becomes increasingly anisotropic away from the center of the sphere.²

A source is *compact* to $\gamma\gamma$ -pair production attenuation if

$$\tau_{\gamma\gamma} \approx n_\gamma \sigma_{\gamma\gamma} R \gtrsim 1. \quad (10.49)$$

Taking $\sigma_{\gamma\gamma} \approx \sigma_T$ (see figure 10.2), we define the compactness parameter [108,264]

$$\ell_\bullet \equiv \left(\frac{L_\gamma}{R} \right) / \left(\frac{4\pi m_e c^3}{\sigma_T} \right) \gtrsim 1. \quad (10.50)$$

A source becomes compact to $\gamma\gamma$ -pair production when $\ell_\bullet \gtrsim 1$, or if L_γ/R exceeds the electron compactness value

$$\frac{4\pi m_e c^3}{\sigma_T} = 4.64 \times 10^{29} \text{ erg s}^{-1} \text{ cm}^{-1}. \quad (10.51)$$

Note that L_γ/R is an observational quantity, with L_γ directly measurable with detectors sensitive to soft γ -rays, and R inferred from the timescale for temporal variability when, as is usually the case, direct imaging of the size of the emission region is not possible.

The Solar luminosity produced in photons near $m_e c^2$ energy within a Solar radius gives $L_\odot/R_\odot \approx 10^{-7} (4\pi m_e c^3/\sigma_T)$. One Solar luminosity released at soft γ -ray energies on the size scale of a football field would become compact.

The production sites of high-energy radiation from black holes must be extremely compact if the γ -ray emission regions are at rest in the stationary frame of the black hole. For example, OSSE measured large-amplitude variability on a timescale ~ 3 days from the blazar PKS 0528 + 134 at $z = 2.06$, $d_L \cong 5 \times 10^{28}$ cm [265]. Its mean flux in the 150–500 keV range during this period was $0.82 (\pm 0.15) \times 10^{-3} \text{ ph cm}^{-2} \text{ s}^{-1} \text{ MeV}^{-1}$, so its apparent isotropic luminosity at $\approx 1/2$ MeV was therefore $L_\gamma \approx 6 \times 10^{48} \text{ erg s}^{-1}$. A three-day variability timescale for a stationary source at $z = 2.06$ corresponds to a size scale $R \approx 2.5 \times 10^{15}$ cm, so that $\ell_\bullet \cong 5000 \gg 1$. Rather than being highly attenuated above \approx a few hundred keV, PKS 0528 + 134 is

²The mean distance to the boundary of a sphere if each photon is emitted isotropically and uniformly throughout a sphere is $\langle R \rangle = 3R/4$.

a prolific source at MeV and 100 MeV γ -ray energies, as shown by COMPTEL and EGRET, suggesting that one of our assumptions is incorrect. From all available evidence, the assumption that is violated is that the source is at rest in the stationary frame.

Models of sources of multi-MeV γ radiation must ensure that the source be transparent to its own γ radiation. γ -ray transparency can be guaranteed if the source is in relativistic motion, as we show in the next section. Another way to avoid the compactness constraint is to assume that all the radiation is from beamed, anisotropic electrons [266]. Models of directed particle beams from black-hole jets are unlikely because a broad pitch-angle distribution is required to radiate synchrotron radiation, but beamed electrons would follow quasi-parallel field lines with small pitch angles. Synchrotron radiation is more easily modeled and understood in a scenario where the magnetic field and plasma move in a bulk outflow.

10.6 MINIMUM DOPPLER FACTOR FROM $\gamma\gamma$ CONSTRAINT

Requiring that $\tau_{\gamma\gamma}(\epsilon_1) < 1$ so that the emission region is transparent to γ -rays gives, using the δ -function result, eqs. (10.34)–(10.36), the minimum Doppler factor

$$\delta_D > \left[\frac{\sigma_T d_L^2 f_{\epsilon_{pk}}}{2m_e c^4 t_{var} \epsilon_{pk}^A} \left(\frac{(1+z)^2 \epsilon_1}{2} \right)^{1-A} \right]^{1/(6-2A)}. \quad (10.52)$$

In eq. (10.52), $A = b$ if $\epsilon_1 < \epsilon_1^{pk}$, i.e., $\delta_D > (1+z)\sqrt{\epsilon_1 \epsilon_{pk}/2}$, and $A = a$ if $\epsilon_1 > \epsilon_1^{pk}$ (here $A = 1 - \alpha$ is the νF_ν index, where the energy index α is defined by the relation $F_\nu \propto \nu^{-\alpha}$) [251]. One can also use the relation [267]

$$\delta_D > \sqrt[6]{\frac{\sigma_T d_L^2 f_\epsilon (1+z)^2 \epsilon_1}{4m_e c^4 t_{var}}},$$

keeping in mind that the expression $\epsilon = 2\delta_D^2 / [(1+z)^2 \epsilon_1]$ relating γ -ray and target photon energy depends on the Doppler factor.

To illustrate the application of the $\gamma\gamma$ opacity constraint, we apply eq. (10.52) to FSRQs such as 3C 279, PKS 0528 + 134, or CTA 102. OSSE and COMPTEL observations [265] of bright blazars show that $f_{\epsilon_{pk}} = 10^{-10} f_{-10} \text{ ergs cm}^{-2} \text{ s}^{-1}$ with $f_{-10} \gtrsim 1$, and $f_{-10} \approx 10$ during bright blazar flares. The νF_ν flux peaks at $\epsilon_{pk} \sim 1\text{--}100$. Photons observed at 100 MeV/GeV energies (i.e., $\epsilon_1 = 1960 E_{\text{GeV}} \gtrsim 200\text{--}2000$) would therefore be preferentially absorbed by photons with energies below the peak of the νF_ν spectrum, so that the case with $A = a$ applies, and $a \sim 0.2\text{--}1$.

Taking $a = 0.5$ for illustration gives

$$\delta_D \gtrsim 8 \left[\frac{d_{28}^2 f_{-10}}{t_4} \left(\frac{1+z}{2} \right) \right]^{1/5} \left(\frac{E_{\text{GeV}}}{\epsilon_{\text{pk}}} \right)^{1/10}. \quad (10.53)$$

Here we define $t_4 = t_{\text{var}}(s)/10^4 \text{ s} \sim 1$. The Fermi Gamma Ray Space Telescope will be able to detect variability from flares at the level of $f_{-10} \sim 1$ on this timescale [268]. For bright blazar flares from distant FSRQs, Fermi could set minimum values of δ_D exceeding ~ 20 , comparable to the largest values inferred from radio observations of superluminal motion [269].

We next consider TeV blazars ($\epsilon_1 = 1.96 \times 10^6 E_{\text{TeV}}$) such as Mrk 421 or Mrk 501 at a distance of $\approx 140 \text{ Mpc}$. TeV photons from sources with $\delta_D \approx 10$ preferentially pair produce with $\sim 1 \text{ keV}$ synchrotron photons. The X-ray synchrotron spectrum from TeV blazars can exceed $f_{-10} \approx 1$, and the flare timescale t_4 may be as low as 0.1 or even lower, depending on results from the ground-based γ -ray telescopes. Using $A = a = b = 0$ for simplicity (a flat νF_ν synchrotron spectrum) gives

$$\delta_D \gtrsim 12 \left[\left(\frac{d_L}{140 \text{ Mpc}} \right)^2 \frac{f_{-10} E_{\text{TeV}}}{t_4} \right]^{1/6}. \quad (10.54)$$

Shorter flares and brighter synchrotron fluxes will potentially imply values of $\delta_D \gtrsim 15$.

The differences between blast-wave and blob geometries do not make a great deal of difference in the resultant expressions for the pair production opacities, as shown in section 5.5.3. Thus we can also apply our results to GRB blast waves.

The prompt hard X-ray/soft γ -ray emission of a GRB, which we assume here to be nonthermal synchrotron radiation, has $\epsilon_{\text{pk}} \sim 1$. GRBs with peak flux $f_{\epsilon_{\text{pk}}} = 10^{-6} f_{-6} \text{ ergs cm}^{-2} \text{ s}^{-1}$, with $f_{-6} \gtrsim 1$, occur every 2–4 weeks over the full sky. Anticipating that $\delta_{D,100} = \delta_D/100 \approx 1$ for GRBs, we see that $\epsilon_1^{\text{pk}} \approx 5000 \delta_{D,100}^2 / \{[(1+z)/2]^2 \epsilon_{\text{pk}}\}$, so that observations of GeV photons from GRBs generally favor the case $\epsilon_1 \lesssim \epsilon_1^{\text{pk}}$. In other words, GeV photons from GRBs are preferentially attenuated by photons on the high-energy portion of the synchrotron spectrum. For illustration, we let $A = b = -1/2$ for a typical value of the spectral index at $\gtrsim \text{MeV}$ energies, and assume that the synchrotron spectrum extends to GeV energies, giving

$$\delta_D \gtrsim 200 \left[\frac{f_{-6} d_{28}^2}{t_{\text{var}}(s)} \left(\frac{1+z}{2} \right)^3 \right]^{1/7} [\epsilon_{\text{pk}} E_{\text{GeV}}^3]^{1/14}. \quad (10.55)$$

Thus Fermi observations of GRBs imply values of $\delta_D \gg 200$ in the brightest and most variable GRBs (with $\Gamma \approx \delta_D \gtrsim 800$ in GRB 080916C), and

will potentially find differences in minimum values of δ_D between different classes of GRBs.

The results agree with previous treatments [267,270,271]. Note the implicit cospatial assumption in the derivation, namely, that the γ -rays are formed in the same region as the lower-energy target photons. Without this assumption, only much smaller values of minimum Doppler factors can be confidently asserted, which depend more on observations at MeV energies rather than at GeV or TeV energies [272]. To demonstrate the reliability of the cospatial assumption requires correlated multiwavelength observations of γ -ray sources.

After leaving the source, γ rays can still be attenuated as they pass through the radiation environment of the black hole [273,274], and then suffer absorption with photons of the EBL.

10.7 CORRELATED γ -RAY AND NEUTRINO FLUXES

Signal detection in neutrino and γ -ray telescopes is improved by rejecting background, most simply done by choosing favored time windows to search for signal. One would logically think that the best time to search for \sim PeV neutrinos is when GRBs are γ -ray luminous and black-hole blazar jets are flaring at GeV or TeV energies, because during γ -ray flaring states, energetic particle acceleration is most vigorous. But photopion production through photohadronic processes, for example, the direct $p\gamma \rightarrow n\pi^+$ process, is enhanced in conditions of high internal photon target density. Under these conditions, the γ ray flux will be strongly attenuated by internal absorption. Thus times of most favorable neutrino detection could also be argued to take place during periods of low γ -ray flux and high optical/X-ray fluxes. Here the relations defining

1. efficient photopion losses of cosmic ray protons on target photons, and
2. $\gamma\gamma$ opacity of γ rays through that same target photon field [275]

are clarified.

The causality constraint implies that the size scale of the emitting region $r'_b \lesssim c\delta_D t_{\text{var}}/(1+z)$, where $t_{\text{var}} = t_0 \text{ s} = 10^r \text{ s}$ is the measured variability timescale, and δ_D is the Doppler factor. From eq. (10.25),

$$\epsilon' n'(\epsilon') \cong 3a_L^2 f_{\epsilon_{\text{pk}}} S(x)/(cr'_b{}^2 \delta_D^4 m_e c^2 \epsilon'), \tag{10.56}$$

where $\epsilon_{\text{pk}} \equiv 10^j$ is the measured photon energy (in units of $m_e c^2$) of the peak of the νF_ν spectrum with peak flux $f_{\epsilon_{\text{pk}}} = 10^{-10} f_{-10} \text{ ergs cm}^{-2} \text{ s}^{-1} = 10^\eta \text{ ergs cm}^{-2} \text{ s}^{-1}$. The rate at which protons lose energy through

photohadronic processes is $t_{\phi\pi}^{\prime-1} \cong \epsilon' n'(\epsilon') \sigma_1 K_1 c$, where $\sigma_1 K_1 \cong 70 \mu\text{b}$, eq. (9.10), and the threshold condition $2\gamma'_p \epsilon' \gtrsim \epsilon'_{\text{thr}} \cong 400$ relates the proper-frame proton Lorentz factor γ'_p and the internal photon energy.

We write the target comoving photon SED from quasi-isotropic emissions as a broken power law, eq. (10.26). The photopion energy-loss rate of ultrarelativistic protons with Lorentz factor γ'_p interacting with photons with energy ϵ'_{pk} near the peak of the νF_ν spectrum is, from the proceeding considerations,

$$\rho_{\phi\pi} = \frac{3\sigma_1 K_1 d_L^2 f_{\epsilon'_{\text{pk}}} (1+z)}{m_e c^4 \delta_D^5 t_{\text{var}}^2 \epsilon_{\text{pk}}}. \quad (10.57)$$

For the model target photon spectrum with $0 < a < 3$, $b < 0$,

$$t_{\phi\pi}^{\prime-1}(\gamma'_p) \cong \rho_{\phi\pi} \begin{cases} 2y^{b-1}/[(1-b)(3-b)], & y \gg 1, \\ 2y^{a-1}/[(1-a)(3-a)], & y \ll 1, 0 < a \lesssim 1, \\ (a-b)/[(a-1)(1-b)], & y \ll 1, 1 \lesssim a < 3, \end{cases} \quad (10.58)$$

where $y \equiv \epsilon'_{\text{thr}}/2\gamma'_p \epsilon'_{\text{pk}} \cong \delta_D^2 \epsilon'_{\text{thr}}/2\gamma_p(1+z)\epsilon_{\text{pk}}$, and the Lorentz factor γ_p of an escaping proton as measured by a local observer is $\gamma_p \cong \delta_D \gamma'_p$. The condition $y = 1$ for the energy E_p of protons interacting with photons with energy ϵ_{pk} implies that

$$E_p^{\phi\pi} \cong \frac{m_p c^2 \delta_D^2 \epsilon'_{\text{thr}}}{2(1+z)\epsilon_{\text{pk}}} \cong \frac{1.9 \times 10^{14} \delta_D^2}{(1+z)\epsilon_{\text{pk}}(\text{keV})} \text{ eV}. \quad (10.59)$$

The radiating fluid element will expand rapidly following energization through shell collisions, or through external shocks formed when the ejecta shell sweeps through the surrounding medium. If ultrarelativistic protons and ions are accelerated in black-hole jets, then photopion processes can be certain to be efficient if the photopion energy-loss rate $\rho_{\phi\pi}$, eq. (10.57), is greater than the inverse of the light travel timescale, $(1+z)/\delta_D t_{\text{var}}$. An UHECR accelerated in a black hole jet will therefore lose a large fraction of its energy into electromagnetic and neutrino radiations when the jet Doppler factor

$$\begin{aligned} \delta_D < \delta_{\phi\pi} &\equiv \left(\frac{3\sigma_1 K_1 d_L^2 f_{\epsilon'_{\text{pk}}}}{m_e c^4 t_{\text{var}} \epsilon_{\text{pk}}} \right)^{1/4} \\ &= 10^{-10.64+(2\ell+\eta-\tau-j)/4} \cong 7.3 d_{28}^{1/2} \left(\frac{f_{-10}}{t_0 \epsilon_{\text{pk}}} \right)^{1/4}. \end{aligned} \quad (10.60)$$

The same radiation field that functions as a target for photomeson production is a source of $\gamma\gamma$ opacity. The photoabsorption optical depth for a γ -ray photon with energy ϵ_1 in a quasi-isotropic radiation field with spectral photon density $n'(\epsilon')$ is given by eqs. (10.34), (10.35), and (10.36). At the Doppler factor $\delta_D = \delta_{\phi\pi}$ that allows for efficient photopion production, the $\gamma\gamma$ optical depth at photon energy ϵ_1^{pk} is, substituting eq. (10.60) into eq. (10.35), simply

$$\tau_{\gamma\gamma}^{\phi\pi} = \frac{\sigma_T}{6\sigma_1 K_1} \cong 1600. \tag{10.61}$$

Whenever photopion production is important, γ rays with energies given by eq. (10.36) have to be highly extinguished by $\gamma\gamma$ processes when interacting with peak target photons with energy $\sim \epsilon_{\text{pk}}$, making it impossible to detect γ rays at these energies. This energy is

$$\begin{aligned} E_\gamma^{\gamma\gamma} &= \frac{2m_e c^2 \delta_{\phi\pi}^2}{(1+z)^2 \epsilon_{\text{pk}}} = \frac{2m_e c^2 d_L}{(1+z)^2 \epsilon_{\text{pk}}^{3/2}} \sqrt{\frac{3\sigma_1 K_1 f_{\epsilon_{\text{pk}}}}{m_e c^4 t_{\text{var}}}} \\ &\cong \frac{10^{-24.26+\ell+(\eta-\tau-3j)/2} \text{ GeV}}{(1+z)^2} \cong \frac{0.055 d_{28} f_{-10}^{1/2}}{(1+z)^2 t_0^{1/2} \epsilon_{\text{pk}}^{3/2}} \text{ GeV}. \end{aligned} \tag{10.62}$$

The energy of protons that interact most strongly with peak target photons through photopion processes under conditions when photopion processes must be important is, from eqs. (10.59) and (10.60),

$$E_p^{\phi\pi} = \frac{m_p c^2 \delta_{\phi\pi}^2 \epsilon'_{\text{thr}}}{2(1+z)\epsilon_{\text{pk}}} \cong 10^{-10+\ell+(\eta-\tau-3j)/2} \text{ eV} \cong 1.0 \times 10^{13} d_{28} \sqrt{\frac{f_{-10}}{t_0 \epsilon_{\text{pk}}^3}} \text{ eV}. \tag{10.63}$$

Table 10.4 lists the jet Doppler factor where photopion losses are guaranteed to be important for protons of escaping energy $E_p^{\phi\pi}$. Protons with this energy undergo photopion interactions primarily with (peak) target photons with energy $\sim \epsilon_{\text{pk}}$. $E_\gamma^{\gamma\gamma}$ is the energy of γ rays that are attenuated through $\gamma\gamma$ -pair production primarily by peak target photons.

For canonical FSRQ values taken from observations of 3C 279 [276] or PKS 0528 + 134 [277], table 10.4 shows that photopion production is already important at Doppler factors of ~ 6 – 16 during times of day-scale optical flaring, and these optical photons effectively extinguish all γ -rays with energies $\gtrsim E_\gamma^{\gamma\gamma} / 1600^{1/(1-b)}$ (cf. figure 10.9); certainly this would include all $\gtrsim 100$ GeV–TeV photons [275]. The ground-based γ -ray telescope MAGIC has detected the FSRQ 3C 279 at ~ 100 GeV [278]. Monitoring of FSRQs during an optical flare would identify periods of likely neutrino emission.

Table 10.4 Doppler factor $\delta_{\phi\pi}$ for guaranteed photopion losses, γ -ray photon energy $E_{\gamma}^{\gamma\gamma}$ for $\gamma\gamma$ attenuation with photons at the peak of the target photon SED, and cosmic-ray energy $E_p^{\phi\pi}$ for photopion interactions with peak target photons (sources at $z = 2$ except for XBL, at $z \approx 0.08$, $d_L = 10^{27}$ cm).

	ℓ	η	τ	j	$\delta_{\phi\pi}$	$E_{\gamma}^{\gamma\gamma}$ (GeV)	$E_p^{\phi\pi}$ (eV)
FSRQ	28.7	-11	5	-5 (5 eV)	9	92	5×10^{17}
IR/optical				-6 (0.5 eV)	16	30×10^3	1.6×10^{19}
FSRQ	28.7	-11	5	-2 (5 keV)	1.6	0.03	1.6×10^{13}
X-ray				-3 (0.5 keV)	2.8	0.92	5×10^{14}
XBL	27	-10	3	-2 (5 keV)	1.3	0.14	3×10^{13}
X-ray				-3 (0.5 keV)	2.3	4.7	9×10^{14}
GRB	28.7	-6	0	0 (511 keV)	160	2.9	2×10^{15}
γ -ray				-1 (51 keV)	280	92	5×10^{16}
X-ray flare		-9	2	-3 (0.5 keV)	50	290	1.6×10^{17}

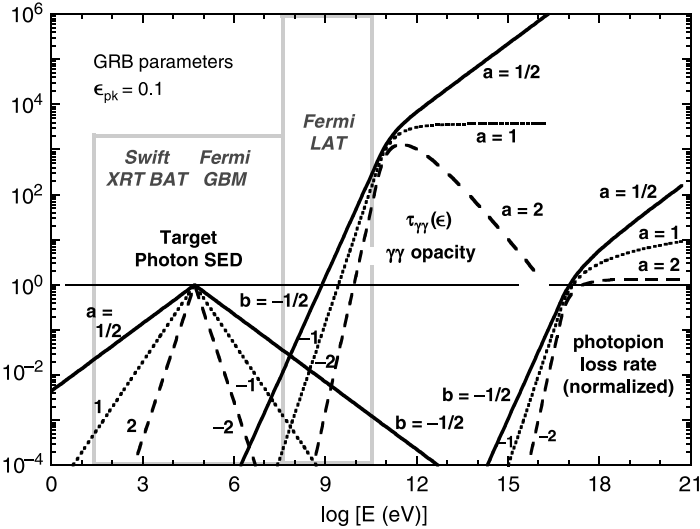


Figure 10.9 Target photon SED, $\gamma\gamma$ opacity $\tau_{\gamma\gamma}(\epsilon_1)$, and normalized photopion energy-loss rate $\iota_{\phi\pi}^{\prime-1}/\rho_{\phi\pi}$ are shown as functions of photon or neutrino energy for parameters of rapidly varying prompt GRB emission from table 10.4. The target photon SED is approximated as a broken target power law, eq. (10.26), with νF_{ν} flux peaking at ϵ_{pk} . When photopion processes are certain to be important for protons with energy $E_p^{\phi\pi}$ that interact with peak target photons with energy $\approx \epsilon_{pk}$, then the $\gamma\gamma$ opacity of γ -rays with energy $E_{\gamma}^{\gamma\gamma}$ is ≈ 1600 . The $\gamma\gamma$ opacity is less than unity at photon energies $\lesssim E_{\gamma}^{\gamma\gamma}/1600^{1/(1-b)}$.

For guaranteed importance of photohadronic production implied by X-ray observations, the Doppler factors of FSRQs and TeV BL Lac objects like Mrk 421 or Mrk 501 have to be unexpectedly small, $\lesssim 3$. If the X-ray flaring timescale of FSRQs were hourly rather than daily, then $\delta_{\phi\pi}$ would more nearly correspond to Doppler factors ~ 5 – 10 as inferred from unification studies and superluminal motion observations of blazars [279]. During such episodes of highly variable X-ray flux, such sources should be invisible at 100 MeV–GeV energies, and \gg TeV neutrinos should be created. For the XBL estimate, 15 minute X-ray flaring timescales have already been assumed [280], so high-energy neutrinos from BL Lacs are less likely than from FSRQs, which are also more likely to be PeV neutrino sources for IceCube, as the external radiation field plays a strong role in neutrino production [95,281].

Prediction for PeV neutrino detection is most favorable for bright GRBs with peak fluxes of $\approx 10^{-6}$ ergs cm^{-2} s^{-1} and peak photon energy in the range 50 keV–0.5 MeV that show $\lesssim 1$ s spikes of emission (figure 10.9). The bulk Lorentz factors, ≈ 100 , are consistent with widely considered outflow speeds in GRBs (see chapter 11). Perhaps 100 MeV photons could be observed, but the Fermi Large Area Telescope (LAT) should see no \gtrsim GeV photons if $\delta_D \lesssim \delta_{\phi\pi}$, which is the most favorable time for detecting 100 TeV–PeV neutrinos and is at an optimal energy for detection with kilometer-scale neutrino telescopes. Bright X-ray flares with durations $\sim 10^2$ s observed hundreds to thousands of seconds after the GRB trigger, like those discovered with Swift [282,283], with blast-wave Doppler factors ≈ 50 , are also promising times to look for neutrinos and a γ -ray spectrum attenuated above ~ 100 GeV.

The condition $\tau_{\gamma\gamma}(\epsilon_1) < 1$ for detected γ rays with energy ϵ_1 gives a minimum Doppler factor δ_D^{\min} , eq. (10.52). If $\delta_D^{\min} \gtrsim \delta_{\phi\pi}$, we should not expect GRBs to be neutrino bright. Breakdown of any of these multivariable predictions would call into question our understanding of the structure of black-hole jets.

10.8 ELECTROMAGNETIC CASCADES

Electromagnetic cascades are important for understanding the development of shower profiles when an UHECR impacts the atmosphere to form an extensive air shower. Nuclear, bremsstrahlung, and Bethe-Heitler pair production processes are important in the development of these hadronically induced electromagnetic cascades. The theoretical analysis is quite involved; see Ref. [12].

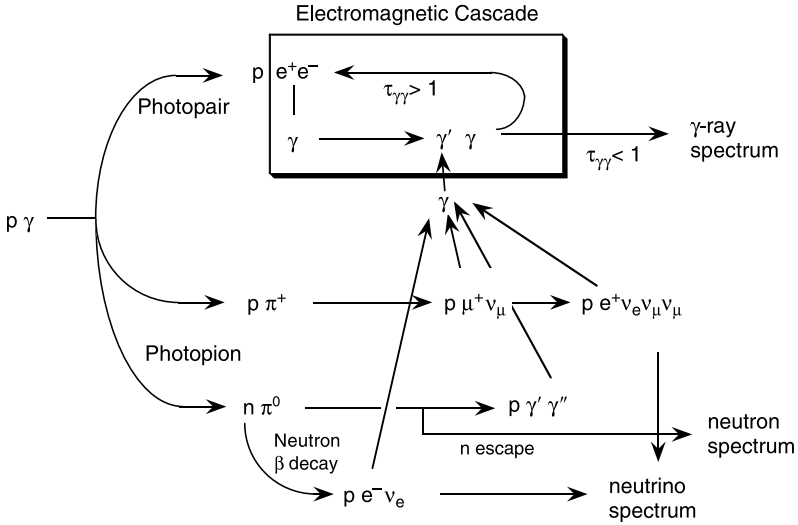


Figure 10.10 Flow diagram of the dominant photohadronic ($p\gamma$) processes involving ultrarelativistic protons and target photons that make an electromagnetic cascade and neutral beam. Photohadronic processes make an injection source of π^0, π^\pm from photopion losses. The lepton and photon π -decay secondaries, along with e^+e^- pairs from photopair processes, produce synchrotron photons and scatter ambient target photons to γ -ray energies. $\gamma\gamma$ attenuation of the synchrotron and Compton-produced γ -rays produce new pair injection sources. Escaping neutrons decay to become UHECR protons.

10.8.1 Cascades in Jets

In high-energy astrophysical sources, a range of cascades can form, depending on the target matter and radiation, the compactness, and magnetic field strength. Energetic electrons can induce an electromagnetic Compton-synchrotron cascade by making γ rays in a region that is optically thick to $\gamma\gamma$ -pair production attenuation. Ultrarelativistic protons and ions will interact with ambient target photons and matter to form secondaries that can initiate an electromagnetic cascade. In Monte Carlo simulations, a cascade tree must be followed (see figure 10.10) to calculate high-energy γ -ray and neutrino spectra formed in black-hole jets.

The photopair ($p\gamma \rightarrow p + e^+ + e^-$) process is the lowest-threshold $p\gamma$ process, and constantly supplies e^\pm pairs over a wide energy range. The two photopion processes ($p\gamma \rightarrow p\pi^0$ and $p\gamma \rightarrow n\pi^+$) have about equal probability to occur. The neutral and charged pions decay as γ rays, muons, and leptons, while making high-energy photons, positrons, and neutrinos.

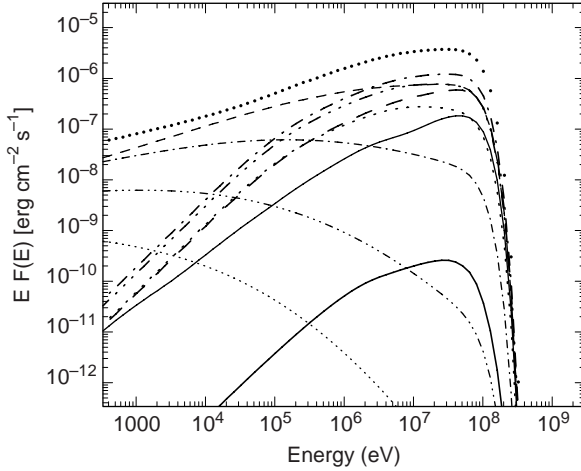


Figure 10.11 Photon energy fluence from an electromagnetic cascade initiated by photopion secondaries in a model GRB, with parameters as given in figure 10.2 and with $\delta_D = 100$. Five generations of Compton (heavy curves) and synchrotron (light curves) are shown. The first through fifth generations are given by solid, dashed, dot-dashed, dot-triple-dashed, and dotted curves, respectively. The total cascade radiation spectrum is given by the upper bold dotted curve. (Figure courtesy of Armen Atoyan.)

While neutrinos escape directly, photons, electrons, and positrons form an electromagnetic cascade (shown in the box in figure 10.10) together with $p\gamma \rightarrow p + e^+ + e^-$ photopairs. Synchrotron radiation and Compton scattering are the dominant electromagnetic processes, followed only by photopair production by electrons and positrons at very high energy. High-energy γ rays can escape from the source if the optical depth to produce e^\pm pairs with ambient soft photons is less than unity.

Neutron and UHE γ -ray escape, and subsequent decay or pair conversion can inject energy and momentum hundreds of kpc from the black hole. This is the basis of the neutral beam model [95], where photohadronic processes in the inner jet lead to bright neutrino fluxes and the escape of 100 TeV–EeV neutrons and γ rays.

Hadronic γ -ray emission components appearing during the prompt phase of GRBs would be caused by a pair-photon cascade initiated by photohadronic processes between high-energy hadrons accelerated in a GRB blast wave and the internal synchrotron radiation field formed by the accelerated nonthermal leptons. Atoyan's calculation [191] of the γ -ray flux from a cosmic-ray proton-induced cascade in a black-hole jet source is shown in figure 10.11. Plotted there are the first five generations of synchrotron

and Compton radiation initiated by the cascade, along with the total emergent radiation spectrum. As can be seen, the cascade radiation approaches the spectrum of an electron distribution cooling by synchrotron losses, that is, a spectrum with photon number index between -1.5 and -2 where $\tau_{\gamma\gamma} < 1$.

This calculation follows a Compton-synchrotron- $\gamma\gamma$ cascade initiated by cosmic-ray protons. The inclusion of ultrarelativistic ions opens photo-nuclear channels discussed in chapter 9, which produce neutrinos and γ -rays. Energy-loss and acceleration of charged secondary muons can alter the results of the cascade calculation including, crucially, the neutrino flux.

10.8.2 Cascades in the Intergalactic Medium

We derive cascade equations for ultrarelativistic electron-positron pairs and Thomson-scattered CMBR photons from the electron and photon continuity equations (Appendix C), though Monte Carlo methods (Appendix D) are required to obtain the most reliable results. Suppose that beamed electrons, also understood to include positrons, are injected by a source into the local ($z \ll 1$) universe with Lorentz factor $\gamma_{\text{TKN}} = 1/4\Theta = 5.5 \times 10^8$. At this point, the electrons begin to Compton-scatter photons in the Thomson regime, so their energy-loss rate is $-\dot{\gamma}_{\text{T}} \simeq \nu_0 \gamma^2$, $\nu_0 = 1.3 \times 10^{-20} \text{ s}^{-1}$.

The electron number distribution at time t , $N_e(\gamma; t)$, is given by

$$\frac{\partial N_e(\gamma; t)}{\partial t} + \frac{\partial}{\partial \gamma} [\dot{\gamma} N_e(\gamma; t)] + \frac{N_e(\gamma; t)}{t_{\text{esc}}(\gamma, t)} = \frac{2cN_{\text{ph}}(2\gamma; t)}{\lambda_{\text{T}}}, \quad (10.64)$$

where $\epsilon_{\text{CMB}} = 1.24 \times 10^{-9}$ and $\lambda_{\text{T}} = (n_{\text{CMB}}\sigma_{\text{T}})^{-1} \cong 1.2 \text{ kpc}$. The photon distribution at time t , $N_{\text{ph}}(\epsilon; t)$, is given by

$$\frac{\partial N_{\text{ph}}(\epsilon; t)}{\partial t} + \frac{cN_{\text{ph}}(\epsilon; t)}{\lambda_{\gamma\gamma}(\epsilon)} = \frac{cN_e(\sqrt{\epsilon/\epsilon_{\text{CMB}}}; t)}{\lambda_{\gamma\gamma}(2\gamma)}. \quad (10.65)$$

As apparently rich as these two coupled equations are, Monte Carlo simulations are required to obtain accurate results, because implicit in the continuity equations above is the use of an average distance for $\gamma\gamma$ attenuation in place of a stochastic distribution of the $\gamma\gamma$ interactions.

When the charged leptons formed in the electromagnetic cascade are deflected out of the beam due to the IGM magnetic fields, pair halos of the type considered in [284] are formed. For recent work, see papers by Murase, Asano, Semikoz *et al.*

10.9 $\gamma\gamma \rightarrow \nu$

The process of muon pair production from $\gamma\gamma$ attenuation is

$$\gamma\gamma \rightarrow \mu^+\mu^- \rightarrow e^+ + \bar{\nu}_\mu + \nu_e + e^- + \nu_\mu + \bar{\nu}_e \quad (10.66)$$

(cf. eq. [8.54]). The $\gamma\gamma \rightarrow$ muon-pair production cross section is derived from quantum electrodynamics in a manner completely analogous to the $\gamma\gamma \rightarrow e^+e^-$ pair production cross section [64] (see eq. [10.1] and section 10.1), but with two changes:

- mass m_e in $r_e = e^2/m_e c^2$ is now replaced by the muon mass m_μ ($m_\mu/m_e = 206.8$), so that the cross section at the muon-pair threshold is a factor of $(m_e/m_\mu)^2$ smaller than the cross section $\sim\sigma_T$ at the electron-pair threshold, and
- the threshold energy, instead of $2m_e c^2$, becomes $2m_\mu c^2 = 2 \times 105.66 \text{ MeV}$.

A δ -function representation for the lowest-order $\gamma\gamma$ production of a pair of particles of mass m is

$$\sigma_{\gamma\gamma \rightarrow m^+m^-} \sim \left(\frac{e^2}{m c^2}\right)^2 \delta\left(s - 2\frac{m^2}{m_e^2}\right) \sim \pi r_e^2 \left(\frac{m_e}{m}\right)^4 \epsilon \delta\left(\epsilon - \frac{2}{\epsilon_1} \frac{m^2}{m_e^2}\right), \quad (10.67)$$

taking $s \approx \epsilon\epsilon_1$.

This process provides a channel for purely leptonic processes—for example, Compton-scattered γ -rays interacting with ambient photons—to make neutrinos. The actual efficiency to make a detectable neutrino flux has not been shown to be comparable to photohadronic processes [285], assuming equal energy or power into nonthermal hadrons as in synchrotron radiation from nonthermal leptons. For the $\gamma\gamma \rightarrow \pi^+\pi^-$ process, see Ref. [286].

Chapter Eleven

Blast-Wave Physics

The methods of blast-wave physics, developed to explain gamma-ray burst (GRB) afterglows, can be used to model emissions from a relativistic flow that is energized through shock formation. The shocks are formed when the relativistic jetted plasma sweeps up material from the surrounding medium at an external shock, or when shocks are formed in collisions between inhomogeneous outflows in a relativistic wind. Because black holes are observed to be sources of collimated relativistic plasma outflows, as most clearly revealed by observations of jets and superluminal motion in Solar mass and supermassive black-hole systems, and also by achromatic breaks in GRB optical afterglow-decay light curves, the techniques of blast-wave physics can be applied to a variety of black-hole systems.

This chapter treats

1. fireball expansion and blast-wave deceleration,
2. blast-wave physics and afterglow theory,
3. relativistic shock hydrodynamics,
4. beaming breaks and jetted emission,
5. the synchrotron self-Compton component,
6. emission in the prompt and early afterglow phases through
 - external shocks and
 - colliding shells,
7. thermal photospheres and neutrons, and
8. GRB cosmology.

Much of the analysis presented here is based on research by Paczyński, Mészáros and Rees, and Piran and Sari and their collaborators.

11.1 FIREBALLS AND RELATIVISTIC BLAST WAVES

Consider an explosion that takes place in a uniform circumburst medium (CBM) with density n_0 . Suppose that the event releases energy at a fixed rate over a timescale Δ_0/c , where Δ_0 is a characteristic size scale of the engine that releases the energy. For long-duration GRBs, this engine is thought to

be the collapse of a massive evolved star's Fe core to a black hole, either directly [18,287], or through intermediate formation of a neutron star [288]. It may also involve the coalescence of compact objects [289,290], or the accretion- or coalescence-induced collapse of a neutron star to a black hole for the short, hard class of GRBs. Consequently the engine's minimum size scale is the Schwarzschild radius of a few-Solar-mass black hole: $\Delta_0/c \gtrsim 30 \mu\text{s}$ or, for impulsive models, a characteristic timescale much shorter than a second.

In hypernova¹ and collapsar models [18,292,293] of GRBs, an active central engine is assumed to emit a jetted relativistic outflow on timescales ranging from fractions of a second to hundreds of seconds, corresponding to the duration of γ -ray emission from the GRB, or even longer for delayed X-ray flares. The apparent isotropic equivalent γ -ray energy E_0 released by a GRB explosion can exceed $\sim 10^{54}$ ergs, with apparent isotropic powers $\gtrsim 10^{51}$ ergs s^{-1} . In comparison, the rest mass energy of a Solar mass of material is $\cong 2 \times 10^{54}$ ergs, and the bolometric luminosity of the universe is $\sim 10^{54}$ ergs s^{-1} .

Given the extreme values of apparent energy release, combined with the short variability times ($\ll 1$ s) measured for GRBs, the best explanation is that the explosion forms a radiation-dominated fireball with injection explosion entropy per baryon $\eta = L/\dot{M}c^2 \gg 1$, where L is the wind power. The energy of the fireball is transformed into the directed kinetic energy of a shell with coasting Lorentz factor

$$\Gamma_0 = E_0/M_0c^2, \quad (11.1)$$

where M_0 is the amount of baryonic matter mixed into the initial explosion.² This relation determines the baryon load of the fireball. When $\Gamma_0 \gg 1$, most system energy is originally in kinetic form and the baryon loading is small.

We begin by assuming that the fireball expands isotropically (jetted outflows are considered in section 11.4). Following the energy release, the fireball expands to keep its total energy constant by transforming the entropy of the explosion into directed kinetic energy. During the early expansion phase, the Lorentz factor Γ of the shell evolves according to the relation $\Gamma(x) \approx x/\Delta_0$ (section 11.7), where x is the distance from the location of the explosion [294,295]. The value of Γ increases until the internal energy of the explosion is converted via baryon-photon coupling into the directed energy of baryons in the blast-wave shell. The rapid expansion and large optical depth of the fireball prevents significant energy loss in the form of escaping photons during the expansion phase. If neutrons remain coupled

¹Hypernovae are unusually energetic supernovae; see Ref. [291].

²The coasting Lorentz factor Γ_0 coincides with η for a fireball that expands adiabatically, which does not apply when neutron escape is important. See section 11.8.

by the time the fireball reaches its coasting Lorentz factor (section 11.9) and the expansion is adiabatic, then the blast-wave plasma shell reaches a coasting Lorentz factor $\Gamma \approx \Gamma_0$ at the coasting distance $x_{\text{co}} \approx \Gamma_0 \Delta_0$. In the stationary frame of the explosion, the shell width is $\Delta \approx \Delta_0$ at $x_{\text{co}} \lesssim x \lesssim x_{\text{spr}}$, and $\Delta \approx x/\Gamma_0^2$ at $x \gtrsim x_{\text{spr}}$, where the spreading distance $x_{\text{spr}} \cong \Gamma_0^2 \Delta_0$. At $x \gtrsim x_{\text{spr}}$, internal motions within the blast-wave shell cause it to spread [296,297].

Adiabatic expansion converts the internal energy of the explosion into directed kinetic energy, with the blast-wave particles nonrelativistic and cold in the comoving frame. Entrained magnetic field in the outwardly moving shell of plasma or field generated through plasma mechanisms [112] cause the fluid shell to sweep up material and field from its surroundings. Interactions of the shell with the external medium [298], or collisions between shells in a relativistic wind [299], inject and dissipate the directed kinetic energy in the form of internal energy that is available to be radiated. The reconversion of energy from the directed outflow to nonthermal broadband radiation from radio through γ -rays depends on particle acceleration and radiation physics in the blast wave, including reverse and forward shock components.

11.1.1 Blast-Wave Deceleration

A basic problem to consider, following Mészáros and Rees [298,300], is blast-wave deceleration that occurs when the relativistic blast-wave shell from an explosive event sweeps up CBM material at an external shock. The accumulation of swept-up material causes the shell to decelerate. For a uniform spherically symmetric CBM, the mass of swept-up material at radius x is $M_{\text{sw}} = 4\pi\mu_0 m_p n_0 x^3/3$, where n_0 is the proton density and μ_0 is a factor accounting for the metallicity of the CBM. Here we consider the simplest case of an ionized H gas and take $\mu_0 = 1$.

The blast wave will start to undergo significant deceleration when an amount of energy comparable to the initial energy E_0 in the blast wave is swept up. Looked at from the comoving frame, each proton from the CBM carries with it an amount of energy $\Gamma_0 m_p c^2$ when captured by the blast wave. After capture and isotropization, the amount of energy carried by the blast wave from this swept-up proton is $\Gamma_0^2 m_p c^2$ as measured in the stationary frame (cf. eq. [5.23]). The condition $\Gamma_0^2 M_{\text{sw}} c^2 = E_0$ gives the deceleration radius

$$x_d \equiv \left(\frac{3E_0}{4\pi\Gamma_0^2 m_p c^2 n_0} \right)^{1/3} \cong 2.6 \times 10^{16} \left(\frac{E_{52}}{\Gamma_{300}^2 n_0} \right)^{1/3} \text{ cm}, \quad (11.2)$$

where $E_0 = E_{52}/10^{52}$ ergs is the total explosion energy including rest mass energy, $\Gamma_{300} = \Gamma_0/300$, and n_0 is the CBM proton density in units of cm^{-3} .

Differential time elements in the stationary (starred), comoving (primed), and observer (unscripted) reference frames satisfy the relations

$$dx = \beta c dt_* = \beta \Gamma c dt' = \beta c \frac{dt}{(1+z)(1-\beta\mu)},$$

where $\theta = \arccos \mu$ is the angle between the direction of outflow and the observer, and $dt = (1+z)dt'/\delta_D$. Hence

$$dt = \frac{(1+z)}{c} dx (\beta^{-1} - \mu) \cong \frac{(1+z)dx}{\Gamma^2 c}. \quad (11.3)$$

The final term in this expression applies to relativistic flows ($\Gamma \gg 1$) observed at $\theta \cong 1/\Gamma$, assuming that the average emitting region is located at cosine angle $\mu \cong \beta$ to the line of sight.

The deceleration time [298,300] as measured by an observer is therefore

$$t_d \equiv (1+z) \frac{x_d}{\beta_0 \Gamma_0^2 c} \\ = (1+z) \left(\frac{3E_0}{4\pi n_0 m_p c^5 \Gamma_0^8} \right)^{1/3} \cong \frac{9.6(1+z)}{\beta_0} \left(\frac{E_{52}}{\Gamma_{300}^8 n_0} \right)^{1/3} \text{ s}, \quad (11.4)$$

where z is the redshift of the source, and the factor $\beta_0^{-1} = 1/\sqrt{1-\Gamma_0^{-2}}$ generalizes [301] the original result of Mészáros and Rees for mildly relativistic and nonrelativistic supernova explosions. The Sedov radius, giving the distance traveled in a uniform CBM when the shell sweeps up an amount of mass energy comparable to the explosion energy, is given by

$$\ell_S = \left(\frac{3E_0}{4\pi m_p c^2 n_0} \right)^{1/3} = \Gamma_0^{2/3} x_d \\ \cong 1.2 \times 10^{18} \left(\frac{E_{52}}{n_0} \right)^{1/3} \text{ cm} \cong 6.6 \times 10^{18} \left(\frac{\mathcal{E}_\odot}{n_0} \right)^{1/3} \text{ cm}. \quad (11.5)$$

The final term is written in units of $\mathcal{E}_\odot = E_0/M_\odot c^2$, where M_\odot is the mass of the Sun. For relativistic explosions, ℓ_S refers to the radius where the blast wave slows to mildly relativistic speeds, i.e., $\Gamma \sim 2$. The Sedov radius of a SN that ejects a $10M_\odot$ envelope can reach several pc or more.

11.1.2 Blast-Wave Equation of Motion

The equation describing the momentum $P = \beta\gamma$ of the relativistic blast wave, which changes as a consequence of the blast wave sweeping up material from the surrounding medium and radiating internal energy, is now

derived. For notational simplicity, energies are written in mass units in this section.

Intuitive Derivation

First we give an intuitive derivation reproducing the asymptotic forms and showing where a more detailed treatment is needed. Applying momentum conservation for the explosion and swept-up mass $m(x)$ gives

$$P \left[M_0 + \int_0^x d\tilde{x} \left(\frac{dm(\tilde{x})}{d\tilde{x}} \right) \Gamma(\tilde{x}) \right] \cong \beta \Gamma [M_0 + m(x) \Gamma(x)] \\ \cong \beta \Gamma [M_0 + kx^3 \Gamma] \cong \text{const},$$

giving the asymptotes $\Gamma \propto x^{-3/2}$ when $\Gamma_0 \gg \Gamma \gg 1$ and $\beta \propto x^{-3}$ when $\Gamma - 1 \ll 1$. For the radiative solution,

$$P \left[M_0 + \int_0^x d\tilde{x} \left(\frac{dm(\tilde{x})}{d\tilde{x}} \right) \right] \cong \beta \Gamma [M_0 + m(x)] \cong \beta \Gamma [M_0 + kx^3] \cong \text{const},$$

giving the asymptotes $\Gamma \propto x^{-3}$ when $\Gamma_0 \gg \Gamma \gg 1$ and $\beta \propto x^{-3}$ when $\Gamma - 1 \ll 1$.

The limits for the adiabatic solution would seem to be obtained through total energy conservation from the expression

$$\Gamma \left[M_0 + \int_0^x d\tilde{x} \Gamma(\tilde{x}) \left(\frac{dm(\tilde{x})}{d\tilde{x}} \right) \right] \cong \Gamma [M_0 + \Gamma m(x)] \cong \Gamma (M_0 + kx^3 \Gamma) \cong \text{const}.$$

This gives the correct relativistic asymptote $\Gamma \propto x^{-3/2}$ when $\Gamma_0 \gg \Gamma \gg 1$, but implies that $\beta \propto x^{-3}$ when $\Gamma - 1 \ll 1$. As is apparent from the numerical results, the change in internal energy due to adiabatic losses becomes important in the nonrelativistic regime so that this estimate is not valid there.

Detailed Derivation

The comoving particle distribution function $N'(p'; x)$, integrated over the volume of the blast-wave shell, is defined so that $N'(p'; x) dp' = [dN'(p'; x)/dp'] dp'$ represents the differential number of particles with momenta between $p' = \beta'_{\text{par}} \gamma'$ and $p' + dp'$ in a blast wave at radius x . In writing this function, we assume that the particles are isotropically distributed in the comoving frame and average over the volume of the blast wave. Global conservation of energy implies that

$$d(\Gamma U_{\text{tot}}) = dm + \Gamma dU_{\text{rad}}. \quad (11.6)$$

Here Γ is the Lorentz factor of the blast wave, dm is the differential change in the swept-up rest-mass energy, U_{tot} is the total internal energy in the comoving frame, and dU_{rad} is the differential change in the comoving internal energy that is radiated from the blast wave. The radiated energy is assumed to be isotropically emitted in the comoving frame.

The quantity

$$U_{\text{tot}} = m_p \int_0^\infty dp' \gamma' N'(p'; x) = M_0 + m(x) + U \quad (11.7)$$

represents the total internal energy, including rest-mass energy, whereas

$$U = m_p \int_0^\infty dp' (\gamma' - 1) N'(p'; x) \quad (11.8)$$

represents the internal energy with rest-mass energy excluded. The total rest mass consists of the sum of the baryon mass M_0 , eq. (11.1), in addition to the swept-up mass

$$m(x) = \int_{x_0}^x d\tilde{x} \left(\frac{dm(\tilde{x})}{d\tilde{x}} \right) = 4\pi m_p \int_{x_0}^x d\tilde{x} \tilde{x}^2 n_{\text{ext}}(\tilde{x}). \quad (11.9)$$

Here $n_{\text{ext}}(x)$ is the density of the external medium, and is assumed for simplicity to have radial symmetry.

The internal energy U in the blast wave increases by the addition of the kinetic energy of the swept-up matter, and decreases due to particle energy losses through adiabatic expansion and radiation. Thus $dU = dU_m + dU_{\text{adi}} + dU_{\text{rad}}$, where $dU_m = (\Gamma - 1)dm$ and dU_{adi} represent the change in internal energy due to swept-up particle kinetic energy and adiabatic losses, respectively. Expanding eq. (11.6) gives $d\{\Gamma[U + M_0 + m(x)]\} = \Gamma dU + \Gamma dm + [U + M_0 + m(x)]d\Gamma$. From this follows the equation of blast-wave evolution:

$$-\frac{d\Gamma}{\Gamma^2 - 1} = \frac{dm + (\Gamma/P^2)dU_{\text{adi}}}{M_0 + m(x) + U}, \quad (11.10)$$

where the blast-wave momentum $P = \sqrt{\Gamma^2 - 1}$. Equation (11.10) can also be written as

$$-\frac{dP}{dx} = \frac{P\Gamma(dm/dx) + (\Gamma^2/P)(dU_{\text{adi}}/dx)}{M_0 + m(x) + U}. \quad (11.11)$$

As the internal energy decreases due to adiabatic losses of the particles, as given by the second term in the numerator on the right-hand side of either eq. (11.10) or (11.11), the rate of change of the blast-wave Lorentz factor likewise becomes smaller. In effect, the energy lost through adiabatic processes is recovered in the kinetic energy of the bulk outflow.

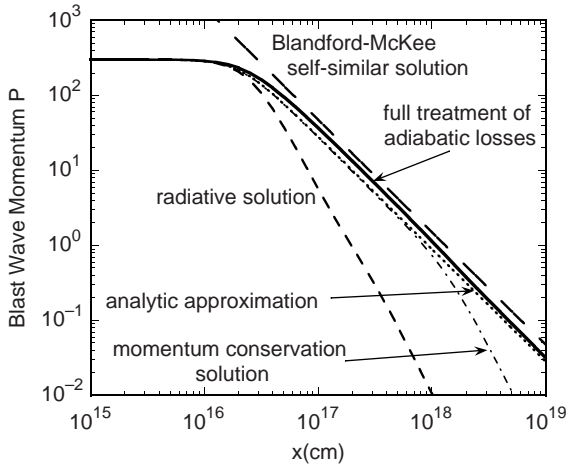


Figure 11.1 Evolution of blast wave momentum $P = \beta\Gamma$ for different assumptions for the particle energy losses [301]. The solid curve labeled “full treatment of adiabatic losses” is a numerical solution of eq. (11.11) that includes adiabatic losses of swept-up particle energy that is transformed into the directed kinetic energy of the outflow. The dotted curve shows the analytic approximation, eq. (11.18). The curve labeled “momentum conservation solution” neglects adiabatic energy losses of the swept-up particles, and the curve labeled “radiative solution” assumes that the internal energy is promptly radiated. Dashed line shows the Blandford-McKee self-similar solution, eq. (11.12).

Figure 11.1 shows a calculation of eq. (11.11) under different assumptions for the particle energy losses [301]. The thermal ejecta particles making up the “ M_0 ” term are assumed to be cold, so that only energy losses of the swept-up particles are considered. The parameters of the calculation are $E_0 = 10^{52} E_{52}$ ergs, $\Gamma_0 = 300\Gamma_{300}$, and $n_0 = n_0 \text{ cm}^{-3}$, with $E_{52} = \Gamma_{300} = n_0 = 1$. The long-dashed curve gives the numerical solution to eq. (11.11), with swept-up particles losing energy through adiabatic losses. The dotted curve gives the analytic solution, eq. (11.18), derived in the argument leading to eq. (11.23). The solid curve gives the momentum conservations solution, where particles suffer no adiabatic losses.

The pioneering treatment of adiabatic and radiative relativistic blast waves, given by Blandford and McKee [302], uses a similarity variable to solve the relativistic hydrodynamic equations of motion. The Lorentz factor of the shocked fluid immediately behind the shock is given for a relativistic adiabatic blast wave in a uniform surrounding medium (see also

Ref. [303]) by

$$\Gamma(x) = \frac{1}{4} \left(\frac{17E}{\pi n_0 m_p c^2 x^3} \right)^{1/2} \cong 47 \frac{\sqrt{E_{52}/n_0}}{x_{17}^{3/2}}, \quad (11.12)$$

where $x = 10^{17} x_{17}$ cm.

Adiabatic Losses

If the internal energy U in the blast wave is dominated by the kinetic energy of a thermal particle distribution, then U changes due to volume expansion according to the relation $U^{-1}(dU_{\text{adi}}/dx) = -(\hat{\gamma} - 1)(d \ln V'/dx)$, where $\hat{\gamma}$ is the ratio of specific heats, V' is the comoving fluid volume, and $\hat{\gamma} = 4/3$ and $5/3$ for relativistic and nonrelativistic monoatomic gases, respectively (see section 9.4). The general case involving a mixed fluid that includes both isotropic thermal and nonthermal particles can be obtained from the expression

$$-\left(\frac{dp'}{dx}\right)_{\text{adi}} = \frac{p'}{3} \frac{d \ln V'}{dx} \quad (11.13)$$

for adiabatic expansion losses. Equation (11.13) reproduces the limiting adiabatic loss forms exhibited by monatomic thermal gases. In the relativistic limit $p' \gg 1$, $d\gamma' \rightarrow -(\gamma'/3)d \ln V'$, and in the nonrelativistic limit $p' \ll 1$, $d(p'^2/2) \rightarrow -(2/3)(\beta'^2/2)d \ln V'$.

The comoving volume of the fluid shell is approximated by the expression

$$V' = 4\pi x^2 \Delta' = 4\pi x^2 \left(\frac{f_{\Delta} x}{\Gamma} \right), \quad (11.14)$$

where Δ' is the comoving width of the blast-wave shell. The shocked fluid shell for the uniform isotropic case has a width $\Delta'_{\text{sh}} \cong x/12\Gamma$, so $f_{\Delta} = 1/12$. The value $f_{\Delta} = 1/12$ can be derived from the shock-jump conditions [304],³ or by noting that conservation of particle number implies $4\pi x^2 \Delta'_{\text{sh}} (4\Gamma n_0) = 4\pi n_0 x^3/3$, for a compression ratio of 4Γ . The differential adiabatic expansion energy-loss rate for particles in a GRB blast wave is therefore given by

$$\left(\frac{dp'}{dx}\right)_{\text{adi}} = -\frac{p'}{x} \left(1 - \frac{1}{3} \frac{d \ln \Gamma}{d \ln x} \right), \quad (11.15)$$

using eqs. (11.13) and (11.14). Note that the second term on the right-hand side in the parentheses of eq. (11.15) is small in comparison with 1 in the limit $\Gamma - 1 \ll 1$.

³ $V' \cong m(x)/[n'(x)m_p]$ in the limits $\Gamma \gg 1$ and $\Gamma - 1 \ll 1$, where $n'(x) = (\hat{\gamma}\Gamma + 1)n_0/(\hat{\gamma} - 1)$ is the downstream comoving density in terms of the external medium density n_0 , which is assumed to be at a nonrelativistic temperature.

The internal energy therefore changes through adiabatic losses according to the relation

$$\frac{dU_{\text{adi}}}{dx} = -m_p \left(\frac{1}{x} - \frac{1}{3} \frac{d \ln \Gamma}{dx} \right) \int_0^\infty dp' \left(\frac{p'^2}{\gamma'} \right) N'(p'; x). \quad (11.16)$$

If only adiabatic losses are important, then eq. (11.15) is easily solved to give

$$p' = p'(x, x_i) = p'_i \left(\frac{x_i}{x} \right) \left(\frac{\Gamma(x)}{\Gamma(x_i)} \right)^{1/3}, \quad (11.17)$$

where p'_i is the momentum of a particle injected at radius x_i when the blast wave was moving with Lorentz factor $\Gamma(x_i)$. Numerical solutions of eq. (11.11) using this expression to calculate adiabatic energy losses are shown in figure 11.1.

Adiabatic (Nonradiative) Blast Waves

An approximate equation describing the evolution of an adiabatic blast wave in a uniform surrounding medium (neglecting the complications of the reverse shock; see section 11.3) from highly relativistic to nonrelativistic speeds is given by

$$P(x) \cong \frac{P_0}{\sqrt{1 + 2(x/x_d)^3}} \cong \begin{cases} \beta_0 \Gamma_0, & \text{for } x_{\text{co}} \ll x \ll x_d, \\ \frac{\beta_0 \Gamma_0}{\sqrt{2}(x/x_d)^{3/2}} = \frac{\beta_0}{\sqrt{2}(x/\ell_S)^{3/2}}, & \text{for } x_d \ll x \ll x_{\text{rad}}. \end{cases} \quad (11.18)$$

Here $P = \beta\Gamma$ [301] is the dimensionless momentum of the shocked fluid, $P_0 = \beta_0\Gamma_0$ is the coasting momentum, and x_{rad} is the distance where the blast wave becomes highly radiative, as occurs for nonrelativistic supernova shocks at late stages in their evolution. Note that the blast-wave speed becomes independent of its initial Lorentz factor Γ_0 during the deceleration phase, which is a feature of the self-similar deceleration phase. Equation (11.18) applies only to adiabatic blast-wave evolution, and reduces to the adiabatic Sedov behavior for nonrelativistic ($\beta_0 \ll 1$) explosions. The radiative state of GRBs—whether they are more likely to be highly radiative or nearly adiabatic—and if this behavior changes from the prompt, gamma-ray luminous to the later afterglow phase, is uncertain [305,306]. The expression for the relativistic ($\Gamma_0 \gg 1$) behavior given by eq. (11.18) is derived below.

In the coasting phase, $P \cong P_0$, and in the relativistic deceleration (or relativistic Sedov) phase, $P \cong P_0(x/x_d)^{-3/2}$. For an on-axis observer, $\mu \cong \beta$, and eqs. (11.3) and (11.18) imply that

$$\frac{x}{x_d} \cong \begin{cases} t/t_d, & \text{for } t/t_d \lesssim 1, \text{ coasting,} \\ (2t/t_d)^{1/4}, & \text{for } 1 \lesssim t/t_d \lesssim \Gamma_0^{8/3}, \text{ relativistic Sedov (RSdv),} \\ \left(\frac{5t}{\sqrt{8}t_d\Gamma_0}\right)^{2/5}, & \text{for } t/t_d \gtrsim \Gamma_0^{8/3}, \text{ (nonrelativistic) Sedov,} \end{cases} \quad (11.19)$$

and

$$\frac{P}{P_0} \cong \begin{cases} 1, & \text{coasting,} \\ \frac{1}{\sqrt{2}}(2t/t_d)^{-3/8}, & \text{RSdv,} \\ 2^{-1/2} \left(\frac{5t}{\sqrt{8}\Gamma_0 t_d}\right)^{-3/5}, & \text{Sedov.} \end{cases} \quad (11.20)$$

These expressions are valid for relativistic GRB explosions, mildly relativistic SNe such as SN 1998bw [307], and nonrelativistic supernova explosions. The dependences

$$x \propto t^{2/5} \quad \text{and} \quad \beta \propto t^{-3/5}$$

in the nonrelativistic Sedov regime are familiar from the physics of SN remnant evolution [308]. The middle asymptote of eqs. (11.19) and (11.20) applies only to relativistic outflows. The Sedov deceleration phase of a relativistic adiabatic blast wave decays with time as

$$P(t) \rightarrow \Gamma(t) \cong \frac{(1+z)^{3/8}}{2^{7/8}(ct)^{3/8}} \left(\frac{3E_0}{4\pi n_0 m_p c^2}\right)^{1/8} \cong 5.4 \left(\frac{1+z}{t_{\text{day}}}\right)^{3/8} \left(\frac{E_{52}}{n_0}\right)^{1/8}, \quad (11.21)$$

where t_{day} is the time measured by the observer in days after the GRB.

Relativistic Adiabatic Blast Waves

In the limit $\Gamma \gg 1$, the second term in the numerator of eq. (11.11) can be neglected in favor of the first term. This simplification is not as easy to justify analytically as numerically. Because both terms are of the same order, that is, $dU_{\text{adi}}/dx \cong -U/x \sim \Gamma dm/dx$, the neglect of the second term is only possible when $\Gamma \gg 1$ because its neglect is balanced by the loss of internal energy U in the denominator of the equation. At relativistic speeds, therefore, eq. (11.11) becomes

$$-\frac{d\Gamma}{\Gamma^2} = \frac{dm}{M_0 + m(x) + U}. \quad (11.22)$$

This expression is often taken as a starting point to derive the relativistic blast-wave equation of motion, whether for adiabatic, radiative, or partially radiative blast waves. Its applicability is somewhat accidental, and does not in any case apply when the blast-wave speed is $\ll c$.

For a relativistic adiabatic blast wave, eq. (11.22) can be solved by noting that $dU = (\Gamma - 1)dm \cong \Gamma dm$, implying $U = M_0[(\Gamma_0/\Gamma) - 1]$. Substituting this expression back into eq. (11.22) gives

$$\Gamma(x) = \frac{\Gamma_0}{\sqrt{1 + 2\Gamma_0 m(x)/M_0}} \rightarrow \frac{\Gamma_0}{\sqrt{1 + 2(x/x_d)^3}} \quad (11.23)$$

where, as before, the final expression holds for a uniform CBM. This expression agrees with the relativistic limit of eq. (11.18). It is easy to show from eqs. (11.19) and (11.20) that, for relativistic adiabatic blast waves,

$$x = \frac{a_{\text{cor}}\Gamma^2 ct}{1+z} \cong \begin{cases} \Gamma^2 ct/(1+z), & \text{coasting,} \\ 4\Gamma^2 ct/(1+z), & \text{RSdv,} \end{cases} \quad (11.24)$$

where the correction factor $a_{\text{cor}} \approx 1$ and 4 in the coasting and the relativistic deceleration phase, respectively.

Radiative Blast Waves

For a strongly radiative blast wave, the adiabatic loss term is negligible because the particles have lost all their internal energy. Letting $U = dU_{\text{adi}}/dx = 0$, we obtain from eq. (11.10) the equation of motion for a radiative blast wave, given by

$$-\frac{d\Gamma}{\Gamma^2 - 1} = \frac{dm}{M_0 + m(x)} \quad (11.25)$$

[302]. This is easily solved to obtain

$$\Gamma(x) = \frac{[1 + m(x)/M_0]^2(\Gamma_0 + 1) + \Gamma_0 - 1}{[1 + m(x)/M_0]^2(\Gamma_0 + 1) - \Gamma_0 + 1}, \quad (11.26)$$

which is valid throughout the nonrelativistic and relativistic regimes.

For a relativistic radiative blast wave, the blast wave enters the nonrelativistic Sedov phase when $m(x) \cong M_0$. Therefore letting $m(x) \ll M_0$ and $\Gamma \gg 1$, eq. (11.25) can be solved to give

$$\Gamma(x) \cong \frac{\Gamma_0}{1 + m(x)\Gamma_0/M_0} \rightarrow \frac{\Gamma_0}{1 + (x/x_d)^3}, \quad (11.27)$$

where the final expression applies to a uniform CBM.

For a relativistic, radiative blast wave in the deceleration phase, therefore, $\Gamma \propto 1/x^3$ and $t \propto \int dx/(\Gamma^2 c) \propto x^7$, so that

$$x \propto t^{1/7} \quad \text{and} \quad \Gamma \propto t^{-3/7}.$$

Relativistic Partially Radiative Blast Waves

If a fraction φ of the swept-up kinetic energy is instantaneously radiated from the blast wave, then $dU = (1 - \varphi)(\Gamma - 1)dm$. Defining $\mathcal{M} = M_0 + m(x) + U$ implies that $d\mathcal{M} = [\varphi + \Gamma(1 - \varphi)]dm$, one obtains

$$-\frac{d\Gamma}{\Gamma^2} = \frac{d\mathcal{M}}{\mathcal{M}[\varphi + \Gamma(1 - \varphi)]} \quad (11.28)$$

in the limit $\Gamma \gg 1$. Equation (11.28) has been used to treat partially radiative blast waves [297,309,310], though assuming that $\varphi \approx \text{const}$ throughout the regime of blast-wave evolution under consideration. In the general case when particle acceleration, escape, and adiabatic losses are considered, eq. (11.11) must be solved numerically.

Equation (11.28) is solved [309] to give

$$\Gamma(x) = \frac{\Gamma_0}{[1 + (2 - \varphi)\Gamma_0 m(x)/M_0]^{1/(2-\varphi)}} = \frac{\Gamma_0}{[1 + (2 - \varphi)(x/x_d)^3]^{1/(2-\varphi)}}, \quad (11.29)$$

which recovers eqs. (11.23) and (11.27) in the adiabatic ($\varphi = 0$) and radiative ($\varphi = 1$) limits, respectively. In the relativistic deceleration regime, therefore,

$$\Gamma(x) \propto x^{-3/(2-\varphi)}, \quad x(t) \propto t^{(2-\varphi)/(8-\varphi)}, \quad \text{and} \quad \Gamma(t) \propto t^{-3/(8-\varphi)}. \quad (11.30)$$

Inhomogeneous External Medium

The blast-wave evolution and radiative signatures depend on the distribution of the external medium density. A more general case beyond the uniform external medium considered up to now, is a radially symmetric density dependence $n(x) \propto x^{-s}$. A special case is $n(x) \propto x^{-2}$, which gives the simplest expression for the density distribution of a preexisting constant speed stellar wind. Distinguishing between wind and uniform density surroundings is important to determine the nature of the progenitor stars of GRBs. For the extension of blast-wave theory to non-uniform surrounding media, including radio predictions, see work by Chevalier and Li [311,312], and Panaitescu and Kumar [313,314]. Application to prompt [315] and afterglow [314,316] modeling of GRBs is complicated by magnetic-field uncertainties (section 11.2).

11.1.3 Dissipated Internal Energy

The kinetic energy swept into the comoving fluid frame per unit proper time at the forward shock is given by

$$\left. \frac{dE'}{dt'} \right|_{\text{FS}} = A(x)n_0m_p c^2(\beta c)\Gamma(\Gamma - 1) \propto \begin{cases} \Gamma^2, & \text{for } \Gamma \gg 1, \\ \beta^3/2, & \text{for } \Gamma - 1 \ll 1 \end{cases} \quad (11.31)$$

[302], where the area $A(x) = 4\pi x^2$ for a spherical blast wave. The factor Γ represents the increase of external medium density due to length contraction, the factor $(\Gamma - 1)m_p$ is the kinetic energy of the swept-up particles, and the factor βc is proportional to the rate at which the particle energy is swept into by the blast wave. This process provides internal energy available to be dissipated in the blast wave.

If some fraction $\varphi \ll 1$ of the internal swept-up energy is instantaneously transformed to radiation at the forward shock, then eqs. (11.19) and (11.20) show that the bolometric radiant luminosity measured by an observer is

$$L_{\text{rad}} = \varphi \Gamma^2 \frac{dE'}{dt'} \propto \varphi x^2 \Gamma^4 \propto \varphi \begin{cases} (t/t_d)^2, & \text{coasting,} \\ (t/t_d)^{-1}, & \text{RSdv,} \end{cases} \quad (11.32)$$

for a relativistic blast wave ($\Gamma > 1$). The final relations make use of eqs. (11.19) and (11.20) for an adiabatic blast wave in the coasting and relativistic Sedov phase. For a radiative blast wave, $\varphi \approx 1$ and $L_{\text{rad}} \propto t^{-10/7}$ in the relativistic deceleration phase, as can be easily shown.

11.2 ELEMENTARY BLAST-WAVE THEORY

Equation (11.32) gives the bolometric luminosity from a relativistic adiabatic blast wave. Blast-wave theory was developed to calculate spectral properties of GRB blast waves, whether from hadrons or electrons. For the production of low frequency ($\nu \lesssim 10^{20}$ Hz; i.e., MeV and below) prompt and afterglow radiation, the most important radiation process in GRBs is probably nonthermal electron synchrotron radiation, though photospheric or Compton emissions may appear below 1 MeV. At higher energies, an SSC component must inevitably accompany synchrotron emission. Here we outline the assumptions and physics leading to the calculation of nonthermal electron synchrotron spectra from decelerating relativistic blast waves, here for the special case of a uniform CBM. For reviews, see Refs. [317,318].

11.2.1 Characteristic Electron Energies

The broadband radio–MeV flux from GRBs is generally thought to be radiated primarily by electrons/leptons rather than ions, for reasons related to time variability, radiative efficiency, and polarization. Low-mass electrons radiate in magnetized flows through a number of processes, but especially via the synchrotron process. However, $\gtrsim m_p/m_e \sim 2000$ of the nonthermal particle energy swept up by the blast wave is in the form of protons or ions rather than electrons. For a radiatively efficient system, physical processes must transfer a large fraction of the swept-up energy to the electron component. In elementary treatments of the blast-wave model, it is simply assumed that a fraction ϵ_e of the forward-shock power is transferred to the electrons/leptons, so that

$$L'_e = \epsilon_e \frac{dE'}{dt'}. \quad (11.33)$$

It is also generally supposed in simple blast-wave model calculations that some mechanism—probably the first-order shock Fermi process—injects electrons with a power-law distribution between electron Lorentz factors $\gamma_{\min} \leq \gamma \leq \gamma_{\max}$ downstream of the shock front. The electron injection spectrum in the comoving frame is therefore described by the expression

$$\frac{dN'_e(\gamma)}{dt'd\gamma} = K_e \gamma^{-p} H(\gamma; \gamma_{\min}, \gamma_{\max}), \quad (11.34)$$

where K_e is the normalization coefficient and p is the injection index.

Minimum Electron Lorentz Factor

Electrons are swept into the comoving frame of the blast wave at the rate $dN'_e/dt' = A(x)n_0c\beta\Gamma$. Assuming that all swept-up electrons are accelerated and none escape, joint normalization of the number and power of the swept-up electrons gives

$$\frac{\gamma_{\min}^{2-p} - \gamma_{\max}^{2-p}}{\gamma_{\min}^{1-p} - \gamma_{\max}^{1-p}} \cong \epsilon_e \left(\frac{p-2}{p-1} \right) \left(\frac{m_p}{m_e} \right) (\Gamma - 1),$$

implying, when $\Gamma \gg 1$, $p > 2$ and $\gamma_{\max} \gg \gamma_{\min}$,

$$\gamma_{\min} \cong \epsilon_e \frac{m_p}{m_e} f(p) \Gamma, \quad \text{where } f(p) \equiv \left(\frac{p-2}{p-1} \right). \quad (11.35)$$

Assuming that ϵ_e remains constant throughout the evolution of an adiabatic blast wave,

$$\gamma_{\min} \propto \Gamma \propto \begin{cases} \text{const,} & \text{coasting,} \\ (t/t_d)^{-3/8}, & \text{RSdv.} \end{cases} \quad (11.36)$$

Cooling Electron Lorentz Factor

Suppose that the dominant energy loss of nonthermal electrons is synchrotron emission. The average energy-loss rate of relativistic electrons, randomly distributed in pitch angles, that lose energy by emitting synchrotron radiation in a tangled magnetic field is given by eq. (7.15), namely,

$$-\dot{\gamma}_{\text{syn}} = \frac{4}{3} c \sigma_{\text{T}} \left(\frac{B^2}{8\pi m_e c^2} \right) \gamma^2, \quad (11.37)$$

The strength of the magnetic field is a major uncertainty. The standard prescription is to assume that the magnetic field energy density is a fixed fraction ϵ_B of the downstream energy density of the shocked fluid. Hence

$$\frac{B^2}{8\pi} = 4\epsilon_B n_0 m_p c^2 (\Gamma^2 - \Gamma) \cong 4\epsilon_B n_0 m_p c^2 \Gamma^2, \quad (11.38)$$

implying

$$B \cong \sqrt{32\pi m_p c^2 \epsilon_B n_0} \Gamma \cong 0.39 \sqrt{\epsilon_B n_0} \Gamma \text{ G}. \quad (11.39)$$

This expression assumes that the compression ratio is 4Γ when $\Gamma \gg 1$, as follows from the shock jump conditions discussed below. Compression of the transverse component of the magnetic field in the CBM gives a different (usually much smaller) estimate of the magnetic field, but the compressional field is assumed to be dominated in relativistic shocks by the magnetic field obtained from eq. (11.38). Recalling that $dx = \beta \Gamma c dt'$, eq. (11.37) gives

$$-\left(\frac{d\gamma}{dx} \right)_{\text{syn}} \cong \frac{16 m_p}{3 m_e} \sigma_{\text{T}} \epsilon_B n_0 \Gamma \gamma^2. \quad (11.40)$$

As described in section 11.1.1, particles lose energy by adiabatic losses due to the expansion of the blast wave. From eq. (11.15), the adiabatic energy-loss rate for relativistic ($\gamma \gg 1$) electrons can be written as

$$-\left(\frac{d\gamma}{dx} \right)_{\text{adi}} = \frac{\gamma}{x} (1 + g/3), \quad \text{where } g \equiv -\frac{d \ln \Gamma}{d \ln x} \quad (11.41)$$

[301], and $g = 3/2$ for an adiabatic blast wave expanding into uniform CBM during the RSdv phase.

Equating eqs. (11.40) and (11.41) gives the “cooling” electron Lorentz factor

$$\gamma_c \cong \frac{9 m_e}{32 m_p \sigma_{\text{T}} \epsilon_B n_0 x \Gamma} \quad (11.42)$$

above which synchrotron losses dominate adiabatic expansion losses. Letting $x \rightarrow a_{\text{cor}} \Gamma^2 ct / (1+z)$, where $a_{\text{cor}} = 1$ and $a_{\text{cor}} = 4$ during the coasting and adiabatic relativistic deceleration phases, respectively (eq. [11.24]),

gives essentially the expression of Ref. [319], namely,

$$\gamma_c = \frac{9m_e(1+z)}{32a_{\text{cor}}m_p\sigma_T\epsilon_B n_0 c \Gamma^3 t}.$$

This expression can also be obtained by defining γ_c through the relation $|\dot{\gamma}_{\text{syn}}(\gamma_c)|dt' = \gamma_c$, with $\Delta t' \cong t' \cong x/\Gamma c \cong \Gamma t/(1+z)$. If ϵ_B remains constant throughout the evolution of the blast wave, then

$$\gamma_c \propto \frac{1}{x\Gamma} \propto \begin{cases} (t/t_d)^{-1}, & \text{coasting,} \\ (t/t_d)^{1/8}, & \text{RSdv.} \end{cases} \quad (11.43)$$

Maximum Electron Lorentz Factor

The maximum electron Lorentz factor γ_{max} in eq. (11.34) is set by three conditions, namely, the available time for acceleration, the condition that the acceleration rate is faster than the radiation-loss rate, and the requirement that the particle Larmor radius $r_L = \gamma m_e c^2/eB$ be smaller than the size scale Δ' of the system [320]. The available time constraint is the most important constraint on particle energies at the earliest times $t \ll t_d$. It, and the condition that the Larmor radius be smaller than the blast-wave width, usually determines the maximum ion energy, as discussed in later chapters. For electrons, by contrast, the maximum energy is most often determined by competition with radiative losses.

The shortest acceleration time scale expected in Fermi processes is $\simeq r_L/c = \gamma m_e c/eB = \gamma/\dot{\gamma}_{\text{acc}}$ [178]. Setting the acceleration rate equal to a constant factor $\hat{\epsilon}_{\text{max}} (\lesssim 1)$ times the maximum particle energy-gain rate $\approx r_L/c$ expected in Fermi processes gives $\dot{\gamma}_{\text{acc}} = \hat{\epsilon}_{\text{max}} eB/m_e c$. Equating $\dot{\gamma}_{\text{acc}}$ with $|\dot{\gamma}_{\text{syn}}|$, assuming that synchrotron emission dominates the radiative losses, implies a maximum particle energy determined by a competition between the radiative energy-loss rate and the acceleration rate, given in terms of particle Lorentz factor by

$$\gamma_{\text{max}} = \left(\frac{6\pi e \hat{\epsilon}_{\text{max}}}{\sigma_T B} \right)^{1/2} \cong \frac{1.2 \times 10^8 \hat{\epsilon}_{\text{max}}^{1/2}}{\sqrt{B(\text{G})}} \cong \frac{2 \times 10^8 \hat{\epsilon}_{\text{max}}^{1/2}}{\epsilon_B^{1/4} n_0 \Gamma^{1/2}}. \quad (11.44)$$

Thus the maximum electron Lorentz factor in the comoving frame is

$$\gamma_{\text{max}} \propto \Gamma^{-1/2} \propto \begin{cases} \text{const,} & \text{coasting,} \\ (t/t_d)^{3/16}, & \text{RSdv.} \end{cases} \quad (11.45)$$

Figure 11.2 illustrates the behavior of γ_{min} , γ_c , and γ_{max} when ϵ_e , ϵ_B , and $\hat{\epsilon}_{\text{max}}$ are assumed to remain constant with time. When $\gamma_c > \gamma_{\text{min}}$, the system is said to be in the weakly cooled regime, whereas it is in the strongly cooled

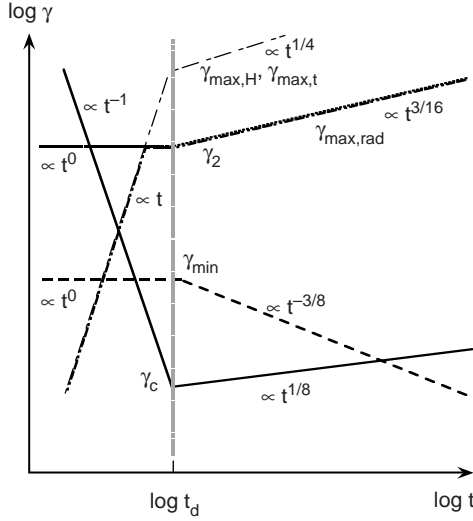


Figure 11.2 Characteristic behavior of the minimum Lorentz factor γ_{\min} , the cooling Lorentz factor γ_c , and the maximum Lorentz factor γ_{\max} with observer time for the strong forward shock of a relativistic adiabatic blast wave, assuming that ϵ_e , ϵ_B , and $\hat{\epsilon}_{\max}$ remain constant with time and that the blast wave expands into a uniform CBM. Also sketched is the limit $\gamma_{\max,t}$ from the available time constraint, and the limit $\gamma_{\max,H}$ from the constraint that the particle Lorentz factor be smaller than the comoving blast-wave width.

regime when $\gamma_c < \gamma_{\min}$ [319]. Figure 11.2 shows that, if the system is in the weakly cooled regime when $t = t_d$, then it is always in the weakly cooled regime under the stated assumptions. Otherwise the system evolves from weakly cooling to strongly cooling behavior when $t < t_d$, and vice versa when $t > t_d$.

These results apply to a scenario with only a strong forward shock. The reverse shock emissions can be neglected for nonrelativistic, or Newtonian reverse shocks (NRSs) [321,322]. When a relativistic reverse shock (RRS) is present, the shocked fluid Lorentz factor Γ evolves from the coasting to the relativistic Sedov phase through an intermediate RRS phase, as described in section 11.3.

11.2.2 Characteristic Synchrotron Frequencies

Electrons with Lorentz factor γ_0 will emit synchrotron radiation at a characteristic observed frequency

$$\nu_0 \cong \frac{eB\gamma_0^2\Gamma}{2\pi m_e c(1+z)} \cong 2.8 \times 10^6 B\gamma_0^2\Gamma/(1+z) \text{ Hz};$$

see eqs. (5.38) and (7.19) with $\delta_D \rightarrow \Gamma$. In dimensionless units, we can therefore relate the received photon energy through the electron γ factor by the expression $\epsilon \cong (B/B_{\text{cr}})\gamma^2\Gamma/(1+z)$, where $B_{\text{cr}} = 4.414 \times 10^{13}$ G is given by eq. (7.22).

Characteristic Synchrotron Frequency Associated with γ_{min}

The dimensionless photon frequency associated with electrons with $\gamma \cong \gamma_{\text{min}}$, eq. (11.35), is therefore

$$\begin{aligned}\epsilon_{\text{min}} &= \frac{\sqrt{32\pi m_p c^2}}{B_{\text{cr}}} \left(\frac{m_p}{m_e}\right)^2 \frac{f^2(p)n_0^{1/2}\epsilon_B\epsilon_e^2\Gamma^4}{(1+z)} \\ &\cong 3.0 \times 10^{-8} \frac{f^2(p)n_0^{1/2}\epsilon_B\epsilon_e^2\Gamma^4}{(1+z)},\end{aligned}$$

so that the characteristic frequency is

$$\nu_m \text{ (Hz)} \cong \frac{3.7 \times 10^{17}}{1+z} \left[\left(\frac{\epsilon_B}{0.01}\right)n_0\right]^{1/2} \left(\frac{\epsilon_e}{0.1}\right)^2 \left(\frac{\Gamma}{100}\right)^4 f^2(p). \quad (11.46)$$

For a relativistic adiabatic blast wave in the deceleration regime,

$$\nu_m \text{ (Hz)} \cong \frac{3 \times 10^{12}(1+z)^{1/2}E_{52}^{1/2}}{t_{\text{day}}^{3/2}} \left(\frac{\epsilon_B}{0.01}\right)^{1/2} \left(\frac{\epsilon_e}{0.1}\right)^2 f^2(p), \quad (11.47)$$

using eq. (11.21) for $\Gamma(t)$.

Cooling Frequency

The dimensionless photon frequency associated with electrons with $\gamma \cong \gamma_c$, eq. (11.42), is

$$\begin{aligned}\epsilon_c &= \frac{\sqrt{32\pi m_p c^2}}{B_{\text{cr}}} \left(\frac{3m_e}{16m_p\sigma_{\text{TC}}}\right)^2 \frac{1+z}{(n_0\epsilon_B)^{3/2}\Gamma^4 t^2} \\ &= \frac{2.3(1+z)}{n_0^{3/2}(\epsilon_B/0.01)^{3/2}(\Gamma/100)^4 t^2 \text{ (s)}}.\end{aligned}$$

The cooling frequency associated with electrons with $\gamma \cong \gamma_c$ is therefore

$$\nu_c \text{ (Hz)} \cong \frac{2.8 \times 10^{20}(1+z)}{(\epsilon_B/0.01)^{3/2} n_0^{3/2} (\Gamma/100)^4 t^2 \text{ (s)}}. \quad (11.48)$$

For a relativistic adiabatic blast wave in the deceleration regime,

$$\nu_c \text{ (Hz)} \cong \frac{4.4 \times 10^{15}}{(\epsilon_B/0.01)^{3/2} n_0 \sqrt{E_{52}(1+z)t_{\text{day}}}}, \quad (11.49)$$

using eq. (11.21).

Maximum Frequency

The dimensionless photon frequency associated with electrons with $\gamma \cong \gamma_{\text{max}}$, eq. (11.44), is

$$\epsilon_{\text{max}} = \frac{9\hat{\epsilon}_{\text{max}}}{4\alpha_f} \frac{\Gamma}{(1+z)},$$

implying a maximum synchrotron frequency

$$\nu_{\text{max}} \text{ (Hz)} \cong \frac{3.7 \times 10^{22} \hat{\epsilon}_{\text{max}} \Gamma}{(1+z)} \cong \frac{2 \times 10^{23} \hat{\epsilon}_{\text{max}} E_{52}^{1/8}}{(1+z)^{5/8} t_{\text{day}}^{3/8} n_0^{1/8}}, \quad (11.50)$$

where the final expression for adiabatic relativistic deceleration again uses eq. (11.21).

Synchrotron Self-Absorption Frequency

At sufficiently low frequencies, a magnetoactive plasma will absorb the synchrotron radiation emitted by electrons in the plasma, as discussed in section 7.8. Here we use the results derived there to obtain an expression the SSA frequency ν_a .

We calculate the SSA coefficient

$$\kappa_{\nu'} = -\frac{1}{8\pi m_e \nu'^2 V'_{\text{bw}}} \int_1^\infty d\gamma \frac{P(\nu', \gamma)}{m_e c^2} \gamma^2 \frac{\partial}{\partial \gamma} \left(\frac{N'(\gamma)}{\gamma^2} \right) \quad (11.51)$$

from eq. (7.141), where the blast-wave volume $V'_{\text{bw}} = 4\pi x^2 \Delta'$ and Δ' is the comoving shell width. The electron distribution is approximated by $N'(\gamma) \cong (s-1)N_e(x)\gamma_0^{s-1}\gamma^{-s}$, as discussed in more detail in the next section.

In the regime $\nu_a < \nu_0 = \min(\nu_m, \nu_c)$, which is the only regime considered here, the calculation of the absorption coefficient is simplified because

we can use the asymptotic form, eq. (7.30), for the synchrotron emissivity function

$$P(\nu) = 3^{1/2} e^3 B \sin \psi F(\nu/\nu_c) \rightarrow \frac{4\pi e^3 B}{\Gamma(1/3)} \left(\frac{\nu}{3\nu_B \gamma^2} \right)^{1/3}. \quad (11.52)$$

The right-hand side of this expression applies in the limit $\nu \ll \nu_c = 3\nu_B \gamma^2/2$, and the pitch angle is set equal to $\pi/2$. Substituting eq. (11.52) into eq. (11.51) and letting the relation $\nu'_a \Delta R = 1$ define the comoving frame SSA frequency ν'_a , we obtain for the observed SSA frequency the expression

$$\nu_a \text{ (Hz)} = \frac{8.8 \Gamma}{(1+z)\gamma_0} \left(\frac{(s+2)(s-1)}{(s+2/3)} \right)^{3/5} \{[x \text{ (cm)}]n_0\}^{3/5} [B \text{ (G)}]^{2/5} \quad (11.53)$$

Case 1. $\nu_c < \nu_m$, $\nu_0 = \nu_c$, and $\gamma_0 = \gamma_c$: In this fast-cooling (fc) regime, $s = 2$ and

$$\nu_a^{\text{fc}} \text{ (MHz)} \cong \frac{10}{(1+z)^{13/5}} \left(\frac{\epsilon_B}{0.01} \right)^{6/5} n_0^{9/5} \left(\frac{\Gamma}{100} \right)^{28/5} t \text{ (s)}^{8/5}, \quad (11.54)$$

which can also be written as

$$\nu_a^{\text{fc}} \text{ (GHz)} \cong \frac{32}{(1+z)^{13/5}} \left(\frac{\epsilon_B}{0.1} \right)^{6/5} n_0^{9/5} \left(\frac{\Gamma}{10} \right)^{28/5} t_{\text{day}}^{8/5}. \quad (11.55)$$

For adiabatic blast-wave evolution in the fast-cooling regime, $\Gamma(t) \propto t^{-3/8}$ and $\nu_a^{\text{fc}} \propto t^{-1/2}$. For radiative blast-wave evolution in the fast-cooling regime, $\Gamma(t) \propto t^{-3/7}$ and $\nu_a^{\text{fc}} \propto t^{-4/5}$.

Case 2. $\nu_m < \nu_c$, $\nu_0 = \nu_m$, and $\gamma_0 = \gamma_m$: In this slow-cooling (sc) regime, $s = p$ and

$$\nu_a^{\text{fc}} \text{ (Hz)} \cong \frac{1.5 \times 10^4}{(1+z)^{8/5} \epsilon_e} \left(\frac{(p-1)^{8/5} (p+2)^{3/5}}{(p-2)(p+2/3)^{8/5}} \right) \epsilon_B^{1/5} n_0^{4/5} \Gamma^{8/5} t^{3/5}, \quad (11.56)$$

For $p = 2.5$,

$$\nu_a^{\text{fc}} \text{ (MHz)} \cong \frac{430}{(1+z)^{8/5} (\epsilon_e/0.1)} \left(\frac{\epsilon_B}{0.01} \right)^{1/5} n_0^{4/5} \left(\frac{\Gamma}{100} \right)^{8/5} t \text{ (s)}^{3/5}. \quad (11.57)$$

This can also be written as

$$\nu_a^{\text{fc}} \text{ (GHz)} \cong \frac{28}{(1+z)^{8/5} (\epsilon_e/0.1)} \left(\frac{\epsilon_B}{0.1} \right)^{1/5} n_0^{4/5} \left(\frac{\Gamma}{10} \right)^{8/5} t_{\text{day}}^{3/5}. \quad (11.58)$$

For adiabatic blast-wave evolution in the slow-cooling regime, $\nu_a^{\text{sc}} \propto \text{const.}$ For radiative blast-wave evolution in the slow-cooling regime, $\nu_a^{\text{sc}} \propto t^{-3/35}$. The SSA frequency appears in the radio regime for typical parameters considered for GRB blast waves in the afterglow phase.

11.2.3 Afterglow Theory

Long-wavelength optical and X-ray afterglows of GRBs were predicted by Mészáros and Rees [323], shortly anticipating their discovery with Beppo-SAX [324]. Here we follow the approach of Sari, Piran, and Narayan [319]. Electrons cool in the comoving fluid frame by synchrotron losses⁴ to Lorentz factor γ_c at observing time t given by eq. (11.42). The distribution of energized electrons is approximated by

$$N'_e(\gamma; x) \cong \frac{N_e(x)}{s-1} \gamma_0^{s-1} \begin{cases} \gamma^{-s} & \text{for } \gamma_0 \leq \gamma \leq \gamma_1, \\ \gamma_1^{-s} (\gamma/\gamma_1)^{-(p+1)} & \text{for } \gamma_1 \leq \gamma \leq \gamma_{\text{max}}, \end{cases} \quad (11.59)$$

where $N_e(x) = 4\pi x^3 n_0/3$ is the total number of nonthermal electrons. The regime where the magnetic field is sufficiently weak that electrons do not cool below γ_{min} is referred to as the *slow-cooling limit*. In this regime, $\gamma_0 = \gamma_{\text{min}}$, $\gamma_1 = \gamma_c$, and $s = p$. In the opposite *fast-cooling limit*, electrons cool through synchrotron radiation losses below γ_{min} , in which case $\gamma_0 = \gamma_c$, $\gamma_1 = \gamma_{\text{min}}$, and $s = 2$. The blast wave's radiative efficiency $\varphi = \epsilon_e \epsilon_{\text{rad}}$, where $\epsilon_{\text{rad}} \cong 1$ in the fast-cooling limit, and $\epsilon_{\text{rad}} = (\gamma_{\text{min}}/\gamma_c)^{p-2}$ in the slow-cooling limit.

For the blast-wave geometry, the νF_ν spectrum

$$f_\epsilon \cong \frac{\Gamma^2}{4\pi d_L^2} \left(\frac{4}{3} c\sigma_T U_B \right) \gamma_s^3 N'_e(\gamma_s; x) \quad \text{with } \gamma_s \cong \sqrt{\frac{\epsilon(1+z)B_{\text{cr}}}{\Gamma B}}, \quad (11.60)$$

recalling that $U_B = B^2/8\pi$ is the magnetic-field energy density in the comoving frame. Substitution of eq. (11.59) into eq. (11.60) gives

$$f_\epsilon = \frac{c\sigma_T}{24\pi^2 d_L^2} \frac{B^2 \Gamma^2 N_e(x)}{s-1} \gamma_s^2 \times \begin{cases} (\gamma_s/\gamma_0)^{1-s} & \text{for } \gamma_0 \leq \gamma_s \leq \gamma_1, \\ (\gamma_1/\gamma_0)^{1-s} (\gamma_s/\gamma_1)^{-p} & \text{for } \gamma_1 \leq \gamma_s \leq \gamma_{\text{max}}. \end{cases} \quad (11.61)$$

⁴Cooling due to Compton losses is considered in section 11.5.

The flux density at frequency ν_0 is given by $F_{\nu_0} = f_{\epsilon_0}/\nu_0$. The relation

$$\nu_0 = \frac{m_e c^2 \epsilon_0}{h} = \frac{m_e c^2}{h} \frac{\Gamma B \gamma_0^2}{B_{\text{cr}}(1+z)}$$

implies that

$$F_{\nu_0} = \frac{\Gamma(1+z)m_e c^2 B \sigma_T}{4\pi d_L^2 3e} \frac{N_e(x)}{s-1} = \frac{\Gamma(1+z)}{12\pi d_L^2} \frac{N_e(x)}{s-1} P_{\nu_0}, \tag{11.62}$$

where

$$P_{\nu_0} = \frac{8\pi}{3} \frac{e^3 B}{m_e c^2} = B \frac{m_e c^2 \sigma_T}{e}$$

is the spectral power of a single electron.⁵ For a uniform CBM with density n_0 , eq. (11.62) can be written, using $x \cong 4\Gamma^2 ct/(1+z)$ (eq. [11.24]), as

$$F_{\nu_0} = \frac{32}{9\pi d_L^2} \frac{hc^4 \sigma_T n_0}{m_e c^2 (s-1)} \frac{\Gamma^7 B B_{\text{cr}}}{(1+z)^2} t^3 \cong \frac{1.7}{d_{28}^2} \frac{(\epsilon_B/0.1)^{1/2} n_0^{3/2} (\Gamma/10)^8 t_{\text{day}}^3}{(1+z)^2 (s-1)} \text{Jy}, \tag{11.63}$$

using eq. (11.38). The value of F_{ν_0} does not depend on whether the system is in the fast- or slow-cooling regime, because it depends simply on the number of swept-up electrons that have accumulated at γ_0 ($f_{\epsilon_0} = \nu_0 F_{\nu_0}$ represents the measured synchrotron energy flux from $N_e(x)$ electrons with Lorentz factor $\gamma \approx \gamma_0$).

Because the self-absorbed νF_ν spectrum is proportional to ϵ^3 when $\epsilon < \epsilon_a < \epsilon_0$, the synchrotron νF_ν flux can be approximated by the expression

$$f_\epsilon = \frac{n_0 c \sigma_T}{18\pi d_L^2} \frac{B^2 \Gamma^2 x^3}{s-1} \times \begin{cases} \gamma_0^2 \left(\frac{\epsilon_a}{\epsilon_0}\right)^{4/3} \left(\frac{\epsilon}{\epsilon_a}\right)^3 & \text{for } \epsilon < \epsilon_a, \\ \gamma_0^2 \left(\frac{\epsilon}{\epsilon_0}\right)^{4/3} & \text{for } \epsilon_a < \epsilon < \epsilon_0, \\ \gamma^{3-s} \gamma_0^{s-1} & \text{for } \epsilon_0 < \epsilon < \epsilon_1, \\ \gamma^{2-p} \gamma_1^{1+p-s} \gamma_0^{s-1} & \text{for } \epsilon_1 < \epsilon < \epsilon_2, \end{cases} \tag{11.64}$$

⁵This expression gives accurate spectral results away from the endpoints of a synchrotron spectrum produced by a distribution of electrons. For the synchrotron spectrum from an electron distribution with a low-energy cutoff, the spectral power is actually distributed over $\approx 2\pi$ in frequency space. Thus the spectrum at $\nu \lesssim \nu_0$ should be divided by 2π to account for the spectral range of the synchrotron spectral power.

where $\epsilon = h\nu/m_e c^2 = \Gamma B\gamma^2/B_{\text{cr}}(1+z)$, $\epsilon_i = h\nu_i/m_e c^2 = \Gamma B\gamma_i^2/B_{\text{cr}}(1+z)$, $i = 0, 1, 2$, and $\epsilon_a = h\nu_a/m_e c^2$ is given by eq. (11.53).

The received spectrum, written in terms of flux density and frequencies, takes the form

$$F_\nu = F_{\nu_0} \times \begin{cases} \left(\frac{\nu_a}{\nu_0}\right)^{1/3} \left(\frac{\nu}{\nu_a}\right)^2 & \text{for } \nu < \nu_a, \\ \left(\frac{\nu}{\nu_0}\right)^{1/3} & \text{for } \nu_a < \nu < \nu_0, \\ \left(\frac{\nu}{\nu_0}\right)^{-(s-1)/2} & \text{for } \nu_0 < \nu < \nu_1, \\ \left(\frac{\nu_1}{\nu_0}\right)^{-(s-1)/2} \left(\frac{\nu}{\nu_1}\right)^{-p/2} & \text{for } \nu_1 < \nu < \nu_2, \end{cases} \quad (11.65)$$

with F_{ν_0} given by eq. (11.63).

Recalling eq. (11.30), which gives the temporal dependence of $\Gamma(t)$ and $x(t)$ for general radiative regimes, we find that the temporal and spectral dependence of the synchrotron spectrum in the fast-cooling regime is

$$f_\epsilon^{\text{fc}} \propto \begin{cases} t^{(23-3\varphi)/[3(8-\varphi)]} \epsilon^3 & \text{for } \epsilon < \epsilon_a, \\ t^{(3-11\varphi)/[3(8-\varphi)]} \epsilon^{4/3} & \text{for } \epsilon_a < \epsilon < \epsilon_0, \\ t^{-2(1+\varphi)/(8-\varphi)} \epsilon^{1/2} & \text{for } \epsilon_0 < \epsilon < \epsilon_1, \\ t^{2(2-\varphi-3p)/(8-\varphi)} \epsilon^{(2-p)/2} & \text{for } \epsilon_1 < \epsilon < \epsilon_2. \end{cases} \quad (11.66)$$

In the slow-cooling regime, the temporal and spectral dependence of the νF_ν spectrum is

$$f_\epsilon^{\text{sc}} \propto \begin{cases} t^{(8-3\varphi)/(8-\varphi)} \epsilon^3 & \text{for } \epsilon < \epsilon_a, \\ t^{(4-3\varphi)/(8-\varphi)} \epsilon^{4/3} & \text{for } \epsilon_a < \epsilon < \epsilon_0, \\ t^{3(2-\varphi-2p)/(8-\varphi)} \epsilon^{(3-p)/2} & \text{for } \epsilon_0 < \epsilon < \epsilon_1, \\ t^{2(2-\varphi-3p)/(8-\varphi)} \epsilon^{(2-p)/2} & \text{for } \epsilon_1 < \epsilon < \epsilon_2. \end{cases} \quad (11.67)$$

Figure 11.3 shows the spectral and temporal dependences of the synchrotron emission from a blast wave that decelerates in a uniform CBM. The parameters of the calculation are $E_{52} = n_0 = 1$, $\epsilon_e = \epsilon_B = 0.1$, and $\Gamma_0 = 300$. The time t_0 occurs when the system transitions from the fast-cooling to the slow-cooling regime. It is defined by the condition that $\gamma_c = \gamma_m$, which implies that

$$t_0 = (1+z) \frac{8E_0 n_0}{3\pi m_p c^3} \left(\frac{m_p}{m_e}\right)^4 \left(\frac{\sigma_T \epsilon_B \epsilon_e f(p)}{1+g/3}\right)^2. \quad (11.68)$$

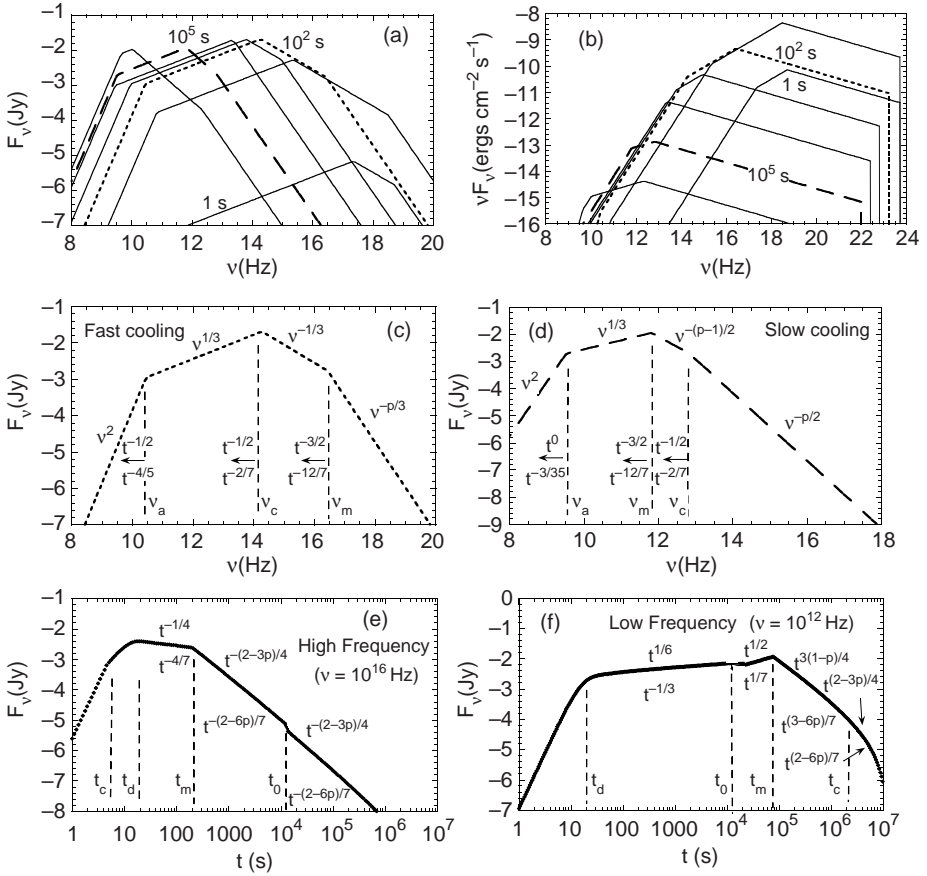


Figure 11.3 Spectral and temporal dependences of the synchrotron emission from a blast wave that decelerates in a uniform surrounding medium. (a) and (b) show the SEDs in F_ν and νF_ν representations, respectively, with SEDs graphed at times from 1 to 10^6 s in factors of 10. (c) and (d) show the SED when the system is in the fast-cooling regime at 100 s, and in the slow-cooling regime at 10^5 s, respectively. The temporal dependences of the characteristic frequencies in the adiabatic and radiative limits are shown by the expressions above and below the arrows, respectively. (e) and (f) show the light curves of the temporal behavior at high (here, at $\nu = 10^{16}$ Hz) and low frequencies (here at $\nu = 10^{12}$ Hz). The temporal dependences of the light curves in the adiabatic and radiative regimes are given above and below the light curves, respectively. After Ref. [325].

Performing the previous analysis for an adiabatic blast wave decelerating in a CBM with a density profile given by $n(x) \propto x^{-s}$ should give spectral differences that could identify a wind medium, as already noted [311–314]. Although a uniform CBM seems to give better agreement with data than a wind CBM in several cases [314], the model uncertainties preclude strong conclusions.

11.3 RELATIVISTIC SHOCK HYDRODYNAMICS

We follow the treatments of Refs. [302,321,322,326] in this section, assuming idealized shock structures. For example, instabilities in the outward-going flow that would lead to a nonuniform blast-wave shell [327] are ignored. Effects of neutron decoupling [328], which occur for sufficiently high Lorentz factor shocks when neutrons decouple from the proton-electron component of the expanding blast-wave shell, are considered in section 11.9.

11.3.1 Relativistic Shock Thermodynamics

Thermodynamic quantities are defined in the comoving fluid frame. We briefly review, without derivation, the equations leading to the strong-shock jump conditions [302]. (For Poynting-flux dominated outflows, see [329].) The structure of a shock is determined by continuity of the particle number $n\beta\Gamma$, energy $w\Gamma^2\beta$, and momentum $w\Gamma^2\beta^2 + p$ fluxes across the shock front. The enthalpy $w = p + e_{\text{tot}}$, where p is the pressure, $e_{\text{tot}} = e_{\text{ke}} + \rho c^2$ is the total energy density, e_{ke} is the kinetic energy density, and $nm c^2 = \rho c^2$ is the particle rest-mass energy density. For a nonrelativistic thermal gas, $e_{\text{ke}} = 3\rho c^2\Theta/2$, where $\Theta = k_B T/m_p c^2$ and T is the fluid temperature. The pressure $p = (\hat{\gamma} - 1)e_{\text{ke}}$, where $\hat{\gamma}$ corresponds to the ratio of specific heats. For a nonrelativistic monatomic ideal gas, $\hat{\gamma} = 5/3$, whereas $\hat{\gamma} = 4/3$ for a relativistic gas. Thus $w = \rho c^2 + \hat{\gamma}e_{\text{ke}}$.

Figure 11.4(a) illustrates the system of a shocked fluid with density n and Lorentz factor Γ encountering a stationary medium with density n_0 . In the strong-shock limit, $p/n \gg p_0/n_0$. This leads to the strong-shock jump condition for the density, given by

$$\frac{n}{n_0} = \frac{\hat{\gamma}\Gamma + 1}{\hat{\gamma} - 1} \rightarrow \begin{cases} 4 + 5\beta^{2/4} \cong 4, & \text{NR } (\Gamma - 1 \ll 1) \\ 4\Gamma + 3, & \text{ER } (\Gamma \gg 1) \end{cases}. \quad (11.69)$$

The asymptotes in the nonrelativistic (NR) and extreme relativistic (ER) limits are given in eq. (11.69).

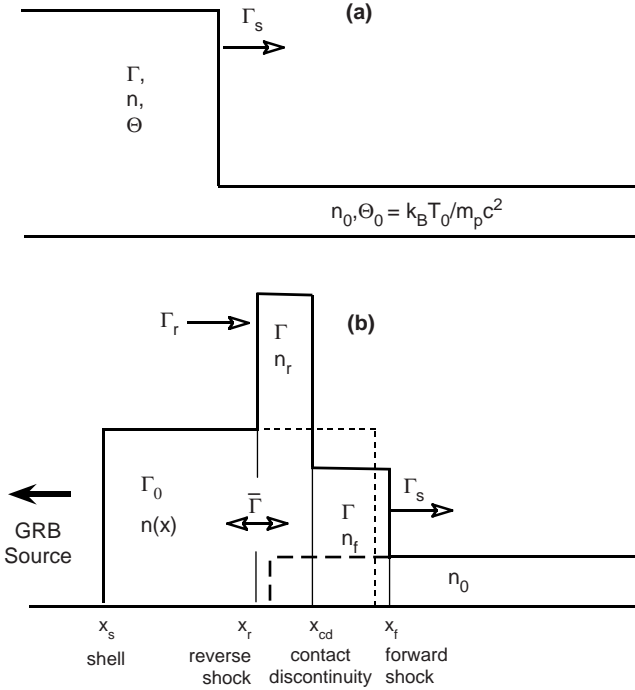


Figure 11.4 Diagrams of the relativistic shock system. (a) Quantities for the basic system consisting of a shocked fluid encountering the stationary external medium. (b) Quantities for the system consisting of the unshocked shell, the reverse and forward shocks, and the stationary external medium.

The strong-shock jump condition for the energy flux takes the form

$$\frac{e_{tot}}{\rho} = \frac{\Gamma w_0}{n_0},$$

implying that

$$\frac{e_{ke}}{\rho c^2} = \Gamma - 1 + \hat{\gamma} \Gamma \left(\frac{e_{ke,0}}{\rho_0 c^2} \right) \rightarrow \begin{cases} \frac{\beta^2}{2} + \frac{5}{2} \Theta_0, & \text{NR,} \\ \Gamma(1 + 2\Theta_0), & \text{ER.} \end{cases} \quad (11.70)$$

Here it is assumed that the unshocked gas is at nonrelativistic temperatures $\theta_0 \ll 1$. This equation affords a very simple interpretation: the kinetic energy density of the shocked fluid is simply equal to the kinetic energy of the swept-up matter plus an additional contribution from the swept-up internal energy.

A third jump condition relates the Lorentz factor Γ of the shocked fluid to the Lorentz factor Γ_{sh} of the shock itself, and is given by

$$\Gamma_{\text{sh}}^2 = \frac{(\Gamma + 1)[\hat{\gamma}(\Gamma - 1) + 1]^2}{\hat{\gamma}(2 - \hat{\gamma})(\Gamma - 1) + 2} \Rightarrow \begin{cases} \beta_{\text{sh}} = \frac{4}{3}\beta, & \text{NR, } \hat{\gamma} = \frac{5}{3}, \\ \Gamma_{\text{sh}} = \sqrt{2}\Gamma, & \text{ER, } \hat{\gamma} = \frac{4}{3}. \end{cases} \quad (11.71)$$

Note that the shock must travel faster than the shocked fluid because of the matter that is accumulated as the shock propagates.

Figure 11.4(b) illustrates the idealized structure of a relativistically expanding shell of matter that encounters a stationary external medium. The shock structure takes the form of a forward shock that accelerates the stationary CBM and a reverse shock that decelerates and gives internal energy to the plasma in the cold relativistic shell. The fluids shocked by the reverse and forward shocks, separated by a contact discontinuity, have the same Lorentz factor Γ and kinetic energy densities. The reverse shock persists until it traverses the shell of width Δ , after which time no further energization is provided by the reverse shock. The shocked fluid is then hydrodynamically connected in the sense that the material can be treated as a causally connected shell whose Lorentz factor evolves according to bulk equations for momentum and energy conservation derived earlier in this chapter.

The notation shown in figure 11.4(b) generalizes the figure 11.4(a) case to include the shock-jump conditions operating at both the forward and reverse shocks. In the coasting phase, the Lorentz factor of the unshocked shell material is Γ_0 , and its density is

$$n(x) = \frac{E_0}{4\pi x^2 \Gamma_0^2 m_p c^2 \Delta(x)}, \quad (11.72)$$

assuming a thin ($\Delta \ll x$), constant width shell. The temperature Θ_{sh} of the unshocked shell material resulting from the GRB explosion is likely to be very small due to the strong adiabatic cooling during the expansion phase, so that $\Theta_{\text{sh}} \ll 1$. In this treatment, we also assume that the temperature of the surrounding medium is also small ($\Theta_0 \ll 1$), and that the blast wave is relativistic ($\Gamma_0 \gg 1$).

The term $\bar{\Gamma}$ is the relative Lorentz factor of the reverse shocked fluid as it encounters the material of the unshocked shell. From figure 11.4(b), we see that

$$\bar{\Gamma} = \Gamma\Gamma_0(1 - \beta\beta_0) \cong \frac{1}{2} \left(\frac{\Gamma}{\Gamma_0} + \frac{\Gamma_0}{\Gamma} \right), \quad (11.73)$$

where the last relation applies in the regime $\Gamma_0, \Gamma \gg 1$ considered here.

When $\Gamma \gg 1$, the shocked fluid behind the forward shock is relativistic, and the density of the forward-shocked fluid is $n_f = (4\Gamma + 3)n_0 \cong 4\Gamma n_0$. The density of the fluid shocked by the reverse shock is $n_r \cong 4\bar{\Gamma}n(x)$, noting from eq. (11.69) that these expressions are not accurate for mildly relativistic reverse shocks. The equality of kinetic-energy densities at the contact discontinuity implies, for fluids made primarily of proton-electron plasma, that

$$\frac{e_{ke}}{m_p c^2} \cong n_f(\Gamma - 1) \cong n_r(\bar{\Gamma} - 1) \cong 4n_0\Gamma^2 \cong 4n(x)(\bar{\Gamma}^2 - \bar{\Gamma}). \quad (11.74)$$

The relativistic shock jump conditions for an isotropic explosion in a uniform CBM therefore imply [322]

$$\frac{n(x)}{n_0} \equiv F = \frac{E_0}{4\pi x^2 \Gamma_0^2 n_0 m_p c^2 \Delta} = \frac{\ell_S^3}{3x^2 \Gamma_0^2 \Delta} = \frac{\Gamma^2}{\bar{\Gamma}^2 - \bar{\Gamma}} \rightarrow \begin{cases} 2\Gamma^2/\bar{\beta}^2, & \text{NRS,} \\ \Gamma^2/\bar{\Gamma}^2, & \text{RRS,} \end{cases} \quad (11.75)$$

where $\bar{\beta} = \sqrt{1 - 1/\bar{\Gamma}^2}$. Because $n(x)/n_0 \propto 1/x^2$, the quantity $\bar{\Gamma}^2 - \bar{\Gamma}$ and the reverse shock speed $c\bar{\beta}(x)$ increases with x , at least when $x \lesssim x_d$ and $\Gamma \cong \Gamma_0$.

The transition from a NRS to a RRS occurs when $F(x_{NR}) \cong \Gamma_0^2$, or when

$$x_{NR} = \frac{\ell_S^{3/2}}{\Gamma_0^2 \Delta^{1/2}} \equiv \xi x_d, \quad (11.76)$$

where

$$\xi \equiv \frac{\ell_S^{1/2}}{\Gamma_0^{4/3} \Delta^{1/2}} = \frac{x_d^{1/2}}{\Gamma_0 \Delta^{1/2}} \cong \frac{54}{\Delta_8^{1/2} \Gamma_{300}^{4/3}} \left(\frac{E_{52}}{n_0} \right)^{1/6}, \quad (11.77)$$

defining the blast-wave width $\Delta = 10^8 \Delta_8$ cm. For $x \ll x_{NR}$, $\Gamma \cong \Gamma_0$, and the reverse shock β -factor at location x is

$$\bar{\beta}(x) = \frac{\sqrt{2}x}{x_{NR}} = \frac{\sqrt{2}\Gamma_0^2 \Delta^{1/2}}{\ell_S^{3/2}} x, \quad (11.78)$$

from eq. (11.75). A NRS crosses the shell at $\Delta'/\bar{\beta}(x_\Delta)c = \Gamma_0 \Delta/\bar{\beta}(x_\Delta)c \cong x_\Delta/\Gamma_0 c$, implying that

$$x_\Delta \equiv \Delta^{1/4} \ell_S^{3/4} = \xi^{-1/2} x_d, \quad (11.79)$$

dropping numerical factors of order unity. The reverse shock will remain nonrelativistic if it crosses the shell before it reaches relativistic speeds, that is, if $x_\Delta < x_{NR}$, which implies that

$$\xi \gg 1 \quad \text{for a NRS.}$$

A GRB blast wave expanding in a uniform surrounding medium will be in the NRS regime for the standard parameters used in eq. (11.77), which are appropriate to an impulsive explosion. If the shell width is \sim lt-seconds or more, then the blast wave may have a RRS.

For a NRS, $\bar{\beta} \ll 1$, $F \gg 4\Gamma_0^2$, and

$$\bar{\beta} \cong \Gamma_0 \sqrt{\frac{2}{F}}, \quad \bar{\Gamma} = \frac{1}{\sqrt{1 - \bar{\beta}^2}}, \quad \Gamma \cong \frac{\Gamma_0}{(1 + \bar{\beta})}. \quad (11.80)$$

For a RRS, $F \ll 4\Gamma_0^2$, $\bar{\Gamma} \gg 1$ and $\bar{\beta} \rightarrow 1$, the shock jump conditions imply $F \cong \Gamma^2/\bar{\Gamma}^2$, so that $\bar{\Gamma} = \Gamma/\sqrt{F} = \frac{1}{2}(\Gamma/\Gamma_0 + \Gamma_0/\Gamma)$, from eq. (11.73). This can be solved to give

$$\Gamma = \frac{\Gamma_0 F^{1/4}}{\sqrt{2\Gamma_0 - F^{1/2}}} \cong \left(\frac{\Gamma_0}{2}\right)^{1/2} F^{1/4} \propto x^{-1/2}. \quad (11.81)$$

The second expression is valid when $F^{1/2} \lesssim 2\Gamma_0$ or $x \gtrsim x_{\text{NR}}$, and the last two expressions hold when $x \gg x_{\text{NR}}$. The relativistic reverse shock crosses the shell when $\Delta'/c \cong x_\Delta/\Gamma c$, or $x_\Delta \cong \Gamma^2 \Delta \cong \Gamma_0 F^{1/2} \Delta/2 = \ell_S^{3/2} \Delta^{1/2}/2x_\Delta$, from which eq. (11.79) is again recovered for the RRS case. After the reverse shock crosses the shell, the shocked shell follows the self-similar Sedov behavior given by (11.18). From eq. (11.81), we see for the RRS case,

$$\bar{\Gamma} \xrightarrow{x_{\text{NR}} < x < x_\Delta} \frac{\Gamma_0 F^{-1/4}}{\sqrt{2\Gamma_0 - F^{1/2}}} \xrightarrow{x_{\text{NR}} \ll x < x_\Delta} \sqrt{\frac{\Gamma_0}{2}} F^{-1/4} \propto x^{1/2},$$

and $\bar{\beta} \cong 1$. Figure 11.5 illustrates the values of Γ and $\bar{\Gamma}$ as a function of F with approximations in various asymptotes.

Definition (11.77) for the spreading radius $x_{\text{spr}} = \Gamma_0^2 \Delta = \xi^{-2} x_d$ implies the ordering

$$\xi^2 x_{\text{spr}} = \xi^{1/2} x_\Delta = x_d = \xi^{-1} x_{\text{NR}}. \quad (11.82)$$

In the NRS case, $\xi \gg 1$, and $x_{\text{spr}} < x_\Delta < x_d < x_{\text{NR}}$, that is, the reverse shock crosses the shell after the shell begins to spread but before the shell begins to decelerate. The evolution of an adiabatic Lorentz factor is described by eq. (11.18) in this case, so that the synchrotron emission as described in the previous sections applies to the NRS case. In the RRS case, $\xi \ll 1$ and the order of the characteristic radii is reversed. Thus $x_{\text{NR}} < x_d < x_\Delta < x_{\text{spr}}$, namely, the reverse shock becomes relativistic before the shell, if treated as a connected hydrodynamic fluid, begins to decelerate. At larger radii and

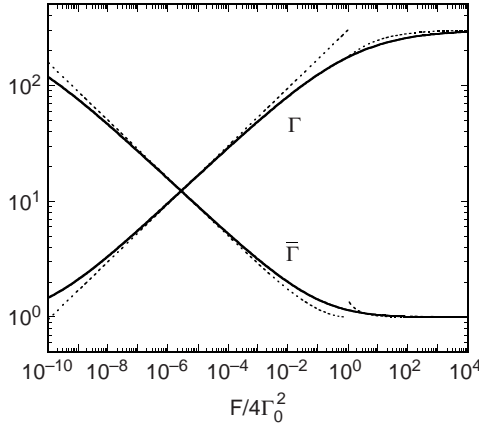


Figure 11.5 Lorentz factor Γ of the shocked fluid in the explosion frame, and Lorentz factor $\bar{\Gamma}$ of the unshocked shell material in the rest frame of the shocked fluid, as a function of $F/4\Gamma_0^2$ when $\Gamma_0 = 300$. Solid curves give numerical solution to eq. (11.75), and dotted curves show approximations given in eqs. (11.80) and (11.81).

later times, the reverse shock crosses the shell and the entire shell begins to uniformly decelerate.

The reverse shock power is $dE'/dt'|_{RS} = A(x)n(x)m_p c^3 \bar{\beta}(\bar{\Gamma}^2 - \bar{\Gamma})$. Comparing with eq. (11.31) and using the shock jump condition (11.75) gives the result that $(dE'/dt'|_{RS})/(dE'/dt'|_{FS}) = \bar{\beta}$, so that roughly equal power is dissipated as internal energy in the forward and reverse shock during the RRS phase. The fraction of power dissipated by the reverse shock is a fraction $\bar{\beta}$ of the forward-shock power in the NRS phase, but this phase lasts only until the blast wave reaches $x = x_\Delta < x_d$; moreover, the shock is nonrelativistic, which reduces the particle acceleration efficiency.

We summarize the results of this section by restating and generalizing the equations for the adiabatic evolution of the relativistic blast wave Lorentz factor $\Gamma (\gg 1)$ and the reverse shock Lorentz factor $\bar{\Gamma}$ in a uniform surrounding medium, neglecting neutron decoupling. In the NRS case,

$$\Gamma(x) \cong \begin{cases} x/\Delta_0 & \text{for } \Delta_0 < x \lesssim \Gamma_0 \Delta_0, \\ \Gamma_0 & \text{for } \Gamma_0 \Delta_0 \lesssim x \lesssim x_d, \\ \Gamma_0 (x/x_d)^{-3/2} & \text{for } x_d \lesssim x \ll \ell_s, \end{cases} \quad (11.83)$$

and $\bar{\Gamma} \cong 1, \bar{\beta} \simeq x/x_{NR} \ll 1$ for $x < x_\Delta$.

In the RRS case,

$$\Gamma(x) \cong \begin{cases} x/\Delta_0 & \text{for } \Delta_0 < x \lesssim \Gamma_0 \Delta_0, \\ \Gamma_0 & \text{for } \Gamma_0 \Delta_0 \lesssim x \lesssim x_{\text{NR}}, \\ \frac{\Gamma_0 f^{1/4}}{\sqrt{2\Gamma_0 - f^{1/2}}} \simeq \sqrt{\frac{\Gamma_0}{2}} f^{1/4} \propto x^{-1/2} & \text{for } x_{\text{NR}} \lesssim x \lesssim x_\Delta, \\ \Gamma_0 (x/x_d)^{-3/2} & \text{for } x_\Delta \lesssim x \ll \ell_S, \end{cases} \quad (11.84)$$

The reverse shock Lorentz factor is given through the expression

$$\bar{\beta}(x)\bar{\Gamma}(x) \cong \begin{cases} \sqrt{2} \frac{\Gamma_0^2 \Delta^{1/2}}{\ell_S^{3/2}} x \cong \frac{x}{x_{\text{NR}}} & \text{for } x \lesssim x_{\text{NR}}, \\ \frac{\Gamma_0 f^{-1/4}}{\sqrt{2\Gamma_0 - f^{1/2}}} \simeq \sqrt{\frac{\Gamma_0}{2}} f^{-1/4} \propto x^{1/2} & \text{for } x_{\text{NR}} \lesssim x \lesssim x_\Delta. \end{cases} \quad (11.85)$$

Figure 11.6 illustrates the generic behavior of Γ and $\bar{\Gamma}$ in the NRS and RRS cases.

11.3.2 Synchrotron Radiation from a Relativistic Reverse Shock

The observing time t and location x of a blast wave with a RRS and shocked fluid Lorentz factor given by eq. (11.84) are related according to the expression

$$t \cong \frac{1+z}{c} \begin{cases} \Delta_0(1 - \Delta_0/x) & \text{for } \Delta_0 \lesssim x \lesssim \Gamma_0 \Delta_0 \\ & \text{(expanding),} \\ x/\Gamma_0^2 + \Delta_0 & \text{for } \Gamma_0 \Delta_0 \lesssim x \lesssim x_{\text{NR}} \\ & \text{(coasting),} \\ \frac{\Delta^{1/2}}{\ell_S^{3/2}} (x^2 - x_{\text{NR}}^2) - \frac{(x - x_{\text{NR}})}{\Gamma_0^2} + \frac{x_{\text{NR}}}{\Gamma_0^2} & \text{for } x_{\text{NR}} \lesssim x \lesssim x_\Delta \\ & \text{(RRS),} \\ \left(\frac{1}{4\Gamma_0^2 x_d^3} (x^4 - x_\Delta^4) + \frac{\Delta^{1/2} x_\Delta^2}{\ell_S^{3/2}} \right), & \text{for } x_\Delta \lesssim x \lesssim \ell_S \\ & \text{(RSdv).} \end{cases} \quad (11.86)$$

The measured period of activity of the central engine is just $t \sim (1+z)\Delta_0/c$, corresponding to the duration of the explosion and generation of the relativistic wind. The relations between times and locations in the coasting

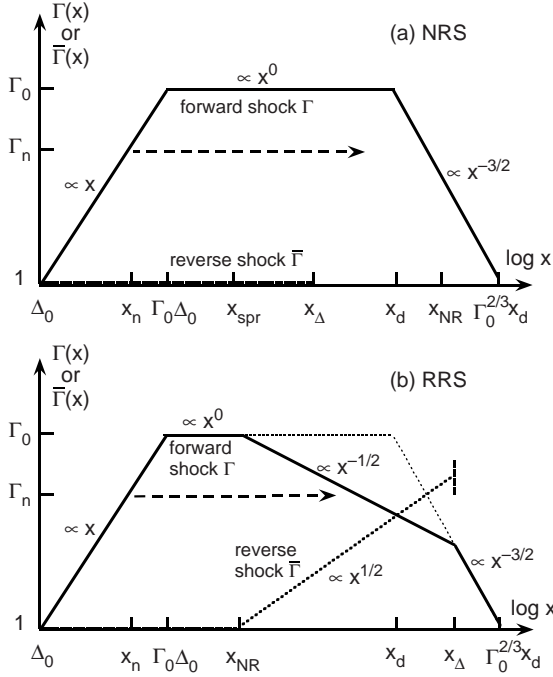


Figure 11.6 Diagrams illustrating the generic behavior of the forward and reverse shocks in the nonrelativistic reverse shock (NRS) case (a) when the reverse shock crosses the shell before it becomes relativistic, and in the relativistic reverse shock (RRS) case (b) when the reverse shock becomes relativistic before crossing the shell. In the NRS case, $\xi \gg 1$, and in the RRS case $\xi \gg 1$, where ξ is defined by eq. (11.77). The dashed line with the arrow indicates a possible decoupling of the neutrons from the expanding fluid.

and relativistic Sedov phases have the same dependences as for the NRS case given by eq. (11.19). In the RRS phase where $x_{NR} \ll x \lesssim x_\Delta$, $x \propto t^{1/2}$ and $\Gamma \propto t^{-1/4}$. We call this regime the asymptotic RRS regime.

The principal dependences of $x(t)$, $\Gamma(t)$, and $\bar{\beta}(t)\bar{\Gamma}(t)$ are given, in the various regimes, by

$$x(t) \propto \begin{cases} \frac{c\Gamma_0^2}{1+z} t \propto t, & t \ll t_{NR} \text{ (coasting)}, \\ \sqrt{\frac{c\ell_S^{3/2} t}{(1+z)\Delta^{1/2}}} \propto t^{1/2}, & t_{NR} \ll t \ll t_\Delta \text{ (asymptotic RRS)}, \\ \left(\frac{4c\Gamma_0^2 x_d^3 t}{1+z}\right)^{1/4} \propto t^{1/4}, & t_\Delta \ll t \ll (1+z)\ell_S/c \text{ (RSdv)}, \end{cases} \quad (11.87)$$

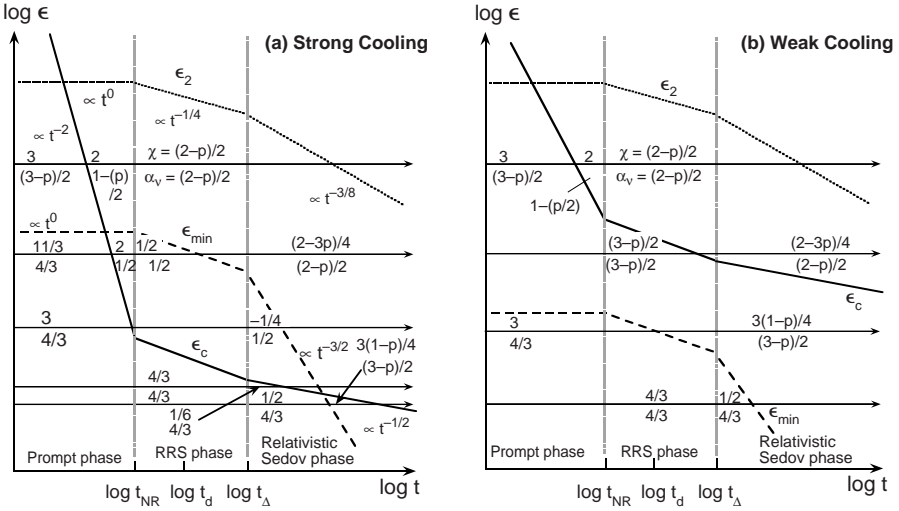


Figure 11.7 Diagram giving temporal indices χ and νF_ν , spectral indices α_ν for a blast wave decelerating in a surrounding uniform medium in (a) strong-cooling and (b) weak-cooling regimes.

$$\Gamma(t) \propto \begin{cases} \text{const,} & \text{coasting,} \\ t^{-1/4}, & \text{asymptotic RRS,} \\ t^{-3/8}, & \text{RSdv,} \end{cases} \quad (11.88)$$

and

$$\bar{\beta}(x)\bar{\Gamma}(x) \propto \begin{cases} x \propto t, & \text{coasting,} \\ x^{1/2} \propto t^{1/4}, & \text{asymptotic RRS.} \end{cases} \quad (11.89)$$

The spectral and temporal indices for a blast wave with a RRS expanding in a uniform CBM are shown in figure 11.7.

11.4 BEAMING BREAKS AND JETS

An observer will receive most emission from those portions of a GRB blast wave that are within an angle $\sim 1/\Gamma$ to the direction to the observer. As the blast wave decelerates by sweeping up material from the CBM, a break in the light curve will occur when the jet opening half angle θ_j becomes smaller than $1/\Gamma$. This is due to a change from a spherical blast-wave geometry, given by eqs. (5.70) and (11.60), to a geometry defined by a localized emission region, as given by eq. (5.71). Assuming that the blast wave decelerates adiabatically in a uniform surrounding medium, the condition

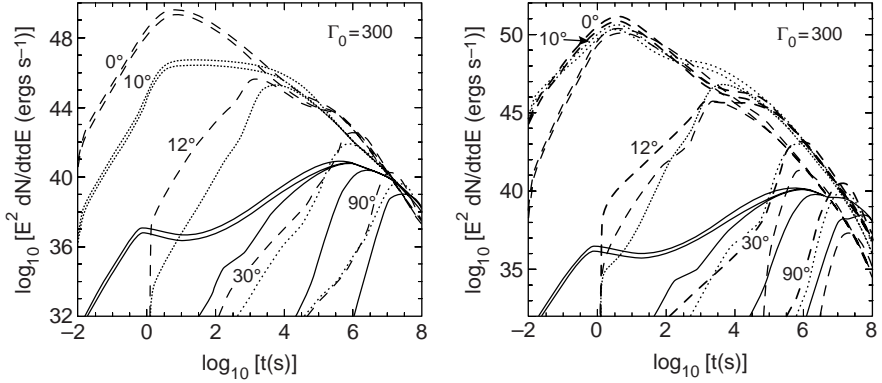


Figure 11.8 Light curves calculated at various observing energies and inclination angles θ for a GRB with a standard parameter set (see text) and opening half-angle $\theta_j = 10^\circ$ of the jet [331]. The initial blast wave Lorentz factor $\Gamma_0 = 300$. Calculations of $\theta = 0^\circ, 10^\circ, 12^\circ, 30^\circ,$ and 90° are shown, with the brighter peak fluxes reached by curves progressively closer to the jet axis. (a) *Left*: Light curves at 8.6 GHz radio (solid curves), V-band optical (dotted), and 3 keV X-ray (dashed) are plotted. The X-ray curves have the angles labeled. (b) *Right*: Light curves at 4.8 GHz radio (solid curves), MeV (dot-dashed), GeV (dotted), and TeV (dashed) are plotted. The MeV curves have the angles labeled.

$\theta_j \cong 1/\Gamma = \Gamma_0^{-1}(x_{\text{br}}/x_d)^{3/2} = \Gamma_0^{-1}(t_{\text{br}}/t_d)^{3/8}$ implies

$$t_{\text{br}} \approx 45(1+z) \left(\frac{E_{52}}{n_0} \right)^{1/3} \theta_j^{8/3} \text{ days}, \quad (11.90)$$

from which the jet angle

$$\theta_j \approx 0.1 \left[\frac{t_{\text{br}}(\text{d})}{1+z} \right]^{3/8} \left(\frac{n_0}{E_{52}} \right)^{1/8} \quad (11.91)$$

can be derived [330]. Note that the beaming angle is only weakly dependent on n_0 and E_0 .

Figure 11.8 shows calculations of a GRB blast wave in a beamed geometry [331] with $\theta_j = 10^\circ$ at different observing angles and energies. The jet emission is assumed to be uniform across its surface and not to spread laterally (see [332] when this is not the case). For the standard parameters used here ($E_{52} = 100$, $\epsilon_B = 10^{-4}$, $\epsilon_e = 0.5$, $n_0 = 100 \text{ cm}^{-3}$, $p = 2.5$), the beaming break occurs at $\sim 10^5$ s, but is obscured at X-ray and optical frequencies by the appearance of an SSC component. The appearance of clearly defined breaks in the light curves of some GRBs, if due to beaming rather than to a variation in the density of the surrounding medium, limits

the ratio ϵ_e/ϵ_B that defines the strength of the SSC component. So-called “orphan” afterglows, which are those GRBs with jets pointed away from our line of sight that become visible upon deceleration of the blast wave, are quite similar in spectral evolution to heavily baryon-loaded, “dirty” fireballs [331,333].

Afterglow modeling of multiwavelength spectra of GRB 980703, GRB 990123, GRB 9905010, and GRB 991216 [314] shows that the blast-wave model predictions are more simply explained with a uniform surrounding CBM than a wind profile ($n(r) \propto r^{-2}$). They derive magnetic field parameters in the range $10^{-4} \lesssim \epsilon_B \lesssim 0.05$ and electron energy-transfer parameters in the range $0.01 \lesssim \epsilon_e \lesssim 0.1$, and obtain low-density surroundings ($\sim 10^{-4} \lesssim n_0 \lesssim 10 \text{ cm}^{-3}$) in their fits. The jet angles θ_j range from 1° to 4° . The beaming factor for a one-sided jet is $\approx 1.3 \times 10^4 [\theta(^{\circ})]^{-2}$, so that many misaligned GRBs sources should exist for every detected GRB.

11.5 SYNCHROTRON SELF-COMPTON RADIATION

Electrons cool in the comoving fluid frame by synchrotron and Compton losses. The Compton y -parameter [310]

$$y_C \equiv \frac{L_C}{L_{\text{syn}}} \cong \frac{U_{\text{syn}}}{U_B}, \quad (11.92)$$

gives the ratio of the (synchrotron-self) Compton and synchrotron powers, and the final expression holds for scattering in the Thomson regime. Primes are omitted.

The total internal energy $U = U_e + U_p + U_B + U_{\text{ph}}$ in the shocked fluid shell is found in the form of nonthermal electron and protons/ions, magnetic field, and photons. The electron energy $U_e = \epsilon_e U$, and the magnetic field energy $U_B = \epsilon_B U$. The photon energy

$$U_{\text{ph}} = U_{\text{syn}} + U_C = \eta_e \epsilon_e U = \frac{\eta_e \epsilon_e U_B}{\epsilon_B}, \quad (11.93)$$

and η_e is the radiative efficiency to convert nonthermal electron energy into radiation. In the fast cooling regime, $\gamma_c < \gamma_{\text{min}}$, and $\eta_e \cong 1$. In the slow-cooling regime, only electrons with $\gamma > \gamma_c$ cool efficiently. The fractional energy in electrons that stongly cool is $\sim (\gamma_{\text{min}}/\gamma_c)^{p-2}$, so

$$\eta_e = \min \left[1, \left(\frac{\gamma_{\text{min}}}{\gamma_c} \right)^{p-2} \right]. \quad (11.94)$$

Dividing eq. (11.93) by U_B gives

$$\frac{U_{\text{syn}}}{U_B} + \frac{U_C}{U_{\text{syn}}} \frac{U_{\text{syn}}}{U_B} = y_C + y_C^2 = \frac{\eta_e \epsilon_e}{\epsilon_B}, \quad (11.95)$$

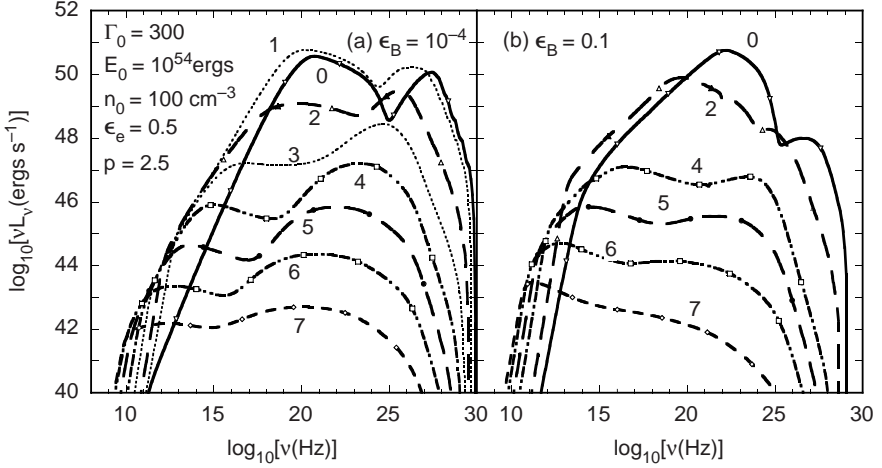


Figure 11.9 Numerical calculation of the synchrotron and SSC emission SEDs from a blast wave with a strong forward shock that decelerates in a uniform surrounding medium. SEDs are labeled by the base 10 logarithm of the observing time in seconds. The left (a) and right (b) panels use $\epsilon_B = 10^{-4}$ and 0.1, respectively.

with solution

$$\gamma_C \equiv \frac{L_C}{L_{\text{syn}}} = \frac{-1 + \sqrt{1 + 4\eta_e \epsilon_e / \epsilon_B}}{2} \rightarrow \begin{cases} \eta_e \epsilon_e / \epsilon_B, & \eta_e \epsilon_e / \epsilon_B \ll 1, \\ \sqrt{\eta_e \epsilon_e / \epsilon_B}, & \eta_e \epsilon_e / \epsilon_B \gg 1. \end{cases} \quad (11.96)$$

The inclusion of a Compton component in blast-wave afterglow modeling can be used to derive analytic [334] and numerical [310,331] spectra and light curves. A standard approximation to treat the Compton component analytically is to use the Thomson cross section truncated for scattering in the Klein-Nishina regime. A numerical simulation [315,331] of the evolving leptonic synchrotron and SSC emission is shown in the external shock model blast-wave calculation of figure 11.9. The parameters of the calculation are given in the figure legend, with injection index $p = 2.5$, $\epsilon_e = 0.5$, and apparent isotropic energy release $E_0 = 10^{54}$ ergs. The blast wave is assumed to form a strong forward shock, and reverse shock emission is not calculated. Internal $\gamma\gamma$ opacity was considered in this calculation. The only difference between the two calculations is the value of $\epsilon_B = 10^{-4}$ and 0.1 in the left and right panels, respectively. The different magnetic field parameters strongly affect the SEDs, with weak cooling in figure 11.9(a) and strong cooling in figure 11.9(b). The relative powers in the synchrotron

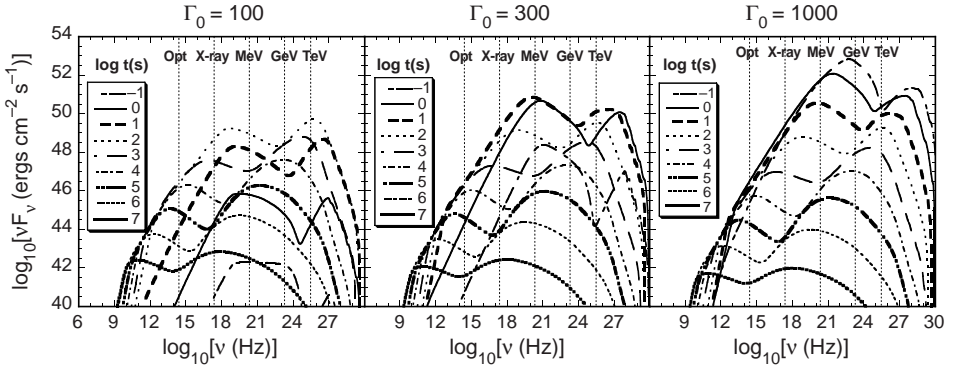


Figure 11.10 Sequence of calculations for GRBs with initial Lorentz factor $\Gamma_0 = 100$ (left), 300 (center), and 1000 (right), using other parameters as in the previous figure, with $\epsilon_B = 10^{-4}$.

and Compton components are inversely proportional to the ϵ_B parameter, in accord with the general trend indicated in eq. (11.96).

As can be seen, external shock emission from a relativistic blast wave is in principle capable of making multi-TeV emission from GRBs. This is also shown in figure 11.10, which shows an external shock relativistic blast-wave model calculation for a standard GRB explosion with different values of Γ_0 . The different baryon-loading parameters could explain different types of GRBs [335], for example, the X-ray flashes. Depending on the redshift of the source, intervening EBL absorption would make it more difficult to detect high-energy γ -ray emission, as considered in the previous chapter.

11.6 THEORY OF THE PROMPT PHASE

The prompt phase of long-duration GRBs, when they are most luminous, lasts from seconds to minutes at ~ 100 keV–MeV energies, as long as 90 minutes at $\gtrsim 100$ MeV energies, and up to $\sim 10^5$ after the start of a burst for keV X-ray flares found with Swift [336]. Within the theoretical blast-wave framework as developed, a central problem concerns the nature of the prompt radiation. In the internal shock model, an active central engine ejects waves of relativistic plasma that overtake and collide to form shocks [337]. The shocks accelerate nonthermal particles that radiate high-energy photons [338]. By contrast, in the external shock model, a single relativistic wave of particles interacts with inhomogeneities in the surrounding medium to accelerate particles that radiate the prompt γ rays.

Some canonical features found in the variable prompt and early afterglow X-ray emission of long-duration GRBs is sketched in figure 11.11 from

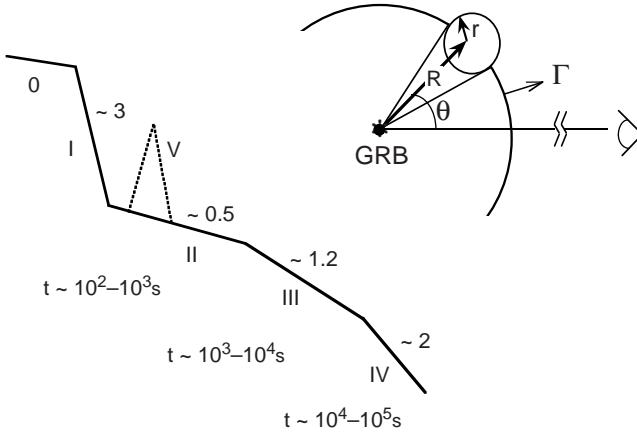


Figure 11.11 Left: Diagram of a generic long-duration GRB light curve at ~ 1 keV, from Swift observations [339,340]. The temporal decay indices α in the form $F_\nu \propto t^{-\alpha} \nu^{-\beta}$ are listed for the prompt phase (0), decay phase (I), plateau phase (II), afterglow phase (III), and jet break phase (IV). X-ray flares (V), seen usually in the early afterglow, are seen as late as $\sim 10^5$ s after a GRB trigger. Right: Sketch of blast-wave/cloud interaction.

Swift observations. A plausible theory of GRB emission must explain these characteristic behaviors.

11.6.1 X-Ray Flares and γ -Ray Pulses from External Shocks

Because the characteristic deceleration time scale, eq. (11.4), is comparable to the typical duration of the long, soft GRBs, of a few tens of seconds, then smooth peaked GRBs can be explained in an external shock model. It is interesting to explore the requirement that external shocks make prompt phase emission, as the answer to this question determines allowed pathways for black-hole formation in a GRB.

As we have seen in section 5.5, if a spherical relativistic shell moving outward with Lorentz factor $\Gamma_0 \gg 1$ is instantaneously illuminated at radius R over the Doppler cone on angular scales $\theta \gtrsim 1/\Gamma_0$ with respect to the line of sight to the observer, then a characteristic emission profile is formed with mean duration $t_{\text{FWHM}} \gtrsim 0.2R/\Gamma_0^2 c$, due to light-travel time delays from different portions of the surface of the shell.

For a single relativistic shell moving to larger radii, successive instantaneous illuminations would form pulses with successively larger durations, contrary to observations, that is, unless the condition of local spherical symmetry was broken on size scales $\ll R/\Gamma_0$ [61]. Interactions of the

blast-wave shell with density inhomogeneities (“clouds”) will break the local spherical symmetry condition [341]. For $\Gamma_0 \approx 300$, comparison with GRB pulse properties implied that density inhomogeneities located $\approx 10^{16}$ cm from the sites of GRBs with sizes $\approx 10^{12}$ – 10^{13} cm are required to make rapidly variable light curves. The duration of the pulse is limited by two basic timescales, the radial and angular timescales.

Radial Timescale

Consider a blast wave intercepting a cloud with size $r \ll R/\Gamma_0$ that is located at an angle θ with respect to the line of sight to the observer. The duration of the received pulse of radiation depends on the light travel-time delays from different portions of the blast wave as it interacts with the cloud. Photons emitted when the blast wave passes through the near and far sides of the cloud are received over a *radial* timescale

$$t_r = \frac{2r}{\beta_0 \Gamma_0 \delta_{\text{DC}}} \cong \frac{r}{\Gamma_0^2 c}. \quad (11.97)$$

The radial timescale varies by a factor ≈ 2 , depending on whether the cloud is located on axis or at an angle $\theta \cong 1/\Gamma_0$ off the observer’s line of sight.

Angular Timescale

Photons emitted from points defining the greatest angular extent of the cloud are received over an *angular* timescale

$$t_{\text{ang}} \cong \frac{r\theta}{c}. \quad (11.98)$$

Note that if $r \rightarrow R/\Gamma_0$ and $\theta \rightarrow 1/\Gamma_0$, then $t_{\text{ang}} \rightarrow R/\Gamma_0^2 c$, as expected. When $\theta \approx 1/\Gamma_0$, $t_{\text{ang}} \approx \Gamma_0 t_r \gg t_r$. Except for those few clouds with $\theta \lesssim 1/\Gamma_0^2$ lying almost exactly along the line of sight to the observer, $t_{\text{ang}} \gg t_r$.

Short-Timescale Variability

Sari and Piran [342] argue that a highly variable light curve is only possible in an external shock model if the radiative efficiency is very low. They define a variability index \mathcal{V} , roughly corresponding to the number of distinct pulses in a GRB light curve, given by $\mathcal{V} = t/\Delta t$, where t is the GRB duration and Δt is a typical pulse width. A highly variable GRB can have $\mathcal{V} \gg 100$. The efficiency η_{eff} to extract energy from a GRB blast wave is given by the ratio of the total area $A_c \cong N_c \pi r^2 \approx \mathcal{V} \pi r^2$ subtended by the N_c clouds within the Doppler beaming cone $\theta \lesssim 1/\Gamma_0$, to the area $A_{\text{bw}} = \pi R^2/\Gamma_0^2$ of the blast wave within the Doppler beaming cone. Thus $\eta_{\text{eff}} = \mathcal{V} \pi r^2 / (\pi R^2/\Gamma_0^2)$.

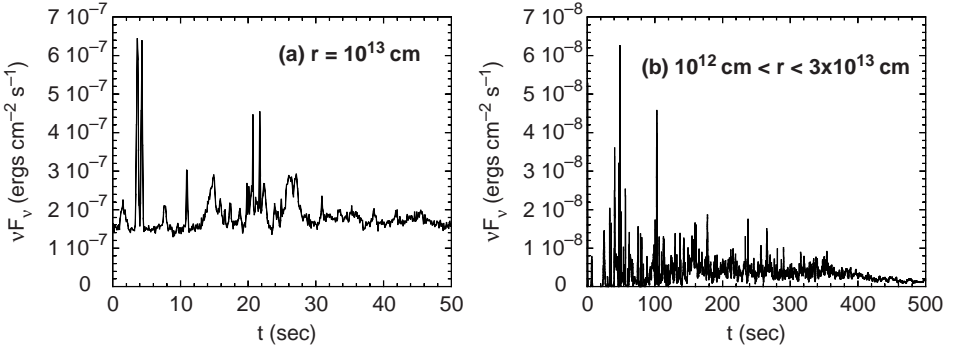


Figure 11.12 Model GRB light curves formed through external shocks with clouds in the circumburst medium. (a) All clouds have radii $r = 10^{13}$ cm. (b) Clouds are chosen with equal partial covering factor per logarithmic interval in cloud size between 10^{12} and 3×10^{13} cm.

They then argue that $\eta_{\text{eff}} \lesssim 1/4\mathcal{V} \ll 1$, so that a highly variable light curve with $\mathcal{V} \gg 1$ must be very inefficient. This expression makes use of the relation $\mathcal{V} < (R/\Gamma_0)/2r$, which follows by assuming that the characteristic duration of a GRB is $t \approx t_{\text{dur}} \approx R/\Gamma_0^2 c$, and that the variability timescale $\Delta t \approx t_{\text{ang}} \approx r/\Gamma_0 c$. This last approximation makes use of an expression for t_{ang} (see eq. [11.98]) that is correct only at $\theta \approx 1/\Gamma_0$. Clouds located at angles $\theta \ll 1/\Gamma_0$ with respect to the line of sight make a disproportionate contribution to the variability of GRB light curves because t_{ang} becomes small and therefore the peak flux of a pulse becomes large for such clouds [341]. The peak pulse flux

$$\phi_{\text{pk}} \propto \frac{\delta_{\text{D}}^{3+\alpha}}{\max(t_r, t_{\text{ang}})} \rightarrow \frac{c\delta_{\text{D}}^{3+\alpha}}{r\theta}, \quad (11.99)$$

where α is the energy spectral index, and the last expression holds for clouds with $\theta \gtrsim 1/\Gamma_0^2$. Here we have used a beaming factor appropriate to isotropic synchrotron radiation in the comoving frame. Specifically,

$$\frac{\phi_{\text{pk}}(\theta = 1/10\Gamma_0)}{\phi_{\text{pk}}(\theta = 1/\Gamma_0)} \cong 10 \cdot 2^{3+\alpha} \cong 80\text{--}160.$$

Hence 1% of clouds at $\theta \cong 1/10\Gamma_0$ produce 8–16% of the fluence in very narrow pulses that are ≈ 100 times brighter than clouds at $\theta \approx 1/\Gamma_0$. This produces highly variable light curves with reasonable ($\gtrsim 10\%$) efficiency.

Figure 11.12 shows calculations of GRB light curves in an external shock scenario from a GRB with apparent isotropic energy release of 10^{53} ergs and $\Gamma_0 = 300$. Clouds, with a partial covering factor of 10%, are assumed

to radiate 10% of their intercepted energy in the form of a photon spectrum with the shape of a Band function [343], which smoothly connects an exponentially cutoff power-law spectrum with number index α to a second power-law spectrum with index β , giving

$$N_B(\epsilon) = k_B \epsilon^\alpha \exp[-\epsilon(\alpha - \beta)/\epsilon_{\text{br}}] H(\epsilon; \epsilon_{\text{min}}^B, \epsilon_{\text{br}}) \\ + k_B \epsilon_{\text{br}}^{\alpha - \beta} \exp(\beta - \alpha) \epsilon^\beta H(\epsilon; \epsilon_{\text{br}}, \epsilon_{\text{max}}^B). \quad (11.100)$$

Here, in this paragraph alone, α and β are the low- and high-energy Band α and Band β indices, typically around -1 and -2.5 , respectively, for long-duration BATSE GRBs, and $E_{\text{br}} = m_e c^2 \epsilon_{\text{br}} \sim 100$ keV is the “break energy.” It can readily be shown that the photon energy E_{pk} of the peak of the νF_ν spectrum is related to E_{br} by

$$E_{\text{pk}} = \frac{(2 + \alpha)E_{\text{br}}}{\alpha - \beta}.$$

The clouds are assumed to be “uniformly randomly” distributed between 10^{16} and 10^{17} cm, that is, the location of the cloud is randomly selected throughout the volume of the shell by Monte Carlo methods provided that the volume of each cloud does not overlap the volume of another cloud. The underlying assumption is that no spatial correlations exist between cloud locations.

In figure 11.12(a), all clouds have the same radius $r = 10^{13}$ cm, and Gaussian noise is added to the simulation at a level typical of BATSE GRBs. Figure 11.12(b) shows a simulation where clouds are chosen with equal partial covering factor per logarithmic interval for clouds with sizes between 10^{12} and 3×10^{13} cm. No noise is added in figure 11.12(b). As can be seen, there is no difficulty in making highly variable light curves in an external shock model, even with a 10% (or larger) partial covering factor.

Thin-Shell Requirement for External Shock Model

A central requirement for strong radiative efficiency in an external shock model for the prompt phase is that a strong forward shock is formed; otherwise the Lorentz factor $\Gamma \ll \Gamma_0$ and the radiation is strongly debeamed. A strong forward shock is formed when $n(x) \gg \Gamma_0^2 n_0$, eq. (11.75), which will occur if the shell remains narrow. We write the shell width

$$\Delta(x) \cong \Delta_0 + \eta_{\text{sh}} \frac{x}{\Gamma_0^2}, \quad (11.101)$$

and the proper number density of the relativistic shell is given by eq. (11.72).

Short-timescale flaring requires (a) a strong forward shock, which from the relativistic shock jump conditions [302] implies a maximum cloud density given by

$$n_{\text{cl}} \lesssim \frac{E_0}{16\pi x^2 \Gamma_0^4 m_p c^2 \Delta(x)}, \quad (11.102)$$

and (b) significant blast-wave deceleration to provide efficient energy extraction, which occurs in clouds with thick columns [341], that is, with densities

$$n_{\text{cl}} \gtrsim \frac{E_0}{4\pi x_0^2 \Gamma_0^2 m_p c^2 \Delta_{\text{cl}}}. \quad (11.103)$$

These two conditions translate into the requirement that

$$\Delta_{\text{cl}} \gtrsim 4\Gamma_0^2 \Delta(x) \quad (11.104)$$

in order to produce short-timescale variability. The short-timescale variability condition [341] for quasi-spherical clouds is

$$\Delta_{\text{cl}} \lesssim \frac{x}{\Gamma_0}. \quad (11.105)$$

Using eq. (11.101) for the shell width, eqs. (11.104) and (11.105) imply the requirement that

$$\eta_{\text{sh}} \lesssim 1/4\Gamma_0 \quad (11.106)$$

in order to produce rapid variability from an external shock. Hence the production of γ -ray pulses and X-ray flares from external shocks depends on whether the GRB blast-wave width spreads in the coasting phase according to eq. (11.101), with $\eta_{\text{sh}} \approx 1$, as is generally argued. In the gas-dynamical study of [296], inhomogeneities in the GRB fireball produce a spread in particle velocities of order $|v - c|/c \sim \Gamma_0^{-2}$, so that $\Delta(x) \sim x/\Gamma_0^2$ when $x \gtrsim \Gamma_0^2 \Delta_0$. This dependence is also obtained in a hydrodynamical analysis [344].

Two points can be made about these relations. First, the spread in Δ considered for a spherical fireball is averaged over all directions. As the fireball expands and becomes transparent, the variation in fluid motions or gas particle directions over a small solid angle $\sim 1/\Gamma_0^2$ of the full sky becomes substantially less. Second, the particles within a magnetized blast-wave shell will expand and adiabatically cool so that the fluid will spread with thermal speed $v_{\text{th}} = \beta_{\text{th}}c$. The comoving width of the blast wave is $\Gamma_0 \Delta_0 + \beta_{\text{th}}c \Delta t' \approx \Gamma_0 \Delta_0 + \beta_{\text{th}}x/\Gamma_0$, so that the spreading radius $x_{\text{spr}} \cong \Gamma_0^2 \Delta_0 / \beta_{\text{th}}$. Adiabatic expansion of nonrelativistic particles can produce a very cold shell with $\beta_0 \lesssim 10^{-3}$, leading to very small shell widths.

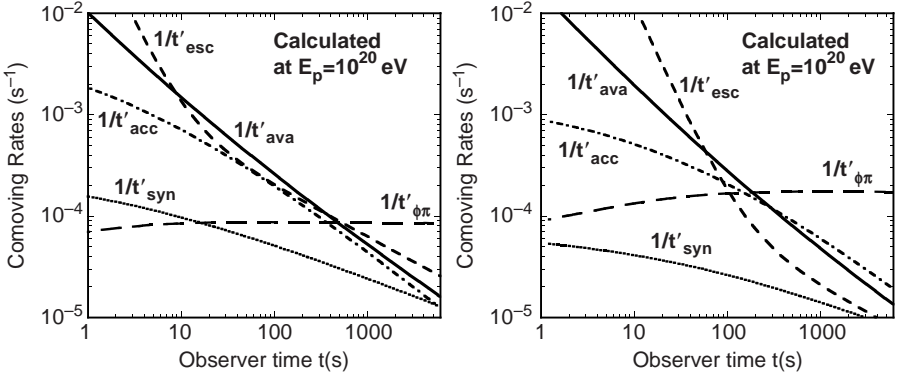


Figure 11.13 Rates and inverse timescales as a function of observer time for 10^{20} eV cosmic-ray protons as measured by a stationary external observer. Left and right panels are results for parameter sets 1 and 2, respectively, with $\zeta_{acc} = 10$.

The requirement on the thinness of $\Delta(x)$ does not apply to the adiabatic self-similar phase, where the width is necessarily $\sim x/\Gamma_0^2$, as implied by the relativistic shock hydrodynamic equations [302]. Even in this case, however, $\Delta \ll x/\Gamma_0^2$ if the blast wave is highly radiative [345]. Under the assumption of a strong forward shock and small clouds in the vicinity of a GRB, highly variable GRB light curves are formed with reasonable efficiency ($\gtrsim 10\%$) to transform blast wave energy into γ rays [341].

Rapid X-Ray Declines from UHECR Escape

If hadrons are accelerated by GRB blast waves, then blast-wave dynamics could be affected by the loss of internal energy when the UHECRs escape, possibly explaining the rapid X-ray declines in the Swift GRB light curves [346]. Photohadronic processes become important when the comoving-frame threshold condition $\epsilon'\gamma' \gtrsim m_\pi/m_e \simeq 200$ is satisfied. The dependence on observer time of the photohadronic energy-loss timescale, the available comoving time t'_{ava} since the start of the GRB explosion, the comoving acceleration time scale $t'_{acc} = \zeta_{acc} m_p c^2 \gamma' / e B c$, written as a factor $\zeta_{acc} \gg 1$ times the Larmor timescale [178], the comoving escape timescale t'_{esc} in the Bohm diffusion approximation, and the proton synchrotron energy loss timescale t'_{spr} is shown in figure 11.13 for protons that would escape the blast wave with 10^{20} eV, in the case of an adiabatic blast wave that decelerates in a uniform surrounding medium. The left-hand panel of figure 11.13 uses the parameter set

$$z = 1, \Gamma_0 = 300, E_{54} = 1, n_0 = 1000 \text{ cm}^{-3}, \epsilon_e = 0.3, \epsilon_B = 0.3,$$

and the right-hand panel uses the parameter set

$$z = 1, \Gamma_0 = 150, E_{54} = 10, n_0 = 1000 \text{ cm}^{-3}, \epsilon_e = 0.1, \epsilon_B = 0.3.$$

$t_d \cong 9.6(1+z)(E_{54}/n_2\Gamma_{300}^8)^{1/3}$ s is ≈ 9 s and ≈ 120 s, respectively.

For these parameters, it takes a few hundred seconds to accelerate protons to energies $\approx 10^{20}$ eV, at which time photohadronic losses and escape start to be important. Photohadronic losses inject electrons and photons into the GRB blast wave. The GRB blast wave rapidly loses internal energy due to the photohadronic processes and particle escape. The blast wave will then rapidly decelerate, producing a rapidly decaying X-ray flux. The electromagnetic cascade emission, in addition to hyper-relativistic electron synchrotron radiation from neutron escape followed by subsequent photohadronic interactions [97], makes a delayed anomalous γ -ray emission component coincident with rapid X-ray declines. Detection of $\sim 10^{14}$ – 10^{16} eV neutrinos formed as photopion secondaries would demonstrate the importance of cosmic ray acceleration in GRBs.

11.6.2 Colliding Shells and Internal Shocks

The relativistic winds formed by the energy released by the black hole are likely to be variable and intermittent on time scales at least as short as or shorter than the light crossing time scale for the Schwarzschild radius [299], which is $\lesssim 10^{-5}(M_{\text{bh}}/M_{\odot})$ s for a Solar mass black hole, and over an hour for a $\sim 10^9 M_{\odot}$ black hole.

Consider two shells ejected into the same part of the sky at different times t_* and $t_* + \Delta t_*$, with the Lorentz factor $\Gamma_2 = \zeta \Gamma_1$ of the second shell larger by a factor of ζ than the first shell, so that it can catch up and intercept it. The interception takes place at the interception radius $r_{\text{int}} = \beta_1 c t_* = \beta_2 c (t_* - \Delta t_*)$, which implies, for $\Gamma_1, \Gamma_2 \gg 1$, $(\zeta^2 - 1)r_{\text{int}} \cong 2\Gamma_2^2 c \Delta t_*$, or

$$\begin{aligned} r_{\text{int}} &\cong 2\Gamma_1^2 c \Delta t_* \cong 2 \times 10^{16} \left(\frac{\Gamma_1}{10}\right)^2 [\Delta t_* \text{ (hr)}] \text{ cm} \\ &\cong 6 \times 10^{14} \left(\frac{\Gamma_1}{100}\right)^2 [\Delta t_* \text{ (s)}] \text{ cm} \end{aligned} \quad (11.107)$$

when $\Gamma_2 \gg \Gamma_1$. The interception radius will be much smaller than the deceleration radius t_{dec} given by eq. (11.4) for variable outflows in GRBs produced on timescales $\Delta t_* \ll 1$ s with $\zeta \gtrsim 1$. Internal shocks in GRBs would then generally take place at much smaller distance scales than the external shock forming the afterglow emission when the blast wave sweeps up stellar wind or CBM material, and the internal and external shocks can be, to first approximation, treated separately.

The relative Lorentz factor of the two shells, from eq. (11.73), is

$$\Gamma_{\text{rel}} = \Gamma_1 \Gamma_2 (1 - \beta_1 \beta_2) \xrightarrow{\Gamma_1 \Gamma_2 \gg 1} \frac{1}{2} (\zeta + \zeta^{-1}). \quad (11.108)$$

For mildly relativistic internal shocks with a range of relative Lorentz factors $1 \lesssim \Gamma_{\text{rel}}, \zeta \lesssim 10$, the Lorentz factor $\hat{\Gamma}$ of the shocked fluid with adiabatic index $\hat{\gamma} = 5/3$ in the explosion frame is, from eq. (11.81),

$$\Gamma_{\text{sf}} \cong 2\Gamma_1 \frac{\Gamma_{\text{rel}} f^{1/4}}{\sqrt{2\Gamma_{\text{rel}} - f^{1/2}}} \cong \sqrt{2\Gamma_{\text{rel}}}\Gamma_1 \cong \sqrt{\Gamma_1 \Gamma_2},$$

where $f = n_2/n_1$ is the ratio of proper-frame densities of shell 2 to shell 1 when they intercept each other, and the final expression assumes that $n_2 \approx n_1$ and $\Gamma_{\text{rel}} \gg 1$. The proper shocked fluid number and energy densities are

$$n_{\text{sf}} = (4\Gamma_{\text{rel}} + 3)n_1 \approx 4\Gamma_{\text{rel}}n_1 \quad \text{and} \quad e_{\text{sf}} = \Gamma_{\text{rel}}n_{\text{sf}} m_p c^2$$

from eqs. (11.69) and (11.70).

Now consider the elastic collisions of shell 2 with mass m_2 intercepting shell 1 with mass m_1 . In an elastic collision, the Lorentz factor of the merged shell is

$$\Gamma_m \cong \sqrt{\frac{m_1 \Gamma_1 + m_2 \Gamma_2}{m_2/\Gamma_2 + m_1/\Gamma_1}} \quad (11.109)$$

[318]. The efficiency to convert the directed kinetic energy of the shells into internal energy is

$$\nu = 1 - \frac{(m_1 + m_2)\Gamma_m}{m_1 \Gamma_1 + m_2 \Gamma_2} \quad (11.110)$$

[347]. The efficiency is greatest when the shells have comparable mass and $\Gamma_2 \gg \Gamma_1$; otherwise $\nu \sim \text{few\%}$ [348,349]. When the contrast between the Γ factors of the shells is large, $\nu \sim 10\text{--}20\%$ is possible. When the Γ_0 contrast is large, however, Doppler boosting would scatter E_{pk} outside the detector waveband, thus reducing the γ -ray detection efficiency. The allowed range of Γ factors of the merged shells are constrained by $\gamma\gamma$ processes.

From eq. (11.107) for the radius where the shells intercept each other, we see that $\Delta t_* \cong r_{\text{int}}/2\Gamma_1^2 c$. A photon emitted with shell 2 will reach the observer at almost the same time as a photon emitted from the shell collision, so that time histories in models of internal shocks closely follow the assumed activity of the central engine. When two shells collide to form a spherical radiating surface, light-travel time effects imply a unique temporal relation between the shell intensity and E_{pk} that depends only on the (measurable) spectral indices of the GRB pulse [350]. The evolution of GRB

pulses do not follow the expected trend, implying that the simplest version of colliding shell physics is incomplete or incorrect [297].

The rapid X-ray declines seen [351] in the light curves of $\sim 30\%$ of GRBs with Swift are explained as due to cessation of central engine activity. If the shells emit uniformly within the Doppler cone of the shocked radiating fluid, then the curvature relation for colliding shells,

$$F_\nu \propto t^{-\alpha} \nu^{-\beta}, \quad \alpha = 2 + \beta$$

(see section 5.5.2 and eq. [5.60]), should be obeyed. This test has been made using the Swift data, with a significant fraction not following this relation, with interesting implications for jet structure [339].

In the standard long-duration GRB picture with relativistic winds and colliding shells, X-ray flares are made when the GRB engine is restarted. Long-lasting GRB central engines can also involve continual injection scenarios with pulsars. For review, see [336,337]. For simulations of colliding shells in GRBs, see [352], and in blazars, [353].

11.7 THERMAL PHOTOSPHERES

The tremendous energy release at the base of a GRB jet forms an opaque, thermal relativistic wind. One motivation to study thermal processes operating in GRB emissions is that the existence of thermal photospheric X/γ emissions may provide an explanation for the Amati and Ghirlanda correlations relating spectral and global properties of GRBs.

11.7.1 The Amati and Ghirlanda Relations

The Amati relation [354] correlates the νL_ν peak photon energy E_{pk} with apparent isotropic energy release $\mathcal{E}_{\text{iso}} = 10^{54} \mathcal{E}_{54}$ ergs according to

$$E_{\text{pk}} \propto \mathcal{E}_{\text{iso}}^{1/2}. \quad (11.111)$$

(In this section, E_{pk} and \mathcal{E}_{iso} are proper-frame quantities.) The Ghirlanda relation [355] correlates E_{pk} with the collimation-corrected absolute X/γ energy release, $\mathcal{E}_{\text{abs}} = 10^{51} \mathcal{E}_{51}$ ergs, according to

$$E_{\text{pk}} \propto \mathcal{E}_{\text{abs}}^{0.7}. \quad (11.112)$$

When $E_{\text{pk}} = 100 \text{ keV}$, $\mathcal{E}_{\text{iso}} \approx 10^{52}$ ergs, and $\mathcal{E}_{\text{abs}} \approx 10^{50}$ ergs in eqs. (11.111) and (11.112), respectively. The absolute and apparent energy releases are related in a top-hat jet geometry by the expression $(1 - \mu_j) \mathcal{E}_{\text{iso}} \cong \mathcal{E}_{\text{abs}}$, so that in the limit of small jet opening angle,

$$\theta_j = \arccos \mu_j \cong \left(\frac{2\mathcal{E}_{\text{iso}}}{\mathcal{E}_{\text{abs}}} \right)^{1/2}.$$

A thermal explanation for the Amati relation, eq. (11.111), is as follows [356]: The measured luminosity $L \cong \Gamma^2 L'$ is Γ^2 times the comoving luminosity $L' \cong 4\pi r^2 \sigma_{\text{SB}} T'^4$. Written in like units, $T \cong E_{\text{pk}} \cong \Gamma T'$, so that

$$L \cong \frac{8\pi r^2 \sigma_{\text{SB}} E_{\text{pk}}^4 \mathcal{E}_{\text{abs}}}{k_j^2 \mathcal{E}_{\text{iso}}}, \quad (11.113)$$

where we assume that the jet opening angle $\theta_j = k_j/\eta$ is inversely proportional to the entropy per baryon $\eta = L/\dot{M}_b c^2$, where \dot{M}_b is the baryonic mass loss rate into the wind.

Because $\mathcal{E}_{\text{iso}} \cong L t_{\text{GRB}}$, where $t_{\text{GRB}} = 10 t_1$ s is the typical duration of a GRB when it is most luminous,

$$E_{\text{pk}} \cong \sqrt{\frac{k_j \mathcal{E}_{\text{iso}}}{r_0}} (8\pi \sigma_{\text{SB}} \mathcal{E}_{\text{abs}} t_{\text{GRB}})^{-1/4} \cong 4 \text{ MeV} \frac{k_j^{1/2} \mathcal{E}_{54}^{1/2}}{r_8^{1/2} \mathcal{E}_{51}^{1/4} t_1^{1/4}}, \quad (11.114)$$

so $E_{\text{pk}} \propto \mathcal{E}_{\text{iso}}^{1/2}$. Here $r_0 = 10^8 r_8$ cm is the size scale in which energy is injected by processes in the vicinity of the newly formed black hole.

The values of \mathcal{E}_{iso} are measured over a range of four orders of magnitude, and the values of t_{GRB} over \sim one order of magnitude, which produces a dispersion in the correlation by a factor $\approx 10^{4/2}/10^{1/4} \cong 100/1.8 \approx 50$. The tight observed correlation between E_{pk} and \mathcal{E}_{iso} would mean, for the thermal photospheric explanation, that k_j , the scaled jet opening angle, and r_0 are relatively constant between GRBs.

11.7.2 Thermodynamics of a Steady Relativistic Wind

The black-hole engine can be described by a steady relativistic wind with four-velocity $u^\alpha = c\Gamma(1, \beta, 0, 0)$ in a spherical geometry with spherical coordinates (t, r, θ, ϕ) in terms of the following model parameters: luminosity L , entropy $\eta = L/\dot{M}c^2$, injection size scale r_0 , and temperature T_0 . The energy-momentum tensor for a perfect fluid is

$$T^{\alpha\beta} = p\eta^{\alpha\beta} + (p + \rho)u^\alpha u^\beta / c^2, \quad (11.115)$$

where ρ is the energy density, including rest-mass energy, of the fluid in a rest frame where it is isotropic, and $\eta^{\alpha\beta}$ is the Minkowski metric, eq. (3.3). For a mixed radiation/matter fluid, $\rho = u + \rho_p$, where u is the energy density of radiation, and ρ_p is the proper (comoving) energy density of matter. Temperature T is given in the local comoving frame where the particle distribution is isotropic (or at rest).

The mass flux four-vector $F^\alpha = \rho_p u^\alpha = c\rho_p \Gamma(1, \beta, 0, 0)$. Conservation of energy requires that the four-divergence of mass flux vanishes, i.e.,

$\partial F^\alpha / \partial x^\alpha = 0$, implying

$$\frac{1}{c} \frac{\partial(\Gamma \rho_p)}{\partial t} + \frac{1}{r^2} \frac{\partial(r^2 \beta \Gamma \rho_p)}{\partial r} = 0.$$

In steady state, $\dot{M} = 4\pi r^2 \beta \Gamma \rho_p c = \text{const}$, so

$$n_p = \frac{\rho_p}{m_p} = \frac{\dot{M}}{4\pi m_p r^2 c \beta \Gamma} = \frac{L}{4\pi m_p c^3 r^2 \beta \Gamma \eta}. \quad (11.116)$$

For a relativistically light plasma, $\eta \gg 1$, $u = aT^4$, $p = u/3$, $\rho = u + \rho_p$, so that

$$T^{\alpha\beta} = \frac{1}{3} a T^4 \eta^{\alpha\beta} + \left(\rho_p + \frac{4}{3} a T^4 \right) u^\alpha u^\beta / c^2. \quad (11.117)$$

Conservation of four-momentum is expressed by $T_{;\beta}^{\alpha\beta} = 0$, or

$$\frac{\partial T^{tt}}{\partial x^t} + \frac{\partial T^{rt}}{\partial x^r} = 0.$$

In steady state, $\partial T^{rt} / \partial x^r = 0$ implies

$$\frac{\partial}{\partial r} \left[r^2 \left(\rho_p + \frac{4}{3} a T^4 \right) \beta \Gamma^2 \right] = 0$$

or

$$L = 4\pi r^2 \beta \Gamma^2 c \rho_p \left(1 + \frac{4}{3} \frac{a T^4}{\rho_p} \right). \quad (11.118)$$

For an adiabatic wind dominated by a relativistic photon or particle gas, $u \propto T^4 \propto V^{-4/3} \propto r^{-4}$ (section 9.4), so that $T \propto r^{-1} \propto n_p^{1/3}$, and

$$\frac{T}{T_0} = \left(\frac{n_p}{n_0} \right)^{1/3} = \left(\frac{\rho_p}{\rho_0} \right)^{1/3}. \quad (11.119)$$

Equation (11.118) can be expressed as

$$L = 4\pi r^2 \beta \Gamma^2 c \rho_p \left[1 + x_0 \left(\frac{\rho_p}{\rho_0} \right)^{1/3} \right], \quad (11.120)$$

where

$$x_0 \equiv \frac{4aT_0^4}{3\rho_0} \quad (11.121)$$

and the subscripts “0” refer to values in the injection volume with radius r_0 . The energy is assumed to be injected at the base of the GRB jet with $\beta\Gamma = 1$, or $\Gamma = \sqrt{2}$, and $n_0 = \dot{M}/4\pi m_p r_0^2 c$, so that, from eq. (11.116),

$$\frac{n_p}{n_0} = \frac{\rho_p}{\rho_0} = \left(\frac{r_0}{r} \right)^2 \frac{1}{\beta\Gamma}.$$

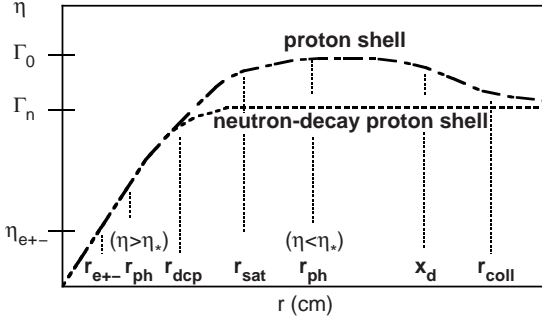


Figure 11.14 Sketch of the behavior of the proton and neutron wind in a fireball with injection entropy per baryon η (see Ref. [357]). The photospheric radius occurs during the expanding wind phase for light relativistic winds with $\eta \gg \eta_*$, and the photospheric radius is found in the coasting phase for heavy relativistic winds with $\eta \ll \eta_*$, where the critical entropy η_* is defined when $r_{ph} = r_{sat}$ is given by eq. (11.129).

Using this result and eq. (11.116) in eq. (11.120) gives [357]

$$x_0 \left(\frac{r}{r_0} \right)^{-2/3} = (\Gamma^2 - 1)^{1/6} \left(\frac{\eta}{\Gamma} - 1 \right) \quad (11.122)$$

for the implicit equation giving the dependence of the radial Lorentz factor $\Gamma(r)$ of a steady relativistic wind. The asymptotes of eq. (11.122) are

$$\Gamma(r) \rightarrow \begin{cases} r/r_0, & 1 \ll r/r_0 \ll \eta, \\ \frac{\eta}{1 + [\eta/(r/r_0)]^{2/3}} \approx \eta, & r/r_0 \gg \eta. \end{cases} \quad (11.123)$$

The saturation radius $r_{sat} = \eta r_0$ defines the radius separating the expanding and coasting regimes of the blast wave. The behavior described by eq. (11.123) is followed until the photons decouple from the outflowing proton-electron plasma at the photospheric radius. See figure 11.14.

11.7.3 Photospheric Radius

The electrons, protons, and photons in the plasma are strongly coupled until the fluid becomes optically thin to Thomson scattering. For the proper-frame electron density n'_e , the Thomson depth defining the photospheric radius r_{ph} is

$$\tau'_T \approx \frac{n'_e \sigma_T r_{ph}}{\Gamma} = 1, \quad (11.124)$$

because the distance r is shortened by a factor Γ^{-1} in the proper frame. Assuming that $n'_e \cong n_p$, that is, a proton-electron plasma rather than a pair plasma with comoving electron density equal to proper-frame proton density, then eq. (11.116) implies with eq. (11.124) the definition of the photospheric radius

$$r_{\text{ph}} = \frac{L\sigma_{\text{T}}}{4\pi m_p c^3 \beta \Gamma^2 \eta}. \quad (11.125)$$

The radiant power released at the photospheric radius is, from eq. (11.118),

$$L_{\gamma} = \frac{16\pi}{3} r_{\text{ph}}^2 c \beta (r_{\text{ph}}) \Gamma^2 (r_{\text{ph}}) a T^4 (r_{\text{ph}}), \quad (11.126)$$

with the remainder of the power leaving the jet in the form of particle kinetic energy or field energy.

Equation (11.118) gives the injection luminosity

$$L \cong \frac{16\pi\sqrt{2}}{3} r_0^2 c a T_0^4 \quad (11.127)$$

of a radiation-dominated fireball, taking the value of $\beta\Gamma = 1$ at the base of the flow by convention. The ratio of eq. (11.127) to eq. (11.126) is

$$\frac{L_{\gamma}}{L} = \left(\frac{r_{\text{ph}}}{r_0}\right)^2 \frac{\Gamma^2(r_{\text{ph}})}{\sqrt{2}} \left(\frac{T(r_{\text{ph}})}{T_0}\right)^4. \quad (11.128)$$

Following [358–360], we define a characteristic flow entropy η_* where the photospheric radius r_{ph} , eq. (11.125), equals the saturation radius $r_s = \eta r_0$, given by

$$\eta_* = \sqrt[4]{\frac{L/r_0}{4\pi m_p c^3 / \sigma_{\text{T}}}} \cong 330 \sqrt[4]{\frac{L_{51}}{r_8}} \quad (11.129)$$

where $r_8 = r/(10^8 \text{ cm})$ and $L_{51} = L/(10^{51} \text{ ergs s}^{-1})$. The quantity $4\pi m_p c^3 / \sigma_{\text{T}} = 8.5 \times 10^{32} \text{ ergs s}^{-1} \text{ cm}^{-1}$ is the proton compactness, analogous to the electron compactness introduced in eq. (10.51). When the entropy $\eta < \eta_*$, there is more baryonic material in the flow, so more opacity, and $r_{\text{ph}} > r_{\text{sat}}$. Conversely, when $\eta > \eta_*$, $r_{\text{ph}} < r_{\text{sat}}$. For a relativistic flow,

$$\frac{r}{r_0} = \frac{\eta_*^4}{\Gamma^2 \eta} \rightarrow \begin{cases} \frac{\eta_*^{4/3}}{\eta^{1/3}} & \text{for } \eta > \eta_*, \quad r < r_{\text{sat}}, \\ \frac{\eta_*^4}{\eta^3} & \text{for } \eta < \eta_*, \quad r > r_{\text{sat}}. \end{cases} \quad (11.130)$$

From eqs. (11.116) and (11.119),

$$\frac{T}{T_0} = \left(\frac{r}{r_0}\right)^{-2/3} (\beta\Gamma)^{-1/3}$$

$$\rightarrow \begin{cases} \left(\frac{r}{r_0}\right)^{-1} & \text{for } r < r_{\text{sat}}, \\ \frac{T(r_{\text{sat}})}{T_0} \frac{T(r)}{T(r_{\text{sat}})} = \eta^{-1} \left(\frac{r}{r_{\text{sat}}}\right)^{-2/3} = \eta^{-1/3} \left(\frac{r}{r_0}\right)^{-2/3} & \text{for } r > r_{\text{sat}}. \end{cases} \quad (11.131)$$

Substituting eqs. (11.123), (11.130), and (11.131) into eq. (11.128) gives

$$\frac{L_\gamma}{L} \rightarrow \begin{cases} 1 & \text{for } \eta > \eta_*, \text{ or } r_{\text{ph}} \ll r_{\text{sat}}, \\ \left(\frac{\eta}{\eta_*}\right)^{8/3} & \text{for } \eta < \eta_* \text{ or } r \gg r_{\text{sat}}, \end{cases} \quad (11.132)$$

for the ratio of total photon luminosity emitted at the photospheric radius compared to the total jet power. This result shows that, if the jet flow entropy is sufficiently large and the baryon-loading sufficiently small that $\eta \gtrsim \eta_*$, then a large fraction of the escaping power can be in the form of photospheric emission.

For a numerical solution for $\Gamma(r)$, note that eq. (11.122) is an implicit equation. The parameters are η , r_0 , L , and either x_0 or T_0 , which are related because $\rho_0 = L/4\pi r_0^2 c^3 \sqrt{2}$ and x_0 is given in terms of T_0 and ρ_0 (eq. [11.121]). Rossi, Beloborodov, and Rees [357] present a more detailed study and numerical solutions of blast-wave evolution with different electron and ion temperatures.

11.7.4 Pair Photosphere

The pair plasma at the base of the jet is a Fermi gas, and obeys Fermi statistics with chemical potential μ and distribution function

$$\bar{n}_k = \frac{1}{\exp[(\varepsilon_k - \mu)/T] + 1}. \quad (11.133)$$

The phase space volume for particles with wavenumber $k = 2\pi/\lambda = 2\pi v/c$ and (dimensional) momentum $p = h\nu/c$ is

$$g d\mathcal{V} = g dV d^3 \vec{p} = g \frac{4\pi k^2 dk}{(2\pi)^3} = 4\pi g \frac{v^2 dv}{c^3} = \frac{4\pi g}{h^3} dV dp p^2. \quad (11.134)$$

The statistical weight $g = 2S + 1 = 2$ for spin $S = 1/2$ leptons counts total states. The lepton density is therefore

$$n'_{e^\pm} = \frac{1}{\pi^2 h^3} \int_0^\infty dp \frac{p^2}{\exp(\gamma/\Theta) + 1}, \quad (11.135)$$

taking $\varepsilon_k \rightarrow m_e \gamma$ for zero chemical potential and (dimensionless) $p = \sqrt{\gamma^2 - 1}$.

In the limit $\Theta \ll 1$, $p \ll 1$,

$$n'_{e^\pm} \simeq 0.7 \frac{(2\Theta)^{3/2} \exp(-1/\Theta)}{\pi^2 \lambda_C^3} \int_0^\infty dy \frac{y^{1/2}}{\exp(y) + 1}. \quad (11.136)$$

Here

$$\begin{aligned} \int_0^\infty dy \frac{y^{1/2}}{\exp(y) + 1} &= \Gamma(3/2)(1 - 2^{-1/2})\zeta(3/2) \\ &= \frac{\sqrt{\pi}}{2} \times 0.2928 \dots \times 2.612 \dots \cong 0.67799 \dots \end{aligned} \quad (11.137)$$

(see Appendix B). The pair photospheric radius r_{e^\pm} is defined through the relation $n'_{e^\pm} \sigma_T r_{e^\pm} / \Gamma \cong 1$, giving

$$r_{e^\pm} = \frac{1.92 \pi^2 \lambda_C^3 \exp(1/\Theta) \Gamma(r)}{\sigma_T \Theta^{3/2}}. \quad (11.138)$$

In the regime $1 \ll r/r_0 \ll \eta$,

$$\Theta = \Theta_0(r_0/r) \quad \text{and} \quad \Gamma(r) = \sqrt{2}(r/r_0),$$

and eq. (11.138) becomes, with $y_{e^\pm} = r/r_0 \Theta_0$

$$\sqrt{y_{e^\pm}} \exp(y_{e^\pm}) \cong \frac{1.92 \sigma_T (r_0 \Theta_0)}{\pi^2 \lambda_C^3} \cong 9 \times 10^{11} r_8 \Theta_0. \quad (11.139)$$

Squaring eq. (11.138) casts it in the form of a Lambert function (Appendix B). It is a simple matter to solve this equation numerically, giving

$$\eta_{e^\pm} = y_{e^\pm} \Theta_0 \cong 26 \Theta_0$$

for the Lorentz factor of the fireball wind where it becomes optically thin to Thomson scattering on the pairs. For values of $\eta \gtrsim 10^2$, thought to be found in GRB jets, the fireball becomes optically thin to pair Thomson scattering well before it becomes optically thin to Thomson scattering with the electrons carried by the baryonic material of the flow. The jet luminosity L injected into the jet normalizes the dimensionless temperature Θ_0 at the base of the jet though the relation

$$L = 4\pi r_0^2 \sigma_{\text{SB}} T^4 \cong 9 \times 10^{51} r_8^2 \Theta_0^4 \text{ ergs s}^{-1}. \quad (11.140)$$

Letting r_{e^\pm} , eq. (11.138), equal to r_{ph} , eq. (11.125), gives the injection entropy where the pair photosphere equals the baryonic photosphere,

$$\bar{\eta} \cong \frac{L/r_0}{(8\pi m_p c^3 / \sigma_T) (y_{e^\pm} \Theta_0)^3} \cong 3 \times 10^5 \frac{L_{51}}{r_8 \Theta_0^3}. \quad (11.141)$$

It is not clear if such relativistically light jets occur in nature.

11.8 THERMAL NEUTRONS

Neutrons in the fireball formed at the base of the GRB outflow are coupled to the ambient protons through proton-neutron nuclear elastic scattering. At a radius where the baryon density in the expanding fireball wind is sufficiently dilute, the neutrons decouple to form a separately streaming wind of particles interacting only through nuclear scattering. Inelastic π -producing nuclear scattering between the two winds produces γ -ray and neutrino signals at $\sim 1\text{--}10\text{ GeV}$ [361]. Later, the neutrons decay into protons, forming two charged proton winds moving at different speeds. In a dynamic situation, the leading proton wind sweeps up material and decelerates, allowing it to be impacted from behind by the neutron-decay proton wind. Nuclear collisions form γ -rays and neutrinos that could be detected at energies $\lesssim \eta\text{ GeV} \approx (\eta/10^3)\text{ TeV}$ [361]. In a steady situation, the neutron-decay products in the wind produce disturbances that can excite shocks [362]. Here we outline the basic theory of this process, first proposed by Derishev and colleagues [328,363].

As we have seen (eq. [11.123]), the Lorentz factors of fluid particles in a spherically symmetric wind evolve with radius r according to

$$\Gamma(r) \simeq \begin{cases} r/r_0, & 1 \lesssim r/r_0 \lesssim \eta, \\ \eta, & r/r_0 \gtrsim \eta. \end{cases} \quad (11.142)$$

A straightforward integration gives the comoving time

$$t'(r) \simeq \begin{cases} \frac{r_0}{c} \ln\left(\frac{2r}{r_0}\right), & r_0 \lesssim r \lesssim \eta r_0, \\ \frac{r}{\eta c} + \frac{r_0}{c} [\ln(2\eta) - 1], & r \gtrsim \eta r_0, \end{cases} \quad (11.143)$$

to reach radius r from injection. Strong elastic nuclear forces keep neutrons coupled if $t'_{np} \lesssim t'$, where the nuclear elastic timescale is given by

$$t'_{np} \simeq (n'_p \sigma_{pn} \beta_p c)^{-1}, \quad (11.144)$$

and $\beta_p \sigma_{pn} \simeq 30\text{ mb}$.

Let the total baryon density $n' = n'_p + n'_n$ be the sum of the proton density n'_p and neutron density n'_n . Defining

$$y \equiv \frac{n'_n}{n'_p} \Rightarrow n'_p = \frac{n'}{1+y} \text{ and } \frac{yn'}{1+y}.$$

The proper baryon and proton densities are

$$n' \cong \frac{L}{4\pi r^2 \Gamma \eta m_p c^3} \quad \text{and} \quad n'_p \cong \frac{L}{4\pi r^2 \Gamma \eta m_p c^3 (1+y)}, \quad (11.145)$$

respectively, from eq. (11.116). Neutrons become decoupled from the protons in the wind, which are bound to the radiation through electrostatic forces with the electrons when $t'_{np} > t'$, that is, when

$$\frac{(1+y)4\pi\Gamma^3\eta m_p c^3 r_0}{L\sigma_{pn}\ln 2\Gamma} > 1. \quad (11.146)$$

Neutrons will decouple if the flow entropy η exceeds η_{dcp} , the critical entropy for decoupling, which is obtained by setting $\eta = \eta_{\text{dcp}}$, giving

$$\begin{aligned} \eta_{\text{dcp}} &\cong (\ln 2\eta_{\text{dcp}})^{1/4} \sqrt[4]{\frac{L\sigma_{pn}}{(1+y)4\pi m_p c^3 r_0}} \\ &\approx 240 \sqrt[4]{\ln\left(\frac{\eta_{\text{dcp}}}{300}\right)} \sqrt[4]{\frac{L_{51}}{(1+y)r_8}}, \end{aligned} \quad (11.147)$$

defining $r_0 = 10^8 r_8 \text{ cm}$ and $L = 10^{51} L_{51} \text{ ergs s}^{-1}$. With eq. (11.146), eq. (11.147) gives the decoupling Lorentz factor of the neutrons,

$$\Gamma_n = \eta_{\text{dcp}} \left(\frac{\eta_{\text{dcp}}}{\eta}\right)^{1/3} = \eta u^{4/3}, \quad (11.148)$$

where

$$u \equiv \eta_{\text{dcp}}/\eta < 1$$

for neutron decoupling. Because $\Gamma = r/r_0$, the decoupling radius

$$r_{\text{dcp}} = r_0 \Gamma_n = r_0 \eta u^{4/3}. \quad (11.149)$$

Consider a sudden release of energy over the stationary frame Δt_* with mean luminosity L . The release is assumed to be long enough that a steady wind is established on a size scale $c\Delta t_* \gg r_{\text{sat}} \sim 10^{10} \text{ cm}$ and short enough that $c\Delta t_* \ll x_d \sim 10^{16} \text{ cm}$, so that the dynamics can be treated as an impulsive release of energy into a uniform CBM or size scales $r \sim x_d$ (eq. [11.2]). When the protons in the wind reach large radii $r \gg x_d$, the observer time is

$$t \cong \frac{(1+z)x_d}{\Gamma_0^2 c} \left[\frac{r}{x_d} + \frac{1}{2} \left(\frac{r}{x_d}\right)^4 \right] \rightarrow \frac{(1+z)x_d}{2\Gamma_0^2 c} \left(\frac{r}{x_d}\right)^4.$$

The location of the neutron-decay proton shell, as a function of observer time t , is given by

$$r \propto \Gamma_n^2 c t / (1+z),$$

provided that $r \gg 900\Gamma_n c s$. The condition that the neutron-decay proton shell intersects the proton shell at the same observer time implies the collision radius

$$r_{\text{coll}} = x_d \left(\frac{\Gamma_0}{\Gamma_n}\right)^{2/3} = x_d u^{-8/9}. \quad (11.150)$$

The observer time of the collision between the two shells is

$$t_{\text{coll}} \cong t_d u^{-32/9}. \quad (11.151)$$

The requirement that the neutrons have decayed before the collision becomes

$$x_d \gg 6 \times 10^{15} \left(\frac{\eta}{300} \right) u^{20/9} \text{ cm}. \quad (11.152)$$

11.9 GRB COSMOLOGY

Beppo-SAX and Swift established the distance scale to long- and short-duration GRBs, respectively. Except for a beaming-factor correction, this also establishes the energy budget of these sources. The apparent isotropic γ -ray energy release, from eq. (4.36), is

$$\mathcal{E}_{\gamma,\text{iso}} = \frac{4\pi d_L^2 \mathcal{F}_\gamma}{1+z}, \quad (11.153)$$

where the GRB γ -ray energy fluence \mathcal{F}_γ is typically $\sim 10^{-7}$ – 10^{-4} ergs cm^{-2} . Using θ_j given by eq. (11.91) for the opening angle of the jet gives a beaming-corrected absolute energy release. Combining eqs. (11.91) and (11.153) gives the jet energy

$$\mathcal{E}_j \text{ (ergs)} \simeq 1.3 \times 10^{50} (1+z)^{-3/4} t_{\text{br}}^{3/4} \left(\frac{\mathcal{E}_{\gamma,\text{iso}}}{10^{52} \text{ ergs}} \right)^{3/4} n_0^{1/4} \eta_\gamma^{1/4} \quad (11.154)$$

[367].

Figure 11.15 from Frail and colleagues [364] shows the result of performing this exercise, and the remarkable mapping of apparent energies $\mathcal{E}_{\gamma,\text{iso}}$ spread over three orders of magnitude to a distribution of beaming-corrected energies $\mathcal{E}_{\gamma,\text{abs}}$ with dispersion of less than one order of magnitude. This “standard energy reservoir,” with $\mathcal{E}_{\gamma,\text{abs}} \sim 5 \times 10^{50}$ ergs, or an absolute energy release $\mathcal{E}_{\text{abs}} \sim 1.5 \times 10^{51}$ ergs for a γ -ray efficiency $\eta_\gamma \cong 1/3$, would represent the long-sought energy scale of GRBs (the most complete pre-Swift study is by Friedman and Bloom [365]).

The clustering of the beaming-corrected energy has led several groups [366,367] of researchers to consider the use of GRBs as standard candles, and therefore as tools for cosmology. The energy is assumed to follow the Ghirlanda relation, eq. (11.112). The dispersion of beaming-corrected energies away from this relation gives the uncertainty in standard energy. The standard energy and its uncertainty can be used to derive the allowed range in cosmological parameters. The low-luminosity GRBs may be identified as a separate population.

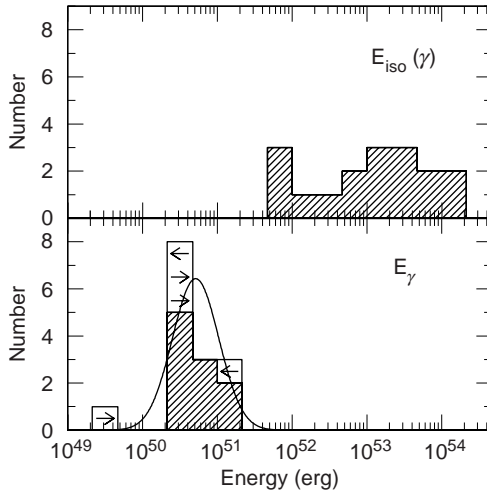


Figure 11.15 Distribution of the apparent isotropic GRB energy of GRBs with known redshifts (top panel) vs. the geometry-corrected energy for those GRBs whose afterglows exhibit the signature of a nonisotropic outflow (bottom panel). Arrows are plotted for five GRBs to indicate upper or lower limits to the geometry-corrected energy [364]. (Figure courtesy of Dale A. Frail, National Radio Astronomy Observatory.)

GRBs are observed to have apparent isotropic energy releases as much as 9×10^{54} ergs (at the time of writing, for GRB 080916C), mainly radiated at ≈ 100 keV–MeV energies. These GRBs could also radiate a large fraction of their energy in the form of high-energy γ rays above ~ 1 GeV. Deviations of spectral models from an empirical Band function, eq. (11.100), can reveal the existence of separate spectral components and test EBL models. The goal of measuring GRB energy release is being realized with the multiwavelength data in GRB studies, now using extensive γ -ray data from the Fermi Gamma Ray Space Telescope and the ground-based arrays.

Chapter Twelve

Introduction to Fermi Acceleration

The subject of particle acceleration is integral to our understanding of energetic nonthermal radiations. Our focus on Fermi acceleration does not preclude the existence of other accelerators based on magnetic reconnection, wakefield acceleration driven by the ponderomotive force of a radiation pulse, shear flows (which can, but need not be, a Fermi mechanism), Weibel or other plasma instability mechanisms, etc. Electrodynamical acceleration, as discussed in relation to neutron stars, pulsars, and magnetars [368], can also operate near black holes, and is studied in chapter 16. Because of its highly developed theoretical basis, and its ability to produce nonthermal power-law particle spectra with number indices near -2 or harder, Fermi acceleration is studied here. For more introduction to Fermi acceleration, see the books by Gaisser [12] and Longair [369].

Consider a test particle physically diffusing through a part of the ISM inhabited by massive magnetized clouds moving randomly in all directions with mean speed $v = |\vec{v}| = \beta c$ (Figure 12.1a). Elastic scattering of the particles by the massive clouds leads, stochastically, to a diffusive energy gain. The scattered particle intercepts a cloud according to a scattering rate, which favors head-on over tail-on collisions, and exits the cloud isotropically from the cloud frame. The particle diffuses physically when cycling between ISM and cloud media, and diffuses in momentum space to higher mean energies in the process of thermal equilibration between the test particle and the clouds. The fractional energy gain per cycle is proportional to v^2 , and therefore this process is called second-order Fermi acceleration (F2).

A shock, by contrast, is a distinct geometry where suprathermal particles can diffuse and cycle through unshocked upstream regions and shocked downstream regions by crossing the shock velocity discontinuity. The particle gains energy, and the statistical systematic energy gain is balanced by convective particle loss downstream where there is no further acceleration. In the idealized case of a semi-infinite forward shock between a fast-moving fluid with speed $u = |\vec{u}| \gg$ local sound speed c_s of the upstream medium, as sketched in figure 12.1, the divergent velocity structure results in a fractional energy gain rate per cycle proportional to u/c ; therefore this process is known as first-order Fermi acceleration (F1).

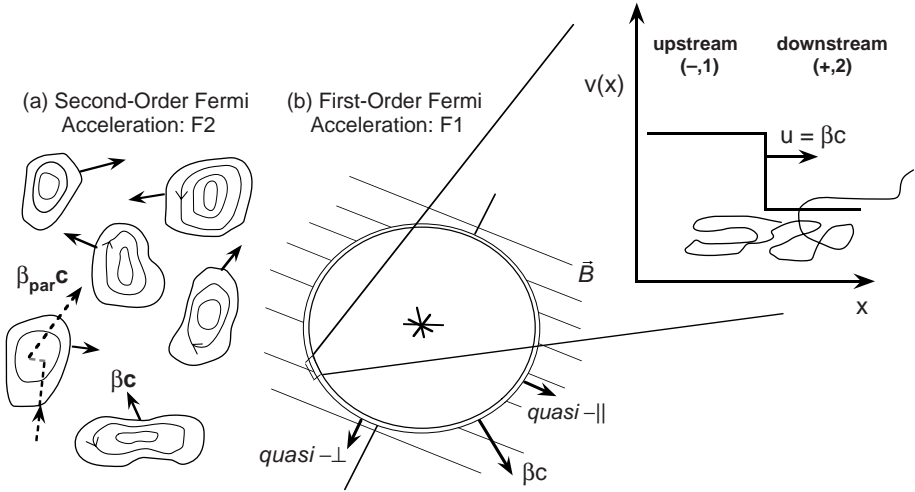


Figure 12.1 The two basic types of Fermi processes. (a) Second-order, stochastic Fermi acceleration, where test particles scatter off randomly moving magnetized mirrors, now reinterpreted as MHD waves. (b) First-order, shock Fermi acceleration, where test particles systematically gain energy by scattering with advancing (converging) scattering centers formed by the shock. Magnetic field shock geometries can have the large-scale magnetic field direction aligned with the shock normal as quasi-parallel ($q\text{-}\parallel$) shocks, and magnetic field directions transverse to the shock normal as quasi-perpendicular ($q\text{-}\perp$) shocks. Blow-up shows the shock structure approximated by an infinite plane parallel geometry.

For nonrelativistic flow speeds, the compression ratio χ is equal to the ratio of downstream to upstream proper particle densities, or upstream to downstream speeds as measured in the shock frame. For a strong shock with $u \gg c_s$ in a uniform density ISM, $\chi \rightarrow 4$; thus the density of the fluid downstream of a strong shock increases by a factor of 4, and the velocity decreases by the same factor (section 13.1). Particles with gyroradii much smaller than the shock width are heated by adiabatic compression, but otherwise convect downstream. Particles with gyroradii much larger than the shock width can sample both sides of the flow, increasing their momenta proportionally to u in each cycle. Because of turbulence generated in both the downstream and upstream fluids, suprathermal particles follow diffusive trajectories. Each roundtrip cycle up- and downstream earns a particle a systematic energy gain, so that the rare few particles that diffuse hundreds of times across the shock can be accelerated to very high energies before convecting downstream.

The subject is introduced by describing the basic features of Fermi acceleration, either through statistical systematic increases in particle energy by cycling across a shock front (F1) or statistical diffusive increases in particle energy by scattering off randomly oriented scatterers (F2). The remainder of this chapter introduces the following:

1. The two Fermi acceleration mechanisms are further described.
2. Dimensional arguments are shown to recover the Kolmogorov and Kraichnan indices for the spectrum of turbulence.
3. Hillas's criterion [320] that the particle gyroradius is smaller than the size scale of the system is shown to rule out many sites as sources of UHECRs.
4. The energy gain per cycle for relativistic particles in Fermi acceleration is derived.
5. Diffusion in physical space, integral to Fermi processes, is discussed.
6. Expressions for maximum particle energies E_{\max} are summarized.

The values of E_{\max} are based on derivations of maximal energy-gain rates integrated over time for first-order acceleration at nonrelativistic and relativistic shocks, and for second-order acceleration in the shocked fluid shell formed by an explosive event.

12.1 STOCHASTIC AND SHOCK FERMI ACCELERATION

In the original formulation of this problem by Fermi [370,371], particles gain energy by scattering off magnetic clouds moving in random directions with mean speeds $\langle v \rangle = c\beta$.

The stochastic and shock Fermi mechanism both rely on scattering charged particles by moving scattering centers. In the case of stochastic, second-order Fermi acceleration, the scattering centers are assumed to be moving in random directions. A test particle elastically scattering off these randomly moving centers will on average pick up more energy than it loses. This is because the rate factor $(1 - \beta_{\text{par}}\beta\mu)$, with its lower value for tail-on collisions, makes a smaller energy loss than for head-on collisions, which tend to increase the particle's energy. A slow general energy increase of the particle takes place at the expense of the kinetic energy of the magnetic clouds.

When second-order acceleration is sufficiently rapid to accelerate supra-thermal particles over the Coulomb barrier, quasi-Maxwellian particle distributions with number index as hard as +1 ($N_e(\gamma) \propto \gamma^{-1}$) are formed with cutoff energies or effective temperatures that may be highly relativistic [372,373].

The first-order Fermi mechanism involves fundamentally different scattering kinematics as a result of the discontinuity in velocity, density, and magnetic field at the shock front. A suprathermal particle samples large volumes around the shock front when its gyroradius is large compared to scales set by the shock width. The effect of the velocity jump when viewed from the stationary ISM is to have advancing scattering centers. Suprathermal particles cycling upstream and downstream across the shock front pick up a systematic energy gain. Remarkably, the convective loss downstream of the accelerated particles balances the energy gain rate and makes, in the test particle limit, a power-law particle distribution with power-law index simply related to the compression ratio of the flow. Important issues here are the origin of the upstream and downstream scattering centers responsible for the particles' diffusive motions, and the effect of the nonthermal particle energy on shock structure and acceleration.

The shock and magnetic-field geometries are usually considered in the two limiting cases of

1. Quasi-parallel ($q\parallel$), where the shock normal is parallel to the magnetic-field direction; and
2. quasi-perpendicular ($q\perp$), where the shock normal is perpendicular to the magnetic-field direction,

as sketched in figure 12.1.

12.2 WAVE TURBULENCE SPECTRUM

A wavevector \vec{k} ($k = |\vec{k}| = 2\pi/\lambda$) description of turbulence is needed to describe gyroresonant acceleration of particles which gain energy by interacting with magnetic scattering centers. These scattering centers, viewed by Fermi as magnetized clouds, are now understood to be magnetohydrodynamic (MHD) (including hydromagnetic or electromagnetic) waves. Gyroresonant interactions of these waves with electrons and protons cause a gradual second-order diffusive increase in the mean energy of the particles.

The spectral wave energy density $w(\vec{k})$ is a local quantity, and depends in general on location. The differential energy density of MHD waves in the momentum element $d^3\vec{k}$ in the direction \vec{k} is defined as $d^3\vec{k} w(\vec{k})$ [374,375]. A better description would consider wave type, polarization, and helicity. By assuming isotropic MHD wave turbulence, and following the arguments of Kolmogorov and Kraichnan outlined below, a simple approximate form for the MHD wave spectrum for parallel, one-dimensional turbulence is

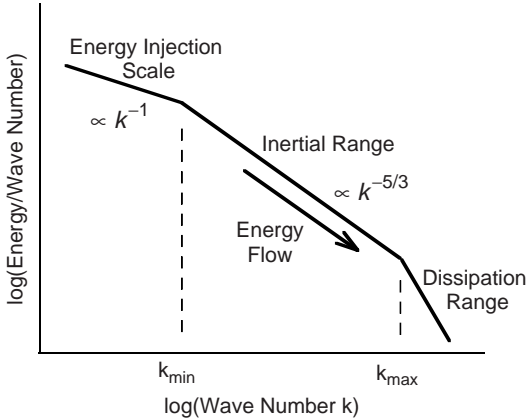


Figure 12.2 Illustration of the wave spectral energy density $w(k)$, including the injection scale at $k \sim k_{\min}$, the inertial range between k_{\min} and k_{\max} , and the dissipation range at $k \gtrsim k_{\max}$. The inverse size scale L^{-1} determines the characteristic wavenumber of the injected turbulence.

given by

$$w(k) \cong w_0 k^{-q} H(k; k_{\min}, k_{\max}), \quad q = \begin{cases} 5/3, & \text{Kolmogorov,} \\ 3/2, & \text{Kraichnan,} \end{cases} \quad (12.1)$$

in the inertial range of cascading turbulence. The units are such that $kw(k)$ is energy density. Turbulence spectral indices q in the range $1 \lesssim q \lesssim 2$ are generally considered. Most of the turbulent energy resides in small-wavenumber, large-size-scale turbulence.

As sketched in figure 12.2, the cascade phenomenology involves the injection of turbulence at small wavenumber $k \approx k_{\min}$, corresponding to the largest or dominant size scale of the system. Turbulence cascades to smaller wavelength structures until it is damped by, for example, microphysical processes or energy extraction by particles through gyroresonant processes. A specific example of interacting waves and particles used to model impulsive Solar flare data is given in Ref. [376].

Kolmogorov Spectrum of Turbulence

Consider a closed system filled with an incompressible fluid filled with eddy turbulence. Each eddy can be characterized by velocity v and size scale R . Energy flows from smaller to larger wavenumbers as eddies cascade from larger to smaller size scale until the eddies reach a size scale where energy dissipation dominates the flow of turbulent energy (figure 12.2). The

cascade phenomenology can be understood as a Reynolds-number-dependent injection of turbulence, with feedback between the particle and wave energy driving the wave spectrum to self-similar form [377].

For the units peculiar to this and the next subsection, energy E is given per unit mass; thus $E \sim v^2$, where the “ \sim ” sign connotes dimensional accuracy. The only microphysical property that enters is the energy dissipation rate per unit mass $\dot{\epsilon}$ (ergs s⁻¹), which determines the end of the turbulent cascade over the dissipation range of wavenumber space.

By dimensional analysis,

$$\dot{\epsilon} \sim v^2 \cdot \frac{v}{\lambda} \sim \frac{v^3}{\lambda} \Rightarrow v \propto (\dot{\epsilon} \lambda)^{1/3}. \quad (12.2)$$

In these units,

$$kw(k) \sim v^2 \sim (\dot{\epsilon} \lambda)^{2/3} \sim \frac{\dot{\epsilon}^{2/3}}{k^{2/3}}, \quad (12.3)$$

and λ refers to the size scale (wavelength) of the turbulence. Thus [378]

$$w(k) \sim k^{-5/3}. \quad (12.4)$$

Most of the wave energy is in waves with $k \sim k_{\min}$.

The frequency spectrum of the magnetic field fluctuations in the Solar wind measured with the magnetometer on *Mariner 10* gave a slope in the inertial range consistent with the Kolmogorov spectrum. Many other studies find a Kolmogorov spectrum for Solar wind turbulence [375].

Kraichnan Spectrum of Turbulence

Kraichnan [379] pointed out that coupled hydromagnetic equations for velocity and magnetic field fluctuations were required to understand energy transfer in the inertial range. Fluid fluctuations would couple turbulence to produce “asymptotically exact equipartition of energy.” Distributing kinetic energy into velocity turbulence on scales k_v^{-1} with energy density $\int_0^\infty dk_v w_{ke}(k_v)$ implies a mean-squared velocity

$$\frac{3}{2} v_0^2 \sim V \int_0^\infty dk_v w_{ke}(k_v) \sim \frac{3}{2} b_0^2 \sim V \int_0^\infty dk w(k),$$

which is of comparable energy density to the MHD turbulent wave energy density. Here b_0 is a characteristic velocity associated with the MHD energy density.

Performing dimensional analysis with $vt \sim 1/k$, but now letting energy depend quadratically on the wave energy density, we have

$$\dot{\epsilon} \sim \frac{E}{tV} \sim \frac{E^2}{Vt v^2} \sim V [kw(k)]^2 \frac{v_0 k}{v_0^2} \sim \frac{V k^3 w^2(k)}{v_0}. \quad (12.5)$$

This gives [380] the form of the Kraichan spectrum of MHD turbulence,

$$w(k) \sim k^{-3/2}. \quad (12.6)$$

12.3 THE HILLAS CONDITION

The maximum particle energy E_{\max} is governed by the condition that the Larmor radius r_L , eq. (7.5), be less than the size scale R of the system. For relativistic particles

$$E < QBR.$$

More precisely, a Fermi acceleration mechanism is, as it must be, ultimately an electrodynamic accelerator. The differential energy gained through Lorentz force in a frame with zero electric field is $dE \cong Q\beta Bdr$, so that the total energy gain

$$E \lesssim Q\beta BR \Rightarrow R \gtrsim \frac{E}{Q\beta B}, \quad \text{or} \quad B_{\mu\text{G}} \gtrsim \frac{E_{20}}{Z\beta(R/\text{Mpc})},$$

the final expression immediately ruling out acceleration processes associated with the Galactic ISM, except possibly for heavy ions like Fe.

Figure 12.3 shows the original figure published by Hillas in 1984 [320] comparing different astrophysical accelerators based on this criterion. This diagram shows how much more effective mildly relativistic or relativistic flows are for acceleration compared to nonrelativistic flows. It shows that large- Z ions, specifically Fe nuclei, are easier to accelerate to 10^{20} eV energies. It rules out many source classes to accelerate 10^{20} eV particles, including most galactic sources other than highly magnetized neutron stars, mainly young pulsars. Based on this diagram, pulsar wind nebulae like the Crab (though not the Crab pulsar itself) would have difficulty on accelerating even cosmic-ray Fe to $\sim 10^{20}$ eV energies.

It is notable that AGNs, galaxy clusters, and $\gtrsim 10^{12}$ G neutron stars are viable candidate UHECR accelerators. The impact of the relativistic motions of the jet fluids in AGN, GRB, and other jet sources was not fully considered by Hillas, and we take up that subject here.

Absent also from this diagram are the GRBs, whose nature and distance scale were unknown at the time that Hillas wrote, though early papers by Paczynski [294] and Goodman [295] in 1986, and earlier by Usov and Chibisov in 1975 [381], saw the possibilities that GRBs are cosmological in nature.

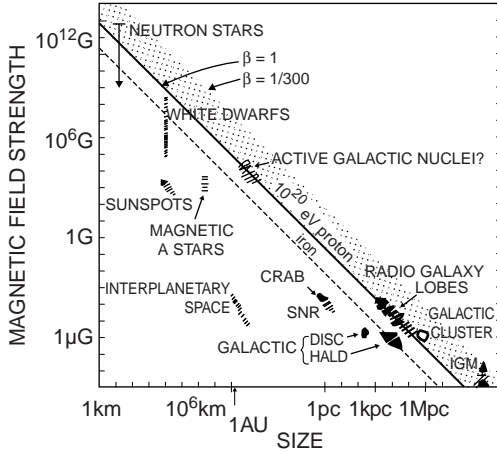


Figure 12.3 Size and magnetic field strength of possible sites of particle acceleration. Objects below the solid (dashed) diagonal line cannot accelerate protons (Fe) to 10^{20} eV [320]. (Figure courtesy of A. M. Hillas.)

12.4 ENERGY GAIN PER CYCLE FROM FERMI ACCELERATION

The particle Lorentz factor in the frame of the fluid moving with speed βc , from the Lorentz transformation eqs. (2.11), is

$$\gamma' = \Gamma \gamma (1 - \beta \beta_{\text{par}} \mu) \xrightarrow{\beta_{\text{par}} \rightarrow 1} \Gamma \gamma (1 - \beta \mu). \tag{12.7}$$

After scattering and becoming isotropized within the moving medium, the particle then escapes and returns back to the original medium, but now with Lorentz factor

$$\gamma_f = \Gamma \gamma' (1 + \beta \beta'_{\text{par}} \mu') \xrightarrow{\beta'_{\text{par}} \rightarrow 1} \Gamma \gamma' (1 + \beta \mu'). \tag{12.8}$$

So, provided that the particle speed $c\beta_{\text{par}} > c\beta$ and further taking the $\gamma \gg 1$, $\beta_{\text{par}} \rightarrow 1$ limit

$$\gamma_f = \Gamma^2 \gamma (1 - \beta \mu) (1 + \beta \mu').$$

For a particle entering and exiting the scattering region with angles $\theta = \arccos(\mu)$ and $\theta' = \arccos(\mu')$, respectively, the fractional energy gain is

$$\frac{\Delta \gamma(\mu, \mu')}{\gamma} = \frac{\gamma(\mu, \mu') - \gamma}{\gamma} = \Gamma^2 (1 - \beta \mu + \beta \mu' - \beta^2 \mu \mu') - 1.$$

The average energy gain per cycle for second-order Fermi acceleration, averaged over entrance and exit angles, is

$$\left(\frac{\Delta\gamma}{\gamma}\right)_{F2} = \frac{\int d\mu' n'(\mu') \int d\mu n(\mu) (1 - \beta\mu) [\Gamma^2 (1 - \beta\mu + \beta\mu' - \beta^2\mu\mu') - 1]}{\int d\mu' n'(\mu) \int d\mu n(\mu) (1 - \beta\mu)}. \quad (12.9)$$

For isotropic particle distributions, the particle directional distribution is given by $n(\mu) = \frac{1}{2}H(\mu; -1, 1)$ and $n(\mu') = \frac{1}{2}H(\mu'; -1, 1)$, and eq. (12.9) gives

$$\left(\frac{\Delta\gamma}{\gamma}\right)_{F2} = \frac{4}{3}\beta^2\Gamma^2 \xrightarrow{\beta \ll 1} \frac{4}{3}\beta^2 \propto \beta^2. \quad (12.10)$$

In the case of first-order Fermi acceleration, the geometry is fundamentally different, involving an infinite planar shock. The average energy gain per cycle in first-order Fermi acceleration, averaged over entrance and exit angles, is

$$\left(\frac{\Delta\gamma}{\gamma}\right)_{F1} = \frac{\int d\mu' n'(\mu') \int d\mu n(\mu) [\Gamma^2\mu(1 - \beta + \beta\mu' - \beta^2\mu\mu') - 1]}{\int d\mu' n'(\mu) \int d\mu n(\mu)}, \quad (12.11)$$

and no longer involves the reaction-rate factor because, in the frame of the shock, there is a velocity discontinuity fixed in the frame of the shock. The flux of particles onto a planar surface is reduced proportionally to μ , μ' for particles with angles $\theta, \theta' \cong \pi/2$. The normalized projection of the flux of particles escaping from the shock is $n'(\mu') = 2\mu'H(\mu'; 0, 1)$. The normalized projection of an isotropic flux of particles onto a plane is $n(\mu) = 2|\mu|H(\mu; -1, 0)$; weighting the flux by μ gives $\int_{-1}^0 d\mu \mu |\mu| = -2/3$. Averaging eq. (12.11) using these fluxes gives

$$\left(\frac{\Delta\gamma}{\gamma}\right)_{F1} = \frac{4}{3}\beta\Gamma^2 + \frac{13}{9}\beta^2\Gamma^2 \xrightarrow{\beta \ll 1} \frac{4}{3}\beta \propto \beta. \quad (12.12)$$

Note the crucial assumption that the accelerated particle distribution is isotropic in the proper frame of the fluid. In fact, this assumption cannot be justified in relativistic, $\Gamma \gg 1$ flows. For nonrelativistic shocks, the relative change in particle momenta per cycle is

$$\left(\frac{\Delta p}{p}\right)_{F1} = \frac{4\beta}{3\beta_{\text{par}}} \xrightarrow{\beta_{\text{par}} \rightarrow 1} \frac{4}{3}\beta. \quad (12.13)$$

12.5 DIFFUSION IN PHYSICAL SPACE

In treatments of particle acceleration, diffusion in momentum space cannot be separated from diffusion in physical space. When no energy losses or

gains take place, however, we can examine the simpler convection-diffusion equation for particle momentum density $n(p, \vec{x})$, given (section 13.2) by

$$\frac{\partial n}{\partial t} = -\vec{\nabla} \cdot (\vec{u}n - \kappa \cdot \vec{\nabla}n), \quad (12.14)$$

where κ is the diffusion tensor. The first term on the right says that the change in the density is proportional to the gradient of the convective flux $\vec{u}n$, and the second term says that the change in density is proportional to the gradient of the diffusive flux $\kappa \cdot \vec{\nabla}n$, which itself is proportional to the gradient of n .

Consider the simplest three-dimensional diffusion scenario without convection and with an isotropic diffusion coefficient. Therefore

$$\frac{\partial n}{\partial t} = \frac{\kappa}{r^2} \frac{\partial^2(r^2n)}{\partial r^2}.$$

Suppose that a source impulsively injects cosmic rays with a power-law spectrum $N(\gamma) = K\gamma^{-p}$. For energy-dependent diffusive propagation, $\kappa = \kappa(\gamma)$, the spectral number density of relativistic cosmic ray ions measured at a distance r away from an impulsive source of cosmic rays that occurred a time t earlier is

$$n(\gamma; r, t) = \frac{K\gamma^{-p}}{\pi^{3/2}r_{\text{dif}}^3} \exp[-(r/r_{\text{dif}})^2]. \quad (12.15)$$

Here the diffusion radius $r_{\text{dif}} \cong 2\sqrt{\kappa(\gamma)t} = 2\sqrt{\lambda ct/3}$, where λ is the diffusion mean free path, and eq. (12.15) assumes that cosmic rays suffer no significant energy losses during transport (see Ref. [196] for the more general case).

In the Bohm diffusion approximation, the diffusion coefficient is defined by the condition that $\lambda = r_L$. Thus the Bohm diffusion coefficient for relativistic particles is $\kappa_B = cr_L/3$. The mean escape timescale from a region of size $\langle R \rangle$, using the Bohm diffusion approximation, is $t_{\text{esc}} = \langle R \rangle^2/2\kappa_B$. The Bohm diffusion approximation serves as a benchmark; particles can be more diffusive than implied by the Bohm approximation if the coherence length of the disordered magnetic field is small compared to the Larmor radius. In contrast, an ordered field can trap particles and impede escape compared to the Bohm approximation.

When $r \ll r_{\text{dif}}$, then

$$n(\gamma; r, t) \propto \frac{\gamma^{-p}}{r_{\text{dif}}^3} \propto \frac{\gamma^{-p-(3/2)(2-q)}}{t^{3/2}} \propto t^{-3/2} \times \begin{cases} \gamma^{-p-1/2} & \text{for } q = 5/3, \\ \gamma^{-p-3/4} & \text{for } q = 3/2. \end{cases} \quad (12.16)$$

The measured spectrum from a bursting source is therefore steepened by $3(2 - q)/2$ units [196,208] when the diffusion coefficient $\kappa \propto \lambda \propto \gamma^{2-q}$ (chapter 14). By comparison, the spectral index is steepened by $(2 - q)$ units for continuous cosmic-ray injection ($q = 1$ for the Bohm approximation).

The theory of cosmic-ray diffusion in the disk and halo of the Galaxy is quite extensive; see, e.g., Refs. [12,114,382,383]. Physical diffusion through regions with different flow speeds is integral to the Fermi mechanism. Consequently a coupled convection-diffusion equation must be examined (chapter 13).

12.6 MAXIMUM PARTICLE ENERGY

The question of maximum particle energy in shocked and turbulent flows is central to the cosmic-ray problem. Lagage and Cesarsky [384] gave an answer to this question for SNR explosions, finding maximum energies

$$E_{\max} \sim 10^{14} Z B_{\mu\text{G}}$$

of ions accelerated in SNR shocks. This energy is well below the proton knee at ≈ 3 PeV, threatening the standard interpretation expressed by Ginzburg and Syrovatskii [385] and Hayakawa [386] that GeV–TeV cosmic rays are accelerated by supernovae. Crucial in making this calculation is the magnetic field and spectrum of wave turbulence in the upstream region responsible for scattering the accelerated particles.

Consider a quasi-homogeneous environment entraining a disordered magnetic field with mean intensity $B_0 = 10^{-6} B_{\mu\text{G}}$ G. An impulsive release of energy into the surroundings forms a shock wave, whose evolution in the coasting and Sedov phase is assumed to follow the behavior of adiabatic blast waves derived in chapter 11. Here we summarize the maximum energy to which a particle can be accelerated in first-order and second-order Fermi processes for a shock wave in this environment. These results are derived in detail in the next two chapters.

The evolution of the blast-wave momentum $P(x) = \beta(x)\Gamma(x)$ in the adiabatic asymptote is described by eq. (11.18) [301], where $P_0 = \sqrt{\Gamma_0^2 - 1} = \beta_0\Gamma_0$ is the initial blast-wave Lorentz factor that defines the baryon loading. The deceleration radius [298,300], eq. (11.2), can be written as

$$\begin{aligned} x_d &\equiv \left(\frac{3(\partial\mathcal{E}_0/\partial\Omega)}{\Gamma_0^2 m_p c^2 \mu_0 n_0} \right)^{1/3} \\ &\cong 6.6 \times 10^{18} \left(\frac{\mathcal{E}_\odot}{\Gamma_0^2 \mu_0 n_0} \right)^{1/3} \text{ cm} \cong 2.1 \left(\frac{\mathcal{E}_\odot}{\Gamma_0^2 \mu_0 n_0} \right)^{1/3} \text{ pc} \quad (12.17) \end{aligned}$$

is defined in terms of \mathcal{E}_\odot , the apparent isotropic energy release of the explosion expressed in units of Solar rest-mass energy, so $\mathcal{E}_\odot = 1 \Leftrightarrow \partial \mathcal{E}_0 / \partial \Omega \cong 1.4 \times 10^{53} \text{ ergs sr}^{-1}$. The term μ_0 gives the average atomic mass of swept-up material in units of m_p , and $\mu_0 \cong 1.4$ for Solar composition material. For a nonrelativistic explosion, $x_d \cong$ the Sedov length $\ell_{\text{Sdv}} = \Gamma_0^{2/3} x_d$.

Maximum Particle Energy at Nonrelativistic Supernova Shocks

As shown in the next chapter, the maximum particle energy possible for a particle accelerated by a quasi-parallel nonrelativistic shock from an explosion with energy \mathcal{E}_\odot and coasting speed $c\beta_0$ taking place in a uniform density environment with density n_0 and mean magnetic field B is

$$E_{\parallel, \text{max}} \simeq 6 \times 10^{15} Z \beta_0 \left(\frac{\mathcal{E}_\odot}{\mu_0 n_0} \right)^{1/3} B_{\mu\text{G}} \text{ eV}. \quad (12.18)$$

The maximum particle energy $E_{\perp, \text{max}}(x_1)$ at x_1 possible for a particle accelerated by a quasi-perpendicular nonrelativistic shock is

$$E_{\perp, \text{max}} \simeq 10^{16} Z \beta_0^{2/3} \left(\frac{\mathcal{E}_\odot}{\mu_0 n_0} \right)^{1/3} B_{\mu\text{G}} \text{ eV}. \quad (12.19)$$

Coasting speeds $\beta_0 c$ are $\beta_0 \sim 10^{-2}$ for Type II SNe and $\beta_0 \lesssim 10^{-1}$ for SNe Ia (table 12.1). This gives results similar to those found by Lagage and Cesarsky [384].

Maximum Particle Energy at Relativistic External Shocks

The maximum energy that can be achieved by relativistic first-order shock acceleration at an external shock is

$$\begin{aligned} E_{\text{max, F1}} &\simeq \bar{\gamma} \Gamma^2(x_0) m c^2 + 3 \times 2^{3/2} q B_{\perp - x_d} \Gamma_0 \\ &\simeq \left[8 \times 10^{13} \bar{\gamma} \Gamma_{300}^2 A + 1.5 \times 10^{16} Z B_{\mu\text{G}} \left(\frac{\mathcal{E}_\odot \Gamma_0}{\mu_0 n_0} \right)^{1/3} \right] \text{ eV}, \quad (12.20) \end{aligned}$$

where $\Gamma = 300 \Gamma_{300}$, and $\bar{\gamma}$ is the Lorentz factor of a particle captured in the first cycle of relativistic shock acceleration.

Besides requiring highly magnetized surroundings, external shock acceleration of $\sim 10^{20}$ eV particles must surmount kinematic difficulties to acceleration [338]. Another approach using first-order shock theory is to have colliding shells, with each shell being highly magnetized.

Table 12.1 Maximum Particle Energy through Fermi Processes in Cosmic Explosions

Explosion type	Outflow speed (km s ⁻¹)	$\langle\beta_0\Gamma_0\rangle$	$\frac{E_{\max,F1} \text{ (eV)}^a}{Z}$	$\frac{E_{\max,F2} \text{ (eV)}^b}{Z}$	t_d^c
SN Ia ^d	$\lesssim 2 \times 10^4$	0.03	$\sim 10^{15}$	$\sim 2 \times 10^{14}$	~ 350 yr
SN II ^d	$\sim 10^3\text{--}2 \times 10^4$	0.01	$\sim 5 \times 10^{14}$	$\sim 2 \times 10^{12}$	~ 200 yr
SN Ib ^{d,e}	$\sim 1.5 \times 10^3\text{--}10^5$	0.1	$\sim 2 \times 10^{15}$	$\sim 2 \times 10^{16}$	~ 700 yr
SN Ic ^e	$\sim 3 \times 10^4\text{--}3 \times 10^5$	0.3	$\sim 4 \times 10^{15}$	$\sim 2 \times 10^{18}$	~ 70 yr
GRBs ^f	3×10^5	~ 300	$\sim 7 \times 10^{16}$	$\sim 10^{20}$	~ 55 s

^a $B_{\mu G} = \mathcal{E}_\odot = 1$, $\mu_0 n_0 = 1 \text{ cm}^{-3}$; $\mu_0 n_0 m_p c^2$ is the mass density of the surrounding medium, assumed homogeneous (section 13.4.3). $\mathcal{E}_\odot \simeq 10^{-3}$, 10^{-2} , and 1 for SNe, hypernovae, and GRBs, respectively.

^b $\epsilon_B = \xi = f_\Delta = \mathcal{E}_\odot = 1$, $\mu_0 n_0 = 1 \text{ cm}^{-3}$, $q = 5/3$ (section 14.8).

^c Deceleration timescale, eq. (11.4), $t_d = x_d/(\Gamma_0 P_0 c)$.

^d Data from [308].

^e Data from [387].

^f Parameters representative of relativistic flows in long-duration GRBs (see figure 11.9).

Maximum Particle Energy in Stochastic Acceleration at Relativistic Shocks

The basic scaling for the maximum energy achieved by stochastic acceleration in a relativistic blast wave is given by the term

$$E_{\max,F2} \equiv q B_* f_\Delta x_d P_0 \simeq 4 \times 10^{20} Z \epsilon_B^{1/2} (\mu_0 n_0)^{1/6} \left(\frac{f_\Delta}{1/12} \right) \beta_0 (\mathcal{E}_\odot \Gamma_{300})^{1/3} \text{ eV.} \quad (12.21)$$

The term f_Δ , which sets the shell width in terms of swept-up material, is nominally set equal to 1/12 for a spherically symmetric explosion in a uniform medium. Stochastic acceleration processes apparently can accelerate particles to $\gtrsim 10^{20}$ eV, but the parameters of the flow— ϵ_B , Γ , n_0 —must be in appropriate (high-end) ranges, or the particles must be ions with relatively large Z .

Hillas [388] points out some other things besides E_{\max} that must be understood for a complete theory of cosmic-ray acceleration, including

1. the cosmic-ray spectral index, anisotropy, and short-residence-time problem;
2. the reason for the low TeV fluxes from SNRs;
3. whether the radiation from SNRs is leptonic or hadronic in origin.

Chapter Thirteen

First-Order Fermi Acceleration

The importance of first-order shock Fermi acceleration in driving ideas about particle acceleration and the origin of the cosmic rays demands a fuller review than a single chapter can provide, but here we present basic results about the first-order Fermi acceleration mechanism that are essential knowledge for deeper study.

We begin by deriving the hydrodynamic relation between Mach number \mathcal{M} and compression ratio χ . The derivation of the convection-diffusion equation for nonrelativistic shocks and nonrelativistic particles is outlined, and the momentum representation of the particle spectrum is extended to relativistic energies. The shock spectral index in nonrelativistic shock acceleration is derived from the convection-diffusion equation and from probability arguments. The solution to the one-dimensional convection-diffusion equation for a velocity jump written in terms of the compression ratio χ is obtained, giving a spectrum $n(p) \propto p^{-2}$ for strong shocks. The underlying required simplification is that scattering centers exist in the fluid to isotropize the particle distribution both upstream and downstream of the shock.

In the test particle limit, spectral steepening occurs for finite-width shocked fluid shells, or when the medium becomes appreciably diffusive. The test particle limit fails due to nonlinear effects from the pressure of the accelerated particles, which flattens the shock transition and hardens the accelerated particle spectrum. Maximum particle energy in first-order Fermi acceleration is derived, and effects of upstream conditioning by the Bell-Lucek mechanism [389,390] are discussed.

Anisotropies are essential to relativistic shock acceleration, so a Fokker-Planck equation in terms of the particle distribution function $f(\mu, p, x)$ is considered [391]. Solving the eigenvalue equation either numerically or analytically gives a number spectral index $A \sim 2.2$ – 2.3 , which is obtained as a limiting case of highly relativistic shocks in the solution by Keshet and Waxman [392]. Kinematic effects limit maximum particle energy from relativistic external shocks [338].

The basic theory of first-order particle acceleration at a nonrelativistic shock was developed by Bell [393,394], Blandford and Ostriker [395],

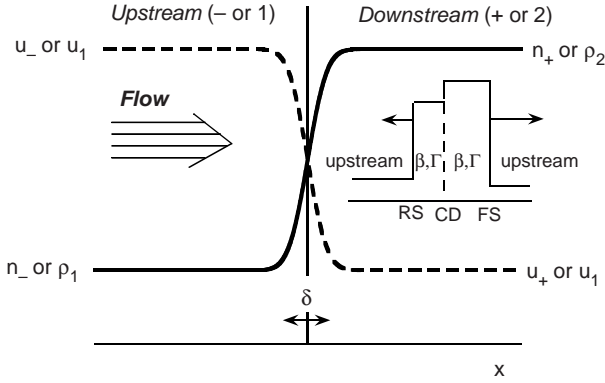


Figure 13.1 Shock geometry in rest frame of shock, with inset showing forward and reverse shock structure.

Krymsky [396], and Axford [397] in the late 1970s. For reviews, see Refs. [398–400].

13.1 NONRELATIVISTIC SHOCK HYDRODYNAMICS

The relationship between the compression ratio χ and Mach number \mathcal{M} for a strong nonrelativistic shock was mentioned in the previous chapter. Here we derive this result.

Conservation of mass, momentum, and energy is satisfied in one dimension by the Rankine-Hugoniot equations generalized for escape:

$$\rho_1 u_1 = \rho_2 u_2 + \Phi_m = \Phi_0, \tag{13.1}$$

$$\rho_1 u_1^2 + P_1 = \rho_2 u_2^2 + P_2 + \Phi_P, \tag{13.2}$$

and

$$\rho_1 u_1 \left(\frac{1}{2} u_1^2 + \frac{\hat{\gamma} P_1}{(\hat{\gamma} - 1) \rho_1} \right) = \rho_2 u_2 \left(\frac{1}{2} u_2^2 + \frac{\hat{\gamma} P_2}{(\hat{\gamma} - 1) \rho_2} \right) + \Phi_E \tag{13.3}$$

[401,402], where the subscript “1” refers to upstream and “2” to downstream (see figure 13.1), $\rho_{1,2}$ and $P_{1,2}$ are the particle mass densities and pressures, respectively, and $\hat{\gamma}$ is the ratio of specific heats ($\hat{\gamma} = 5/3$ for a nonrelativistic monatomic ideal gas). In this expression, the terms Φ_m , Φ_P , and Φ_E represent particle, momentum, and energy flux, respectively, lost from the system.

Defining the compression ratio

$$\chi = \frac{u_1}{u_2}, \tag{13.4}$$

eq. (13.1) becomes

$$\rho_2 = \chi \rho_1 N', \quad N' \equiv 1 - \frac{\Phi_m}{\Phi_0}. \tag{13.5}$$

The upstream (preshock) Mach number $\mathcal{M}_1 = u_1/c_s$, where $c_s = \sqrt{\hat{\gamma} P_1/\rho_1}$ is the local sound speed. Thus

$$\mathcal{M}_1^2 = \frac{\rho_1 u_1^2}{\hat{\gamma} P_1}.$$

Defining

$$Y = P_2/P_1,$$

eq. (13.2) becomes

$$Y = \hat{\gamma} \mathcal{M}_1^2 \left(1 - \frac{N'}{\chi} \right) + 1. \tag{13.6}$$

Defining

$$D \equiv \frac{1}{2} \rho_1 u_1^3,$$

eq. (13.3) can be rewritten as a quadratic in χ , given by

$$\chi^2 \left(1 + \frac{2}{(\hat{\gamma} - 1)\mathcal{M}_1^2} - \frac{\Phi_E}{D} \right) - \frac{2\chi\hat{\gamma}}{(\hat{\gamma} - 1)} \left(1 + \frac{1}{\mathcal{M}_1^2} \right) + \left(\frac{\hat{\gamma} + 1}{\hat{\gamma} - 1} \right) N' = 0. \tag{13.7}$$

For a lossless adiabatic shock wave, $\Phi_E = 0$ and $\Phi_m = 0$, $N' = 1$, and eq. (13.7) reduces to a quadratic with solution

$$\chi = \frac{\hat{\gamma} + 1}{\hat{\gamma} - 1 + 2/\mathcal{M}_1^2}. \tag{13.8}$$

When $\mathcal{M}_1 \gg 1$, $\chi \rightarrow 4$ for a gas with $\hat{\gamma} = 5/3$. It follows from eq. (13.4) that

$$u_1 = \frac{\chi u}{\chi - 1}, \quad u_2 = \frac{u}{\chi - 1},$$

so $u_1 \rightarrow 4u/3$ and $u_2 \rightarrow u/3$ in the limit $\mathcal{M} \gg 1$.

Again in the limit of a large-Mach-number shock, $\mathcal{M}_1 \gg 1$, but now allowing for particle or energy losses, eq. (13.7) can be solved for χ , giving

$$\chi = \frac{[\hat{\gamma}/(\hat{\gamma} - 1)] \pm \sqrt{[\hat{\gamma}/(\hat{\gamma} - 1)]^2 - (1 - \Phi_E/D)N'[(\hat{\gamma} + 1)/(\hat{\gamma} - 1)]}}{1 - \Phi_E/D}. \tag{13.9}$$

The positive root is physically interesting, as the negative root gives $\chi < 1$. If the particle flux lost is small compared to the influx, $\Phi_m \ll \Phi_0 = \rho_1 u_1$, and eq. (13.9) gives, with $\hat{\gamma} = 5/3$,

$$\chi = \frac{5/2 + \sqrt{25/4 - 4(1 - \Phi_E/D)}}{1 - \Phi_E/D} \xrightarrow{\Phi_E/D \ll 1} 4 + \frac{16\Phi_E}{3D} + \mathcal{O}\left(\frac{\Phi_E^2}{D^2}\right). \quad (13.10)$$

When the energy lost is small, that is, for a nonradiative shock, $\Phi_E \ll 1$ and $\chi \rightarrow 4$ for a large-Mach-number shock in a $\hat{\gamma} = 5/3$ gas.

For a relativistic gas, $\hat{\gamma} = 4/3$. The compression ratio of an adiabatic shock in a relativistic shock can be as large as $\chi = 7$. The inclusion of accelerated particle energy in the hydrodynamic description of the gas changes the adiabatic index and the acceleration efficiency, as described in section 13.3.4.

13.2 CONVECTION-DIFFUSION EQUATION

The density of particles differential in momentum p is $n = n(p, \vec{x})$, with units $dN/dV dp$. The convection-diffusion equation describing n is

$$\frac{\partial n}{\partial t} + \vec{\nabla} \cdot (\vec{u}n - \kappa \cdot \vec{\nabla}n) - \frac{1}{3}(\vec{\nabla} \cdot \vec{u}) \frac{\partial(pn)}{\partial p} = 0, \quad (13.11)$$

where κ is the diffusion tensor. We sketch the derivation of this result, assuming the flow speed $|\vec{u}| \ll$ particle speed $|\vec{v}|$.

The invariant phase space density for nonrelativistic particles with velocity \vec{v} is

$$f(\vec{v}) = \frac{dN}{d\mathcal{V}} = \frac{dN}{dV d^3\vec{v}} \quad (13.12)$$

(section 2.4). The shock frame is unprimed, and the frames with isotropic particle distributions are primed (see figure 13.1). For strong nonrelativistic shocks, the upstream flow in the shock frame is approaching with speed $u_- = 4\beta c/3$, and the downstream flow is receding with speed $u_+ = \beta c/3$, so that $u = u_- - u_+ = \beta c$. The velocity discontinuity acts as a source of free energy to be tapped by test particles.

In the nonrelativistic shock limit, particle velocities in the shock frame and frame K' in which the particle distribution is isotropic are related by $\vec{v} = \vec{v}' + \vec{u}$, so that

$$f(\vec{v}) = f'(\vec{v}') = f'(|\vec{v} - \vec{u}|) \cong f'(v) - u\mu \frac{\partial f'(v)}{\partial v}. \quad (13.13)$$

Here $\theta = \arccos \mu$ is the angle of the particle velocity with respect to the direction of the flow, and the final expression uses a Taylor expansion in u/v .¹

Assuming isotropy of the particle distributions in the upstream and downstream flows, the differential particle density satisfies the particle conservation equation

$$\frac{\partial n}{\partial t} + \vec{\nabla} \cdot \vec{S}_c + \frac{\partial}{\partial p} S_p = 0, \quad (13.14)$$

where \vec{S}_c is the physical flux of particles, and S_p is the momentum-space flux. The convective flux across a planar surface is

$$\frac{dN}{dA dt} = \oint d\Omega_{\vec{v}} \int dv v^2 f(\vec{v}) v \cos \theta, \quad (13.15)$$

and the integration is over angles in velocity space.

The differential flux across the shock defined by the direction \vec{u} is therefore

$$\vec{S}_{\text{cnv}} = \frac{dN}{dA dt dp} = \frac{2\pi}{m} \int_{-1}^1 d\mu v^3 \mu \left(f'(v) - u\mu \frac{\partial f'}{\partial v} \right) = -\frac{4\pi}{3m} v^3 \vec{u} \frac{\partial f'(v)}{\partial v}. \quad (13.16)$$

From the definition of the invariant phase space density, eq. (13.12),

$$n'(v') \equiv \frac{dN}{dV dv} = \oint d\Omega_{\vec{v}'} v'^2 f'(\vec{v}') = 4\pi v'^2 f'(\vec{v}'). \quad (13.17)$$

For the stationary frame,

$$n(v) = \oint d\Omega_{\vec{v}} f(\vec{v}) v^2 = 2\pi \int_{-1}^1 d\mu \left(f'(v) - u\mu \frac{\partial f'}{\partial v} \right) = 4\pi v^2 f'(v), \quad (13.18)$$

so $f'(v) = n(v)/4\pi v^2$. Substitution into eq. (13.16) gives

$$\vec{S}_{\text{cnv}} = -\frac{1}{3m} v^3 \vec{u} \frac{\partial}{\partial v} \left(\frac{n(v)}{v^2} \right) = -\frac{\vec{u}}{3} p^3 \frac{\partial}{\partial p} \left(\frac{n}{p^2} \right) = \vec{u} \left(n - \frac{1}{3} \frac{\partial(pn)}{\partial p} \right), \quad (13.19)$$

rewriting the expression in terms of momentum $p = mv$.

The diffusive flux $\vec{S}_{\text{dif}} = -\kappa \cdot \vec{\nabla} n$ is proportional to the gradient of the particle density, so the total flux in physical space from combined convective and diffusive processes is

$$\vec{S}_{\text{cnv+dif}} = -\kappa \cdot \vec{\nabla} n + \left(n - \frac{1}{3} \frac{\partial(pn)}{\partial p} \right) \vec{u}. \quad (13.20)$$

¹The Compton-Getting anisotropy $\Delta I(\mu)/\langle I \rangle = (\gamma_{\text{CR}} + 2)\beta\mu$ of the cosmic-ray intensity follows from this expression, where $\gamma_{\text{CR}} (\cong 2.75$ from ~ 10 GeV–100 TeV) is the number index of the cosmic-ray spectrum [391]; see eq. (8.44).

The flux in momentum space can be obtained by recognizing that particles increase their energy in response to work being performed by pressure gradients. The pressure $P = pvn/3$, so that the force per unit volume is $-\vec{\nabla}P = -\frac{v}{3}\vec{\nabla}(pn)$. The energy dissipation rate is $d\mathcal{E}/dt = -\vec{F} \cdot \vec{u}$, and the flux in momentum space is

$$S_p = \frac{\partial p}{\partial t} = \frac{1}{v} \frac{\partial \mathcal{E}}{\partial t} = \frac{1}{3} \vec{u} \cdot \vec{\nabla}(pn), \quad (13.21)$$

which, combined with eq. (13.20), gives eq. (13.11).

13.3 NONRELATIVISTIC SHOCK ACCELERATION

In the previous section, we freely moved between velocity and momentum representations for particles with speed much in excess of the shock speed. From the Lorentz transformation equation for the parallel component of momentum, eq. (2.13),

$$\beta'_{\text{par}} \gamma' \mu' = p' \mu' = \Gamma \gamma (\beta_{\text{par}} \mu - \beta) = \Gamma p \mu - P \gamma \xrightarrow{\beta_{\text{par}} \rightarrow 1} \gamma (\Gamma \mu - P). \quad (13.22)$$

The transformation at nonrelativistic speeds was $\vec{v} = \vec{v}' + \vec{u}$ or, in momentum representation for the component along the direction of \vec{u} ,

$$p\mu = p'\mu' + P,$$

which has the same form as eq. (13.22) and the same appearance as eq. (13.13) in velocity. Because momentum is the space component of a four-vector, which reduces to velocity in the nonrelativistic limit, the momentum representation is a more convenient description of the particle distribution function across a shock.

In this section, we derive the momentum spectral index of particles from the convection-diffusion equation. Absence of a natural scale in momentum for an infinite planar geometry suggests that power-law spectra are solutions to the particle distribution function formed by a shock discontinuity [403].

13.3.1 Spectral Index from Convection-Diffusion Equation

In one spatial dimension, eq. (13.11) takes the form

$$\frac{\partial n}{\partial t} + \frac{\partial(un)}{\partial x} - \frac{\partial}{\partial x} \left(\kappa \frac{\partial n}{\partial x} \right) = \frac{1}{3} \left(\frac{\partial u}{\partial x} \right) \frac{\partial(pn)}{\partial p}. \quad (13.23)$$

We look for steady solutions. Integration of eq. (13.23) over x from $x \rightarrow -\infty$ to $x = x_+ > 0$ gives

$$u_+n_+ - u_-n_- - \kappa_+ \left. \frac{\partial n}{\partial x} \right|_{x_+} + \kappa_- \left. \frac{\partial n}{\partial x} \right|_{x \rightarrow -\infty} = \frac{u}{3} \left. \frac{\partial (pn)}{\partial p} \right|_{x \cong x_+}. \quad (13.24)$$

The intermediate terms vanish, leaving

$$\frac{\partial (pn_+)}{\partial p} = \frac{3(u_+n_+ - u_-n_-)}{u}. \quad (13.25)$$

With $u = u_- - u_+$ and $\chi = u_-/u_+$, eq. (13.25) can be rearranged to give

$$\frac{\partial n_+}{\partial \ln p} = -A_{\text{tp}}n_+ + \frac{3\chi}{\chi - 1}n_-, \quad (13.26)$$

where

$$A_{\text{tp}} \equiv \frac{2 + \chi}{\chi - 1} = \frac{u_- + 2u_+}{u_- - u_+} \quad (13.27)$$

is the test-particle number index.

Equation (13.26) can be solved by substituting $n_+ = \exp(-A_{\text{tp}} \ln p)g(p)$, reducing this equation to

$$\frac{\partial g(p)}{\partial \ln p} = \frac{3\chi}{\chi - 1} \exp(-A_{\text{tp}} \ln p)n_-, \quad (13.28)$$

with solution

$$g(p) = \frac{3\chi}{\chi - 1} \int_0^p dp' p'^{-(1+A_{\text{tp}})}n_-(p'), \quad (13.29)$$

so that

$$n_+(p) = \frac{3u_-}{u} p^{-A_{\text{tp}}} \int_0^p dp' n_-(p') p'^{(A_{\text{tp}}-1)}. \quad (13.30)$$

Far upstream, a δ -function injection momentum spectrum of particles, $n_-(p') \propto \delta(p' - \bar{p}')$, is transformed into a power law

$$n_+(p) \propto p^{-A_{\text{tp}}}$$

with index A_{tp} given by eq. (13.27).

The function $g(p)$ represents the number of injected particles, so that at momenta larger than the injection momenta,

$$n_+ = n_+(p) = g(p) \times p^{-A_{\text{tp}}} \propto p^{-A_{\text{tp}}}.$$

For strong nonrelativistic shocks, $\chi \rightarrow 4$ (section 13.1) and $A_{\text{tp}} \rightarrow 2$. The shock provides a mechanism to distribute energy over a large range. Practical limits from available time, system size, and the duration of the Fermi process itself limit the particle energy to a calculable maximum.

13.3.2 Spectral Index from Probability Arguments

The average increase in momentum for a particle making a complete cycle in first-order Fermi acceleration at a nonrelativistic shock is, from eq. (12.12), given by

$$\left(\frac{\Delta p}{p}\right)_{\text{F1}} \cong \frac{4}{3}\beta, \quad (13.31)$$

where $u = \beta c = u_- - u_+$. The average particle momentum after k cycles is, when $\beta \ll 1$,

$$p_k = p_0 \prod_{i=1}^k \left(1 + \frac{4}{3}\beta\right) \cong p_0 \left(1 + \frac{4\beta k}{3}\right) \cong p_0 \exp\left(\frac{4}{3}\beta k\right),$$

where p_0 is the injection momentum, so $k = (3/4\beta) \ln(p/p_0)$. The probability per cycle of particle escape downstream from the shock is given by the factor $4u_+/c = 4\beta_+$, as Bell [393] showed. Taking this result at face value for the moment, the change in the integral number of particles per cycle is therefore

$$\frac{dN}{dk} = -4\beta_+ N,$$

so that

$$N = N_0 \exp\left[-\frac{3\beta_+}{\beta} \ln\left(\frac{p}{p_0}\right)\right] = N_0 \left(\frac{p}{p_0}\right)^{-3\beta_+/\beta}. \quad (13.32)$$

Because $N \sim pN(p)$ is an integral number of particles,

$$N(p) \propto \left(\frac{p}{p_0}\right)^{-1-(3\beta_+/\beta)} \propto p^{-(\chi+2)/(\chi-1)} \propto p^{-A_{\text{sp}}}. \quad (13.33)$$

The factor $4u_+/c$ for particle escape downstream is obtained by recognizing that the fraction of particles that escape downstream is the ratio of the convective flux downstream to the flux entering from upstream. The convective flux downstream is $n_0 u_+$. The flux entering from upstream is

$$\Phi_x = \frac{dN}{dA dt} \Big|_x = \int_0^{2\pi} d\phi \int_0^1 d\mu \int_0^\infty dv \mu v^3 f(\vec{v}) = \pi \int_0^\infty dv v^3 f(v). \quad (13.34)$$

Because the total particle density $n_0 = 4\pi \int_0^\infty dv v^2 f(v)$,

$$\frac{d\Phi_x}{dv} = \pi v^3 f(v) = \frac{1}{4}v \frac{dn_0}{dv}.$$

For relativistic particles, $\Phi_x = cn_0/4$, and the escape probability \mathcal{P}_{esc} per cycle is $\mathcal{P}_{\text{esc}} = 4n_0 u_+/n_0 c = 4\beta_+$ [399,404]. The return probability,

that is, the probability that a particle completes a complete cycle without being convected downstream where it no longer samples the shock, is

$$\mathcal{P}_{\text{ret}} = 1 - \mathcal{P}_{\text{esc}} = 1 - 4\frac{u_+}{c} = 1 - 4\beta_+ = \left(\frac{v - u_+}{v + u_+}\right)^2 \quad (13.35)$$

for relativistic particles accelerated at nonrelativistic shocks [405].

13.3.3 Finite Shell Width

As illustrated in the inset to figure 13.1, the spatial extent of the downstream reverse and forward shocked fluids limits particle acceleration in the test particle limit. The steady-state, time-independent diffusion-convection equation, eq. (13.23), is

$$\frac{\partial}{\partial x} \left(un - \kappa \frac{\partial n}{\partial x} \right) = \frac{1}{3} \left(\frac{\partial u}{\partial x} \right) \frac{\partial (pn)}{\partial p} \cong 0, \quad (13.36)$$

where the last relation is true provided we evaluate the expression away from the shock discontinuity where the velocity gradient, $\partial u/\partial x$, vanishes.

Following the treatment of Ellison [402], the solution to eq. (13.36) is, by inspection, given by

$$n_1(x) = c_1 \exp\left(\frac{u_1 x}{\kappa_1}\right) + c_2, \quad x \leq 0, \quad (13.37)$$

$$n_2(x) = c_3 \exp\left(\frac{u_1 x}{\kappa_1}\right) + c_4, \quad x > 0, \quad (13.38)$$

with boundary conditions

$$n_1(x \rightarrow -\infty) = n_-, \quad n_2(x = a) = 0.$$

The relations

$$\begin{aligned} c_1 &= c_3(1 - \mathcal{B}_2) - n_-, \\ c_2 &= n_-, \\ c_4 &= -\mathcal{B}_2 c_3 \end{aligned} \quad (13.39)$$

follow, where

$$\mathcal{B}_{1,2} \equiv \exp\left(\frac{au_{1,2}}{\kappa_{1,2}}\right). \quad (13.40)$$

Continuity of particle flux reads

$$\Phi_x \equiv \left(-\kappa \frac{\partial n}{\partial x} + \frac{2}{3} un - \frac{pu}{3} \frac{\partial n}{\partial p} \right) \Big|_x = \text{const.} \quad (13.41)$$

The upstream particle flux at the shock is

$$\Phi_{x-} = \frac{2}{3}u_1n_- - \frac{u_1}{3}[c_3(1 - \mathcal{B}_2)n_-] - \frac{pu_1}{3} \frac{\partial c_3}{\partial p}(1 - \mathcal{B}_2). \quad (13.42)$$

The downstream particle flux at the shock is

$$\Phi_{x+} = -\frac{u_2c_3}{3}(1 + 2\mathcal{B}_2) - \frac{pu_2}{3} \frac{\partial c_3}{\partial p}(1 - \mathcal{B}_2). \quad (13.43)$$

Equating the two particle fluxes yields the equation

$$p \frac{\partial c_3}{\partial p} + A'c_3 = D'n_-, \quad (13.44)$$

where

$$D' = \frac{3u_1}{(1 - \mathcal{B}_2)u}$$

and

$$A' = \frac{u_1 + 2u_2}{u} - \frac{3u_2}{(1 - \mathcal{B}_2)u} = A_{\text{tp}} + \frac{3}{(\mathcal{B}_2 - 1)(\chi - 1)}. \quad (13.45)$$

The solution to eq. (13.44) can be written

$$c_3 = D' p^{-A'} \int_0^p dp' p'^{(A'-1)} n_-, \quad (13.46)$$

as can be verified by direct substitution. The solution for the downstream particle distribution is

$$n_2(p, x) = \frac{3u_1}{u(\mathcal{B}_2 - 1)} \left[\mathcal{B}_2 - \exp\left(\frac{u_2x}{\kappa_2}\right) \right] p^{-A'} \int_0^p dp' n_-(p') p'^{(A'-1)}. \quad (13.47)$$

Noting that

$$\frac{[\mathcal{B}_2 - \exp(u_2x/\kappa_2)]}{\mathcal{B}_2 - 1} = \frac{1 - \exp[u_2(x - a)/\kappa_2]}{1 - \exp(-u_2a/\kappa_2)},$$

we see that in the regime $u_2a/\kappa_2 \gg 1$

$$n_2(p, x) \cong \frac{3u_1n_-}{u} p^{-A'} \int_0^p dp' n_-(p') p'^{(A'-1)}. \quad (13.48)$$

For a δ -function injection of particles upstream, $n_-(p') = n_0\delta(p' - p'_0)$, and

$$n_2(p, x \ll a) \cong \frac{3u_1n_-}{u} p^{-A'} H(p - p_0) \propto p^{-A'}. \quad (13.49)$$

In the regime $u_2 a / \kappa_2 \ll 1$,

$$n_2(p, x) \rightarrow \frac{3u_1 n_-}{u} \left(1 - \frac{x}{a}\right) p^{-A'} H(p - p_0) \propto p^{-A'}. \quad (13.50)$$

From eq. (13.45), the modified spectral index

$$A' = \frac{\chi + 2}{\chi - 1} + \frac{3}{[\exp(u_2 a / \kappa_2) - 1](\chi - 1)} \xrightarrow{u_2 a / \kappa_2 \ll 1} A_{\text{tp}} + \frac{3\kappa_2}{au_2} \quad (13.51)$$

resulting from diffusion in a finite medium is seen to introduce a spectral steepening compared to the test-particle spectral index A_{tp} , eq. (13.27), obtained for nonrelativistic shock acceleration of a test particle in an infinite medium. Formation of a hard spectrum with $A' \cong 2$ requires the downstream shocked fluid width $a \gg \kappa_2 / u_2$ and $\mathcal{M}_1 \gg 1$ so that $\chi - 1 \gtrsim 1$.

When $\kappa = \kappa(p)$, interesting behaviors are obtained for the accelerated particle distribution function. Models for the diffusion coefficient based on pitch-angle scattering with MHD turbulence are derived in the next chapter. From particle kinetic theory, the isotropic diffusion coefficient can be written as

$$\kappa = \frac{1}{3} \lambda v = \kappa_0 \beta_{\text{par}} (\mathcal{R} / \mathcal{R}_0)^{\alpha_{\mathcal{R}}},$$

where λ is the mean free path, v is the particle speed, and $\mathcal{R} = pc / |Ze|$ is the rigidity. The introduction of an energy-dependent diffusion coefficient softens the spectrum at energies above a characteristic energy defined by $\kappa(\gamma_2) \cong au_2$ when $\alpha_{\mathcal{R}} > 0$.

13.3.4 Cosmic-Ray Pressure and Shock Width

The shock structure has been naively treated as a step-function discontinuity, in which case every test particle samples the same compression ratio χ . With particle pressure in the equation for momentum conservation, eq. (13.2) can be written as

$$\rho_0 u_0^2 + P_0 = \rho(x) u^2(x) + P_g(x) + P_{\text{CR}}(x), \quad (13.52)$$

where far-upstream quantities have subscript “0,” $P_g(x)$ is the gas pressure, and

$$P_{\text{CR}}(x) = \frac{1}{3} \int_{p_{\text{inj}}}^{p_{\text{max}}} d\tilde{p} 4\pi \tilde{p}^3 v(\tilde{p}) f(x, \tilde{p}) \quad (13.53)$$

is the cosmic-ray pressure. Because this pressure is spread out over different length scales, the modified shock structure hardens the accelerated relativistic particle distribution, because increasingly energetic particles sample

larger ranges of the upstream shock region, with consequently a larger range of speeds and therefore compression ratios. The shock structure consists of a precursor shock upstream and a subshock with a sharp transition [405]. Nonrelativistic particles primarily sample the subshock, and relativistic particles sample the range of compression ratios in the precursor.

Rewriting the one-dimensional convection-diffusion equation, eq. (13.23), in terms of the momentum phase-space distribution function

$$f(p, x) = \frac{n(p, x)}{4\pi p^2} \quad (13.54)$$

and including a source term $\mathfrak{q}(p, x)$ gives

$$\frac{\partial f}{\partial t} = \frac{\partial}{\partial x} \left(\kappa \frac{\partial f}{\partial x} \right) - u \frac{\partial f}{\partial x} + \frac{1}{3} \frac{\partial u}{\partial x} \left(p \frac{\partial f}{\partial x} \right) + \mathfrak{q}(p, x). \quad (13.55)$$

If we assume a solution of the form $f(p) = Kp^{-\varpi}$, then $n(p) = 4\pi Kp^{2-\varpi}$, and

$$n(>p) = 4\pi \int_p^\infty d\tilde{p} \tilde{p}^2 f(\tilde{p}) = \frac{pn(p)}{\varpi - 3}. \quad (13.56)$$

Hence

$$\varpi \equiv -\frac{\partial f(p)}{\partial p} = 3 - \frac{\partial \ln n(>p)}{\partial \ln p}. \quad (13.57)$$

From eq. (13.56),

$$n(>p + \Delta p) = 4\pi \int_{p+\Delta p}^\infty d\tilde{p} \tilde{p}^2 f(\tilde{p}) = \mathcal{P}_{\text{ret}} n(>p), \quad (13.58)$$

where $\Delta p = 4\beta p/3$ is the momentum change per cycle, and the integral particle density is reduced over this momentum difference by the return probability $\mathcal{P}_{\text{ret}} = 1 - 4\beta_+$, eq. (13.35). Expanding the integral spectrum

$$n(>p + \Delta p) \cong n(>p) + \Delta p \frac{\partial n(>p)}{\partial p}$$

gives the result

$$\frac{\partial \ln n(>p)}{\partial \ln p} = \frac{-3\beta_+}{\beta}. \quad (13.59)$$

With eq. (13.57), we have

$$\varpi = 3 + \frac{3\beta_+}{\beta} = \frac{3\beta_-}{\beta_- - \beta_+} = 2 + A_{\text{tp}}. \quad (13.60)$$

Generalizing eq. (13.60) and letting $u_- = \beta_-c \rightarrow u_p$, $\beta_+c = u_2$, Berezhko [406] shows

$$\varpi_p = \frac{3u_p}{u_p - u_2} + \frac{d \ln(u_p - u_2)}{d \ln p} = \frac{3u_p}{u_p - u_2} + \frac{1}{(u_p - u_2)} \frac{du_p}{d \ln p}. \quad (13.61)$$

The term u_p has the meaning of the average fluid velocity that a particle with momentum p samples during diffusion. The particle distribution function can then be written as

$$f(p) \cong \frac{\mathfrak{Q}}{4\pi p_{inj}^3} \exp\left(-\int_{p_{inj}}^p \frac{d\tilde{p}}{\tilde{p}} \varpi_{\tilde{p}}\right) \quad (13.62)$$

[407]. For relativistic particles accelerated at nonrelativistic shocks,

$$\varpi_p = 3.5 + \frac{3.5 - 0.5\chi_{sub}}{2\chi - \chi_{sub} - 1} \xrightarrow{\chi \gg \chi_{sub} \gg 1} 3.5, \quad (13.63)$$

where χ_{sub} is the compression ratio of the subshock. Nonlinear effects from the pressure of the cosmic rays on the shock structure cause the relativistic cosmic-ray spectrum to be as hard as -1.5 , considerably harder than the -2 limit in first-order test-particle acceleration. See also Refs. [408–410].

13.3.5 Maximum Particle Energy in Nonrelativistic Shock Acceleration

We now perform standard derivations to determine maximum energies of particles in nonrelativistic first-order shock Fermi acceleration [384,390, 411,412].

Consider relativistic nonthermal particles with $v = \beta_{par}c \approx c$, and Lorentz factor $\gamma \gg 1$. As usual, $u = \beta(x)c = \beta c$ is the speed of the relativistic flow moving with Lorentz factor Γ in the stationary frame, and the blast-wave evolution is described by its bulk momentum $P = \beta\Gamma$. In the comoving primed frame stationary with respect to the shock, the upstream ($-$) flow approaches with speed $u_- = \beta_-c = 4\beta c/3$ and the downstream ($+$) flow recedes with speed $u_+ = \beta_+c = \beta c/3$ and $u = u_- - u_+ = \beta c$.

Momentum Gain Rate for Quasi-Parallel Shocks

Let $p = \sqrt{\gamma^2 - 1}$ represent the dimensionless momentum of a particle with Lorentz factor γ' in the comoving shock frame. Then

$$\dot{p}_{FI} \cong \frac{\Delta p}{t_{cyc}}, \quad (13.64)$$

where the cycle time t_{cyc} is given by the diffusive properties of the upstream and downstream regions. The average change in particle momentum over a

complete cycle for relativistic test particles with $p \gg 1$ is $\Delta p = 4\beta p/3$ when $\beta \ll 1$ (eq. [12.12]), provided that there are scatterers in the upstream and downstream flow to isotropize the particles. In a one-dimensional flow,

$$t_{\text{cyc}} = \frac{4}{v} \left(\frac{\kappa_-}{u_-} + \frac{\kappa_+}{u_+} \right) = \frac{4}{vu_-} (\kappa_- + \chi \kappa_+) \quad (13.65)$$

[411], where $\chi = u_-/u_+ = \rho_+/\rho_-$ is the compression ratio, ρ is the mass density, and the spatial diffusion coefficient

$$\kappa_{\pm} = \frac{1}{3} \lambda_{\pm} v = \frac{1}{3} \eta_{\pm} r_{L\pm} v = \frac{1}{3} \eta_{\pm} r_{L\pm}^0 p v.$$

Here we write diffusion coefficients in terms of the parameters η_{\pm} that give the particle mean free paths scaled to the values implied by the Bohm diffusion limit evaluated in the local magnetic field.

In the Bohm diffusion approximation, the diffusion mean-free path is set equal to the Larmor radius, so $\eta_{\pm} = 1$. Thus the Bohm approximation is

$$\kappa_{B\pm} = \frac{1}{3} r_{L\pm} v,$$

where the Larmor radius

$$r_{L\pm} = r_{L\pm}^0 p = \frac{mc^2}{QB_{\pm}} p. \quad (13.66)$$

The Bohm approximation is a limit if we assume that regions can only be more diffusive than the Bohm approximation, i.e., $\eta_{\pm} > 1$, which limits maximum acceleration rate.

In $q\parallel$ shocks, $B_-/B_+ \cong 1$. Hence

$$\begin{aligned} \dot{p}_{\parallel} &\cong \frac{u_- \beta}{r_{L-}^0 (\eta_- + \chi \frac{B_-}{B_+} \eta_+)} \\ &\cong \frac{u^2}{cr_{L-}^0} \left(\frac{\chi}{\chi - 1} \right) \frac{1}{\eta_- + \chi \eta_+} \lesssim \frac{u^2}{cr_{L-}^0} \left(\frac{\chi}{\chi^2 - 1} \right) \equiv \dot{p}_{\parallel, \text{max}}. \end{aligned} \quad (13.67)$$

The last relation defines the Bohm-diffusion-limit maximum acceleration rate for $q\parallel$ shocks.

For $q\parallel$ shocks, particle acceleration through the shock Fermi mechanism proceeds more rapidly in less diffusive media. Assuming there exist scattering centers to isotropize the particles over a distance $\lambda = \eta r_L$, $\kappa_{\parallel} \propto \eta$ for $q\parallel$ shocks. The rate $\dot{p}_{\parallel} \propto \kappa_{\parallel}^{-1} \propto \eta^{-1}$ is thus largest when $\eta \rightarrow 1$. The maximum rate at which relativistic particles gain energy in a nonrelativistic quasi-parallel shock is

$$\dot{\gamma}_{\parallel, \text{max}} \approx \frac{u^2}{cr_{L-}^0} \left(\frac{\chi}{\chi^2 - 1} \right). \quad (13.68)$$

Momentum Gain Rate for Quasi-Perpendicular Shocks

In q-⊥ shocks, the situation is somewhat different. A scattering event shifts a particle in the \hat{x} direction by a mean distance r_L ; therefore $\lambda \rightarrow r_L$. The effective particle drift speed is reduced by a factor η^{-1} because particles are confined within the gyroradius scale size r_L . Hence $\kappa_{\perp} \cong r_L v / 3\eta$, or $\kappa_{\perp} \cong \kappa_{\parallel} / (1 + \eta^2)$ [413], implying

$$\kappa_{\perp\pm} = \frac{\eta_{\pm}}{1 + \eta_{\pm}^2} \frac{r_{L\pm} v}{3}, \quad r_{L+}^o = \frac{B_-}{B_+} r_{L-}^o = \frac{1}{\chi} r_{L-}^o. \tag{13.69}$$

Equations (13.64), (13.65), and (13.69) together give

$$\dot{p}_{\perp} \cong \frac{u^2}{cr_{L-}^o} \left(\frac{\chi}{\chi - 1} \right) \left(\frac{\eta_-}{1 + \eta_-^2} + \frac{\eta_+}{1 + \eta_+^2} \right)^{-1} \lesssim \frac{u^2}{cr_{L-}^o} \frac{\chi\eta}{\chi^2 - 1} \equiv \dot{p}_{\perp, \max}. \tag{13.70}$$

In this expression, $\eta = \min(\eta_-, \eta_+)$.

For this analysis to apply, two conditions must hold: first, the particle distribution must be isotropic. To maintain an isotropic particle distribution requires

$$\eta \lesssim v/u \sim 1/\beta \tag{13.71}$$

for relativistic particles [413]. Second, if shock drift takes particles to regions of smaller obliquenesses, then the acceleration rate is reduced [413,414]. Particles will drift along a q-⊥ shock to scatter in a region of smaller obliqueness in a homogeneous medium with a directed magnetic field when

$$\frac{\eta r_{L-}}{x} \lesssim \theta_{1/2}. \tag{13.72}$$

Let R_a be the ratio of the energy gain rate at a shock with obliqueness $\cos^{-1} \mu$ to that for the energy-gain rate in the q-∥ case. Jokipii [413] finds

$$R_a(\mu) = \frac{1 + \chi[\mu^2 + \chi^2(1 - \mu^2)]^{-1/2}}{\mu^2 + \frac{1 - \mu^2}{1 + \eta^2} + \chi \frac{[\mu^2 + \chi^2(1 - \mu^2)/(1 + \eta^2)]}{[\mu^2 + \chi^2(1 - \mu^2)]^{3/2}}} \rightarrow \begin{cases} 1 & \text{for } \mu = 1 \text{ (q-}\parallel\text{)}, \\ 1 + \eta^2 & \text{for } \mu = 0 \text{ (q-}\perp\text{)}. \end{cases} \tag{13.73}$$

The relative energy-gain rates scale proportionally to η^2 , and the energy and momentum gain rate \dot{p}_{\perp} for particle acceleration at q-⊥ shocks is enhanced by a factor proportional to η with respect to the Bohm diffusion limit [414]. Eqs. (13.67) and (13.70) span the range of particle acceleration rates in diffusive first-order nonrelativistic shock acceleration.

When $\mu \ll 1$, that is, for nearly perpendicular shocks,

$$R_a \xrightarrow{\mu \ll 1} \frac{1 + \eta^2}{1 + \frac{1}{2}\mu^2(1 + \eta^2)(1 + \chi^{-2})}. \quad (13.74)$$

The ratio of the q_{\perp} to q_{\parallel} acceleration rates declines by a factor of 2 when $R_a(\eta_{1/2}) = \frac{1}{2}R_a(0) = (1 + \eta^2)/2$, implying $\eta_{1/2} = \sqrt{2/(1 + \eta^2)(1 + \chi^{-2})} \cong \sqrt{2/(1 + \eta^2)}$, where the last relation applies for strong shocks. Thus $\eta_{1/2} = \cos(\pi/2 - \theta_{1/2}) \cong \theta_{1/2} \simeq 2^{1/2}/\eta$, when $\eta \gg 1$. From eq. (13.72), $\eta r_{L-}/x \lesssim 2^{1/2}/\eta$ so that $\eta \lesssim \sqrt{x/r_{L-}}$. With the results of eq. (13.71), $\eta_{-} \lesssim \min[\beta^{-1}, \sqrt{x/r_{L-}}]$.

Distance Differentials and Energy Gains

To consider the total energy gain by a particle, it is necessary to relate distance, time, and shock location. Let Γ_{sh} be the Lorentz factor of the shock and (as usual) Γ the Lorentz factor of the shocked fluid, and consider the relativistic shock jump condition for a strong shock, eq. (11.71) [302,415]. For a nonrelativistic shock in a nonrelativistic monotonic gas with $\hat{\gamma} = 5/3$, $\beta_{\text{sh}} = \beta_{-} = 4\beta/3$ and $\beta_{+} = \beta/3$, as already noted. For highly relativistic shocks with $\hat{\gamma} = 4/3$, $\Gamma_s = \Gamma_{-} = \sqrt{2}\Gamma$ and $\Gamma_{+} = \sqrt{9/8}$, implying that the downstream speed $c\beta_{+} = c/3$.

A nonrelativistic shock advances a differential distance $dx = \beta_{\text{sh}}\Gamma_{\text{sh}}cdt' \rightarrow \beta_{\text{sh}}cdt' = u_{-}dt' \cong u_{-}dt$ during the differential time element dt measured in the stationary frame of the external medium in which the explosion source is assumed to be at rest. From the expression for the compression ratio, eqs. (13.4) and (13.8), for a nonrelativistic shock,

$$dx = \frac{\chi}{\chi - 1} udt, \quad (13.75)$$

so that

$$\left. \frac{dp}{dx} \right|_{\parallel} = \frac{\beta}{r_{\text{L}}^o} (\eta_{-} + \chi\eta_{+})^{-1} \lesssim \frac{\beta}{r_{\text{L}}^o} \quad (13.76)$$

and

$$\left. \frac{dp}{dx} \right|_{\perp} = \frac{\beta}{r_{\text{L}}^o} \left(\frac{\eta_{-}}{1 + \eta_{-}^2} + \frac{\eta_{+}}{1 + \eta_{+}^2} \right)^{-1} \lesssim \frac{\eta\beta}{r_{\text{L}}^o}, \text{ provided } \eta \lesssim \max \left(\beta^{-1}, \sqrt{\frac{x}{r_{\text{L}}}} \right). \quad (13.77)$$

The condition $\sqrt{x/r_{\text{L}}} < \beta^{-1} \Rightarrow E > \beta^2 x QB$, and this condition generally holds when evaluating maximum particle energies. The condition $\eta \lesssim \sqrt{x/r_{\text{L}}} \Rightarrow \eta^2 \lesssim (\eta\beta)^{-1}$ or $\eta \lesssim \beta^{-1/3}$, which is obtained by making the approximation $r_{\text{L}} \simeq r_{\text{L}}^o |dp/dx|_{\perp x} \simeq \eta\beta x$. Because $\min(\beta^{-1}, \beta^{-1/3}) = \beta^{-1/3}$

for all $\beta < 1$, we find $|dp/dx|_{\perp x} \simeq \beta^{2/3}/r_L^0$. Thus the maximum energy gain per unit distance for quasi-parallel and quasi-perpendicular nonrelativistic shocks is

$$\left. \frac{dE}{dx} \right|_{\parallel, \max} \simeq \beta Q B_- \quad (13.78)$$

and

$$\left. \frac{dE}{dx} \right|_{\perp, \max} \simeq \beta^{2/3} Q B_- \quad (13.79)$$

13.3.6 Maximum Particle Energy in Nonrelativistic Shocks

We assume that the upstream medium surrounding the explosion entrains a magnetic field with mean intensity $B_- = B_0 = 10^{-6} B_{\mu G}$ G. Importantly, we assume that the accelerated diffusing cosmic rays do not affect this upstream magnetic field value. For a homogeneous surrounding medium, blast-wave evolution is assumed to follow the behavior of the coasting and adiabatic Sedov solutions. The solution fails at x_{rad} when the shocked material becomes highly radiative (see later). The maximum particle energy at blast-wave location $x_1 = y_1 x_d$ possible for a particle accelerated from energy $E_{\parallel, \max}(x_0)$ at location $x_0 = y_0 x_d$ by a q- \parallel nonrelativistic shock is, after integrating eq. (13.78), given by

$$E_{\parallel, \max}(x_1) \cong E_{\parallel, \max}(x_0) + \beta_0 Q B_0 I_{\parallel}(y_0, y_1), \quad (13.80)$$

where

$$I_{\parallel}(y_0, y_1) \equiv \int_{y_0}^{y_1} \frac{dy}{\sqrt{1+y^3}} \cong \begin{cases} y_1 - y_0 & \text{for } y_0 < y_1 \lesssim 1, \\ 3 - y_0 - 2y_1^{-1/2} & \text{for } y_0 \lesssim 1 \lesssim y_1, \\ 2(y_0^{-1/2} - y_1^{-1/2}) & \text{for } 1 \lesssim y_0 < y_1. \end{cases} \quad (13.81)$$

Thus $E_{\parallel, \max} \simeq 3 \times \beta_0 Q B_0 x_d$, noting that $\int_0^{\infty} dy/\sqrt{1+y^3} \cong 2.8$. Consequently,

$$E_{\parallel, \max} \simeq 9500 Z \beta_0 \left(\frac{\mathcal{E}_{\odot}}{\mu_0 n_0} \right)^{1/3} B_{\mu G} \text{ ergs} \simeq 6 \times 10^{15} Z \beta_0 \left(\frac{\mathcal{E}_{\odot}}{\mu_0 n_0} \right)^{1/3} B_{\mu G} \text{ eV}. \quad (13.82)$$

The maximum particle energy $E_{\perp, \max}(x_1)$ at x_1 possible for a particle accelerated from energy $E_{\perp, \max}(x_0)$ at location x_0 by a q- \perp nonrelativistic shock is, integrating eq. (13.79), given by

$$E_{\perp, \max}(x_1) \cong E_{\perp, \max}(x_0) + \beta_0^{2/3} Q B_0 I_{\perp}(y_0, y_1), \quad (13.83)$$

where

$$I_{\perp}(y_0, y_1) \equiv \int_{y_0}^{y_1} \frac{dy}{(1+y^3)^{1/3}} \cong \begin{cases} y_1 - y_0 & \text{for } y_0 < y_1 \lesssim 1, \\ 1 - y_0 + \ln y_1 & \text{for } y_0 \lesssim 1 \lesssim y_1, \\ \ln(y_1/y_0) & \text{for } 1 \lesssim y_0 < y_1. \end{cases} \quad (13.84)$$

Thus $E_{\perp, \max} \simeq [3 + \ln(x_1/10x_d)]\beta_0^{2/3} Q B_0 x_d$, noting that $\int_0^{y_1} dy/\sqrt{1+y^3} \cong 3.15 + \ln(y_1/10)$. The distance where radiative losses start to dominate is at $x_{\text{rad}} \cong 20(E_{\text{ke}}/10^{51} \text{ ergs})^{0.29} n_0^{-0.41} \text{ pc}$ [416,417], where E_{ke} is the kinetic energy of the explosion. In the most extreme case of transrelativistic flows with large kinetic energy, $y_1 \sim 10^2$, so that the maximum value taken by I_{\perp} is ≈ 5 . Consequently,

$$\begin{aligned} E_{\perp, \max} &\simeq 1.6 \times 10^4 Z \beta_0^{2/3} \left(\frac{\mathcal{E}_{\odot}}{\mu_0 n_0} \right)^{1/3} B_{\mu\text{G}} \text{ ergs} \\ &\simeq 10^{16} Z \beta_0^{2/3} \left(\frac{\mathcal{E}_{\odot}}{\mu_0 n_0} \right)^{1/3} B_{\mu\text{G}} \text{ eV}. \end{aligned} \quad (13.85)$$

13.3.7 Amplification of Upstream Medium Magnetic Field

A crucial assumption made in the previous derivation is that the upstream magnetic field is unaffected by the approaching shock wave and the accelerated particle distribution, and so is given by an interstellar value of order a few μG , so $B_{\mu\text{G}} \sim 1$. Cosmic rays diffuse upstream, amplify the magnetic field, and excite Alfvénic and other MHD turbulence through particle streaming instabilities [418,419]. The enhanced magnetic-field energy effectively increases the density of scattering centers and decreases the scattering mean free path to make the medium less diffusive ($\eta \sim 1$). This increases the energy-gain rate (eqs. [13.67] and [13.70]) and therefore the maximum cosmic-ray energy [411].

Alfvén waves are hydromagnetic waves supported by magnetic field tension against density perturbations of the thermal ions with mean mass density ρ_0 , and travel with speed $v_A = B/\sqrt{4\pi\rho_0}$ (see section 14.3), so

$$\beta_A = \frac{v_A}{c} = \frac{B}{\sqrt{4\pi\mu_0 n_0 m_p c^2}} \cong 7.3 \times 10^{-6} \frac{B_{\mu\text{G}}}{\sqrt{\mu_0 n_0}}. \quad (13.86)$$

The energy density in Alfvénic turbulence is

$$U_A \cong \left(\frac{\Delta B}{B} \right)^2 U_B \equiv \left(\frac{\Delta B}{B} \right)^2 \frac{B^2}{8\pi} = \left(\frac{\Delta B}{B} \right)^2 \frac{1}{2} \rho_0 v_A^2, \quad (13.87)$$

where $(\Delta B/B)^2$ is the ratio of turbulent MHD and large-scale magnetic field energy densities.

Energy is dissipated into Alfvénic turbulence by PdV work proportional to the gradient $\partial P_{\text{CR}}(x)/\partial x$ of the cosmic-ray pressure, eq. (13.53), on a characteristic timescale proportional to $\Delta x/v_A$, where Δx is the distance over which the cosmic-ray pressure changes significantly. Thus the rate at which Alfvénic turbulence energy density is generated is given by

$$\frac{dU_A}{dt} = \frac{\partial U_A}{\partial t} + v_{\text{sh}} \frac{\partial U_A}{\partial x} = v_A \frac{\partial P_{\text{CR}}(x)}{\partial x}. \quad (13.88)$$

In steady state, $v_{\text{sh}} \partial U_A / \partial x = v_A \partial P_{\text{CR}}(x) / \partial x$. Integrating over x gives $U_A \approx v_A / v_{\text{sh}} P_{\text{CR}}$, so that with eq. (13.87)

$$\left(\frac{\Delta B}{B} \right)^2 \approx \frac{\rho_0 v_{\text{sh}} v_A}{2U_B} \left(\frac{P_{\text{CR}}}{\frac{1}{2} \rho_0 v_{\text{sh}}^2} \right) = \frac{\beta_{\text{sh}}}{\beta_A} \left(\frac{P_{\text{CR}}}{\frac{1}{2} \rho_0 v_{\text{sh}}^2} \right). \quad (13.89)$$

The quantity in parentheses represents the efficiency for the conversion of the directed kinetic energy into cosmic rays, and may approach unity [420]. A value of 0.1 might be more realistic, otherwise if it were larger the cosmic-ray energy would be lost to MHD turbulence.

For a shock speed $v_{\text{sh}} = \beta_{\text{sh}} c \equiv 10^{-2} \beta_{-2} c$,

$$\frac{\beta_{\text{sh}}}{\beta_A} \cong 1400 \frac{\beta_{-2} \sqrt{\mu_0 n_0}}{B_{\mu\text{G}}},$$

and the energy density in MHD turbulence could potentially be increased orders of magnitude by cosmic-ray streaming. The perturbed magnetic field, from eq. (13.89),

$$\Delta B (\mu\text{G}) \cong 12 \left[B_{\mu\text{G}} \beta_{-2} \sqrt{\mu_0 n_0} \left(\frac{P_{\text{CR}}}{\frac{1}{2} \rho_0 v_{\text{sh}}^2} \right) / 0.1 \right]^{1/2}. \quad (13.90)$$

For ISM magnetic fields $B_{\mu\text{G}} \lesssim 10$, the amplified magnetic field can reach values as large as a few hundred μG in the optimistic case of a mildly relativistic shock, $\beta_{-1} \sim 10$, that converts streaming cosmic-ray energy into Alfvénic turbulence with high efficiency.

Once $\Delta B/B$ exceeds unity, the plasma becomes fully turbulent and the problem becomes nonlinear, so the applicability of the above estimate is uncertain. Bell and Lucek numerically [389] and analytically [390] treat amplification of the upstream magnetic field by streaming cosmic rays. They find that the streaming energy is efficiently transferred to the magnetic field in accord with eq. (13.90).

Substitution of eq. (13.90) into eq. (13.85) gives the maximum energy possible in nonrelativistic shock acceleration,

$$E_{\text{NR,max}} \simeq 2 \times 10^{15} Z \sqrt{B_{\mu\text{G}}} \beta_{-2}^{5/3} \left(\frac{\mathcal{E}_{\odot}^{1/3}}{(\mu_0 n_0)^{1/12}} \text{eV} \right) \sqrt{\left(\frac{P_{\text{CR}}}{\frac{1}{2} \rho_0 v_{\text{sh}}^2} \right)} / 0.1. \quad (13.91)$$

This estimate gives acceleration of protons to maximum energies near the knee of the cosmic-ray spectrum at ~ 3 PeV for Type II SNe, the most common type. For mildly relativistic Type Ib/c SNe, efficient conversion of streaming energy into Alfvén waves, $B_{\mu\text{G}} \sim 10$, and diffusion in the Bohm limit with the amplified magnetic field, the maximum energy in nonrelativistic shock acceleration cannot be substantially increased above $\approx 10^{17} Z$ eV, unless the upstream field is substantially larger [384]. One possibility is that the explosion takes place in the presupernova stellar wind [421], optimistically reaching maximum energies $\approx 10^{17} Z$ eV for the winds of a massive OB or Wolf-Rayet star.

In spite of not reaching ultrahigh energies, first-order Fermi acceleration at supernova shocks is the leading mechanism to explain the origin of the Galactic cosmic rays. Galactic supernovae have adequate energy to power Galactic cosmic rays, and the mechanism efficiently produces hard power-law cosmic-ray spectra independent of specific details about the diffusion process or magnetic field geometry.

13.4 RELATIVISTIC SHOCK ACCELERATION

The success of nonrelativistic diffusive shock acceleration, and the evidence for relativistic jetted outflows, has spurred the effort to extend the theory to relativistic shocks. The underlying assumption in nonrelativistic theory that the accelerated particle distribution is isotropized by scattering in the upstream and downstream fluid frames is violated in relativistic shock acceleration due to anisotropy induced by relativistic beaming.

In the frame of strong nonrelativistic shocks, the upstream flow approaches at speed $4u/3$ and the downstream flow recedes at the speed $u/3$. In the frame of highly relativistic, $\Gamma \gg 1$ shocks, the shock Lorentz factor

$$\Gamma_{\text{sh}} = \sqrt{2}\Gamma, \quad (13.92)$$

from eq. (11.71), so that the Lorentz factor of the receding downstream fluid is

$$\Gamma_{\text{ds}} = \frac{3}{2\sqrt{2}} \quad \text{and} \quad \beta_{\text{ds}} = \frac{1}{\sqrt{3}}. \quad (13.93)$$

13.4.1 Fokker-Planck Equation for a Stationary, Parallel Shock

The simplest geometry of relativistic shock acceleration is a stationary shock with a parallel magnetic field. The transport equation for this case, and for the case of oblique shocks, was derived in the papers by Kirk and Schneider [422] and Kirk and Heavens [423], respectively.

The particle distribution function $f(\mu, p, t)$ is used to describe anisotropic particle distributions in the simplest case of a one-dimensional, gyrotropic flow, where the phase of the particles in the Larmor orbits are random. Particles diffuse by pitch-angle scattering according to the Fokker-Planck transport equation

$$\frac{df}{dt} = \frac{\partial f}{\partial t} + \vec{v} \cdot \vec{\nabla} f = \frac{\partial}{\partial \mu} \left(D_{\mu\mu} \frac{\partial f}{\partial \mu} \right). \quad (13.94)$$

On other timescales, the particles diffuse in momentum space, for example, due to energy losses.

The diffusion coefficients are given in terms of the spectrum of plasma waves in the plasma, which in turn depend on the particle distribution function, so that the treatment as expressed by simplification of eq. (13.94) is quasi-linear. For isotropic turbulence making isotropic pitch-angle scattering,

$$D_{\mu\mu} \sim \frac{(\Delta\mu)^2}{t_{\text{scat}}} \sim \frac{(\Delta\psi)^2}{t_{\text{scat}}} \left(\frac{\Delta\mu}{\Delta\psi} \right)^2 \sim (1 - \mu^2) \frac{(\Delta\psi)^2}{t_{\text{scat}}} \propto (1 - \mu^2),$$

where t_{scat} is the characteristic timescale for isotropization through pitch-angle scattering. The last expression refers to isotropic turbulence and an isotropic pitch-angle scattering coefficient ($\Delta\psi$ independent of direction).

Thus we write eq. (13.94) as

$$\frac{\partial f}{\partial t} + v\mu \frac{\partial f}{\partial x} = \frac{\partial}{\partial \mu} D_{\mu\mu}(p)(1 - \mu^2) \frac{\partial f}{\partial \mu}, \quad (13.95)$$

and the newly defined diffusion coefficient $D_{\mu\mu}(p)$ is independent of μ in quasi-linear theory for certain properties of the waves. Transforming to the shock frame with variables x_{sh} and t_{sh} and considering the steady situation $\partial f / \partial t = 0$ gives the transport equation [422]

$$G(\beta + \mu) \frac{\partial f(\mu, p, x_{\text{sh}})}{\partial x_{\text{sh}}} = \frac{\partial}{\partial \mu} (1 - \mu^2) \frac{\partial f(\mu, p, x_{\text{sh}})}{\partial \mu}, \quad (13.96)$$

and $G = [(1 - \mu^2)D_{\mu\mu}(p)]^{-1}$. By solving the eigenvalue problem [422, 424], general solutions are obtained upstream and downstream of the shock. The two solutions are matched at the shock to obtain the spectral index and anisotropic distribution by taking into account a sufficient number of eigenfunctions.

13.4.2 Spectral Index in Relativistic Shock Acceleration

The spectral index in relativistic shock acceleration has been studied numerically [425,426] and analytically [391,424]. Values of number index between 2.2 and 2.3 were calculated numerically, in agreement with analytic results obtained by solution of an eigenfunction equation for the stationary transport equation describing the particle anisotropy [422,424]. Keshet and Waxman [392] obtain an index $\varpi = 38/9$, that is, a number index of $20/9 = 2.22$.

They start with eq. (13.96) in the form

$$\gamma(\beta + \mu) \frac{\partial f(\mu, p, \tau)}{\partial \tau} = \frac{\partial}{\partial \mu} (1 - \mu^2) \frac{\partial f(\mu, p, \tau)}{\partial \mu}, \quad (13.97)$$

applied to particles in the downstream or upstream frame. The variable $\tau \equiv \gamma^{-1} \int^x D_2(p, \tilde{x}) d\tilde{x}$ assumes the separation $D_{\mu\mu} = D_1(\mu) D_2(p, x) = (1 - \mu^2) D(\mu) D_2(p, x)$ of the diffusion coefficient.

The boundary conditions on the particle distribution functions are

$$f_u(\mu_u, p_u, \tau = 0) = f_d(\mu_u, p_u, \tau = 0)$$

and

$$f_u(\mu_u, p_u, \tau \rightarrow -\infty) = 0 \quad \text{and} \quad f_d(\mu_u, p_u, \tau \rightarrow \infty) = f_\infty p_d^{-s}.$$

By inspection of the vanishing of the left-hand side of eq. (13.97), it is clear that $\partial j / \partial \mu = 0$ at $\mu = \beta$, where $j = D_{\mu\mu} (\partial f / \partial \mu)$ is the diffusive flux. Thus it makes sense to expand the particle distribution function f about the variable $\mu + \beta$.

Doing this leads to a relation between the particle spectral index s_{iso} for upstream and downstream fluid speeds, $\beta_u c$ and $\beta_d c$, respectively, and the parameters characterizing anisotropies of the particle distribution function and diffusion coefficient at the shock front. The transport equation is expanded in various powers of anisotropy parameters, considering limiting forms of the shock front distributions. Assuming essentially isotropic turbulence downstream of the shock gives

$$s_{\text{iso}} = (3\beta_u - 2\beta_u \beta_d^2 + \beta_d^3) / (\beta_u - \beta_d). \quad (13.98)$$

For highly relativistic shocks,

$$s_{\text{iso}}(\beta_u \rightarrow 1, \beta_d \rightarrow 1/3) = \frac{38}{9} = 4.222 \dots, \quad (13.99)$$

in good agreement with numerical simulations. See Ref. [392] for details.

13.4.3 Maximum Particle Energies in Relativistic Shock Acceleration

It is simplest to work in the frame of the upstream medium to calculate the maximum energy of particles accelerated by a relativistic external shock. In the first cycle, a particle increases its energy by a factor Γ^2 but, due to kinematics of escape and capture, the particle increases its energy by only a factor ≈ 2 in successive cycles, as shown by Gallant and Achterberg [338]. This is because a particle is captured by the advancing relativistic shock when the particle is deflected by an angle $\theta_d \sim 1/\Gamma_s$, so that the upstream cycle time is $t_u \sim (\Gamma_s \omega_{\perp-})^{-1}$. Here the particle gyration frequency in the upstream medium is $\omega_{\perp-} = v/r_{L-}$, where v is the particle speed and the particle deflection is determined by $B_{\perp-}$, the transverse component of the magnetic field in the upstream region. As a result, the nonthermal particle distribution function at relativistic shock is highly anisotropic [422]. The cycle time is dominated by the upstream transit time [338].

Because the energy increases by a factor $\cong 2$ during a single cycle, the momentum gain rate following the first cycle in relativistic shock acceleration is

$$\dot{p}_{\text{rel}} \simeq \frac{2p}{t_u} \simeq \frac{2cQB_{\perp-}\Gamma_s}{mc^2}, \tag{13.100}$$

provided $\Gamma_s \gg 1$. Because $dx = \beta_s c dt$, $|dE/dx|_{\text{rel}} \simeq 2QB_{\perp-}\Gamma_s$, and we have

$$E_{\text{rel}}(x_1) \simeq E_{\text{rel}}(x_0) + 2^{3/2}QB_{\perp-}\Gamma_0 x_d I_{\parallel}(y_0, y_1). \tag{13.101}$$

If the particles are captured in the first cycle with Lorentz factor $\bar{\gamma}$, then the energy from the first cycle of Fermi acceleration in the stationary frame is $\approx \Gamma^2 \bar{\gamma} mc^2$ [427]. The maximum energy that can be achieved by relativistic first-order shock acceleration at an external shock is therefore

$$E_{\text{rel,max}} \simeq \bar{\gamma} \Gamma^2(x_0) mc^2 + 3 \times 2^{3/2}QB_{\perp-}x_d \Gamma_0 \\ \simeq \left[8 \times 10^{13} \bar{\gamma} \Gamma_{300}^2 A + 10^{17} Z B_{\mu G} \left(\frac{\mathcal{E}_{\odot} \Gamma_{300}}{\mu_0 n_0} \right)^{1/3} \right] \text{eV}, \tag{13.102}$$

where $\Gamma = 300\Gamma_{300}$. From eq. (13.102), we see that it is difficult to accelerate particles to energies larger than a factor $\sim 2^{1/3}\Gamma_0^{1/3}$ over $E_{\perp,\text{max}}$, given by eq. (13.85), unless a preexisting energetic particle distribution with Lorentz factors $\bar{\gamma}$ is found in the vicinity of the explosion. Higher energies can be obtained though single-cycle acceleration than through continuous Fermi acceleration if $\Gamma_0 > \Gamma \gtrsim 2 \times 10^4 (Z B_{\mu G}/A \bar{\gamma})^{3/5} (\mathcal{E}_{\odot}/\mu_0 n_0)^{1/5}$, as can be verified by comparing the two terms in eq. (13.102).

Following the deceleration of the blast wave from relativistic speeds, little subsequent acceleration occurs because of the size-scale limitation on non-relativistic flows to be able to capture the diffusing particles. This condition implies $r_{L-} < x$, which means that $E \lesssim 10^{15} Z B_{\mu G}[x \text{ (pc)}] \text{ eV}$. Noting this constraint, equations [13.82] and [13.85] provide reasonable estimates of the largest particle energy that can be obtained through first-order Fermi acceleration in nonrelativistic and mildly relativistic external shocks of supernovae and black-hole jets.

Chapter Fourteen

Second-Order Fermi Acceleration

The mean energy gain per cycle in second-order Fermi acceleration was derived in section 12.4. Revisiting this point, let us consider a test particle that changes energy by first entering a magnetized cloud, scattering around until isotropized, and then leaving the cloud, as shown in figure 14.1. If γ_1 is the initial Lorentz factor of the particle, then its Lorentz factor in the cloud is $\gamma'_1 = \Gamma\gamma_1(1 - \beta\beta_1\mu_1)$, where $\arccos \mu_1$ is the angle between the cloud direction of motion and the direction of the particle. For isotropic elastic scattering, the Lorentz factor γ'_2 of the scattered particle is the same as the initial Lorentz factor, so that $\gamma'_2 = \gamma'_1$. After leaving the scattering cloud, the particle's Lorentz factor in the stationary frame is $\gamma_2(\mu'_2) = \Gamma\gamma'_2(1 + \beta\beta'_2\mu'_2)$.

Averaging the particle energy, assuming isotropic scattering in the frame of the magnetized cloud, gives

$$\langle \gamma_2 \rangle = \frac{1}{2} \int_{-1}^{+1} d\mu'_2 \gamma_2(\mu'_2) = \Gamma\gamma'_2 = \Gamma^2\gamma_1(1 - \beta\beta_1\mu_1).$$

In the course of performing a cycle by entering the cloud, scattering around, and isotropically exiting to the surrounding medium, the relative change of the particle energy or Lorentz factor is

$$\begin{aligned} \frac{\Delta\gamma}{\gamma_1} &= \Gamma^2(1 - \beta\beta_1\mu_1) - 1 \\ &= \frac{1 - \beta\beta_1\mu_1}{1 - \beta^2} - 1 \xrightarrow{\beta \ll 1, \beta_1 \rightarrow 1} -\beta\beta_1\mu_1 + \beta^2 + \mathcal{O}(\beta^3). \end{aligned}$$

Averaging the mean energy loss over the rate factor gives

$$\begin{aligned} \left\langle \frac{\Delta\gamma}{\gamma_1} \right\rangle &= \frac{\int_{-1}^1 d\mu_1 (1 - \beta\mu_1) (\Delta\gamma/\gamma_1)}{\int_{-1}^1 d\mu_1 (1 - \beta\mu_1)} = \left(1 + \frac{\beta_1}{3}\right) \beta^2 \Gamma^2 \\ &\xrightarrow{\beta_1 \rightarrow 1} \frac{4\beta^2 \Gamma^2}{3} \xrightarrow{\beta \ll 1} \frac{4\beta^2}{3} \propto \beta^2. \end{aligned} \quad (14.1)$$

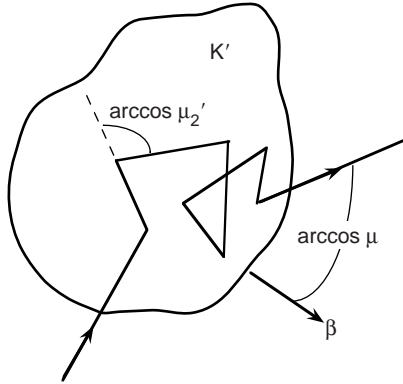


Figure 14.1 Second-order Fermi acceleration due to elastic scattering with magnetized clouds moving in random directions.

This process is referred to as “second-order” acceleration because the relative energy change in a cycle is proportional to the square of the speed of the magnetized clouds. Since Fermi’s time, the magnetized clouds have been replaced with MHD waves that cause diffusion in direction and energy due to pitch-angle scattering and second-order energy changes as the particles are accelerated and decelerated by gyroresonant interactions with MHD plasma waves.

A presentation of second-order Fermi theory is given here that is based on gyroresonant scattering of particles by plasma waves. The resonance condition that couples the MHD wave and particle motions is introduced, followed by a summary of plasma waves that can produce second-order acceleration. A description of diffusive particle acceleration is presented. The Ramaty-Lee equation for hard-sphere diffusive scattering is derived, and more general solutions are mentioned. The chapter ends with a derivation of maximum particle energy achievable by second-order processes in the shocked fluid shells made by nonrelativistic and relativistic outflows.

Implicit in the treatment of second-order acceleration is the correctness of the diffusion approximation. A momentum-diffusion equation is not valid when the momentum changes are large compared with the total particle momentum. Large, ~ 1 radian pitch-angle changes per interaction also renders the pitch-angle diffusion equation invalid. Typically, particles will diffuse along large scale magnetic field, which itself could have a complex geometry. The diffusion approximation is also invalid in a system where the magnetic field is so strong that electrons lose energy and are forced to follow the large-scale magnetic field direction, like in pulsars or magnetars. Only scenarios where the diffusion approximation applies are considered here.

14.1 POWER-LAW PARTICLE SPECTRA FROM SECOND-ORDER FERMI ACCELERATION

The remarkable feature about statistical or stochastic second-order Fermi acceleration is that it naturally makes a power-law spectrum of accelerated relativistic particles. Consider that the number of particles surviving without escape to Lorentz factor γ is just the exponential factor

$$N(>\gamma) \propto \exp\left(-\int_{\gamma_i}^{\gamma} \frac{d\gamma'}{\dot{\gamma}_{\text{acc}} t_{\text{esc}}}\right).$$

We have just seen that $\dot{\gamma}_{\text{acc}} \cong 4\beta^2\gamma/(3t_{\text{cyc}})$, where t_{cyc} is the time to complete a complete cycle in Fermi acceleration. Assuming that particles escape from the system of magnetic scattering clouds with timescale $t_{\text{esc}} = f_{\text{cyc}} t_{\text{cyc}}$, then

$$N(\gamma) \propto \left(\frac{\gamma}{\gamma_i}\right)^{-(1+3/4\beta^2 f_{\text{cyc}})}. \quad (14.2)$$

The main difficulty in arguing that this mechanism is responsible for cosmic-ray acceleration, as Fermi himself recognized, is that this model lacks an explanation as to why the index $(1 + 3/4\beta^2 f_{\text{cyc}})$ coincides with the measured number index (≈ 2.7) of the cosmic rays.

14.2 THE RESONANCE CONDITION

Waves in magnetized plasma have, in general, an electric field component transverse to the ambient magnetic field \mathbf{B}_0 , as well as a component parallel to \mathbf{B}_0 . These two components strongly affect charged particle motion through resonant interactions. A resonant interaction between a particle and the transverse electric field of a wave occurs when the Doppler-shifted wave frequency is a multiple of the particle cyclotron frequency in the particle guiding-center frame. Additionally, the sense of rotation of the transverse electric field and the particle gyration must be the same.

Depending on the initial relative phase of the particle and wave, the particle will see either an accelerating or a decelerating electric field along its transverse direction of motion over a substantial fraction of a cyclotron period, resulting in a relatively large energy gain or loss, respectively.

A MHD wave with frequency ω and wavenumber k is in resonance with an electron with Lorentz factor γ when the resonance condition,

$$\omega - k_{\parallel} v_{\parallel} + \zeta_{\pi} \zeta_q \frac{l\Omega}{\gamma} = 0 \quad (14.3)$$

is satisfied. Here

$$\Omega = \frac{|Q|B}{mc}$$

is the nonrelativistic gyrofrequency of the particle with charge Q and mass m , k_{\parallel} and v_{\parallel} are the parallel wavenumber and parallel particle speed, respectively, and B is the intensity of the large-scale magnetic field. The polarization index $\varsigma_{\pi} = +1$ (-1) for right-hand circularly polarized R (left-hand circularly polarized L) waves, and the charge index $\varsigma_q = +1$ (-1) for positively (negatively) charged particles; different conventions are also adopted [428]. The harmonic number l is equal to zero for resonance with the parallel electric field, but is equal to $\pm 1, \pm 2, \dots$ for resonance with the transverse electric field.

The resonance condition can be derived by transforming to the guiding center frame of the particle moving with velocity $v_z \hat{z} = c\beta_z \hat{z}$ along the direction of the magnetic field. The frequency of the wave in the particle's rest frame, given by $\omega_c = \gamma_z(\omega - v_z k)$ where $\gamma_z = (1 - \beta_z^2)^{-1/2}$, is equal to the gyrofrequency of the particle in the guiding center rest frame $\Omega_{gc} = \gamma_z(\varsigma_q \Omega / \gamma)$. Hence $|\omega - kv_z| = |\varsigma_q \Omega / \gamma|$ [429].

For the electron, proton, and ion cyclotron frequencies, we define

$$\Omega_e = \frac{eB}{m_e c}, \quad \Omega_p = \frac{eB}{m_p c}, \quad \text{and} \quad \Omega_i = \frac{ZeB}{m_i c},$$

respectively, where $m_i = Am_p$ is the ionic mass. Note that these various frequencies are defined in terms of a large-scale magnetic field of strength B . If the energy density in the plasma waves starts to approach $B^2/8\pi$, then the field becomes disordered and there may be no well-defined gyrofrequency. We work in the *quasi-linear* approximation where $\int_0^{\infty} dk w(k) \ll B^2/8\pi$.

Resonances with $l \neq 0$ primarily change the transverse particle momentum and therefore its pitch angle. The pitch-angle scattering accompanies not only diffusion in momentum space but also diffusion in physical space. When the resonance condition is not satisfied, the time over which a particle can be influenced by a wave is much shorter, and the effect on the particle becomes negligible. For $l = 0$, resonance between a particle and the parallel electric field occurs when the parallel phase speed of the particle approximately equals the parallel phase speed of the wave. Depending on whether the parallel particle speed is slightly less than or greater than the parallel phase speed, the particle will become trapped in a potential trough and either be accelerated up to phase speed or decelerated down to this speed, respectively.

The $l = +1$ case is called the normal Doppler resonance, and is relevant when the handedness of the transverse electric field of the wave is the same

as that for the gyrational motion of the particle; $l = -1$ corresponds to the anomalous Doppler resonance, which is appropriate when the handedness of the field and particle are opposite. The transverse electric field can be decomposed into right- and left-hand circularly polarized components, so that both $l = \pm 1$ should be considered for a given wave and particle.

14.3 PLASMA WAVES

The frequency and wave vector \vec{k} are related through the warm-plasma dispersion relations [430]. The phase speed v_ϕ and group speed v_g are defined as

$$v_\phi = \frac{\omega}{k} \quad \text{and} \quad v_g = \frac{\partial \omega}{\partial k}. \quad (14.4)$$

Waves can be modulated and made to carry information; these waves travel with speed $v_g < c$ as compared to v_ϕ , the phase speed of a wave crest in an infinite wave train of MHD waves, which can exceed c in plasma but carries no information.

The generation of electron plasma waves with a parallel electric field that could contribute to resonant acceleration is not considered here. Here we consider, for simplicity, only the cold-plasma approximation, and parallel propagating circularly polarized modes in a fully ionized hydrogen plasma. Calculating these modes and the associated diffusion coefficients is the province of plasma astrophysics, and can only be briefly summarized here [383, 429–432].

The cold-plasma approximation, which involves neglecting the particle temperatures, results in a much simpler dispersion relation for electron waves, which is also accurate when the waves are near a cyclotron frequency or other natural frequency of the system, such as the electron plasma frequency [433]. The plasma frequency ω_p is defined by

$$\omega_p^2 = \frac{4\pi n_0 e^2}{m_e} + \frac{4\pi n_0 e^2}{m_p} \cong \frac{4\pi n_0 e^2}{m_e}. \quad (14.5)$$

Defining

$$a_\beta = \frac{\omega_p^2}{\Omega_e^2} \cong \frac{m_e c^2 n_e}{2U_B}, \quad (14.6)$$

where n_e is the electron density and $U_B = B^2/8\pi$, the cold-plasma dispersion relation takes the form

$$\frac{k^2 c^2}{\Omega_e^2} = \frac{\omega^2}{\Omega_e^2} \left(1 - \frac{a_\beta}{[(\omega/\Omega_e) - \zeta_q][(\omega/\Omega_e) + \zeta_q(m_e/m_p)]} \right). \quad (14.7)$$

The Alfvén speed

$$v_A = \frac{B}{\sqrt{4\pi n_p m_p}}, \quad (14.8)$$

so that

$$\beta_A = \frac{v_A}{c} = \sqrt{\frac{m_e}{m_p a_\beta}}. \quad (14.9)$$

Note that $a_\beta = 4\pi m_e c^2 n_e / B^2 \sim u_{\text{par}} / u_B$ is the plasma beta factor, with $a_\beta \ll 1$ for magnetically dominated (low-beta) plasmas, and $a_\beta \gg 1$ in (high-beta) plasmas with particles dominating the energy density. From eq. (14.9),

$$a_\beta = \frac{m_e}{m_p \beta_A^2}. \quad (14.10)$$

Equation (14.10) shows that $\beta_A > \sqrt{m_e / m_p}$ for a low- β plasma.

The R and L waves resonate with Ω_e and Ω_p , respectively. Each mode also has a plasma cutoff that depends on the value of (ω_p / Ω_e) .

From eq. (14.7), $kc = \omega \sqrt{1 - a_\beta m_p / m_e}$ for $\omega \ll \Omega_p$ and $kc = \omega \sqrt{1 - a_\beta / (\omega / \Omega_e)}$ for $\Omega_p \ll \omega \ll \Omega_e$. In the first case, when $\omega \ll \Omega_p$, we have the high-frequency, small-wavevector Alfvén wave branch with

$$\omega = \frac{kc\beta_A}{\sqrt{1 - \beta_A^2}}. \quad (14.11)$$

As the frequency approaches Ω_p , the L waves become proton cyclotron waves and cease to propagate in the plasma. The R waves in the second case have dispersion relation

$$\omega \cong \frac{k^2 c^2}{a_\beta \Omega_e} = \frac{k^2 c^2 \Omega_e}{\omega_p^2}. \quad (14.12)$$

These low-frequency waves, which can gyroresonate with low-energy suprathermal electrons are called whistlers. Figure 14.2 gives the dispersion relation for a magnetized plasma with $\omega_p / \Omega_e = \sqrt{10}$ [429].

Plasma waves may be electronic or ionic, and electrostatic or electromagnetic. Electrostatic electron waves are electron density perturbations that propagate at thermal speeds $v_{\text{th}} = \sqrt{2k_B T / m_e}$. These are plasma oscillations, or Langmuir waves, with dispersion relation

$$\omega^2 = \omega_p^2 + v_{\text{th}}^2. \quad (14.13)$$

When a magnetic field is present, electrostatic electron waves with transverse components meet a resonance at the electron plasma frequency. These are upper hybrid oscillations, with dispersion relation

$$\omega^2 = \omega_p^2 + \Omega_e^2. \quad (14.14)$$

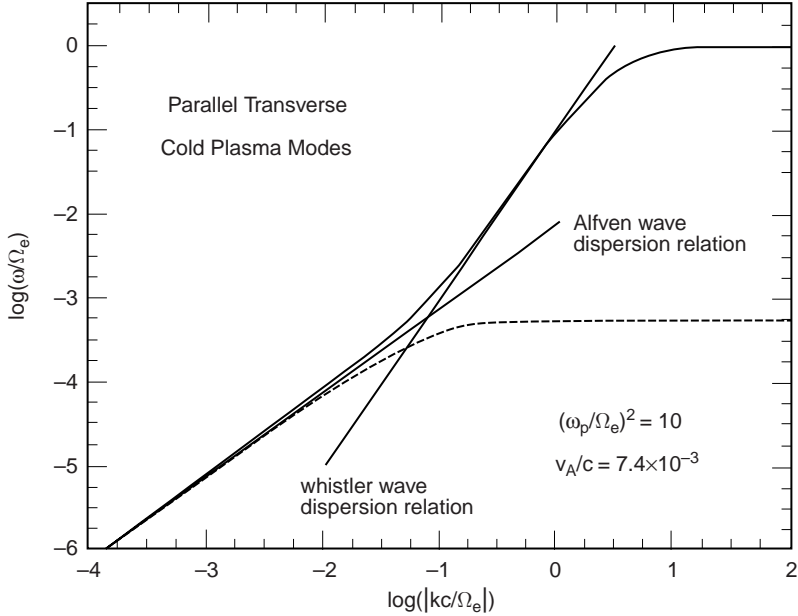


Figure 14.2 Normalized dispersion relations for parallel transverse waves in a cold hydrogen plasma. The solid curves are for right-hand circularly polarized waves, which become the fast-mode branch when $\omega \ll \Omega_p$ and the whistler branch at $\Omega_p \lesssim \omega \lesssim \Omega_e$. The dashed curve is for left-hand circularly polarized waves, which are the shear Alfvén waves when $\omega \ll \Omega_p$ [429]. (Figure courtesy of J. Steinacker and J. Miller.)

An electrostatic ionic density disturbance propagates more slowly than an electron plasma wave due to the greater mass of the ions. These are ion acoustic, or ion sound waves. When a field is present, and the wave has a transverse component along the field direction ($\hat{k} \times \vec{B}_0 \neq 0$), ion density waves meet the ion-cyclotron resonance. These are electrostatic ion-cyclotron waves, with dispersion relation

$$\omega^2 = \Omega_i^2 + k^2 v_i^2, \tag{14.15}$$

and $v_i = \sqrt{k_B T / m_i}$.

Electromagnetic waves propagating in an unmagnetized plasma have the well-known dispersion relation

$$\omega^2 = \omega_p^2 + k^2 c^2. \tag{14.16}$$

When a magnetic field is present and $\vec{k} \parallel \vec{B}$, electromagnetic electron waves propagate with dispersion relation

$$c^2 k^2 = \omega^2 - \frac{\omega_p^2}{1 \pm \Omega_e/\omega}, \quad \begin{cases} + & \text{for L waves} \\ - & \text{for R or whistler waves.} \end{cases} \quad (14.17)$$

Other electromagnetic electron waves are the ordinary and extraordinary waves.

The nonrelativistic cold-temperature parallel-propagating ($\vec{k} \parallel \vec{B}$) Alfvén wave is dispersionless, with dispersion relation

$$\omega = v_A |k_{\parallel}|. \quad (14.18)$$

When $\vec{k} \perp \vec{B}$, magnetosonic waves with dispersion relation

$$\frac{\omega^2}{k^2} = c^2 \frac{v_i^2 + v_A^2}{c^2 + v_A^2} \quad (14.19)$$

can propagate.

When $\omega \ll \Omega_p$, the L mode is referred to as the shear Alfvén wave, while the R mode is referred to as the fast-mode wave. Both have dispersion relation $\omega = v_A |k_{\parallel}|$. The shear Alfvén mode has a resonance at $\omega = \Omega_p$. As $\omega \rightarrow \Omega_p$, k_{\parallel} on the shear Alfvén branch approaches infinity, and waves in this regime are called ion-cyclotron waves. The fast-mode waves pass through Ω_p and become whistlers in the regime $\Omega_p \ll \omega \ll \Omega_e$, where Ω_e is the electron gyrofrequency. The whistler dispersion relation, from eq. (14.12) or eq. (14.17), is

$$k_{\parallel}^2 = \frac{\omega_p^2 \omega}{c^2 \Omega_e}. \quad (14.20)$$

As $\omega \rightarrow \Omega_e$, whistlers become electron cyclotron waves.

For parallel waves, higher-order gyroresonances are not as important as the $l = \pm 1$ values. Inserting the low-frequency dispersion relation into the resonance condition, eq. (9.13), we have that, for protons, $\omega - kv\mu - \zeta\pi\zeta_q(\Omega_p/\gamma) = 0$, where μ is the cosine of the pitch angle. When $\omega \ll \Omega_p$, $kv\mu \cong \Omega_p/\gamma$. Thus

$$k = \frac{\Omega_p}{v|\mu|\gamma} = \frac{\Omega_p}{cp|\mu|} \ll \frac{\Omega_p}{v_A}.$$

The Alfvén dispersion relation $\omega = kv_A (\ll \Omega_p)$ then implies that protons can resonate with shear Alfvén waves via $l = +1$, or with fast-mode waves via $l = -1$, when their momenta $p = \beta\gamma$ satisfy the relation

$$p \gg \frac{\beta_A}{|\mu|}. \quad (14.21)$$

This is the threshold conditions for protons to gyroresonate with Alfvén waves. Sub-Alfvénic protons can also resonate with waves, but of frequency above the region of applicability of the Alfvén dispersion relation. Equation (14.3) shows that low-energy particles will resonate with waves of frequency comparable to the particle cyclotron frequency which, in the case of protons, are ion-cyclotron waves.

Similarly, electrons can gyroresonate with fast-mode waves via $l = +1$, or shear Alfvén waves via $l = -1$ if their dimensionless momentum satisfies

$$p \gg \frac{m_p \beta_A}{m_e |\mu|}. \quad (14.22)$$

Even if the threshold condition is satisfied, it is of course also required to have sufficient energy in the form of MHD waves to gyroresonate with the particle. It is generally assumed, for simplicity, that there is equal energy in forward- and backward-propagating L and R waves.

For whistlers,

$$\Omega_p \lesssim \frac{c^2 \Omega_e k^2}{\omega_p^2} = \Omega_e \left(\frac{\Omega_e}{\omega_p} \right)^2 \frac{1}{(p\mu)^2} \lesssim \Omega_e,$$

using the resonance condition $k \approx \Omega_e/(cp|\mu|)$ in the regime $\omega \ll \Omega_p/\gamma$. Because $(\Omega_e/\omega_p)^2 = (m_p/m_e)\beta_A^2$, the threshold condition for electrons to gyroresonate with whistlers takes place in the regime defined by the condition

$$\sqrt{\frac{m_p}{m_e}} \beta_A \lesssim p|\mu| \lesssim \frac{m_p}{m_e} \beta_A. \quad (14.23)$$

14.4 DIFFUSIVE PARTICLE ACCELERATION

The effect of a spectrum of waves upon the particle phase-space distribution function $f(\vec{p})$ can be determined by solving a diffusion equation for $f(\vec{p})$ in momentum $\vec{p} = \gamma \vec{\beta}_{\text{par}}$ space. The diffusion coefficients can be derived from a Fokker-Planck equation for the particle distribution function [383, 434, 437] and in a Hamiltonian formulation for the variation of the phase-space distribution functions [429]. If the pitch angle changes appreciably on a timescale much less than the acceleration timescale, then the distribution is isotropic over the latter timescale, and this two-dimensional diffusion equation can be averaged over μ to obtain a diffusion equation in p -space only. In this case, acceleration is characterized by a single momentum diffusion coefficient $D(p)$, with units of t^{-1} .

The convective and diffusive nature of the acceleration is best seen by examining the momentum diffusion equation

$$\frac{\partial f}{\partial t} = \frac{1}{p^2} \frac{\partial}{\partial p} \left(p^2 D(p) \frac{\partial f}{\partial p} \right). \quad (14.24)$$

The convection coefficient (or systematic energy-gain rate) in the Fokker-Planck equation is related to $D(p)$ by

$$\frac{1}{mc^2} \left\langle \frac{dE}{dt} \right\rangle = \frac{1}{p^2} \frac{\partial}{\partial p} [\beta p^2 D(p)], \quad (14.25)$$

and E is the particle energy. The mean rate of change of momentum due to stochastic acceleration is given by

$$\left\langle \frac{dp}{dt} \right\rangle = \frac{1}{p^2} \frac{\partial}{\partial p} [p^2 D(p)] \quad (14.26)$$

[436, 437].

Various formalisms have been developed to derive the pitch-angle-averaged momentum diffusion coefficient $D(p)$ from coefficients for diffusion in momentum and pitch angle. By analyzing the equation of motion of a particle in the presence of a background magnetic field of strength B_0 on which is superposed a fluctuating electromagnetic field from small-amplitude electric and magnetic fields due to parallel cold-plasma waves, the collisionless Boltzmann equation for the distribution function f_0 can be derived. It takes the form

$$\frac{\partial f_0}{\partial t} + \vec{v} \cdot (\vec{\nabla} f_0) + \frac{dp}{dt} \frac{\partial f_0}{\partial p} + \frac{d\psi}{dt} \frac{\partial f_0}{\partial \psi} + \frac{d\phi}{dt} \frac{\partial f_0}{\partial \phi} = S_0, \quad (14.27)$$

where ψ and ϕ are the particle's pitch angle and azimuth, respectively, and S_0 is a source function. This function can be written as

$$\begin{aligned} \frac{\partial f_0}{\partial t} + v\mu \frac{\partial f}{\partial z} - \langle S_0 \rangle &= \frac{\partial}{\partial \mu} \left(D_{\mu\mu} \frac{\partial f}{\partial \mu} + D_{\mu p} \frac{\partial f}{\partial p} \right) \\ &+ \frac{1}{p^2} \frac{\partial}{\partial p} \left(p^2 D_{p\mu} \frac{\partial f}{\partial \mu} + p^2 D_{pp} \frac{\partial f}{\partial p} \right), \end{aligned} \quad (14.28)$$

with the Fokker-Planck diffusion coefficients D_{pp} , $D_{\mu p}$, and $D_{\mu\mu}$ given in terms of k - and ω -integrals over waves satisfying the resonance condition.

The momentum diffusion coefficient and the spatial (parallel) diffusion coefficient $\kappa_{\parallel}(p)$ are related to the Fokker-Planck diffusion coefficients through the expressions

$$D(p) = \frac{1}{2} \int_{-1}^{+1} d\mu \left(D_{p\mu} - \frac{D_{\mu p}^2}{D_{\mu\mu}} \right) \quad (14.29)$$

[435], and

$$\kappa_{\parallel}(p) = \frac{v^2}{8} \int_{-1}^{+1} d\mu \frac{(1 - \mu^2)^2}{D_{\mu\mu}} \quad (14.30)$$

[438], where $v = \beta_{\text{par}}c$ is the particle speed.

Another approach [404] is to use the collisionless Boltzmann equation for the evolution of the particle distribution function $f(\vec{r}, \vec{p}, t)$ in response to the exact electromagnetic fields, given by

$$\frac{\partial f}{\partial t} + \vec{v} \cdot \nabla f + \left[Ze \left(\frac{\vec{v}}{c} \times \vec{B} \right) + \vec{\mathcal{E}} \right] \cdot \frac{\partial f}{\partial \vec{p}} = 0. \quad (14.31)$$

The particle distribution function evolves because of correlations between the fluctuating force components at different times along the trajectories. Writing $f = f_0 + \bar{f}$, where \bar{f} is the evolving part of the particle distribution function, one obtains

$$\frac{\partial \bar{f}}{\partial t} + \vec{v} \cdot \nabla \bar{f} + \left[Ze \left(\frac{\vec{v}}{c} \times \vec{B} \right) + \vec{\mathcal{E}} \right] \cdot \frac{\partial \bar{f}}{\partial \vec{p}} = \frac{\partial}{\partial \vec{p}} \cdot \bar{D} \cdot \frac{\partial \bar{f}}{\partial \vec{p}}. \quad (14.32)$$

The diffusion term

$$\bar{D} \cdot \frac{\partial \bar{f}}{\partial \vec{p}} = \left(D_{\mu\mu} \frac{\partial \bar{f}}{\partial \mu} + D_{\mu p} \frac{\partial \bar{f}}{\partial p} \right) \hat{\mu} + \left(D_{p\mu} \frac{\partial \bar{f}}{\partial \mu} + D_{pp} \frac{\partial \bar{f}}{\partial p} \right) \hat{p}. \quad (14.33)$$

The diffusion coefficients for particles interacting with parallel transverse waves, derived using a Hamiltonian formulation of the collisionless Boltzmann equation, are [429]

$$D_{\mu\mu} = \Omega^2 m^2 \frac{v^2}{p^2} (1 - \mu^2) \int_0^\infty d\omega \int_{-\infty}^{+\infty} dk \left(1 - \frac{\omega\mu}{kv} \right)^2 \times \frac{|\Delta B_{k,\omega}|^2}{B_0^2} \frac{\delta(\omega - \omega_k^{-\zeta\pi})}{kv\mu - \omega - \zeta\pi\zeta_q\Omega} \quad (14.34)$$

and

$$D_{pp} = \Omega^2 m^2 (1 - \mu^2) \int_0^\infty d\omega \int_{-\infty}^{+\infty} dki \frac{\omega^2}{k^2} \frac{|\Delta B_{k,\omega}|^2}{B_0^2} \frac{\delta(\omega - \omega_k^{-\zeta\pi})}{kv\mu - \omega - \zeta\pi\zeta_q\Omega}. \quad (14.35)$$

Here a more physical approach to this problem is presented which, though lacking rigor, give intuitive expressions for the diffusion coefficients having the correct dependencies on μ , p , and B .

14.5 APPROXIMATE DERIVATION OF DIFFUSION COEFFICIENTS

The various Fokker-Planck diffusion coefficients represent the mean-squared change of $\Delta\mu$ and Δp per unit time according to

$$D_{\mu\mu} \approx \frac{(\Delta\mu)^2}{t_g}, \quad D_{pp} \approx \frac{(\Delta p)^2}{t_g}, \quad D_{\mu p} \approx D_{p\mu} \approx \frac{(\Delta\mu\Delta p)}{t_g}, \quad (14.36)$$

and appropriate averaging is performed in accurate treatments. The gyrotime

$$t_g \equiv \frac{1}{\omega_L} = \frac{\gamma mc}{QB} = \frac{\gamma r_{L0}}{c} \quad (14.37)$$

is the time to execute a radian in a Larmor orbit (recall that it is independent of pitch angle; see eq. [7.3]). The Larmor length

$$r_{L0} = \frac{mc^2}{QB}. \quad (14.38)$$

Consider particle acceleration by low-frequency ($\omega \ll \Omega_p$) waves. The spectral density of low-frequency parallel waves of type i , assuming symmetry and equipartition [i.e., $w(k_{\parallel}) = w(-k_{\parallel})$], is normalized by

$$\xi_i \equiv \frac{W_i^{\text{tot}}}{U_B} = \frac{2V}{U_B} \int_0^{\infty} dk_{\parallel} w(k_{\parallel}). \quad (14.39)$$

If the wave spectrum can be described by the function in eq. (12.1),

$$w(k) \cong w_0 k^{-q} H(k; k_{\min}, k_{\max}) \quad (14.40)$$

(q is the wave spectral index). Dropping the \parallel subscripts for simplicity, and letting $k_{\max} \rightarrow \infty$, then

$$kW(k) \equiv Vkw(k) = \frac{q-1}{2} \xi_i U_B \left(\frac{k}{k_{\min}} \right)^{1-q}. \quad (14.41)$$

14.5.1 Pitch-Angle Diffusion Coefficient

We derive the pitch-angle diffusion coefficient $D_{\mu\mu}$ by noting that the change in pitch angle over a gyrotime is reasonably related to the ratio of magnetic field fluctuations ΔB to the background large-scale magnetic field of intensity B according to

$$\Delta\psi \approx \frac{\Delta B}{B}.$$

Because $\mu = \cos \psi$, $\Delta\psi = \Delta\mu/\sqrt{1 - \mu^2}$, so that

$$\left| \frac{\Delta B}{B} \right|^2 \approx \frac{(\Delta\mu)^2}{1 - \mu^2} = \frac{k w(k)}{U_B},$$

so that $(\Delta\mu)^2 = k w(k)(1 - \mu^2)/U_B$.

From the normalization of the wave energy spectrum, eq. (14.41), and eq. (14.36),

$$D_{\mu\mu} \approx \frac{c}{\gamma r_{L0}} \frac{q-1}{2} \xi_i (1 - \mu^2) \left(\frac{k}{k_{\min}} \right)^{1-q}. \quad (14.42)$$

The condition for gyroresonant interaction with waves with frequency $\omega \ll \Omega/\gamma$ is $k \cong 1/(pr_{L0}|\mu|)$, so that eq. (14.42) becomes

$$D_{\mu\mu} \approx \frac{q-1}{2} \xi_i \beta_{\text{par}} c k_{\min} (k_{\min} r_{L0})^{q-2} |\mu|^{q-1} (1 - \mu^2) p^{q-2}. \quad (14.43)$$

This expression is independent of the type of wave mode. Moreover, note that $D_{\mu\mu} \sim |\mu|^{q-1}$, so that the diffusion coefficient vanishes when $\mu = \cos \psi = 0$, or $\psi = \pi/2$. This is known as the *resonance gap* problem. Schlickeiser [437] argues that there is no resonance gap when both L and R waves traveling in both directions are found in the plasma.

14.5.2 Momentum Diffusion Coefficient

Consider a relativistic particle with Lorentz factor γ_1 . The mean change in its momentum when completing a cycle in second-order Fermi acceleration is, from eq. (14.1),

$$\Delta p = \frac{\gamma \Delta\gamma}{p} = \frac{\gamma_1}{\beta} \frac{\Delta\gamma}{\gamma_1} = \frac{4}{3} \beta \Gamma^2 \gamma_1 \xrightarrow{\beta \ll 1} \frac{4}{3} \beta \gamma_1 \simeq \beta \gamma_1 \rightarrow \beta_g \gamma_1,$$

where β_g is the group velocity of the resonant wave. The averaging over angles washes out the first-order term in second-order Fermi acceleration, making this process generally slower and less efficient than first-order Fermi acceleration, and consequently often overlooked in astrophysical problems.

The Fokker-Planck momentum diffusion coefficient

$$\begin{aligned} D_{pp} &\approx \frac{(\Delta p)^2}{t_g} \approx (\beta_g \gamma)^2 D_{\mu\mu} \\ &\approx \frac{q-1}{2} \xi_i (c k_{\min}) \beta_g^2 (k_{\min} r_{L0})^{q-2} |\mu|^{q-1} (1 - \mu^2) \frac{p^q}{\beta_{\text{par}}}. \end{aligned} \quad (14.44)$$

Rather than use eq. (14.29), the diffusion coefficient can be estimated through the relation by $D(p) \approx \frac{1}{2} \int_{-1}^{+1} d\mu D_{pp}$. For stochastic acceleration

of particles by Alfvén waves, $\beta_g = \beta_A$, and

$$D_A(p) \cong \frac{\pi}{2} \left(\frac{q-1}{q(q+2)} \right) \xi_i (ck_{\min}) \beta_A^2 (r_{L0} k_{\min})^{q-2} \frac{p^q}{\beta_{\text{par}}}, \quad (14.45)$$

and we have included a multiplicative factor to agree with more accurate treatments [434, 436].

For whistler waves, $\beta_g \rightarrow \beta_w = 2c\Omega_e k / \omega_p^2 = 2(m_p/m_e)\beta_A^2 (ck/\Omega_e)$. The resonance condition for whistler waves when $\omega \ll \Omega_e$ is $k \approx \Omega_e / (cp|\mu|)$, so that $ck/\Omega_e = 1/p\mu$ and $\beta_w \approx 2(m_p/m_e)(\beta_A^2/p|\mu|)$. The Fokker-Planck momentum diffusion coefficient for whistler waves is therefore

$$D_{pp}^w \approx \frac{q-1}{2} \zeta_w \left(\frac{m_p}{m_e} \right)^2 (ck_{\min}) \beta_A^4 (k_{\min} r_{L0})^{q-2} |\mu|^{q-3} (1-\mu^2) \frac{p^q}{\beta_e}, \quad (14.46)$$

and ζ_w is the ratio of MHD wave energy in whistlers compared to U_B . The approximation $D(p) \approx \frac{1}{2} \int_{-1}^{+1} d\mu D_{pp}$ indicates that the momentum diffusion coefficient for electrons gyroresonating with whistlers has the form

$$D_w(p) \propto \zeta_w \left(\frac{m_p}{m_e} \right)^2 (ck_{\min}) \beta_A^4 (k_{\min} r_{L0})^{q-2} \frac{p^{q-2}}{\beta_e}.$$

A more accurate derivation [439] that takes into account waves from the fast-mode through the whistler regimes is given by

$$D_w(p) \approx \frac{\pi}{4} (q-1) \zeta_w \left(\frac{m_p}{m_e} \right)^2 (ck_{\min}) \beta_A^4 (k_{\min} r_{L0})^{q-2} \frac{p^{q-2}}{\beta_e} \times \left(\frac{2}{q(2+q)} + \frac{(p/43\beta_A)^{2-q}}{2-q} + \frac{(p/43\beta_A)^{-q}}{q} \right). \quad (14.47)$$

Equation (14.47) can be shown to reduce to the Alfvén fast-mode expression, eq. (14.45), in the appropriate regime. The diffusion coefficient can be written in the form

$$D(p) \cong \frac{\pi}{2} \frac{\beta_A^4}{\beta} \frac{Q^2}{A} \int_{k_\ell}^{k_u} dk k \left(1 - \frac{k_0^2}{k^2} \right) w(k), \quad (14.48)$$

with $k_u = \sqrt{A/Q}/\beta_A$ and $k_\ell = \max(k_0, A/Q\beta_A)$. More detailed and exhaustive derivations of $D_{p\mu}$ and $D_{\mu p}$ are given by Melrose [434], Schlickeiser [383], and the Hamiltonian method [376, 429, 432].

14.6 ENERGY GAIN AND DIFFUSIVE ESCAPE RATES

From eq. (14.25) and the momentum diffusion coefficients, one obtains the systematic energy-gain rate for either shear Alfvén or fast mode waves

given by

$$\left\langle \frac{d\gamma}{dt} \right\rangle_A = \frac{\pi}{2} \left(\frac{q-1}{q} \right) (ck_{\min}) \beta_A^2 \xi_i (k_{\min} r_{L0})^{q-2} p^{q-1}. \quad (14.49)$$

The functional dependence of this expression can be obtained by noting that the particle pitch angle ψ changes by $\sim \Delta B/B$ during one gyrotime $t_g = r_{L0}/c$, where B now refers to the mean magnetic field in the shocked fluid plasma. The isotropization time scale from pitch-angle diffusion is $t_{\text{iso}} \cong t_g/(\Delta B/B)^2$. Changes in ψ due to gyroresonant interactions of particles with resonant plasma waves is described by relating the mean-squared magnetic fluctuation to the ξ_i , the ratio of wave energy in mode i to $B^2/8\pi$, according to $(\Delta B/B)^2 \approx \bar{k}W(\bar{k})/U_B$. The resonant wavenumber is assigned through the resonance condition $\omega - k_{\parallel}v_{\parallel} = \ell\Omega/\gamma$, but for low-frequency waves and $\psi \cong \pi/2$, we can let $k \approx 1/pr_{L0}$ [374]. Assuming isotropy of forward- and backward-moving waves gives the normalization $W_0 = \xi_i U_B (q-1)/2k_{\min}$. Hence $t_{\text{iso}}^{-1} \cong c\xi_i (q-1)(r_{L0}k_{\min}p)^{q-1}/(2r_{L0})$, $\dot{p} \simeq p_A^2 t_{\text{iso}}^{-1}$ and

$$\dot{p}_{F2} \cong \frac{2}{3} p_A^2 \xi_i (q-1) \left(\frac{c}{r_{L0}} \right) (r_{L0}k_{\min}p)^{q-1}. \quad (14.50)$$

The term $r_{L0}k_{\min}p$ in the parentheses of equation (14.50) gives the comoving gyroradius in units of the inverse of the smallest turbulence wavenumber k_{\min} found in the shocked fluid. If $k_{\min} \sim 1/R$, then the relation $r_{L0}k_{\min}p \lesssim 1$ is an expression of the Hillas [320] condition. When this condition is satisfied, then $\dot{p}_{F2} \lesssim p_A^2 c/r_{L0}$. According to this prescription, the relative momentum increase per gyroperiod can greatly exceed the Larmor rate c/r_L , which depends on relativistic scattering centers. If relativistic MHD waves do exist, but do not gyroresonate with particles, then acceleration at a rate as indicated by this expression may not be possible.

The characteristic timescale for a particle starting from low energy to reach Lorentz factor $\gamma \gg 1$ through gyroresonant interactions with Alfvén waves is given by

$$t_{EA} \equiv \left| \frac{1}{\gamma-1} \left\langle \frac{d\gamma}{dt} \right\rangle_A \right|^{-1} \cong \frac{2}{\pi} \left(\frac{q}{q-1} \right) \frac{t_{\text{dyn}}}{\beta_A^2 \xi_i} \gamma^{2-q}, \quad (14.51)$$

and we set $k_{\min} \rightarrow R^{-1}$.

The systematic energy-gain rate for gyroresonant interaction of electrons with whistler waves, from eqs. (14.47) and (14.25), is

$$\left\langle \frac{d\gamma}{dt} \right\rangle_w = \frac{\pi}{2} \left(\frac{q-1}{2-q} \right) \xi_i \left(\frac{m_p}{m_e} \right)^2 (ck_{\min}) \beta_A^4 (k_{\min} r_{L0})^{q-2} p^{q-3} \\ \times (1-\gamma^{-1}) \left[\left(\frac{p}{43\beta_A} \right)^{2-q} - 1 \right]. \quad (14.52)$$

The characteristic timescale for a particle starting from low energy to reach Lorentz factor $\gamma \gg 1$ through gyroresonant interactions with whistler waves is given by

$$t_{Ew} = \frac{2}{\pi} \left(\frac{m_e}{m_p} \right)^{1+q/2} \left(\frac{q-2}{q-1} \right) \frac{t_{lc}}{\beta_A^{2+q} \xi_R} \left(\frac{r_{L0}}{R} \right)^{2-q} p^2 \left[\left(\frac{43\beta_A}{p} \right)^{2-q} - 1 \right]^{-1} \quad (14.53)$$

The acceleration timescales for electron interactions with whistlers, eq. (14.53), and with low-frequency fast-mode waves, eq. (14.51), are not continuous, owing to the discontinuity in the dispersion relations. Employing the correct dispersion relation for R waves from low to high frequencies is necessary to obtain continuous energy gains and time scales throughout the whistler and fast-mode regime [429, 439].

Equations (14.30) and (14.43) imply that the parallel spatial diffusion coefficient due to gyroresonant interactions with Alfvén waves is given by

$$\kappa_{\parallel}^A(p) = \frac{vp^{2-q}}{(q-1)(2-q)(4-q)} \frac{(k_{\min} r_{L0})^{2-q}}{\xi_i k_{\min}}. \quad (14.54)$$

For magnetic field lines directed radially outward, the diffusive escape time

$$t_d^A \approx \frac{R^2}{4\kappa_{\parallel}^A} \approx \frac{t_{lc}}{4} (q-1)(2-q)(4-q) \xi_i (k_{\min} R) (r_{L0} k_{\min})^{q-2} \frac{p^{q-2}}{\beta_{\text{par}}}, \quad (14.55)$$

where $t_{lc} \equiv R/c$ is the light-crossing time scale for the system. For Kraichnan or Kolmogorov wave turbulence spectra, therefore, the particle escape time decreases with increasing particle energy.

The pitch-angle scattering Fokker-Planck coefficient for electrons interacting with whistlers is given by eq. (14.43) with $r_{L0} = eB/m_e c^2$. Following the procedure for the Alfvén mode gives the diffusive escape time of electrons due to scattering by whistlers, namely,

$$t_d^w \approx \frac{\pi}{4} (q-1) t_{lc} \xi_R (k_{\min} R) (r_{L0} k_{\min})^{q-2} \frac{p^{q-2}}{\beta_{\text{par}}} \\ \times \left(\frac{(p/43\beta_A)^{q-2} - 1}{q-2} - \frac{(p/43\beta_A)^{q-4} - 1}{q-4} \right). \quad (14.56)$$

Equation (14.56) generalizes eq. (14.55) to include both the Alfvén and whistler interactions, and reduces to eq. (14.55) in the limit $p \gg \beta_A \sqrt{m_p/m_e}$.

14.7 MOMENTUM DIFFUSION EQUATION

The convective and diffusive nature of the acceleration is best revealed by writing the resulting momentum diffusion equation with no systematic losses, but with momentum-dependent exponential escape timescale $T(p)$ and source function $\dot{n}(t)$. Written in terms of the particle momentum spectrum $n(p) = 4\pi p^2 f(p)$ rather than the distribution function $f(p)$, the diffusion equation takes the form

$$\frac{\partial n}{\partial t} = \frac{\partial}{\partial p} \left(D(p) \frac{\partial n}{\partial p} \right) - \frac{\partial}{\partial p} [A(p)n] - \frac{n}{T(p)} + \dot{n}(p, t). \quad (14.57)$$

where

$$A(p) \equiv \frac{2D(p)}{p}.$$

For Alfvén waves, $D_A(p) \propto p^q$, as can be seen from eq. (14.45). Writing $D(p) = \mathcal{D}p^q$, $A(p) = \mathcal{A}p^{q-1}$, and $T(p) = T_0 p^s$, and letting $p \rightarrow x$ to improve its appearance, then G , the Green's function,¹ is a solution of the equation

$$\frac{\partial G}{\partial y} = x^q \frac{\partial^2 G}{\partial x^2} + (q-a)x^{q-1} \frac{\partial G}{\partial x} - [a(q-1)x^{q-2} + \theta x^{-s}]G + \delta(x-x_0)\delta(y). \quad (14.58)$$

Here the reduced time $y = \mathcal{D}t$, $\theta \equiv 1/\mathcal{D}y_0$, and a is an index of an assumed additional systematic energy gain term with p dependence proportional to p^{q-1} . This equation can also be written in the Fokker-Planck form

$$\frac{\partial G}{\partial y} = \frac{\partial^2}{\partial x^2} (x^q G) - \frac{\partial}{\partial x} [(q+2+a)x^{q-1}G] - \theta x^{2-q}G + \delta(x-x_0)\delta(y), \quad (14.59)$$

where the identification $s = q - 2$ follows by relating the diffusive escape time scale, eq. (14.55), with the systematic energy gain rate in second-order acceleration, eq. (14.49).

¹The Green's function is the solution to a differential equation with δ -function source terms in space and time. For Green's function methods to solve differential equations see, e.g., Ref. [440].

14.7.1 Ramaty-Lee Spectrum for Hard-Sphere Scattering

The application of the diffusion equation for hard-sphere scattering to particle acceleration in Solar flares was done by Ramaty [441]. The magnetized fluid elements of Fermi are replaced by hard spheres with radius r_{hs} and effectively infinite mass moving in random directions with the same nonrelativistic speed βc . All particles are scattered with equal cross section πr_{hs}^2 . The diffusion coefficient for hard-sphere scattering is

$$D_{\text{hs}}(p) = \frac{1}{3} \frac{(\beta c)^2}{\lambda_{\text{sc}} c} \beta_{\text{par}} p^2 \equiv \frac{1}{3} \alpha_{\text{hs}} \beta_{\text{par}} p^2 \propto p^2, \quad (14.60)$$

where βc is the speed of the hard spheres, $\lambda_{\text{sc}} = 1/(\pi r_{\text{hs}}^2 n_{\text{sc}})$ is the scattering mean free path, and n_{sc} is the density of hard spheres. Thus $q = 2$ for hard-sphere scattering.

With $q = 2$, eq. (14.59) becomes, retaining the possibility of an additional acceleration term,

$$\frac{\partial G}{\partial y} = x^2 \frac{\partial^2 G}{\partial x^2} + (2 - a)x \frac{\partial G}{\partial x} - (a + \theta)G + \delta(x - x_0)\delta(y). \quad (14.61)$$

Equation (14.61) can be solved by the Laplace transform method. The Laplace transform

$$L = \mathcal{L}\{G\} = \int_0^\infty dy G(x, y) \exp(-y\lambda), \quad (14.62)$$

so

$$\mathcal{L} \left\{ \frac{\partial G}{\partial y} \right\} = \int_0^\infty dy \frac{\partial G}{\partial y} \exp(-y\lambda) = -G(y=0) + \lambda L \equiv G(0) + \lambda L$$

and

$$x^2 \frac{\partial^2}{\partial x^2} \int_0^\infty dy \exp(\lambda y) G = x^2 \frac{\partial^2 L}{\partial x^2} \equiv x^2 L''.$$

The Laplace transform of eq. (14.61) gives the normal differential equation

$$x^2 L'' + (2 - a)x L' - (a + \theta + \lambda)L = -G(0) = -\frac{\delta(x - x_0)}{\mathcal{D}}; \quad (14.63)$$

the final relation derives from the initial condition for $G(p, t)$.

The solution of the homogeneous equation, valid for $x \neq x_0$, is obtained by assuming a solution in the form $L = Kx^{j-1}$, where j is a solution of the quadratic

$$j = \frac{a + 1 \pm \sqrt{(a + 1)^2 + 4(\theta + \lambda)}}{2}.$$

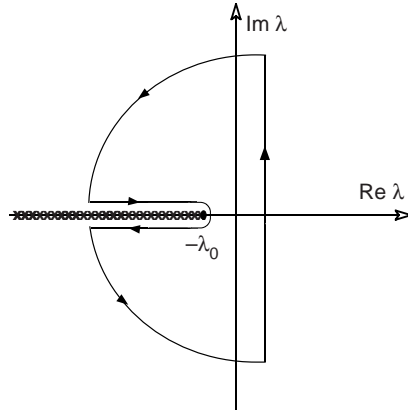


Figure 14.3 Contour for the integration of eq. (14.65).

We write $j_{1,2} = [(a + 1)/2] \pm \mu$, where $\mu = \sqrt{\lambda_0 + \bar{\lambda}}$ and $\lambda_0 = [(a + 1)/2]^2 + \theta$. Note that $j_1 > 0$ and $j_2 < 0$. As $x \rightarrow x_0$, one sees that we take the $+$ root for $x \rightarrow x_0$ and the $-$ root for $x \rightarrow \infty$. Therefore

$$L = K_1 x^{j_1-1} H(x_0 - x) + K_2 x^{j_2-1} H(x - x_0).$$

Continuity of L at $x = x_0$ implies $K_2 = K_1 x_0^{j_1-j_2}$. Also, the derivative jump condition

$$\int_{x_0-\varepsilon}^{x_0+\varepsilon} [x^2 L'' + (2-a)xL' - (a+\theta+\lambda)L] = -\frac{1}{\mathcal{D}}$$

gives the result through partial integrations in the limit $\varepsilon \rightarrow 0$ that

$$K_1 = -\frac{x_0^{-j_1}}{\mathcal{D}(j_2 - j_1)}, \quad K_2 = -\frac{x_0^{j_2}}{\mathcal{D}(j_2 - j_1)}. \tag{14.64}$$

Hence

$$L = \frac{1}{2\mathcal{D}\mu x_0} \left[\left(\frac{x}{x_0}\right)^{j_1-1} H(x_0 - x) + \left(\frac{x}{x_0}\right)^{j_2-1} H(x - x_0) \right]. \tag{14.65}$$

The inverse Laplace transform is defined by

$$G(x, y) = \frac{1}{2\pi i} \int_{c_1-i\infty}^{c_1+i\infty} d\lambda \exp(\lambda y) L(x, \lambda). \tag{14.66}$$

The singularity at $\mu = \sqrt{\lambda_0 + \bar{\lambda}} = 0$ in eq. (14.65) suggests that we integrate around the contour shown in figure 14.3, avoiding the singularity at $\lambda = -\lambda_0$. After performing the inversion, one obtains for the Green's function solution to eq. (14.61) the result

$$G(x, y) = \frac{\exp(-\theta y)}{\mathcal{D}x\sqrt{4\pi y}} \exp\left(-\frac{1}{4y}[\ln(x/x_0) - (a+1)y]^2\right). \tag{14.67}$$

For impulsive injection and no escape, the particle energy distribution in the asymptote for relativistic particle energies takes the form

$$N(E, t) \propto E^{-1} \exp\{-3[\ln(E/E_0) - \alpha_{\text{hs}}t]/(4\alpha_{\text{hs}}t)\}$$

[441], where E_0 is the injection energy. For continuous injection and energy-independent escape time t_{esc} , the relativistic particle distribution becomes

$$N(E, t) \propto (E/E_0)^{[1-\sqrt{9+12/(\alpha_{\text{hs}}t_{\text{esc}})}]/2}$$

[442], with a power-law form. Solutions for hard-sphere scattering are shown in the top panels of figure 14.4.

14.7.2 Green's Function Solution

The Laplace transform of eq. (14.59) is

$$\begin{aligned} z^2 \frac{d^2 L}{dz^2} + \frac{a+1}{q-2} z \frac{dL}{dz} + \left(\frac{(1-q)(2+a)}{(2-q)^2} - \frac{z^2}{4} - \frac{sz}{c_0(2-q)^2} \right) L \\ = -\frac{c_0 \delta(z-z_0)}{2-q} \left(\frac{z}{c_0} \right)^{(3-2q)/(2-q)}, \end{aligned} \quad (14.68)$$

where

$$z(x) \equiv \frac{2\sqrt{\theta}}{2-q} x^{2-q}, \quad z_0(x_0) \equiv \frac{2\sqrt{\theta}}{2-q} x_0^{2-q}, \quad (14.69)$$

and

$$c_0 \equiv \frac{2\sqrt{\theta}}{2-q}. \quad (14.70)$$

The Green's function $G = (x_0, x, y)$ can be found using the complex Mellin inversion integral [436], with general closed-form solution

$$G = \frac{2-q}{x_0} \left(\frac{x}{x_0} \right)^{(a+1)/2} \frac{\sqrt{zz_0\xi}}{1-\xi} \exp\left(-\frac{(z+z_0)(1+\xi)}{2(1-\xi)}\right) I_{\beta-1}\left(\frac{2\sqrt{zz_0\xi}}{1-\xi}\right), \quad (14.71)$$

where $I_{\beta-1}$ is a modified Bessel function of the first kind of order $\beta-1$ (see Appendix B).

$$\begin{aligned} z(x) \equiv \frac{2\sqrt{\theta}}{2-q} x^{2-q}, \quad z_0(x_0) \equiv \frac{2\sqrt{\theta}}{2-q} x_0^{2-q}, \\ \beta \equiv \frac{a+3}{2-q}, \quad \text{and} \quad \xi(y) \equiv e^{2(q-2)y\sqrt{\theta}}. \end{aligned} \quad (14.72)$$

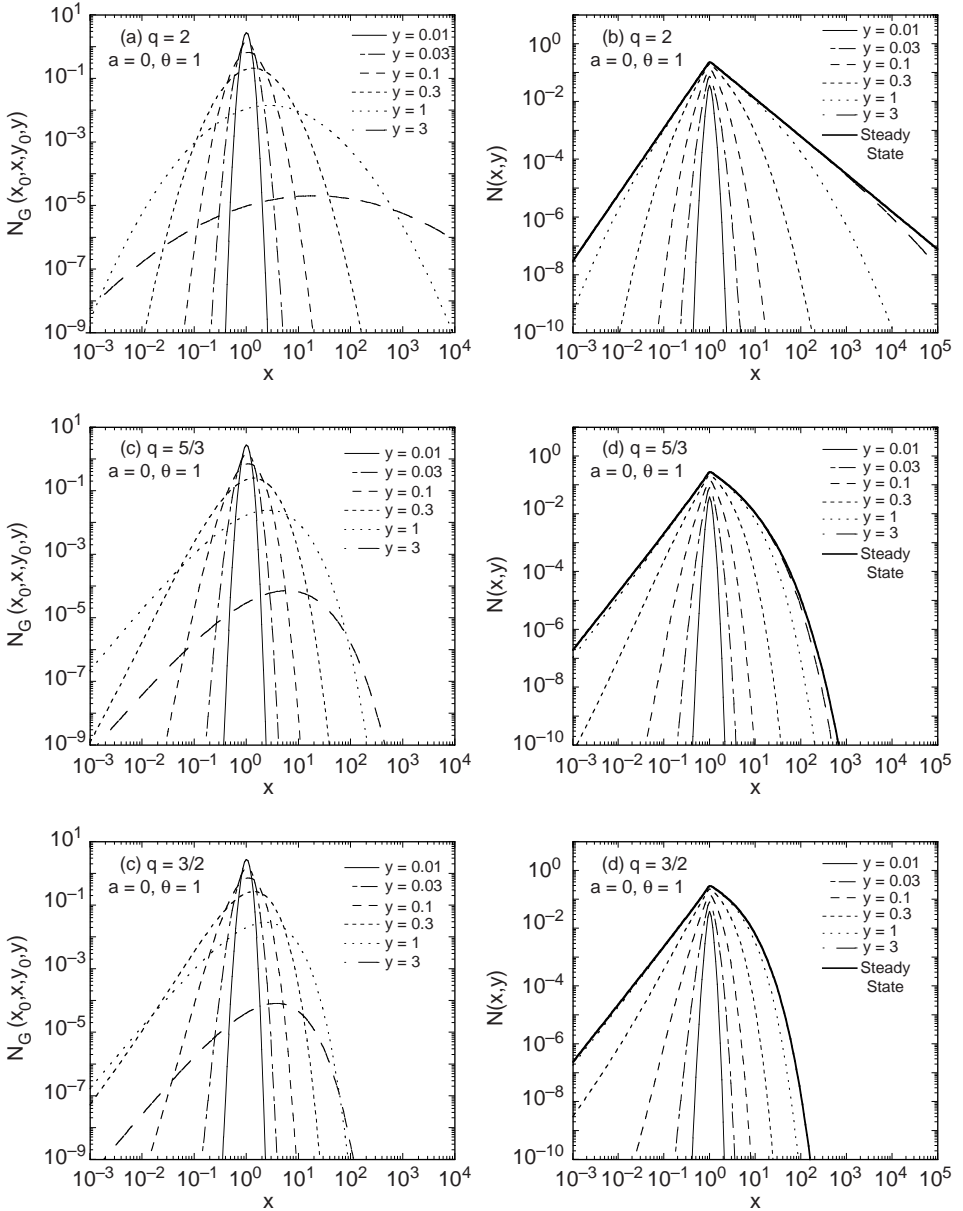


Figure 14.4 Green's function solutions to the time-dependent stochastic particle acceleration equation, eq. (14.58) or (14.59), for $x_0 = 1, \theta = 1$, and $a = 0$, for values of $q = 2$ (top), $5/3$ (middle), $3/2$ (lower). *Left panels:* δ -function injection in time and momentum. *Right panels:* Continuous injection and the approach to steady state. The reduced time variable is y .

Note that the solution for G depends on the time parameter y representing the “age” of the injected particles.

The exact solution for the time-dependent Green’s function describing the evolution of a monoenergetic initial spectrum with $q < 2$ is given by eq. (14.71). In the hard-sphere case with $q = 2$, eq. (14.71) reduces to the result [443]

$$G(q = 2) = \frac{e^{-\gamma y}}{2x_0\sqrt{\pi y}} \left(\frac{x}{x_0}\right)^{(a+1)/2} \exp\left(\frac{-(\ln x - \ln x_0)^2}{4y}\right) \quad (14.73)$$

(cf. eq. [14.67]), where

$$\gamma \equiv \frac{(a+1)^2}{4} + 2 + a + \theta. \quad (14.74)$$

Equation (14.71) is plotted in figure 14.4 for parameters as labeled. The steady-state solution at $x \geq x_0 = 1$ is a power-law spectrum when $q = 2$, whereas it is a curving spectrum at $q < 2$. For research on second-order Fermi acceleration processes in a variety of cosmic environments, see the work by Petrosian and Liu, e.g., [444].

14.8 MAXIMUM PARTICLE ENERGY IN SECOND-ORDER FERMİ ACCELERATION

The energy gain in second-order Fermi acceleration can be seen to result from the *elastic* deflection of a particle in the *wave frame*, which for Alfvén waves, moves along the magnetic field with a velocity $\pm\beta_{Ac}$ (the phase speed) for forward and backward waves propagating along the field. In the wave frame, the electric field associated with the waves vanishes, and the particle energy is unchanged by the wave-particle interaction, which reduces to pure pitch-angle scattering in that frame.

We derived the relative energy gain in one cycle of second-order Fermi acceleration in the nonrelativistic ($\beta \ll 1$) limit (eq. [14.1]). The second-order acceleration rate of particles resulting from interactions with Alfvén waves therefore scales as

$$\left(\frac{dp'}{dt'}\right)\Big|_{F2} \propto \beta_A^2 \gamma_A^2 p' \equiv p_A^2 p'.$$

We now extend these expressions to relativistic scatterers.

The flow behind a relativistic blast wave is relativistically hot. If the blast-wave Lorentz $\Gamma \gg 1$, then

$$P = \frac{e}{3} = \frac{4}{3}\Gamma^2 \rho_- c^2, \quad n = 4\Gamma n_-, \quad \text{and} \quad B \approx 4\Gamma B_{-1},$$

with the subscript “-” referring to upstream quantities. For a cold upstream medium, then $\rho_- = \mu n_{p-} m_p c^2$, and n_{p-} is the upstream density, assumed to be dominated by protons. The quantity e is the proper thermal energy density in the downstream flow, P is the pressure, B is the shock-compressed comoving magnetic field, and B_{\perp} is the upstream transverse field.

The Alfvén speed in a relativistically hot gas is given by [445]

$$\beta_A = \frac{v_A}{c} = \frac{B}{\sqrt{4\pi(e + P + B^2/4\pi)}}. \tag{14.75}$$

Taking $P = e/3$, the associated Lorentz factor γ_A is

$$\gamma_A = \frac{1}{\sqrt{1 - \beta_A^2}} = \sqrt{1 + \frac{3B^2}{16\pi e}}, \tag{14.76}$$

so that

$$p_A = \beta_A \gamma_A = \sqrt{\frac{3B^2}{16\pi e}} = \sqrt{\frac{3\epsilon_B}{2}}, \tag{14.77}$$

where $\epsilon_B = B^2/8\pi e$ is the fraction of total energy in magnetic field energy, and is essentially equivalent to the ϵ_B parameter in blast-wave physics. Even if the field is amplified to equipartition, $\epsilon_B \rightarrow 1$, the quantity p_A is of order unity. Thus we take $p_A^2 = 3\epsilon_B/2$ as the scaling for the relativistic momenta of Alfvén waves.

14.8.1 Gyroresonant Stochastic Acceleration

Particle acceleration through stochastic gyroresonant processes is written as $\dot{p}'_{F2} \cong \Delta p'/t_{\text{iso}}$, where t_{iso} is the pitch-angle isotropization timescale in the comoving fluid frame. When $p' \gg 1$, the fractional change in momentum over this time period is

$$\frac{\Delta p'}{p'} \cong \gamma_A^2(1 + \beta_A^2/3) - 1 = 4p_A^2/3 \rightarrow 2\epsilon_B. \tag{14.78}$$

Equation (14.78) represents the mean fractional momentum change from elastic scattering off relativistic scattering centers. The quantity β_{Ac} , which represents the speed of the scattering centers, reduces to the Alfvén speed in the weakly turbulent quasilinear regime.

The downstream Larmor radius depends on the strength of the downstream magnetic field, given by

$$B_+ \cong \max(\chi\Gamma B_{\perp-}, B_*\sqrt{\Gamma^2 - \Gamma}), \tag{14.79}$$

where the first term represents the compression of the upstream transverse magnetic field, and the second term defines the downstream field in the manner of eq. (11.39). The compression ratio $\chi = 4$ for strong shocks whether or not the shocks are relativistic.

When $B_* > \chi B_{\perp-}/\sqrt{1-1/\Gamma}$, that is, when, $n_{0\epsilon_B} \gtrsim 2 \times 10^{-10} B_{\mu G}^2/\beta^2 \text{ cm}^{-3}$, the turbulent field dominates the compressive field. The value of ϵ_B cannot be too small, however; otherwise particles will not be captured by the blast wave. We parameterize $k_{\min} = f_{\Delta} x/\Gamma$ in terms of the characteristic scale of the blast-wave shell [296]. The value $f_{\Delta} = 1/12$ corresponds to the hydrodynamic width of the blast wave [301, 304]. For $f_{\Delta} \approx 1/12$, the size scale of the MHD turbulence corresponds to the physical scale of the comoving blast-wave width.

With the result that $\beta_A \rightarrow p_A = \sqrt{3\epsilon_B/2}$, then $p_A^2 = 3\epsilon_B/2$. For relativistic flows, $p_A \gg 1$ if $\epsilon_B \Gamma \gg 1$, and the energy gain rate through gyroresonant stochastic acceleration can exceed c/r_{L+}^0 under these circumstances. For nonrelativistic flows, $p_A \rightarrow \beta_A = \epsilon_B^{1/2} \beta$, provided that the turbulent field exceeds the compressive field. The implied energy-gain rate from second-order Fermi acceleration is

$$\left. \frac{dE'}{dx} \right|_{\text{F2}} = \frac{4}{3} \epsilon_B \xi (q-1) \left(\frac{\Gamma-1}{\beta_{\text{sh}} \Gamma_{\text{sh}}} \right) Q B_* \sqrt{\Gamma^2 - \Gamma} \left(\frac{E'}{Q B_* \sqrt{1-\Gamma^{-1}} f_{\Delta} x} \right)^{q-1}, \quad (14.80)$$

and ξ is the ratio of plasma turbulence to magnetic-field energy density (section 14.6). Equation (14.80) reduces for nonrelativistic and relativistic flows to

$$\left. \frac{dE'}{dx} \right|_{\text{F2,NR}} = 2^{-3/2} \epsilon_B \xi (q-1) Q B_* \beta^2 \left(\frac{2^{1/2} E'}{Q B_* f_{\Delta} x \beta} \right)^{q-1} \quad \text{for } \Gamma - 1 \ll 1 \quad (14.81)$$

and

$$\left. \frac{dE'}{dx} \right|_{\text{F2,ER}} = \frac{2^{3/2}}{3} \epsilon_B \xi (q-1) Q B_* \Gamma \left(\frac{E'}{Q B_* f_{\Delta} x} \right)^{q-1} \quad \text{for } \Gamma \gg 1, \quad (14.82)$$

respectively.

14.8.2 Stochastic Energization in Nonrelativistic Shocks

For an adiabatic blast wave in a uniform surrounding medium, the nonrelativistic expression (14.81) can be integrated to give

$$E'^{2-q}(x_1) = E'^{2-q}(x_0) + \left(\frac{2^{q/2} \epsilon_B \xi}{4 f_{\Delta}} (q-1)(2-q) \beta_0 I_{2N} \right) (Q B_* f_{\Delta} x_d \beta_0)^{2-q}, \quad (14.83)$$

where

$$I_{2N} = I_{F2,NR}(y_0, y_1, q) \equiv \int_{y_0}^{y_1} \frac{dy y^{1-q}}{(1+y^3)^{(3-q)/2}}$$

$$\cong \begin{cases} (2-q)^{-1}(y_1^{2-q} - y_0^{2-q}) & \text{for } y_0 < y_1 \lesssim 1, \\ \frac{1-y_0^{2-q}}{2-q} + \frac{2(1-y_1^{-(q-1)/2})}{q-1} & \text{for } y_0 \lesssim 1 \lesssim y_1, \\ 2(q-1)^{-1}(y_0^{-(q-1)/2} - y_1^{-(q-1)/2}) & \text{for } 1 \lesssim y_0 < y_1, \end{cases} \quad (14.84)$$

and $y_i = x_i/QB_*f_\Delta$. The largest possible value of I_{2N} is given by the middle branch of eq. (14.89), and $I_{2N}(0, \infty, 5/3) \cong I_{2N}(0, \infty, 3/2) \cong 6$.

When $E'(x_1) \gg E'(x_0)$ and $x_1 \gg x_0$,

$$E(x_1) \cong E'(x_1) \cong \left(\frac{2^{q/2}}{4} \frac{\epsilon_B \xi}{f_\Delta} (q-1)(2-q)\beta_0 I_{2N} \right)^{1/(2-q)} QB_*f_\Delta x_d \beta_0. \quad (14.85)$$

The maximum energy of particles accelerated by second-order Fermi acceleration in a nonrelativistic blast wave is defined by the quantity $KQB_*f_\Delta x_d \beta_0$, where K is the coefficient of the quantity $QB_*f_\Delta x_d \beta_0$ in eq. (14.85), given by

$$K \equiv \left(\frac{2^{q/2}}{4} \frac{\epsilon_B \xi}{f_\Delta} (q-1)(2-q)\beta_0 I_{2N} \right)^{1/(2-q)}$$

$$\rightarrow \begin{cases} 2 \times 10^{-7} \left(\frac{\epsilon_B \xi \beta_{-2}(I_{2N}/6)}{f_\Delta} \right)^3 & \text{for } q = 5/3, \\ 4 \times 10^{-5} \left(\frac{\epsilon_B \xi \beta_{-2}(I_{2N}/6)}{f_\Delta} \right)^2 & \text{for } q = 3/2. \end{cases} \quad (14.86)$$

The measured ejecta speed from Types Ia, II, and Ib SNe are in the range $\beta_0 \sim 0.005\text{--}0.05$ (table 12.1), so we take as a basic scaling $\beta_0 = 10^{-2}\beta_{-2}$ for nonrelativistic shocks from SNe. The quantity

$$QB_*f_\Delta x_d \beta_0 \cong 8 \times 10^{18} Z \epsilon_B^{1/2} (\mu_0 n_0)^{1/6} f_\Delta \beta_{-2} \mathcal{E}_\odot^{1/3} \text{ eV}. \quad (14.87)$$

Equations (14.86) and (14.87) imply maximum particle energies $E_{\max} \propto 2 \times 10^{12} Z \beta_{-2}^4 \text{ eV}$ for $q = 5/3$ and $E_{\max} \propto 3 \times 10^{14} Z \beta_{-2}^3 \text{ eV}$ for $q = 3/2$, when the quantity $\epsilon_B \xi / f_\Delta \cong 1$. Though this quantity could arguably be much smaller than unity, it cannot be much larger. Comparison of these energies with the values given by eqs. (13.82) and (13.85) shows why stochastic processes are generally discounted as being important in nonrelativistic shock physics. When $\beta_0 \rightarrow 1$, the second-order acceleration rate can become, however, more rapid than the first-order Fermi acceleration

rate. This is simply because the second-order rate does not depend on the field strength in the upstream medium, but on the much stronger downstream field strength.

14.8.3 Stochastic Energization in Relativistic Flows

The relativistic expression (14.82) can be integrated to give

$$E'^{2-q}(x_1) = E'^{2-q}(x_0) + \left(\frac{2^{3/2}}{3} \frac{\epsilon_B \xi}{f_\Delta} (q-1)(2-q)\Gamma_0 I_{2E} \right) (QB_* f_\Delta x_d)^{2-q}, \quad (14.88)$$

where

$$I_{2E} = I_{F2,ER}(y_0, y_1, q) \equiv \int_{y_0}^{y_1} \frac{dy y^{1-q}}{\sqrt{1+y^3}}$$

$$\cong \begin{cases} (2-q)^{-1}(y_1^{2-q} - y_0^{2-q}) & \text{for } y_0 < y_1 \lesssim 1, \\ \frac{1-y_0^{2-q}}{2-q} + \frac{1-y_1^{-q+1/2}}{q-1/2} & \text{for } y_0 \lesssim 1 \lesssim y_1, \\ (q-1/2)^{-1}(y_0^{-q+1/2} - y_1^{-q+1/2}) & \text{for } 1 \lesssim y_1 < y_2. \end{cases} \quad (14.89)$$

The largest possible value of I_{2E} is given by the middle branch of eq. (14.89), and $I_{2E}(0, \infty, 5/3) \cong 27/7$, $I_{2E}(0, \infty, 3/2) \cong 3$.

When $E'(x_1) \gg E'(x_0)$ and $x_1 \gg x_0$,

$$E(x_1) \cong \Gamma(x_1) E'(x_1) \cong \left(\frac{2^{3/2}}{3} \frac{\epsilon_B \xi}{f_\Delta} (q-1)(2-q) I_{2E} \right)^{1/(2-q)} QB_* f_\Delta x_d \Gamma_0. \quad (14.90)$$

Equation (14.90) shows that the maximum energy of particles accelerated by second-order Fermi acceleration in a relativistic blast wave occurs near the deceleration scale. The basic scaling for this maximum energy is given by the energy

$$QB_* f_\Delta x_d P_0 \cong 7.7 \times 10^{20} Z \epsilon_B^{1/2} (\mu_0 n_0)^{1/6} f_\Delta \beta_0 (\mathcal{E}_\odot \Gamma_0)^{1/3} \text{ eV} \quad (14.91)$$

(cf. eq. [14.87]), where we have generalized the expression so that the scalings (14.87) [446] for nonrelativistic Sedov and relativistic adiabatic flows are recovered. Note the dependence of the maximum accelerated energy given by eq. (14.90) on the factor $\xi \epsilon_B / f_\Delta$. When $\epsilon_B \xi / f_\Delta \simeq 1$ near the deceleration radius, then stochastic acceleration processes in relativistic blast waves can in principle accelerate particles to energies of $\approx 10^{20} Z$ eV, limited by competition with adiabatic and radiation losses and escape from

the system. The acceleration of particles to such energies remains however hypothetical due to poorly understood wave-particle interaction physics in relativistic plasmas dominated by electromagnetic energy [447, 448], and the existence of turbulence on different scales.

Comparison with Adiabatic Losses

Particle acceleration by stochastic Fermi acceleration will proceed only if adiabatic losses are small, which applies to particles with energies that satisfy $|dE'/dx|_{F2} \gg kE'/x$. For nonrelativistic flows, adiabatic losses can be neglected for particles with energies

$$E \lesssim 2^{-1/2} \left(\frac{\epsilon_B \beta}{2k f_\Delta} (q - 1) \right)^{1/(2-q)} Q B_* f_\Delta \beta x \tag{14.92}$$

(see eq. [14.81]). For the relativistic gain rate (14.82), adiabatic losses can be neglected when

$$E \simeq \Gamma E' \lesssim \left(\frac{2^{3/2}}{3k} \frac{\Gamma \epsilon_B \xi}{f_\Delta} (q - 1) \right)^{1/(2-q)} Q B_* f_\Delta \Gamma x. \tag{14.93}$$

Note again the extreme sensitivity to the factor $\xi \epsilon_B \beta \Gamma / f_\Delta$ on second-order particle acceleration processes. As can be seen, adiabatic losses become important near the maximum particle energies obtained by solving the particle energy evolution with location x in both the nonrelativistic and relativistic cases.

Competition between Stochastic Acceleration and Diffusive Escape

The escape timescale $t'_{\text{esc}} \approx N\lambda/v'$ depends only upon pitch-angle diffusion. The number of scattering events to travel distance Δ' is $N \cong (\Delta'/\lambda)^2$, where $\lambda \cong v' t_{\text{iso}} \simeq 2v' r_L (r_{L+} k_{\text{min}})^{1-q} / [c\xi(q - 1)]$. The timescale to travel distance Δ' is therefore $t'_{\text{esc}} = c\Delta'^2 \xi (q - 1) k_{\text{min}} (r_{L+} k_{\text{min}})^{q-2} / (2v'^2)$. For relativistic particles, $v' \rightarrow c$, and

$$t'_{\text{esc}} \cong \frac{\Delta'}{c} \max \left[1, \frac{\xi(q - 1)}{2} (\Delta' k_{\text{min}}) (r_{L+} k_{\text{min}})^{q-2} \right]. \tag{14.94}$$

When $r_{L+} \gtrsim k_{\text{min}}^{-1} [\xi(q - 1)(\Delta' k_{\text{min}})/2]^{1/(2-q)}$, the escape time is governed by the transit time, so particles diffusively escape when $E' \lesssim \mathcal{E}' [\xi(q - 1)(\Delta' k_{\text{min}})/2]^{1/(2-q)}$, where $\mathcal{E}' = Q B_+ / k_{\text{min}} \approx Q B_+ R'$. Depending on the precise value of $k_{\text{min}} \Delta'$, diffusive escape is unimportant when $E' \gg \mathcal{E}'$, where at the highest energies, particles escape with increasingly straight trajectories.

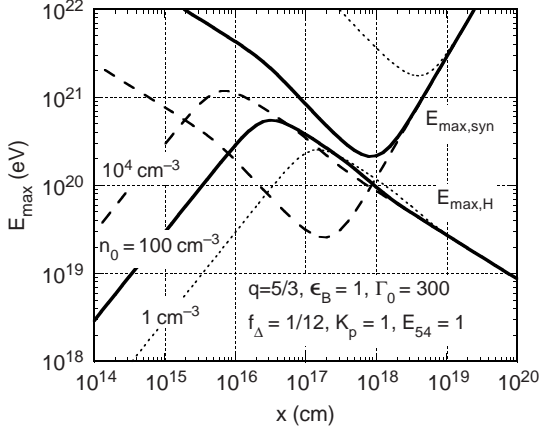


Figure 14.5 Maximum proton energy $E_{\max,H}$ as a function of blast-wave location x implied by the Hillas condition obtained by comparing the Larmor radius and blast-wave width and stochastic acceleration rate, given eq. (14.91), with the synchrotron cooling rate, eq. (14.95). Changes in $E_{\max,H}$ and $E_{\max,\text{syn}}$ for different values of n_0 are shown, with parameters given in the figure legend [301].

Comparison between Stochastic Energy Gain and Synchrotron Radiation Losses

The synchrotron energy-loss rate for particles with randomly oriented pitch angles in a magnetic field with mean strength B is given by (equation 7.49)

$$-\dot{\gamma}'_{\text{syn}} = 4c\sigma_{\text{T}}Z^4(B^2/8\pi m_e c^2)p'^2/[3A^3(m_p/m_e)^3].$$

Hence

$$-\dot{\gamma}'_{\text{syn}} = \frac{16}{3} \frac{\mu_0 Z^4}{A^3} \frac{c\sigma_{\text{T}}\epsilon_B \mu_0 n_0 \Gamma(\Gamma-1)}{(m_p/m_e)^2} p'^2 \cong -\dot{p}'_{\text{syn}}. \quad (14.95)$$

Equating this rate to the stochastic energy-gain rate (14.50) gives the maximum particle momentum achievable due to the competition with synchrotron losses. The result is

$$p_{\max,\text{syn}} \cong \Gamma \left[\frac{K_p}{\Delta'} \left(\frac{r_{\text{L}}^0}{\Delta'} \right)^{q-2} \frac{3A^3}{16\mu_0 Z^4} \frac{(m_p/m_e)^2}{\sigma_{\text{T}}\epsilon_B \mu_0 n_0 \Gamma(\Gamma-1)} \right]^{1/(3-q)}. \quad (14.96)$$

The maximum particle energy from second-order Fermi acceleration, compared to limitations placed by synchrotron energy losses, is given in figure 14.5 [301]. Acceleration and diffusive escape of particles with energies $\gg 10^{18}$ eV from second-order Fermi processes in relativistic blast waves has been proposed as the mechanism that accelerates UHECRs (see chapter 17).

Chapter Fifteen

The Geometry of Spacetime

15.1 INTRODUCTION

The presence of a massive object (compact or otherwise) deforms the ambient Minkowski geometry of spacetime in accordance with the Einstein equation. The gravitational field is described by the metric tensor $g_{\mu\nu}$ of the manifold. On any region of the manifold we can place a coordinate system (t, x^1, x^2, x^3) such that t is a timelike coordinate, and x^i are spacelike for $i = 1, 2, 3$. The metric tensor can then be written in the form

$$g = g_{tt}dt \otimes dt + g_{ii}dt \otimes dx^i + g_{ii}dx^i \otimes dt + g_{ij}dx^i \otimes dx^j. \quad (15.1)$$

Here $g_{\mu\nu} = g_{\nu\mu}$, and since t is a timelike coordinate, $g_{tt} < 0$. At every point of our manifold, the tangent space is isomorphic to Minkowski space. In particular, the timelike vectors are contained within two lightcones. We may designate either of the lightcones as future directed. After having chosen the orientation of the future cone at one point, one must extend this to every point of the manifold in a continuous manner assigning light cones as future directed and past directed consistently. It may not be possible to do this in general if the manifold has a nontrivial topology. In the event that such a designation can be made, we say that the manifold is *time orientable*. By going into a local Minkowski tangent frame at any point p of the manifold, we can easily see that any two distinct causal (timelike or lightlike) vectors at p belong to the same light cone if and only if their inner product is less than zero. In addition to time orientability, if the metric satisfies the Einstein equation for an appropriate energy momentum tensor, the manifold is physically relevant and is a candidate *spacetime*.

The spacetime is determined by the gravitational interactions of all the matter and other causal fields in it. In turn, the geometry determines the motion of all matter and the time evolution of the fields it contains. Therefore, it is necessary to solve for the geometry and the fields (including matter) at the same time. This is nearly an impossible task save for a few ideal, but very important, examples. There is however a practical solution to this problem. Gravitation is a very weak force. Consequently, it takes a large amount of energy and momentum to deform the geometry of spacetime. Thus, it is

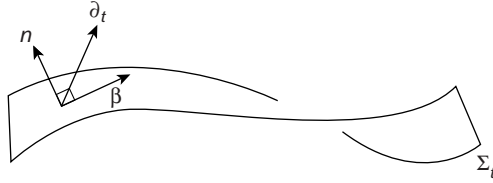


Figure 15.1 Σ_t is a sample spacelike surface which may in general be curved and evolve in time.

possible to introduce the concept of a fixed ambient spacetime in which other particles and fields may evolve. For example, in the absence of massive stars and black holes, we may take the ambient geometry to be Minkowski. This is the situation in special relativity. The Minkowski metric describes perfect vacua. However, we may still talk about particles falling in it, and solve the *twin paradox* problem for example. Our situation will be very similar. We will fix the ambient geometry so that it describes the gravitational field of a rotating star or a black hole. In chapter 16, we will consider the nature of electromagnetic fields and currents in this fixed geometry.

15.2 SPLITTING SPACETIME INTO SPACE AND TIME

It will be convenient in our discussions to visualize spacetime as time-stacked slices of absolute space. These spacelike slices are three-dimensional manifolds whose geometry, as we shall see, is described by the metric $\gamma_{ij} \equiv g_{ij}$. In general, the metric coefficients can be a function of time, in which case, the properties of the absolute space also become time dependent. For the case of a stationary spacetime however, the metric coefficients are by definition time independent. Stationary spacetimes will be of great significance for us since it will be sufficient in describing the ambient exterior geometry of stars and black holes. When this happens, the nature of absolute space will not evolve with time and can therefore be thought of as a curved space counterpart of the familiar Galilean notion of space. We will rewrite eq. (15.1) in a form that will make the foliation of the geometry into spacelike slices manifest, i.e., we shall give meaning to the various components of the metric tensor $g_{\mu\nu}$. The discussion here will be applicable in general, and shall not require the stationarity of spacetime.

Consider a spacelike hypersurface Σ_t obtained by fixing the value of the timelike coordinate t . Henceforth, such hypersurfaces will be referred to as absolute space. The geometric nature of the various slices of absolute space

will in general evolve in time. Clearly,

$$T(\Sigma_t) = \text{span} \left\{ \frac{\partial}{\partial x^i} \right\}. \tag{15.2}$$

From eq. (15.1), we see that the induced metric on our $3d$ absolute space is given by

$$\hat{\gamma} = g_{ij} dx^i \otimes dx^j \equiv \gamma_{ij} dx^i \otimes dx^j \tag{15.3}$$

since $dt = 0$ on Σ_t . Let \tilde{t} denote the timelike vector field $\partial/\partial t$ and let n be the unit normal vector field on Σ_t that points in the direction of increasing t (as shown in figure 15.1). We pick the time coordinate t such that \tilde{t} is future pointing. Consequently, n is timelike and future pointing and so $g(n, \tilde{t}) < 0$. The *lapse function* α is the component of \tilde{t} in the direction of n , i.e.,

$$\alpha \equiv -g(\tilde{t}, n). \tag{15.4}$$

To obtain the components of n , define a three-dual vector in our absolute space by

$$\beta = \beta_i dx^i \equiv g_{ti} dx^i. \tag{15.5}$$

The corresponding tangent vector (which we also denote as β) is given by

$$\beta = \beta^i \frac{\partial}{\partial x^i} = \gamma^{ij} \beta_j \frac{\partial}{\partial x^i}. \tag{15.6}$$

We raise β by the induced metric $\hat{\gamma}$ since it belongs to $T(\Sigma_t)$. Vector fields like β will be given a new life in our absolute space. We shall refer to vectors belonging to $T(\Sigma_t)$ as spatial vectors. They are, however, to be distinguished from spacelike vectors. Spacelike vectors can have a component along \tilde{t} . Spatial vectors are three-dimensional. Since n is normal to $T(\Sigma_t)$

$$g(n, \partial_i) = 0. \tag{15.7}$$

In components, the above equation becomes

$$\beta_j n^t + \gamma_{ij} n^i = 0. \tag{15.8}$$

From eq. (15.4) we get

$$g_{tt} n^t + \beta_i n^i = -\alpha \tag{15.9}$$

and since n is a unit timelike vector

$$g_{tt} (n^t)^2 + 2\beta_i n^i n^t + \gamma^{ij} n^i n^j = -1. \tag{15.10}$$

Equations (15.8)–(15.10) can be solved immediately to obtain

$$n = \frac{1}{\alpha} (\partial_t - \beta^i \partial_i). \tag{15.11}$$

Equivalently,

$$\partial_t = \alpha n + \beta^i \partial_i. \quad (15.12)$$

We now proceed to write the spacetime metric components in terms of α and β :

$$\begin{aligned} g_{tt} &= g(\tilde{t}, \tilde{t}) = g(\alpha n + \beta, \alpha n + \beta) \\ &= -\alpha^2 + 2\alpha g(n, \beta) + g(\beta, \beta). \end{aligned}$$

Therefore, we get that

$$g_{tt} = \beta^2 - \alpha^2.$$

The spacetime metric eq. (15.1) can now be written in the form

$$g = (\beta^2 - \alpha^2)dt \otimes dt + \beta_i [dt \otimes dx^i + dx^i \otimes dt] + \gamma_{ij} dx^i \otimes dx^j. \quad (15.13)$$

β is traditionally called the *shift* vector.

Lowering the index to obtain the one-form corresponding to n^μ , we see that

$$n_\mu = \frac{1}{\alpha} (g_{t\mu} - g_{\mu i} \beta^i).$$

Therefore,

$$n_t = \frac{1}{\alpha} (g_{tt} - g_{ti} \beta^i) = \frac{1}{\alpha} (\beta^2 - \alpha^2 - \beta_i \beta^i) = -\alpha$$

and

$$n_j = \frac{1}{\alpha} (g_{tj} - g_{ji} \beta^i) = 0.$$

That is,

$$n_\mu = (-\alpha, 0, 0, 0).$$

It is now easy to verify that in matrix form

$$g_{\mu\nu} = \begin{bmatrix} \beta^2 - \alpha^2 & \beta_1 & \beta_2 & \beta_3 \\ \beta_1 & & & \\ \beta_2 & & \gamma_{ij} & \\ \beta_3 & & & \end{bmatrix}.$$

It is not too difficult to obtain a projection operator from $T(M) \rightarrow T(\Sigma_t)$. The interested reader is referred to the footnote below.¹ A quick calculation reveals that

$$\sqrt{-g} \equiv \sqrt{-\det(g)} = \alpha \sqrt{\det(\hat{\gamma})} \equiv \alpha \sqrt{\hat{\gamma}},$$

¹Let X be any vector in $T(M)$. Then clearly, by an orthogonal decomposition

$$X = -g(X, n) n + \chi$$

where $\det(g)$ and $\det(\hat{\gamma})$ are the determinants of the matrix representations of g and $\hat{\gamma}$ (the induced spatial metric given in eq. [15.3]). It is important to distinguish the tensor g from the square root of the absolute value of its determinant $\sqrt{|g|} = \sqrt{-g}$ (this rule applies to metric tensors of spacetime and the absolute spaces). It should be clear to the reader by now that the absolute spaces are hardly unique. They depend entirely on the time function t that was chosen.

It is usual to give the invariant interval ds^2 of a spacetime instead of the metric tensor g . They are of course, closely related. Let α be any curve in our spacetime parameterized by the variable τ as given in eq. (3.43). Then

$$ds^2 \equiv g(\dot{\alpha}, \dot{\alpha})d\tau^2. \tag{15.14}$$

Clearly, it is sufficient to give the expression for ds^2 instead of the metric tensor g . It will be useful to briefly consider some simple examples from a 3 + 1 space and time point of view. As remarked earlier, far from regions of strong gravitation the Minkowski spacetime will be adequate in describing the background geometry. Here

$$ds^2 = -dt^2 + dx^2 + dy^2 + dz^2, \tag{15.15}$$

where (t, x, y, z) are the spacetime coordinates. Here (as per the notation above) $\alpha = 1$, $\beta_i = 0$, and $\gamma_{ij} = \delta_{ij}$, where as usual $\delta_{ij} = 1$ if $i = j$, and 0 otherwise. The absolute spaces are the usual Cartesian space \mathfrak{R}^3 with coordinates (x, y, z) endowed with the metric

$$\hat{\gamma} = dx \otimes dx + dy \otimes dy + dz \otimes dz. \tag{15.16}$$

It will be instructive to write the above metric using the familiar spherical coordinate system. In this case

$$ds^2 = -dt^2 + dr^2 + r^2(d\theta^2 + \sin^2 \theta d\varphi^2). \tag{15.17}$$

The coordinates used are (t, r, θ, φ) , where $x = r \sin \theta \cos \varphi$, $y = r \sin \theta \sin \varphi$, and $z = r \cos \theta$. Once again $\alpha = 1$, $\beta_i = 0$, and the nontrivial

for some unique $\chi^i \partial_i \in T(\Sigma_t)$, where $g(n, \chi) = 0$ from eq. (15.7). But clearly,

$$X^\mu = -g(X, n) n^\mu + g(X, n) n^\mu = -g(X, n) n^\mu + (g_\nu^\mu + n^\mu n_\nu) X^\nu.$$

Therefore,

$$h_{\mu\nu} = g_{\mu\nu} + n_\mu n_\nu$$

is the projection operator we need. In components

$$h_{\mu\nu} = \begin{bmatrix} \beta^2 & \beta_1 & \beta_2 & \beta_3 \\ \beta_1 & & & \\ \beta_2 & & \gamma_{ij} & \\ \beta_3 & & & \end{bmatrix}.$$

As expected, the purely spatial components of the tensors g and h agree.

components of $\hat{\gamma}$ are $\gamma_{rr} = 1$, $\gamma_{\theta\theta} = r^2$, and $\gamma_{\varphi\varphi} = r^2 \sin^2 \theta$. Since all we have done is a coordinate change, the absolute spaces continues to be flat, and in spherical coordinates (r, θ, φ) , the spatial metric takes the form

$$\hat{\gamma} = dr \otimes dr + r^2(d\theta \otimes d\theta + \sin^2 \theta d\varphi \otimes d\varphi). \quad (15.18)$$

For the case of the Schwarzschild metric

$$ds^2 = -\left(1 - \frac{2M}{r}\right) dt^2 + \left(1 - \frac{2M}{r}\right)^{-1} dr^2 + r^2(d\theta^2 + \sin^2 \theta d\varphi^2). \quad (15.19)$$

Since there are no mixed time and space components in the metric, here $\beta_i = 0$ and $\alpha^2 = (1 - 2M/r)$. The coordinate t is timelike when $r > 2M$, and in this region, the absolute space is described by the metric

$$\hat{\gamma} = \left(1 - \frac{2M}{r}\right)^{-1} dr \otimes dr + r^2(d\theta \otimes d\theta + \sin^2 \theta d\varphi \otimes d\varphi). \quad (15.20)$$

15.3 THE KERR METRIC

Ever since its inception in 1963 [449], the Kerr solution is the only candidate metric to describe the exterior gravitational field of an electrically neutral, massive, stationary, compact object. From a theoretical point of view, the Kerr solution has been supported by uniqueness theorems of varying sophistication. But the physical relevancy of the Kerr solution can be discerned only by careful astrophysical observations of rapidly rotating compact objects. The observational data has to be then matched up with theoretical predications and calculations. Therefore, it is crucial that we strive to do physics in a Kerr background. As a first step, in this section, we will describe the salient properties of the Kerr solution. The discussion here is merely functional. The reader is referred to the exhaustive book on Kerr geometry by Barrett O'Neill [450]. However, the analysis that follows is sufficient and self-contained.

The Kerr metric describes the time-independent, axis-symmetric gravitational field of a collapsed object that has retained its angular momentum. All matter having collapsed, the Kerr metric (where defined) satisfies the vacuum Einstein equation

$$R_{\mu\nu} = 0. \quad (15.21)$$

$R_{\mu\nu}$ is the Ricci tensor defined in eq. (A.69). In the Boyer-Lindquist coordinate system (t, r, θ, φ) , the Kerr metric takes the form

$$ds^2 = g_{tt} dt^2 + 2\beta_\varphi dt d\varphi + \gamma_{rr} dr^2 + \gamma_{\theta\theta} d\theta^2 + \gamma_{\varphi\varphi} d\varphi^2. \quad (15.22)$$

Here

$$\begin{aligned}
 g_{tt} &= -1 + \frac{2Mr}{\rho^2}, & g_{t\varphi} \equiv \beta_\varphi &= \frac{-2Mr a \sin^2 \theta}{\rho^2}, \\
 \gamma_{rr} &= \frac{\rho^2}{\Delta}, & \gamma_{\theta\theta} &= \rho^2, & \gamma_{\varphi\varphi} &= \frac{\Sigma^2 \sin^2 \theta}{\rho^2},
 \end{aligned}
 \tag{15.23}$$

where

$$\begin{aligned}
 \rho^2 &= r^2 + a^2 \cos^2 \theta, \\
 \Delta &= r^2 - 2Mr + a^2,
 \end{aligned}$$

and

$$\Sigma^2 = (r^2 + a^2)^2 - \Delta a^2 \sin^2 \theta.$$

Additionally

$$\alpha^2 = \frac{\rho^2 \Delta}{\Sigma^2}, \quad \beta^2 = \frac{\beta_\varphi^2}{\gamma_{\varphi\varphi}},$$

$$\sqrt{\hat{\gamma}} = \sqrt{\frac{\rho^2 \Sigma^2}{\Delta}} \sin \theta, \quad \text{and} \quad \sqrt{-g} = \rho^2 \sin \theta.$$

Here, M can be interpreted as the mass and aM the angular momentum of the black hole. It is convenient to pick the time orientation of the Kerr metric consistently so that as $r \rightarrow \infty$ and \tilde{t} is future directed. The metric coefficient functions are independent of t and φ as expected from the assumed symmetry. When $a \rightarrow 0$, the Kerr metric reduces to the Schwarzschild metric given by eq. (3.48). The Schwarzschild metric is both static and spherically symmetric, and consequently describes the end product of a non-rotating spherically symmetric collapse. The contravariant form of the Kerr metric tensor is given by

$$\begin{aligned}
 g &= -\frac{\Sigma^2}{\rho^2 \Delta} \partial_t \otimes \partial_t - \frac{2aMr}{\rho^2 \Delta} \partial_t \otimes \partial_\varphi - \frac{2aMr}{\rho^2 \Delta} \partial_\varphi \otimes \partial_t + \frac{\Delta}{\rho^2} \partial_r \otimes \partial_r \\
 &+ \frac{1}{\rho^2} \partial_\theta \otimes \partial_\theta + \frac{(\Delta - a^2 \sin^2 \theta)}{\rho^2 \Delta \sin^2 \theta} \partial_\varphi \otimes \partial_\varphi.
 \end{aligned}
 \tag{15.24}$$

We will find the following relationships obeyed by the components of the Kerr metric in Boyer-Lindquist coordinates useful. Since they can be easily verified by algebraic manipulation, we state them without proof:

$$a \sin^2 \theta g_{tt} + g_{t\varphi} = -a \sin^2 \theta,
 \tag{15.25}$$

$$(r^2 + a^2)g_{t\varphi} + a\gamma_{\varphi\varphi} = a \sin^2 \theta \Delta, \quad (15.26)$$

$$(r^2 + a^2)g_{tt} + ag_{t\varphi} = -\Delta, \quad (15.27)$$

and

$$a \sin^2 \theta g_{t\varphi} + \gamma_{\varphi\varphi} = (r^2 + a^2) \sin^2 \theta. \quad (15.28)$$

It is clear that the Kerr metric is singular at $\rho^2 = 0$. This is a true singularity of the geometry and cannot be removed away by a coordinate transformation as can be verified by computing scalar quantities at $\rho^2 = 0$ which do not change with coordinate systems. In particular the contraction of the Riemann tensor with itself is not well defined at $\rho^2 = 0$. Explicitly, $R_{\mu\nu\alpha\beta} R^{\mu\nu\alpha\beta} \rightarrow \infty$ as $\rho^2 \rightarrow 0$. The singularity at $\rho^2 = r^2 + a^2 \cos^2 \theta = 0$, has an additional interesting feature in that it happens only when $\theta = \pi/2$. For an excellent, but brief, description of the true Kerr singularity and related matters, see Chandrashekar [451].

On the other hand, the singularity when $\Delta = 0$ in the contravariant form of the Kerr metric is unphysical. These apparent singularities are located at $r = r_{\pm}$, where

$$r_{\pm} = M \pm \sqrt{M^2 - a^2} \quad (15.29)$$

are the roots to the equation $\Delta = 0$. To understand the properties of these surfaces and the region bounded by them, we will have to rewrite the Kerr metric in a coordinate system that is well behaved at $r = r_{\pm}$. We will get to these matters shortly.

15.3.1 The Geodesic Equation and Its Integrability in Kerr Geometry

The nature of the Kerr geodesics will play a vital role in understanding the process of energy extraction from black holes. Energy extraction from rotating black holes will be our chief concern in the following chapter. In a four-dimensional spacetime we would need four constants along geodesics to successfully integrate the geodesic equation. It is clear that we should expect at least three such quantities:

1. The speed of a geodesic is a conserved quantity. In particular, the geodesic tangent vector u satisfies $u^2 = q^2$ where $q^2 = -1$ and $q^2 = 0$ for timelike and null geodesics, respectively.
2. Since the Kerr metric is time independent, we would expect a conserved quantity that is related to the energy of the particle.
3. Owing to the axial symmetry of the geometry, or equivalently φ independence of the metric functions, the angular momentum of the particle corresponding to the geodesic would remain a constant.

Indeed, a fourth conserved quantity exists [452], and as such has enabled a complete geometric analysis of the Kerr spacetime. But, before we embark on deriving the fourth Carter's constant (as it is called), lets quantify the remaining two items above. Let u denote the tangent vector of a proper-time parameterized geodesic, i.e.,

$$u(\tau) = \dot{t}\partial_t + \dot{r}\partial_r + \dot{\theta}\partial_\theta + \dot{\varphi}\partial_\varphi. \tag{15.30}$$

Here, (as always) the overdot refers to the derivative with respect to proper time τ . The symmetry properties of the Kerr geometry are reflected in its Killing vectors. A vector field ξ is Killing if it satisfies the following equation:

$$\nabla_\mu \xi_\nu + \nabla_\nu \xi_\mu = 0. \tag{15.31}$$

It is not difficult to see that along any geodesic, $g(\xi, u) = \text{const}$, where u is the geodesic tangent:

$$u g(\xi, u) = g(u^\mu \nabla_\mu \xi, u) + g(\xi, \nabla_u u) = 0.$$

In the above equation

$$u^\mu u^\nu \nabla_\mu \xi_\nu = 0,$$

since the symmetric sum of an antisymmetric object is trivial. Since the metric coefficients in the Kerr geometry are independent of t , \tilde{t} is a Killing vector field. To check this, we see if \tilde{t} satisfies the Killing equation. Note that

$$\nabla_\mu \tilde{t}_\nu + \nabla_\nu \tilde{t}_\mu = g_{\nu\gamma} \nabla_\mu \tilde{t}^\gamma + g_{\mu\gamma} \nabla_\nu \tilde{t}^\gamma. \tag{15.32}$$

But,

$$\begin{aligned} g_{\nu\gamma} \nabla_\mu \tilde{t}^\gamma &= g_{\nu\gamma} \Gamma_{\mu\alpha}^\gamma \tilde{t}^\alpha = g_{\nu\gamma} \Gamma_{\mu t}^\gamma = \frac{1}{2} g_{\nu\gamma} g^{\gamma\alpha} (\partial_\mu g_{\alpha t} + \partial_t g_{\mu\alpha} - \partial_\alpha g_{\mu t}) \\ &= \frac{1}{2} (\partial_\mu g_{\nu t} - \partial_\nu g_{\mu t}). \end{aligned}$$

Substituting the above into eq. (15.32) we find

$$\nabla_\mu \tilde{t}_\nu + \nabla_\nu \tilde{t}_\mu = \frac{1}{2} (\partial_\mu g_{\nu t} - \partial_\nu g_{\mu t} + \partial_\nu g_{\mu t} - \partial_\mu g_{\nu t}) = 0,$$

i.e., \tilde{t} satisfies the Killing equation (15.31). In a similar manner we can show that $m = \partial_\varphi$ is a Killing vector field of the Kerr geometry. Since Killing vectors give rise to conserved quantities, we are now able to define the constants of motion arising from \tilde{t} and m . The energy E of the geodesic is given by

$$E = -g(\tilde{t}, u) = -(g_{t\dot{t}}\dot{t} + g_{t\dot{\varphi}}\dot{\varphi}). \tag{15.33}$$

The angular momentum L of the geodesic with four-velocity u is given by

$$L = g(m, u) = (g_{t\varphi}\dot{t} + \gamma_{\varphi\varphi}\dot{\varphi}). \quad (15.34)$$

Clearly, E and L are constant along each geodesic. There is a slight abuse of terminology here. For the case of particles with mass, since our timelike geodesics are of unit speed, the quantities E and L defined above corresponds to the energy and angular momentum per unit mass of the particle. It should be clear that the definitions above will determine the time evolution of the geodesic coordinates t and φ . The geodesic equations for t and φ in eq. (15.30) are

$$\dot{t} = \frac{\Sigma^2 E - 2aMrL}{\rho^2 \Delta} \quad (15.35)$$

and

$$\dot{\varphi} = \frac{2aMrE \sin^2 \theta + (\rho^2 - 2Mr)L}{\rho^2 \Delta \sin^2 \theta}. \quad (15.36)$$

This can be seen by substituting expressions for the metric coefficients in eqs. (15.33) and (15.34). The energy of the geodesic is given by

$$-E = \left(-1 + \frac{2Mr}{\rho^2}\right) \dot{t} - \frac{2aMr \sin^2 \theta}{\rho^2} \dot{\varphi}. \quad (15.37)$$

Similarly, from eqs. (15.23) and (15.34) we see that

$$L = -\frac{2aMr \sin^2 \theta}{\rho^2} \dot{t} + \frac{\Sigma^2 \sin^2 \theta}{\rho^2} \dot{\varphi}. \quad (15.38)$$

The above two equations can be inverted to obtain eqs. (15.35) and (15.36).

The promised fourth conserved quantity along Kerr geodesics is not so immediately obtained. The most efficient way of deriving the remaining constant of motion is by recalling that the geodesic equation is implied by an Euler-Lagrange set of equations. Having a Lagrangian in our possession lends itself to the sometimes very powerful set of equations of the Hamilton-Jacobi theory. Following Carter [452], we shall show below that the action is indeed completely separable in this case, and that, all the independent conserved quantities of geodesic motion can be obtained using the Hamilton-Jacobi formalism.

The Lagrangian for geodesic motion is given by (eq. [3.38])

$$\mathbf{L}(x^\mu, \dot{x}^\mu, \tau) = \frac{1}{2} g_{\mu\nu} \dot{x}^\mu \dot{x}^\nu. \quad (15.39)$$

Here, x^μ are the coordinates, and can therefore in our case take on values t, r, θ , and φ . In relativity theory, the proper time parameter τ takes on

the usual role of time. To pass from a Lagrangian formalism to Hamilton's method, we must first obtain the conjugate momenta. By definition,

$$P_\mu = \frac{\partial \mathbf{L}}{\partial \dot{x}^\mu} = g_{\mu\nu} \dot{x}^\nu, \tag{15.40}$$

where P_μ are the generalized momenta. Therefore, the Hamiltonian $H \equiv H(x^\mu, P_\mu, \tau)$ becomes

$$H = P_\mu \dot{x}^\mu - \mathbf{L} = \frac{1}{2} g^{\mu\nu} P_\mu P_\nu. \tag{15.41}$$

The Hamiltonian here is not an explicit function of τ and therefore is a conserved quantity. Clearly, $H = q^2/2$. To utilize the Hamilton-Jacobi method we must introduce a function S such that it is a function of τ , the old coordinates t, r, θ, φ and the new set of conserved quantities of geodesic motion: q^2, E, L, K . Here, K will turn out to be Carter's constant. That is,

$$S = S(\tau, t, r, \theta, \varphi, q^2, E, L, K). \tag{15.42}$$

In addition, S is related to the conjugate momenta of the old coordinates as follows.

$$\partial_t S = P_t, \quad \partial_r S = P_r, \quad \partial_\theta S = P_\theta, \quad \text{and} \quad \partial_\varphi S = P_\varphi. \tag{15.43}$$

From eqs. (15.41) and (15.43) we get that

$$H = \frac{1}{2} g^{\mu\nu} \partial_\mu S \partial_\nu S. \tag{15.44}$$

The Hamilton-Jacobi equation $\partial_\tau S + H = 0$ can now be written in the form

$$\partial_\tau S + \frac{1}{2} g^{\mu\nu} \partial_\mu S \partial_\nu S = 0. \tag{15.45}$$

From eqs. (15.24) and (15.45) we have

$$\begin{aligned} 2\partial_\tau S = & \frac{\Sigma^2}{\rho^2 \Delta} (\partial_t S)^2 + \frac{4aMr}{\rho^2 \Delta} \partial_t S \partial_\varphi S - \frac{\Delta}{\rho^2} (\partial_r S)^2 - \frac{1}{\rho^2} (\partial_\theta S)^2 \\ & - \frac{(\Delta - a^2 \sin^2 \theta)}{\rho^2 \Delta \sin^2 \theta} (\partial_\varphi S)^2. \end{aligned} \tag{15.46}$$

Assuming separability, let us try to write S in the form

$$S = -\frac{1}{2} q^2 \tau - Et + L\varphi + S_r(r) + S_\theta(\theta). \tag{15.47}$$

As suggested S_r is dependent only on r and S_θ only on θ . Here the τ dependence of S was chosen so that

$$\partial_\tau S = -\frac{1}{2} q^2 = -\frac{1}{2} g^{\mu\nu} P_\mu P_\nu = -H,$$

as required by the Hamilton-Jacobi equation. From eqs. (15.46) and (15.47) we get

$$\left[\Delta \left(\frac{dS_r}{dr} \right)^2 - \frac{C^2}{\Delta} - q^2 r^2 \right] + \left[\left(\frac{dS_\theta}{d\theta} \right)^2 + \frac{D^2}{\sin^2 \theta} - q^2 a^2 \cos^2 \theta \right] = 0. \quad (15.48)$$

Here,

$$C = C(r) = (r^2 + a^2)E - aL \quad \text{and} \quad D = D(\theta) = L - aE \sin^2 \theta. \quad (15.49)$$

The terms in the first square bracket above are functions of r alone, while in the second square bracket they are functions of only θ . This gives us the necessary separation constant K . Set

$$\Delta \left(\frac{dS_r}{dr} \right)^2 - \frac{C^2}{\Delta} - q^2 r^2 = -K \quad (15.50)$$

and

$$\left(\frac{dS_\theta}{d\theta} \right)^2 + \frac{D^2}{\sin^2 \theta} - q^2 a^2 \cos^2 \theta = K. \quad (15.51)$$

Define functions $R(r)$ and $\Theta(\theta)$ by

$$R(r) \equiv C^2 + \Delta (q^2 r^2 - K) \quad (15.52)$$

and

$$\Theta(\theta) \equiv K + q^2 a^2 \cos^2 \theta - \frac{D^2}{\sin^2 \theta}. \quad (15.53)$$

Therefore, modulo an irrelevant additive constant, we get the following expression for S :

$$S = -\frac{1}{2}q^2\tau - Et + L\varphi + \int \frac{\sqrt{R}}{\Delta} dr + \int \sqrt{\Theta} d\theta. \quad (15.54)$$

The result we need is obtained from the requirement

$$\frac{\partial S}{\partial q^2} = 0 = -\frac{1}{2}\tau + \int \frac{1}{2\sqrt{R}\Delta} \frac{\partial R}{\partial q^2} dr + \int \frac{1}{2\sqrt{\Theta}} \frac{\partial \Theta}{\partial q^2} d\theta \quad (15.55)$$

and

$$\frac{\partial S}{\partial K} = 0 = \int \frac{1}{2\sqrt{R}\Delta} \frac{\partial R}{\partial K} dr + \int \frac{1}{2\sqrt{\Theta}} \frac{\partial \Theta}{\partial K} d\theta. \quad (15.56)$$

Taking the derivative with respect to proper time after substituting the explicit form of R in eq. (15.55), we get

$$1 = \frac{r^2}{\sqrt{R}} \dot{r} + \frac{a^2 \cos^2 \theta}{\sqrt{\Theta}} \dot{\theta}. \quad (15.57)$$

Similarly, from eq. (15.56) we see that

$$\frac{\dot{r}}{\sqrt{R}} = \frac{\dot{\theta}}{\sqrt{\Theta}}. \tag{15.58}$$

Therefore, the geodesic equations for r and θ in eq. (15.30) for the Kerr geometry are given by

$$\rho^4 \dot{r}^2 = R(r) \tag{15.59}$$

and

$$\rho^4 \dot{\theta}^2 = \Theta(\theta). \tag{15.60}$$

Here, the Carter constant K brought about a separation of variables, thus permitting the integrability of Kerr geodesic equations (15.59) and (15.60).

Null geodesics that stay on a constant value of θ will be important to our analysis. For null geodesics $q^2 = 0$. Here, we will also set $K = 0$, $E = 1$, and $L = a \sin^2 \theta$. When this happens, from eq. (15.53) we see that $\dot{\theta} = 0$ as required, for only then is $L = a \sin^2 \theta$ is a constant of motion. Consequently, from the above derived equations of motion, we see that the components of the geodesic tangent vectors take the simple form

$$i = \frac{r^2 + a^2}{\Delta}, \quad \dot{r} = \pm 1, \quad \dot{\theta} = 0 \quad \text{and} \quad \dot{\varphi} = \frac{a}{\Delta}.$$

It will be convenient to define the following two null geodesic tangent vectors:

$$l_+ = \frac{1}{\Delta} [(r^2 + a^2)\partial_t + \Delta\partial_r + a\partial_\varphi] \tag{15.61}$$

and

$$l_- = \frac{1}{\Delta} [(r^2 + a^2)\partial_t - \Delta\partial_r + a\partial_\varphi]. \tag{15.62}$$

Here l_+ is outgoing ($\dot{r} > 0$), and l_- is infalling ($\dot{r} < 0$).

As was mentioned before, the Boyer-Lindquist coordinates fail at $r = r_+$. Even the null geodesics defined above are not valid when $\Delta = 0$. In order for our analysis to be valid beyond this value of r , we must be able to transform all the relevant quantities to a coordinate system that is well defined across this region. This is the central purpose of the Kerr-Schild coordinate system that we will discuss in the following section.

15.3.2 The Kerr Metric in Kerr-Schild Coordinates

As expected, the coordinate transformation will be singular at $r = r_+$ if the new coordinates are to remove the existing unphysical singularity. Clearly,

this is the case below. The Kerr-Schild coordinates are \bar{t} , \bar{r} , $\bar{\theta}$, and $\bar{\varphi}$. They are related to the Boyer-Lindquist coordinates by the following relations:

$$\bar{r} = r, \quad \bar{\theta} = \theta, \quad d\bar{t} = dt + \frac{2Mr}{\Delta} dr, \quad \text{and} \quad d\bar{\varphi} = d\varphi + \frac{a}{\Delta} dr. \quad (15.63)$$

The overbar is placed on r and θ so that no confusions arise while performing coordinate transformations. We will have plenty of opportunities to compare various components of tensors in the Boyer-Lindquist and Kerr-Schild coordinates. Therefore, it will be crucial to establish the transformation properties as early as possible. Clearly,

$$\begin{bmatrix} d\bar{t} \\ d\bar{r} \\ d\bar{\theta} \\ d\bar{\varphi} \end{bmatrix} = \begin{bmatrix} 1 & G & 0 & 0 \\ 0 & 1 & 0 & 0 \\ 0 & 0 & 1 & 0 \\ 0 & H & 0 & 1 \end{bmatrix} \begin{bmatrix} dt \\ dr \\ d\theta \\ d\varphi \end{bmatrix}, \quad (15.64)$$

where

$$G = \frac{2Mr}{\Delta} \quad \text{and} \quad H = \frac{a}{\Delta}. \quad (15.65)$$

We can write the above equation as

$$d\bar{x}^\mu = A_\nu^\mu dx^\nu. \quad (15.66)$$

Here, as will be the case always, “barred” quantities refer to the Kerr-Schild objects, and the “unbarred” objects are the equivalent Boyer-Lindquist objects. Also, A_ν^μ is the transformation matrix defined in eq. (15.64). For a one-form X ,

$$\bar{X}_\mu d\bar{x}^\mu = \bar{X}_\mu A_\nu^\mu dx^\nu \equiv X_\nu dx^\nu, \quad (15.67)$$

i.e. in component form

$$X_\nu = A_\nu^\mu \bar{X}_\mu. \quad (15.68)$$

Taking the inverse of A_ν^μ we find

$$\bar{X}_\mu = (A^{-1})_\mu^\nu X_\nu, \quad (15.69)$$

where

$$(A^{-1})_\mu^\nu = \begin{bmatrix} 1 & -G & 0 & 0 \\ 0 & 1 & 0 & 0 \\ 0 & 0 & 1 & 0 \\ 0 & -H & 0 & 1 \end{bmatrix}. \quad (15.70)$$

It is now a trivial matter to work out the transformation properties of vectors,

$$d\bar{x}^\mu \left(\frac{\partial}{\partial \bar{x}^\nu} \right) = \delta_\nu^\mu, \quad (15.71)$$

where δ_v^μ is the Kronecker delta. Let

$$\frac{\partial}{\partial \bar{x}^v} = B_v^\beta \frac{\partial}{\partial x^\beta}. \tag{15.72}$$

Then, using eq. (15.66), eq. (15.71) becomes

$$A_\alpha^\mu dx^\alpha \left(B_v^\beta \frac{\partial}{\partial x^\beta} \right) = \delta_v^\mu. \tag{15.73}$$

Therefore

$$A_\alpha^\mu B_v^\alpha = \delta_v^\mu, \tag{15.74}$$

i.e.,

$$B_v^\alpha = (A^{-1})_v^\alpha. \tag{15.75}$$

Therefore from eq. (15.72) and the above equation we get the transformation properties for the components of a vector Y ,

$$\bar{Y}^\alpha = A_\beta^\alpha Y^\beta. \tag{15.76}$$

Equations (15.69) and (15.76) can be used to transform general tensors. We are now in a position to compute the metric tensor in the Kerr-Schild coordinate system. Various metric identities listed in eqs. (15.25)–(15.28) will be required to simplify the expressions. To illustrate the nature of the simplifications, will carry out the calculation of $\bar{g}_{\bar{r}\bar{r}}$ explicitly, leaving the others to the reader to verify:

$$\bar{g}_{\bar{r}\bar{r}} = B_1^\alpha B_1^\beta g_{\alpha\beta} = (G^2 g_{tt} + GH g_{t\varphi}) + (GH g_{t\varphi} + H^2 \gamma_{\varphi\varphi}) + \gamma_{rr}. \tag{15.77}$$

But,

$$(G^2 g_{tt} + GH g_{t\varphi}) = \frac{G}{\Delta} (2Mr g_{tt} + a g_{t\varphi}) = \frac{G}{\Delta} [(r^2 + a^2) g_{tt} + a g_{t\varphi} - \Delta g_{tt}].$$

Using eq. (15.27), the above equation gives

$$(G^2 g_{tt} + GH g_{t\varphi}) = -G (1 + g_{tt}). \tag{15.78}$$

Similary, using eq. (15.26) we find that

$$(GH g_{t\varphi} + H^2 \gamma_{\varphi\varphi}) = H (a \sin^2 \theta - g_{t\varphi}). \tag{15.79}$$

Placing eqs. (15.78) and (15.79) in eq. (15.77), we get

$$\bar{g}_{\bar{r}\bar{r}} = 1 + \frac{2Mr}{\rho^2}.$$

In a similar manner, we find that in Kerr-Schild coordinates the metric components in the basis $\{\bar{t}, \bar{r}, \bar{\theta}, \bar{\varphi}\}$ become

$$\bar{g}_{\mu\nu} = \begin{bmatrix} z-1 & z & 0 & -za \sin^2 \theta \\ z & 1+z & 0 & -a \sin^2 \theta(1+z) \\ 0 & 0 & \rho^2 & 0 \\ -za \sin^2 \theta & -a \sin^2 \theta(1+z) & 0 & \Sigma^2 \sin^2 \theta / \rho^2 \end{bmatrix}, \quad (15.80)$$

where $z = 2Mr/\rho^2$. As required, the metric above is not singular when $\Delta = 0$. In going to a 3 + 1 space and global time formalism, we must remember that, here we have different foliations of space. Spacelike slices in the two coordinate systems are not equivalent. On spacelike slices $d\bar{t} = 0$, the three-metric in a basis $\{\bar{r}, \bar{\theta}, \bar{\varphi}\}$ become

$$\bar{\gamma}_{ij} = \begin{bmatrix} 1+z & 0 & -a \sin^2 \theta(1+z) \\ 0 & \rho^2 & 0 \\ -a \sin^2 \theta(1+z) & 0 & \Sigma^2 \sin^2 \theta / \rho^2 \end{bmatrix}. \quad (15.81)$$

Also

$$\bar{\alpha} = 1/\sqrt{1+z} \quad \text{and} \quad \bar{\beta} = zd\bar{r} - za \sin^2 \theta d\bar{\varphi}. \quad (15.82)$$

Lowering the above one-form β using eq. (15.81), the shift vector becomes

$$\bar{\beta} = \frac{z}{1+z} \frac{\partial}{\partial \bar{r}}. \quad (15.83)$$

Having removed the coordinate singularity at $\Delta = 0$, we are able to meaningfully extend our analysis beyond the $r = r_+$ mark.

15.3.3 The Ergosphere

The causal character of the coordinate function t changes even outside the event horizon. To see this explicitly, let us locate the set of points such that $g_{tt} = 0$. This is given by the surface

$$r_{\text{erg}}(\theta) = M + \sqrt{M^2 - a^2 \cos^2 \theta}. \quad (15.84)$$

Therefore, $g_{tt} > 0$ in the region

$$r_+ < r < r_{\text{erg}}(\theta), \quad (15.85)$$

and consequently $\tilde{t} \equiv \partial_t$ becomes spacelike in the above region. We shall refer to the region defined by eq. (15.85) as the *ergosphere* (see figure 15.2).

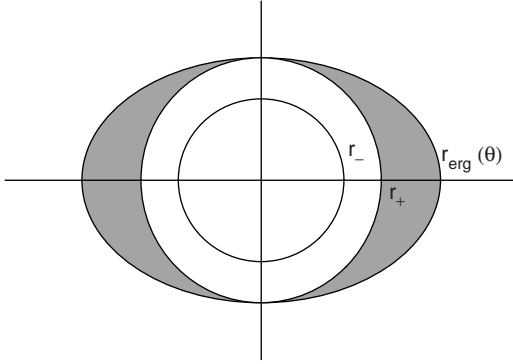


Figure 15.2 r_{\pm} locate the horizons of the Kerr geometry. The shaded region is the ergosphere.

When $r > r_{\text{erg}}$, \tilde{t} is timelike and future directed (as per our choice of time orientation). Inside the ergosphere we can no longer use \tilde{t} as our candidate future-pointing timelike vector. Therefore, the nature of the future cones inside the ergosphere becomes unclear. The same problem exists beyond $r = r_+$ (as we shall see below, this region brings about other interesting features). Both of these issues can now be handled in one stroke. To this end, let us write the null geodesic l_- in the Kerr-Schild coordinate system. We will denote the corresponding Kerr-Schild vector as \bar{l}_- . Using the transformations listed above we get from eq. (15.62) that

$$\bar{l}_- = \partial_{\tilde{t}} - \partial_{\tilde{r}}. \tag{15.86}$$

The above vector field is well defined so long as the Kerr-Schild coordinate system is. As $r \rightarrow \infty$ we have that $g(\bar{l}_-, \tilde{t}) \rightarrow -1$. Therefore, \bar{l}_- is asymptotically future pointing. But, since \bar{l}_- is nowhere vanishing, for consistency reasons \bar{l}_- is future pointing everywhere. *Therefore, we shall take the time-cone containing \bar{l}_- as the future cone at every point in the region defined by $r_- < r$ since the Kerr-Schild coordinates is single valued and well defined in this region.* In particular, \bar{l}_- prescribes the future cone in the ergosphere.

Even though \tilde{t} is not timelike in the ergosphere, the coordinate function t does increase for observers in the ergosphere. To see this, note that eq. (15.24) implies that

$$g_{\mu\nu} \nabla^{\mu} t \nabla^{\nu} t = g^{\mu\nu} \nabla_{\mu} t \nabla_{\nu} t = g^{tt} < 0. \tag{15.87}$$

Therefore, $\nabla^{\mu} t$ is timelike in the ergosphere. Since \bar{l}_- is future pointing,

$$g_{\mu\nu} \bar{l}^{\mu} \nabla^{\nu} t = \bar{l}^{\mu} \nabla_{\mu} t = l^0 = \frac{r^2 + a^2}{\Delta} > 0 \tag{15.88}$$

implies that $\nabla^\mu t$ is past-directed timelike in the ergosphere. Consequently, for an observer with future-pointing four-velocity u

$$0 < g_{\mu\nu} u^\mu \nabla^\nu t = u^\mu \nabla_\mu t = \dot{t}. \quad (15.89)$$

Therefore, for an observer in the ergosphere with four-velocity $u(\tau) = (\dot{t}, \dot{r}, \dot{\theta}, \dot{\varphi})$

$$\dot{t} > 0. \quad (15.90)$$

In the ergosphere, since \tilde{t} is spacelike, an observer cannot remain static. A *static* observer is one whose curve traced out in the spacetime has a fixed value of r , θ , and φ . The required rotation of an observer in the ergosphere can be thought of as an extreme case of frame dragging. At best, all we can have are stationary observers. Stationary observers move along constant values of r and θ . More precisely, as an object with mass falls into the ergosphere, it starts to rotate along with the black hole. This can be seen as follows:

Let $\alpha(\tau)$ be the curve traced out the by a stationary observer. The four-velocity of the observer then takes the form

$$\dot{\alpha} = u(\tau) = (\dot{t}, 0, 0, \dot{\varphi}).$$

We also require that

$$-1 = u^2 = [(\beta^2 - \alpha^2)\dot{t}^2 + \gamma_{\varphi\varphi}\dot{\varphi}^2 + 2\beta_\varphi\dot{t}\dot{\varphi}]. \quad (15.91)$$

If such an observer is to be static, $\dot{\varphi}$ must vanish. Inside the ergosphere, all but the last term on the right hand side of eq. (15.91) is positive. Therefore, for eq. (15.91) to hold true

$$\beta_\varphi \dot{\varphi} < 0$$

for timelike curves, since $\dot{t} > 0$ even in the ergosphere. From eq. (15.23) the above inequality remains true only when

$$a \dot{\varphi} > 0.$$

In particular, there are no static observers in the ergosphere, for the observer is forced to rotate along with the black hole.

15.3.4 The Event Horizon

In the region $r_- < r < r_+$, $\Delta < 0$. Since Δ changes sign in this region, $-\partial_r$ is necessarily timelike. We will now show that $-\partial_r$ is contained in the same timecone as L_- ; or equivalently we need that

$$g(-\partial_r, L_-) < 0. \quad (15.92)$$

Using the transformation matrix constructed above we see that

$$-\frac{\partial}{\partial r} = -G \frac{\partial}{\partial \tilde{t}} - \frac{\partial}{\partial \tilde{r}} - H \frac{\partial}{\partial \tilde{\varphi}}. \tag{15.93}$$

Therefore,

$$g(-\partial_r, l_-) = -[G(\tilde{g}_{\tilde{t}\tilde{t}} - \tilde{g}_{\tilde{r}\tilde{r}})] + H[(\tilde{g}_{\tilde{t}\tilde{\varphi}} - \tilde{g}_{\tilde{\varphi}\tilde{r}})] - (\tilde{g}_{\tilde{r}\tilde{r}} - \tilde{\gamma}_{\tilde{r}\tilde{r}}) = \frac{\rho^2}{\Delta}. \tag{15.94}$$

Since $\Delta < 0$ in the region of interest, we have the necessary result. Consequently, $-\partial_r$ is future pointing and timelike when $r_- < r < r_+$.

This claim leads to a very important result in general relativity. For a particle with future-pointing four-velocity u ,

$$g(u, -\partial_r) < 0 \rightarrow \dot{r} < 0,$$

when $r_- < r < r_+$. Therefore, if a particle (massless or otherwise) enters the region $r < r_+$, it will have necessarily have to move along decreasing values of r until it is thrown into the region $r < r_-$ where Δ is positive and $-\partial_r$ is no longer timelike. Therefore $r = r_+$ forms a one-way membrane. Particles entering it may never escape, thus $r = r_+$ is referred to as the *event horizon* and it forms the boundary of the *black-hole* region. Consequently, what happens beyond $r = r_-$ will never affect physics (and indeed life) in our region of the spacetime, i.e., for values of large r , since particles in the region $r < r_-$ may never enter the region $r > r_-$. For this reason, $r = r_-$ is called the *Cauchy horizon*. Figure 15.2 shows the ergosphere and the horizons of the Kerr black hole when $a^2 < M^2$.

15.4 THE PENROSE PROCESS

As early as 1969, Roger Penrose [453] pointed out the possibility of extracting energy from rotating black holes. As we shall see, such an extraction of energy is possible only due to the existence of the ergosphere.

We begin our analysis with a few preliminaries. Outside the ergosphere \tilde{t} is future pointing and timelike. Therefore, for a particle (regardless of its mass) moving along a geodesic outside the ergosphere we have that

$$g(u, \tilde{t}) < 0. \tag{15.95}$$

From eq. (15.33), we have that the energy E of such an object must be greater than zero. Positivity of E is, however, not a requirement for causal geodesics in the ergosphere (since \tilde{t} is not timelike here). Naturally, particles flowing along geodesics with $E < 0$ will not be able to escape

the ergosphere into the asymptotically flat region, since the energy E in this region must be a positive quantity for the four-velocity of the particle to be future pointing. For a future-pointing causal four-velocity u we need $\dot{t} > 0$ and $\dot{\varphi} > 0$ in the ergosphere. From eqs. (15.35) and (15.36), we see that this is possible for geodesics so long as

$$\Sigma^2 E > 2aMrL \quad (15.96)$$

and

$$2aMrE \sin^2 \theta > (2Mr - \rho^2)L. \quad (15.97)$$

As usual, here E and L are the energy and angular momentum constants associated with the geodesics. Notice, in the ergosphere $(2Mr - \rho^2) > 0$. Clearly, if we want orbits with $E < 0$, we must also have that $L < 0$. We shall see below that the above relations will place a restriction on the amount of energy that can be extracted from the black hole. Thus, we see that geodesics in the ergosphere are permitted to have “negative” values of energy E . Such “*negative-energy*” particles can be used for energy extraction from Kerr black holes. It is important to note that these particles are never observed in regions outside $r > r_{\text{erg}}(\theta)$.

Let us consider the simplest example put forth by Penrose in some detail. Our presentation of the Penrose process leans heavily on [451]. To extract energy from the black hole we would send an object with four momentum p_0 toward the hole via a timelike geodesic. Inside the ergosphere, this object is set to decay into two photons. One photon with negative energy will fall into the black hole, whereas the other photon would escape from the ergosphere into regions of large r . Conservation of energy would then imply that the photon emerging from the ergosphere will have a greater total energy than the initial particle with mass. To see how this would happen let us set up the necessary notation:

1. The four-momentum of the initial infalling particle (along a timelike geodesic):

$$p_0 = m (\dot{t}_0, \dot{r}_0, \dot{\theta}_0, \dot{\varphi}_0). \quad (15.98)$$

2. The four-momentum of the decayed photon with negative energy (along a lightlike geodesic) that falls into the hole:

$$p_1 = (\dot{t}_1, \dot{r}_1, \dot{\theta}_1, \dot{\varphi}_1). \quad (15.99)$$

3. The four-momentum of the decayed photon that escape into regions of large r (along a lightlike geodesic):

$$p_2 = (\dot{t}_2, \dot{r}_2, \dot{\theta}_2, \dot{\varphi}_2). \quad (15.100)$$

At the point of decay $r = r_d$ (for $r_+ < r_d < r_{\text{erg}}(\theta)$), conservation of four-momentum would imply

$$p_0 = p_1 + p_2. \tag{15.101}$$

For simplicity, we would want all these geodesics to lie in the $\theta = \pi/2$ plane. Now, its just a matter of calculating the various geodesics constants for the three particle to make sure that all of what we want can be done consistently. To this end, lets recall the results of eqs. (15.59) and (15.60) and specialize it to the $\theta = \pi/2$ plane. The r and θ coordinates of all the geodesics above must satisfy

$$\rho^4 \dot{r}^2 = R(r) \equiv C^2 + \Delta(q^2 r^2 - K) \tag{15.102}$$

and

$$\rho^4 \dot{\theta}^2 = \Theta(\theta) \equiv K + q^2 a^2 \cos^2 \theta - \frac{D^2}{\sin^2 \theta}, \tag{15.103}$$

where

$$C = C(r) = (r^2 + a^2)E - aL \quad \text{and} \quad D = D(\theta) = L - aE \sin^2 \theta.$$

As before, here, K is the Carter's constant. Since we want all geodesics to be in the $\theta = \pi/2$ plane, following eq. (15.103), we set

$$K_0 = D_0^2, \quad K_1 = D_1^2, \quad \text{and} \quad K_2 = D_2^2. \tag{15.104}$$

The subscripts on all quantities refer to the particle labels as given in eqs. (15.98)–(15.100). We will also pick the initial object to have unit mass, and we will drop it from rest at infinity, i.e.,

$$m = 1 \quad \text{and} \quad E_0 = 1. \tag{15.105}$$

At $r = r_d$, contracting the four-momentum conservation equation eq. (15.101) with the Killing vectors of the Kerr geometry, we get the conservation of energy and angular momentum relations, i.e.,

$$1 = E_1 + E_2 \quad \text{and} \quad L_0 = L_1 + L_2. \tag{15.106}$$

The above equations will not uniquely specify the remaining constants. One way to insist on eq. (15.101), and a safe return of our energetic photon is to require that $r = r_d$ is the only turning point of all the three geodesics. That is we require that at $r = r_d$ we have that $\dot{r}_0 = \dot{r}_1 = \dot{r}_2 = 0$. Then clearly, eq. (15.106) will ensure that

$$(\dot{t}_0, 0, 0, \dot{\phi}_0) = (\dot{t}_1, 0, 0, \dot{\phi}_1) + (\dot{t}_2, 0, 0, \dot{\phi}_2), \tag{15.107}$$

since \dot{t} and $\dot{\phi}$ are given by eqs. (15.35) and (15.36). To impose the turning point condition in eq. (15.102), we set $\dot{r}_0 = 0$ at $r = r_d$ for $E_0 = 1$ and

$q^2 = -1$, and solve for L_0 . This gives

$$L_0 = \frac{1}{2M - r_d} \left(2aM - \sqrt{2Mr_d \Delta_{r_d}} \right). \quad (15.108)$$

Here, $r = 2M$ locates the outer boundary of the ergosphere in the $\theta = \pi/2$ plane, and $\Delta_{r_d} = \Delta(r = r_d)$. For r_d close to the event horizon, $\Delta \approx 0$ and so $L_0 > 0$ (we picked the appropriate root for the quadratic equation for L_0 in eq. [15.102] so that this happens). Similarly, from eq. (15.102), setting $\dot{r}_1 = 0$ at $r = r_d$ for as yet arbitrary but negative E_1 gives

$$L_1 = \frac{1}{2M - r_d} \left(2aM + r_d \sqrt{\Delta_{r_d}} \right) E_1. \quad (15.109)$$

Here, we set $q^2 = 0$, since this geodesic describes a photon. Clearly, when E_1 is less than zero, so is L_1 . Finally, for photon number 2 we get in a similar manner that

$$L_2 = \frac{1}{2M - r_d} \left(2aM - r_d \sqrt{\Delta_{r_d}} \right) E_2. \quad (15.110)$$

With little difficulty we obtain from eqs. (15.106), (15.108), (15.109), and (15.110) the values for the photon energies:

$$E_1 = -\frac{1}{2} \left(\sqrt{\frac{2M}{r_d}} - 1 \right) \quad \text{and} \quad E_2 = \frac{1}{2} \left(\sqrt{\frac{2M}{r_d}} + 1 \right). \quad (15.111)$$

Indeed, the gain in energy in this process is given by

$$\Delta E = E_2 - E_0 = E_2 - 1 = \frac{1}{2} \left(\sqrt{\frac{2M}{r_d}} - 1 \right) = -E_1 \quad (15.112)$$

as expected. This is the Penrose process.

As we have seen, negative energy particles in the ergosphere have negative angular momentum. As the black hole swallows such particles, the mass and the angular momentum of the black hole decrease. This will also lead to a decrease in the ergosphere region. Once the ergosphere vanishes, we cannot continue further with the extraction process. This places a natural limit on the amount of energy we can extract from the black hole. We now proceed to calculate this limit.

Consider the geodesic that describes the negative energy photon (or any other particle in general) that falls into the hole. From remarks made earlier, we know that for such a geodesic, in the ergosphere $\dot{t} \geq 0$ and $\dot{\phi} \geq 0$. Therefore, at the event horizon, as the particle enters the black hole, from eqs. (15.96) and (15.97) we get the single condition

$$E \geq \Omega_H L. \quad (15.113)$$

Here, eqs. (15.96) and (15.97) were evaluated at $r = r_+$ (i.e., $\Delta = 0$), and

$$\Omega_H = \frac{a}{r_+^2 + a^2} = \frac{a}{2Mr_+}. \tag{15.114}$$

Ω_H is usually referred to as the angular velocity of the event horizon. After the negative energy particle falls into the black hole, it suffers a mass and angular momentum decrease subject to the condition

$$\delta M \geq \Omega_H \delta J. \tag{15.115}$$

Here, $J = aM$ is the angular momentum of the black hole. To consider the time evolution of the Kerr black hole, which is subject to energy extraction, let us assume that this process is done in a very slow manner so that we may employ the adiabatic approximation. That is, the black-hole geometry continues to be described by the Kerr metric with its new value of M and J , i.e.,

$$M \rightarrow M + \delta M \quad \text{and} \quad J \rightarrow J + \delta J. \tag{15.116}$$

Of course $\delta J = \delta(aM) = M \delta a + a \delta M$. Christodoulou [454] defines the irreducible mass of the black hole as

$$M_{\text{irr}}^2 = \frac{1}{2} \left(M^2 + \sqrt{M^4 - J^2} \right) = \frac{1}{2} M \left(M + \sqrt{M^2 - a^2} \right). \tag{15.117}$$

To obtain the utility and the meaning of the above expression, lets compute the variation of the irreducible mass. We will do this in the usual manner by taking its variational derivative. Consider variations of the type

$$M \rightarrow M + \lambda \delta M \quad \text{and} \quad a \rightarrow a + \lambda \delta a. \tag{15.118}$$

Here λ is the variational parameter. By definition

$$\begin{aligned} \delta M_{\text{irr}}^2 &= \left. \frac{dM_{\text{irr}}^2}{d\lambda} \right|_{\lambda=0} \\ &= \frac{1}{2} \delta M (M + \sqrt{M^2 - a^2}) + \frac{1}{2} M \left(\delta M + \frac{2M \delta M - 2a \delta a}{2\sqrt{M^2 - a^2}} \right) \\ &= \frac{1}{2\sqrt{M^2 - a^2}} [(2Mr_+ - a^2) \delta M - aM \delta a]. \end{aligned} \tag{15.119}$$

But from eq. (15.115)

$$(2Mr_+ - a^2) \delta M > a \delta J - a^2 \delta M = aM \delta a. \tag{15.120}$$

The above two equations imply that

$$\delta M_{\text{irr}}^2 > 0.$$

Therefore, the irreducible mass of a black hole cannot decrease as it expels energy and angular momentum. Equation (15.117) can be inverted to give:

$$M^2 = M_{\text{irr}}^2 + \frac{J^2}{4M_{\text{irr}}^2}. \quad (15.121)$$

Now consider a Kerr black hole with some initial value of mass and angular momentum M_i and J_i . We can at best extract energy from the hole such that $\delta M_{\text{irr}}^2 = 0$ (the theoretical ideal). At the end of the energy extraction process, the mass of the black hole has now been reduced to the value $M = M_{\text{irr}}(M_i, J_i)$. From the above equation we see that this happens when the new $J = 0$, i.e., the ergosphere has disappeared. Consequently, the term

$$\frac{J^2}{4M_{\text{irr}}^2} \quad (15.122)$$

can be thought of as the extractable rotational energy of the black hole. Since $J_i^2 = M_i^2$ for a maximally rotating Kerr black hole, the percent of energy that can be extracted from the hole is given by

$$\left(1 - \frac{M_{\text{irr}}}{M_i}\right) \times 100\% = \left(1 - \frac{1}{\sqrt{2}}\right) \times 100\% \approx 29\%. \quad (15.123)$$

Thus we see that the astrophysical black hole has little in common with its proverbial counterpart.

15.5 HAWKING RADIATION

It has been well known for some time now that black holes can also radiate energy by means of a purely quantum mechanical process [455]. Unlike the Penrose process, Hawking radiation from black holes does not require an ergosphere. When considering particle production in the presence of a strong gravitational field, we enter the realm of quantum field theory in curved spacetime—a topic that is well outside the scope of this book. However, the essential features of this process can be understood with the slightest knowledge of quantum field theory (or even the quantum mechanical harmonic oscillator for that matter). In this section, we will carefully outline this radiation process. For computational simplicity, we will restrict our discussion to scalar particles.

15.5.1 Scalar Fields in Curved Spacetime

Consider a massless scalar field ϕ in a curved spacetime whose equation of motion is given by

$$\nabla_\mu \nabla^\mu \phi = 0. \quad (15.124)$$

Just as in our applications of classical general relativity, we will continue our discussion here within the 3 + 1 formalism used before. Consider a particular foliation of the background spacetime into spacelike slices Σ . On Σ we define an inner product on functions ϕ that satisfy eq. (15.124),

$$(\phi_1, \phi_2) = i \int (\phi_2^* \nabla_n \phi_1 - \phi_1 \nabla_n \phi_2^*) dV. \tag{15.125}$$

As usual, n is the unit timelike vector field that is orthogonal to Σ and $dV = \sqrt{\hat{\gamma}} d^3x$ is the volume element on the spacelike hyperspaces, and $*$ denotes complex conjugation. The inner product defined above is independent of the spacelike slice chosen. To see this, consider integrable functions ϕ_1 and ϕ_2 that satisfy eq. (15.124) such that they vanish at spatial infinity. Let Σ_1 be the spacelike surface at $t = t_1$, and Σ_2 be the spacelike surface at $t = t_2$ with $t_2 > t_1$. Let B be the four-dimensional volume bounded by the surface. Then

$$(\phi_1, \phi_2)_{\Sigma_1} - (\phi_1, \phi_2)_{\Sigma_2} = i \int_{\partial B} (\phi_2^* \nabla_n \phi_1 - \phi_1 \nabla_n \phi_2^*) dV, \tag{15.126}$$

but

$$i \int_{\partial B} (\phi_2^* \nabla_n \phi_1 - \phi_1 \nabla_n \phi_2^*) dV = i \int_{\partial B} (\phi_2^* \nabla_\mu \phi_1 - \phi_1 \nabla_\mu \phi_2^*) n^\mu dV, \tag{15.127}$$

and since n is a unit normal vector, we get from the four-dimensional version of the divergence theorem that

$$i \int_{\partial B} (\phi_2^* \nabla_\mu \phi_1 - \phi_1 \nabla_\mu \phi_2^*) n^\mu dV = i \int_B \nabla_\mu (\phi_2^* \nabla^\mu \phi_1 - \phi_1 \nabla^\mu \phi_2^*) \sqrt{-g} d^4x. \tag{15.128}$$

But the integrand in the right-hand side of the above equations vanishes due to eq. (15.124):

$$\nabla_\mu (\phi_2^* \nabla^\mu \phi_1 - \phi_1 \nabla^\mu \phi_2^*) = \phi_2^* \nabla_\mu \nabla^\mu \phi_1 - \phi_1 \nabla_\mu \nabla^\mu \phi_2^* = 0. \tag{15.129}$$

From eqs. (15.126)–(15.129) we see that

$$(\phi_1, \phi_2)_{\Sigma_1} = (\phi_1, \phi_2)_{\Sigma_2} \tag{15.130}$$

as claimed. It should be noted that the inner product defined above is not positive definite. In particular,

$$(f, f) = -(f^*, f^*). \tag{15.131}$$

In order to proceed with the canonical quantization of the scalar field, we must choose a complete set of basis functions $\{\phi_k, \phi_k^*\}$ that satisfy

eq. (15.124) such that

$$(\phi_k, \phi_{k'}) = \delta(k - k'), \quad (15.132)$$

which implies that

$$(\phi_k^*, \phi_{k'}^*) = -\delta(k - k'), \quad (15.133)$$

along with the requirement that

$$(\phi_k, \phi_{k'}^*) = 0. \quad (15.134)$$

Here k is just a convenient label. The above equation is consistent with the requirement that $(f, f^*) = 0$ for any smooth function f . Here $\delta(k - k')$ is the usual delta-function such that

$$\int dk g(k) \delta(k - k') = g(k')$$

for any smooth function g .

15.5.2 The Quantum Field for a Scalar Particle in a Flat Spacetime

In Minkowski space, for example, the positively normed functions are given by

$$\phi_{\mathbf{k}} = \frac{1}{\sqrt{(2\pi)^3}} \frac{1}{\sqrt{2\omega}} e^{-i(\omega t - \mathbf{k} \cdot \mathbf{x})} \quad (15.135)$$

for any three-vector \mathbf{k} . Here $\omega \equiv \sqrt{m^2 + \mathbf{k}^2}$. The quantum field for the scalar particle can be written as

$$\phi(x) = \int d^3\mathbf{k} a_{\mathbf{k}} \phi_{\mathbf{k}}(x) + a_{\mathbf{k}}^\dagger \phi_{\mathbf{k}}^*(x), \quad (15.136)$$

where $a_{\mathbf{k}}$ and $a_{\mathbf{k}}^\dagger$ are annihilation and creation operators such that their commutators are given by

$$[a_{\mathbf{k}}, a_{\mathbf{k}'}^\dagger] = \delta(\mathbf{k} - \mathbf{k}') \quad (15.137)$$

and

$$[a_{\mathbf{k}}, a_{\mathbf{k}'}] = 0 = [a_{\mathbf{k}}^\dagger, a_{\mathbf{k}'}^\dagger]. \quad (15.138)$$

The adjoint $a_{\mathbf{k}}^\dagger$ of the operator $a_{\mathbf{k}}$ is defined so that

$$\langle f | a_{\mathbf{k}}^\dagger g \rangle \equiv \langle a_{\mathbf{k}} f | g \rangle \quad (15.139)$$

for every $|f\rangle$ and $|g\rangle$ in the Hilbert space of multiparticle states with inner product denoted by

$$\langle g|f\rangle.$$

Since quantum field theory in flat spacetime is invariant under Lorentz transformations, the vacuum state $|0\rangle$ is defined by the conditions

$$a_{\mathbf{k}}|0\rangle = 0 \quad \text{for every three-vector } \mathbf{k}. \quad (15.140)$$

This vacuum is well defined in the sense that all inertial observers agree on its meaning. Any other inertial observer will see a vacuum as well. Multiparticle states are obtained by the action of the creation operators on the vacuum state. For example, a two-particle state with momentum three-vectors \mathbf{k}_1 and \mathbf{k}_2 are given by

$$a_{\mathbf{k}_1}^\dagger a_{\mathbf{k}_2}^\dagger |0\rangle. \quad (15.141)$$

The number operator

$$W_{\mathbf{k}} \equiv a_{\mathbf{k}}^\dagger a_{\mathbf{k}}$$

counts the number of particles with momentum \mathbf{k} and energy $\omega \equiv \sqrt{m^2 + \mathbf{k}^2}$ in a given multiparticle state, for clearly

$$N_{\mathbf{k}}(a_{\mathbf{k}}^\dagger)^n |0\rangle = n (a_{\mathbf{k}}^\dagger)^n |0\rangle.$$

The notion of particle content is taken for granted in flat space quantum field theory. In other words, suppose you have an n -particle state in one inertial frame, then all other inertial observers seen an n -particle state. This is true because all observers are related to each other by a mere Lorentz transformation. As we shall see below, this will not be the case when noninertial agents conduct observations.

15.5.3 Particle Creation in Curved Spacetime

In curved spacetime, there is no unique complete set of functions $\{\phi_k\}$. Consider a spacetime which is stationary in the infinite past (the *in* region) and in the infinite future (the *out* region). Let $\{\phi_k\}$ and $\{\psi_k\}$ be a complete set of positively normed solutions of eq. (15.124) such that

$$(\phi_k, \phi_{k'}) = (\psi_k, \psi_{k'}) = \delta(k - k'), \quad (15.142)$$

and consequently

$$(\phi_k^*, \phi_{k'}^*) = (\psi_k^*, \psi_{k'}^*) = -\delta(k - k'), \quad (15.143)$$

along with the requirement that

$$(\phi_k, \phi_{k'}^*) = (\psi_k, \psi_{k'}^*) = 0. \quad (15.144)$$

Since $\{\phi_k\}$ and $\{\psi_k\}$ reside in the same space, it is possible to make the following expansion:

$$\phi_j = \int dk (\alpha_{jk} \psi_k + \beta_{jk} \psi_k^*). \quad (15.145)$$

α_{jk} and β_{jk} are in general complex numbers and are referred to as Bogoliubov coefficients. The orthonormalization condition eq. (15.142) implies that

$$\begin{aligned} (\phi_j, \phi_{j'}) &= \int dk ds (\alpha_{jk} \psi_k + \beta_{jk} \psi_k^*, \alpha_{j's} \psi_s + \beta_{j's} \psi_s^*) \\ &= \int dk ds [(\alpha_{jk} \psi_k, \alpha_{j's} \psi_s) + (\beta_{jk} \psi_k^*, \beta_{j's} \psi_s^*)] \\ &= \int dk ds [\alpha_{jk} \alpha_{j's}^* (\psi_k, \psi_s) + \beta_{jk} \beta_{j's}^* (\psi_k^*, \psi_s^*)]. \end{aligned}$$

Therefore, the Bogoliubov coefficients satisfy

$$\int dk (\alpha_{jk} \alpha_{j'k}^* - \beta_{jk} \beta_{j'k}^*) = \delta(j - j'). \quad (15.146)$$

Similarly, eq. (15.144) gives

$$\int dk (\alpha_{jk} \alpha_{j'k} - \beta_{jk} \beta_{j'k}) = 0. \quad (15.147)$$

Equation (15.145) can be inverted to give

$$\psi_j = \int dk (\alpha_{jk}^* \phi_k - \beta_{jk} \phi_k^*). \quad (15.148)$$

We further assume that $\phi_k \propto e^{-i\omega t}$ in the *in* region (as $t \rightarrow -\infty$) and that $\psi_k \propto e^{-i\omega t}$ in the *out* region (as $t \rightarrow +\infty$). Here ω is a fixed positive function of k . Such solutions are possible since the spacetime is stationary when $t \rightarrow \pm\infty$. The in-vacuum is such that

$$a_k |0\rangle_{\text{in}} = 0 \quad (15.149)$$

for every in annihilation operator a_k . a_k^\dagger are creation operators associated with a_k such that the set $\{a_k, a_k^\dagger\}$ satisfy eqs. (15.137) and (15.138). The number of particles present in the far past can be calculated by using the in number operator

$$N_{\text{in},k} \equiv a_k^\dagger a_k.$$

We define the out vacuum in an analogous manner:

$$b_k |0\rangle_{\text{out}} = 0 \quad (15.150)$$

for every *out* annihilation operator b_k , and b_k^\dagger are creation operators associated with b_k that satisfy eqs. (15.137) and (15.138) as well. Also, the number of particles present in the far future can be calculated by using the *out* number operator

$$N_{\text{out},k} \equiv b_k^\dagger b_k.$$

The quantum field for the scalar particle in a curved spacetime is given by

$$\phi(x) = \int dk a_k \phi_k(x) + a_k^\dagger \phi_k^*(x). \tag{15.151}$$

Equivalently,

$$\phi(x) = \int dk b_k \psi_k(x) + b_k^\dagger \psi_k^*(x). \tag{15.152}$$

To avoid any notational confusion, we restate that ϕ denotes the quantum field operator for the scalar particle, whereas $\{\phi_k\}$ are the positively normed bases functions that have a positive frequency in the *in* region (i.e., $\phi_k \propto e^{-i\omega t}$ as $t \rightarrow -\infty$, where $\omega = \omega(k) > 0$). The argument x locates points in spacetime. Since $a_j = (\phi, \phi_j)$ we can use eq. (15.145) to obtain

$$\begin{aligned} a_j &= \int ds (b_s \psi_s + b_s^\dagger \psi_s^*, \phi_j) \\ &= \int ds dk (b_s \psi_s + b_s^\dagger \psi_s^*, \alpha_{jk} \psi_k + \beta_{jk} \psi_k^*). \end{aligned}$$

Therefore,

$$a_j = \int dk (\alpha_{jk}^* b_k - \beta_{jk}^* b_k^\dagger). \tag{15.153}$$

Similarly, using the fact that $b_k = (\phi, \psi_k)$ and eq. (15.148), we get that

$$b_j = \int dk (\alpha_{kj} a_k + \beta_{kj}^* a_k^\dagger). \tag{15.154}$$

Now, consider the circumstance where you have the *in* state as the vacuum $|0\rangle_{\text{in}}$. If the curvature of spacetime can indeed create particles, the expectation value of the number of particles with mode j in the *out* region is given by

$${}_{\text{in}}\langle 0|N_{\text{out},j}|0\rangle_{\text{in}} = {}_{\text{in}}\langle 0|b_j^\dagger b_j|0\rangle_{\text{in}}. \tag{15.155}$$

Using the expansion given in eq. (15.154) we get that

$${}_{\text{in}}\langle 0|N_{\text{out},j}|0\rangle_{\text{in}} = \int dk ds {}_{\text{in}}\langle 0|(\beta_{kj} a_k + \alpha_{kj}^* a_k^\dagger)(\alpha_{sj} a_s + \beta_{sj}^* a_s^\dagger)|0\rangle_{\text{in}}.$$

Therefore,

$$\text{in} \langle 0 | N_{\text{out},j} | 0 \rangle_{\text{in}} = \int dk |\beta_{kj}|^2. \quad (15.156)$$

It turns out that it is a generic feature of black hole spacetimes that the above quantity is nontrivial. It is this process of particle creation that leads to Hawking radiation.

15.5.4 Particle Creation in Rindler Spacetime

The simplest case of particle creation occurs when detectors are carried by non-inertial observers in Minkowski spacetime. Specifically, let us consider the two-dimensional (2D) Rindler spacetime as defined by the metric

$$g = -(\kappa x)^2 dt \otimes dt + dx \otimes dx. \quad (15.157)$$

Here $-\infty < t < \infty$. Since this metric is singular at $x = 0$, we will restrict our spatial coordinate to $0 < x < \infty$. Also, $\kappa > 0$, is a constant that is included for dimensional consistency. To understand the geometry of this spacetime, consider coordinates (u, v) defined by

$$\kappa u = \kappa t - \ln x \quad \text{and} \quad \kappa v = \kappa t + \ln x. \quad (15.158)$$

The Rindler spacetime is covered by $-\infty < u < \infty$ and $-\infty < v < \infty$. In this coordinate system the metric becomes

$$g = -\frac{\kappa^2}{2} e^{\kappa(v-u)} (du \otimes dv + dv \otimes du). \quad (15.159)$$

Let us make a further coordinate transformation given by

$$\bar{u} = -e^{-\kappa u} \quad \text{and} \quad \bar{v} = e^{\kappa v}. \quad (15.160)$$

In this coordinate system the metric becomes

$$g = -\frac{1}{2} (d\bar{u} \otimes d\bar{v} + d\bar{v} \otimes d\bar{u}). \quad (15.161)$$

Here $\bar{u} < 0$ and $\bar{v} > 0$ describes the original Rindler spacetime. But the metric in eq. (15.161) has no coordinate singularities, and therefore can be extended to all values of \bar{u} and \bar{v} . It is easily seen that when $-\infty < \bar{u} < \infty$ and $-\infty < \bar{v} < \infty$, eq. (15.161) describes the 2D Minkowski metric by the following coordinate transformation:

$$\bar{t} = \frac{\bar{v} + \bar{u}}{2} \quad \text{and} \quad \bar{x} = \frac{\bar{v} - \bar{u}}{2}. \quad (15.162)$$

In the \bar{t}, \bar{x} coordinate system

$$g = -d\bar{t} \otimes d\bar{t} + d\bar{x} \otimes d\bar{x}. \quad (15.163)$$

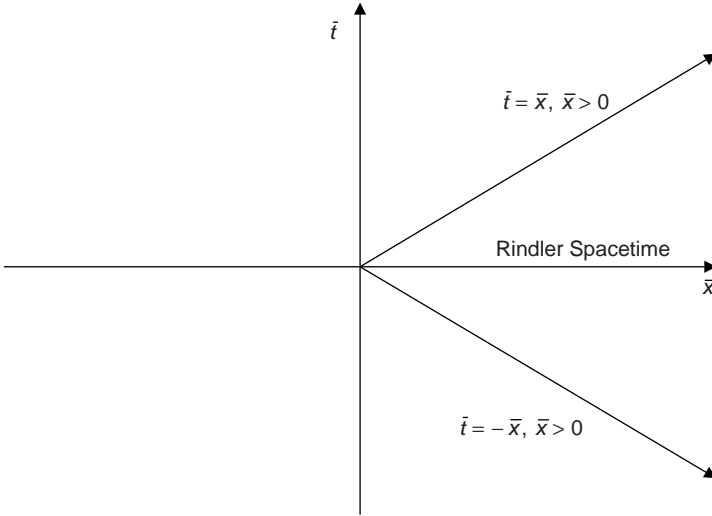


Figure 15.3 The Rindler spacetime is the wedge $\bar{x} > |\bar{t}|$ of the Minkowski geometry.

What we have shown here is that the Rindler spacetime is contained within the Minkowski geometry. A quick calculation reveals that $x = \sqrt{\bar{x}^2 - \bar{t}^2}$. Therefore, as shown in figure 15.3, the Rindler spacetime is simply the wedge $\bar{x} > |\bar{t}|$ of the Minkowski geometry.

The null geodesics

$$l = \dot{t} \partial_t + \dot{x} \partial_x \tag{15.164}$$

of the Rindler spacetime are such that

$$-(\kappa x)^2 \dot{t}^2 + \dot{x}^2 = 0. \tag{15.165}$$

Here, the overdot refers to the derivative with respect to an affine parameter. The above equation is easily integrated by noting that

$$(dt/dx)^2 = \frac{1}{(\kappa x)^2}. \tag{15.166}$$

Consequently, along null geodesics

$$\kappa t \pm \ln x = \text{const.} \tag{15.167}$$

Clearly, $u = \text{const}$ and consequently $\bar{u} = \text{const}$ delineate the outgoing null geodesics. Similarly, $v = \text{const}$ and consequently $\bar{v} = \text{const}$ delineate the infalling null geodesics. The boundary

$$\bar{t} = \bar{x}, \quad \bar{x} > 0 \tag{15.168}$$

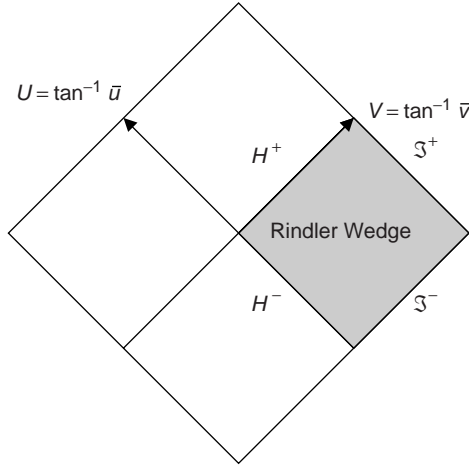


Figure 15.4 The asymptotic structure of the Rindler spacetime. The coordinate transformation $U = \tan^{-1} \bar{u}$ and $V = \tan^{-1} \bar{v}$ brings points at infinity closer.

denotes the future horizon H^+ of the Rindler spacetime, and

$$\bar{t} = -\bar{x}, \quad \bar{x} > 0 \tag{15.169}$$

denotes the past horizon H^- of the Rindler spacetime. The region

$$\bar{v} = \infty \quad \text{and} \quad \bar{u} < 0 \tag{15.170}$$

is the future null infinity \mathfrak{S}^+ of the Rindler spacetime, since all outgoing null geodesics with $\bar{u} = \text{const}$ move along increasing values of \bar{v} . Similarly, the region

$$\bar{u} = -\infty \quad \text{and} \quad \bar{v} > 0 \tag{15.171}$$

is the past null infinity \mathfrak{S}^- of the Rindler spacetime. Figure 15.4 depicts the asymptotic structure of the Rindler geometry.

A static observer in Rindler coordinates

$$x = \text{const} = x_0$$

moves along the tangent vector field

$$\partial_t = \kappa(-\bar{u} \partial_{\bar{u}} + \bar{v} \partial_{\bar{v}}). \tag{15.172}$$

Since

$$g_{tt} = \kappa^2 g(-\bar{u} \partial_{\bar{u}} + \bar{v} \partial_{\bar{v}}, -\bar{u} \partial_{\bar{u}} + \bar{v} \partial_{\bar{v}}) = \kappa^2 \bar{u} \bar{v} \tag{15.173}$$

(note that $\bar{u}\bar{v} < 0$ in the Rindler region), the proper velocity k of such an observer is given by

$$k = \frac{1}{\sqrt{-\bar{u}\bar{v}k^2}} \partial_t = \frac{1}{\sqrt{-\bar{u}\bar{v}}} (-\bar{u} \partial_{\bar{u}} + \bar{v} \partial_{\bar{v}}). \quad (15.174)$$

The acceleration a^μ of this observer is by definition

$$a^\mu = \nabla_k k^\mu. \quad (15.175)$$

But

$$\nabla_{\partial_t} \bar{u}\bar{v} = [-\bar{u} \partial_{\bar{u}} + \bar{v} \partial_{\bar{v}}] \bar{u}\bar{v} = -\bar{u} \bar{v} + \bar{v} \bar{u} = 0. \quad (15.176)$$

Therefore

$$a = \frac{1}{-\bar{u}\bar{v}} \left\{ \nabla_{-\bar{u} \partial_{\bar{u}}} [-\bar{u} \partial_{\bar{u}} + \bar{v} \partial_{\bar{v}}] + \nabla_{\bar{v} \partial_{\bar{v}}} [-\bar{u} \partial_{\bar{u}} + \bar{v} \partial_{\bar{v}}] \right\}. \quad (15.177)$$

Also, in the (\bar{u}, \bar{v}) coordinates, from eq. (15.161), we see that the metric coefficients are constants, and therefore from eq. (A.57) we get that

$$\Gamma_{\alpha\beta}^\mu = 0. \quad (15.178)$$

Therefore,

$$a = - \left\{ \frac{1}{\bar{v}} \partial_{\bar{u}} + \frac{1}{\bar{u}} \partial_{\bar{v}} \right\}. \quad (15.179)$$

The magnitude of proper acceleration for the Rindler observer then becomes

$$|a| = \sqrt{g(a, a)} = \sqrt{\frac{1}{-\bar{u}\bar{v}}} = \frac{1}{x}. \quad (15.180)$$

Therefore, Rindler observers lie on orbits of constant acceleration that increases without bound as they approach the horizon $x = 0$.

For the Rindler spacetime we will consider the boundary

$$\mathcal{S}_{\text{in}} = \mathcal{H}^- \cup \mathcal{S}^- \quad (15.181)$$

as the *in* region. For the *in* region, it will be convenient to use the (\bar{u}, \bar{v}) coordinate system when writing the solutions ϕ_k . In particular, the solutions of positive frequency are outgoing on \mathcal{H}^- and can be written as

$$\phi_{\omega, \rightarrow} = \frac{1}{\sqrt{2\pi}} \frac{1}{\sqrt{2\omega}} e^{-i\omega\bar{u}}. \quad (15.182)$$

The \rightarrow denotes “outgoing.” Note that $\bar{u} = \bar{t} - \bar{x}$, and so a point of constant phase moves in the increasing direction of \bar{x} . Similarly, the solutions of positive frequency are ingoing on \mathcal{S}^- and can be written as

$$\phi_{\omega, \leftarrow} = \frac{1}{\sqrt{2\pi}} \frac{1}{\sqrt{2\omega}} e^{-i\omega\bar{v}}. \quad (15.183)$$

The \leftarrow denotes “ingoing.” The quantum field operator in the *in* region can be written as

$$\phi_{\text{in}} = \int d\omega [a_{\omega} \phi_{\omega, \leftarrow} + a_{\omega}^{\dagger} \phi_{\omega, \leftarrow}^* + c_{\omega} \phi_{\omega, \rightarrow} + c_{\omega}^{\dagger} \phi_{\omega, \rightarrow}^*]. \quad (15.184)$$

Here a_{ω}^{\dagger} create infalling particles, and c_{ω}^{\dagger} create outflowing particles in the *in* region. As these particles enter the Rindler spacetime, the particle content are now measured by accelerating detectors. Consequently, we will use the Rindler coordinates (u, v) in the *out* region,

$$\mathcal{S}_{\text{out}} = \mathcal{H}^+ \cup \mathfrak{S}^+. \quad (15.185)$$

The equation of motion (eq. [15.124]) can be written using ordinary derivatives as

$$\frac{1}{\sqrt{-g}} \partial_{\mu} \sqrt{-g} \partial^{\mu} \psi = 0. \quad (15.186)$$

Here $\sqrt{-g} = \kappa^2 e^{\kappa(v-u)}/2$ as can be seen from eq. (15.159). It is now easily verified that the equation of motion becomes:

$$\partial_v \partial_u \psi = 0. \quad (15.187)$$

The solutions of positive frequency are infalling on \mathcal{H}^+ (see figure 15.5) and are given by

$$\psi_{\omega, \leftarrow} = \frac{1}{\sqrt{2\pi}} \frac{1}{\sqrt{2\omega}} e^{-i\omega v}, \quad (15.188)$$

and the solutions of positive frequency that reach \mathfrak{S}^+ are given by

$$\psi_{\omega, \rightarrow} = \frac{1}{\sqrt{2\pi}} \frac{1}{\sqrt{2\omega}} e^{-i\omega u}. \quad (15.189)$$

The quantum field operator in the *out* region can be written as

$$\phi_{\text{out}} = \int d\omega [b_{\omega} \psi_{\omega, \leftarrow} + b_{\omega}^{\dagger} \psi_{\omega, \leftarrow}^* + d_{\omega} \psi_{\omega, \rightarrow} + d_{\omega}^{\dagger} \psi_{\omega, \rightarrow}^*]. \quad (15.190)$$

Here b_{ω}^{\dagger} create infalling particles, and d_{ω}^{\dagger} create outflowing particles in the *out* region.

If we are looking for the number of particles of mode ω in the \mathfrak{S}^+ region, we must calculate the relevant Bogolubov coefficient $\beta_{\omega'\omega}$ and then integrate the absolute value squared of this amplitude over ω' . From eq. (15.145) we see that

$$\beta_{\omega'\omega} = -(\phi_{\omega', \rightarrow}, \psi_{\omega, \rightarrow}^*) - (\phi_{\omega', \leftarrow}, \psi_{\omega, \rightarrow}^*). \quad (15.191)$$

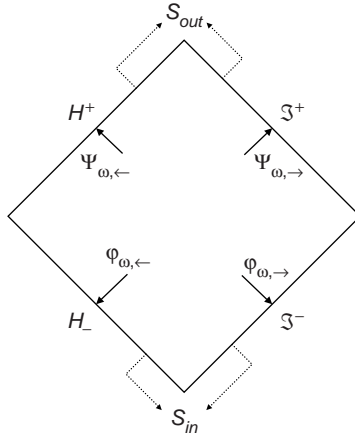


Figure 15.5 Infalling and outgoing modes in the *in* and *out* states of the Rindler geometry.

Due to the invariant nature of the inner product, we will evaluate $\beta_{\omega'\omega}$ along $0 < \bar{x} < \infty$ when $\bar{t} = 0$. Let

$$\beta_{1, \omega'\omega} = -(\phi_{\omega', \rightarrow}, \psi_{\omega, \rightarrow}^*) \tag{15.192}$$

and

$$\beta_{2, \omega'\omega} = -(\phi_{\omega', \leftarrow}, \psi_{\omega, \rightarrow}^*). \tag{15.193}$$

Here we will evaluate $\beta_{1, \omega'\omega}$ explicitly. A similar calculation for $\beta_{2, \omega'\omega}$ is left as an exercise. In this case

$$\beta_{1, \omega'\omega} = -i \int_0^\infty d\bar{x} [\psi_{\omega, \rightarrow} (\partial_{\bar{t}} \phi_{\omega', \rightarrow}) - \phi_{\omega', \rightarrow} (\partial_{\bar{t}} \psi_{\omega, \rightarrow})] |_{\bar{t}=0} \tag{15.194}$$

since $\nabla_n = \partial_{\bar{t}}$ on scalar functions and $dV \rightarrow d\bar{x}$ in one spatial dimension. The first term in the above integral yields

$$\begin{aligned} \xi_{\omega'\omega} &\equiv -i \int_0^\infty d\bar{x} \psi_{\omega, \rightarrow} (\partial_{\bar{t}} \phi_{\omega', \rightarrow}) |_{\bar{t}=0} \\ &= \frac{-i}{4\pi\sqrt{\omega'\omega}} \int_0^\infty d\bar{x} e^{-i\omega u} (-i\omega') e^{-i\omega'\bar{u}} |_{\bar{t}=0} \\ &= \frac{-\omega'}{4\pi\sqrt{\omega'\omega}} \int_0^\infty d\bar{x} e^{i\omega'\bar{x}} \bar{x}^{i\omega/\kappa} \end{aligned} \tag{15.195}$$

since $\kappa u = -\ln(-\bar{u})$ and $\bar{u} = -\bar{x}$ when $\bar{t} = 0$. Since $\xi_{\omega'\omega}$ is analytic in the upper half of the complex plane of the variable \bar{x} , we can rotate our contour of integration axis to upper imaginary axis when $\omega' > 0$ (see figure 15.6).

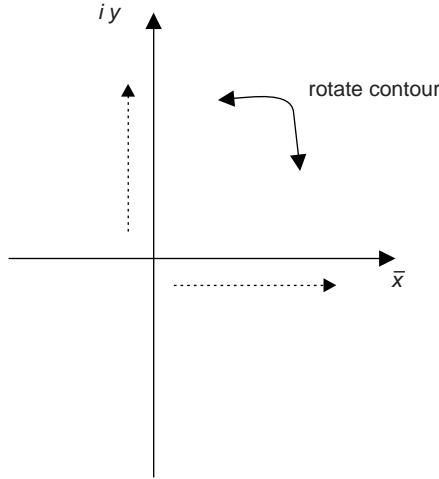


Figure 15.6 Rotated contour of integration for $\xi_{\omega'\omega}$ when $\omega' > 0$.

This is effectively a coordinate substitution $y = -i\omega'\bar{x}$. Then

$$\xi_{\omega'\omega} = \frac{-i(-i\omega')^{-i\omega/\kappa}}{4\pi\sqrt{\omega'\omega}} \int_0^\infty e^{-y} y^{i\omega/\kappa} dy. \quad (15.196)$$

Therefore

$$\xi_{\omega'\omega} = \frac{1}{4\pi\sqrt{\omega'\omega}} \frac{\omega}{\kappa} (-i\omega')^{-i\omega/\kappa} \Gamma(i\omega/\kappa). \quad (15.197)$$

Here $\Gamma(s) = \int_0^\infty dz e^{-z} z^{s-1}$. Similarly, the second term in the integral of eq. (15.194) gives the exact same result as above, i.e.,

$$\zeta_{\omega'\omega} \equiv i \int_0^\infty d\bar{x} \phi_{\omega',\rightarrow} (\partial_{\bar{t}} \psi_{\omega,\rightarrow})|_{\bar{t}=0} = \frac{1}{4\pi\sqrt{\omega'\omega}} \frac{\omega}{\kappa} (-i\omega')^{-i\omega/\kappa} \Gamma(i\omega/\kappa). \quad (15.198)$$

Since there is no scattering in Rindler spacetime, $\psi_{\omega,\rightarrow}$ could only have originated in the H^- region. This is now easily verified by showing that $\beta_{2,\omega'\omega} = 0$. We will not show the parallel calculation for $\beta_{2,\omega'\omega}$; however, we note that the two integrals for $\beta_{2,\omega'\omega}$ (analogous to $\xi_{\omega'\omega}$ and $\zeta_{\omega'\omega}$ for $\beta_{1,\omega'\omega}$) are equal and opposite in this case, and hence cancel each other. Therefore from eqs. (15.194), (15.197), and (15.198) we get

$$\beta_{\omega'\omega} = \frac{1}{2\pi\sqrt{\omega'\omega}} \frac{\omega}{\kappa} (-i\omega')^{-i\omega/\kappa} \Gamma(i\omega/\kappa). \quad (15.199)$$

It immediately follows that

$${}_{\text{in}}\langle 0|N_{\text{out},\omega}|0\rangle_{\text{in}} = \int d\omega' |\beta_{\omega'\omega}|^2 = \int d\omega' \frac{1}{2\pi\omega'\kappa} \frac{1}{e^{2\pi\omega/\kappa} - 1}. \quad (15.200)$$

Here we have used the identity $|\Gamma(ix)|^2 = \pi/(x \sinh \pi x)$ and that

$$(-i)^{(-i\omega/\kappa)} = e^{(-i\pi/2)(-i\omega/\kappa)} = e^{-\pi\omega/2\kappa}$$

in calculating $|\beta_{\omega'\omega}|^2$. The integral in eq. (15.200) is divergent since we are calculating the number of pure modes created by the Rindler spacetime. Pure modes are orthonormal, but they are not square integrable. Had we carefully worked with normalizable wave packets, we would indeed produce normalizable results. From eq. (15.200) we see that the Rindler observer is submerged in a thermal bath of scalar particles such that the absolute temperature T is given by

$$kT = \frac{\hbar\kappa}{2\pi}. \quad (15.201)$$

Here k_B is the Boltzmann constant. This is the Unruh effect. The reader is referred to [42] for a detailed study of the Unruh effect and its physical interpretation.

15.5.5 Particle Creation in Schwarzschild Geometry

Consider a spherical collapse of matter into a Schwarzschild black hole. At some point during the collapse, the future horizon H^+ appears in the spacetime. Scalar modes from the past null infinity \mathfrak{S}^- propagate toward H^+ and fall into the hole, yet others propagate to the future null infinity \mathfrak{S}^+ due to the curvature in the geometry created by the strong gravitational field. Therefore, when we calculate $\beta_{\omega'\omega}$ for this process, we must carefully connect the modes at \mathfrak{S}^+ to \mathfrak{S}^- . The full calculation is beyond the scope of our discussion. Here, we simply present the results. The blackbody temperature of the Schwarzschild black hole is given by [42,455]

$$k_B T_H = \frac{\hbar c^3}{8\pi GM}, \quad \text{i.e.,} \quad T_H \approx 6 \times 10^{-8} (M_\odot/M) \text{ K}. \quad (15.202)$$

Here we have restored all the fundamental constants, and M is the mass of the black hole and T_H is the Hawking temperature. Clearly, the Hawking temperature is vanishingly small for supermassive black holes. From Stephan's law, it is possible to get a quick estimate on the lifetime of a black

hole (in the following calculation we will ignore any effects due to back reaction):

$$\frac{d}{dt}(Mc^2) = -\sigma_{\text{SB}} A T_H^4. \quad (15.203)$$

The effective area of a Schwarzschild black hole $A \sim M^2$ since $r = 2M$ locates the event horizon. Therefore, we have that

$$\frac{dM}{dt} \sim \frac{1}{M^2} \quad (15.204)$$

and hence

$$\tau \sim M^3 \quad (15.205)$$

where τ is the lifetime of the black hole. From eqs. (15.202) and (15.205) we see that the Hawking effect does not play a significant role in the radiative properties of a supermassive black hole.

Hypothetical black holes of significantly smaller mass, $\lesssim 5 \times 10^{14}$ g, would radiate a steady γ -ray emission to contribute to the diffuse extragalactic γ -ray background, according to Page and Hawking [456,457], and evaporating black holes would make submicrosecond bursts of ~ 250 MeV γ rays. Searches using the EGRET [458] place upper limits on the space density of evaporating low-mass black holes, which will improve with the Fermi Gamma Ray Space Telescope.

Chapter Sixteen

Black-Hole Electrodynamics

We have seen in chapter 15 that energy and angular momentum can be extracted from rotating black holes. Extraction of energy using particles does not seem to be a very efficient process in an astrophysical setting [459]. Energetic jets that emanate from supermassive black holes probably rely on electromagnetic fields and currents for their existence. To undertake a study of these matters we shall begin by looking at the equations of electrodynamics in a curved background whose metric is written in the form given by eq. (15.13). Just as we did with the metric, we shall rewrite the usual covariant form of Maxwell's equations in spacetime (i.e., using the Maxwell tensor) in the familiar three-vector formalism that utilizes the electric and magnetic fields. These three-vectors will turn out to be spatial vectors that live in our absolute space. If we choose to employ a coordinate transformation that uses a different foliation of space (and we will), we must be careful in recalculating the three-vectors.

16.1 3+1 ELECTRODYNAMICS

Since we rely on intuition, following Komissarov [460], we will decompose the Maxwell tensor and its dual to components that we are familiar with. The 3+1 formalism of electrodynamics was pioneered by MacDonald and Thorne particularly to study the magnetospheres of black holes [461,462]. Thorne went on to formulate the membrane paradigm wherein he introduces a fictitious membrane just outside the event horizon of the black hole [463]. Prescribing a suitable boundary condition on this membrane allows one to proceed with techniques familiar from classical electrodynamics. However, the membrane paradigm restricts analysis to regions away from the event horizon. Since we will be concerned with the stringent condition imposed by the event horizon, we will not follow the membrane paradigm. However, the 3+1 decomposition will prove useful to our analysis. For the remainder of the chapter, we shall restrict ourselves to stationary spacetimes. This will not pose any difficulty since later on we wish to consider the magnetosphere

of a Kerr black hole. In general, stationary spacetimes come with a timelike Killing vector \tilde{t} . We will use a coordinate system (t, x^1, x^2, x^3) such that $\tilde{t} \equiv \partial_t$. This is the case for the Kerr metric in the Boyer-Lindquist coordinate system. The metric coefficients in such an adapted coordinate system become time independent, i.e., $\partial_t g_{\mu\nu} = 0$. Consequently, our absolute spaces do not evolve in time.

In general, Maxwell equations can be written in the form

$$\nabla_\beta *F^{\alpha\beta} = 0, \quad (16.1)$$

$$\nabla_\beta F^{\alpha\beta} = I^\alpha. \quad (16.2)$$

Here, the Maxwell tensor F that describes the electromagnetic field is anti-symmetric. I is the current four-vector, ∇ is the covariant derivative of the geometry, and $*F$ is the the two-form given by

$$*F^{\alpha\beta} \equiv \frac{1}{2} \epsilon^{\alpha\beta\mu\nu} F_{\mu\nu}, \quad (16.3)$$

or equivalently

$$F^{\alpha\beta} = -\frac{1}{2} \epsilon^{\alpha\beta\mu\nu} *F_{\mu\nu}. \quad (16.4)$$

Here $\epsilon_{\alpha\beta\mu\nu}$ is the completely antisymmetric Levi-Civita tensor density of spacetime defined in eq. (A.41) such that

$$\epsilon_{0123} = \sqrt{-g} = \alpha \sqrt{\hat{\gamma}}. \quad (16.5)$$

Since our absolute spaces do not evolve in time, let us fix a candidate absolute space Σ_0 at $t = t_0$. On Σ_0 we define spatial vectors E and B by the relation

$$B^i = \alpha *F^{it} \quad (16.6)$$

where α is defined by eq. (15.4), and

$$E_i = \frac{1}{2} \alpha \tilde{\epsilon}_{ijk} *F^{jk}. \quad (16.7)$$

Of course, spatial vectors are raised and lowered by the metric $\hat{\gamma}$, specifically $E^i = \hat{\gamma}^{ij} E_j$. Here, the Levi-Civita tensor density of the absolute space Σ_0 is fixed by setting $\tilde{\epsilon}_{123} = \sqrt{\hat{\gamma}}$. Of course, all metric coefficients are understood to be evaluated at $t = t_0$, but this will not directly affect us since they are time independent in our adapted coordinate system. Similarly, we define dual field tangent vectors D and H by

$$D^i = \alpha F^{ti} \quad (16.8)$$

and

$$H_i = \frac{1}{2} \alpha \tilde{\epsilon}_{ijk} F^{jk}. \tag{16.9}$$

It is also possible to define the electric field vector as

$$E_i = F_{it}. \tag{16.10}$$

To see that the above equation is consistent with eq. (16.7) we note that:

$$E_i = \frac{1}{2} \alpha \tilde{\epsilon}_{ijk} *F^{jk} = \frac{1}{2} \alpha \tilde{\epsilon}_{ijk} \frac{1}{2} \epsilon^{jk\mu\nu} F_{\mu\nu}.$$

Since ijk are spatial indices, either μ or ν must take on the label t in the right-hand side above ($j \neq k \neq \mu \neq \nu$). Therefore, using the antisymmetry property of the tensors above,

$$E_i = \frac{1}{2} \alpha \tilde{\epsilon}_{ijk} \epsilon^{tjkl} F_{tl} = -\frac{1}{2} \tilde{\epsilon}_{ijk} \tilde{\epsilon}^{jkl} F_{tl},$$

since

$$\epsilon^{0ijk} = \frac{-1}{\alpha} \tilde{\epsilon}^{ijk},$$

as can be easily seen by raising the Levi-Civita tensor defined by eq. (16.5). To obtain E we must first compute $\tilde{\epsilon}_{ijk} \tilde{\epsilon}^{jkl}$. $\{i, j, k\}$ and $\{j, k, l\}$ should take on distinct values in the above contraction since $\tilde{\epsilon}_{ijk}$ is a totally antisymmetric tensor. But these indices can take on only values 1, 2, and 3. Therefore we see that

$$\tilde{\epsilon}_{ijk} \tilde{\epsilon}^{jkl} \propto \delta_i^l.$$

To get the proportionality constant we note that

$$\tilde{\epsilon}_{1jk} \tilde{\epsilon}^{jkl} = \tilde{\epsilon}_{123} \tilde{\epsilon}^{23l} + \tilde{\epsilon}_{132} \tilde{\epsilon}^{32l} = [1 + (-1)(-1)] \delta_1^l = 2\delta_1^l.$$

Therefore,

$$E_i = -\delta_i^l F_{tl} = F_{it} \tag{16.11}$$

as desired. In a similar manner B , D and H can be defined in an alternate way.

It is easy to see that

1.

$$B^i = \frac{1}{2} \tilde{\epsilon}^{ijk} F_{jk}, \tag{16.12}$$

2.

$$D^i = \frac{1}{2} \tilde{\epsilon}^{ijk} *F_{jk}, \quad (16.13)$$

and

3.

$$H_i = *F_{ti}. \quad (16.14)$$

Equations (16.6)–(16.14) can be used to construct the matrix representations of the Maxwell tensor and its dual. Accordingly,

$$F^{\mu\nu} = \frac{1}{\sqrt{-g}} \begin{bmatrix} 0 & \sqrt{\hat{\gamma}} D^1 & \sqrt{\hat{\gamma}} D^2 & \sqrt{\hat{\gamma}} D^3 \\ -\sqrt{\hat{\gamma}} D^1 & 0 & H_3 & -H_2 \\ -\sqrt{\hat{\gamma}} D^2 & -H_3 & 0 & H_1 \\ -\sqrt{\hat{\gamma}} D^3 & H_2 & -H_1 & 0 \end{bmatrix}, \quad (16.15)$$

$$F_{\mu\nu} = \begin{bmatrix} 0 & -E_1 & -E_2 & -E_3 \\ E_1 & 0 & \sqrt{\hat{\gamma}} B^3 & -\sqrt{\hat{\gamma}} B^2 \\ E_2 & -\sqrt{\hat{\gamma}} B^3 & 0 & \sqrt{\hat{\gamma}} B^1 \\ E_3 & \sqrt{\hat{\gamma}} B^2 & -\sqrt{\hat{\gamma}} B^1 & 0 \end{bmatrix}, \quad (16.16)$$

$$*F_{\mu\nu} = \begin{bmatrix} 0 & H_1 & H_2 & H_3 \\ -H_1 & 0 & \sqrt{\hat{\gamma}} D^3 & -\sqrt{\hat{\gamma}} D^2 \\ -H_2 & -\sqrt{\hat{\gamma}} D^3 & 0 & \sqrt{\hat{\gamma}} D^1 \\ -H_3 & \sqrt{\hat{\gamma}} D^2 & -\sqrt{\hat{\gamma}} D^1 & 0 \end{bmatrix}, \quad (16.17)$$

and

$$*F^{\mu\nu} = \frac{1}{\sqrt{-g}} \begin{bmatrix} 0 & -\sqrt{\hat{\gamma}} B^1 & -\sqrt{\hat{\gamma}} B^2 & -\sqrt{\hat{\gamma}} B^3 \\ \sqrt{\hat{\gamma}} B^1 & 0 & E_3 & -E_2 \\ \sqrt{\hat{\gamma}} B^2 & -E_3 & 0 & E_1 \\ \sqrt{\hat{\gamma}} B^3 & E_2 & -E_1 & 0 \end{bmatrix}. \quad (16.18)$$

These relations can be viewed as the natural generalization of their flat space counterpart (eqs. [3.27] and [3.28]). From the above expressions we see that the Maxwell tensor and its dual can be obtained from E , B , D , and H . We will let the above vector fields on Σ_0 become time dependent in accordance with Maxwell's equations such that

$$F^{\mu\nu}(t, x^1, x^2, x^3) = F^{\mu\nu}\{D(t; x^1, x^2, x^3), H(t; x^1, x^2, x^3)\} \quad (16.19)$$

and

$$F_{\mu\nu}(t, x^1, x^2, x^3) = F_{\mu\nu}\{E(t; x^1, x^2, x^3), B(t; x^1, x^2, x^3)\}. \quad (16.20)$$

By expressions like $E = E(t; x^1, x^2, x^3)$, we mean the time-evolved spatial vector E on Σ_0 at the point (x^1, x^2, x^3) . Similar remarks apply to the dual tensors, i.e., they are generated by the following dependence:

$$*F^{\mu\nu}(t, x^1, x^2, x^3) = *F^{\mu\nu}\{E(t; x^1, x^2, x^3), B(t; x^1, x^2, x^3)\} \quad (16.21)$$

and

$$*F_{\mu\nu}(t, x^1, x^2, x^3) = *F_{\mu\nu}\{D(t; x^1, x^2, x^3), H(t; x^1, x^2, x^3)\}. \quad (16.22)$$

The strength of the above definitions for E , B , D , and H is that the two covariant Maxwell's equations (eqs. [16.1] and [16.2]) reduce to the familiar four (frame-dependent) Maxwell's equations of electrodynamics, as we shall now show. To see the implications of the homogenous Maxwell equation, we first evaluate

$$\nabla_\beta *F^{\alpha\beta} = \partial_\beta *F^{\alpha\beta} + \Gamma_{\beta\lambda}^\alpha *F^{\lambda\beta} + \Gamma_{\beta\lambda}^\beta *F^{\alpha\lambda}. \quad (16.23)$$

Substituting the value for the contracted Christoffel symbol from eq. (A.64), we find that

$$\nabla_\beta *F^{\alpha\beta} = \frac{1}{\sqrt{-g}} \partial_\beta \{\sqrt{-g} *F^{\alpha\beta}\} + \Gamma_{\beta\lambda}^\alpha *F^{\lambda\beta}. \quad (16.24)$$

The last term on the right-hand side in the above equation vanishes since we taking the symmetric sum of an antisymmetric object. Therefore, the homogeneous Maxwell equation (eq. [16.1]) gives

$$\frac{1}{\sqrt{-g}} \partial_\beta \{\sqrt{-g} *F^{\alpha\beta}\} = 0. \quad (16.25)$$

Taking the time component of the above equation we get

$$\frac{1}{\sqrt{\hat{\gamma}}} \partial_i \{\sqrt{\hat{\gamma}} \alpha *F^{ti}\} = 0. \quad (16.26)$$

This implies that in a stationary ambient spacetime, in our adapted coordinate system, the magnetic field B is divergence-free, i.e.,

$$\tilde{\nabla} \cdot B = 0. \quad (16.27)$$

Here $\tilde{\nabla}$ is the covariant derivative of Σ_0 induced by the spacetime metric. When the index α takes on spatial values, from eq. (16.25) we get

$$\frac{1}{\sqrt{-g}} \partial_i \{\sqrt{-g} *F^{jt}\} + \frac{1}{\sqrt{-g}} \partial_i \{\sqrt{-g} *F^{ji}\} = 0. \quad (16.28)$$

Clearly,

$$\frac{1}{\sqrt{-g}} \partial_t \{ \sqrt{-g} * F^{jt} \} = \frac{1}{\alpha} \partial_t \{ \alpha * F^{jt} \} = \frac{1}{\alpha} \partial_t B^j. \quad (16.29)$$

To compute the second term in eq. (16.28) note that

$$\tilde{\epsilon}^{ijk} \tilde{\epsilon}_{klm} * F^{lm} = [\delta_l^i \delta_m^j - \delta_l^j \delta_m^i] * F^{lm} = -2 * F^{ji}.$$

Therefore,

$$\begin{aligned} \frac{1}{\sqrt{\hat{\gamma}}} \partial_i \{ \sqrt{\hat{\gamma}} \alpha * F^{ji} \} &= -\frac{1}{\sqrt{\hat{\gamma}}} \partial_i \left\{ \sqrt{\hat{\gamma}} \frac{1}{2} \alpha \tilde{\epsilon}^{ijk} \tilde{\epsilon}_{klm} * F^{lm} \right\} \\ &= -\tilde{\epsilon}^{ijk} \tilde{\nabla}_i \left\{ \alpha \frac{1}{2} \tilde{\epsilon}_{klm} * F^{lm} \right\}. \end{aligned}$$

Consequently, from eq. (16.7),¹

$$\frac{1}{\sqrt{\hat{\gamma}}} \partial_i \{ \sqrt{\hat{\gamma}} \alpha * F^{ji} \} = \tilde{\epsilon}^{jik} \tilde{\nabla}_i E_k. \quad (16.30)$$

Therefore, from eqs. (16.28), (16.29), and (16.30) we get that

$$\partial_t B + \tilde{\nabla} \times E = 0. \quad (16.31)$$

Here,

$$(\tilde{\nabla} \times E)^i \equiv \tilde{\epsilon}^{ijk} \tilde{\nabla}_j E_k. \quad (16.32)$$

Since the inhomogenous Maxwell's equations are obtained in exactly the same way, we leave the details as an exercise.

When the ambient metric is stationary, in an adapted coordinate system wherein $\tilde{t} = \partial_t$ is the timelike Killing vector field, the dual electric and magnetic fields D and H on Σ_0 satisfy

$$\tilde{\nabla} \cdot D = \rho_c \quad (16.33)$$

and

$$-\partial_t D + \tilde{\nabla} \times H = J, \quad (16.34)$$

¹Note:

$$\tilde{\epsilon}^{jik} \tilde{\epsilon}_{jik} = 3!.$$

Therefore,

$$2 \tilde{\epsilon}^{jik} \tilde{\nabla}_m \tilde{\epsilon}_{jik} = 0,$$

which in turn implies that

$$\tilde{\nabla}_m \tilde{\epsilon}_{jik} = 0.$$

where $\rho_c = \alpha I^t$ and $J^k = \alpha I^k$. Here ρ_c is the charge density and J is the electric three-current.

Clearly, F and $*F$ are not independent, therefore, we cannot expect E and B to be independent of D and H . Given E and B we must be able to obtain an expression for D and H . In special relativity, in regions of ignorable electric and magnetic susceptibilities, $E = D$ and $B = H$. Here, we will see that the corresponding relations are nontrivial. Gravitation induces a mixing of the various electromagnetic vector fields. The vacuum constitutive relations between the electromagnetic vector fields in a stationary spacetime are given by

$$\alpha D = E - \beta \times B \tag{16.35}$$

and

$$H = \alpha B - \beta \times D. \tag{16.36}$$

These results follow from a direct computation. Here we will outline the calculations for eq. (16.35). We can obtain D from eq. (16.15), while E and B can be obtained from eq. (16.18). The tensors in eqs. (16.15) and (16.18) are related by

$$F^{\mu\nu} = -\frac{1}{2}\epsilon^{\mu\nu\alpha\beta} *F_{\alpha\beta} = -\frac{1}{2}\epsilon^{\mu\nu\alpha\beta} g_{\alpha\lambda} g_{\beta\theta} *F^{\lambda\theta}. \tag{16.37}$$

Therefore,

$$\begin{aligned} \alpha D^i &= \alpha^2 F^{ti} = -\frac{\alpha^2}{2}\epsilon^{tijk} g_{j\lambda} g_{k\theta} *F^{\lambda\theta} \\ &= -\frac{\alpha^2}{2} \left(\frac{-\tilde{\epsilon}^{ijk}}{\alpha} \right) [g_{jt} g_{km} *F^{tm} + g_{jm} g_{kt} *F^{mt} + g_{jm} g_{kn} *F^{mn}]. \end{aligned} \tag{16.38}$$

Therefore

$$\alpha D^i = \frac{\alpha \tilde{\epsilon}^{ijk}}{2} [\beta_j \hat{\gamma}_{km} (-B^m / \alpha) + \beta_k \hat{\gamma}_{jm} (B^m / \alpha) + \hat{\gamma}_{jm} \hat{\gamma}_{kn} *F^{mn}]. \tag{16.39}$$

But

$$\frac{\alpha}{2} \tilde{\epsilon}^{ijk} [\beta_j \hat{\gamma}_{km} (-B^m / \alpha) + \beta_k \hat{\gamma}_{jm} (B^m / \alpha)] = -(\beta \times B)^i$$

and from eq. (16.7)

$$\frac{\alpha}{2} \tilde{\epsilon}^{ijk} \hat{\gamma}_{jm} \hat{\gamma}_{kn} *F^{mn} = \frac{\alpha}{2} \hat{\gamma}^{il} \tilde{\epsilon}_{lmn} *F^{mn} = E^i.$$

Using the above two equations and eq. (16.39) we get eq. (16.35). Equation (16.36) should follow from a similar calculation and is left as an exercise.

Equations (16.27), (16.31), (16.33), and (16.34) should be solved together with eqs. (16.35) and eq. (16.36) to obtain the expressions for the electromagnetic field vectors. As a consistency check, notice that very far from the Kerr black hole, $\alpha \rightarrow 1$ and $\beta \rightarrow 0$, and therefore the constitutive relations reduce to their special relativistic counterpart. It is also possible to introduce the usual scalar and vector potential. Let U_μ be the four-vector potential for the Maxwell tensor $F_{\mu\nu}$, i.e.,

$$F_{\mu\nu} = \partial_\mu U_\nu - \partial_\nu U_\mu. \quad (16.40)$$

Then

$$E_i = F_{it} = -\partial_t \Phi - \partial_t A_i, \quad (16.41)$$

where $-\Phi = U_t$ and $A_i = U_i$. Therefore

$$E = -\tilde{\nabla} \Phi - \partial_t A. \quad (16.42)$$

The magnetic field can also be obtained from the four-potential.

$$\begin{aligned} B^i &= \frac{1}{2} \tilde{\epsilon}^{ijk} F_{jk} = \frac{1}{2} \tilde{\epsilon}^{ijk} [\partial_j A_k - \partial_k A_j] \\ &= \frac{1}{2} \tilde{\epsilon}^{ijk} [\tilde{\nabla}_j A_k - \tilde{\nabla}_k A_j] = \tilde{\epsilon}^{ijk} \tilde{\nabla}_j A_k = (\tilde{\nabla} \times A)^i. \end{aligned} \quad (16.43)$$

Here, we have used the fact that the Christoffel symbols are symmetric in the lower indices in the above calculations (i.e., $\Gamma_{jk}^i = \Gamma_{kj}^i$). Therefore,

$$B = \tilde{\nabla} \times A, \quad (16.44)$$

as expected.

16.2 THE ENERGY-MOMENTUM TENSOR

While the currents affect the fields (eqs. [16.1] and [16.2]), they themselves are not immune to prevailing electromagnetic field. The resulting dynamics is however finely balanced by the following principle:

$$\nabla_\mu T_\nu^\mu = 0, \quad (16.45)$$

where $T^{\mu\nu}$ is the total energy momentum of the system. Consider, for example, the electromagnetic field. Here the energy-momentum tensor is given by [464]

$$(T_{\text{em}})^\mu_\nu = F^{\mu\alpha} F_{\nu\alpha} - \frac{1}{4} (F_{\alpha\beta} F^{\alpha\beta}) \delta_\nu^\mu. \quad (16.46)$$

When there is no matter field present, we want the above energy-momentum tensor to be divergence-free. It is easily verified that this is indeed the case.

$$\nabla_{\mu}(T_{\text{em}})_{\nu}^{\mu} = (\nabla_{\mu} F^{\mu\alpha})F_{\nu\alpha} + F^{\mu\alpha}\nabla_{\mu}F_{\nu\alpha} - \frac{1}{2}F^{\alpha\beta}\nabla_{\nu}F_{\alpha\beta}.$$

But

$$\begin{aligned} F^{\mu\alpha}\nabla_{\mu}F_{\nu\alpha} &= \frac{1}{2}[F^{\alpha\beta}\nabla_{\alpha}F_{\nu\beta} + F^{\beta\alpha}\nabla_{\beta}F_{\nu\alpha}] \\ &= -\frac{1}{2}[F^{\alpha\beta}\nabla_{\alpha}F_{\beta\nu} + F^{\alpha\beta}\nabla_{\beta}F_{\nu\alpha}]. \end{aligned}$$

Therefore

$$\nabla_{\mu}(T_{\text{em}})_{\nu}^{\mu} = -F_{\nu\alpha}I^{\alpha} - \frac{1}{2}F^{\alpha\beta}[\nabla_{\nu}F_{\alpha\beta} + \nabla_{\alpha}F_{\beta\nu} + \nabla_{\beta}F_{\nu\alpha}]. \quad (16.47)$$

The last term in the right-hand side of the equation above vanishes. To see this, note that from eq. (16.1) we get

$$\epsilon^{\alpha\beta\mu\nu}\nabla_{\beta}F_{\mu\nu} = 0. \quad (16.48)$$

Therefore, when β , μ , and ν are all different

$$\nabla_{\beta}F_{\mu\nu} + \nabla_{\mu}F_{\nu\beta} + \nabla_{\nu}F_{\beta\mu} = 0. \quad (16.49)$$

But the above equation is easily seen to be true if any of the two indices are the same (owing to the antisymmetry of $F_{\mu\nu}$). Consequently, eq. (16.49) is identically true. And so

$$\nabla_{\mu}(T_{\text{em}})_{\nu}^{\mu} = -F_{\nu\alpha}I^{\alpha}. \quad (16.50)$$

Therefore, as promised in eq. (16.45), for “pure” electromagnetic fields when the current vector is absent ($I^{\alpha} = 0$), we get that

$$\nabla_{\mu}(T_{\text{em}})_{\nu}^{\mu} = 0. \quad (16.51)$$

When the electromagnetic fields interact with charges and currents, the above equation is slightly modified. Here,

$$\nabla_{\mu} [T_{\text{em}}^{\mu\nu} + T_{\text{matter}}^{\mu\nu}] = 0, \quad (16.52)$$

where $T_{\text{matter}}^{\mu\nu}$ is the energy-momentum tensor of the matter fields present. The nature of the matter fields will not concern us directly.

The “divergence-free” nature of the energy-momentum tensor will be used later in the chapter to construct expressions for the total energy and angular momentum of the electromagnetic field in the vicinity of a Kerr

black hole. To facilitate this, we proceed to calculate the relevant components of the energy-momentum tensor of the electromagnetic field. We begin by computing $(T_{\text{em}})^t_t$:

$$(T_{\text{em}})^t_t = F^{t\alpha} F_{t\alpha} - \frac{1}{4}(F_{\alpha\beta} F^{\alpha\beta}). \quad (16.53)$$

But

$$F^{t\alpha} F_{t\alpha} = F^{ti} F_{ti} = \frac{1}{\alpha} D^i \cdot (-E_i) \quad (16.54)$$

and

$$(F_{\alpha\beta} F^{\alpha\beta}) = 2F_{ti} F^{ti} + F_{ij} F^{ij} = \frac{-2}{\alpha} D \cdot E + F_{ij} F^{ij}. \quad (16.55)$$

To simplify the last term in the above equation we note that

$$B^i H_i = \frac{1}{2} \tilde{\epsilon}^{ijk} F_{jk} \frac{1}{2} \alpha \tilde{\epsilon}_{ilm} F^{lm}.$$

Therefore,

$$B^i H_i = \frac{1}{2} \alpha F_{jk} F^{lm} \delta_l^i \delta_m^k = \frac{1}{2} \alpha F_{ij} F^{ij}. \quad (16.56)$$

From eqs. (16.53)–(16.56) we see that

$$(T_{\text{em}})^t_t = -\frac{1}{2\alpha}(E \cdot D + B \cdot H). \quad (16.57)$$

The computation of the remaining useful components of the electromagnetic energy-momentum tensor yield

$$(T_{\text{em}})^i_t = -\frac{1}{\alpha}(E \times H)^i \quad (16.58)$$

and

$$(T_{\text{em}})^t_i = \frac{1}{\alpha}(D \times B)_i \equiv \frac{1}{\alpha} \gamma_{ij}(D \times B)^j. \quad (16.59)$$

If any notion of energy and angular momentum of electromagnetic field should exist in a curved spacetime, it should arise from the symmetries of the background geometry. Although, at this point, we are not committing to a particular background configuration, we will assume that the geometry is endowed with two Killing vector fields: \tilde{t} , which is asymptotically time-like, and m , whose integral curves are closed and spacelike. As mentioned before, in our adapted coordinate system $\tilde{t} = \partial_t$. The asymptotically time-like Killing vector field \tilde{t} can be used to obtain the Poynting equation:

$$\begin{aligned} \nabla_\mu [(T_{\text{em}})^\mu_\nu \tilde{t}^\nu] &= [\nabla_\mu (T_{\text{em}})^\mu_\nu] \tilde{t}^\nu + (T_{\text{em}})^\mu_\nu \nabla_\mu \tilde{t}^\nu \\ &= -F_{\nu\alpha} I^\alpha \tilde{t}^\nu + (T_{\text{em}})^{\mu\nu} \nabla_\mu \tilde{t}_\nu. \end{aligned}$$

The first term on the right-hand side of the above equation comes from eq. (16.50). $T_{\text{em}}^{\mu\nu}$ is a symmetric tensor, while $\nabla_\mu \tilde{t}_\nu$ is antisymmetric as can be seen from the Killing equation (15.31). Therefore, the second term on the right-hand side of the equation above vanishes, and so we have

$$\nabla_\mu [(T_{\text{em}})^\mu_\nu \tilde{t}^\nu] = -F_{ii} I^i = \frac{E_i J^i}{\alpha}. \quad (16.60)$$

Consequently,

$$\frac{1}{\alpha \sqrt{\hat{\gamma}}} \partial_t [\alpha \sqrt{\hat{\gamma}} T_t^t] + \frac{1}{\alpha \sqrt{\hat{\gamma}}} \partial_i [\alpha \sqrt{\hat{\gamma}} T_t^i] = \frac{E \cdot J}{\alpha}.$$

Multiplying the above equation by $-\alpha$ and by noting that $\sqrt{\hat{\gamma}}$ is time independent, we get that

$$\partial_t e + \tilde{\nabla} \cdot S = -E \cdot J. \quad (16.61)$$

Here

$$e = -\alpha T_t^t \quad \text{and} \quad S = E \times H.$$

Equation (16.61) is the curved space version of the Poynting equation. The analogous equation generated by m is given by

$$\partial_t l + \tilde{\nabla} \cdot L = -(\rho_c E + J \times B) \cdot m, \quad (16.62)$$

where

$$l = \alpha T_\varphi^t \quad \text{and} \quad L = -(E \cdot m) D - (H \cdot m) B + \frac{1}{2}(E \cdot D + B \cdot H) m.$$

16.3 THE BLANDFORD-ZNAJEK PROCESS

Based on the work of Ruffini and Wilson [465], and Goldreich and Julian [466], Blandford and Znajek in their seminal paper proposed a viable mechanism by which energy and angular momentum can be extracted from a rotating black hole [467]. Stray charges in the magnetosphere set up by an accretion disc get accelerated sufficiently to produce photons. These photons will in turn produce electron-positron pairs. When charges are produced freely in this manner, an approximately force-free magnetosphere is set up in the vicinity of the black hole. They then showed that such force-free magnetospheres will permit solutions that allow for the extraction of energy from the rotating black hole.

From an observational point of view, the release of energy occurs over a significant amount of time that we are only too content to study the steady-state properties of such phenomena. In addition to time independence, we

shall very naturally impose the condition of axis symmetry. For concreteness, we shall let the Kerr metric describe the ambient geometry of spacetime. Unless otherwise stated, we shall do our calculations in the Boyer-Lindquist coordinate system. Additionally, much like the ambient geometry, we will take U_μ , E , B , D , H , ρ_c , and J to be independent of the coordinates t and φ .

We will presently quantify what we mean by “force-free” in the context of a fluid of charges in the magnetosphere. In this case, since the individual charges do not feel a net electromagnetic force, there is no way for the electromagnetic charges and fields to exchange energy. Therefore, we would expect the energy-momentum tensors of matter and electromagnetic fields to be divergence-free separately, i.e., we require that

$$\nabla_\mu T_{\text{matter}}^{\mu\nu} = 0, \quad (16.63)$$

and consequently

$$\nabla_\mu T_{\text{em}}^{\mu\nu} = 0. \quad (16.64)$$

Therefore, from eq. (16.50) we have that

$$F_{\nu\alpha} I^\alpha = 0. \quad (16.65)$$

This is the force-free condition that we will enforce. In the 3 + 1 formalism, this reduces to the usual result in special relativity. The t component of the above equation gives

$$F_{ti} I^i = -\frac{E_i J^i}{\alpha} = 0, \quad (16.66)$$

and the spatial components give

$$F_{it} \frac{\rho_c}{\alpha} + F_{ij} \frac{J^j}{\alpha} = 0. \quad (16.67)$$

But

$$(J \times B)_i = \tilde{\epsilon}_{ijk} J^j B^k = \tilde{\epsilon}_{ijk} J^j \frac{1}{2} \tilde{\epsilon}^{klm} F_{lm} = F_{ij} J^j. \quad (16.68)$$

Therefore, when the charges and currents in the magnetosphere of a stationary black hole are not subject to a net electromagnetic force, we have that

$$E \cdot J = 0 \quad (16.69)$$

and

$$\rho_c E + J \times B = 0. \quad (16.70)$$

Taking the inner product of eq. (16.70) with the magnetic field B , we find that

$$E \cdot B = 0. \quad (16.71)$$

Definition 16.1 Any spatial vector A in Σ_0 can be decomposed uniquely into the form

$$A = A_P + A_T \quad (16.72)$$

where $A_P = A^r \partial_r + A^\theta \partial_\theta$ and $A_T = A^\varphi \partial_\varphi$. A_P and A_T are referred to as the poloidal and toroidal components of A , respectively. Clearly,

$$E_T = 0 \quad (16.73)$$

since

$$E_\varphi = \partial_\varphi U_t - \partial_t U_\varphi = 0$$

from the assumed symmetry of the problem. Therefore, eq. (16.71) implies that

$$E_P \cdot B_P = 0. \quad (16.74)$$

From eq. (16.73) and eq. (16.74) we see that there exists a purely toroidal vector

$$\omega = \Omega \partial_\varphi$$

such that

$$E = -\omega \times B. \quad (16.75)$$

Additionally, since E_P is perpendicular to B_P and J_P (from the force free condition), and since poloidal vectors are two dimensional,

$$J_P \propto B_P. \quad (16.76)$$

In our analysis of the force-free stationary axis-symmetric magnetosphere of the Kerr black hole, it will be convenient to introduce the notion of a poloidal function and poloidal surfaces. The relationship between $E = E_P$, B_P and J_P is shown in figure 16.1.

Definition 16.2 Surfaces of constant A_φ are called *equipotential surfaces*. Here A_φ is the toroidal component of the three-vector potential A . Functions that are constant on equipotential surfaces are called *equipotential surface functions*.

Functions on Σ_0 that we consider here are functions of only r and θ (from the assumed symmetries of the situation). Therefore equipotential surfaces

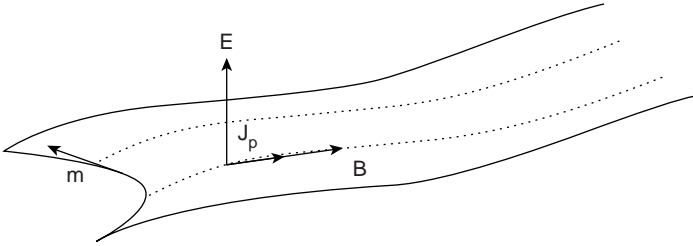


Figure 16.1 3 + 1 Electrodynamics.

are curves in the r - θ plane that have been rotated about the symmetry axis. Clearly, a function f is an equipotential surface function if and only if

$$A_{\varphi,\theta} \partial_r f = A_{\varphi,r} \partial_\theta f.$$

Since (see eq. [16.84])

$$B_P = \frac{1}{\sqrt{\hat{\gamma}}} [A_{\varphi,\theta} \partial_r - A_{\varphi,r} \partial_\theta], \quad (16.77)$$

we have that

$$f \text{ is an equipotential surface function if and only if } B \cdot \tilde{\nabla} f = 0. \quad (16.78)$$

We will now show that Ω is an equipotential surface function. From eqs. (16.31) and (16.75) we see that

$$\tilde{\nabla} \times (\omega \times B) = 0. \quad (16.79)$$

Therefore,

$$\begin{aligned} (\tilde{\nabla} \times (\omega \times B))^i &= \tilde{\epsilon}^{ilm} \tilde{\epsilon}_{mjk} \tilde{\nabla}_l \omega^j B^k \\ &= \delta_j^i \delta_k^l \tilde{\nabla}_l \omega^j B^k - \delta_j^l \delta_k^i \tilde{\nabla}_l \omega^j B^k \\ &= \tilde{\nabla}_j (\omega^i B^j) - \tilde{\nabla}_j (\omega^j B^i). \end{aligned}$$

That is,

$$(\tilde{\nabla}_B \omega - \tilde{\nabla}_\omega B) - (\tilde{\nabla} \cdot \omega) B = 0. \quad (16.80)$$

But,

$$\tilde{\nabla}_j \omega^j = \delta_3^j \Omega_{,j} + \Omega \Gamma_{3j}^j = \delta_3^j \Omega_{,\varphi} + \Omega (\ln \sqrt{\gamma})_{,\varphi} = 0 \quad (16.81)$$

from axial symmetry. Also,

$$0 = \tilde{T}(B, \omega) = (\tilde{\nabla}_B \omega - \tilde{\nabla}_\omega B) - [B, \omega]. \quad (16.82)$$

Here \tilde{T} is the torsion tensor of the absolute space. Finally

$$[B, \omega] = B \cdot \tilde{\nabla} \Omega \partial_\varphi - \Omega (\partial_\varphi B^j) \partial_j = B \cdot \tilde{\nabla} \Omega \partial_\varphi \tag{16.83}$$

since the components of B are φ independent. Equations (16.79)–(16.83) imply that

$$B \cdot \tilde{\nabla} \Omega = 0.$$

Therefore, from eq. (16.78), Ω is an equipotential surface function. There are two other important equipotential surface functions. Using eqs. (16.34) and (16.76) we get that H_φ is an equipotential surface function, and from eq. (16.75) we see that the same is true for the scalar potential Φ .

16.3.1 Explicit Expressions for the Fields and Currents

In this section, we will write the field variables in terms of the equipotential surface functions A_φ and Ω . Consequently, as we shall see, the dynamics of the force-free, stationary, axis-symmetric magnetosphere of the Kerr black hole will be governed by two equipotential surface functions. From the very definition of the three-vector potential we have that

$$B_P = \frac{1}{\sqrt{\hat{\gamma}}} (A_{\varphi,\theta} \partial_r - A_{\varphi,r} \partial_\theta). \tag{16.84}$$

Consequently, eq. (16.75) implies that

$$E_P = - d \int \Omega dA_\varphi. \tag{16.85}$$

The above integral is meaningful, since Ω can be written as a function of A_φ . Equation (16.35) gives the expression for the dual of the electric field:

$$D = D_P = -\frac{1}{\alpha} (\Omega + \beta^\varphi) dA_\varphi. \tag{16.86}$$

Similarly, from eq. (16.36) the poloidal component of the dual of the magnetic field is given by

$$H_P = (\alpha^2 - \beta^2 - \beta_\varphi \Omega) \frac{B_P}{\alpha}. \tag{16.87}$$

The electric charge density is determined by the divergence of D_P , and from eq. (16.86) we get

$$\begin{aligned} -\sqrt{\hat{\gamma}} \rho_c = & \partial_r \left(\frac{1}{\alpha \sqrt{\hat{\gamma}}} (\gamma_{\varphi\varphi} \Omega + \beta_\varphi) \gamma_{\theta\theta} A_{\varphi,r} \right) \\ & + \partial_\theta \left(\frac{1}{\alpha \sqrt{\hat{\gamma}}} (\gamma_{\varphi\varphi} \Omega + \beta_\varphi) \gamma_{rr} A_{\varphi,\theta} \right). \end{aligned} \tag{16.88}$$

The toroidal current vector can be obtained by computing the φ component of the curl in eq. (16.34):

$$\begin{aligned}
 -\sqrt{\hat{\gamma}} J^\varphi = H_{r,\theta} - H_{\theta,r} = \partial_r \left(\frac{1}{\alpha\sqrt{\hat{\gamma}}} (\alpha^2 - \beta^2 - \beta_\varphi \Omega) \gamma_{\theta\theta} A_{\varphi,r} \right) \\
 + \partial_\theta \left(\frac{1}{\alpha\sqrt{\hat{\gamma}}} (\alpha^2 - \beta^2 - \beta_\varphi \Omega) \gamma_{rr} A_{\varphi,\theta} \right). \quad (16.89)
 \end{aligned}$$

The poloidal current is completely determined by H_φ and is given by

$$\sqrt{\hat{\gamma}} J_P = H_{\varphi,\theta} \partial_r - H_{\varphi,r} \partial_\theta. \quad (16.90)$$

Finally,

$$B_\varphi = H_\varphi / \alpha.$$

In the next section we will show that indeed H_φ , and thus B_φ and J_P , is uniquely determined by A_φ and Ω as well (modulo an integration constant).

16.3.2 The Force-Free Constraint Equation

The explicit expressions derived above reflect the time and axis symmetry of the problem. In this section, we will make sure that all the requirements of the force-free condition are met. Since H_φ is an equipotential surface function, from eq. (16.90) we have that

$$J_P = \frac{1}{\sqrt{\hat{\gamma}}} \frac{dH_\varphi}{dA_\varphi} (A_{\varphi,\theta} \partial_r - A_{\varphi,r} \partial_\theta) = \frac{dH_\varphi}{dA_\varphi} B_P, \quad (16.91)$$

as claimed in eq. (16.76). Therefore, since $E \cdot B = 0$ we see that eq. (16.69) is automatically satisfied. The expressions above do not however fully incorporate the force-free condition given by eq. (16.70). We will rectify this deficiency immediately. Since E_P is perpendicular to B_P , we can take $\{E_P, B_P, m\}$ as an orthogonal basis for our absolute space. Since J_P is proportional to B_P , clearly,

$$(J \times B) \cdot m = 0.$$

Therefore,

$$(\rho_c E + J \times B) \cdot m = 0 \quad (16.92)$$

and

$$(\rho_c E + J \times B) \cdot B_P = 0. \quad (16.93)$$

It remains to verify that eq. (16.70) is satisfied when projected onto E_P :

$$\begin{aligned} \rho_c E \cdot E_P + (J \times B) \cdot E_P &= \rho_c E^2 + ((J_P + J_T) \times (B_P + B_T)) \cdot E_P \\ &= \rho_c E^2 + ((J_P \times B_T) + (J_T \times B_P)) \cdot E_P = 0 \end{aligned} \quad (16.94)$$

since J_P is parallel to B_P . To simplify the terms above we use the following relations:

$$E^2 = \frac{\Omega^2}{\gamma_{rr}\gamma_{\theta\theta}} [\gamma_{\theta\theta}(A_{\varphi,r})^2 + \gamma_{rr}(A_{\varphi,\theta})^2] \quad (16.95)$$

and

$$E_r B_\theta - E_\theta B_r = \frac{\Omega}{\sqrt{\gamma}} [\gamma_{\theta\theta}(A_{\varphi,r})^2 + \gamma_{rr}(A_{\varphi,\theta})^2]. \quad (16.96)$$

Substituting eq. (16.91) in eq. (16.94) along with the above two equations gives the result that for the magnetosphere of a stationary, axis-symmetric, Kerr black hole to be force-free, H_φ must satisfy the following equation:

$$\frac{1}{2} \frac{dH_\varphi^2}{dA_\varphi} = -\alpha(\rho_c \Omega \gamma_{\varphi\varphi} - J_\varphi). \quad (16.97)$$

As it turns out, this is not a trivial requirement, and we must impose the resulting constraint while we search for solutions.

Two remarks are in order. Since H_φ is an equipotential surface function, the right-hand side of eq. (16.97) must also be an equipotential surface function. This would severely restrict the allowable forms of Ω and A_φ . We view this as a constraint on the equipotential surface functions. Second, as claimed at the end of the previous section we see that H_φ and thus B_φ is determined by the functions Ω and A_φ since ρ_c and J_φ are determined by them as well.

16.3.3 The Znajek Regularity Condition

As we cross into the ergosphere, the electromagnetic field vectors may lose their original meaning since \tilde{t} is not timelike there. This is not necessarily catastrophic. The equations developed above continue to hold regardless of their physical interpretation. This is not however the case at the event horizon, where the Boyer-Lindquist coordinates cease to be valid. The careful practitioner of relativistic astrophysics must transform the equations to a meaningful coordinate at the event horizon such as the Kerr-Schild system developed in chapter 3. Znajek [468] was the first to do this careful analysis

using the tetrad method. We shall present the results of his work in the 3 + 1 formalism.

From eqs. (16.35) and (16.36) we see that

$$\bar{\alpha} \bar{H} = \bar{\alpha}^2 \bar{B} - \bar{\beta} \times \bar{E} + \bar{\beta} \times (\bar{\beta} \times \bar{B}) = \bar{\alpha}^2 \bar{B} - \bar{\beta} \times \bar{E} + \bar{\beta} (\bar{\beta} \cdot \bar{B}) - \bar{B} \bar{\beta}^2. \quad (16.98)$$

All “barred” quantities are objects in the Kerr-Schild system. In particular

$$\sqrt{\bar{\gamma}} = \sqrt{\det \bar{\gamma}_{ij}}.$$

Taking the $\bar{\varphi}$ component of the above equation we get

$$\bar{\alpha} \bar{H}_{\bar{\varphi}} - \bar{B}^{\bar{r}} [\bar{\gamma}_{\bar{\varphi}\bar{r}} (\bar{\alpha}^2 - \bar{\beta}^2) + \bar{\beta}_{\bar{\varphi}} \bar{\beta}_{\bar{r}}] + \sqrt{\bar{\gamma}} \bar{\beta}^{\bar{r}} \bar{\gamma}^{\bar{\theta}\bar{\theta}} \bar{E}_{\bar{\theta}} = \bar{B}^{\bar{\varphi}} [(\bar{\alpha}^2 - \bar{\beta}^2) \bar{\gamma}_{\bar{\varphi}\bar{\varphi}} + \bar{\beta}_{\bar{\varphi}}^2]. \quad (16.99)$$

From the forms of the various components of the metric coefficients in the Kerr-Schild coordinates given in chapter 15 we see that

$$(\bar{\alpha}^2 - \bar{\beta}^2) \bar{\gamma}_{\bar{\varphi}\bar{\varphi}} + \bar{\beta}_{\bar{\varphi}}^2 = \Delta \sin^2 \theta. \quad (16.100)$$

Therefore, for $\bar{B}^{\bar{\varphi}}$ to be well defined at the event horizon we must have that at $r = r_+$

$$\bar{\alpha} \bar{H}_{\bar{\varphi}} - \bar{B}^{\bar{r}} [\bar{\gamma}_{\bar{\varphi}\bar{r}} (\bar{\alpha}^2 - \bar{\beta}^2) + \bar{\beta}_{\bar{\varphi}} \bar{\beta}_{\bar{r}}] + \sqrt{\bar{\gamma}} \bar{\beta}^{\bar{r}} \bar{\gamma}^{\bar{\theta}\bar{\theta}} \bar{E}_{\bar{\theta}} = 0. \quad (16.101)$$

To understand what this means to us, we must rewrite the above equation in Boyer-Lindquist coordinates.

From eq. (15.69), we see that the Maxwell tensor transforms according to

$$\bar{F}_{\mu\nu} = (A^{-1})_{\mu}^{\alpha} (A^{-1})_{\nu}^{\beta} F_{\alpha\beta}. \quad (16.102)$$

From the explicit form of the transformation matrix A^{-1} we see that $\bar{F}_{\mu\nu} = F_{\mu\nu}$ as long as $\mu, \nu \neq r$. The same goes for the dual tensor $*F$. In particular,

$$-\Omega = \frac{E_{\theta}}{\sqrt{\hat{\gamma}} B^r} = \frac{F_{\theta t}}{F_{\theta\varphi}} = \frac{\bar{F}_{\bar{\theta}\bar{t}}}{\bar{F}_{\bar{\theta}\bar{\varphi}}} = \frac{\bar{E}_{\bar{\theta}}}{\sqrt{\bar{\gamma}} \bar{B}^{\bar{r}}}, \quad (16.103)$$

and

$$\bar{H}_{\bar{\varphi}} = H_{\varphi}.$$

Using the above two equations in eq. (16.101), we get that at the event horizon

$$\frac{\bar{\alpha}}{\alpha} \left(\alpha H_{\varphi} - \frac{\sqrt{-g}}{\sqrt{-\bar{g}}} B^r [\bar{\gamma}_{\bar{\varphi}\bar{r}} (\bar{\alpha}^2 - \bar{\beta}^2) + \bar{\beta}_{\bar{\varphi}} \bar{\beta}_{\bar{r}} + \bar{\gamma} \bar{\beta}^{\bar{r}} \bar{\gamma}^{\bar{\theta}\bar{\theta}} \Omega] \right) = 0. \quad (16.104)$$

Here, $\bar{\gamma} = \sqrt{\bar{\gamma}^2}$. In obtaining the above equation, we also used the fact that

$$\sqrt{-g} = \alpha \sqrt{\hat{\gamma}} = \bar{\alpha} \sqrt{\bar{\gamma}} = \sqrt{-\bar{g}} = \rho^2 \sin \theta.$$

Simple calculations reveal that

$$\det \bar{\gamma}_{ij} \equiv \bar{\gamma} = \sin^2 \theta (1 + z) \rho^4$$

and that

$$\bar{\gamma}_{\bar{\varphi}\bar{r}} (\bar{\alpha}^2 - \bar{\beta}^2) + \bar{\beta}_{\bar{\varphi}} \bar{\beta}_{\bar{r}} + \bar{\gamma} \bar{\beta}^{\bar{r}} \bar{\gamma}^{\bar{\theta}\bar{\theta}} \Omega = \sin^2 \theta (2Mr\Omega - a).$$

Equation (16.104) which is valid at the event horizon, then takes on the form

$$H_\varphi|_{r_+} = \frac{\sin^2 \theta}{\alpha} B^r (2Mr\Omega - a) \Big|_{r_+} \tag{16.105}$$

in Boyer-Lindquist coordinates. This is the Znajek regularity condition. As mentioned before, eq. (16.105) has to hold true for $\bar{B}^{\bar{\varphi}}$ to be well defined at the event horizon.

16.3.4 Energy and Angular-Momentum Extraction from the Force-Free Magnetosphere

It will be convenient to have the expressions for the terms that calculate the rate of extraction of energy and angular momentum from the black hole. We will specialize the general results obtained in section 3.2 to our specific purposes. Consider a Gaussian surface in our absolute space Σ_0 given by the region bounded by $r_+ < r_1$ and $r_2 \rightarrow \infty$. In the force-free case, we see from eq. (16.61) that

$$\frac{d}{dt} \int_{r_1}^{r_2} e dV = - \left(\int_{r_2} S \cdot n dA - \int_{r_1} S \cdot n dA \right). \tag{16.106}$$

Here, $n = \sqrt{\gamma^{rr}} \partial_r$. The area integral is done over surfaces $r = r_1$ and $r = r_2$. In our steady-state case, there are no time-dependent phenomena. What that means is that the energy that flows out of $r = r_2$ must also flow through $r = r_1$. Therefore, the rate of total electromagnetic energy extracted from the black hole is given by

$$\frac{d\mathcal{E}}{dt} = \int_{r_2=\infty} S \cdot n dA. \tag{16.107}$$

Similarly, the rate of extraction of total angular momentum is given by

$$\frac{d\mathcal{L}}{dt} = \int_{r_2=\infty} L \cdot n dA. \tag{16.108}$$

Clearly,

$$L_P = -H_\varphi B_P,$$

and since

$$S_P = \frac{1}{\sqrt{\gamma}}[-E_r H_\varphi \partial_\theta + E_\theta H_\varphi \partial_r] = -\Omega B^\theta H_\varphi \partial_\theta - \Omega B^r H_\varphi \partial_r,$$

the poloidal component of the Poynting vector is

$$S_P = (E \times H)_P = \Omega L_P.$$

Therefore, for the form of n given above,

$$B \cdot n \, dA = B^r \gamma_{rr} \sqrt{\gamma^{rr}} \{ \sqrt{\gamma_{\theta\theta} \gamma_{\varphi\varphi}} \, d\theta \, d\varphi \}.$$

Thus, we have that

$$\frac{d\mathcal{E}}{dt} = - \int_{r_2=\infty} \Omega H_\varphi B^r \sqrt{\hat{\gamma}} \, d\theta \, d\varphi \quad (16.109)$$

and

$$\frac{d\mathcal{L}}{dt} = - \int_{r_2=\infty} H_\varphi B^r \sqrt{\hat{\gamma}} \, d\theta \, d\varphi. \quad (16.110)$$

Under this circumstance, the energy and angular momentum of the black hole decrease at rates given by

$$\frac{\delta M}{\delta t} = - \frac{d\mathcal{E}}{dt} \quad \text{and} \quad \frac{\delta J}{\delta t} = - \frac{d\mathcal{L}}{dt}. \quad (16.111)$$

Equation (16.109) gives the expression for the rate of extraction of energy from the black hole under the Blandford-Znajek mechanism.

16.4 GEODESIC CURRENTS IN THE MAGNETOSPHERE

As a simplifying assumption, we write the current-density vector in a force-free magnetosphere as

$$I^\nu = F(r, \theta) u^\nu, \quad (16.112)$$

where $u^\nu(r, \theta)$ is a geodesic congruence of the form

$$u^\nu = \left(\dot{t}, \frac{\sqrt{R}}{\rho^2}, \frac{\sqrt{\Theta}}{\rho^2}, \dot{\varphi} \right). \quad (16.113)$$

Here, \dot{t} , $\dot{\varphi}$, R , and Θ are as given in eqs. (15.35), (15.36), (15.59), and (15.60). The function $F(r, \theta)$ is such that the charge density and the current spatial vector are given by

$$\rho_c = \alpha F \dot{t}, \quad J^\varphi = \alpha F \dot{\varphi}, \quad \text{and} \quad J_P = \alpha F \left(\frac{\sqrt{R}}{\rho^2}, \frac{\sqrt{\Theta}}{\rho^2} \right). \quad (16.114)$$

Since J_P is parallel to B_P , eq. (16.78) tells us that, when the force-free magnetosphere is filled with geodesic currents, a function f is an equipotential surface function iff

$$J_P f = 0 = \sqrt{R} \partial_r f + \sqrt{\Theta} \partial_\theta f, \tag{16.115}$$

i.e., the charges flow along equipotential surfaces. Conservation of current implies

$$\nabla_\mu I^\mu = 0,$$

i.e.,

$$\partial_r \left(F \frac{\sqrt{R}}{\rho^2} \sqrt{-g} \right) + \partial_\theta \left(F \frac{\sqrt{\Theta}}{\rho^2} \sqrt{-g} \right) = 0. \tag{16.116}$$

This is actually an equation for F . It is very reasonable to assume that force-free currents can be described by eq. (16.112). In this case, we can understand the physical origin for the equations describing the charge density ρ and the toroidal current density J^φ (eqs. [16.88] and [16.89]). It is important to develop a physical understanding of these objects, since they are the only undetermined nonequipotential surface functions to appear in the constraint equation. From eqs. (15.35), (16.88), and (16.114) we see after substituting the expressions for the metric coefficients that

$$\begin{aligned} -F \sin \theta \frac{(\Sigma^2 E - 2aMrL)}{\Delta} &= \partial_r \left(\sin \theta (\Sigma^2 \Omega - 2aMr) \frac{A_{\varphi,r}}{\rho^2} \right) \\ &+ \partial_\theta \left(\sin \theta (\Sigma^2 \Omega - 2aMr) \frac{A_{\varphi,\theta}}{\rho^2 \Delta} \right). \end{aligned} \tag{16.117}$$

Both sides of the equation have similar features. There is more in common to the two sides than one might initially suspect. E and L are constant along a geodesic. That does not imply that E and L are constant over the magnetosphere. The integral curve of each J_P can have a different value for E and L . That is, much like Ω , E and L are equipotential surface functions. The above equation lends credence to the form of the current density four-vector we have chosen. This feature is seen again in the expression for J^φ (the other important term in the constraint equation). From eqs. (15.36), (16.89), and (16.114), we see after substituting the expressions for the metric coefficients

that

$$\begin{aligned}
 -F \frac{[2aMrE \sin^2 \theta + (\rho^2 - 2Mr)L]}{\sin \theta \Delta} &= \partial_r \left([2aMr\Omega \sin^2 \theta \right. \\
 &+ (\rho^2 - 2Mr)] \frac{A_{\varphi,r}}{\rho^2 \sin \theta} \Big) + \partial_\theta \left([2aMr\Omega \sin^2 \theta + (\rho^2 - 2Mr)] \frac{A_{\varphi,\theta}}{\rho^2 \Delta \sin \theta} \right).
 \end{aligned} \tag{16.118}$$

This is an expected expression considering eq. (16.117). In eqs. (16.117) and (16.118) we must keep in mind that

$$J_P \Omega = J_P E = J_P L = 0. \tag{16.119}$$

This is the only preset requirement for E and L . Since eq. (16.112) prescribes J_P (eq. [16.114]), we shall now consider its implications.

$$\sqrt{\hat{\gamma}} J_P = H_{\varphi,\theta} \partial_r - H_{\varphi,r} \partial_\theta = \sqrt{-g} \left(F \frac{\sqrt{R}}{\rho^2} \partial_r + F \frac{\sqrt{\Theta}}{\rho^2} \partial_\theta \right). \tag{16.120}$$

Therefore,

$$\sqrt{-g} F \frac{\sqrt{R}}{\rho^2} = H_{\varphi,\theta} \tag{16.121}$$

and

$$\sqrt{-g} F \frac{\sqrt{\Theta}}{\rho^2} = -H_{\varphi,r}. \tag{16.122}$$

But $H_{\varphi,\theta,r} = H_{\varphi,r,\theta}$ imply that

$$\partial_r \left(F \frac{\sqrt{R}}{\rho^2} \sqrt{-g} \right) + \partial_\theta \left(F \frac{\sqrt{\Theta}}{\rho^2} \sqrt{-g} \right) = 0. \tag{16.123}$$

But this is exactly eq. (16.116), which is satisfied by F , so there is no extra consistency requirement from the form of J_P . Finally we turn our attention to H_φ . Equations (16.121) and (16.122) explicitly show that H_φ satisfies eq. (16.115), which is consistent with the requirement that H_φ is an equipotential surface function. In terms of eq. (16.114), the constraint equation for H_φ takes the form

$$\begin{aligned}
 -\frac{1}{2} \frac{dH_\varphi^2}{dA_\varphi} &= \alpha (\rho_c \Omega \gamma_{\varphi\varphi} - J_\varphi) = \frac{\alpha^2 \gamma_{\varphi\varphi}}{\alpha \sqrt{\hat{\gamma}}} (\sqrt{\hat{\gamma}} \rho_c \Omega - \sqrt{\hat{\gamma}} J^\varphi) \\
 &= \Delta \sin^2 \theta (I^0 \Omega - I^\varphi).
 \end{aligned} \tag{16.124}$$

Therefore,

$$-\frac{1}{2} \frac{dH_\varphi^2}{dA_\varphi} = \Delta \sin^2 \theta F (\dot{t} \Omega - \dot{\varphi}). \tag{16.125}$$

16.5 AN EXACT SOLUTION

It is actually possible to extract an exact set of solutions to the constraint equation above, which is consistent with all the requirements of the force-free, stationary, axis-symmetric electrodynamics on a Kerr background [469]. However, as we shall see these solutions will not explain the phenomenon of energy extraction. Nonetheless, this may serve as a guide for the future researcher in the search for other solutions.

From eqs. (15.35) and (15.36) we see that

$$a \sin^2 \theta \Delta \left(\frac{\dot{t}}{a \sin^2 \theta} - \dot{\varphi} \right) = C(r), \tag{16.126}$$

where $C(r)$ is defined in eq. (15.49). Comparing the equation above with eq. (16.125), we see that considerable simplification of terms occur if Ω can be chosen as $(a \sin^2 \theta)^{-1}$. It is a remarkable coincidence that this choice of Ω does satisfy all the necessary requirements and even the Znajek regularity condition eq. (16.105). Since we are guessing the form of Ω , it will be convenient to write A_φ in terms of Ω .

Definition 16.3 Let Λ be the equipotential surface function such that

$$dA_\varphi = -\Lambda d\Omega. \tag{16.127}$$

In terms of Λ and Ω , the constraint equation eq. (16.97) takes the form

$$\begin{aligned} \frac{1}{2\Lambda} \frac{dH_\varphi^2}{d\Omega} = & \frac{\alpha \gamma_{\varphi\varphi}}{\sqrt{\hat{\gamma}}} \left[\Omega \partial_r \left[\frac{\Lambda}{\alpha \sqrt{\hat{\gamma}}} (\gamma_{\varphi\varphi} \Omega + \beta_\varphi) \gamma_{\theta\theta} \Omega_{,r} \right] \right. \\ & + \Omega \partial_\theta \left(\frac{\Lambda}{\alpha \sqrt{\hat{\gamma}}} (\gamma_{\varphi\varphi} \Omega + \beta_\varphi) \gamma_{rr} \Omega_{,\theta} \right) \\ & + \partial_r \left(\frac{\Lambda}{\alpha \sqrt{\hat{\gamma}}} (\beta^2 - \alpha^2 + \beta_\varphi \Omega) \gamma_{\theta\theta} \Omega_{,r} \right) \\ & \left. + \partial_\theta \left(\frac{\Lambda}{\alpha \sqrt{\hat{\gamma}}} (\beta^2 - \alpha^2 + \beta_\varphi \Omega) \gamma_{rr} \Omega_{,\theta} \right) \right], \tag{16.128} \end{aligned}$$

where we have used eqs. (16.88) and (16.89) for the expressions for ρ and J_φ .

Definition 16.4 Let Ω_- be our particular choice of Ω , i.e.,

$$\Omega_- \equiv \frac{1}{a \sin^2 \theta}. \tag{16.129}$$

The nature of the equipotential surfaces is fixed by our choice of Ω . Since Ω is only a function of θ , $\theta = \text{const}$ are equipotential surfaces. That is, the r derivatives of all equipotential surface functions vanish. When $\Omega_{,r} = 0$, the constraint equation takes the form

$$\begin{aligned} \frac{1}{2\Lambda} \frac{dH_\varphi^2}{d\Omega} &= \frac{\alpha\gamma_{\varphi\varphi}}{\sqrt{\hat{\gamma}}} \left[\Omega \partial_\theta \left(\frac{\Lambda}{\alpha\sqrt{\hat{\gamma}}} (\gamma_{\varphi\varphi}\Omega + \beta_\varphi) \gamma_{rr} \Omega_{,\theta} \right) \right. \\ &\quad \left. + \partial_\theta \left(\frac{\Lambda}{\alpha\sqrt{\hat{\gamma}}} (\beta^2 - \alpha^2 + \beta_\varphi\Omega) \gamma_{rr} \Omega_{,\theta} \right) \right]. \end{aligned} \quad (16.130)$$

Expanding the terms, we find that

$$\begin{aligned} \frac{1}{2\Lambda} \frac{dH_\varphi^2}{d\Omega} &= \sin\theta \left(\frac{\Lambda(\Omega_{-,\theta})}{\sin\theta} \right)_{,\theta} \frac{\beta^2 - \alpha^2 + 2\beta_\varphi\Omega_- + \gamma_{\varphi\varphi}\Omega_-^2}{\rho^2} \\ &\quad + \Lambda\Omega_-(\Omega_{-,\theta}) \frac{[\gamma_{\varphi\varphi}\Omega_- + \beta_\varphi]_{,\theta}}{\rho^2} + \Lambda(\Omega_{-,\theta}) \frac{[\beta^2 - \alpha^2 + \beta_\varphi\Omega_-]_{,\theta}}{\rho^2}. \end{aligned} \quad (16.131)$$

The Kerr metric coefficients in Boyer-Lindquist coordinates satisfy

$$\begin{aligned} \beta^2 - \alpha^2 + 2\beta_\varphi\Omega_- + \gamma_{\varphi\varphi}\Omega_-^2 &= \frac{\rho^2}{a^2 \sin^2\theta}, \\ \beta^2 - \alpha^2 + \beta_\varphi\Omega_- &= -1, \\ \gamma_{\varphi\varphi}\Omega_- + \beta_\varphi &= \frac{r^2 + a^2}{a}. \end{aligned} \quad (16.132)$$

Substituting the above expressions in our constraint equation, we get

$$\frac{1}{2\Lambda} \frac{dH_\varphi^2}{d\Omega} = \frac{1}{a^2 \sin\theta} \left(\frac{\Lambda\Omega_{-,\theta}}{\sin\theta} \right)_{,\theta}. \quad (16.133)$$

The right-hand side of the equation above is clearly an equipotential surface function since, much like Ω_- , it is not r dependent. Therefore, we can consistently integrate to obtain H_φ as a function of only θ . There is still freedom in choosing $\Lambda(\theta)$. What we have shown is that $\Omega = \Omega_-$ is an exact solution to the constraint equation (eq. [16.97]) where Λ is any arbitrary equipotential surface function.

16.6 FIELDS AND ENERGY EXTRACTION FOR THE Ω_- SOLUTION

Equation (16.133) can be easily integrated by observing that

$$\frac{dH_\varphi^2}{d\theta} = \frac{4}{a^4} \frac{d}{d\theta} \left(\frac{\Lambda \cos \theta}{\sin^4 \theta} \right)^2 \quad (16.134)$$

to give

$$H_\varphi^2 = \left(\frac{2\Lambda \cos \theta}{a^2 \sin^4 \theta} \right)^2 + H_{\varphi 0}^2. \quad (16.135)$$

Here $H_{\varphi 0}^2$ is an integration constant. The poloidal component of the magnetic field is given by

$$B^r = -\frac{\Lambda \Omega_{-, \theta}}{\sqrt{\hat{\gamma}}} = \frac{2}{a} \Lambda \frac{\cos \theta}{\sqrt{\hat{\gamma}} \sin^3 \theta}. \quad (16.136)$$

For B^r as given above, we see that H_φ satisfies the Znajek regularity condition (eq. [16.105]) at the event horizon when we pick the positive root in eq. (16.135) for $H_{\varphi 0}^2 = 0$, i.e.,

$$H_\varphi = \frac{2\Lambda \cos \theta}{a^2 \sin^4 \theta}. \quad (16.137)$$

We now proceed to calculate the remaining nontrivial components of the fields and current consistent with our choice of Ω_- . From eq. (16.75) and above we get

$$E_\theta = -\frac{2}{a^2} \Lambda \frac{\cos \theta}{\sin^5 \theta}. \quad (16.138)$$

The charge density is calculated from eq. (16.88), and is given by

$$\rho_c = \frac{-2(r^2 + a^2)}{a^2 \Delta \sqrt{\hat{\gamma}}} \partial_\theta \left(\Lambda \frac{\cos \theta}{\sin^4 \theta} \right). \quad (16.139)$$

The expression for the toroidal component of the current density vector is given by eq. (16.89), and in our case, this reduces to

$$J^\varphi = \frac{-2}{a \Delta \sqrt{\hat{\gamma}}} \partial_\theta \left(\Lambda \frac{\cos \theta}{\sin^4 \theta} \right). \quad (16.140)$$

Finally, from eq. (16.90) we see that

$$J^r = \frac{2}{a^2 \sqrt{\hat{\gamma}}} \partial_\theta \left(\Lambda \frac{\cos \theta}{\sin^4 \theta} \right). \quad (16.141)$$

The efforts to solve for the fields and currents for the force-free magnetosphere of a Kerr black hole have been largely numerical in nature. To date, this is the only known, exact, analytical solution to the problem that has been presented in the last thirty years since it was formulated [467]. The appearance of the various powers of $\sin\theta$ in the denominator of the above expressions do not create any real divergences in the solution along the symmetry axis, since as yet Λ has not been prescribed. In fact, a simple transformation of the type $\Lambda \rightarrow \Lambda \sin^5\theta$ removes all problems of apparent divergences. But, when it comes to the chief issue of energy extraction from the black hole, it appears that we are not so lucky. From eq. (16.109) we see that

$$\frac{d\mathcal{E}}{dt} = -\frac{8\pi}{a^4} \int_0^\pi \frac{\Lambda^2 \cos^2\theta}{\sin^9\theta} d\theta \leq 0, \quad (16.142)$$

and similarly, from eq. (16.110), we get

$$\frac{d\mathcal{L}}{dt} = -\frac{8\pi}{a^3} \int_0^\pi \frac{\Lambda^2 \cos^2\theta}{\sin^7\theta} d\theta \leq 0. \quad (16.143)$$

There the solution generated by $\Omega = \Omega_-$ does not allow for energy extraction from the black hole regardless of the form of the equipotential surface function Λ .

By writing the charge and current three-vector in its covariant form we get that

$$I^\nu = -\frac{2}{a^2\alpha\sqrt{\hat{\gamma}}} \frac{d}{d\theta} \left(\Lambda \frac{\cos\theta}{\sin^4\theta} \right) l_-^\nu, \quad (16.144)$$

where l_-^ν is the infalling null geodesic of the Kerr geometry given in eq. (15.62). It is of course nice that these charges move along geodesics since we are considering the force-free magnetosphere, but the fact that they move along null geodesics suggests that these charged particles are massless: a feature that makes our solution less practical.

16.7 AN APPROXIMATE SOLUTION

As shown above, the solution generated by $\Omega = \Omega_-$ has not proven quite useful. However, the question remains as to whether there are other solutions where equipotential surfaces are surfaces of constant θ . As we shall show in the next section, the solution presented above is the unique exact solution that satisfies all the requirements of force-free, stationary, axis-symmetric dynamics when $\Omega = \Omega(\theta)$. But we shall temporarily abandon our search for exact solutions. Instead, we look for solutions to order r^{-2} such that

$\Omega_{,r} = 0$, which we shall assume for the remainder of this section. So once again we impose the condition that $\Omega = \Omega(\theta)$. To $\mathcal{O}(r^{-3})$ the constraint equation (eq. [16.97]) becomes

$$\begin{aligned}
 -\frac{1}{2f(\theta)} \frac{dH_\varphi^2}{d\theta} &= -\Omega \sin \theta \frac{d}{d\theta} (f\Omega \sin \theta) \\
 &+ \frac{\sin \theta}{r^2} \left[-a^2 \Omega \sin^2 \theta \frac{d}{d\theta} (f\Omega \sin \theta) + \frac{d}{d\theta} \left(\frac{f}{\sin \theta} \right) \right] + 2M \frac{\sin \theta}{r^3} \\
 &\times \left[a\Omega \frac{d}{d\theta} [f \sin \theta (1 - a\Omega \sin^2 \theta)] - \frac{d}{d\theta} \left(\frac{f}{\sin \theta} (1 - a\Omega \sin^2 \theta) \right) \right],
 \end{aligned}
 \tag{16.145}$$

where $f(\theta) \equiv -\Lambda \Omega_{,\theta} \equiv A_{\varphi,\theta}$. The above expansion to $\mathcal{O}(r^{-3})$ was obtained for future reasons.

The solution we seek for H_φ to $\mathcal{O}(r^{-2})$ must satisfy the condition that $H_\varphi = H_\varphi(\theta)$. If to $\mathcal{O}(r^{-2})$ H_φ is to be a function of θ alone, then f and Ω must satisfy

$$a^2 \Omega \sin^2 \theta \frac{d}{d\theta} (f\Omega \sin \theta) = \frac{d}{d\theta} \left(\frac{f}{\sin \theta} \right)
 \tag{16.146}$$

to make the r^{-2} term trivial. Defining $g \equiv f\Omega \sin \theta$ and $h \equiv (\Omega \sin^2 \theta)^{-1}$, it is possible to integrate the above equation. Consequently eq. (16.146) becomes

$$\frac{a^2}{h} \frac{d}{d\theta} g = \frac{d}{d\theta} (gh).
 \tag{16.147}$$

This can be easily integrated to give

$$g = \frac{Q_0}{\sqrt{|a^2 - h^2|}}.
 \tag{16.148}$$

Here Q_0 is an integration constant. Resubstituting the definitions of g and h into eq. (16.146), we see that when $\Omega \neq \Omega_-$ the unique solution for f in terms of Ω is given by

$$f = \frac{Q_0 \sin \theta}{\sqrt{|(a\Omega \sin^2 \theta)^2 - 1|}}.
 \tag{16.149}$$

Consequently, by ignoring all r -dependent terms in eq. (16.145) we get

$$\begin{aligned}
 \frac{dH_\varphi^2}{d\theta} &= 2f\Omega \sin \theta \frac{d}{d\theta} (f\Omega \sin \theta) = \frac{d}{d\theta} (f\Omega \sin \theta)^2 \\
 &\Rightarrow H_\varphi^2 = \pm H_0^2 + (f\Omega \sin \theta)^2
 \end{aligned}
 \tag{16.150}$$

to $\mathcal{O}(r^{-2})$. Clearly, the expression for H_φ given above, since it is only a function of θ , is an equipotential surface function. Let us impose this r -independent expression for H_φ in the Znajek regularity condition eq. (16.105). This gives

$$\pm H_0^2 = \frac{\sin^2 \theta}{\rho_+^4} [(4r_+^2 M^2 - \rho_+^4) \Omega^2 - 4r_+ M a \Omega + a^2] f^2. \quad (16.151)$$

Using eq. (16.150), when $H_0 = 0$, we can eliminate the function f and the above quadratic equation for Ω can be solved to obtain

$$\Omega_\pm \equiv \frac{a}{2Mr_+ \pm \rho_+^2}. \quad (16.152)$$

Incidentally, notice that

$$\Omega_- = \frac{a}{2Mr_+ - \rho_+^2} = \frac{1}{a \sin^2 \theta} \quad (16.153)$$

as before. The Ω_- solution is of no further interest to us.

Let us consider the consequence of the choice $\Omega = \Omega_+$. In this case, the nonvanishing components of the fields are

$$B^r = \frac{1}{\sqrt{\hat{\gamma}}} f = \frac{1}{\sqrt{\hat{\gamma}}} \frac{Q_0 \sin \theta}{2\rho_+} \frac{\sqrt{a\Omega_H}}{\Omega_+}, \quad (16.154)$$

and from the explicit formula for the electric field we find that

$$E_\theta = -\sqrt{\hat{\gamma}} \Omega_+ B^r.$$

Also

$$\alpha B_\varphi = H_\varphi = -\sqrt{\hat{\gamma}} \Omega_+ B^r \sin \theta. \quad (16.155)$$

As before

$$\Omega_H = a/2Mr_+$$

is the angular velocity of the event horizon and $\rho_+ = \sqrt{r_+^2 + a^2 \cos^2 \theta}$. The charge density in the magnetosphere is given by eq. (16.88). To $\mathcal{O}(r^{-2})$,

$$\rho_c \approx -\frac{Q_0 \sqrt{a \Omega_H}}{2 r^2 \sin \theta} \frac{d}{d\theta} \left(\frac{\sin^2 \theta}{\rho_+} \right). \quad (16.156)$$

Clearly, Q_0 has dimensions of charge. It is interesting to note that, while B satisfies $\nabla \cdot B = 0$, we find that

$$\int_{r>2M} B \cdot n \, dA \neq 0. \quad (16.157)$$

For our case,

$$\int_{r>2M} B \cdot n \, dA = \frac{Q_0 \pi a}{\sqrt{r_+^2 + a^2}} \left(\frac{\sqrt{r_+^2 + a^2}}{a} + \frac{(3r_+^2 + 2a^2)}{a^2} \sinh^{-1} \frac{a}{r_+} \right). \quad (16.158)$$

This is not an unexpected result; after all, the region bounded by $r < 2M$ is not a closed region wherein the fields are completely well defined. The ring singularity of the Kerr black hole (which is removed from our space-time) creates interesting topological and geometric effects. This is one such. Solutions of this type are referred to as “monopole” solutions. One should not mistake this to mean that there are net magnetic charges in general relativistic electrodynamics.

In the limit when $a \ll M$

$$B^r \rightarrow \frac{1}{\sqrt{\gamma}} Q_0 \sin \theta$$

and

$$\Omega_+ \rightarrow \frac{a}{8M^2}. \quad (16.159)$$

This is the monopole solution derived by Blandford and Znajek [467] (also see [460]). In their approach, Blandford and Znajek found a perturbative solution by requiring that a is very small when compared to the mass of the black hole. We did not pose any restriction of this type. Therefore, the solutions for the fields and currents corresponding to $\Omega = \Omega_+$ generalizes the Blandford-Znajek monopole solution to accommodate the case of a black hole for all values of $a^2 < M^2$ [470]. Blandford and Znajek also proposed that we can split the solution where Q_0 can have opposite signs above and below the equatorial plane, so that the resulting solution gives a trivial net magnetic flux. This discontinuity would be introduced by the currents in the equatorial plane possibly stemming from the accretion disk.

Unlike the exact solution we developed previously, the Ω_+ solution does indeed permit the extraction of energy and angular momentum. From the expression for the fields corresponding to the Ω_+ solution, we see from eq. (16.109) that the rate of energy extraction per unit area is given by

$$\frac{d^2 \mathcal{E}}{dA dt} \approx \frac{a \Omega_H}{r^2} \left(\frac{Q_0}{2} \right)^2 \frac{\sin^2 \theta}{\rho_+^2}. \quad (16.160)$$

Clearly, for this solution, most of the extraction of energy takes place along the equatorial plane (when $\sin \theta$ is a maximum); see figure 16.2. That is, the solution developed here cannot as such be used to account for jet formation

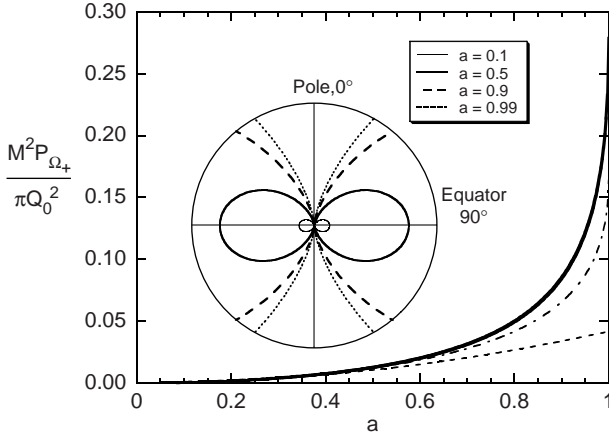


Figure 16.2 Energy-loss rate for the Ω_+ solution as a function of spin parameter a for $M = 1$. The heavy solid curve is the expression given by eq. (16.161), the short-dashed curve shows the asymptote given in eq. (16.173) for $a \ll 2M$, and the dot-dashed curve plots $(2/3)\Omega_H^2$. Inset shows angular distribution of emitted power.

from black holes. However, the formalism here does permit solutions that allow for the extraction of energy and angular momentum from rotating Kerr black holes. Upon completing the above integral we find that the rate of energy extraction, or power, of the Ω_+ solution is

$$P_{\Omega_+} = \frac{d\mathcal{E}}{dt} = \frac{\pi Q_0^2}{ar_+} \left(\arctan \frac{a}{r_+} - \frac{a}{2M} \right). \quad (16.161)$$

In a similar manner we can compute the rate of extraction of angular momentum:

$$\frac{d\mathcal{L}}{dt} = \frac{2\pi}{3} Q_0^2 \Omega_H + \frac{1}{\Omega_H} \frac{d\mathcal{E}}{dt}. \quad (16.162)$$

From eq. (16.111) we see that the mass and the total angular momentum of the black hole change by the amounts

$$\frac{\delta M}{\delta t} = -\frac{d\mathcal{E}}{dt} \quad \text{and} \quad \frac{\delta J}{\delta t} = -\frac{d\mathcal{L}}{dt}. \quad (16.163)$$

Therefore,

$$\frac{\delta J}{\delta t} + \frac{2\pi}{3} Q_0^2 \Omega_H = \frac{1}{\Omega_H} \frac{\delta M}{\delta t}; \quad (16.164)$$

consequently,

$$\frac{\delta J}{\delta t} \leq \frac{1}{\Omega_H} \frac{\delta M}{\delta t}. \quad (16.165)$$

As we have seen, the above inequality ensures that the mass of the hole is always greater than its angular momentum. When all the angular momentum is spent, the ergosphere disappears, and the extraction of energy is brought to a halt. Therefore, this process cannot lead to the formation of a naked singularity.

16.8 UNIQUENESS OF THE Ω_- SOLUTION

In this section we will show that $\Omega = \Omega_-$ is the only exact solution possible when we impose the condition that $\Omega_{,r} = 0$. Consequently, as in the previous section $\Omega = \Omega(\theta)$. From eq. (16.151) we see that

$$f^2 = \frac{\pm H_0^2 \rho_+^4}{a} \frac{\Omega_+ \Omega_-^2}{(\Omega - \Omega_+)(\Omega - \Omega_-)}. \tag{16.166}$$

Here the \pm factor is to ensure that $f^2 \geq 0$. Similarly, we find from eq. (16.149) that

$$f^2 = \frac{Q_0^2}{a^2 \sin^2 \theta |(\Omega - \Omega_-)(\Omega + \Omega_-)|}. \tag{16.167}$$

Setting the right-hand sides of the last two equations equal to each other, we get

$$Q_0^2 |\Omega - \Omega_+| = H_0^2 \rho_+^4 \Omega_+ \Omega_- |\Omega + \Omega_-|. \tag{16.168}$$

The above equation has the unique solution

$$\Omega = \tilde{\Omega}_\pm = \frac{\tilde{A} \Omega_+ \pm \tilde{B} \Omega_-}{\tilde{A} \mp \tilde{B}}. \tag{16.169}$$

Here $\tilde{B} = H_0^2 \rho_+^4 \Omega_+ \Omega_-$ and $\tilde{A} = Q_0^2 \neq 0$. When $Q_0 = 0$, the radial component of the magnetic field is trivial and no extraction of energy is possible. If $H_0 = 0$, we see that $\tilde{\Omega}_\pm \rightarrow \Omega_+$. Therefore, the Ω_- solution is never described by $\tilde{\Omega}_\pm$. If $\Omega = \tilde{\Omega}_\pm$ is to be realized by an exact solution, then f is given by eq. (16.149). It is only necessary to show that $\Omega = \tilde{\Omega}_\pm$, along with f as given in eq. (16.149), does not satisfy eq. (16.145) to order $1/r^3$, for then $\tilde{\Omega}_\pm$ could never be an r -independent exact solution. Vanishing of the $1/r^3$ term in eq. (16.145) implies that

$$\frac{dg^2}{d\theta} \sin \theta (1 - a \tilde{\Omega}_\pm \sin^2 \theta) = 2g^2 \cos \theta (a \tilde{\Omega}_\pm \sin^2 \theta + 1). \tag{16.170}$$

Here $g = f(1 - a \tilde{\Omega}_\pm \sin^2 \theta)$. Inserting the expression for f and $\tilde{\Omega}_\pm$ in the definition of g , we find that

$$g^2 = \frac{1}{r_+^2 + a^2} |(H_0^2 \rho_+^4 - Q_0^2 \rho_+^2 \sin^2 \theta)|. \tag{16.171}$$

Inserting eq. (16.171) in eq. (16.170) we find that

$$-\frac{2Mr_+Q_0^2}{a^2} = \sin^4\theta [Q_0^2a^2\sin^2\theta - Q_0^2\rho_+^2 - 2H_0^2a^2\rho_+^2]. \quad (16.172)$$

The above equation will not be satisfied because the left-hand side is independent of θ , unlike the right-hand side. Therefore, we reach a contradiction, and $\Omega = \tilde{\Omega}_\pm$ is not an exact solution that satisfies the Znajek event horizon regularity condition. We have also shown that $\Omega = \Omega_-$ is an exact solution that is consistent with the event horizon regularity condition. Hence we get the following result [469]: *when equipotential surfaces are surfaces of constant θ , the unique class of solutions to the stationary, axisymmetric force-free magnetosphere that is regular on the event horizon of a Kerr black hole is generated by the function $\Omega = \Omega_-$. The entire degree of freedom in this theory lies in the r -independent but otherwise arbitrary function Λ .*

Unfortunately, from eqs. (16.142) and (16.143) we see that it is impossible to extract energy and angular momentum from a stationary, axisymmetric force-free magnetosphere that is regular on the event horizon of a Kerr black hole when $\Omega_{,r} = 0$. While it is clear from analytical grounds that the Blandford-Znajek mechanism describe a process by which extraction of energy and angular momentum from a black hole can happen in an astrophysical setting, the extent to which it might explain jet physics is still an open question. The above result of the uniqueness of Ω_- implies that the search for new solutions must incorporate a dependence of the radial coordinate into equipotential surfaces.

16.9 ENERGY EXTRACTION FOR THE Ω_+ SOLUTION

The approximate Ω_+ solution, eq. (16.152), generalizes the Blandford-Znajek (BZ) split monopole solution to all values of $0 < a < M$ and leads to positive energy extraction. We suppose that this solution accurately gives the black-hole rotational energy extraction, and that the collimation problem can be handled separately through geometrical or magnetic field effects (by bringing in the radial dependence of Ω).

If so, the black-hole power through the BZ process is given by eq. (16.161), with asymptotes

$$P_{\Omega_+} \cong \frac{\pi Q_0^2}{M^2} \times \begin{cases} \frac{1}{6} \left(\frac{a}{2M}\right)^2 & \text{for } a/2M \ll 1, \\ \frac{\pi}{4} - \frac{1}{2} \cong 0.285 & \text{for } a \rightarrow M, \end{cases} \quad (16.173)$$

noting that r_+ shrinks from $2M$ to M as the spin parameter increases from $a \ll M$ to $a \rightarrow M$.

The charge Q_0 can be related to the radial component of the magnetic field, B^r , from eq. (16.154), giving

$$Q_0 = \frac{2\sqrt{\hat{\gamma}}\rho_+\Omega_+}{\sin\theta\sqrt{a\Omega_H}} B^r \xrightarrow{\theta\approx\pi/2} \frac{2\sqrt{\hat{\gamma}}\sqrt{r_+^2+a^2}\Omega_+}{\sqrt{a\Omega_H}} B^r, \quad (16.174)$$

evaluating the magnetic field threading the event horizon at the equator.

To obtain the magnetic field threading the event horizon, we will now calculate the magnetic field intensity in the Kerr-Schild coordinate system:

$$\bar{B} = \sqrt{\bar{\gamma}_{\bar{r}\bar{r}}(\bar{B}^{\bar{r}})^2 + \bar{\gamma}_{\bar{\theta}\bar{\theta}}(\bar{B}^{\bar{\theta}})^2 + 2\bar{\gamma}_{\bar{r}\bar{\phi}}\bar{B}^{\bar{r}}\bar{B}^{\bar{\phi}} + \bar{\gamma}_{\bar{\phi}\bar{\phi}}(\bar{B}^{\bar{\phi}})^2}. \quad (16.175)$$

Unlike B^ϕ , the Znajek regularity condition will force $\bar{B}^{\bar{\phi}}$ to be finite at the event horizon. It is easily verified using eqs. (15.69) and (16.16) that

$$\sqrt{\bar{\gamma}}\bar{B}^{\bar{\phi}} = \bar{F}_{\bar{r}\bar{\theta}} = G E_\theta + \sqrt{\hat{\gamma}}B^\phi + H\sqrt{\hat{\gamma}}B^r = 0$$

for the Ω_+ solution. Similarly,

$$\bar{B}^{\bar{\theta}} = 0 \quad \text{and} \quad \sqrt{\bar{\gamma}}\bar{B}^{\bar{r}} = \sqrt{\gamma}B^r.$$

Then $\bar{B} = f(\theta)\sqrt{\bar{\gamma}_{\bar{r}\bar{r}}/\bar{\gamma}}$, where

$$f \equiv \frac{Q_0 \sin\theta}{2\rho_+} \frac{\sqrt{a\Omega_H}}{\Omega_+},$$

and $\sqrt{\bar{\gamma}_{\bar{r}\bar{r}}/\bar{\gamma}} = 1/\rho^2 \sin\theta \rightarrow r_+^{-2}$ when $r = r_+$ and $\bar{\theta} = \theta = \pi/2$. Thus

$$\bar{B}|_{r=r_+, \theta=\pi/2} = \frac{f(\theta = \pi/2)}{r_+^2}. \quad (16.176)$$

which gives

$$Q_0^2 = \frac{4r_+^2(r_+^2+a^2)^2}{(2M+r_+)^2} \bar{B}^2. \quad (16.177)$$

Consequently, the BZ power for the Ω_+ solution is

$$P_{\Omega_+} \cong 4\pi \bar{B}^2 \frac{(r_+^2+a^2)^2}{(2M+r_+^2)^2} \left(\frac{r_+}{a}\right) \left(\arctan \frac{a}{r_+} - \frac{a}{2M}\right) \\ \rightarrow \frac{8\pi}{3} \bar{B}^2 M^2 \begin{cases} \left(\frac{a}{2M}\right)^2 & \text{for } a/2M \ll 1, \\ \left(\frac{2}{9}\right) \left(\frac{\pi}{4} - \frac{1}{2}\right) \cong 0.0634\dots & \text{for } a \rightarrow M. \end{cases} \quad (16.178)$$

16.10 BLANDFORD-ZNAJEK PROCESS IN ASTROPHYSICAL SOURCES

Adopting the notation that $B = 10^i B_i$ G and $M = 10^j M_\odot M_j$ and restoring units gives

$$\frac{8\pi}{3} c B^2 M^2 = 5.5 \times 10^{47} B_4^2 M_9^2 \text{ ergs s}^{-1}. \quad (16.179)$$

The two asymptotes of eq. (16.178) are

$$P_{\Omega_+} (\text{ergs s}^{-1}) \rightarrow 10^{47} B_4^2 M_9^2 \begin{cases} 1.4 \left(\frac{a}{M}\right)^2 & \text{for } a/2M \ll 1, \\ 0.35 & \text{for } a \rightarrow M, \end{cases} \quad (16.180)$$

so the power extracted through the BZ power given by the Ω_+ solution is, roughly,

$$P_{\Omega_+} \simeq 4 \times 10^{46} B_4^2 M_9^2 \left(\frac{a}{M}\right)^2 \text{ ergs s}^{-1}. \quad (16.181)$$

Astronomical observations can be used to deduce the magnetic field threading the event horizon. The estimate in eq. (7.73), obtained by normalizing the magnetic field energy density to the density of radiant photons, when substituted in eq. (16.182), gives the power

$$P_{\Omega_+} \simeq \frac{2 \times 10^{47}}{\tilde{R}_0} \ell_{\text{Edd}} M_9 \left(\frac{a}{M}\right)^2 \text{ ergs s}^{-1}. \quad (16.182)$$

Thus the BZ power for the Ω_+ solution is limited to values

$$P_{\Omega_+} \lesssim 2 \times 10^{47} \ell_{\text{Edd}} M_9 \text{ ergs s}^{-1}, \quad (16.183)$$

taking $\tilde{R}_0 \cong r_+/M$. For Solar-mass black holes, this power is at the level

$$P_{\Omega_+} \lesssim 5 \times 10^{38} \ell_{\text{Edd}} \left(\frac{M}{3M_\odot}\right) \text{ ergs s}^{-1}. \quad (16.184)$$

Accretion scenarios that could be effectively Eddington limited, at least over long timescales, probably operate in wind-fed X-ray binaries and AGNs. The Eddington luminosity is, from eq. (6.133),

$$L_{\text{Edd}} \simeq 10^{47} M_9 \text{ ergs s}^{-1}, \quad (16.185)$$

and is comparable to the BZ power, eq. (16.182).

The Eddington limit $\ell_{\text{Edd}} \leq 1$ cannot, however, be considered a fundamental limiting luminosity in all cases. Gamma-ray bursts, if due to the formation of a few Solar-mass black holes at redshifts near unity, reach instantaneous powers $\gtrsim 10^{51}$ ergs s⁻¹, so that $\ell_{\text{Edd}} \sim 10^{12}$. Blandford-Znajek

energy extraction through a massive nuclear torus accreting on the a newly formed, rapidly rotating black hole could extract the spin energy and power the GRB. Jet collimation can be a consequence of effects in the accretion-disk magnetospheric. The solution presented here accurately describes the BZ process near a black hole if the energy extraction and jet formation problem can be separated.

The formation of jets by the BZ process has driven many recent studies, both numerical and theoretical. For recent work, see, for example, Punsly [471], Levinson [472], McKinney and Narayan [473,474], and Königl [475].

Chapter Seventeen

High-Energy Radiations from Black Holes

Energy from a black hole is generated by one of three mechanisms: (i) the release of gravitational potential energy by accretion of matter onto a black hole; (ii) dissipation of rotational energy stored in black-hole spin; and (iii) Hawking radiation from low-mass, evaporating black holes. For case (i), the energy of accreting matter is surely the source of the luminous UV and X-rays detected from radio-quiet Seyfert AGNs, reaching to $\approx 10^{46}$ ergs s^{-1} , and X-ray binaries in the Galaxy as bright as $\approx 10^{39}$ ergs s^{-1} . For case (iii), no evidence for evaporating black holes was found with EGRET [458], and it would be a great but unexpected discovery for the Fermi Gamma Ray Space Telescope to detect evaporating black holes.

Several lines of evidence, including superluminal motion, brightness temperature, Compton limits on the Doppler factor, and $\gamma\gamma$ attenuation, lead to the conclusion that nonthermal radiations emitted by black holes are produced by jets of collimated relativistic plasma outflows. If, for case (ii), the energetic nonthermal radiations of radio and γ -ray loud sources are powered by the rotational energy of the black hole—an important and interesting question that only detailed studies using theory as presented here can answer—then this could explain the very different properties and powers of radio-quiet and radio-loud black holes, which in the latter cases reach apparent luminosities $\gtrsim 10^{49}$ ergs s^{-1} for supermassive black-hole blazars, and $\gtrsim 10^{51}$ ergs s^{-1} for GRBs. The extreme black-hole-jet environment where the energy is dissipated provides appropriate conditions for particle acceleration to the highest energies. When they leave the black-hole accelerators, these particles become high-energy cosmic rays.

Cosmic rays were discovered by Victor Hess in 1912, UHECR air showers were discovered by Rossi and Auger in the 1930s, and intense, highly variable sources of cosmic γ rays were discovered with the Vela satellites and the COS-B and Compton γ -ray observatories in the last half of the twentieth century. The Pierre Auger Observatory (PAO) recently observed clustering in the arrival direction of UHECRs, opening the field of charged-particle astronomy. The lower energy, \sim GeV–PeV cosmic rays are widely believed to be accelerated by supernova remnant shocks from exploding stars in the Galaxy, but conclusive evidence for this hypothesis has not yet been found.

According to the black-hole spin paradigm examined here, the $\gtrsim 10^{17}\text{--}10^{18}$ eV UHECRs are accelerated in the even more extreme environments of a black hole by the release of its rotational energy. Black holes have the properties needed to explain the extraordinary energies and powers of the γ -ray and multiwavelength radiations from AGNs and GRBs: they are compact and can release large amounts of energy on short time scales. If they accelerate ultrahigh-energy particles, they will unavoidably make γ rays and neutrinos, so the sources of cosmic rays must, at some predictable flux level, be γ -ray and neutrino sources.

Therefore we propose, based on many related theoretical ideas, for example, by Vietri [427] and Waxman [476] for GRBs, and by Berezhinsky [217, 230], and Mannheim and Biermann [477] for blazars, and work by Atoyan and the authors [95, 191, 208], that collimated relativistic jets from black holes emit γ rays and neutrinos and accelerate the UHECRs. The very different properties of radio quiet and radio loud sources are ultimately related to the spin of the black hole, following Blandford's hypothesis [478]. To confirm this black-hole spin paradigm requires calculations of γ -ray, neutrino, and cosmic-ray signatures, and comparison of theory and model results with the evolving astronomical and astroparticle data bases. Tying UHECR acceleration to the spin of a black hole would involve, at least, statistical studies of the properties of galaxies hosting nonthermal radio/ γ -ray emitting black holes.

Our understanding of the most luminous, highly variable sources of radiation in nature is far from complete. Whether the mechanism powering these luminous emissions is an accretion process, a Penrose process for extracting black-hole spin energy, or some hybrid of the two, is unclear. The black-hole spin paradigm for radio/ γ -ray emitting blazars will be tested by new observations over the next decade, when γ -ray, astroparticle and neutrino observatories more sensitive than ever before will provide confirming or contrary evidence for this hypothesis.

17.1 γ RAYS

The EGRET experiment on the *Compton Observatory* discovered that blazar AGNs and GRBs are powerful sources of nonthermal γ rays [479], and the Whipple Observatory discovered that X-ray-selected BL Lac objects including Mrk 421 [480] and Mrk 501 are strong sources of TeV γ rays. The new air-Cherenkov TeV telescopes *HESS*, *MAGIC*, and *VERITAS*, the large field-of-view Milagro and HAWC water Cherenkov telescopes, and new discoveries with *AGILE* and Fermi are building on these results in unexpected ways. (See Refs. [175, 481, 482] for reviews of γ -ray sources.)

Except for lineless blazars like 0716 + 714 with no confirmed redshift, BL Lac objects and FSRQs detected with EGRET have mean redshifts ≈ 0.3 and ≈ 1 , respectively. The brightest FSRQ flares reach apparent powers of $\sim 10^{49}$ ergs s^{-1} , ≈ 2 – 3 orders of magnitude greater than the brightest apparent powers of the most luminous BL Lac objects. The misaligned population of blazars, namely radio galaxies like Centaurus A and M87 are also found to be a class of γ -ray sources with EGRET and HESS, with 3C 84 in the Perseus cluster recently detected with Fermi.

Concerning GRBs, we had before Fermi only fragmentary evidence about γ -ray emission from five EGRET spark chamber GRBs and a few BATSE GRBs also seen with the EGRET calorimeter, most without redshifts. The γ -ray properties of different classes of GRBs will probably be very different. This is likewise true for candidate Galactic black hole sources, for example, LS 5039 and other high-mass microquasars like Cyg X-1, a radio-emitting X-ray binary with strong dynamical evidence for a black-hole primary. New classes of γ -ray sources may soon be discovered, e.g., extreme blazars or evaporating black holes.

Gamma-ray telescopes will advance studies on γ rays from black holes, including the topics discussed in sections 17.1.1–17.1.5.

17.1.1 Modeling γ Rays from Black Holes

Large new γ -ray and multiwavelength databases from black-hole sources will allow physical models of black-hole jets to be tested and jet properties to be extracted. Two analytical methods can be employed.

Acceleration, Injection, Energy Loss, and Spectral Fitting

In standard time-dependent leptonic models of black-hole jet sources (e.g., [100, 483]), the low- and high-energy components in the SEDs are simultaneously fit by injecting relativistic electrons into the model jet and allowing the electrons to evolve through radiative and adiabatic cooling. The injection spectrum is usually approximated by a power law with low- and high-energy cutoffs. The evolution of the comoving electron distribution function $N'(\gamma'; t')$ is usually described by the particle continuity equation

$$\frac{\partial N'(\gamma'; t')}{\partial t'} + \frac{\partial}{\partial \gamma'}[\dot{\gamma}' N'(\gamma'; t')] + \frac{N'(\gamma'; t')}{t'_{\text{esc}}(\gamma', t')} = \dot{N}'(\gamma'; t'). \quad (17.1)$$

Solutions to this equation give the electron distribution, from which the multiwavelength spectrum of black-hole jet sources can be calculated for comparison with data.

Appendix C gives elementary solutions to the particle continuity equation for specific injection and energy losses. Internal attenuation, pair reinjection,

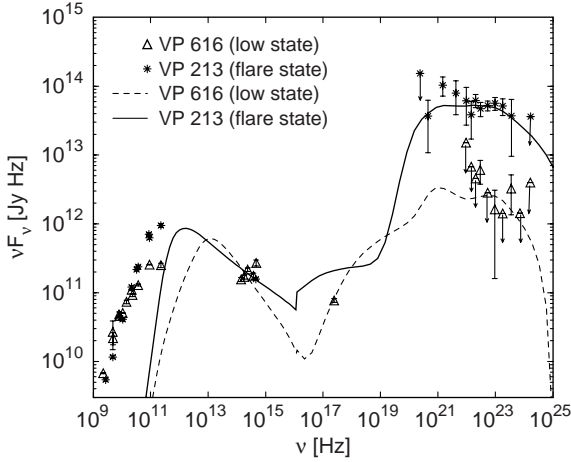


Figure 17.1 Relativistic jet model of PKS 0528 + 134 [277]. (Figure courtesy of M. Böttcher.)

anisotropy, and light-travel time effects are considered in advanced models, giving predictions for temporal evolution that can be tested with multiwavelength light curves. Figure 17.1 shows an example of a spectral model fit to PKS 0528 + 134, a FSRQ at $z = 2.07$ [277] ($4\pi d_L^2 \times 10^{13} \text{ Jy Hz} = 3 \times 10^{48} \text{ ergs s}^{-1}$).

New Methodology for Multiwavelength Analysis

Another approach developed here and in [72] is to assume that the radio/optical/X-ray νF_ν flux is nonthermal lepton synchrotron radiation, and use this SED and the variability data to deduce the electron distribution in the jet by solving eq. (7.116) for a model electron spectrum. The derived electron distribution can then be used to calculate the high-energy SSC component using eq. (7.117). The SSC spectrum is precisely calculated from the inferred electron distribution and a small set of well-constrained observables. Allowed values of mean magnetic field B and Doppler factor δ_D (for a given variability time and implied size scale of the emitting region) are obtained by fitting the multiwavelength spectrum of a relativistic jet source, implying absolute jet luminosities.

An application of this method to the X/ γ -ray spectrum of PKS 2155-304 at $z = 0.116$ is shown in figure 17.2 [72] ($4\pi d_L^2 \times 10^{-9} \text{ ergs s}^{-1} \text{ cm}^{-2} = 3.3 \times 10^{46} \text{ ergs s}^{-1}$). A synchrotron/SSC model requires $\delta_D \gtrsim 60$ and absolute jet powers $\gtrsim 2 \times 10^{46} \text{ ergs s}^{-1}$, calling into question whether this model is correct.

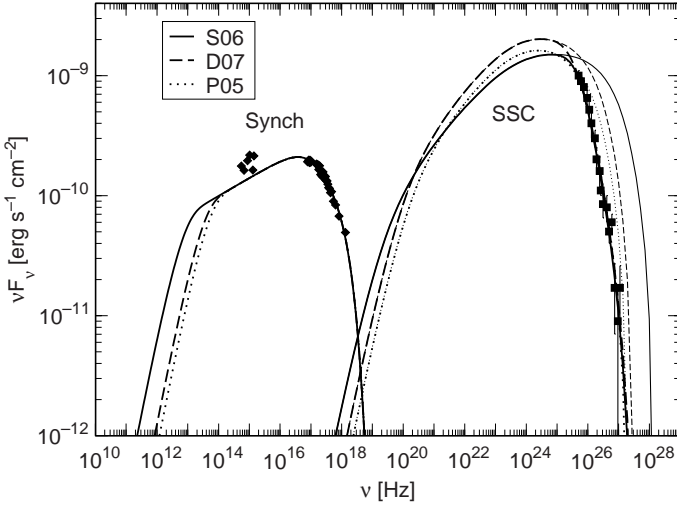


Figure 17.2 Relativistic synchrotron/SSC jet model [72] for the July 2006 flares of PKS 2155-304 [25, 484], using different EBL models [261, 262].

The spectrum from external Compton scattering in a standard one-zone blazar model is given, in general, by the fourfold integral, eq. (6.97). This equation can be solved for a variety of external radiation fields, including a point source from behind the jet, and accretion-disk and scattered radiation fields [73]. Figure 17.3 shows a calculation of a jet source for a FSRQ.

Knowing precisely the leptonic signatures of a relativistic jet model, we can examine theoretically the different hadronic signatures and compare with γ -ray data to determine whether relativistic jets of black holes accelerate UHECRs.

17.1.2 Statistics of Black-Hole Sources

The (“log N –log S ”) integral rate $\dot{N}(> \phi_p)$ at which an observer detects events with flux greater than ϕ_p is given by

$$\frac{d\dot{N}(> \phi_p)}{d\Omega} = \frac{c}{H_0} \int_0^{z_{\max}(\phi_p)} dz d_{\text{evt}}^2(z) \dot{n}_{\text{co}}(z) \mathcal{Y}_{\text{tr}}[\phi_p(z)], \quad (17.2)$$

where $\dot{n}_{\text{co}}(z)$ is the comoving rate density ($\text{cm}^{-3} \text{s}^{-1}$) of events at redshift z (eq. [4.45]; [485]). The term $\mathcal{Y}_{\text{tr}}[\phi_p]$ is a detector-dependent quantity, and gives the detection (“trigger”) efficiency to detect an event with peak flux ϕ_p in the waveband where the detector is most sensitive. Well above detector threshold, $\mathcal{Y}_{\text{tr}}[\phi_p] \cong 1$. The function $\phi_p(z)$ relates the measured flux over different wavebands to the peak source directional jet luminosity. The event-rate distance $d_{\text{evt}}(z)$, eq. (4.46), is plotted as a function of z in figure 4.3,

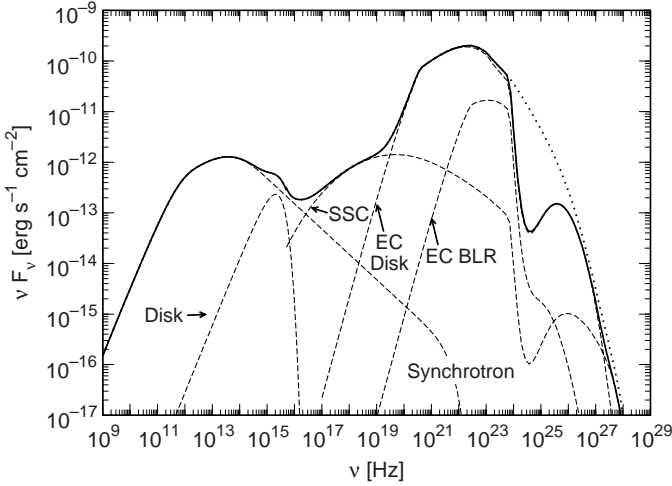


Figure 17.3 Multiwavelength spectral model of a FSRQ, including accretion disk radiation, and synchrotron, SSC, and external Compton (EC) scattered disk and BLR components, as labeled. Model includes internal and source $\gamma\gamma$ attenuation. (Figures 17.2 and 17.3 courtesy of Justin Finke.)

incidentally showing that there is not very much effective volume in the high-redshift universe.

Equation (17.2), when supplemented by a physical model of relativistic jet sources [52, 53, 486], can be used to fit flux or fluence distributions. Statistical analysis of extragalactic source counts is a powerful technique [29] to test jet structure, the redshift-dependent formation rate of sources, luminosity and density evolution, and the relationship between different classes of black-hole sources.

17.1.3 Blazar Physics

The Fermi Gamma Ray Space Telescope is providing an all-sky scanning mission giving a GeV γ -ray data base containing as many as thousands of radio-loud AGN and GRBs over a wide range of redshifts and fluxes. From these results, combined with data taken with ground-based γ -ray telescopes and correlated with multiwavelength and multichannel observations we can, by joining statistical analysis and blazar modeling efforts, answer some open questions in black hole research, including:

1. *Unification.* Significant progress will be made in connecting different subclasses of AGN and testing the unification hypothesis [279] that luminous Fanaroff-Riley 2 (FR2) radio galaxies [487] are the parent

population of radio-loud quasars and FSRQs, and low-luminosity FR I radio galaxies are the parent population of BL Lac objects. The space densities and emissivities of different classes of jetted sources, important for cosmic-ray studies and black-hole fueling scenarios, can be determined.

2. *Blazar main sequence.* Blazar subclasses exhibit a trend characterized by decreasing bolometric luminosities, a shift of the peak frequencies of their broadband spectral components towards higher values, and a decreasing fraction of power in γ rays compared with lower-frequency radiation [488, 489]. The blazar main sequence is argued [490] to result from the decreasing energy density of the external radiation field, leading to a decreasing amount of Compton cooling.
3. *Blazar evolution.* An evolutionary scenario may link these blazar subclasses in terms of a reduction of the black hole fueling with time. As the circumnuclear material accretes to fuel the central engine, less gas and dust is left to scatter accretion-disk radiation and produce an external Compton-scattered component in blazar spectra. This chronology produces an evolution with time from FSRQ \rightarrow BL Lac objects [491], with the BZ process playing an important role [492].

17.1.4 GRB Classes

The distance scale is crucial for solving the question of source origin. As demonstrated by short-hard and long-soft GRB studies, both apparent isotropic and beaming-corrected energies can be derived. Separation of GRBs by energy release and redshift distribution has led to the recognition of a low-luminosity GRB population. In the same way, absolute and beaming-corrected energy releases, unusual spectral states, and anomalous γ -ray emission components can be used to define different classes of GRBs.

With the dozen or so GRBs that the Fermi LAT and the hundreds of GRBs that the Fermi Gamma ray Burst Monitor (GBM) will significantly detect per year, the simplest method to examine the γ -ray properties of GRBs, as shown in figure 17.4, is to plot the ratio of fluences in the Fermi LAT (20 MeV– $>$ 300 GeV) and GBM (8 keV–40 MeV) wavebands [493]. Fluence ratio is one way to search for distinct classes of GRBs, compared to hardness/duration diagrams [494] or energies [495, 496].

17.1.5 Unresolved and Diffuse γ -Ray Background

The intensity of the diffuse and unresolved γ -ray EBL from EGRET observations and analysis [33, 34] is shown in figure 17.5 (compare figure 1.3). It is decomposed into contributions from blazars [52], separated into FSRQs

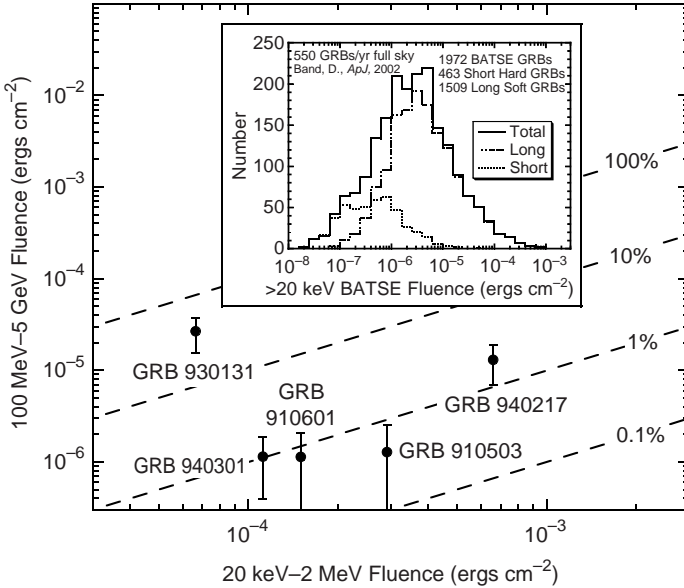


Figure 17.4 Search for different classes of GRB sources in terms of fluence ratios [493]. Shown are the BATSE fluence distribution (upper panel; figure courtesy Nicola Omodei), and EGRET and BATSE fluences, in units of $\text{ergs cm}^{-2} \text{s}^{-1}$, for five GRBs detected with the spark chamber on EGRET (lower panel).

and BL Lacs, and the superposed emissions from numerous faint sources where the γ rays are formed primarily by interactions of cosmic rays accelerated by supernovae in star-forming galaxies and by structure formation shocks in clusters of galaxies [497,499]. (For the diffuse γ -ray intensity from the Hawking radiation of evaporating mini-black holes, see [457].) Particle and radiation fields are connected because photohadronic interactions of UHECRs with the EBL form cascade γ rays that contribute a truly diffuse component to the γ -ray EBL [498].

17.2 COSMIC RAYS

The origin of the cosmic rays has been one of the central problems in astrophysics since Baade and Zwicky [500] commented on the connection between cosmic rays and supernovae in 1934. The hypothesis that cosmic rays, at least the Galactic cosmic rays between $\sim \text{GeV/nuc}$ and $\approx 10^{14} - 10^{17} \text{ eV}$, are accelerated by supernova remnant shock waves is reasonable because it passes the basic tests of available power and a plausible

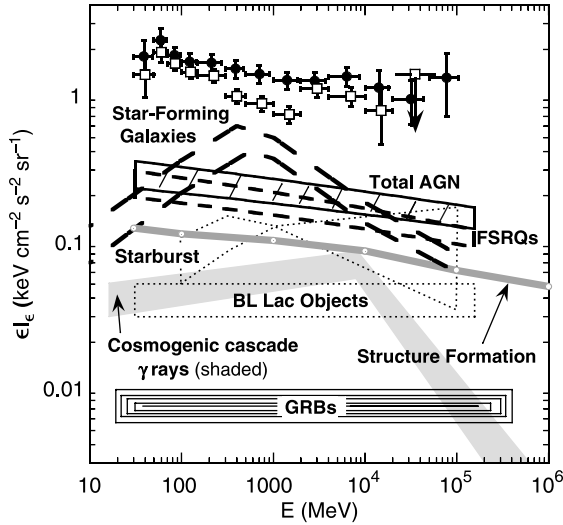


Figure 17.5 Decomposition of the diffuse/unresolved γ -ray background measured with EGRET [33,34,497]. Shaded region shows estimate for cascade γ rays induced by UHECRs formed by sources evolving as AGNs [498].

acceleration mechanism, especially given results of first-order shock Fermi acceleration theory, reviewed here (see [12, 114]).

Featureless power-law hard X-rays from SNRs like SN 1006, interpreted as nonthermal synchrotron radiation from cosmic-ray electrons, lead us to think that SNRs are sites of cosmic-ray electron acceleration. The identification of sites of hadronic acceleration in Galactic SNRs has however been more difficult. EGRET's point spread function was too large to convincingly identify a SNR as a source of γ -rays. The HESS spectra on SNRs may be interpreted as leptonic or hadronic emissions. Milagro finds ~ 10 TeV γ -ray excesses in the Cygnus region of unknown origin.

The confirming γ -ray signature of the acceleration of the hadronic cosmic rays is the π^0 γ -ray bump at ≈ 70 MeV in a photon number spectrum [385, 386]. Fermi could provide the crucial data to determine if the solution to the origin of cosmic rays can be settled by γ -ray astronomy. This is a difficult problem, because it depends on background subtraction, line-of-sight integrations, presence of clouds of target material, and arguments regarding the age and distance of the SNR.

Depending on the spectral hardness and diffusivity of TeV–PeV cosmic rays, neutrinos could be detected from interactions of cosmic rays with the gas and dust in the OB associations. The detection and interpretation of γ -ray and neutrino signals from SNRs should solve the problem of Galactic cosmic-ray origin.

17.2.1 Acceleration of Cosmic Rays at Supernova Remnant Shocks

The momentum gain rate from first-order Fermi acceleration at an external shock is, from eqs. (13.78) and (13.100),

$$\dot{p}_{\text{F1}} \simeq \frac{(\Gamma - 1)c}{r_{\text{L}-}^o} \simeq \dot{p}'_{\text{F1}}. \quad (17.3)$$

The momentum gain rate from second-order Fermi acceleration in the co-moving shocked fluid frame is, from eqs. (14.50) and (14.77),

$$\dot{p}'_{\text{F2}} \simeq \frac{\epsilon_B \xi (q - 1)c}{r_{\text{L}+}^o} (r_{\text{L}+}^o k_{\text{min}} p')^{q-1}. \quad (17.4)$$

Note that $\dot{p}'_{\text{F1}} \propto \text{const}$ and $\dot{p}'_{\text{F2}} \propto p'^{q-1}$, recalling that q is the index of the wave turbulence.

The rate of stochastic second-order processes is negligible in comparison with the first-order rate when $\beta_0 \ll 0.1$. As the flow speed becomes marginally relativistic, first-order processes can accelerate particles to sufficiently high energies that second-order acceleration then starts to become important [372]. At relativistic flow speeds, the second-order process can easily dominate.

Table 12.1 gives a listing of flow speeds and ejecta energies obtained from spectral line observations of SNe [308] and GRBs. Particle acceleration to the knee of the cosmic ray spectrum by SNe requires large explosions taking place in tenuous surroundings [384]. This is feasible for SNe if cosmic rays primarily originate from Type Ia SNe, as Type II and Type Ib/c SNe are thought to be associated with young massive stars in dense, gaseous environments. In the latter case, though, upstream amplification of the magnetic field can enhance acceleration to reach, for mildly relativistic outflows, $\approx 10^{17}$ eV.

The situation is far more complex. Acceleration efficiency is probably a function of Mach number, so that different classes of SNe differ widely in their efficiency to accelerate cosmic rays. A clumpy or a wind-type environment would have different maximum energies than a uniform medium. (Outflow velocities of ejected matter from SN 1987A reached $2\text{--}3 \times 10^4$ km s⁻¹, more than twice as fast as a typical Type II SN [308].) SNe and hypernovae may eject mass outflows with a range of speeds [501]. Mildly relativistic outflows are deduced from radio observations of the Type Ic SN 1998bw associated with GRB 980425 [307, 387], so that hadronic cosmic-ray acceleration to the knee of the cosmic-ray spectrum is possible from Type Ic SNe. But even if shocks of SNRs accelerate cosmic rays, this mechanism has trouble in accounting for the origin of cosmic rays with energies $\gtrsim 10^{17}$ eV.

17.2.2 Acceleration of UHECRs at Relativistic Blast Waves

The maximum particle energy for a cosmic-ray ion accelerated by second-order Fermi processes at an external shock of a relativistic blast wave can easily be derived. Consider a blast wave with apparent isotropic energy $E_0 = 10^{52} E_{52}$ ergs and Lorentz factor $\Gamma_0 = 300\Gamma_{300}$, sweeping up an external medium with density $n_0 \text{ cm}^{-3}$. The volume of the shocked shell for a spherically symmetric explosion at distance x from the engine is $V' = 4\pi x^2 \Delta'$, where the shell width $\Delta' = x/12\Gamma$. The Hillas condition [320] for maximum particle energy E'_{max} is that the particle Larmor radius is less than the size scale of the system; thus

$$r'_L = \frac{E'_{\text{max}}}{QB'} = \frac{E_{\text{max}}}{Z\Gamma eB'} < \Delta'. \quad (17.5)$$

The largest particle energy is reached at the deceleration radius $x = x_d$, from eq. (11.2). Hence $E_{\text{max}} \cong ZeB'x_d/12$.

The mean magnetic field $B' \cong 0.4(\epsilon_B n_0)^{1/2} \Gamma \text{ G}$, from eq. (11.39), giving

$$E_{\text{max}} \cong 8 \times 10^{19} Z n_0^{1/6} \epsilon_B^{1/2} \Gamma_{300}^{1/3} E_{52}^{1/3} \text{ eV} \quad (17.6)$$

[301,446], so that second-order processes in the shocked fluid shell of a relativistic blast wave that sweeps up material from the surrounding medium can, in the right environment, accelerate particles to ultrahigh energies. Acceleration to ultrahigh energies through first-order relativistic shock acceleration requires a highly magnetized surrounding medium [338], but mildly relativistic shocks in the colliding shells of relativistic black-hole jet sources are also able to accelerate particles to $\gtrsim 10^{20}$ eV energies.

17.2.3 Charged-Particle Astronomy

The Auger discovery [14] of clustering in the arrival directions of $\gtrsim 60 \text{ EeV}$ UHECRs along the supergalactic plane (SGP) rules out a Galactic origin of UHECRs. By correlating the UHECR arrival directions with directions to AGNs in the Véron-Cetty and Véron (VCV) catalog [502], with 694 active galaxies at $d \lesssim 100 \text{ Mpc}$, the Auger collaboration finds that UHECRs with $E \gtrsim 60 \text{ EeV}$ correlate with the directions to AGNs within 50–100 Mpc. UHECRs are deflected in transit by the Galactic [503] and the intergalactic magnetic field.

The clustering energy $E_{\text{cl}} \cong 60 \text{ EeV}$ separates UHECRs formed mainly by sources along the SGP at $d \lesssim d_{\text{cl}}$ from lower-energy UHECRs formed nearby and on $\gtrsim 75 \text{ Mpc}$ scales. A high-significance steepening in the UHECR spectrum at $E \cong 10^{19.6} \text{ eV} \cong 4 \times 10^{19} \text{ eV}$ and at $E \cong 10^{19.8} \text{ eV} \cong 6 \times 10^{19} \text{ eV}$ was recently reported, respectively, by the PAO [183] and

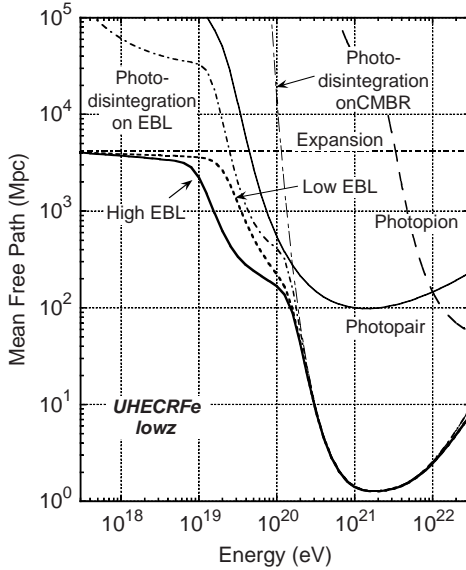


Figure 17.6 Effective energy-loss mean free path of Fe in low and high EBLs of figure 10.5.

HiRes [182] collaborations. These results confirm the prediction of Greisen, Zatsepin, and Kuzmin [10, 11] that interactions of UHECRs with CMBR photons cause a break in the UHECR spectral intensity near 10^{20} eV.

The simplest explanation is that more distant UHECRs fail to arrive here at Earth due to energy and photodisintegration losses. Figure 17.6 shows the effective energy-loss MFP of UHECR Fe from photopion, photopair, photodisintegration, and universal expansion losses, as described in chapters 9 and 10, for the low and high EBLs of figure 10.5 [504]. This distance is ≈ 200 Mpc at 10^{20} eV and a factor of 2 larger at 60 EeV. The PAO clustering results would apparently rule out that $\gtrsim 60$ EeV had a significant UHECR Fe composition.

Figure 17.7 shows the energy-loss MFP of UHECR He, N, and Fe in the low and high EBLs. If we accept the Auger results, keeping in mind calibration uncertainties [505, 506] and the approximate meaning of an effective MFP, then figures 17.6 and 17.7 show that UHECR ions up to perhaps Ne ($A = 20$) would lose their energy or be destroyed within ≈ 100 Mpc. An abundance of light ions [505] would be required if there is significant ionic composition in the UHECRs.

For protons, the clustering energy is similar to the GZK energy because they both represent the energy where detection of $\gtrsim 60$ EeV cosmic rays at the $\gtrsim 100$ Mpc scale is obscured by photopion energy losses with the

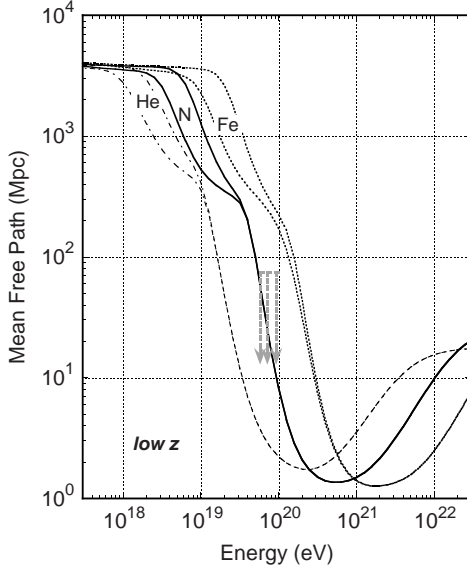


Figure 17.7 Effective energy-loss mean free paths of UHECR He, N, and Fe ions, as labeled, in low and high EBLs of figure 10.5.

CMBR. The energy-loss mean free path gives the mean distance over which a particle with energy E loses $\approx 1 - e^{-1} \cong 63\%$ of its energy.

The GZK horizon radius giving the mean distance from which protons detected with energy $10^{20} E_{20}$ eV originate depends in general on injection spectra and source evolution [203], but a model-independent definition that reduces to $r_{\phi\pi}(E_{20})$ for energy-independent energy loss considers the average distance from which a proton with measured energy E had energy eE . The horizon distance, defined this way, is given by

$$r_{\text{hrz}}(E_{20}) = \int_{E_{20}}^{eE_{20}} \frac{dx}{x} r_{\phi\pi}(x) \cong \frac{1.1 E_{20}^2 \exp(4/E_{20})}{1 + 1.6 E_{20}^2/13.7} \text{Mpc}, \quad (17.7)$$

where the last expressions gives the proton horizon on CMBR photons alone, using eq. (9.17).

Using the phenomenological fits to the low and high EBLs at optical and IR frequencies, represented as a superposition of blackbodies in figure 10.5, gives the corrected horizon distance shown in figure 17.8. The horizon distance for $\gtrsim 57$ (75, 100) EeV UHECR protons is $\gtrsim 200$ (100, 50) Mpc. A GZK horizon smaller than 40 Mpc applies to protons with $E \gtrsim 100$ EeV. This explains the clustering observations for UHECR protons. Differences in the energy scale between the two experiments, which have $\approx 20\%$

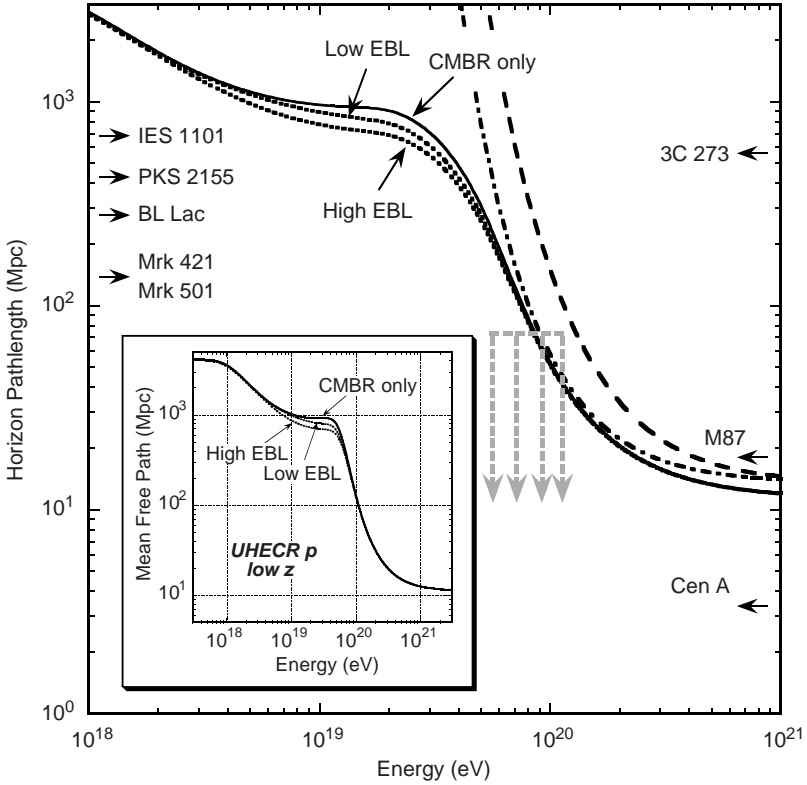


Figure 17.8 Heavy dotted curves give the horizon distance for UHECR protons as a function of total proton energy, using the local CMBR and the low and high EBL target radiation field, from figure 10.5. The analytic approximation to photopion energy-loss mean free path, eq. (9.16) or (9.17), is given by the dashed curve, and the UHECR proton horizon, eq. (17.7), by the dot-dashed curve, for CMBR only. Auger clustering results [14] are indicated by the shaded arrows. Distances to key radio galaxies are shown, and inset shows UHECR proton energy-loss MFPs.

uncertainties due to systematic effects, could reconcile the discrepancies between the HiRes and Auger GZK energies as determined from the spectral break (see figure 9.9), and would be compatible with GZK losses of UHECRs with a predominantly proton composition.

The dip energy can be viewed as a consequence of photopair effects on UHECR protons [506], either from GRBs [208] or AGNs [507]. It could also involve photodisintegration and photopair energy losses of ions interacting with photons of the EBL.

17.2.4 UHECR Propagation

Three-dimensional diffusive propagation was described in section 12.5. Detailed propagation models follow trajectories in specified magnetic field geometries [203, 508]. If the magnetic field is tangled on size scales $\sim \lambda_{\text{coh}}$, where λ_{coh} is the coherence length of the magnetic field, then cosmic rays from a source at distance d passing through a medium with mean magnetic field $B = 10^{-12} B_{-12}$ G are deflected by the angle [476, 509]

$$\theta_d \simeq \frac{d}{2r_L \sqrt{N_{\text{inv}}}} \cong \frac{dZeB}{2E\sqrt{N_{\text{inv}}}} \simeq 0.04^\circ Z \frac{B_{-12} d(100 \text{ Mpc})}{(E/60 \text{ EeV})\sqrt{N_{\text{inv}}}}. \quad (17.8)$$

Here $N_{\text{inv}} \cong d/\lambda_{\text{coh}} \gtrsim 1$ is the number of inversions of the magnetic field, and the Larmor radius of a particle with energy E and charge Ze is $r_L \cong 65(E/60 \text{ EeV})/(ZB_{-12})$ Gpc. If the UHECRs originated from AGNs in the Véron-Cetty and Véron catalog [502], taking $d \cong 75$ Mpc and $\theta_d \cong 3^\circ$ gives $B_{-12} \lesssim 100(E/60 \text{ EeV})\sqrt{N_{\text{inv}}}/Z$ in order that the deflections are not greater than 3° .

The Galactic magnetic field could, however, cause the deflections [503]. Approximating the Galactic magnetic field by a magnetic disk with characteristic height h_{md} gives a deflection angle $\theta_{\text{diff}} \approx h_{\text{md}} \csc b/r_L$, where b is the Galactic latitude of the UHECR source. Thus

$$\theta_{\text{diff,MW}} \cong 0.9^\circ \frac{Zh_{\text{md}}(\text{kpc})B(\mu\text{G})}{\sin b(E/60 \text{ EeV})}. \quad (17.9)$$

Mean magnetic fields B in the ≈ 0.2 kpc thick gaseous disk of the Galaxy are $\approx 3\text{--}5 \mu\text{G}$, but could fall to $\ll 1 \mu\text{G}$ in the kpc-scale halo. Deflection angles $\lesssim 3^\circ$ from Cen A ($b = 19.4^\circ$, galactic longitude $\ell = 309.5^\circ$, declination -43° , distance $d \cong 3.4$ Mpc) would seem to restrict UHECRs to protons or light- Z nuclei and a small ($\lesssim 0.1 \mu\text{G}$) Galactic halo magnetic field, consistent with results in section 17.2.3.

The equation for the time delay due to the deflection of UHECRs from an impulsive source is

$$\Delta t \cong \frac{d}{6c} \theta_d^2 \lesssim \frac{34Z^2 B_{-12}^2 d^3 (100 \text{ Mpc})}{(E/60 \text{ EeV})^2} \text{ yr} \quad (17.10)$$

[476, 509]. Recurrent events over days or shorter could be observed from UHECRs powered by nearby GRBs from Cen A or low luminosity GRBs like GRB980425/SN1998bw ($d \cong 36$ Mpc) if the magnetic field of the IGM is sufficiently weak or disordered.

17.2.5 UHECR Source Power Requirements

Maximum particle energy in relativistic flows characterized by apparent jet power L is given by a simple theoretical argument.

The particle energy density of a cold relativistic wind with apparent isotropic luminosity L and Lorentz factor $\Gamma = 1/\sqrt{1 - \beta^2}$ at radius R from the source is

$$u_p = \frac{L}{4\pi R^2 \beta \Gamma^2 c},$$

from eq. (11.116). If a fraction ϵ_B of the power is channeled into magnetic field B' in the fluid frame, then $RB'\Gamma = \sqrt{2\epsilon_B L/\beta c}$, implying maximum particle energies $E'_{\max} \cong QB'(R/\beta\Gamma)$, so

$$E_{\max} \cong E'_{\max} \Gamma \cong \left(\frac{Ze}{\Gamma}\right) \sqrt{\frac{2\epsilon_B L}{\beta}} c \cong 2 \times 10^{20} Z \mathcal{A} \sqrt{\epsilon_B \left(\frac{L}{10^{46} \text{ ergs s}^{-1}}\right)} \text{ eV}.$$

This simple, optimistic estimate does not explain how to transform directed particle kinetic energy into magnetic field energy in a cold wind, and leaves out physical limitations, for example, the acceleration time limiting the highest energy particles in supernova remnant shocks. Nevertheless, this equation is recovered in more detailed studies, where the factor $\mathcal{A} \ll 1$. Assuming a Fermi acceleration scenario for the sources of UHECRs therefore restricts sources to those with apparent isotropic powers to $\gtrsim 10^{46} \text{ ergs s}^{-1}$, that is, blazars and GRBs.

We also consider another argument that black holes are luminous enough to accelerate $10^{20} E_{20} \text{ eV}$ UHECR protons or ions [510]. In a region of size R and magnetic field B , electromagnetic forces can accelerate a particle to a maximum energy of $E_{\max} > E_{\text{par}} \simeq Ze\beta BR$. The available time in the comoving frame is shortened by bulk Lorentz factor Γ , so that the effective size for acceleration is $\approx R/\Gamma$, and $BR > \Gamma E_{\text{par}}/Ze\beta$. The required power of the magnetized flow is

$$L \approx 2 \times 4\pi R^2 v \times \frac{B^2}{8\pi} \approx \beta c (BR)^2 \approx \frac{c\Gamma^2 E_{\text{par}}^2}{Z^2 e^2 \beta} \cong \frac{3 \times 10^{45}}{Z^2} \frac{\Gamma^2}{\beta} E_{20}^2 \text{ ergs s}^{-1}, \quad (17.11)$$

including a factor of 2 for the plasma jet kinetic power. If the nonthermal luminosity is a good measure of jet power, then we can decide whether different source classes are good candidate UHECR sources.

For GRBs, $\Gamma \approx 300$, and $L_{\text{GRB}} \gg 10^{50} (\Gamma/300)^2 E_{20}^2 / Z^2 \text{ ergs s}^{-1}$. Apparent isotropic X/γ powers of long-duration GRBs are regularly measured in excess of $10^{50} \text{ ergs s}^{-1}$ [365], so long-duration GRBs are a viable candidate for UHECR acceleration. For the low-luminosity GRBs, which may only reach $\approx 10^{48} - 10^{50} \text{ ergs s}^{-1}$ [495], higher- Z ions can still be accelerated to super-GZK energies if Γ remains large.

For blazars, $L_{\text{blazars}} \gg 3 \times 10^{45} \Gamma^2 E_{20}^2 / Z^2 \text{ ergs s}^{-1}$. The γ -ray evidence shows that powerful radio galaxies, and even lower-luminosity radio

galaxies like Centaurus A during flaring periods, could be the sources of UHECRs.

17.3 NEUTRINOS

Multimessenger astronomy will truly come of age when PeV neutrinos are detected from extragalactic sources beyond the γ -ray horizon. Instruments at the kilometer scale have the critical size needed to open this window and detect sources.

A source of neutrinos should also be bright in direct or cascade GeV–TeV γ -rays coproduced in the pion/neutrino production process. Consequently, detectable neutrino production should be accompanied by high-energy γ -ray fluences, which should exceed the level $\sim 10^{-4}$ ergs cm^{-2} to be bright enough to be detected with km-scale neutrino detectors. The detection efficiency in water or ice of ultrarelativistic upward-going muon neutrinos (ν_μ) with energy of $100\epsilon_T$ TeV is

$$P_{\nu\mu}(\epsilon_T) \simeq 10^{-4} P_{-4} \epsilon_T^\chi, \quad \chi = 1 \text{ for } \epsilon_T < 1 \text{ and } \chi = 0.5 \text{ for } \epsilon_T > 1$$

[181, 226]. Parameterizing the GRB neutrino $\nu\mathcal{F}_\nu$ fluence spectrum by a power law with index a_ν , so $\nu\mathcal{F}_\nu = 10^{-4} \phi_{-4} \epsilon_T^{a_\nu}$ erg cm^{-2} , then the number of neutrinos detected with a km-scale ν detector such as IceCube or the proposed northern hemisphere neutrino telescope KM3NeT is

$$\begin{aligned} N_\nu &\approx \int d\epsilon_T \frac{\nu\mathcal{F}_\nu}{\epsilon_T^2} \frac{P_{\nu\mu}(\epsilon_T) A_\nu}{(160 \text{ erg}/100 \text{ TeV})} \\ &\simeq 0.6 \frac{\phi_{-4} P_{-4} A_{10}}{1 - a_\nu} \begin{cases} 1 + (1 - a_\nu^{-1})(1 - \epsilon_T^{a_\nu}), & \text{for } \epsilon_T < 1, \\ \epsilon_T^{a_\nu - 1/2}, & \text{for } \epsilon_T > 1. \end{cases} \end{aligned} \quad (17.12)$$

For a neutrino spectrum that is flat in $\nu\mathcal{F}_\nu$, that is, $a_\nu \cong 0$, $N_\nu(\epsilon_T < 1) \simeq \phi_{-4} P_{-4} A_{10} (1 + \frac{1}{2} \ln \epsilon_T^{-1})$ and $N_\nu(\epsilon_T > 1) \simeq \phi_{-4} P_{-4} A_{10} / \sqrt{\epsilon_T}$. The IceCube detector is especially sensitive to cosmic neutrino sources at ~ 100 TeV–PeV energies, as cosmic-ray-induced background may become too large at lower energies, and the flux becomes too small at higher energies.

The detection of a single ν_μ therefore requires a ν_μ fluence $\gtrsim 10^{-4}$ erg cm^{-2} above 1 TeV. Since the energy release in high-energy neutrinos and electromagnetic secondaries is about equal, this energy will be reprocessed in a pair-photon cascade and emerge in the form of observable radiation at γ -ray energies, and this radiation cannot exceed the measured

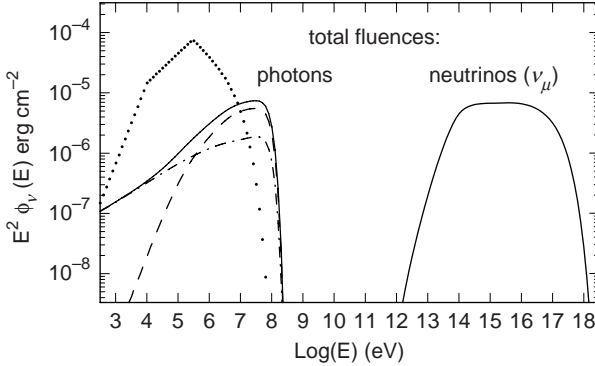


Figure 17.9 Energy fluence of photons and photomeson muon neutrinos for a collapsar-model GRB with hard X-ray fluence $\Phi_{\text{tot}} = 3 \times 10^{-4} \text{ erg cm}^{-2}$ and $\delta_D = 100$. The dotted curve shows the fluence of a GRB used for calculations, and the dashed and dot-dashed curves show the Compton and synchrotron contributions to the photon fluence from the electromagnetic cascade initiated by secondaries from photomeson processes, respectively.

fluence in this regime. Thus the γ -ray photon fluence \mathcal{F}_γ accompanying the neutrino production must be $\gtrsim 10^{-4} \text{ ergs cm}^{-2}$ for an UHECR source to be detected with a km-scale neutrino telescope such as IceCube. Because the neutrino fluence will be spread over several orders of magnitude, it is necessary that $\mathcal{F}_\gamma \gtrsim \text{few} \times 10^{-4} \text{ ergs cm}^{-2}$ in order to produce a sufficient neutrino fluence for detection, given that the ν_μ fluence will generally be smaller than the photon fluence even in the optimistic case that the photon radiation originates substantially from hadronic processes [511].

For comparison, ≈ 2 GRBs per year are expected with X/ γ -fluence $> 3 \times 10^{-4} \text{ ergs cm}^{-2} \text{ s}^{-1}$ at hard X-ray/soft γ -ray energies [512] (figure 17.4). The day-long fluence of a bright γ -ray blazar flare with flux brighter than $\gtrsim 200 \times 10^{-8} \text{ ph} (> 100 \text{ MeV}) \text{ cm}^{-2} \text{ s}^{-1}$ exceeds $10^{-4} \text{ ergs cm}^{-2}$, and we expect a blazar flare this bright should occur every few weeks [268].

Figure 17.9 shows calculations [191,513] of photomeson neutrino production for a collapsar model GRB with $\Phi_{\text{tot}} = 3 \times 10^{-4} \text{ erg cm}^{-2}$ and $\delta_D = 100$, as well as the accompanying electromagnetic radiation induced by pair-photon cascades from the secondary electrons and γ rays made by the same photomeson interactions [97]. (Not shown is the leptonic SSC component.) The same energy required to power the leptonic synchrotron radiation is deposited in the form of relativistic protons in this calculation, so that the baryon-load factor $f_{\text{CR}} = 1$. The dotted curve shows the primary lepton synchrotron radiation spectrum that was assumed for the calculation.

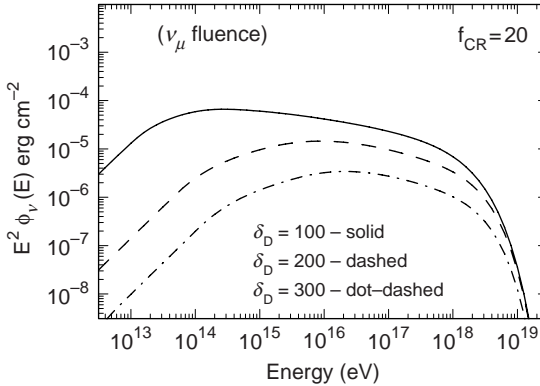


Figure 17.10 The fluences of muon neutrinos calculated for a GRB at $z = 1$ with X-ray/MeV γ -ray fluence of 3×10^{-4} ergs cm^{-2} and Doppler factors $\delta_D = 100, 200,$ and 300 , and a nonthermal baryon-loading factor $f_{\text{CR}} = 20$. (Figures 17.9 and 17.10 courtesy of Armen Atoyan.)

The total number of ν_μ expected with IceCube is $\cong 0.1$. The total fluence of cascade photons shown here is contributed by lepton synchrotron (dot-dashed) and Compton (dashed) emissions induced by hadronic processes. The level of the fluence of the cascade photons is $\approx 10\%$ of the primary synchrotron radiation. This means that the maximum allowed baryon load $f_{\text{CR}} \lesssim 10\text{--}30$ in order not to overproduce the primary synchrotron radiation fluence, which could possibly be of hadronic origin.

Figure 17.10 shows the neutrino fluences expected in the collapsar GRB scenario from a model burst with photon fluence $\Phi_{\text{rad}} = 3 \times 10^{-4}$ erg cm^{-2} at redshift $z = 1$ [513]. The value of the baryon-loading parameter f_{CR} is set equal to 20 in this calculation. The numbers of muon neutrinos that would be detected from a single GRB with IceCube for these parameters and with $\delta_D = 100, 200,$ and 300 are $N_\nu = 1.32, 0.105,$ and 0.016 , respectively, limited by the high-energy radiation fluence. If the radiation fluence at MeV–GeV energies is larger than the hard X-ray fluence, a possibility that the Fermi telescope is answering, then the expected number of detected neutrinos could be increased correspondingly. Observations of γ -ray emission not easily explained with leptonic models, for example, the anomalous γ -ray component in GRB 941017 [514], could be a feature of relativistic hadron acceleration in these sources.

Figure 17.11 is a hybrid plot of lengths for particles and photons of different energies. Its interest for neutrino physics is that any source of UHECRs, if from a collimated relativistic jet, produces a distinctive γ -ray signature from $\gamma\gamma$ cascades on the EBL. For IGM magnetic fields that are very disordered or weak, then the hadronic cascade will produce an

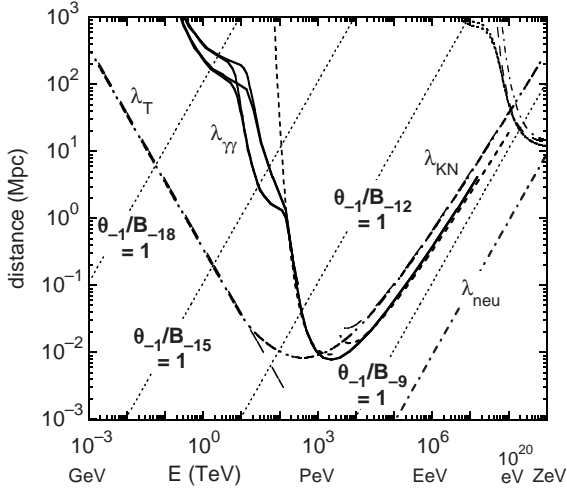


Figure 17.11 Mean free paths for attenuation of γ rays by the EBL ($\lambda_{\gamma\gamma}$; for corrections from radio EBL, see [515]), for Compton-scattering energy loss of relativistic electrons or positrons with the CMBR in the Thomson (λ_T) and Klein-Nishina (λ_{KN}) regimes, and neutron decay (λ_{neu}). The particle or photon energy is denoted E (TeV). The photopion horizon and energy-loss pathlengths for protons, from figure 17.8, are shown for comparison. Dotted lines give length scales for a lepton to be deflected by $0.1\theta_{\perp}$ rad in a magnetic field from 10^{-9} to 10^{-18} G, as labeled. Photohadronic processes that induce such high-energy electromagnetic primaries will also be strong sources of neutrinos.

≈ 100 GeV–multi-TeV flux from sources of UHECRs at distances \approx few hundred Mpc–Gpc. A strong neutrino source will be accompanied by a flux of neutrons and γ rays. The neutrons transfer energy to lobes or the surrounding galactic environment, while the γ rays materialize and form an electromagnetic cascade. Observations with the IceCube neutrino detector will determine whether black holes power neutral beams.

17.4 CONCLUDING REMARKS

In this study, we have tried to join black-hole engine and high-energy radiation physics to give an understanding of observations of energetic nonthermal emissions from candidate black-hole sources, seen as sites of energy release, plasma ejection, particle acceleration, and radiation. We have concentrated on energy extraction from spinning black holes through Penrose processes, namely, *the spin paradigm*, with the spin of the black hole as the

decisive variable separating thermal black holes largely powered by accretion from nonthermal black holes in radio galaxies, γ -ray blazars, and jetted sources like GRBs and microquasars whose radiative output is dominated by nonthermal emissions.

Based on a Blandford-Znajek process for electromagnetically extracting rotational energy from a black hole, we found a solution with energy extraction valid for general values of the spin angular momentum parameter a . The power output peaks, however, along the equator, contrary to the picture of oppositely-directed collimated jets. The geometry of matter currents setting up the black-hole magnetospheric fields could play a role, but the jet-formation problem was not treated here.

Instead, we considered whether spinning black holes eject relativistic outflows, and make shocks that accelerate the ultrahigh-energy cosmic rays, at the same time making γ -ray luminous sources. Evidence challenging this hypothesis would be given by special characteristics of the host galaxies or progenitor populations; by high-energy neutrino observations of GRBs or blazars or other sources; by anomalous γ -ray signatures associated with hadronic acceleration and energy losses in relativistic shock waves; and by evidence for cosmic-ray sources based on the arrival direction studies of UHECRs, for example, from special types of galaxies (e.g., radio, star-forming, or infrared luminous).

The advent of the IceCube neutrino telescope at the South Pole and the launch of Fermi in 2008, accompanied by major advances in ground-based cosmic-ray and γ -ray observatories, autonomously repointing telescopes, and a network of multiwavelength observers, will provide the important data to determine whether black holes accelerate the ultrahigh-energy cosmic rays and make hadronic radiations. Our understanding is already being challenged by new results from ground-based γ -ray observatories, the Pierre Auger Observatory, and the Fermi Gamma-ray Space Telescope. Detection of multi-TeV–PeV neutrino sources and sources of cosmogenic neutrinos with IceCube and UHE neutrino observatories could succeed in establishing the sources of Galactic and extragalactic cosmic rays and solve a puzzle reaching back a century. In the meantime, searches for energetic radiations from black holes in the extreme universe continue to surprise.

Appendix A

Essential Tensor Calculus

A.1 INTRODUCTION

This chapter provides the supplemental material that is necessary for a reader unfamiliar with tensor calculus and/or differential geometry to follow parts of the book. The description here is elementary, and it is our hope that a background in vector calculus is sufficient prerequisite. There are plenty of excellent books on the subject of differential geometry, some of which we include here as reference. For an introduction to the subject, see the books by Synge and Schild [516], Kay [517], and Bishop and Goldberg [518]. For a more advanced introduction suitable for physicists, see O'Neill [519] and Curtis and Miller [520].

A.2 THE TANGENT VECTOR

In order to formulate a general description of a tangent vector, let us consider the simplest possible example: Consider the Cartesian space \mathfrak{R}^2 on which we impose a coordinate system (x, y) in the usual manner. A vector at any point $p \in \mathfrak{R}^2$ is spanned by the two unit vectors $\{e_x, e_y\}$. e_x is the unit vector pointing along curves $y = \text{const}$ along the increasing direction of the x coordinate, and e_y is the unit vector pointing along curves $x = \text{const}$ along the increasing direction of the y coordinate. Any vector χ at p can be written in the form

$$\chi = \chi^x e_x + \chi^y e_y. \quad (\text{A.1})$$

Here χ^x and χ^y are just numbers. A vector field A on the other hand can be written in the form

$$A(x, y) = A^x(x, y)e_x + A^y(x, y)e_y. \quad (\text{A.2})$$

This vector field is defined wherever the functions A^x and A^y are. We say the vector field A is smooth whenever A^x and A^y are smooth functions of x and y . At any point $p = (x_0, y_0)$, in the domain of the tangent vector field A

$$A(x_0, y_0) = A^x(x_0, y_0)e_x + A^y(x_0, y_0)e_y \quad (\text{A.3})$$

is a tangent vector.

A vector is also characterized by its transformation property. To understand how vector fields transform, let us now use the polar coordinate system (r, θ) to describe $\mathfrak{R}^2 - 0$. In the polar coordinate system, the origin is removed from \mathfrak{R}^2 for the usual reason. The polar coordinates are defined by

$$x = r \cos \theta \quad \text{and} \quad y = r \sin \theta.$$

The unit vectors

$$e_r = \cos \theta e_x + \sin \theta e_y \quad \text{and} \quad e_\theta = -\sin \theta e_x + \cos \theta e_y.$$

The above transformation of unit vectors can be written as

$$e_r = \frac{\partial x}{\partial r} e_x + \frac{\partial y}{\partial r} e_y \quad \text{and} \quad e_\theta = \frac{1}{r} \left(\frac{\partial x}{\partial \theta} e_x + \frac{\partial y}{\partial \theta} e_y \right).$$

Let us compare the above equation with

$$\frac{\partial}{\partial r} = \frac{\partial x}{\partial r} \frac{\partial}{\partial x} + \frac{\partial y}{\partial r} \frac{\partial}{\partial y} \quad \text{and} \quad \frac{\partial}{\partial \theta} = \frac{\partial x}{\partial \theta} \frac{\partial}{\partial x} + \frac{\partial y}{\partial \theta} \frac{\partial}{\partial y}.$$

We see that the basis vectors transform like partial derivatives. The $1/r$ in e_θ is there for normalization reasons since here we are looking at the transformation properties of unit vectors. Therefore, we see that there is a 1:1 correspondence between the basis for tangent vectors and partial derivatives. Let us generalize the result that we have obtained, keeping in mind that we are just looking for a basis set for the tangent vector fields (not necessarily an orthonormal set).

We would like to do tensor calculus on a general smooth surface and not just on \mathfrak{R}^n as we have done above. Examples of these surfaces are a 3d sphere, a 2d ball (the boundary of a sphere) and a torus. In relativity, we will even be concerned with 4d spaces. Regardless of the details, an n -dimensional smooth space will have n smooth coordinate functions $\{x^i|_{i=1}^n\}$ defined on it. In the language of differential geometry the space itself is referred to as a *manifold*. In an arbitrary manifold M with coordinates $\{x^i|_{i=1}^n\}$, the vector fields are objects spanned by the quantities

$$\frac{\partial}{\partial x^i}$$

for $i = 1, 2, \dots, n$. The most general tangent vector A at the point $p \in M$ can be written as

$$A(p) = A^i(p) \frac{\partial}{\partial x^i}. \quad (\text{A.4})$$

Here, we have used the Einstein summation convention that repeated indices with one upper and one lower implies summation, i.e.,

$$A^i \frac{\partial}{\partial x^i} \equiv \sum_{i=1}^n A^i \frac{\partial}{\partial x^i}. \quad (\text{A.5})$$

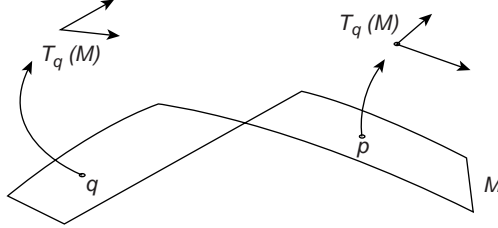


Figure A.1 $T_p(M)$ and $T_q(M)$.

The set of all tangent vectors at $p \in M$ forms the tangent vector space at p and is denoted as $T_p(M)$, as shown in figure A.1.

The most general tangent vector fields have the appearance

$$A(x) = A^i(x) \frac{\partial}{\partial x^i} . \tag{A.6}$$

Here x is any point of interest on the manifold where the coordinates are well defined. The tangent vector field A is defined wherever all the $A^i(x)$ are. A^i are the components of the vector field A . Also $\partial/\partial x^i$ is sometimes written as ∂_i . Very often, the basis vectors ∂_i are ignored and the vector (or vector field) $A^i(x)\partial_i$ is simply denoted as A^i . The restriction of a tangent vector field to a point p of the manifold is a tangent vector at p . The collection of all the tangent vectors spaces of all the points on the manifold forms the *tangent bundle*: $T(M)$. Naturally, tangent vector fields live on the tangent bundle. The transformation property of vectors fields can be deduced from the familiar chain rule.

Consider a change of coordinates from $\{x^i\}$ to $\{\bar{x}^i\}$ for $i = 1, 2, \dots, n$. Then

$$A(x) = A^i(x) \frac{\partial}{\partial x^i} = A^i(x) \frac{\partial \bar{x}^j}{\partial x^i} \frac{\partial}{\partial \bar{x}^j} \equiv \bar{A}^j(\bar{x}) \frac{\partial}{\partial \bar{x}^j} . \tag{A.7}$$

Here, the point x is short for (x^1, x^2, \dots, x^n) , and \bar{x} is the corresponding point in the “barred” coordinate system, and \bar{A}^j are components of the vector field A in the transformed coordinate system. In component form, the transformation property of tangent vectors become

$$\bar{A}^j(\bar{x}) = A^i(x) \frac{\partial \bar{x}^j}{\partial x^i} . \tag{A.8}$$

Definition. Tangent vectors at any point p of the manifold take smooth functions at p to a real number in a linear fashion by the prescription

$$A(f)|_p = A^i(p) \left. \frac{\partial f}{\partial x^i} \right|_{\hat{p}} . \tag{A.9}$$

Here f is any smooth function.

Clearly, eq. (A.9) is a linear map since

$$A(af + bg) = a A(f) + b A(g). \quad (\text{A.10})$$

Here f and g are smooth functions and a and b are numbers. In differential geometry this is how tangent vectors are defined. It turns out that the rest of the properties can be derived from the above definition.

A.3 DUAL VECTORS

A dual vector at a point $p \in M$ is a linear functional on the tangent vectors at p , i.e., a dual vector at a point takes a tangent vector at the same point and converts it to a number in a linear fashion.

Definition. For a smooth function f on the manifold, let the differential of f , denoted as df , be the linear functional on tangent vectors defined by

$$df(A) = A(f) = A^i \frac{\partial f}{\partial x^i}. \quad (\text{A.11})$$

It is easy to verify that the action of a differential of a function on a tangent vector is a function linear map, i.e.,

$$df(gA + hB) = g df(A) + h df(B). \quad (\text{A.12})$$

Here A and B are vectors, and g and h are functions.

The coordinate differentials form a basis for the dual vectors since

$$dx^i(\partial_j) = \frac{\partial x^i}{\partial x^j} = \delta_j^i.$$

Indeed, any dual vector A at the point p of the manifold can be written in the form

$$A(p) = A_i(p)dx^i. \quad (\text{A.13})$$

As in the case of tangent vector fields, the notion of dual vector at p can be extended to dual vector fields by allowing the point p to vary. The transformation properties of dual vectors follow from the expression above

$$A(x) = A_i(x)dx^i = A_i(x) \frac{\partial x^i}{\partial \bar{x}^j} d\bar{x}^j = \bar{A}_j(\bar{x})d\bar{x}^j = \bar{A}(\bar{x}). \quad (\text{A.14})$$

As before, we employ a coordinate transformation from $\{x^i\}$ to $\{\bar{x}^i\}$. Here the point \bar{x} is the corresponding point to x in the new coordinate system,

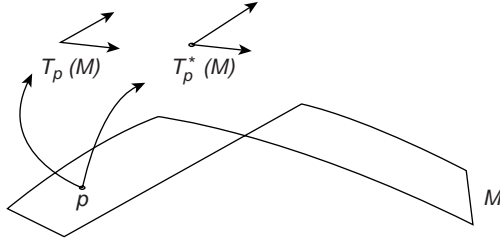


Figure A.2 $T_p(M)$ and $T_p^*(M)$.

and \bar{A}_j are components of the dual vector field A in the transformed coordinate system. In component form the transformation relation for dual vectors become

$$\bar{A}_j(\bar{x}) = A_i(x) \frac{\partial x^i}{\partial \bar{x}^j}. \tag{A.15}$$

Let us consider the action of a general dual vector A on a tangent vector χ

$$A(\chi) = A_i dx^i (\chi^j \partial_j) = A_i \chi^j dx^i (\partial_j) = A_i \chi^j \delta_j^i = A_i \chi^i. \tag{A.16}$$

The resulting function $A_i \chi^i$ obtained by *contraction* of indices is coordinate invariant, and hence is a scalar function. This is easily verified by the transformation properties eqs. (A.8) and (A.15).

$$\bar{A}_j \bar{\chi}^j(\bar{x}) = A_i \frac{\partial x^i}{\partial \bar{x}^j} \chi^k \frac{\partial \bar{x}^j}{\partial x^k} = A_i \chi^k \frac{\partial x^i}{\partial x^k} = A_i \chi^i(x). \tag{A.17}$$

Therefore we see that contraction is a coordinate-invariant action.

Definition. The set of all dual vectors at a point $p \in M$ forms the dual space at that point p denoted as $T_p^*(M)$, and the set of all dual spaces forms the cotangent bundle: $T^*(M)$ (see figure A.2).

Traditionally, tangent vectors are called contravariant vectors and dual vectors are referred to as covariant vectors. For a smooth function f ,

$$df = (\partial_i f) dx^i \equiv f_{,i} dx^i.$$

A.4 THE SPACE $T^{**}(M)$

As one might expect, the dual space at a point p will have its own dual space: the set of all linear functionals on the dual vectors at p denoted as $T_p^{**}(M)$. Let $\{E_i\}$ be a basis for $T_p^{**}(M)$ such that

$$E_i(dx^j) = \delta_i^j. \tag{A.18}$$

Then any $\chi \in T_p^{**}(M)$ can be written in the form $\chi = \chi^i E_i$. The action of such an object with a dual vector $A = A_j dx^j$ is given by

$$\chi(A) = \chi^i E_i(A_j dx^j) = \chi^i A_j E_i(dx^j) = \chi^i A_i.$$

The space $T_p^{**}(M)$ can be defined on all points of the manifold, and as a result we get the bundle $T^{**}(M)$. From the above equation, and eq. (A.16) we see that $T_p^{**}(M)$ can easily be identified with the original tangent space $T_p(M)$ by the following map

$$E_i \longleftrightarrow \partial_i. \quad (\text{A.19})$$

In this manner we can think of a tangent vector as a dual to the covariant vectors. Therefore, there are no new spaces that can be constructed by a search for dual spaces, and discussions here for this reason are limited to the tangent and the cotangent bundle.

It is important to remember that the action of a dual on a vector and vice-versa is essentially a contraction, and therefore, they are a coordinate independent process.

A.5 TENSORS

The tangent vectors and dual vectors can be used to construct multilinear functionals. Consider objects of type

$$dx^i \otimes dx^j.$$

We can view this as a multilinear functional on two tangent vectors, i.e.,

$$\begin{aligned} dx^i \otimes dx^j(A, B) &= dx^i \otimes dx^j(A^m \partial_m, B^n \partial_n) \\ &\equiv dx^i(A^m \partial_m) \cdot dx^j(B^n \partial_n) = A^i B^j. \end{aligned}$$

Here A and B are tangent vectors. \otimes is referred to as a “tensor” product. The most general tensor that can take two tangent vectors and return a scalar can be written in the form

$$T = T_{ij} dx^i \otimes dx^j.$$

The action of the tensor T on tangent vectors A and B is given by

$$T(A, B) = T_{ij} dx^i \otimes dx^j(A, B) = T_{ij} dx^i(A^m \partial_m) \cdot dx^j(B^n \partial_n) = T_{ij} A^i B^j.$$

Once again, we see that the end product is a coordinate independent contraction. Clearly,

$$\{dx^i \otimes dx^j\} \Big|_{i,j=1}^n$$

is a set of basis for tensors of type T mentioned above. The (ij) th component of such a tensor is obtained by the action

$$T(\partial_i, \partial_i) = T_{ij}.$$

In a similar manner we can construct tensors T of type (r, s) at any point $p \in M$ as a multilinear functional on r many dual vectors and s many-tangent vectors:

$$T : T_P^*(M) \times T_P^*(M) \times \dots \times T_P^*(M) \times T_P(M) \times T_P(M) \times \dots \times T_P(M) \rightarrow \mathfrak{R}. \tag{A.20}$$

In the above expression, there are r many $T_P^*(M)$ and s many $T_P(M)$. The components of such a tensor in an arbitrary coordinate basis can be obtained by the formula

$$T^{i_1 i_2 \dots i_r}{}_{j_1 j_2 \dots j_s} = T(dx^{i_1}, dx^{i_2}, \dots, dx^{i_r}, \partial_{j_1}, \partial_{j_2}, \dots, \partial_{j_s}). \tag{A.21}$$

To write the basis for such a tensor we need a dual basis for $\{dx^i\}$ and $\{E_i\}$. Therefore,

$$T = T^{i_1 i_2 \dots i_r}{}_{j_1 j_2 \dots j_s} E_{i_1} \otimes E_{i_2} \otimes \dots \otimes E_{i_r} \otimes dx^{j_1} \otimes dx^{j_2} \otimes \dots \otimes dx^{j_s} \tag{A.22}$$

with the understanding that for tensor basis, E_i acting on dx^j has the same effect as dx^j acting on ∂_i . These tensors at a point can be extended to tensor fields in an obvious manner. The above definition makes tensors multifunction-linear objects, i.e.,

$$T(A, B, \alpha C + \beta D, \dots, E) = \alpha T(A, B, C, \dots, E) + \beta T(A, B, D, \dots, E). \tag{A.23}$$

Here α and β are functions on the manifold and A, B, C, D, E are either covariant or contravariant vectors acting on a tensor of an appropriate type. This property would hold true at any entry of tensors of arbitrary type. Tensor products can also be used to construct other tensors. For example, if T is a tensor of type (r, s) and S is a tensor of type (l, m) , then $T \otimes S$ is a tensor of type $(r + l, s + m)$ whose components are given by

$$(T \otimes S)^{i_1 \dots i_r p_1 \dots p_l}{}_{j_1 \dots j_s q_1 \dots q_m} = T^{i_1 \dots i_r}{}_{j_1 \dots j_s} S^{p_1 \dots p_l}{}_{q_1 \dots q_m}. \tag{A.24}$$

The transformation properties of tensors under an arbitrary coordinate change can be deduced from from eqs. (A.8) and (A.15) as

$$\bar{T}^{i_1 i_2 \dots i_r}{}_{j_1 j_2 \dots j_s}(\bar{x}) = T^{l_1 l_2 \dots l_r}{}_{m_1 m_2 \dots m_s} \frac{\partial \bar{x}^{i_1}}{\partial x^{l_1}} \dots \frac{\partial \bar{x}^{i_r}}{\partial x^{l_r}} \frac{\partial x^{m_1}}{\partial \bar{x}^{j_1}} \dots \frac{\partial x^{m_s}}{\partial \bar{x}^{j_s}}. \tag{A.25}$$

It is also possible to convert a tensor of type (r, s) to type $(r - 1, s - 1)$ by contracting the i_j th contravariant and the j_k th covariant indices. In component form:

$$CT^{i_1 i_2 \dots i_{r-1}}{}_{j_1 j_2 \dots j_{s-1}} = \sum_{\sigma} T^{i_1 i_2 \dots \sigma \dots i_r}{}_{j_1 j_2 \dots \sigma \dots j_s}. \quad (\text{A.26})$$

For exactly the same reason as in eq. (A.17), the above contraction is not dependent on the coordinate basis chosen.

A.6 THE METRIC TENSOR

The metric tensor is of type $(0, 2)$. It takes two tangent vectors and returns a scalar. It is usual to reserve the letter g to describe the metric tensor.

Definition. The inner product of any two vectors A and B is given by the scalar

$$A \cdot B \equiv g(A, B).$$

For a tensor of type $(0, 2)$ to be a metric tensor, it must satisfy two properties:

1. g must be a symmetric tensor, i.e., $g(A, B) = g(B, A)$ for any two tangent vectors A and B .
2. g must be nondegenerate, i.e., if the inner product of a vector A with all the tangent vectors at a point vanishes, then A must vanish at that point. Explicitly,

$$g(A, \cdot) = 0 \Rightarrow A = 0.$$

Definition. Since g_{ij} is a nondegenerate tensor, given a metric tensor g , there is a unique tensor of type $(2, 0)$ denoted as g^{ij} such that

$$g_{ij} g^{jk} = \delta_i^k. \quad (\text{A.27})$$

The tensor g^{ij} is also referred to as the metric tensor.

1. The metric tensor g_{ij} induces a well-defined map from $T(M) \rightarrow T^*(M)$ given by

$$A_i(x) = g_{ij}(x) A^j(x) \quad (\text{A.28})$$

for any $A^j \in T(M)$.

2. The metric tensor g^{ij} induces a well-defined map from $T^*(M) \rightarrow T(M)$ given by

$$A^i(x) = g^{ij}(x) A_j(x) \quad (\text{A.29})$$

for any $A_j \in T^*(M)$.

Arbitrary tensor indices can be raised and lowered in a similar manner. For example

$$T^{i_1 i_2 \dots i_{l-1} i_l i_{l+1} \dots i_r}{}_{j_1 j_2 \dots j_s} = g_{i_l \sigma} T^{i_1 i_2 \dots i_{l-1} \sigma i_{l+1} \dots i_r}{}_{j_1 j_2 \dots j_s}. \quad (\text{A.30})$$

It is not necessary that the metric is positive definite; more definitely, there could be nontrivial vectors A such that

$$g(A, A) \leq 0. \quad (\text{A.31})$$

In fact, this is the case in relativistic physics. Spacetime is in general a 4d manifold. There are three classes of tangent vectors. Lightlike vectors are nontrivial vectors whose inner product with itself vanishes. Timelike vectors u , on the other hand, satisfy $g(u, u) < 0$. Spacelike tangent vectors X are familiar objects from classical physics with $g(X, X) > 0$.

In general, the metric tensor on a manifold has the form

$$g = g_{\mu\nu} dx^\mu \otimes dx^\nu. \quad (\text{A.32})$$

This metric can induce a metric on the various submanifolds of the original manifold. For concreteness, let μ, ν take on the values 1, 2, 3. Consider the submanifold defined by the surface $x^3 = \text{const}$. Then on the 2d manifold we have an induced metric of the form

$$\hat{g} = g_{ij} dx^i \otimes dx^j, \quad (\text{A.33})$$

where $\{i, j\}$ take on the values $\{1, 2\}$, since on this submanifold $dx^3 = 0$.

A.7 THE VOLUME ELEMENT AND THE LEVI-CIVITA TENSOR

We know from classical analysis that under a coordinate change from $\{x^i\}$ to $\{\bar{x}^i\}$

$$\int f(x) d^n x = \int \bar{f}(\bar{x}) J(x, \bar{x}) d^n \bar{x}. \quad (\text{A.34})$$

Here, by definition $\bar{f}(\bar{x}) = f(x)$ and the Jacobian of the transformation $J(x, \bar{x})$ is given by the determinant of the transformation matrix. Explicitly,

$$J(x, \bar{x}) = \left| \frac{\partial x^\mu}{\partial \bar{x}^\nu} \right|. \quad (\text{A.35})$$

As always, the upper indices refer to rows, and the lower indices refer to columns. On the other hand, the metric tensor transforms accordingly:

$$\bar{g}_{\mu\nu}(\bar{x}) = \frac{\partial x^\alpha}{\partial \bar{x}^\mu} g_{\alpha\beta}(x) \frac{\partial x^\beta}{\partial \bar{x}^\nu}. \quad (\text{A.36})$$

Taking the determinant on both sides we find that when $J(x, \bar{x}) > 0$

$$\sqrt{|\bar{g}(\bar{x})|} = J(x, \bar{x}) \sqrt{|g(x)|}. \quad (\text{A.37})$$

Here $|g|$ is the absolute value of the determinant of the matrix $g_{\mu\nu}$. Therefore, since

$$\begin{aligned} \int \bar{f}(\bar{x}) \sqrt{|\bar{g}(\bar{x})|} d^n \bar{x} &= \int f(x) \sqrt{|g(x)|} J(x, \bar{x}) \frac{d^n x}{J(x, \bar{x})} \\ &= \int f(x) \sqrt{|g(x)|} d^n x, \end{aligned} \quad (\text{A.38})$$

we can take

$$\sqrt{|g(x)|} d^n x \quad (\text{A.39})$$

as the invariant volume element. The above volume element is invariant only when the coordinate systems are such that eq. (A.37) holds true. Therefore, we must make sure that we pick coordinate systems that are “positively oriented,” i.e., if $\{x^i\}$ is chosen as a positively oriented frame, all other coordinate systems $\{\bar{x}^i\}$ should be such that

$$J(x, \bar{x}) > 0;$$

otherwise, we must make sure to insert a “ $-$ ” sign manually. In general relativity, since the determinant of the spacetime metric is negative, the above volume element becomes

$$\sqrt{-g(x)} d^4 x. \quad (\text{A.40})$$

In differential geometry, we call eq. (A.39) the volume element regardless of the dimension of the manifold; for example, if $n = 1$, then eq. (A.39) reduces to the line element, while if $n = 2$, eq. (A.39) becomes the area element, and so on.

In a similar manner, it can be shown [44] that the Levi-Civita tensor

$$\epsilon_{\mu\nu\alpha\beta} = \begin{cases} \sqrt{|g(x)|} & \text{for even permutations of } \mu\nu\alpha\beta, \\ -\sqrt{|g(x)|} & \text{for odd permutations of } \mu\nu\alpha\beta, \\ 0 & \text{if any two indices are equal } \mu\nu\alpha\beta \end{cases} \quad (\text{A.41})$$

is a well-defined tensor when coordinate transformations are restricted to systems where $J(x, \bar{x}) > 0$.

A.8 THE COVARIANT DERIVATIVE

The goal here is to be able to take derivatives of tensors in a coordinate-independent way. Derivatives of tensors are taken with respect to a tangent vector. This derivative should not affect the tensor type, i.e., the derivative of an (r, s) tensor is another (r, s) tensor. By ∇_X we mean the covariant derivative with respect to the tangent vector X . Following is a list of properties that we would like the derivative operator to have:

1.

$$\nabla_X(aT + bS) = a\nabla_X T + b\nabla_X S. \tag{A.42}$$

Here $a, b \in \mathfrak{R}$ and T and S are tensors of arbitrary type. Additionally,

$$\nabla_{fX+gY} T = f\nabla_X T + g\nabla_Y T. \tag{A.43}$$

Here f and g are functions and Y is any tangent vector.

2. For scalar functions f

$$\nabla_X f = X(f). \tag{A.44}$$

3. For arbitrary tensors T and S

$$\nabla_X(T \otimes S) = (\nabla_X T) \otimes S + T \otimes \nabla_X S. \tag{A.45}$$

This is nothing more than the usual product rule for derivatives. A scalar function f can be thought of a tensor of type $(0, 0)$ where $f \otimes T \equiv fT$.

4.

$$\nabla_X C T = C \nabla_X T. \tag{A.46}$$

Here C is a contraction of any pair of covariant and contravariant indices.

These properties do not by any means fix the covariant derivative, to fix this, we will need to develop the notion of the torsion tensor.

Definition. The Lie bracket $[X, Y]$ of two tangent vector fields $X = X^i \partial_i$ and $Y = Y^j \partial_j$ is a vector field given by the expression

$$[X, Y] = (Y^i_j X^j - X^i_j Y^j) \partial_i. \tag{A.47}$$

Note that the above expression satisfies

$$[X, Y]f = XYf - YXf$$

for any scalar function f .

Definition. The torsion tensor T is of type $(1, 2)$ and is given by

$$T(W, X, Y) = W(\nabla_X Y - \nabla_Y X - [X, Y]). \tag{A.48}$$

Here X and Y are tangent vector fields, and W is a dual vector field. T as defined above is a tensor, i.e., its truly a function linear object. It is not difficult to show that

1. $T(fW + gZ, X, Y) = f T(W, X, Y) + g T(Z, X, Y)$.
2. $T(W, fX + g\chi, Y) = f T(W, X, Y) + g T(Z, \chi, Y)$.
3. $T(W, X, fY + g\chi) = f T(W, X, Y) + g T(Z, X, \chi)$.

Here X, Y , and χ are vector fields, W and Z are dual vector fields, and f and g are functions. Hence, $T = T_{kj}^i \partial_i \otimes dx^k \otimes dx^j$.

We will now show that there exists a unique covariant derivative on a manifold such that

- 1.

$$\nabla_X g = 0 \quad (\text{A.49})$$

for a prescribed metric tensor g on the manifold, and

2. the torsion tensor $T = 0$.

To see this, let us fix a coordinate system and set

$$\nabla_{\partial_\mu} \partial_\nu = \Gamma_{\mu\nu}^\alpha \partial_\alpha. \quad (\text{A.50})$$

$\Gamma_{\mu\nu}^\alpha$ are called connection coefficients or Christoffel symbols. Using the properties satisfied by the covariant derivative, we see that

$$\nabla_X Y^\nu \partial_\nu = (XY^\nu) \partial_\nu + X^\mu Y^\nu \Gamma_{\mu\nu}^\alpha \partial_\alpha. \quad (\text{A.51})$$

Here Y is vector field and X is a tangent vector at the point we wish to take the derivative. Since $W(X) = W_\mu X^\mu$, the properties of the covariant derivative imply that

$$\nabla_{\partial_\mu} dx^\nu = -\Gamma_{\alpha\mu}^\nu dx^\alpha. \quad (\text{A.52})$$

Here $W \in T^*(M)$ and $X \in T(M)$.

Since the torsion tensor $T = 0$, and since $[\partial_\mu, \partial_\nu] = 0$ for coordinate vector fields, we get that

$$\nabla_{\partial_\mu} \partial_\nu = \nabla_{\partial_\nu} \partial_\mu,$$

i.e.,

$$\Gamma_{\mu\nu}^\alpha = \Gamma_{\nu\mu}^\alpha.$$

This is the feature we need from our torsion-free requirement. Now let us consider the implication of the requirement that the covariant derivative of the metric is trivial. Using the product rule and eq. (A.52)

$$\begin{aligned} \nabla_X g_{\mu\nu} dx^\mu \otimes dx^\nu &= X(g_{\mu\nu}) dx^\mu \otimes dx^\nu - g_{\mu\nu} X^\beta \Gamma_{\alpha\beta}^\mu dx^\alpha \otimes dx^\nu \\ &\quad - g_{\mu\nu} X^\beta \Gamma_{\alpha\beta}^\nu dx^\mu \otimes dx^\alpha = 0. \end{aligned} \quad (\text{A.53})$$

After changing dummy variables so that all tensor products in the above equations are of the form $dx^\mu \otimes dx^\nu$, and setting $X = \partial_\lambda$ we get

$$\partial_\lambda g_{\mu\nu} = g_{\alpha\nu} \Gamma_{\lambda\mu}^\alpha + g_{\alpha\mu} \Gamma_{\lambda\nu}^\alpha. \tag{A.54}$$

Let us rewrite the above equation by permutations of subscripts:

$$\partial_\mu g_{\nu\lambda} = g_{\alpha\lambda} \Gamma_{\mu\nu}^\alpha + g_{\alpha\nu} \Gamma_{\mu\lambda}^\alpha, \tag{A.55}$$

$$\partial_\nu g_{\lambda\mu} = g_{\alpha\mu} \Gamma_{\nu\lambda}^\alpha + g_{\alpha\lambda} \Gamma_{\nu\mu}^\alpha. \tag{A.56}$$

Equation (A.54) + eq. (A.55) – eq. (A.56) gives

$$\Gamma_{\mu\lambda}^\alpha = \frac{1}{2} g^{\nu\alpha} [\partial_\lambda g_{\mu\nu} + \partial_\mu g_{\nu\lambda} - \partial_\nu g_{\lambda\mu}]. \tag{A.57}$$

We have the result we want. The connection coefficients are completely specified, and hence it is unique. Equations (A.50) and (A.52) along with the expressions for the connection coefficients (eq. [A.57]) enable us to take derivatives of arbitrary tensor fields.

Let $\alpha(\tau) = (x^1(\tau), \dots, x^n(\tau))$ be a curve with tangent u^μ , i.e.,

$$u^\mu = \frac{dx^\mu}{d\tau}. \tag{A.58}$$

Then, by definition, α is a geodesic if

$$\nabla_u u = 0. \tag{A.59}$$

From eq. (A.51), in component form

$$\ddot{x}^\mu + \Gamma_{\alpha\beta}^\mu \dot{x}^\alpha \dot{x}^\beta = 0. \tag{A.60}$$

Comparing with eq. (3.40), we see that eq. (A.59) is consistent with the previous definition of a geodesic.

A.9 THE DIVERGENCE THEOREM

The divergence of a vector field is given by

$$\nabla \cdot V = \nabla_{\partial_\mu} V^\mu = \partial_\mu V^\mu + \Gamma_{\mu\lambda}^\mu V^\lambda. \tag{A.61}$$

From eq. (A.57) we see that

$$\Gamma_{\mu\lambda}^\mu = \frac{1}{2} g^{\mu\alpha} \partial_\lambda g_{\alpha\mu}. \tag{A.62}$$

But, for any matrix G

$$\text{Tr} \{G^{-1} \partial_\lambda G\} = \partial_\lambda \{\ln \text{Det } G\}. \tag{A.63}$$

Therefore, from above, eq. (A.62) becomes

$$\Gamma_{\mu\lambda}^{\mu} = \frac{1}{\sqrt{|g|}} \partial_{\lambda} \sqrt{|g|}. \quad (\text{A.64})$$

As usual $\sqrt{|g|} = \sqrt{|\text{Det } g_{\mu\nu}|}$. Consequently, the expression for the divergence of a tangent vector field becomes

$$\nabla_{\partial_{\mu}} V^{\mu} = \frac{1}{\sqrt{|g|}} \partial_{\mu} (\sqrt{|g|} V^{\mu}). \quad (\text{A.65})$$

Since we will have occasion to use the 3d divergence theorem, we will state the familiar result without proof. For any 3d manifold M with boundary ∂M , and a positive definite metric g ,¹ we have that

$$\int_M \nabla \cdot V \, dV = \int_{\partial M} g(V \cdot n) \, dA. \quad (\text{A.66})$$

Here dV is the volume element of the manifold ∂M , which is a 2d submanifold and has an induced metric prescribed on it. Using the induced metric we can construct a volume element which we denote as dA . n is the outward-pointing unit normal on ∂M . Of course, any vector n is normalized by dividing the vector by its magnitude $\sqrt{g(n, n)}$. It is possible to generalize the divergence theorem to a four-dimensional spacetime as well.

A.10 THE EINSTEIN EQUATION

Let X , Y , and Z be tangent vector fields, and let W be a dual vector field. The Riemann curvature tensor is defined by

$$R(X, Y, Z, W) = [\nabla_X \nabla_Y W - \nabla_Y \nabla_X W - \nabla_{[X, Y]} W] Z. \quad (\text{A.67})$$

The Riemann curvature tensor is of type (1, 3). In component form eq. (A.67) becomes

$$R_{\alpha\beta\mu}{}^{\nu} X^{\alpha} Y^{\beta} Z^{\mu} W_{\nu} = X^{\alpha} Y^{\beta} [\nabla_{\partial_{\alpha}} \nabla_{\partial_{\beta}} W - \nabla_{\partial_{\beta}} \nabla_{\partial_{\alpha}} W]_{\nu} Z^{\nu}, \quad (\text{A.68})$$

since on smooth functions $[\partial_a, \partial_b] = 0$. The contracted Riemann tensor gives the Ricci tensor $R_{\mu\nu}$:

$$R_{\mu\nu} = R_{\mu\alpha\nu}{}^{\alpha}. \quad (\text{A.69})$$

The scalar curvature R is given by

$$R = R_{\mu}{}^{\mu}. \quad (\text{A.70})$$

¹A metric g is positive definite if $g(X, X) \geq 0$ for every $X \in T(M)$, and the equality is realized only for a trivial tangent vector.

The Einstein equation for the gravitational field $g_{\mu\nu}$ is

$$R_{\mu\nu} - \frac{1}{2}Rg_{\mu\nu} = 8\pi T_{\mu\nu}. \quad (\text{A.71})$$

Here $T_{\mu\nu}$ is the energy-momentum tensor of the nongravitational fields present. In vacuum, $T_{\mu\nu} = 0$ and therefore by contracting the Einstein equation we find that the scalar curvature vanishes in this case. Consequently, the vacuum Einstein equation is given by

$$R_{\mu\nu} = 0. \quad (\text{A.72})$$

Appendix B

Mathematical Functions

B.1 THE GAMMA FUNCTION AND ERROR FUNCTION

The Gamma function

$$\Gamma(n) = \int_0^{\infty} dx x^{n-1} \exp(-x). \quad (\text{B.1})$$

Thus

$$\Gamma(n+1) = n\Gamma(n). \quad (\text{B.2})$$

When n is a whole number, $\Gamma(n) = (n-1)!$, and $\Gamma(1/2) = \int_0^{\infty} dx x^{-1/2} \exp(-x) = 2 \int_0^{\infty} dt \exp(-t^2) = \sqrt{\pi}$, so that $\Gamma(3/2) = \sqrt{\pi}/2$. This definite integral is related to the error function, defined by

$$\operatorname{erf}(x) = \frac{2}{\sqrt{\pi}} \int_0^x dt \exp(-t^2) = -\operatorname{erf}(-x) \rightarrow \begin{cases} \frac{2}{\sqrt{\pi}} \exp(-x^2) & \text{if } x \gg 1, \\ 1 - \frac{\exp(-x^2)}{x\sqrt{\pi}} & \text{if } x \gg 1. \end{cases} \quad (\text{B.3})$$

B.2 MODIFIED BESSEL FUNCTIONS OF THE SECOND KIND

Modified Bessel functions R satisfy the differential equation

$$\frac{d^2 R}{dx^2} + \frac{1}{x} \frac{dR}{dx} - \left(1 + \frac{n^2}{x^2}\right) R = 0, \quad (\text{B.4})$$

with n an integer. Being second-order, eq. (B.4) has two linearly independent solutions $I_n(x)$ and $K_n(x)$, which prove to be Bessel functions of pure imaginary argument (eq. [B.4] becomes Bessel's equation when $-(1 + n^2/x^2)$ is replaced by $+(1 - n^2/x^2)$). The Bessel function of the second kind of order n , $K_n(x)$, satisfies

$$K_n(x) = \frac{x^n}{1 \cdot 3 \cdot 5 \cdot \dots \cdot (2n-1)} \int_0^{\infty} d\theta \operatorname{sh}^{2n}(\theta) \exp(-x \operatorname{ch}\theta) \quad (\text{B.5})$$

and the integral formula

$$K_n(x) = \frac{\Gamma(n + \frac{1}{2})(2x)^n}{\sqrt{\pi}} \int_0^\infty \frac{\cos t \, dt}{(t^2 + x^2)^{n+1/2}}. \tag{B.6}$$

Among its properties is the relation

$$\frac{d}{dx}(x^n K_n) = -x^n K_{n-1}. \tag{B.7}$$

The asymptotes of $K_n(x)$, also valid for fractional order, are

$$K_n(x) \rightarrow \begin{cases} -\ln(x/2) - \gamma_E + \dots & \text{if } n = 0, \\ \frac{\Gamma(n)}{2} \left(\frac{2}{x}\right)^n + \dots & \text{if } n \neq 0, \end{cases} \text{ for } x \ll 1, \tag{B.8}$$

where $\gamma_E = 0.577216\dots$ is Euler's constant, and

$$K_n(x) \rightarrow \left(\frac{\pi}{2x}\right)^{1/2} \exp(-x) \left(1 + \frac{4n^2 - 1}{8x} + \dots\right) \text{ for } x \gg 1. \tag{B.9}$$

A useful representation for numerical evaluation of the modified Bessel functions appearing in the synchrotron radiation formulae is [521]

$$K_n(x) = \frac{1}{2} \left(\frac{\exp(-x)}{2} + \sum_{j=1}^\infty \cosh(nj/2) \exp[-x \cosh(j/2)] \right). \tag{B.10}$$

B.3 EXPONENTIAL INTEGRAL FUNCTION

The exponential integral function

$$E_i(x) = - \int_{-x}^\infty dt \frac{e^{-t}}{t} = \gamma_E + \ln x + \sum_{k=1}^\infty \frac{x^k}{k \cdot k!} \tag{B.11}$$

is a special case of the incomplete Gamma function

$$\Gamma(n, x) = \int_x^\infty dt t^{n-1} \exp(-t), \tag{B.12}$$

and extends the exponential integral

$$E_1(x) = \int_x^\infty dt \frac{e^{-t}}{t} = -E_i(-x) \tag{B.13}$$

to values of the negative real numbers. The exponential integral function can also be expanded as

$$E_1(x) \rightarrow \frac{\exp(-x)}{x} \left[\sum_{k=0}^N \frac{k!}{(-x)^k} + \mathcal{O}\left(\frac{N!}{x^N}\right) \right]. \tag{B.14}$$

B.4 PLANCK'S FUNCTION

The expression for $u(\epsilon, \Omega) = I_\epsilon(\Omega)/c$, eq. (5.15), gives the spectral blackbody energy density

$$u_{\text{bb}}(\epsilon) = 4\pi u_{\text{bb}}(\epsilon, \Omega) = \frac{8\pi m_e c^2}{\lambda_C^3} \frac{\epsilon^3}{\exp(\epsilon/\Theta) - 1}$$

$$\rightarrow \frac{8\pi m_e c^2}{\lambda_C^3} \begin{cases} \Theta \epsilon^2, & \epsilon \ll \Theta, & \text{Rayleigh-Jeans regime,} \\ \epsilon^3 e^{-\epsilon/\Theta}, & \epsilon \gg \Theta, & \text{Wien regime.} \end{cases} \quad (\text{B.15})$$

The blackbody energy density

$$u_{\text{bb}} = \int_0^\infty d\epsilon u_{\text{bb}}(\epsilon) = aT^4 = \frac{8\pi^5 m_e c^2}{15\lambda_C^3} \Theta^4$$

$$= \frac{\pi^2 \alpha_f}{15} B_{\text{cr}}^2 \Theta^4 = 9.36 \times 10^{24} \Theta^4 \text{ ergs cm}^{-3} = 0.12 u_{\text{cr}} \Theta^4, \quad (\text{B.16})$$

in terms of the critical magnetic-field energy density $u_{\text{cr}} = B_{\text{cr}}^2/8\pi = 7.75 \times 10^{25} \text{ ergs cm}^{-3}$ associated with the critical magnetic field B_{cr} (eq. [7.22]).

B.5 BERNOULLI NUMBERS AND RIEMANN ζ FUNCTION

When dealing with Planck's function, integrals of the form

$$\int_0^\infty dx \frac{x^{n-1}}{\exp(ax) - 1} = \frac{\Gamma(n)}{a^n} \zeta(n) \quad (\text{B.17})$$

for $n > 0$ are often encountered. The quantity

$$\zeta(n) = \sum_{i=1}^\infty \frac{1}{i^n} = \prod_{\substack{p \geq 2 \\ p \text{ prime}}} \frac{1}{1 - p^{-n}} \quad (\text{B.18})$$

is the Riemann zeta function, with the final expression giving the Euler product. Some values of the zeta function are, $\zeta(1) \rightarrow \infty$, $\zeta(3/2) = 2.612\dots$, $\zeta(2) = \pi^2/6 = 1.6449\dots$, $\zeta(5/3) = 1.341\dots$, $\zeta(3) = 1.202\dots$, $\zeta(7/2) = 1.127\dots$, and $\zeta(4) = \pi^4/90 = 1.08232\dots$

When dealing with fermions, integrals of the form

$$\int_0^\infty dx \frac{x^{2n-1}}{\exp(ax) + 1} = \frac{\Gamma(2n)}{a^{2n}} (1 - 2^{1-2n}) \zeta(2n) = \frac{(2^{2n-1} - 1)\pi^{2n}}{2na^{2n}} B_n \quad (\text{B.19})$$

are met. Here B_n are the Bernoulli numbers defined by the contour integral

$$B_n = \frac{n!}{2\pi i} \oint \frac{dz}{z^{n+1}} \frac{z}{\exp(z) - 1}, \tag{B.20}$$

with analytic solution for even orders

$$B_{2n} = \frac{(-1)^{n-1} 2(2n)!}{(2\pi)^{2n}} \zeta(2n). \tag{B.21}$$

Perhaps the most well-known Bernoulli number is related to the integral

$$\int_0^\infty dx \frac{x^3}{e^x - 1} = \frac{4\pi^4}{2} B_2 = \frac{\pi^4}{15}.$$

Some values of B_i are $B_1 = 1/6, 1/30, 1/42, 1/30, 5/66, 691/2730, 7/6$ for $i = 1, 2, \dots, 7$.

B.6 WHITTAKER FUNCTIONS

The Whittaker functions are solutions to the differential equation

$$\frac{d^2 W_{\kappa,\mu}(x)}{dt^2} + \left(-\frac{1}{4} + \frac{\kappa}{z} + \frac{(1/4) - \mu^2}{z^2} \right) W_{\kappa,\mu}(x) = 0 \tag{B.22}$$

and can be expressed in the form of a confluent hypergeometric function.

B.7 LAMBERT W FUNCTION

The Lambert W function is solved by inverting the equation

$$z = W(z) \exp[W(z)] \tag{B.23}$$

for the complex number z . Some values of W are $W(0) = 0, W(1) = \Omega = 0.56714\dots, W(e) = 1$; here Ω is the Omega constant. For example, the solution to eq. (11.139) is $y_{e^\pm} = W(2K^2)/2$, where K is the constant on the right-hand side of this equation. See Ref. [522] for more properties of the Lambert W function.

Appendix C

Solutions of the Continuity Equation

We consider solutions of the continuity equation

$$\frac{\partial n(\gamma; t)}{\partial t} + \frac{\partial}{\partial \gamma}[\dot{\gamma} n(\gamma; t)] + \frac{n(\gamma; t)}{t_{\text{esc}}(\gamma, t)} = \dot{n}(\gamma; t) \quad (\text{C.1})$$

in various limits (for inclusion of a diffusion term, see Ref. [523]). Here $n(\gamma; t)$ is the spectral number density (units of $\text{cm}^{-3} \gamma^{-1}$) of particles with Lorentz factor γ at time t , $\dot{\gamma}$ is the energy-gain rate (energy loss is negative energy gain), and $\dot{n}(\gamma; t)$ (units of $\text{cm}^{-3} \gamma^{-1} \text{s}^{-1}$) is the source term. The escape term $t_{\text{esc}}(\gamma, t)$ can be equated with the diffusive escape timescale from the system, or with the timescale for catastrophic losses, such as those which occur in the extreme Klein-Nishina limit for electrons, or in secondary nuclear processes for hadronic collisions.

Case (i). Time Independent with No Escape Term

The continuity equation takes the form

$$\frac{\partial}{\partial \gamma}[\dot{\gamma} n(\gamma)] = \dot{n}(\gamma). \quad (\text{C.2})$$

Equation (C.2) has solution

$$n(\gamma) = \frac{1}{|\dot{\gamma}|} \int_{\gamma}^{\infty} d\gamma' \dot{n}(\gamma') \quad (\text{C.3})$$

for an energy-loss process with $\dot{\gamma} < 0$. Now consider the case of Thomson or synchrotron energy-loss processes of the form $\dot{\gamma} = -v_0 \gamma^2$, and power-law injection

$$\dot{n}(\gamma) = k_e \gamma^{-s} H(\gamma; \gamma_1, \gamma_2), \quad (\text{C.4})$$

with injection index s . Normalization to the total electron emissivity $\dot{\epsilon}_e$ (ergs $\text{cm}^{-3} \text{s}^{-1}$) gives

$$k_e = \frac{(s-2)\dot{\epsilon}_e}{(\gamma_1^{2-s} - \gamma_2^{2-s})m_e c^2} \quad (\text{C.5})$$

(compare eq. [6.64]). The solution of eq. (C.3) is

$$n(\gamma) = \frac{k_e}{v_0 \gamma^2} \int_{\max(\gamma, \gamma_1)}^{\gamma_2} d\gamma' \gamma'^{-s} = \frac{k_e}{v_0(s-1)} \gamma^{-2} \left[\max(\gamma, \gamma_1)^{1-s} - \gamma_2^{1-s} \right]. \tag{C.6}$$

Therefore

$$n(\gamma) \propto \begin{cases} \gamma^{-2} & \text{if } \gamma \leq \gamma_1, \\ \gamma^{-(1+s)} & \text{if } \gamma_1 \leq \gamma \ll \gamma_2, \end{cases} \tag{C.7}$$

and the effect of Thomson or synchrotron losses is to make the spectral index of the steady-state cooling spectrum one unit steeper than the injection index for $\gamma_1 \ll \gamma \leq \gamma_2$. For the case $s = 2$, the spectrum breaks from $n(\gamma) \propto \gamma^{-2}$ to $n(\gamma) \propto \gamma^{-3}$ at $\gamma = \gamma_1$.

Now consider the steady-state spectrum for particles subject to acceleration energy gains of the form $\dot{\gamma} = v_a \gamma^{-v}$. Equation (C.2) has solution

$$n(\gamma) = \frac{\gamma^v}{v_a} \int_1^\gamma d\gamma' \dot{n}(\gamma'). \tag{C.8}$$

For monoenergetic electron injection $\dot{n}(\gamma) = \dot{n}_0 \delta(\gamma' - \bar{\gamma})$, the steady-state electron spectrum is $n(\gamma) = \dot{n}_0 \gamma^v / v_a$ for $\gamma \geq \bar{\gamma}$. For power-law injection given by eq. (C.4),

$$n(\gamma) = \frac{k_e \gamma^v}{v_a(s-1)} \left[\gamma_1^{1-s} - \min(\gamma, \gamma_2)^{1-s} \right] \propto \gamma^v \quad \text{if } \gamma_1 \ll \gamma \text{ and } s > 1. \tag{C.9}$$

For $s < 1$, $n(\gamma) \propto \gamma^{-v-s+1}$, when $\gamma_1 \ll \gamma \leq \gamma_2$, and $n(\gamma) \propto \gamma^{-v}$ for $\gamma > \gamma_2$. In realistic situations, energy losses or escape will alter this dependence at sufficiently large Lorentz factors.

Case (ii). Time Independent with Energy-Dependent Escape Term

The continuity equation takes the form

$$\frac{\partial}{\partial \gamma} [\dot{\gamma} n(\gamma)] + \frac{n(\gamma)}{t_{\text{esc}}(\gamma)} = \dot{n}(\gamma). \tag{C.10}$$

Equation (C.10) has the solution

$$n(\gamma) = |\dot{\gamma}|^{-1} \int_\gamma^\infty d\gamma' \dot{n}(\gamma') \exp \left(- \int_\gamma^{\gamma'} \frac{d\gamma''}{t_{\text{esc}}(\gamma'') |\dot{\gamma}(\gamma'')|} \right) \tag{C.11}$$

for an energy-loss process $\dot{\gamma} < 0$. Consider Thomson or synchrotron energy-loss processes of the form $\dot{\gamma} = -v_0 \gamma^2$, and an energy-independent

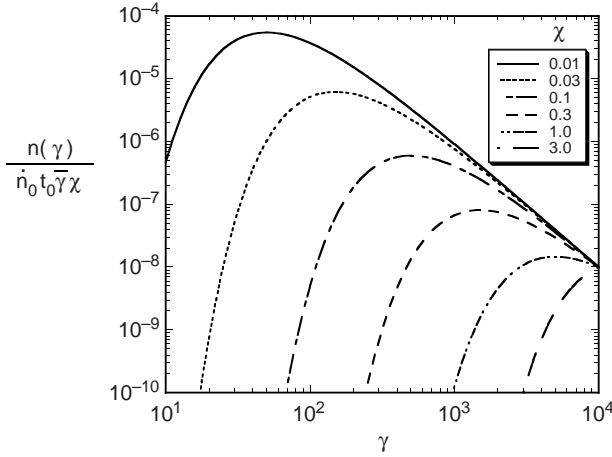


Figure C.1 Solution (C.13) to the time-independent continuity equation with losses proportional to γ^{-2} , constant escape time t_0 , and monoenergetic injection at $\gamma = \bar{\gamma} = 10^4$.

escape timescale $t_{\text{esc}}(\gamma) = t_0$. Equation (C.11) becomes

$$n(\gamma) = \frac{\exp(-1/v_0 t_0 \gamma)}{v_0 \gamma^2} \int_{\gamma}^{\infty} d\gamma' \dot{n}(\gamma') \exp(1/v_0 t_0 \gamma'). \quad (\text{C.12})$$

For monoenergetic injection $\dot{n}(\gamma') = \dot{n}_0 \delta(\gamma' - \bar{\gamma})$,

$$\gamma^2 n(\gamma) = \frac{\dot{n}_0}{v_0} \exp\left[\chi \left(1 - \frac{\bar{\gamma}}{\gamma}\right)\right] H(\gamma; 1, \bar{\gamma}). \quad (\text{C.13})$$

Figure C.1 shows $n(\gamma; \chi)$ as a function of γ for different values of $\chi \equiv 1/v_0 t_0 \bar{\gamma}$.

For power-law injection given by eq. (C.4),

$$\gamma^2 n(\gamma) = \frac{k_e \exp(-1/v_0 t_0 \gamma)}{v_0} (v_0 t_0)^{s-1} \int_{y_1}^{y_2} dy y^{s-2} \exp(y), \quad (\text{C.14})$$

where $y_1 = (v_0 t_0 \gamma_2)^{-1}$ and $y_2 = [v_0 t_0 \max(\gamma, \gamma_1)]^{-1}$. The solution is analytic for the case $s = 2$, with result

$$n(\gamma) = \frac{k_e t_0}{\gamma^2} \exp(-1/v_0 t_0 \gamma) \{ \exp[1/v_0 t_0 \max(\gamma, \gamma_1)] - \exp(1/v_0 t_0 \gamma_2) \} \\ \propto \begin{cases} \gamma^{-2} & \text{if } \gamma \ll 1/v_0 t_0, \\ \gamma^{-3} & \text{if } \gamma \gg 1/v_0 t_0. \end{cases} \quad (\text{C.15})$$

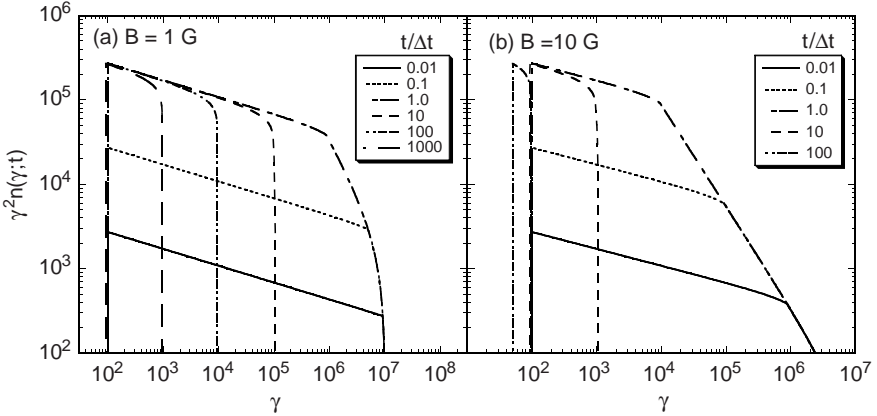


Figure C.2 Solution (C.16) to the time-dependent continuity equation with losses proportional to γ^{-2} , constant escape time t_0 , and power-law electron injection function proportional to $\gamma^{-s} H(\gamma; \gamma_1, \gamma_2) H(t; 0, \Delta t)$, with $\gamma_1 = 10^2$, $\gamma_2 = 10^7$, and $s = 2.2$. Panel (a) has $B = 1$ G, and panel (b) has $B = 10$ G.

The general behavior for the steady-state electron spectrum with power-law injection index s is a power-law spectrum proportional to γ^{-s} at $\gamma \ll 1/\nu_0 t_0$, breaking to a power-law spectrum $\propto \gamma^{-(s+1)}$ at $\gamma \gg 1/\nu_0 t_0$, as can be seen from eq. (C.14).

Case (iii). Time Dependent with Time-Independent Energy-Dependent Escape

Equation (C.1), with $t_{\text{esc}}(\gamma, t) \rightarrow t_{\text{esc}}(\gamma)$ and $\dot{\gamma} = d\gamma/dt < 0$, has solution

$$n(\gamma, t) = \frac{1}{|d\gamma/dt|} \int_{\gamma}^{\infty} d\gamma' \dot{n}(\gamma'; t') \exp\left(-\int_{\gamma}^{\gamma'} \frac{1}{t_{\text{esc}}(\gamma'')} \frac{d\gamma''}{|d\gamma(\gamma'')/dt|}\right), \tag{C.16}$$

where

$$t' = t - \int_{\gamma}^{\gamma'} \frac{d\gamma''}{|d\gamma(\gamma'')/dt|}. \tag{C.17}$$

For Thomson-synchrotron losses, $-d\gamma/dt = \nu_0 \gamma^2$, a constant escape timescale $t_{\text{esc}}(\gamma) = t_0$, and injection function $\dot{n}(\gamma', t') = k_e \gamma'^{-s} H(\gamma'; \gamma_1, \gamma_2)$

$H(t'; 0, \Delta t)$, the solution to eq. (C.16) is

$$\gamma^2 n(\gamma, t) = \frac{k_e}{\nu_0} \exp\left(\frac{-1}{\nu_0 t_0 \gamma}\right) \times \int_{\max\{\gamma, \gamma_1, [\gamma^{-1} - \nu_0(t - \Delta t)]^{-1}\}}^{\min[\gamma_2, (\gamma^{-1} - \nu_0 t)^{-1}]} d\gamma' \gamma'^{-s} \exp\left(\frac{1}{\nu_0 t_0 \gamma'}\right). \quad (\text{C.18})$$

The solution is analytic in the asymptote $\nu_0 t_0 \gg 1$. Figure C.2 is a graph of $\gamma^2 n(\gamma; t)$ as a function of γ in this limit for different times in units of the injection timescale $\Delta t = 800$ s. The electron emissivity $\dot{\epsilon}_e = 1/800 \text{ erg cm}^{-3} \text{ s}^{-1}$, so that $\dot{\epsilon}_e \Delta t = 1 \text{ erg cm}^{-3}$. Note the stronger cooling taking place on the right-hand panel with $B = 10$ G than on the left-hand panel with $B = 1$ G.

Appendix D

Basics of Monte Carlo Calculations

The standard random number generators on Fortran or c systems yield values randomly but uniformly distributed on $(0, 1)$. Every simulation or integration typically is reduced to an average or an integral over auxiliary variables x on $(0, 1)$, with values of x to be supplied by the random number generator.

Case (1). Values of y are to be chosen to follow a parent distribution $f(y)$ on $a \leq y \leq b$. Define the normalized cumulative distribution

$$F(y) = \frac{\int_a^y dy' f(y')}{\int_a^b dy' f(y')}, \quad F(a) = 0, \quad F(b) = 1. \quad (\text{D.1})$$

Then solve $x = F(y)$ or $y = F^{-1}(x)$.

Case (1a). Analytic inversion is possible. The standard example is $f(y) = \exp(-\lambda y)$ on $0 \leq y < \infty$ (radioactive decay, absorption of photons, etc.) It is fairly common, although not necessary, to invert the limits in the cumulative distribution,

$$F(y) = \frac{\int_y^\infty dy' \exp(y')}{\int_0^\infty dy' \exp(y')} = \exp(-\lambda y) = x, \quad y = -\frac{1}{\lambda} \ln x. \quad (\text{D.2})$$

When x_i are chosen randomly on $(0, 1)$, then $y_i = \ln x_i / \lambda$ are distributed in an exponential decrease on $(0, \infty)$.

Case (1b). No analytic inversion is possible. Tabulate $F(y_i)$ versus y_i . The “mesh” of points can be defined by choosing either the set y_i or the set $F(y_i)$. Then solve $x = F(y)$ by inverse interpolation of the table. If either the mesh of y_i or the mesh of $F(y_i)$ has equal intervals, then higher-order interpolation is possible, but linear interpolation producing a histogram approximating $f(y)$ is always possible.

Case (2). Linear rescaling. The standard example is angular integration

$$I = \oint d\Omega f(\theta, \phi) = \int_{-1}^1 d \cos \theta \int_0^{2\pi} d\phi f(\theta, \phi). \quad (\text{D.3})$$

Set $\cos \theta = 2x_\theta - 1$, $d \cos \theta = 2dx_\theta$, and $\phi = 2\pi x_\phi$, $d\phi = 2\pi dx_\phi$.

Therefore

$$I = 4\pi \int_0^1 dx_\theta \int_0^1 dx_\phi f(2x_\theta - 1, 2\pi x_\phi) \rightarrow 4\pi \sum_{i=1}^N f(2x_{\theta_i} - 1, 2\pi x_{\phi_i}). \quad (\text{D.4})$$

Case (3). Nonlinear rescaling. The standard example is relativistic thermal averaging.

$$\bar{G} = \int_{E=mc^2}^{\infty} dE' G(E') \exp(-E'/k_B T). \quad (\text{D.5})$$

Similarly to case (1a), define an auxiliary variable

$$x = F(E) = \frac{\int_E^{\infty} dE' \exp(-E'/k_B T)}{\int_{mc^2}^{\infty} dE' \exp(-E'/k_B T)} = \exp[-(E - mc^2)/k_B T], \quad (\text{D.6})$$

so that $E = mc^2 - k_B T \ln x$, or $\exp(-E/k_B T)dE = -k_B T \exp(-mc^2/k_B T)dx$. Hence

$$\begin{aligned} \bar{G} &= k_B T \exp(-mc^2/k_B T) \int_0^1 G(mc^2 - k_B T \ln x) dx \\ &\rightarrow k_B T \exp(-mc^2/k_B T) \frac{1}{N} \sum_{i=1}^N G(mc^2 - k_B T \ln x_i). \end{aligned} \quad (\text{D.7})$$

Appendix E

Supplementary Information

Table E.1 Astronomical Constants—Gaussian (cgs) Units

Physical quantity	Symbol	Value	Units
Solar mass	M_{\odot}	1.989×10^{33}	g
Solar luminosity	L_{\odot}	3.826×10^{33}	ergs/s
Solar radius	r_{\odot}	6.960×10^{10}	cm
Solar constant	Φ_{\odot}	1.353×10^6	ergs/cm ² s
Astronomical unit	AU	1.496×10^{13}	cm
parsec	pc	3.085678×10^{18}	cm

Source: AIP 50th Anniversary *Physics Vade Mecum* [524].

Table E.2 Physical Constants—Gaussian (cgs) Units

Physical quantity	Symbol	Value	Units
Boltzmann constant	k_B	1.3807×10^{-16}	ergs/deg (K)
Elementary charge	e	4.8032×10^{-10}	statcoulomb (statcoul)
Electron mass	m_e	9.1094×10^{-28}	g
		0.510 999	MeV
Proton mass	m_p	1.6726×10^{-24}	g
		938.27	MeV
Neutron mass	m_n	1.6749×10^{-24}	g
		939.57	MeV
Neutron mean life	t_n	886	s
Gravitational constant	G	6.6726×10^{-8}	dyne cm ² /g ²
Planck constant	h	6.6261×10^{-27}	erg s
	$\hbar = h/2\pi$	1.0546×10^{-27}	erg s
Speed of light in vacuum	c	2.9979×10^{10}	cm/s
Proton/electron mass ratio	m_p/m_e	1.8362×10^3	

Table E.3 Physical Constants—Gaussian (cgs) Units

Physical quantity	Symbol	Value	Units
Classical electron radius	$r_e = e^2/m_e c^2$	2.8179×10^{-13}	cm
Thomson cross section	$\sigma_T = 8\pi r_e^2/3$	6.6525×10^{-25}	cm ²
Compton wavelength of electron	$\lambda_C = h/m_e c$	2.4263×10^{-10}	cm
Fine-structure constant	$\lambda_C = \hbar/m_e c$	3.8616×10^{-11}	cm
	$\alpha_f = e^2/\hbar c$	7.2974×10^{-3}	
	α_f^{-1}	137.04	
Stefan-Boltzmann constant	$\sigma_{SB} = \frac{2\pi^5 k_B^4}{15c^2 h^3}$	5.6705×10^{-5}	erg/(cm ² s K ⁴)
Radiation constant	$a = 4\sigma_{SB}/c$	7.566×10^{-15}	erg/(cm ³ K ⁴)
Critical magnetic field	$B_{cr} = m_e^2 c^3 / e \hbar$	4.414×10^{13}	G
Frequency associated with 1 eV		2.4180×10^{14}	Hz
π^\pm mass	m_{π^\pm}	139.57	MeV
π^\pm mean life	τ_{π^\pm}	2.6030×10^{-8}	s
π^0 mass	m_{π^0}	134.96	MeV
π^0 mean life	τ_{π^0}	0.83×10^{-16}	s
μ^\pm mass	m_{μ^\pm}	105.66	MeV
μ^\pm mean life	τ_{μ^\pm}	2.197×10^{-6}	s

Source: *NRL Plasma Formulary* [123]; *Review of Particle Properties* [525].

Table E.4 Commonly Used Symbols

Physical quantity	Symbol
Bulk Lorentz factor	Γ
Christoffel symbol	$\Gamma_{\mu\nu}^\alpha$
Lorentz transformation	$\Lambda^\mu{}_\nu$
Dimensionless temperature	$\Theta = k_B T / mc^2$
Compton scattering kernel	Ξ_C
Thomson scattering kernel	Ξ_T
Absolute space at time t	Σ_t
Star formation rate factor	$\Sigma(z)$
Energy flux	Φ
Direction vector	$\vec{\Omega}$
Cyclotron frequency of particle of type i	Ω_i
Angular momentum of the electromagnetic field	Ω

Table E.4 Continued

Physical quantity	Symbol
Energy spectral index	α
Lapse function	α
Shift vector	β
Bulk β -factor	$\beta = \sqrt{1 - \Gamma^{-2}}$
Particle β -factor	$\beta_{\text{par}} = \sqrt{1 - \gamma^{-2}}$
Particle Lorentz factor	γ
Induced metric on absolute space	$\hat{\gamma}_{\mu\nu}$
Square root of the determinant of the absolute space metric	$\sqrt{\hat{\gamma}}$
Doppler factor	δ_{D}
Dimensionless photon energy	ϵ
Stationary frame photon energy	$\epsilon_s = \epsilon_z = (1 + z)\epsilon$
Dimensionless magnetic field	$\epsilon_B = B/B_{\text{cr}}$
Blast-wave parameters	ϵ_e, ϵ_B
Levi-Civita tensor of spacetime	$\epsilon_{\mu\nu\alpha\beta}$
Levi-Civita tensor of absolute space	$\tilde{\epsilon}_{ijk}$
Minkowski metric	$\eta_{\mu\nu}$
Baryon-loading factor	η
Absorption coefficient	κ
Wavelength	λ
Cosine of scattering angle	μ
Metallicity correction to mass density	μ_0
Photon frequency	ν
Charge density	ρ_c
Cross section	σ
Thomson depth	τ_{T}
Quantum field for a scalar particle	ϕ
Spectral flux	$\phi(\epsilon)$
Comoving coordinate	χ
Scattering angle	ψ
Angular frequency	ω
Three-vector potential	A
Atomic weight	A
Poloidal vector	A_P
Toroidal vector	A_T
Magnetic field	\vec{B}, B
Critical magnetic field	B_{cr}

Table E.4 Continued

Physical quantity	Symbol
Electric field dual	D
Diffusion coefficient	D_{ij}
Particle energy	E
Photon energy	E_γ
Electric field	\vec{E}, E
Aggregate energy	\mathcal{E}
Maxwell tensor	$F^{\mu\nu}$
Dual Maxwell tensor	$*F^{\mu\nu}$
Flux density	$F(\epsilon; \Omega), F_\nu$
Fluence	\mathcal{F}
Magnetic field dual	H
Intensity	I_ϵ
Blackbody intensity	$I_\epsilon^{\text{bb}}(\Theta)$
Black-hole angular momentum	J
Current density vector	J, J^i
Carter constant	K
Particle angular momentum per unit mass	L
Mass of a black hole	M
Poynting power, jet power	P_p, P_j
Bulk momentum	$P = \beta\Gamma$
Charge	Q
Scalar curvature	R
Schwarzschild radius	R_S
Expansion scale factor	$R(t)$
Riemann curvature tensor	$R_{\mu\nu\alpha\beta}$
Ricci tensor	$R_{\mu\nu}$
Poynting vector	S
Spectral function	$S(x)$
Flux density	$S(\nu)$
Temperature	T
Energy-momentum tensor	$T^{\mu\nu}$
Tangent bundle	$T(M)$
Cotangent bundle	$T^*(M)$
Four-vector potential	U_μ
Magnetic field energy density	$U_B = B^2/8\pi$
Critical magnetic field energy density	$U_{\text{cr}} = B_{\text{cr}}^2/8\pi$
Phase space volume	\mathcal{V}
Atomic charge	Z

Table E.4 Continued

Physical quantity	Symbol
Rising index of νF_ν spectrum	a
Angular momentum per unit mass of a black hole	a
Falling index of νF_ν spectrum	b
Luminosity distance	d_L
Angular diameter distance	d_A
Invariant interval	ds^2
Dual vector basis	dx^μ
Energy density of type \dot{z}	$e_{\dot{z}}$
νF_ν flux	f_ϵ
Invariant phase space density	$f(v)$
Shell width parameter	f_Δ
Metric tensor	$g_{\mu\nu}$
Hubble constant (units of $100 \text{ km s}^{-1} \text{ Mpc}^{-1}$)	h
Emissivity	$j_s(\epsilon, \Omega)$
Wavevector	k
Number emissivity	$\dot{n}_s(p, \Omega)$
Unit normal	n^μ
Electron number density	n_e
Dimensionless momentum	$p = \beta_{\text{par}}\gamma$
Four-momentum	p^μ
Index of wave spectrum	q
Comoving radius of emitting region	r'_b
Larmor radius	r_L
Time (variability timescale)	$t(t_{\text{var}}, \Delta t_{\text{var}})$
Specific spectral energy density	$u(\epsilon, \Omega)$
Four-velocity	u^μ, v^μ
Dimensionless magnetic field energy density	$u_B = U_B/m_e c^2$
Velocity	v
Wave turbulence energy density	$w(k)$
Spacetime coordinates	x^μ
Redshift	z
Tensor product	\otimes
Dirac delta function	$\delta(k - k')$
Inner product of functions	$(\phi_k, \phi_{k'})$
Adjoint of operator A	A^\dagger

Table E.4 Continued

Physical quantity	Symbol
Commutator of operators A and B	$[A, B]$
Inner product of quantum states $ f\rangle$ and $ g\rangle$	$\langle f g\rangle$
Complex conjugate of function ϕ	ϕ^*
Covariant derivative of spacetime	∇
Covariant derivative of space	$\tilde{\nabla}$
Cross product	\times
Tangent vector basis	∂_μ
Set of n -tuples of real numbers	\mathfrak{R}^n

Appendix F

Glossary and Acronym List

AGASA	Akeno giant air shower array
AGILE	Astro-Rivelatore Gamma a Immagini L'Eggero, launched 23 April 2007
AGN	Active galactic nucleus (nuclei)
ANITA	Antarctic Impulsive Transient Antenna
ARIANNA	Antarctic Ross Ice Shelf Antenna Neutrino Array
AU	Astronomical unit
BATSE	Burst and Transient Source Experiment, on CGRO
Beppo-SAX	X-ray satellite, 30 April 1996–30 April 2002
Blazar	Radio galaxy with radio jet pointed toward observer
BL Lac	BL Lacertae object; lineless or nearly lineless blazar
BLR	Broad line region
BZ	Blandford-Znajek
CBM	Circumburst medium
CGRO	Compton Gamma Ray Observatory, 5 April 1991–4 June, 2000
CMB(R)	Cosmic microwave background (radiation)
COMPTEL	Compton Telescope, on CGRO
EBL	Extragalactic background light
EGRET	Energetic Gamma Ray Experiment Telescope, on CGRO
ERF	Electron rest frame
FGST	Fermi Gamma-ray Space Telescope, formerly GLAST
FR1(2)	Fanaroff-Riley 1(2) radio galaxies
FS	Forward shock
FSRQ	Flat spectrum radio quasar; blazar with strong emission lines
GBM	GLAST (or GRB) Burst Monitor on FGST
GDR	Giant dipole resonance
GLAST	Gamma-ray Large Area Space Telescope, launched 11 June 2008, renamed FGST

GRB	Gamma-ray burst
GZK	Cutoff in the UHECR spectrum predicted by Greisen, Zatsepin, and Kuzmin
HAWC	High-Altitude Water Cherenkov detector in Mexico
HiRes	High-Resolution Fly's Eye in Utah
HESS	High-Energy Stereoscopic System, array of air Cherenkov telescopes in Namibia
IceCube	South Pole Neutrino Observatory, reaches km scale in 2012
IGM	Intergalactic medium
INTEGRAL	INTErnational Gamma Ray Astrophysics Laboratory, launched 17 October 2002
IR	Infrared
ISM	Interstellar medium
KASCADE	KARlsruhe Shower Core and Array Detector in Germany
KM3NeT	Proposed km-scale neutrino telescope in the Mediterranean Sea
LAT	Large-Area Telescope on Fermi/GLAST
LIGO	Laser Interferometer Gravitational Wave Observatory
LISA	Laser Interferometer Space Antenna
LS	Laboratory system
MAGIC	Major Atmospheric Gamma ray Imaging Cherenkov telescope in Canary Islands
MFP	Mean free path
Milagro	All-sky ground-based TeV γ -ray telescope in New Mexico
MHD	Magnetohydrodynamic
NRS	Nonrelativistic reverse shock
OSSE	Oriented Scintillation Spectrometer Experiment, on CGRO
PAO	Pierre Auger Observatory in Argentina
RS	Reverse shock
RRS	Relativistic reverse shock
RSdv	Relativistic Sedov
SGP	Supergalactic plane
SN	Supernova
SNR	Supernova remnant
SFH	Structure formation history
SFR	Star formation rate
SS	Shakura-Sunyaev

SSA	Synchrotron self-absorption
SSC	Synchrotron self-Compton
Swift	GRB satellite, launched 20 November 2004
UHE(CR)	Ultrahigh energy (cosmic ray)
VERITAS	Very Energetic Radiation Imaging Telescope Array System in Arizona
VLBI	Very Long Baseline Interferometer
VLBA	Very Long Baseline Array
WMAP	Wilkinson Microwave Anisotropy Probe, launched 30 June 2001
XBL	X-ray selected BL Lac Object

This page intentionally left blank

References

CHAPTER 1: INTRODUCTION

- [1] Frank, J., King, A., and Raine, D. 1992. *Accretion Power in Astrophysics*, (Cambridge: Cambridge University Press).¹
- [2] Krolik, J. H. 1999. *Active Galactic Nuclei: from the Central Black Hole to the Galactic Environment* (Princeton, N.J.: Princeton University Press).
- [3] Peterson, B. M. 1997. *An Introduction to Active Galactic Nuclei* (Cambridge: Cambridge University Press).
- [4] Synge, J. L. 1957. *The Relativistic Gas* (Amsterdam: North-Holland).
- [5] Bisnovatyi-Kogan, G. S., Zel'dovich, Y. B., and Syunyaev, R. A. 1971. *Soviet Astronomy*, 15, 17.
- [6] Zdziarski, A. A. 1982. *Astronomy & Astrophysics*, 110, L7.
- [7] Dermer, C. D., and Liang, E. P. 1989. *Astrophysical Journal*, 339, 512.
- [8] Svensson, R. 1984. *Monthly Notices of the Royal Astronomical Society*, 209, 175.
- [9] Plaga, R. 2008. *Nature*, 453, 48.
- [10] Greisen, K. 1966. *Physical Review Letters*, 16, 748.
- [11] Zatsepin, G. T., and Kuz'min, V. A. 1966. *Pis'ma v Zhurnal Eksperimental'noi i Teoreticheskoi Fiziki (JETP Letters)* 4, 78.
- [12] Gaisser, T. K. 1990. *Cosmic Rays and Particle Physics* (New York: Cambridge University Press).
- [13] Healy, M. D., and the Pierre Auger Collaboration. 2007. In *Proceedings of the 30th International Cosmic Ray Conference*, Mérida, Mexico, arXiv:0710.0025.
- [14] The Pierre Auger Collaboration. 2007. *Science*, 318, 939.
- [15] Bahcall, J. N. 1989. *Neutrino Astrophysics* (New York: Cambridge University Press).
- [16] Learned, J. G., and Mannheim, K. 2000. *Annual Review of Nuclear and Particle Science*, 50, 679.
- [17] Flanagan, É. É., and Hughes, S. A. 1998. *Physical Review D*, 57, 4535.
- [18] Woosley, S. E. 1993. *Astrophysical Journal*, 405, 273.
- [19] Collmar, W., et al. 1997. *Astronomy & Astrophysics*, 328, 33.

¹Reference appears in chapter where it first appears.

- [20] Wehrle, A. E., et al. 1998. *Astrophysical Journal*, 497, 178.
- [21] Zombeck, M. V. 1990. *Handbook of Space Astronomy and Astrophysics*, 2nd ed. (Cambridge: Cambridge University Press).
- [22] Genzel, R., and Eckart, A. 1999. Page 3 in *The Central Parsecs of the Galaxy*, ed. Falcke, H., et al. (San Francisco: Astronomy Society of the Pacific).
- [23] Ghez, A. M., et al. 2003. *Astrophysical Journal Letters*, 586, L127.
- [24] Bower, G. C., et al. 2004. *Science*, 304, 704.
- [25] Aharonian, F., et al. 2007. *Astrophysical Journal Letters*, 664, L71.
- [26] Begelman, M. C., Fabian, A. C., and Rees, M. J. 2008. *Monthly Notices of the Royal Astronomical Society*, 384, L19.
- [27] Magorrian, J., et al. 1998. *Astronomical Journal*, 115, 2285.
- [28] McLure, R. J., and Dunlop, J. S. 2002. *Monthly Notices of the Royal Astronomical Society*, 331, 795.
- [29] Schmidt, M. 1968. *Astrophysical Journal*, 151, 393.
- [30] Waxman, E., and Bahcall, J. 1999. *Physical Review D*, 59, 023002.
- [31] Fixsen, D. J., Cheng, E. S., Gales, J. M., Mather, J. C., Shafer, R. A., and Wright, E. L. 1996. *Astrophysical Journal*, 473, 576.
- [32] Madau, P., Ghisellini, G., and Fabian, A. C. 1994. *Monthly Notices of the Royal Astronomical Society*, 270, L17.
- [33] Sreekumar, P., et al. 1998. *Astrophysical Journal*, 494, 523.
- [34] Strong, A. W., Moskalenko, I. V., and Reimer, O. 2004. *Astrophysical Journal*, 613, 956.

CHAPTER 2: RELATIVISTIC KINEMATICS

- [35] Blumenthal, G. R., and Gould, R. J. 1970. *Reviews of Modern Physics*, 42, 237.
- [36] Landau, L. D., and Lifschitz, E. M. 1962. *The Classical Theory of Fields* (Reading, Mass.: Addison-Wesley).
- [37] Gould, R. J. 2006. *Electromagnetic Processes* (Princeton, NJ: Princeton University Press).

CHAPTER 3: INTRODUCTION TO CURVED SPACETIME

- [38] Taylor, E. F. 1992. In *Spacetime Physics: Introduction to Special Relativity*, ed. Taylor, E. F., and Wheeler, J. A. (New York: W. H. Freeman).
- [39] Stephani, H. 2004. *Relativity: An Introduction to Special and General Relativity*, 3rd ed. (Cambridge: Cambridge University Press).
- [40] Carroll, S. M. 2004. *Spacetime and Geometry* (San Francisco, Calif.: Addison-Wesley).

- [41] Schwarzschild, K. 1916. *Sitzungsberichte Deutsche Akademie der Wissenschaften zu Berlin, Kl. Math.-Phys. Tech.*, 189.
- [42] Wald, R. M. 1984. *General Relativity* (Chicago: University of Chicago Press).

CHAPTER 4: PHYSICAL COSMOLOGY

- [43] Peebles, P. J. E. 1971. *Physical Cosmology* (Princeton, N.J.: Princeton University Press).
- [44] Weinberg, S. 1972. *Gravitation and Cosmology* (New York: Wiley).
- [45] Felten, J. E., and Isaacman, R. 1986. *Reviews of Modern Physics*, 58, 689.
- [46] Peebles, P. J. E. 1993. *Principles of Physical Cosmology* (Princeton, N.J.: Princeton University Press).
- [47] Longair, M. S. 1998. *Galaxy Formation* (New York: Springer).
- [48] Gould, R. J. 1980. General Relativity and Cosmology, unpublished lecture notes.
- [49] Spergel, D. N., et al. 2003. *Astrophysical Journal Supplements*, 148, 175.
- [50] Bennett, C. L., et al. 2003. *Astrophysical Journal Supplements*, 148, 1.
- [51] Totani, T. 1999. *Astrophysical Journal*, 511, 41.
- [52] Dermer, C. D. 2007. *Astrophysical Journal*, 659, 958.
- [53] Le, T., and Dermer, C. D. 2007. *Astrophysical Journal*, 661, 394.

CHAPTER 5: RADIATION PHYSICS OF RELATIVISTIC FLOWS

- [54] Mihalas, D. 1970. *Stellar Atmospheres* (San Francisco: Freeman).
- [55] Dermer, C. D., and Schlickeiser, R. 1994. *Astrophysical Journal Supplements*, 90, 945.
- [56] Lind, K. R., and Blandford, R. D. 1985. *Astrophysical Journal*, 295, 358.
- [57] Rees, M. 1966. *Nature*, 211, 468.
- [58] Unwin, S. C., Cohen, M. H., Biretta, J. A., Pearson, T. J., Seielstad, G. A., Walker, R. C., Simon, R. S., and Linfield, R. P. 1985. *Astrophysical Journal*, 289, 109.
- [59] Zensus, J. A., and Pearson, P. J. 1987. *Superluminal Radio Sources* (Cambridge: Cambridge University Press).
- [60] Granot, J., Piran, T., and Sari, R. 1999. *Astrophysical Journal*, 513, 679.
- [61] Fenimore, E. E., Madras, C. D., and Nayakshin, S. 1996. *Astrophysical Journal*, 473, 998.
- [62] Kumar, P., and Panaitescu, A. 2000. *Astrophysical Journal Letters*, 541, L51.
- [63] Dermer, C. D. 2004. *Astrophysical Journal*, 614, 284.

CHAPTER 6: COMPTON SCATTERING

- [64] Jauch, J. M., and Rohrlich, R. 1976. *The Theory of Photons and Electrons* (New York: Springer-Verlag).
- [65] Heitler, W. 1954. *The Quantum Theory of Radiation* (New York: Dover).
- [66] Reynolds, S. P. 1982. *Astrophysical Journal*, 526, 38.
- [67] Jones, F. C. 1968. *Physical Review*, 167, 1159.
- [68] Dermer, C. D., and Schlickeiser, R. 1993. *Astrophysical Journal*, 416, 484.
- [69] Dermer, C. D., Schlickeiser, R., and Mastichiadis, A. 1992. *Astronomy & Astrophysics*, 256, L27.
- [70] Sikora, M., Begelman, M. C., and Rees, M. J. 1994. *Astrophysical Journal*, 421, 153.
- [71] Georganopoulos, M., Kirk, J. G., and Mastichiadis, A. 2001. *Astrophysical Journal*, 561, 111; (e) 2004, 604, 479.
- [72] Finke, J., Dermer, C. D., and Böttcher, M. 2008. *Astrophysical Journal*, 686, 181.
- [73] Dermer, C. D., Finke, J., Krug, H., and Böttcher, M. 2009. *Astrophysical Journal* 692, 32.
- [74] Dermer, C. D., Sturmer, S. J., and Schlickeiser, R. 1997. *Astrophysical Journal Supplements*, 109, 103.
- [75] Dermer, C. D., and Schlickeiser, R. 2002. *Astrophysical Journal*, 575, 667.
- [76] Shakura, N. I., and Sunyaev, R. A. 1973. *Astronomy & Astrophysics*, 24, 337.
- [77] Liang, E. P., and Narayan, R. 1997. Page 461 in *Proceedings of the Fourth Compton Symposium, Part 1*, ed. Dermer, C., Strickman, M., and Kurfess, J. (New York: AIP).
- [78] Shapiro, S., and Teukolsky, S., 1983. *Black Holes, White Dwarfs, and Neutron Stars* (New York: John Wiley and Sons).
- [79] Dermer, C. D. 1995. *Astrophysical Journal*, 446, L63.
- [80] Blandford, R. D., and Levinson, A. 1995. *Astrophysical Journal*, 441, 79.
- [81] Sikora, M. 1997. Page 494 in *Proceedings of the Fourth Compton Symposium, Part 1*, ed. Dermer, C., Strickman, M., and Kurfess, J. (New York: AIP).
- [82] Kaspi, S., and Netzer, H. 1999. *Astrophysical Journal*, 524, 71.
- [83] Donea, A.-C., and Protheroe, R. J. 2003. *Astroparticle Physics*, 18, 377.

CHAPTER 7: SYNCHROTRON RADIATION

- [84] Jackson, J. D. 1962. *Classical Electrodynamics* (New York: John Wiley & Sons).
- [85] Brainerd, J. J., and Petrosian, V. 1987. *Astrophysical Journal*, 320, 703.
- [86] Rybicki, G. B., and Lightman, A. P. 1979. *Radiative Processes in Astrophysics* (New York: John Wiley & Sons).

- [87] Ginzburg, V. L., and Syravotskii, S. I. 1965. *Annual Review of Astronomy and Astrophysics*, 3, 297.
- [88] Pacholczyk, A. G. 1970. *Radio Astrophysics: Nonthermal Processes in Galactic and Extragalactic Sources* (San Francisco: Freeman).
- [89] Panaitescu, A., and Mészáros, P. 1999. *Astrophysical Journal*, 526, 707.
- [90] Ghisellini, G., Guilbert, P. W., and Svensson, R. 1988. *Astrophysical Journal*, 334, L5.
- [91] Crusius, A., and Schlickeiser, R. 1986. *Astronomy & Astrophysics*, 164, L16.
- [92] Katz, B., and Waxman, E. 2008. *Journal of Cosmology and Astro-Particle Physics*, 1, 18.
- [93] Michel, F. C. 1982. *Reviews of Modern Physics*, 54, 1.
- [94] Tavecchio, F., Maraschi, L., and Ghisellini, G. 1998. *Astrophysical Journal*, 509, 608.
- [95] Atoyan, A. M., and Dermer, C. D. 2003. *Astrophysical Journal*, 586, 79.
- [96] Celotti, A., and Fabian, A. C. 1993. *Monthly Notices of the Royal Astronomical Society*, 264, 228.
- [97] Dermer, C. D., and Atoyan, A. 2004. *Astrophysical Journal*, 611, L9.
- [98] Gould, R. J. 1979. *Astronomy & Astrophysics*, 76, 306.
- [99] Ghisellini, G., Maraschi, L., and Treves, A. 1985. *Astronomy & Astrophysics*, 146, 204.
- [100] Böttcher, M., Mause, H., and Schlickeiser, R. 1997. *Astronomy & Astrophysics*, 324, 395.
- [101] Tucker, W. H. 1975. *Radiation Processes in Astrophysics* (Cambridge, Mass.: MIT Press).
- [102] Sobelman, I. I., 1979. *Atomic Spectra and Radiative Transitions* (New York: Springer-Verlag).
- [103] Atoyan, A., and Dermer, C. D. 2004. *Astrophysical Journal*, 613, 151.
- [104] Burbidge, G. R., Jones, T. W., and O'Dell, S. L. 1974. *Astrophysical Journal*, 193, 43.
- [105] Jones, T. W., O'Dell, S. L., and Stein, W. A. 1974. *Astrophysical Journal*, 192, 261.
- [106] Nelson, R. W., and Wasserman, I. 1991. *Astrophysical Journal*, 371, 265.
- [107] Aloisio, R., and Blasi, P. 2002. *Astroparticle Physics*, 18, 195.
- [108] Guilbert, P. W., Fabian, A. C., and Rees, M. J. 1983. *Monthly Notices of the Royal Astronomical Society*, 205, 593.
- [109] de Jager, O. C., Harding, A. K., Michelson, P. F., Nel, H. I., Nolan, P. L., Sreekumar, P., and Thompson, D. J. 1996. *Astrophysical Journal*, 457, 253.
- [110] Dermer, C. D., and Atoyan, A. 2004. *Astronomy & Astrophysics*, 418, L5.
- [111] Medvedev, M. V. 2000. *Astrophysical Journal*, 540, 704.
- [112] Medvedev, M. V., and Loeb, A. 1999. *Astrophysical Journal*, 526, 697.

CHAPTER 8: BINARY PARTICLE PROCESSES

- [113] Mannheim, K., and Schlickeiser, R. 1994. *Astronomy & Astrophysics*, 286, 983.
- [114] Berezhinskii, V. S., Bulanov, S. V., Dogiel, V. A., and Ptuskin, V. S. 1990. In *Astrophysics of Cosmic Rays*, ed. V. L. Ginzburg (Amsterdam: North-Holland).
- [115] Silberberg, R., and Tsao, C. H. 1990. *Physics Reports*, 191, 351.
- [116] Purcell, W. R., et al. 1997. *Astrophysical Journal*, 491, 725.
- [117] Weidenspointner, G., et al. 2007. In *The Obscured Universe*, Proceedings of the 6th INTEGRAL Workshop, arXiv:astro-ph/0702621.
- [118] Gould, R. J. 1972. *Physica*, 60, 145.
- [119] Gould, R. J. 1972. *Physica*, 58, 379.
- [120] Gould, R. J. 1972. *Physica*, 62, 555.
- [121] Shapiro, S. L., Lightman, A. P., and Eardley, D. M. 1976. *Astrophysical Journal*, 204, 187.
- [122] Mahadevan, R., Narayan, R., and Krolik, J. 1997. *Astrophysical Journal*, 486, 268.
- [123] Huba, J. D. 1994. *NRL Plasma Formulary*, revised 2004.
- [124] Miller, J. A., Larosa, T. N., and Moore, R. L. 1996. *Astrophysical Journal*, 461, 445.
- [125] Abraham, P. B., Brunstein, K. A., and Cline, T. L. 1966. *Physical Review*, 150, 1088.
- [126] Boldt, E., and Serlemitsos, P. 1969. *Astrophysical Journal*, 157, 557.
- [127] Baring, M. G., Jones, F. C., and Ellison, D. C. 2000. *Astrophysical Journal*, 528, 776.
- [128] Baring, M. G. 1991. *Monthly Notices of the Royal Astronomical Society*, 253, 388.
- [129] Budnev, V. M., Ginzburg, I. F., Meledin, G. V., and Serbo, V. G. 1975. *Physics Reports*, 15, 181.
- [130] Stepney, S. 1983. *Monthly Notices of the Royal Astronomical Society*, 202, 467.
- [131] Zdziarski, A. A., and Svensson, R. 1989. *Astrophysical Journal*, 344, 551.
- [132] Gould, R. J. 1975. *Astrophysical Journal*, 196, 689.
- [133] Haug, E., 1975. *Zeitschrift Naturforschung*, 30a, 1099.
- [134] Haug, E., 1985. *Physical Review D*, 31, 2120; (e) 32, 1594.
- [135] Svensson, R. 1982. *Astrophysical Journal*, 258, 335.
- [136] Gould, R. J. 1980. *Astrophysical Journal*, 238, 1026; (e) 243, 677.
- [137] Dermer, C. D. 1986. *Astrophysical Journal*, 307, 47.
- [138] Wang, X.-Y., Razzaque, S., and Mészáros, P. 2008. *Astrophysical Journal*, 677, 432.

- [139] Lin, R. P., et al. 2002. *Solar Physics*, 210, 3.
- [140] Simpson, J. A. 1983. *Annual Reviews of Nuclear and Particle Physics*, 33, 323.
- [141] Dermer, C. D. 1986. *Astronomy & Astrophysics*, 157, 223.
- [142] Perl, M. 1974. *High Energy Hadron Physics* (New York: John Wiley & Sons).
- [143] Murphy, R. J., Dermer, C. D., and Ramaty, R. 1987. *Astrophysical Journal Supplements*, 63, 721.
- [144] Aharonian, F. A., and Atoyan, A. M. 1996. *Astronomy & Astrophysics*, 309, 917.
- [145] Hagedorn, R. 1973. *Relativistic Kinematics* (Reading, Mass.: Benjamin).
- [146] Moskalenko, I. V., and Strong, A. W. 1998. *Astrophysical Journal*, 493, 694.
- [147] Blasi, P., and Colafrancesco, S. 1999. *Astroparticle Physics*, 12, 169.
- [148] Stecker, F. W. 1971. *Cosmic Gamma Rays* (Baltimore, Md.: Mono Book Co.).
- [149] Badhwar, G. D., Golden, R. L., and Stephens, S. A. 1977. *Physical Review D*, 15, 820.
- [150] Particle Data Group. 1984. *Reviews of Modern Physics*, 56, S232.
- [151] Stephens, S. A., and Badhwar, G. D. 1981. *Astrophysics & Space Science*, 76, 213.
- [152] Commins, E. 1973. *Weak Interactions* (New York: McGraw-Hill).
- [153] Orth, C. D., and Buffington, A. 1976. *Astrophysical Journal*, 206, 312.
- [154] Berrington, R. C., and Dermer, C. D. 2003. *Astrophysical Journal*, 394, 709.
- [155] Mori, M. 1997. *Astrophysical Journal*, 478, 225.
- [156] Kamae, T., Karlsson, N., Mizuno, T., Abe, T., and Koi, T. 2006. *Astrophysical Journal*, 647, 692, (e) 2007, 662, 779.
- [157] Kelner, S. R., Aharonian, F. A., and Bugayov, V. V. 2006. *Physical Review D*, 74, 034018.
- [158] Pfrommer, C., and Enßlin, T. A. 2004. *Astronomy & Astrophysics*, 413, 17.
- [159] Harris, M. J. 1997. Page 418 in *Proceedings of the Fourth Compton Symposium, Part 1*, ed. Dermer, C., Strickman, M., and Kurfess, J. (New York: AIP).
- [160] Ling, J. C., Mahoney, W. A., Wheaton, W. A., and Jacobson, A. S. 1987. *Astrophysical Journal Letters*, 321, L117.
- [161] Liang, E. P., and Dermer, C. D. 1988. *Astrophysical Journal Letters*, 325, L39.
- [162] Ramaty, R., and Mészáros, P. 1981. *Astrophysical Journal*, 250, 384.
- [163] Bussard, R. W., Ramaty, R., and Drachman, R. J. 1979. *Astrophysical Journal*, 228, 928.
- [164] Crannell, C. J., Joyce, G., Ramaty, R., and Werntz, C. 1976. *Astrophysical Journal*, 210, 582.

- [165] Guessoum, N., Skibo, J. G., Ramaty, R. 1997. Page 113 in the *Second INTEGRAL Workshop*, ed. Winkler, C., Courvoisier, T., and Durouchoux, P. (Noordwijk, The Netherlands: European Space Agency Publications Division).
- [166] Guessoum, N., Jean, P., and Gillard, W. 2005. *Astronomy & Astrophysics*, 436, 171.
- [167] Burdyuzha, V. V., and Kauts, V. L. 1994. *Astrophysical Journal Supplements*, 92, 549.
- [168] Wallyn, P., Mahoney, W. A., Durouchoux, P., and Chapuis, C. 1996. *Astrophysical Journal*, 465, 473.
- [169] Zurek, W. H. 1985. *Astrophysical Journal*, 289, 603.
- [170] Guessoum, N., Ramaty, R., and Lingenfelter, R. E. 1991. *Astrophysical Journal*, 378, 170.
- [171] Dermer, C. D., and Murphy, R. J. 2001. Page 115 in *Proceedings of the Fourth INTEGRAL Workshop* (Noordwijk, The Netherlands: European Space Agency Publications Division).
- [172] Murphy, R. J., Share, G. H., Skibo, J. G., and Kozlovsky, B. 2005. *Astrophysical Journal Supplements*, 161, 495.
- [173] McKee, C. F., and Ostriker, J. P. 1977. *Astrophysical Journal*, 218, 148.
- [174] Diehl, R., Prantzos, N., and von Ballmoos, P. 2006. *Nuclear Physics A*, 777, 70.
- [175] Schönfelder, V. 2001. *The Universe in Gamma Rays* (New York: Springer).
- [176] Woosley, S. E., and Weaver, T. A. 1995. *Astrophysical Journal Supplements*, 101, 181.
- [177] Ramaty, R., Kozlovsky, B., and Lingenfelter, R. E. 1996. *Astrophysical Journal*, 456, 525.

CHAPTER 9: PHOTOHADRONIC PROCESSES

- [178] Rachen, J. P., and Mészáros, P. 1998. *Physical Review D*, 58, 123005.
- [179] Koers, H.B.J., and Wijers, R.A.M.J. 2007. arXiv:0711.4791.
- [180] Deyoung, T., Razzaque, S., and Cowen, D. F. 2007. *Astroparticle Physics*, 27, 238.
- [181] Gaisser, T. K., Halzen, F., and Stanev, T. 1995. *Physics Reports*, 258, 173.
- [182] Abbasi, R. U., et al. 2008. *Physical Review Letters*, 100, 101101.
- [183] The Pierre Auger Collaboration. 2008. arXiv:0806.4302, *Physical Review Letters*, 101, 061101.
- [184] Allard, D., Ave, M., Busca, N., Malkan, M. A., Olinto, A. V., Parizot, E., Stecker, F. W., and Yamamoto, T. 2006. *Journal of Cosmology and Astroparticle Physics*, 9, 5.

- [185] Stecker, F. W. 1979. *Astrophysical Journal*, 228, 919.
- [186] Mücke, A., Engel, R., Rachen, J. P., Protheroe, R. J., and Stanev, T., 2000. *Computer Physics Communications*, 124, 290.
- [187] Mücke, A., Rachen, J. P., Engel, R., Protheroe, R. J., and Stanev, T. 1999. *Publications of the Astronomical Society of Australia*, 16, 160.
- [188] Baldini, A., Flamini, V., Moorhead, W. G., and Morrison, D. R. O. 1988. In *Landolt-Bornstein, New Ser., Vol. I/12b*, ed. H. Schopper (Berlin: Springer).
- [189] Rachen, J. P. 1996. PhD thesis, Max Planck Institute für Radioastronomie, Bonn, Germany.
- [190] Hagiwara, K., et al. 2002. *Physical Review D*, 66, 010001.
- [191] Dermer, C. D., and Atoyan, A. 2003. *Physical Review Letters*, 91, 071102.
- [192] Lock, W. O., and Measday, D. F. 1970. *Intermediate Energy Nuclear Physics* (London: Methuen).
- [193] Stanev, T., Engel, R., Mücke, A., Protheroe, R. J., and Rachen, J. P. 2000. *Physical Review D*, 62, 093005.
- [194] Berezhinskii, V. S., and Grigor'eva, S. I. 1988. *Astronomy & Astrophysics*, 199, 1.
- [195] Berezhinsky, V., Gazizov, A. Z., and Grigorieva, S. I. 2005. *Physics Letters B*, 612, 147.
- [196] Atoyan, A. M., Aharonian, F. A., and Völk, H. J. 1995. *Physical Review D*, 52, 3265.
- [197] Mastichiadis, A., Marscher, A. P., and Brecher, K. 1986. *Astrophysical Journal*, 300, 178.
- [198] Blumenthal, G. R. 1970. *Physical Review D*, 1, 1596.
- [199] Chodorowski, M. J., Zdziarski, A. A., and Sikora, M. 1992. *Astrophysical Journal*, 400, 181.
- [200] Dermer, C. D., and Schlickeiser, R. 1991. *Astronomy & Astrophysics*, 252, 414.
- [201] Jost, R., Luttinger, J. M., and Slotnick, M. 1950. *Physical Review*, 80, 189.
- [202] Stepney, S., and Guilbert, P. W. 1983. *Monthly Notices of the Royal Astronomical Society*, 204, 1269.
- [203] Harari, D., Mollerach, S., and Roulet, E. 2006. *Journal of Cosmology and Astro-Particle Physics*, 11, 12.
- [204] Madau, P., Pozzetti, L., and Dickinson, M. 1998. *Astrophysical Journal*, 498, 106.
- [205] Dermer, C. D. Page 202, in *High Energy Gamma-Ray Astronomy*, ed. Aharonian, F. A., and Völk, H. (New York: AIP), astro-ph/0010564.
- [206] Hopkins, A. M., and Beacom, J. F. 2006. *Astrophysical Journal*, 651, 142.
- [207] Sanders, D. B. 2004. *Advances in Space Research*, 34, 535.
- [208] Wick, S. D., Dermer, C. D., and Atoyan, A. 2004. *Astroparticle Physics*, 21, 125.

- [209] Gronwall, C. 1999. Page 335 *After the Dark Ages: When Galaxies were Young (the Universe at $2 \leq z \leq 5$)*, ed. Holt, S., and Smith, E. (New York: AIP).
- [210] Treyer, M. A., et al. 1998. *Monthly Notices of the Royal Astronomical Society*, 300, 303.
- [211] Tresse, L., and Maddox, S. J. 1998. *Astrophysical Journal*, 459, 691.
- [212] Lilly, S. J., LeFevre, O., Hammer, F., and Crampton, D. 1998. *Astrophysical Journal*, 460, L1.
- [213] Connolly, A. J., et al. 1997. *Astrophysical Journal*, 486, L11.
- [214] Madau, P., et al. 1996. *Monthly Notices of the Royal Astronomical Society*, 283, 1388.
- [215] Pettini, M., et al. 1998. *Astrophysical Journal*, 508, 539.
- [216] Blain, A. W., et al. 1999. *Monthly Notices of the Royal Astronomical Society*, 309, 715.
- [217] Berezhinsky, V., Gazizov, A., and Grigorieva, S. 2006. *Phys. Rev. D*, 74, 043005.
- [218] Sanders, D. B., and Mirabel, I. F. 1996. *Annual Review of Astronomy and Astrophysics*, 34, 749.
- [219] Bahcall, J., and Waxman, E. 2001. *Physical Review D*, 64, 023002.
- [220] Fowler, J. W., Fortson, L. F., Jui, C. C. H., Kieda, D. B., Ong, R. A., Pryke, C. L., and Sommers, P. 2001. *Astroparticle Physics*, 15, 49.
- [221] Takeda, M., et al. 1998. *Physical Review Letters*, 81, 1163.
- [222] Mannheim, K., Protheroe, R. J., and Rachen, J. P. 2001. *Physical Review D*, 63, 023003.
- [223] Abbasi, R. U., et al. 2005. *Physics Letters B* 619, 271.
- [224] Berezhinsky, V., Gazizov, A., and Grigorieva, S. 2004, *Nuclear Physics B*, 136, 147.
- [225] Barwick, S. W., et al. 2006. *Physical Review Letters*, 96, 171101.
- [226] Karle, A., for the IceCube Collaboration. 2003. *Nuclear Physics B (Proceedings Supplement)* 118, 388.
- [227] Barwick, S., et al. 2006. Page 276 in *Proceedings of the TeV Particle Astrophysics II Workshop*, ed. Halzen, F., Karle, A., and Montaruli, T. (Philadelphia: Institute of Physics).
- [228] Semikoz, D. V., and Sigl, G. 2004. *Journal of Cosmology and Astroparticle Physics*, 04, 003.
- [229] Weiler, T. J. 1999. *Astroparticle Physics*, 11, 303.
- [230] Berezhinsky, V. 2006. *Nuclear Physics B (Proceedings Supplements)*, 151, 260.
- [231] Goldhaber, M., and Teller, E. 1948. *Physical Review*, 74, 1046.
- [232] Roy, R. R., and Nigam, B. P. 1967. *Nuclear Physics: Theory and Experiment* (New York: John Wiley & Sons).

- [233] Danos, M., and Fuller, E. G. 1965. *Annual Review of Nuclear and Particle Science*, 15, 29.
- [234] Puget, J. L., Stecker, F. W., and Bredekamp, J. H. 1976. *Astrophysical Journal*, 205, 638.
- [235] Stecker, F. W., and Salamon, M. H. 1999. *Astrophysical Journal*, 512, 521.
- [236] Anchordoqui, L. A., Hooper, D., Sarkar, S., and Taylor, A. M. 2008. *Astroparticle Physics*, 29, 1.
- [237] Paar, N., Vretenar, D., and Ring, P. 2005. *Physical Review Letters*, 94, 182501.
- [238] Anders, E., and Grevesse, N. 1989. *Geochimica et Cosmochimica Acta*, 53, 197.
- [239] Karakula, S., and Tkaczyk, W. 1993. *Astroparticle Physics*, 1, 229.
- [240] Hooper, D., Sarkar, S., and Taylor, A. M. 2007. *Astroparticle Physics*, 27, 199.
- [241] Ave, M., Busca, N., Olinto, A. V., Watson, A. A., and Yamamoto, T. 2005. *Astroparticle Physics*, 23, 19.

CHAPTER 10: PAIR PRODUCTION

- [242] Aharonian, F., et al. 2006. *Nature*, 440, 1018.
- [243] Nikishov, A. I. 1961. *Zh. Experiments. i Theo. Fiz.*, 41, 549.
- [244] Gould, R. J., and Schröder, G. P. 1967. *Physical Review*, 155, 1404.
- [245] Brown, R. W., Mikaelian, K. O., and Gould, R. J. 1973. *Astrophysics Letters*, 14, 203.
- [246] Moskalenko, I. V., Porter, T. A., and Strong, A. W. 2006. *Astrophysical Journal Letters*, 640, L155.
- [247] Becker, P. A., and Kafatos, M. 1995. *Astrophysical Journal*, 453, 83.
- [248] Levinson, A., and Blandford, R. 1995. *Astrophysical Journal*, 449, 86.
- [249] Liu, H. T., and Bai, J. M. 2006. *Astrophysical Journal*, 653, 1089.
- [250] Zdziarski, A. A., and Lightman, A. P. 1985. *Astrophysical Journal*, 294, L79.
- [251] Dermer, C. D. 2005. Page 1385 in *The Tenth Marcel Grossmann Meeting*, ed. Novello, M., Perez Bergliaffa, S., and Ruffini, R. (Singapore: World Scientific Publishing).
- [252] Svensson, R., and Zdziarski, A. 1990. *Astrophysical Journal*, 349, 415.
- [253] Hauser, M. G., and Dwek, E. 2001. *Annual Review of Astronomy and Astrophysics*, 39, 249.
- [254] Stecker, F. W., and de Jager, O. C. 1997. Page 39 in *Proceedings of the Kruger National Park Symposium on TeV Gamma Ray Astronomy*, ed. de Jager, O. C. (Potchefstroom, South Africa: Westprint).
- [255] Mukherjee, R., et al. 1997. *Astrophysical Journal*, 490, 116.

- [256] Kneiske, T. M., Bretz, T., Mannheim, K., and Hartmann, D. H. 2004. *Astronomy & Astrophysics*, 413, 807.
- [257] Mazin, D., and Raue, M. 2007. *Astronomy & Astrophysics*, 471, 439.
- [258] Aharonian, F., et al. 2007. *Astronomy & Astrophysics*, 470, 475.
- [259] Malkan, M. A., and Stecker, F. W. 1998. *Astrophysical Journal*, 496, 13.
- [260] Malkan, M. A., and Stecker, F. W. 2001. *Astrophysical Journal*, 555, 641.
- [261] Stecker, F. W., Malkan, M. A., and Scully, S. T. 2006. *Astrophysical Journal*, 648, 774; (e) 2007, 658, 1392.
- [262] Primack, J. R., Bullock, J. S., and Somerville, R. S. 2005. Page 23 in *High Energy Gamma-Ray Astronomy*, ed. Aharonian, F. A., Völk, H. J., and Horns, D. (New York: AIP).
- [263] Fazio, G. G., and Stecker, F. W. 1970. *Nature*, 226, 135.
- [264] Bonometto, S., and Rees, M. J. 1971. *Monthly Notices of the Royal Astronomical Society*, 152, 21.
- [265] McNaron-Brown, K., et al. 1995. *Astrophysical Journal*, 451, 575.
- [266] Woltjer, L., 1966. *Astrophysical Journal*, 146, 597.
- [267] Dondi, L., and Ghisellini, G. 1995. *Monthly Notices of the Royal Astronomical Society*, 273, 583.
- [268] Dermer, C. D., and Dingus, B. L. 2004. *New Astronomy Review*, 48, 537.
- [269] Vermeulen, R. C., and Cohen, M. H. 1994. *Astrophysical Journal*, 430, 467.
- [270] Lithwick, Y., and Sari, R. 2001. *Astrophysical Journal*, 540, 555.
- [271] Baring, M. G. 2006. *Astrophysical Journal*, 650, 1004.
- [272] Dermer, C. D., and Gehrels, N. 1995. *Astrophysical Journal*, 447, 103; (e) 1996, 456, 412.
- [273] Böttcher, M., and Dermer, C. D. 1995. *Astronomy & Astrophysics*, 302, 37.
- [274] Reimer, A. 2007. *Astrophysical Journal*, 665, 1023.
- [275] Dermer, C. D., Ramirez-Ruiz, E., and Le, T. 2007. *Astrophysical Journal Letters*, 664, L67.
- [276] Hartman, R. C., et al. 2001. *Astrophysical Journal*, 558, 583.
- [277] Mukherjee, R., et al. 1999. *Astrophysical Journal*, 527, 132.
- [278] MAGIC Collaboration. 2008. *Science*, 320, 1752.
- [279] Urry, C. M., and Padovani, P. 1995. *Proceedings of the Astronomical Society of the Pacific*, 107, 803.
- [280] Błażejowski, M., et al. 2005. *Astrophysical Journal*, 630, 130.
- [281] Atoyan, A., and Dermer, C. D. 2001. *Physical Review Letters*, 87, 221102.
- [282] O'Brien, P. T., et al. 2006. *Astrophysical Journal*, 647, 1213.
- [283] Murase, K., and Nagataki, S. 2006. *Physical Review Letters*, 97, 051101.
- [284] Aharonian, F. A., Coppi, P. S., and Völk, H. J. 1994. *Astrophysical Journal Letters*, 423, L5.
- [285] Razzaque, S., Mészáros, P., and Waxman, E. 2006. *Physical Review D*, 73, 103005.
- [286] Brodsky, S. J., and Lepage, G. P. 1981. *Physical Review D*, 24, 1808.

CHAPTER 11: BLAST-WAVE PHYSICS

- [287] MacFadyen, A. I., and Woosley, S. E. 1999. *Astrophysical Journal*, 524, 262.
- [288] Vietri, M., and Stella, L. 1998. *Astrophysical Journal Letters*, 507, L45.
- [289] Eichler, D., Livio, M., Piran, T., and Schramm, D. N. 1989. *Nature*, 340, 126.
- [290] Narayan, R., Piran, T., and Shemi, A. 1991. *Astrophysical Journal*, 379, L17.
- [291] Paczyński, B. 1998. *Astrophysical Journal Letters*, 494, L45.
- [292] Mészáros, P., and Rees, M. J. 2001. *Astrophysical Journal Letters*, 556, L37.
- [293] MacFadyen, A. I., Woosley, S. E., and Heger, A. 2001. *Astrophysical Journal*, 550, 410.
- [294] Paczyński, B. 1986. *Astrophysical Journal*, 308, L43.
- [295] Goodman, J. 1986. *Astrophysical Journal*, 308, L47.
- [296] Mészáros, P., Laguna, P., and Rees, M. J. 1993. *Astrophysical Journal*, 415, 181.
- [297] Piran, T. 1999. *Physics Reports*, 314, 575.
- [298] Rees, M. J., and Mészáros, P. 1992. *Monthly Notices of the Royal Astronomical Society*, 258, 41P.
- [299] Rees, M. J., and Mészáros, P. 1994. *Astrophysical Journal Letters*, 430, L93.
- [300] Mészáros, P., and Rees, M. J. 1993. *Astrophysical Journal*, 405, 278.
- [301] Dermer, C. D., and Humi, M. 2001. *Astrophysical Journal*, 536, 479.
- [302] Blandford, R. D., and McKee, C. F. 1976. *Physics of Fluids*, 19, 1130.
- [303] Sari, R. 1997. *Astrophysical Journal Letters*, 489, L37.
- [304] Panaitescu, A., Mészáros, P., and Rees, M. J. 1998. *Astrophysical Journal*, 503, 314.
- [305] Waxman, E. 1997. *Astrophysical Journal*, 485, L5.
- [306] Vietri, M. 1997. *Astrophysical Journal*, 478, L9.
- [307] Kulkarni, S. R., et al. 1998. *Nature*, 395, 663.
- [308] Lozinskaya, T. A. 1992. *Supernovae and Stellar Wind in the Interstellar Medium* (AIP: New York).
- [309] Böttcher, M., and Dermer, C. D. 2000. *Astrophysical Journal*, 532, 281.
- [310] Moderski, R., Sikora, M., and Bulik, T. 2000. *Astrophysical Journal*, 529, 151.
- [311] Chevalier, R. A., and Li, Z.-Y. 1999. *Astrophysical Journal Letters*, 520, L29.
- [312] Chevalier, R. A., and Li, Z.-Y. 2000. *Astrophysical Journal*, 536, 195.
- [313] Panaitescu, A., and Kumar, P. 2000. *Astrophysical Journal*, 543, 66.
- [314] Panaitescu, A., and Kumar, P. 2001. *Astrophysical Journal*, 554, 667.
- [315] Chiang, J., and Dermer, C. D. 1999. *Astrophysical Journal*, 512, 699.
- [316] Wijers, R.A.M.J., and Galama, T. J. 1999. *Astrophysical Journal*, 523, 177.
- [317] Zhang, B., and Mészáros, P. 2004. *International Journal of Modern Physics A*, 19, 2385.

- [318] Piran, T. 2005. *Reviews of Modern Physics*, 76, 1143.
- [319] Sari, R., Piran, T., and Narayan, R. 1998. *Astrophysical Journal*, 497, L17.
- [320] Hillas, A. M. 1984. *Annual Review of Astronomy and Astrophysics*, 22, 425.
- [321] Sari, R., Narayan, R., and Piran, T. 1996. *Astrophysical Journal*, 473, 204.
- [322] Sari, R., and Piran, T. 1995. *Astrophysical Journal*, 455, L143.
- [323] Mészáros, P., and Rees, M. J. 1997. *Astrophysical Journal*, 476, 232.
- [324] Costa, E., et al. 1997. *Nature*, 387, 783.
- [325] Hurley, K., Sari, R., and Djorgovski, S. G. 2003. Page 587 in *Compact Stellar X-Ray Sources*, ed. Lewin, W., and van der Klis, M. (Cambridge: Cambridge University Press).
- [326] Kobayashi, S., Piran, T., and Sari, R. 1999. *Astrophysical Journal*, 513, 679.
- [327] Kang, H., Jones, T. W., and Ryu, D. 1992. *Astrophysical Journal*, 385, 193.
- [328] Derishev, E. V., Kocharovsky, V. V., and Kocharovsky, V. V. 1999. *Astrophysical Journal*, 521, 640.
- [329] Lyutikov, M., and Blandford, R. 2003. astro-ph/0312347.
- [330] Sari, R., Piran, T., and Halpern, J. 1999. *Astrophysical Journal*, 519, L17.
- [331] Dermer, C. D., Chiang, J., and Mitman, K. E. 2000. *Astrophysical Journal*, 537, 785.
- [332] Rhoads, J. E. 1999. *Astrophysical Journal*, 525, 737.
- [333] Huang, Y. F., Dai, Z. G., and Lu, T. 2002. *Monthly Notices of the Royal Astronomical Society*, 332, 735.
- [334] Sari, R., and Esin, A. A. 2001. *Astrophysical Journal*, 548, 787.
- [335] Dermer, C. D., Chiang, J., and Böttcher, M. 1999. *Astrophysical Journal*, 513, 656.
- [336] Zhang, B. 2007. *Chinese Journal of Astronomy and Astrophysics*, 7, 1.
- [337] Mészáros, P. 2006. *Reports of Progress in Physics*, 69, 2259.
- [338] Gallant, Y. A., and Achterberg, A. 1999. *Monthly Notices of the Royal Astronomical Society*, 305, L6.
- [339] Zhang, B., Fan, Y. Z., Dyks, J., Kobayashi, S., Mészáros, P., Burrows, D. N., Nousek, J. A., and Gehrels, N. 2006. *Astrophysical Journal*, 642, 354.
- [340] Nousek, J. A., et al. 2006. *Astrophysical Journal*, 642, 389.
- [341] Dermer, C. D., and Mitman, K. E. 1999. *Astrophysical Journal*, 513, L5.
- [342] Sari, R., and Piran, T. 1997. *Astrophysical Journal*, 485, 270.
- [343] Band, D., et al. 1993. *Astrophysical Journal*, 413, 281.
- [344] Piran, T., Shemi, A., and Narayan, R. 1993. *Monthly Notices of the Royal Astronomical Society*, 263, 861.
- [345] Cohen, E., Piran, T., and Sari, R. 1998. *Astrophysical Journal*, 509, 717.
- [346] Dermer, C. D. 2007. *Astrophysical Journal*, 664, 384.
- [347] Kobayashi, S., Piran, T., and Sari, R. 1997. *Astrophysical Journal*, 490, 92.
- [348] Kumar, P., and Piran, T. 2000. *Astrophysical Journal*, 535, 152.
- [349] Beloborodov, A. M. 2000. *Astrophysical Journal Letters*, 539, L25.

- [350] Soderberg, A. M., and Fenimore, E. E. 2001. Page 87 in *Gamma-ray Bursts in the Afterglow Era*, ed. Costa, E., Frontera, F., and Hjorth, J. (Berlin: Springer-Verlag), 87.
- [351] O'Brien, P. T., et al. 2006. *Astrophysical Journal*, 647, 1213.
- [352] Daigne, F., and Mochkovitch, R. 1998, *Monthly Notices of the Royal Astronomical Society*, 296, 275.
- [353] Spada, M., Ghisellini, G., Lazzati, D., and Celotti, A. 2001. *Monthly Notices of the Royal Astronomical Society*, 325, 1559.
- [354] Amati, L., et al. 2002. *Astronomy & Astrophysics*, 390, 81.
- [355] Ghirlanda, G., Ghisellini, G., and Lazzati, D. 2004. *Astrophysical Journal*, 616, 331.
- [356] Thompson, C., Mészáros, P., and Rees, M. J. 2007. *Astrophysical Journal*, 666, 1012.
- [357] Rossi, E. M., Beloborodov, A. M., and Rees, M. J. 2006. *Monthly Notices of the Royal Astronomical Society*, 369, 1797.
- [358] Mészáros, P., and Rees, M. J. 2000. *Astrophysical Journal*, 530, 292.
- [359] Mészáros, P., Ramirez-Ruiz, E., Rees, M. J., and Zhang, B. 2002. *Astrophysical Journal*, 578, 812.
- [360] Pe'er, A., Ryde, F., Wijers, R. A. M. J., Mészáros, P., and Rees, M. J. 2007. *Astrophysical Journal Letters*, 664, L1.
- [361] Bahcall, J. N., and Mészáros, P. 2000. *Physical Review Letters*, 85, 1362.
- [362] Beloborodov, A. M. 2003. *Astrophysical Journal Letters*, 585, L19.
- [363] Derishev, E. V., Kocharovsky, V. V., and Kocharovsky, V. V. 1999. *Astronomy & Astrophysics*, 345, L51.
- [364] Frail, D. A., et al. 2001. *Astrophysical Journal Letters*, 562, L55.
- [365] Friedman, A. S., and Bloom, J. S. 2005. *Astrophysical Journal*, 627, 1.
- [366] Ghirlanda, G., Ghisellini, G., Lazzati, D., and Firmani, C. 2004. *Astrophysical Journal Letters*, 613, L13.
- [367] Dai, Z. G., Liang, E. W., and Xu, D. 2004. *Astrophysical Journal Letters*, 612, L101.

CHAPTER 12: INTRODUCTION TO FERMI ACCELERATION

- [368] Arons, J. 2003. *Astrophysical Journal*, 589, 871.
- [369] Longair, M. S. 1994. *High Energy Astrophysics. Vol. 2: Stars, the Galaxy and the Interstellar Medium* (Cambridge: Cambridge University Press).
- [370] Fermi, E. 1949. *Physical Review*, 75, 1169.
- [371] Fermi, E. 1954. *Astrophysical Journal*, 119, 1.
- [372] Schlickeiser, R. 1984. *Astronomy & Astrophysics*, 136, 227.
- [373] Schlickeiser, R. 1985. *Astronomy & Astrophysics*, 143, 431.

- [374] Biermann, P. L., and Strittmatter, P. A. 1987. *Astrophysical Journal*, 322, 643.
- [375] Goldstein, M. L., Roberts, D. A., and Matthaues, W. H. 1995. *Annual Review of Astronomy and Astrophysics*, 33, 283.
- [376] Miller, J. A., and Roberts, D. A. 1995. *Astrophysical Journal*, 452, 912.
- [377] Eilek, J. A., and Henriksen, R. N. 1984. *Astrophysical Journal*, 277, 820.
- [378] Kolmogorov, A. 1941. *Akademiia Nauk SSSR Doklady*, 30, 301.
- [379] Kraichnan, R. H. 1965. *Physics of Fluids*, 8, 1385.
- [380] Zhou, Y., and Matthaues, W. H. 1990. *Journal of Geophysical Research*, 95, 14881.
- [381] Usov, V. V., and Chibisov, G. V. 1975. *Soviet Astronomy*, 19, 115.
- [382] Ginzburg, V. L., and Ptuskin, V. S. 1976. *Reviews of Modern Physics*, 48, 161.
- [383] Schlickeiser, R. 2002. *Cosmic Ray Astrophysics* (Berlin: Springer-Verlag).
- [384] Lagage, P. O., and Cesarsky, C. J. 1983. *Astronomy & Astrophysics*, 125, 249.
- [385] Ginzburg, V. L., and Syrovatskii, S. I. 1964. *The Origin of Cosmic Rays* (New York: Macmillan).
- [386] Hayakawa, S. 1969. *Cosmic Ray Physics* (New York: Wiley-Interscience).
- [387] Weiler, K. W., Panagia, N., Sramek, R. A., van Dyk, S. D., Montes, M. J., and Lacey, C. K. 2001. Page 198 in *Supernovae and Gamma-Ray Bursts: the Greatest Explosions since the Big Bang*, ed. Livio, M., Panagia, N., and Sahu, K. (Cambridge: Cambridge University Press).
- [388] Hillas, A. M. 2005. *Journal of Physics G: Nuclear Physics*, 31, 95.

CHAPTER 13: FIRST-ORDER FERMI ACCELERATION

- [389] Lucek, S. G., and Bell, A. R. 2000. *Monthly Notices of the Royal Astronomical Society*, 314, 65.
- [390] Bell, A. R., and Lucek, S. G. 2001. *Monthly Notices of the Royal Astronomical Society*, 321, 433.
- [391] Forman, M. A. 1970. *Planetary and Space Science*, 18, 25.
- [392] Keshet, U., and Waxman, E. 2005. *Physical Review Letters*, 94, 111102.
- [393] Bell, A. R. 1978. *Monthly Notices of the Royal Astronomical Society*, 182, 147.
- [394] Bell, A. R. 1978. *Monthly Notices of the Royal Astronomical Society*, 182, 443.
- [395] Blandford, R. D., and Ostriker, J. P. 1978. *Astrophysical Journal Letters*, 221, L29.
- [396] Krymskii, G. F. 1977. *Akademiia Nauk SSSR Doklady*, 234, 1306.
- [397] Axford, I. W. 1981. *International Cosmic Ray Conference*, 12, 155.

- [398] Drury, L. O'C. 1983. *Reports on Progress in Physics*, 46, 973.
- [399] Blandford, R. D., and Eichler, D. 1987. *Physics Reports*, 154, 1.
- [400] Kirk, J. G. 1994. Page 225 in *Saas-Fee Lecture Notes on Plasma Astrophysics*, ed. Benz, A. O., and Courvoisier, T. J.-L. (Berlin: Springer-Verlag).
- [401] Zeldovich, Y. B., and Raizer, Y. P. 1966. *Elements of Gasdynamics and the Classical Theory of Shock Waves* (New York: Academic Press).
- [402] Ellison, D. C. 1982. Ph.D. Thesis, Catholic University, Washington, D.C.
- [403] Michel, F. C. 1981. *Astrophysical Journal*, 247, 664.
- [404] Forman, M. A., and Webb, G. M. 1985. *American Geophysical Union Geophysical Monograph Series*, 35, 91.
- [405] Berezhko, E. G., and Ellison, D. C. 1999. *Astrophysical Journal*, 526, 385.
- [406] Berezhko, E. G. 1996. *Astroparticle Physics*, 5, 367.
- [407] Blasi, P. 2002. *Astroparticle Physics*, 16, 429.
- [408] Malkov, M. A. 1997. *Astrophysical Journal*, 485, 638.
- [409] Ellison, D. C., Baring, M. G., and Jones, F. C. 1996. *Astrophysical Journal*, 473, 1029.
- [410] Jones, F. C., and Ellison, D. C. 1991. *Space Science Reviews*, 58, 259.
- [411] Lagage, P. O., and Cesarsky, C. J. 1983. *Astronomy & Astrophysics*, 118, 223.
- [412] Blasi, P., Amato, E., and Caprioli, D. 2007. *Monthly Notices of the Royal Astronomical Society*, 375, 1471.
- [413] Jokipii, J. R. 1987. *Astrophysical Journal*, 313, 842.
- [414] Baring, M. G., Ellison, D. C., Reynolds, S. P., Grenier, I. A., and Goret, P. 1999. *Astrophysical Journal*, 513, 311.
- [415] Landau, L. D., and Lifshitz, E. M. 1959. *Fluid Mechanics* (New York: Pergamon).
- [416] Chevalier, R. A. 1974. *Astrophysical Journal*, 188, 501.
- [417] Falle, S. A. E. G. 1981. *Monthly Notices of the Royal Astronomical Society*, 195, 1011.
- [418] Wentzel, D. G. 1974. *Annual Review of Astronomy and Astrophysics*, 12, 71.
- [419] Skilling, J. 1975. *Monthly Notices of the Royal Astronomical Society*, 172, 557.
- [420] Völk, H. J., Drury, L. O., and McKenzie, J. F. 1984. *Astronomy & Astrophysics*, 130, 19.
- [421] Völk, H. J., and Biermann, P. L. 1988. *Astrophysical Journal Letters*, 333, L65.
- [422] Kirk, J. G., and Schneider, P. 1987. *Astrophysical Journal*, 315, 425.
- [423] Kirk, J. G., and Heavens, A. F. 1989. *Monthly Notices of the Royal Astronomical Society*, 239, 995.
- [424] Achterberg, A., Gallant, Y. A., Kirk, J. G., and Guthmann, A. W. 2001. *Monthly Notices of the Royal Astronomical Society*, 328, 393.
- [425] Bednarz, J., and Ostrowski, M. 1998. *Physical Review Letters*, 80, 3911.

- [426] Ostrowski, M., and Bednarz, J. 2002. *Astronomy & Astrophysics*, 394, 1141.
 [427] Vietri, M. 1995. *Astrophysical Journal*, 453, 883.

CHAPTER 14: SECOND-ORDER FERMI ACCELERATION

- [428] Lee, M. A., and Ip, W.-H. 1987. *Journal of Geophysics Research*, 92, 11041.
 [429] Steinacker, J., and Miller, J. A. 1992. *Astrophysical Journal*, 393, 764.
 [430] Stix, T. H. 1992. *The Theory of Plasma Waves* (New York: McGraw-Hill).
 [431] Kulsrud, R. M. 2005. *Plasma Physics for Astrophysics* (Princeton, N.J.: Princeton University Press).
 [432] Miller, J. A., and Steinacker, J. 1992. *Astrophysical Journal*, 399, 284.
 [433] Swanson, P. G. 1989. *Plasma Waves* (New York: McGraw-Hill).
 [434] Melrose, D. B. 1980. *Plasma Astrophysics* (New York: Gordon & Breach).
 [435] Miller, J. A., and Ramaty, R. 1989. *Astrophysical Journal*, 344, 973.
 [436] Becker, P. A., Le, T., and Dermer, C. D. 2006. *Astrophysical Journal*, 647, 539.
 [437] Schlickeiser, R. 1989. *Astrophysical Journal*, 336, 243.
 [438] Jokipii, J. R., 1966. *Astrophysical Journal*, 146, 480.
 [439] Dermer, C. D., Miller, J. A., and Li, H. 1996. *Astrophysical Journal*, 456, 106.
 [440] Arfken, G. 1970. *Mathematical Methods for Physicists* (New York: Academic Press).
 [441] Ramaty, R. 1979. Page 135 in *Particle Acceleration Mechanisms in Astrophysics*, ed. Arons, J., McKee, C., and Max, C. (AIP: New York).
 [442] Miller, J. A., Guessoum, N., and Ramaty, R. 1990. *Astrophysical Journal*, 361, 701.
 [443] Park, B. T., and Petrosian, V. 1995. *Astrophysical Journal*, 446, 699.
 [444] Petrosian, V., and Liu, S. 2004. *Astrophysical Journal*, 610, 550.
 [445] Lichnerowicz, A. 1967. *Relativistic Hydrodynamics and Magnetohydrodynamics* (New York: Benjamin).
 [446] Vietri, M. 1998. *Astrophysical Journal*, 507, 40.
 [447] Usov, V. V. 1994. *Monthly Notices of the Royal Astronomical Society*, 267, 1035.
 [448] Mészáros, P., Rees, M. J., and Papathanassiou, H. 1994. *Astrophysical Journal*, 432, 181.

CHAPTER 15: THE GEOMETRY OF SPACETIME

- [449] Kerr, R. P. 1963. *Physical Review Letters*, 11, 237.
 [450] O'Neill, B. 1995. *The Geometry of Kerr Black-Holes* (Wellesley, Mass.: A. K. Peters).

- [451] Chandrasekhar, S. 1992. *The Mathematical Theory of Black Holes* (New York: Oxford University Press).
- [452] Carter, B. 1968. *Physical Review*, 174, 1559.
- [453] Penrose, R. 1969. *Rivista del Nuovo Cimento*, 1, 252.
- [454] Christodoulou, D. 1970. *Physical Review Letters*, 25, 1596.
- [455] Hawking, S. W. 1975. *Communications in Mathematical Physics*, 43, 199.
- [456] Hawking, S. W. 1974. *Nature*, 248, 30.
- [457] Page, D. N., and Hawking, S. W. 1976. *Astrophysical Journal*, 206, 1.
- [458] Fichtel, C. E., et al. 1994. *Astrophysical Journal*, 434, 557.

CHAPTER 16: BLACK-HOLE ELECTRODYNAMICS

- [459] Bardeen, J. M., Press, W. H., and Teukolsky, S. A. 1972. *Astrophysical Journal*, 178, 347.
- [460] Komissarov, S. S. 2004. *Monthly Notices of the Royal Astronomical Society*, 350, 427.
- [461] MacDonald, D., and Thorne, K. S. 1982. *Monthly Notices of the Royal Astronomical Society*, 198, 345.
- [462] Thorne, K. S., and MacDonald, D. 1982. *Monthly Notices of the Royal Astronomical Society*, 198, 339.
- [463] Thorne, K. S., Price, R. H., and MacDonald, D. A. 1986. *Black Holes: The Membrane Paradigm* (New Haven, Conn.: Yale University Press).
- [464] Jackson, J. D. 1979. *Classical Electrodynamics* (New York: Wiley).
- [465] Ruffini, R., and Wilson, J. R. 1975. *Physical Review D*, 12, 2959.
- [466] Goldreich, P., and Julian, W. H. 1969. *Astrophysical Journal*, 157, 869.
- [467] Blandford, R. D., and Znajek, R. L. 1977. *Monthly Notices of the Royal Astronomical Society*, 179, 433.
- [468] Znajek, R. L. 1977. *Monthly Notices of the Royal Astronomical Society*, 179, 457.
- [469] Menon, G., and Dermer, C. D. 2007. *General Relativity and Gravitation*, 39, 785.
- [470] Menon, G., and Dermer, C. D. 2005. *Astrophysical Journal*, 635, 1197.
- [471] Punsky, B. 2001. *Black Hole Gravitohydromagnetics* (New York: Springer).
- [472] Levinson, A. 2006. Page 119 in *Trends in Black Hole Research*, ed. Kreitler, P. V. (New York: Nova Science Publishers).
- [473] McKinney, J. C., and Narayan, R. 2007. *Monthly Notices of the Royal Astronomical Society*, 375, 513.
- [474] McKinney, J. C., and Narayan, R. 2007. *Monthly Notices of the Royal Astronomical Society*, 375, 531.
- [475] Königl, A. 2007. *Revista Mexicana de Astronomia y Astrofisica*, 27, 91.

CHAPTER 17: HIGH-ENERGY RADIATIONS FROM BLACK HOLES

- [476] Waxman, E. 1995. *Physical Review Letters*, 75, 386.
- [477] Mannheim, K., and Biermann, P. L. 1989. *Astronomy & Astrophysics*, 221, 211.
- [478] Blandford, R. D. 1990. Page 161 in *Saas-Fee Advanced Course of the Swiss Society for Astrophysics and Astronomy: Active Galactic Nuclei*, ed. Courvoisier, T. J.-L., and Mayor, M. (Berlin: Springer-Verlag).
- [479] Hartman, R. C., et al. 1999. *Astrophysical Journal Supplements*, 123, 79.
- [480] Punch, M., et al. 1992. *Nature*, 358, 477.
- [481] Torres, D. F., Romero, G. E., Dame, T. M., Combi, J. A., and Butt, Y. M. 2003. *Physics Reports*, 382, 303.
- [482] Torres, D. F. 2003. In *Cosmic Gamma-ray Sources*, ed. Cheng, K. S., and Romero, G. E. (Dordrecht: Kluwer), astro-ph/0308069.
- [483] Moderski, R., Sikora, M., Coppi, P. S., and Aharonian, F. 2005. *Monthly Notices of the Royal Astronomical Society*, 363, 954.
- [484] Foschini, L., et al. 2007. *Astrophysical Journal Letters*, 657, L81.
- [485] Böttcher, M., and Dermer, C. D. 2000. *Astrophysical Journal*, 529, 635.
- [486] Mücke, A., and Pohl M. 2000. *Monthly Notices of the Royal Astronomical Society*, 312, 177.
- [487] Fanaroff, B. L., and Riley, J. M. 1974. *Monthly Notices of the Royal Astronomical Society*, 167, 31P.
- [488] Sambruna, R., Maraschi, L., and Urry, C. M. 1996. *Astrophysical Journal*, 463, 444.
- [489] Fossati, G., Maraschi, L., Celotti, A., Comastri, A., and Ghisellini, G. 1998. *Monthly Notices of the Royal Astronomical Society*, 299, 433.
- [490] Ghisellini, G., Celotti, A., Fossati, G., Maraschi, L., and Comastri, A. 1998. *Monthly Notices of the Royal Astronomical Society*, 301, 451.
- [491] Böttcher, M., and Dermer, C. D. 2002. *Astrophysical Journal*, 564, 86.
- [492] Cavaliere, A., and D'Elia, V. 2002. *Astrophysical Journal*, 571, 226.
- [493] Le, T., Dermer, C. D. 2008. *Astrophysical Journal*, in press, arXiv: 0807.0355.
- [494] Kouveliotou, C., Meegan, C. A., Fishman, G. J., Bhat, N. P., Briggs, M. S., Koshut, T. M., Paciesas, W. S., and Pendleton, G. N. 1993. *Astrophysical Journal Letters*, 413, L101.
- [495] Soderberg, A. M., et al. 2004. *Nature*, 430, 648.
- [496] Soderberg, A. M., et al. 2006. *Nature*, 442, 1014.
- [497] Dermer, C. D. 2007. Page 127 in *The Multi-Messenger Approach to High-Energy Gamma-Ray Sources*, ed. Paredes, J. M., Reimer, O., and Torres, D. F. (New York: Springer).

- [498] Kalashev, O. E., Semikoz, D. V., and Sigl, G. 2007. arXiv:0704.2463.
- [499] Pavlidou, V., and Fields, B., 2002. *Astrophysical Journal Letters*, 575, L5.
- [500] Baade, W., and Zwicky, F. 1934. *Physical Review*, 46, 76.
- [501] Wang, X.-Y., Razzaque, S., Mészáros, P., and Dai, Z.-G. 2007. *Physical Review D*, 76, 083009.
- [502] Véron-Cetty, M.-P., and Véron, P. 2006. *Astronomy & Astrophysics*, 455, 773.
- [503] The Pierre Auger Collaboration. 2008. *Astroparticle Physics*, 29, 188.
- [504] Dermer, C. D. 2009. In *Proceedings of the 30th International Cosmic Ray Conference*, Mérida, Yucatan, Mexico (in press), arXiv:0711.2804.
- [505] Watson, A. A. 2008. arXiv:0801.2321.
- [506] Berezhinsky, V. 2008. In *The International Conference on Topics in Astroparticle and Underground Physics (TAUP) 2007*, ed. Inoue, K., Suzuki, A., and Mitsui, T. (in press), arXiv:0801.3028.
- [507] Aloisio, R., Berezhinsky, V., Blasi, P., Gazizov, A., Grigorieva, S., and Hnatyk, B. 2007. *Astroparticle Physics*, 27, 76.
- [508] Alvarez-Muñiz, J., Engel, R., and Stanev, T. 2002. *Astrophysical Journal*, 572, 185.
- [509] Waxman, E., and Coppi, P. 1996. *Astrophysical Journal Letters*, 464, L75.
- [510] Waxman, E. 2004. *New Journal of Physics*, 6, 140.
- [511] Halzen, F., and Hooper, D. 2002. *Reports of Progress in Physics*, 65, 1025.
- [512] Briggs, M. S., et al. 1999. *Astrophysical Journal*, 524, 82.
- [513] Dermer, C. D., and Atoyan, A. 2006. *New Journal of Physics*, 8, 122.
- [514] González, M. M., Dingus, B. L., Kaneko, Y., Preece, R. D., Dermer, C. D., and Briggs, M. S. 2003. *Nature*, 424, 749.
- [515] Coppi, P. S., and Aharonian, F. A. 1997. *Astrophysical Journal Letters*, 487, L9.

APPENDIX A: ESSENTIAL TENSOR CALCULUS

- [516] Synge, J. L., and Schild, A. 1978. *Tensor Calculus* (New York: Dover).
- [517] Kay, L. 1988. *Schaum's Outline of Tensor Calculus* (New York: McGraw-Hill).
- [518] Bishop, R. L., and Goldberg, S. I. 1980. *Tensor Analysis on Manifolds* (New York: Dover).
- [519] O'Neill, B. 1983. *Semi-Riemannian Geometry With Applications to Relativity* (New York: Academic Press).
- [520] Curtis, W. D., and Miller, F. R. 1985. *Differential Manifolds and Theoretical Physics* (New York: Academic Press).

APPENDIX B: MATHEMATICAL FUNCTIONS

- [521] Kostroun, V. O. 1980. *Nuclear Instruments and Methods*, 172, 371.
- [522] Corless, R. M., Gonnet, G. H., Hare, D. E. G., Jeffrey, D. J., and Knuth, D. E. 1996. *Advances in Computational Mathematics*, 5, 329.

APPENDIX C: SOLUTIONS OF THE CONTINUITY EQUATION

- [523] Syrovatskii, S. I. 1959. *Soviet Astronomy*, 3, 22.

APPENDIX E: SUPPLEMENTARY INFORMATION

- [524] Anderson, H. L., ed. 1981. *Physics Vade Mecum* (New York: AIP).
- [525] Montanet, L., et al. 1994. *Physical Review D*, 50, 1173.

Index

- abundances: meteoritic, 222; solar photospheric, 222
- acceleration mechanisms: electrodynamic, 314 (*See* black-hole electrodynamics); Fermi (*See* Fermi acceleration)
- accretion, 2, 13, 452; accretion disk, 105–106; far-field approximation of, 109–110, 113; near-field approximation of, 109–112; Shakura-Sunyaev, 105–108; transformed fields of, 108–111; two-temperature, 164
- active galactic nuclei, 1
- adiabatic energy losses, 187, 202–204, 265
- adiabatic expansion, 203–204, 260
- affine parameter, 31, 409
- afterglow theory, 278–282
- Alfvén speed, 344, 356; in relativistic gas, 373
- Alfvén waves. *See* plasma waves
- Amati relation, 303–304
- angular timescale, 296
- ANITA, 218–219, 505
- annihilation radiation, 180–185
- astroparticle spectrum, 5
- Auger Observatory. *See* Pierre Auger Observatory
- background radiation; cosmic microwave, 13, 55; infrared and optical, 13; X-ray, 13; γ -ray, 13, 458–459
- Band function, 298, 313
- BATSE, 298, 454, 459, 505
- beaming, 18, 64; for blob geometry, 60; for spherical-shell geometry, 68
- beaming patterns, 113
- Bell-Lucek mechanism, 345
- Beppo-SAX, 278, 312, 505
- Bernoulli numbers, 490–491
- Bessel function, 3, 157, 370, 488–489
- Bethe-Heitler pair production, 197, 253
- binary particle collision processes, 160–186
- black hole, 397; angular momentum of, 385; annihilation radiation from, 161–185; energy extraction from, 398, 400; Hawking (or evaporating), 416, 452, 459; irreducible mass of, 401–402; Kerr, 401–402, 429, 431, 433, 442, 445; mass of, 1, 11, 385; Schwarzschild, 33, 106–108, 415–416; spin paradigm for, 452–453, 471–472
- black-hole electrodynamics, 417–451
- blackbody radiation, 53–55; transformation of, 57–58
- Blandford-Znajek process, 427, 436, 448–449, 450–451, 472
- Blandford-Znajek split monopole solution, 445, 448
- blast waves: adiabatic, 266–268; deceleration of, 260–269; equation of motion for, 261–269; partially radiative, 269; physics of, 258–313; radiative, 268–269
- blast-wave cooling regimes; slow, 273, 277–280, 290; fast (or strongly), 273–274, 277–280, 290
- blast-wave deceleration radius, 260, 324
- blast-wave deceleration timescale, 261
- blast-wave frequency; cooling, 275–276; minimum, 275; maximum, 276; synchrotron self-absorption, 276–277
- blazars, 9, 213, 246–248, 251–253, 453–454; evolution of, 458; models of, 454–456
- blazar main sequence, 458
- BL Lac objects, 243, 453
- blob geometry, 60–62, 68–69, 130, 136
- blue bump, 108

- Bohm diffusion approximation, 323, 340
 Boltzmann equation, 360–361
 Boyer-Lindquist coordinates, 384–385, 391–392, 418, 428, 433–435, 440
 Breit-Wigner distribution, 176, 194, 242
 bremsstrahlung, 160, 166–169; energy-loss rate for, 167; production spectra of, 168–169; suprathermal proton, 166; thermal energy emissivity of, 168
 brightness temperature, 146–147; maximum, 150–153
 broad-line region, 114, 236, 457
- Carter constant, 391
 cascades, 253–256; in gamma-ray bursts, 469–470; in the intergalactic medium, 256, 470–471; in jets, 254–256; turbulent plasma wave, 318
 Christoffel symbols, 31, 33–34, 421, 424, 484
 coherence length. *See* magnetic field, coherence length
 comoving coordinates, 38
 comoving density, 46
 comoving UHECR proton density, 208–209
 compact, 228, 246
 compactness parameter, 245–247
 compression ratio, 315, 328–329, 340
 COMPTEL, 185, 247, 505
 Compton catastrophe, 154
 Compton cross section, 71–79; double, or radiative, 168; moments of, 79
 Compton effect, 70–71
 Compton energy-loss rates, 81–83
 Compton scattering, 70–116; of external radiation fields 94–96, 103–104 (*See* external Compton scattering; isotropic spectral head-on comparisons for, 86–88; kernel for, 78; spectral head-on approximations for, 83–84, 93–94
 Compton Gamma Ray Observatory, 9, 161, 185, 505
 Compton-synchrotron logarithm, 139
 Compton γ parameter, 292–293
 continuity equation, 454, 492–496
 continuous energy losses, 197
 contraction, 477
 contravariant vectors, 25–26, 477
- convection-diffusion equation, 330–332
 cosmic microwave background radiation, 12, 55
 cosmic rays, 5–7, 13, 160, 170, 452; abundances of, 222; accelerated by supernovae, 346, 452, 459–461, demodulated spectrum of, 171, 180; diffusion of, 324; energy density of, 214; maximum energy of, 324–326
 cosmological constant, 41
 cosmological principle, 39
 cosmology: Einstein-de Sitter, 43; flat, 43; Friedmann, 39–43; Λ CDM, 45, 46, 239
 cospatial assumption, 249
 Coulomb cross section, 160
 Coulomb diffusion coefficient, 165
 Coulomb energy loss rate, 161–165
 Coulomb force, 162
 Coulomb logarithm, 162–163
 Coulomb scattering, 160
 covariant derivative, 418, 483–485
 covariant vectors, 26, 477–478
 cross section, 21; annihilation, 181; Bhabha, 160; Compton, 71–73; Coulomb, 160; exclusive, 172; $\gamma\gamma$ pair production, 228, 229; inclusive, 172; inelastic nuclear, 172–173; Klein-Nishina, 73; Møller, 160; photonuclear, 220–223; photopair, 198–199; photopion, 191–194, 205 (multi-pion, 205–206; single pion, 205–206); spallation, 170; Thomson, 72
 curvature relation, 64–65, 303
 curved space, 29, 35
- deflection angle, 158, 466
 density: critical, 42; energy, 53, 57, 61; mass, 42
 diffusion: in momentum space, 360, 367; in physical space, 322–324
 diffusion approximation, 352
 diffusion coefficients, 359–361; approximate derivation of, 362–363; Hamiltonian formulation of, 361
 dilogarithm function, 143
 dispersion relation, 355

- distance: angular diameter, 45; event-rate, 46, 456; luminosity, 44–46; propagation, 44; proper, 44
- divergence theorem, 403, 485–486
- Doppler beaming, 64
- Doppler effect, 18–19
- Doppler factor, 18–19; Compton limits on, 153–154; minimum value from $\gamma\gamma$ constraint, 247–248
- Doppler resonance, 354–355
- dot product, 25
- dual vectors, 28, 476–479
- Eddington luminosity, 106, 450
- EGRET, 9, 13, 135, 219, 247, 416, 452–454, 458–460, 505
- electromagnetic cascades, 253–256
- electromagnetic spectrum, 4
- electromagnetic waves, 357
- emissivity, 51
- Einstein coefficients, 145–146
- Einstein equation, 32, 379, 384, 486–487
- electron cyclotron waves, 358
- electron plasma frequency, 162, 355
- energy flux, 8, 44, 51–52, 59
- energy-momentum tensor, 304–305, 424–426, 487
- entropy per baryon, 259
- ergosphere, 394–398, 400, 402, 433, 447
- Euler's constant, 83, 489
- event horizon, 33, 394, 396–397, 400–401, 417, 433–435, 441, 448–450
- event rate, 45–47
- exponential integral function, 209, 489
- external Compton scattering, 94–116; of accretion disk, 108–111; blazar model with, 456–457; of broad-line region, 114–116; of cosmic microwave background radiation, 103–104; of isotropic photons, 99–101; in Thomson limit, 96–99, 101–102
- extragalactic background light (EBL), 227, 237–238; calculations of, 244; empirical fit to, 240–242; measurements of, 240
- Fazio-Stecker relation, 244. *See* gamma-ray horizon
- Fermi acceleration: introduction to, 314–326; first-order (shock), 317, 321–322, 327–350 (—nonrelativistic: maximum particle energy for, 339–344; spectral index in, 332–337; —relativistic: maximum particle energy for, 349; spectral index in, 348) second-order (stochastic), 316, 321–322, 351–378 (diffusive escape rate in, 364–366; energy gain rates for, 366–367; maximum particle energy for, 372–378)
- Fermi Gamma ray Space Telescope, 238, 248, 252–253, 313, 452–454, 457–458, 472; 505; GBM, 458; LAT, 506, 253, 458, 505
- Feynman scaling, 177
- fine structure constant, 129
- flat spectrum radio quasars, 243, 251–252, 454–458
- fluence, 44, 312
- flux, 8; νF_ν flux, 8, 52, 59–60, 278–279
- flux density, 8, 143–145, 279
- Fokker-Planck coefficients, 359–364
- Fokker-Planck equation 347, 360
- four vectors, 16, 25
- four-vector acceleration, 119
- four-vector force, 32, 118
- four-vector momentum, 16–18, 27
- four-vector velocity, 26, 32
- future cone, 395
- galaxies: infrared luminous, 213; Milky Way, 1, 5, 244; Seyfert, 13, 108, 452
- Gamma function, 55, 195, 488
- gamma-gamma absorption, 230–236; in anisotropic radiation fields, 235–236; by blackbody radiation, 231–232; intrinsic source spectra with, 243–244; by modified blackbody, 233; by power-law radiation, 233–235, 237
- gamma-gamma opacity of the universe, 237–244
- gamma-gamma pair horizon, 236
- gamma-gamma pair production cross section; δ -function approximation for, 236–237; exact, 228–229
- gamma-ray bursts, 1, 9, 213, 248–249, 252–253; blast-wave physics of, 258–313; cascade radiation, 255; classes of, 258–259, 294, 312, 458; collapsar model, 259; colliding shell model, 294, 301–303; cosmology,

- 312–313; deceleration radius, 260, 324; external shock model for, 294; luminosity, 259; model light curves, 297; prompt phase, 294–303; rapid X-ray decline, 295, 300–301; standard energy reservoir in, 312–313; thin-shell requirement, 298–300
- gamma-ray horizon, 238, 244–245
- gamma rays: from blazars, 453–459; detectors of, 228, 253, 453–454, 472; Galactic cosmic-ray induced, 171–180; neutrino correlations with, 249–253, 468–469; nuclear line, 185–186; from supernova remnants, 170; UHECR-induced cascade, 219
- Gaunt factor, 168–169
- GBM. *See* Fermi GBM
- general relativity, 25, 32, 403
- geodesic: definition of, 30, 32, 485; null, 32, 36–37
- geodesic currents, 436–437
- geodesic equation, 30–31; for Kerr metric, 386–391, 397–398; for Schwarzschild metric, 34–35
- Ghirlanda relation, 303–304
- giant dipole resonance, 220–225
- GLAST, 505. *See* Fermi Gamma ray Space Telescope
- gravitational radius, 106
- gravitational redshift, 35
- gravitational waves, 7–8
- Green's function, 367, 370–372
- Greisen-Zatsepin-Kuzmin (GZK), 7, 188–189, 195–197, 218, 462–463
- gyrofrequency, 354
- GZK energy, 196–197
- GZK horizon, 211, 464–465
- GZK neutrinos; *see* neutrinos, cosmogenic (or GZK)
- HAWC, 506, 453
- Hawking black hole. *See* black hole, Hawking
- Hawking radiation, 402, 408, 452, 459
- Hawking temperature, 416
- head-on approximation, 74, 77
- HESS gamma-ray telescope, 11, 228, 453–454, 460, 506
- Hillas condition, 320–321, 378
- HiRes, 189, 215–216, 463, 465, 506
- Horizon: gamma-ray (*See* gamma-ray horizon); UHECR, 211, 464–465
- Hubble constant, 40, 42
- Hubble relation, 39
- hypernova, 259, 326
- hyper-relativistic electrons, 156–158
- IceCube neutrino observatory, 7, 218–219, 468–472, 506
- impact parameter, 161–162
- inclusive cross section for pion production, 173–174
- inelasticity, 173–174, 187, 189–190, 203
- INTEGRAL, 161, 185, 506
- intensity, 49–51; diffuse neutrino, 207; diffuse γ -ray, 208
- internal energy, 261–265, 270
- interstellar medium: dust in, 182; phases of, 183–185
- invariant cross section, 176
- invariant energy, 175, 189, 228–229
- invariant quantities, 53
- ion-cyclotron waves, 357–359
- ionization losses, 163
- isobar (*See also* resonance); model, 175–176
- isospin statistics, 193–194
- Jacobian, 20, 481
- jet angle, 291, 303
- jet models: beam-on-target, 169; mass-loaded, 169–170
- jet power, 135–138
- jitter radiation, 158–159
- Kerr metric, 33, 384–397; in Boyer-Lindquist coordinates, 384–386, 418, 428, 440; in Kerr-Schild coordinates, 391–395
- Kerr singularity, 386
- Killing vector, 387, 399, 418, 422, 426–427
- kinematic invariants, 19–21
- Kirchoff's law, 146
- Klein-Nishina scattering; cross section for, 73; δ -function approximation for, 81; energy-loss rate for, 82–83; mean free path in blackbody radiation field for, 83; moments of, 80; regime of, 70–73; spectral index for isotropic scattering in, 91

- knock-on electrons, 165–166
 Kolmogorov spectrum of turbulence, 318–319
 Kraichnan spectrum of turbulence, 318–320

 Lambert function, 309, 491
 Laplace transform, 368–369
 lapse function, 381
 Larmor angular frequency, 117, 119
 Larmor formula, 119
 Larmor radius, 6, 117, 273
 Larmor timescale, 120, 362
 LAT. *See* Fermi LAT
 length contraction, 15
 Levi-Civita tensor, 418–419, 481–482
 lightcone, 36–37, 379
 light cylinder, 132
 LIGO, 7–8, 506
 LISA, 7–8, 506
 Lorentz factor; bulk coasting, 259; cooling electron, 272; maximum electron, 273; minimum electron, 273; particle, 5, 21, 26; relative, 284
 Lorentz force equation, 117
 Lorentz invariance, 14
 Lorentz transformation, 14–17, 28
 luminosity: apparent, 1, 259; Eddington, 106, 450
 luminosity density, 48, 209
 luminosity distance, 8, 44–45

 Mach number, 329
 MAGIC, 251, 453, 506
 magnetic field, 117; amplification of, 344; in blast-wave physics, 272; coherence length of, 158–159, 323, 466; critical, 121, 129; equipartition, 131–135; of Milky Way, 466
 magnetohydrodynamic (MHD) waves, 317, 352, 355. *See* plasma waves
 magnitude, 9–10
 magnitude scale, 10
 manifold, 379, 474–476, 478–479, 481–482, 484, 486
 Maxwell-Boltzmann distribution, 3, 168
 Maxwell's equations, 28–29, 417–418, 420–422
 Maxwell tensor, 29, 417–418, 420, 424, 434

 Medium: circumburst, 260, 269, 282; interstellar. *See* interstellar medium; intergalactic, 244, 256
 Metric: Kerr (*See* Kerr metric); Minkowski (*See* Minkowski metric); Robertson-Walker (*See* Robertson-Walker metric); Schwarzschild (*See* Schwarzschild metric)
 metric tensor, 379–380, 480–481
 microquasars, 454
 Milagro, 453, 460, 506
 Minkowski metric, 25–28, 304, 380, 408
 Monte Carlo calculations, 182, 197–198, 256, 298
 momentum diffusion equation, 367
 multiplicity, 172, 205–206
 muon: decay, 177; production, 177

 naked singularity, 447
 neutral beam model, 255, 471
 neutrinos: bound on intensity of (*See* Waxman-Bahcall bound); from cascades in the intergalactic medium, 470–471; cosmogenic (or GZK), 195, 204–207, 213–215, 218–219, 225; detectors of, 7, 188–189, 215, 218, 468–469; from gamma-ray bursts, 469–470; gamma-ray correlations with, 249–253, 468–469; from $\gamma\gamma$ processes, 257; MeV, 7; oscillations of, 188, 214; from photodisintegration, 225–226; from photopion processes, 187–188, 193; from pion decay, 172; sources of (buried, 215; exotic, 219); from supernova remnants, 460
 neutron: β decay of, 193, 205, 225, 254; lifetime of, 193; mean free path of, 202; secondary, 190–193; thermal, 310–312
 neutron decoupling, 310–312

 one-zone (blob) model, 130, 136
 optical depth, 51; $\gamma\gamma$, 238–239, 241–242; Thomson depth, 3
 orphan afterglows, 292
 OSSE, 161, 185, 246–247, 506

- pair photosphere, 308–309
- pair production: Bethe-Heitler, 197–198
(*See* photopair production); dip in UHECR spectrum, 218, 465; direct, 166; $\gamma\gamma$, 193, 227–257
- Penrose process, 397–400, 453
- photodisintegration: cross section for, 220–223; effective energy-loss rate for, 224–225
- photodisintegration mean free path, 195
- photodisintegration reaction rate, 222–224
- photoerosion. *See* photodisintegration
- photohadronic interaction rate, 189
- photohadronic mean free path, 195–196
- photohadronic processes, 187–226
- photonuclear. *See* photodisintegration
- photopair cascade, 254
- photopair cross section, 198–199
- photopair production: energy-loss rate and timescale for (approximate, 198–201; numerical, 201–202); inelasticity of, 187, 203; mean free path for, 196, 201–202; threshold of, 198
- photopion cascade, 254
- photopion cross section, 191–193
- photopion (or photomeson) production; energy-loss rate and timescale for, 194–195; inelasticity of, 187, 203; mean free path for, 196–197; threshold of, 190
- photosphere, 303–309
- photospheric radius, 306–307
- Pierre Auger Observatory, 7, 189, 214–216, 219, 452, 462–463, 465, 472, 506
- pion decay, 177, 187
- pion production, 172–177
- pitch angle, 119–120
- pitch-angle diffusion coefficient, 362–363
- Planck's (blackbody) function, 54, 145, 490
- plasma waves; Alfvén waves, 344, 356; Langmuir waves, 356; magnetosonic waves, 358; turbulence, 317–318; whistler waves, 356–357, 359
- polarization: of plasma waves, 354; of synchrotron radiation, 157
- poloidal, 105, 429, 431–432, 436, 441
- positronium, 181–184
- Poynting flux, 132, 282
- pressure, 52, 282, 332
- proper time, 16, 32
- pygmy dipole resonance, 221–222
- quantum synchrotron regime, 121
- quasi-linear approximation, 354
- radial timescale, 296
- radiation reaction, 119, 156
- radiative transfer equation, 51, 146, 213
- radioactive nuclei, 185–185
- Ramaty-Lee spectrum, 368–370
- Rankine-Hugoniot equations, 328
- reaction rate, 21–23; particle-particle, 22; particle-photon, 23; photon-photon, 23
- redshift: cosmological, 1, 38; gravitational, 35; obscuration (for UHECRs, 210–211; for gamma rays, 245)
- relativistic shock hydrodynamics, 282–290
- resonances, 191; multipion, 193–194; single-pion, 192–194
- resonance condition, 393–394
- resonance gap problem, 363
- Ricci tensor, 384, 486
- Riemann curvature tensor, 486
- Riemann zeta function, 55, 195, 490
- rigidity, 117, 337
- Rindler spacetime, 408–415
- Robertson-Walker metric, 36, 37, 48
- scaling model, 176–177
- Schwarzschild metric, 33–34, 384
- Schwarzschild radius, 10
- secondary nuclear production, 169–180; δ -function approximation to, 173; isobar model for, 175–176; scaling model for, 176–180
- secondary production spectra, 23–24; particle-particle, 24; particle-photon, 24; photon-photon, 24
- Sedov phase, 267
- Sedov radius, 261
- self absorption. *See* synchrotron self absorption
- Seyfert galaxies. *See* galaxies, Seyfert
- Shakura-Sunyaev accretion disk, 105–108

- shift vector, 382, 394
 shock acceleration. *See* Fermi acceleration
 shock; forward, 283–284; quasi-parallel, 317, 340; quasi-perpendicular, 317, 340–341; reverse, 283–284 (relativistic, 274, 285–290; nonrelativistic, 274, 285–290)
 shock jump conditions, 282–284
 slab approximation, 144, 228
 source function, 51
 spacetime: curved, 25–35 (particle creation in, 405; scalar fields in, 402); geometry of, 379–416; Minkowski, 26, 36–37, 383, 408
 special relativity, 14, 25
 spherical shell geometry, 63–69
 spin paradigm. *See* black holes, spin paradigm for
 star formation rate, 209, 211–213, 215–216
 statistics: of black-hole sources, 456–457; with V/V_{max} method, 12
 stochastic energy losses, 197
 stopping power: in cold plasma, 161–163; in thermal plasma, 164–165
 structure formation history, 46, 212
 superluminal motion, 62–63, 253
 suprathermal proton bremsstrahlung, 166
 supernova, supernova remnants, 128, 185–186, 267, 461; outflow speeds in, 326, 375
 Swift, 507, 213, 216–217, 253, 294–295, 300, 303, 312
 synchrotron radiation, 117–159; δ -function approximation for, 129–130; elementary emissivity of, 122–127; energy-loss rate by, 119, 126–127; from power-law electrons, 127–129
 synchrotron self absorption, 143–153; coefficient of, 144, 148–150
 synchrotron self-absorption frequency, 150, 276–277
 synchrotron self-absorption spectrum, 154–155
 synchrotron self-Compton radiation, 135, 138–142; energy-loss rate by, 143; in gamma-ray bursts, 292–294
 synchrotron/synchrotron self-Compton model, 142–143, 455–456
 tangent bundle, 475
 tangent vector, 473–478, 26, 32, 381, 386–387, 483–484
 tensor calculus, 473–487
 tensor product, 26, 478
 tensors, 478–480
 thermalization, 3, 160, 163–164; of positrons, 181–183
 Thomson scattering: δ -function approximation for, 80, 92; energy-loss rate in, 82; moments of, 79; regime of, 70–73; spectral index from, 90; spectrum in δ -function approximation for, 92
 Thomson scattering cross section, 72
 time dilation, 15
 time orientable, 379
 timing studies, 10–11
 toroidal vector, 429
 torsion tensor, 431, 483–484
 transformations of: accretion-disk radiation field, 108–111; energy, 39, 56; external radiation fields, 57–59; photon and particle distributions, 56; time, 39
 triplet pair production, 198
 ultra-high energy cosmic rays: acceleration of, 462; arrival direction correlation of, 462; detectors for, 7, 189, 214, 472; evolution with redshift of, 208–209; from gamma-ray bursts, 300–301; injection spectrum of, 209; interactions of, 187–188; luminosity density of, 209, 216; power requirements for, 466–468; propagation of, 466; sources of, 452–453; spectrum of, 6, 13, 215–218
 unification hypothesis, 457–458
 units of electron rest mass, 2
 Unruh effect, 415
 variability timescale, 68; in gamma ray bursts, 296–297

- vectors: dual (covariant), 26;
 - tangent (contravariant), 26, 32
- volume element: in curved spacetime, 403, 481–482, 486; in flat space, 46, 48, 63, 144, 204; momentum, 20
- VERITAS, 453, 507
- VLBA, 10, 152, 507
- VLBI, 137, 152, 507
- wavevector, 317
- Waxman-Bahcall bound, 13, 213–215
- Whistlers. *See* plasma waves
- Whittaker functions, 126, 491
- WMAP, 43, 45, 507
- Znajek regularity condition, 433–435, 439, 441, 444, 449